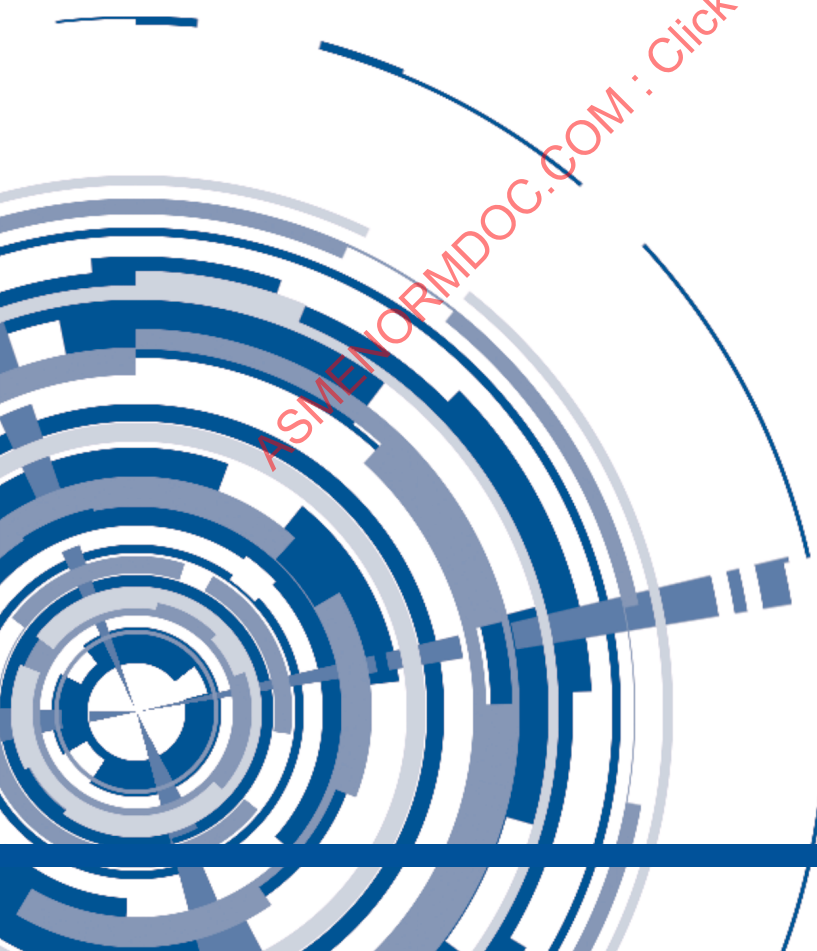


# ASME PTB-15-2023

## Full Matrix Capture Training Manual

ASME NORMDOC.COM : Click to view the full PDF of ASME PTB-15-2023



PTB-15-2023

# FULL MATRIX CAPTURE TRAINING MANUAL

ASMENORMDOC.COM : Click to view the full PDF of ASME PTB-15-2023



Date of Issuance: June 28, 2023

This publication was prepared by ASME Standards Technology, LLC (“ASME ST-LLC”) and sponsored by The American Society of Mechanical Engineers (“ASME”), Pressure Technology Codes & Standards.

Neither ASME, ASME ST-LLC, the authors, nor others involved in the preparation or review of this document, nor any of their respective employees, members or persons acting on their behalf, makes any warranty, express or implied, or assumes any legal liability or responsibility for the accuracy, completeness or usefulness of any information, apparatus, product or process disclosed, or represents that its use would not infringe upon privately owned rights.

Reference herein to any specific commercial product, process or service by trade name, trademark, manufacturer or otherwise does not necessarily constitute or imply its endorsement, recommendation or favoring by ASME or others involved in the preparation or review of this document, or any agency thereof. The views and opinions of the authors, contributors and reviewers of the document expressed herein do not necessarily reflect those of ASME or others involved in the preparation or review of this document, or any agency thereof.

ASME does not “approve,” “rate”, or “endorse” any item, construction, proprietary device, or activity.

ASME does not take any position with respect to the validity of any patent rights asserted in connection with any items mentioned in this document, and does not undertake to insure anyone utilizing a standard against liability for infringement of any applicable letters patent, nor assume any such liability. Users of a code or standard are expressly advised that determination of the validity of any such patent rights, and the risk of infringement of such rights, is entirely their own responsibility.

Participation by federal agency representative(s) or person(s) affiliated with industry is not to be interpreted as government or industry endorsement of this code or standard.

ASME is the registered trademark of The American Society of Mechanical Engineers.

No part of this document may be reproduced in any form,  
in an electronic retrieval system or otherwise,  
without the prior written permission of the publisher.

The American Society of Mechanical Engineers  
Two Park Avenue, New York, NY 10016-5990  
ISBN No. 978-0-7918-7623-7

Copyright © 2023  
THE AMERICAN SOCIETY OF MECHANICAL ENGINEERS  
All Rights Reserved

**TABLE OF CONTENTS**

Acknowledgements ..... xxii

Foreword ..... xxiii

1 HISTORY ..... 1

    1.1 ASME History ..... 1

    1.2 ASME and FMC ..... 3

    1.3 History of FMC and TFM ..... 5

    1.4 Equivalence of Early Developments ..... 6

2 FMC-TFM ..... 7

    2.1 Full Matrix Capture (FMC) ..... 7

        2.1.1 Principle for Firing and Data Collection ..... 7

        2.1.2 FMC Signal Characteristics ..... 7

        2.1.3 Typical FMC Signal Explained ..... 8

        2.1.4 Alternative Firing and Data Collection Methods ..... 10

            2.1.4.1 Half Matrix Capture ..... 10

            2.1.4.2 Sparse Acquisition ..... 11

        2.1.5 FMC Processes Using Different TR Methods ..... 12

            2.1.5.1 Different Methods ..... 12

            2.1.5.2 Pulse Echo ..... 12

            2.1.5.3 FMC-TFM for Pitch/Catch ..... 13

            2.1.5.4 Considerations ..... 13

        2.1.6 FMC Data Size and Storage ..... 14

            2.1.6.1 The Full Data Set ..... 14

            2.1.6.2 A-Scan Sample Count for Time Base Range ..... 14

            2.1.6.3 A-Scan Sample Size (Actual) ..... 14

        2.1.7 FMC Data Storage ..... 15

            2.1.7.1 Size ..... 15

    2.2 Total Focusing Method (TFM) ..... 15

        2.2.1 TFM General ..... 15

        2.2.2 Principle for Data Reconstruction ..... 16

            2.2.2.1 B-Scan ..... 19

            2.2.2.2 A Note on TFM and Noise ..... 19

    2.3 Wave Type, Reconstruction Mode ..... 20

        2.3.1 Naming Conventions ..... 20

            2.3.1.1 Reconstruction Mode ..... 20

            2.3.1.2 Path ..... 20

            2.3.1.3 Beam ..... 20

            2.3.1.4 The Problem with Ray Tracing ..... 20

        2.3.2 TFM Modes ..... 20

        2.3.3 Some Flaw Strategies ..... 22

        2.3.4 Beam Spread Considerations ..... 22

        2.3.5 Self-Tandem Modes ..... 25

        2.3.6 Effects of Thickness ..... 26

    2.4 Amplitude Fidelity ..... 28

        2.4.1 Amplitude Fidelity in Signal Processing ..... 28

        2.4.2 Grid Construction ..... 30

        2.4.3 TFM Grid Resolution ..... 31



2.5	Scan Plan.....	34
2.5.1	Defining the Specimen and the Probe .....	36
2.5.2	Scan Plan for Specific Flaws.....	36
2.5.3	Locating the TFM Grid .....	37
2.5.4	Scan Plan Design.....	37
2.5.4.1	Volumetric Flaw (Void) in TT-TT Mode.....	37
2.5.4.2	Toe Crack in TT-TT Mode.....	38
2.5.4.3	Lack of Fusion T-T Mode .....	38
2.5.4.4	TT-TT Mode .....	39
2.5.4.5	Incomplete Penetration in T-T .....	39
2.5.4.6	Conclusion.....	39
2.6	Fourier and Hilbert Transforms.....	40
2.6.1	Time vs. Frequency Representation of Signals (Fourier Transform).....	40
2.6.1.1	Frequency representation of signals .....	40
2.6.1.2	Frequency Representation of A-scan .....	42
2.6.1.3	Examples in NDT.....	42
2.6.1.4	Example #1: Signal Filtering.....	42
2.6.1.5	Example #2: Probe bandwidth checking .....	44
2.6.2	Hilbert Transform.....	45
2.6.2.1	What is a Hilbert Transform?.....	45
2.6.2.2	How Can Hilbert Transform be Used in NDT?.....	45
2.6.2.3	What is the Envelope of a Signal?.....	45
2.6.2.4	Why Represent an A-Scan Signal with its Envelope Rather Than in an RF Form? ..	45
2.6.2.5	Conclusions .....	49
2.6.2.6	The Hilbert Transform is a Mathematical Function .....	49
2.6.2.7	Where the Hilbert Transform May Be Used .....	50
2.6.2.8	How the Hilbert Transform Can Be Used to Extract the Envelope of a Signal .....	52
2.6.2.9	How the Hilbert Transform Can Be Used for TFM Reconstruction .....	53
2.6.2.10	Computing a Hilbert Transform .....	53
3	TFMs.....	56
3.1	Synthetic Aperture Focusing Technique .....	56
3.1.1	Data Collection.....	56
3.1.2	Post Processing.....	57
3.1.3	Resolution.....	58
3.2	Virtual Source Aperture .....	59
3.3	Migration and Inverse Wave Extrapolation (IWEX), crossover between NDT and Geophysics .....	60
3.3.1	History of Migration in Geophysics.....	60
3.3.2	Examples of crossover between geophysics and NDT.....	61
3.3.3	Difference Between Basic FMC-TFM and IWEX.....	62
3.3.4	Data Displays Used for IWEX .....	62
3.3.5	Electronics Hardware .....	65
3.4	Iterative TFM .....	65
3.5	Adaptive TFM—A Framework.....	68
3.5.1	Basic Process.....	68
3.5.2	Metallurgical Study .....	69
3.5.3	Material Anisotropy Distribution Model.....	69
3.5.4	Material Properties and Wave Propagation in an Elastic Media.....	70
3.5.5	Cauchy Tensor, Christoffel Matrix, and Key Velocity Parameters.....	71

3.5.6	The Slowness Surface, Slowness Curves .....	71
3.5.7	Group velocity and Phase velocity .....	72
3.5.8	Detection of Anisotropic Characteristics.....	73
3.5.9	Path Dependent Adaptation Process.....	74
3.5.10	Model Evolution.....	75
3.5.11	Degrees of Freedom .....	75
3.5.12	TFM Process .....	76
3.6	PWI-ML .....	76
3.6.1	Plane Wave Imaging .....	76
3.7	Sectorial Total Focusing.....	78
3.7.1	STF, LTF, CTF Processes (Techniques but not Methods).....	78
3.8	TFMi™.....	80
3.8.1	Terminology .....	80
3.8.2	FMC Acquisition Characteristics .....	81
3.8.3	Propagation Modes.....	84
3.8.4	Region of Interest .....	84
3.8.5	Image Sensitivity.....	86
3.8.6	TFMi.....	86
3.8.7	Advantages of TFMi .....	88
3.9	Phase Coherence Imaging .....	88
3.9.1	What is PCI?.....	89
3.9.2	Interpreting PCI data .....	91
3.9.3	Conclusion.....	92
4	INSTRUMENTS .....	93
4.1	Hardware Challenges .....	93
4.1.1	The Challenge Posed by FMC.....	93
4.1.2	TFM Image Data Rate.....	93
4.1.3	The TFM Calculation Challenge.....	93
4.1.4	FPGA Performance.....	94
4.1.5	GPU Performance .....	94
4.1.6	FPGA/GPU Comparison .....	95
4.1.7	Adaptive and Iterative TFM.....	96
4.2	Deployment Schemes/Scanning Equipment.....	97
4.2.1	Introduction .....	97
4.2.2	Manual Scanning.....	97
4.2.3	Nonautomated Scanner.....	97
4.2.4	Semi-automated Scanner.....	98
4.2.5	Fully Automated Scanner.....	99
4.2.6	Application Specific .....	100
4.2.7	Conclusion.....	101
5	ARRAYS .....	102
5.1	Abstract .....	102
5.2	Basic Overview of Ultrasonic Transducers and Their Construction.....	102
5.2.1	What is a Transducer? .....	102
5.2.2	The Piezoelectric Effect .....	102
5.2.3	Types of Transducers .....	103
5.2.4	Basic Construction .....	104
5.2.5	Piezocomposite.....	106
5.3	Transducer Arrays .....	107

5.3.1	Linear Arrays.....	107
5.3.2	Construction of Transducer Arrays .....	108
5.3.3	Matrix Arrays .....	109
5.3.4	Common Configurations of Arrays Used in NDE .....	111
5.4	Transducer Sound Fields.....	113
5.4.1	Basic Beam Modeling.....	113
5.4.2	Near Field Distance.....	114
5.4.3	Focusing Flat and Curved Oscillators, Spot Size and Depth of Field.....	115
5.4.4	Beam Divergence/Array Element Performance .....	117
5.5	Array Design for FMC .....	119
5.5.1	Goal of FMC/TFM Imaging.....	119
5.5.2	Near Field Imaging.....	120
5.5.3	Angle Limitation/Constant Focal Ratio (F/D).....	121
5.5.4	Selection of Array Parameters (Active Plane).....	124
5.5.4.1	Frequency .....	124
5.5.4.2	Pitch/System Channels.....	125
5.5.4.3	Algorithms for Setting Active and Passive Plane Parameters.....	126
5.5.4.4	Linear Imaging FMC.....	126
5.5.4.5	Sectorial Imaging FMC.....	127
5.5.5	Strategy for Setting Passive Plane Parameters.....	128
5.5.6	Flat or Focused? .....	130
5.6	Transducer Standards .....	131
5.7	Conclusions and Recommendations.....	131
6	MODELING .....	132
6.1	General benefits of weld simulation.....	132
6.1.1	Effects of Material on Inspection Results .....	132
6.1.2	Better Understanding of Results via Simulation .....	134
6.2	Inspection Simulation.....	136
6.3	Using Modeling for TFM Inspection .....	140
6.3.1	Probe Selection.....	140
6.3.2	Mode of Propagation Selection.....	141
6.3.3	Modeling as TFM Scan Plan Assistance Tool .....	143
6.3.4	Example of Modeling as TFM Scan Plan Assistance Tool on ERW pipe .....	143
7	ADVANTAGES AND LIMITATIONS OF FMC/TFM VERSUS PAUT .....	147
7.1	Advantages.....	147
7.1.1	Accurate Visualization.....	147
7.1.2	Improved Resolution .....	149
7.1.3	Sound Propagation (dead zone).....	150
7.1.4	Near Surface Resolution.....	152
7.2	Limitations .....	152
7.2.1	Selection of the Correct Mode of Propagation for the Type of Flaws .....	152
7.2.2	Part Geometry and Material Definition.....	153
7.2.3	Attenuation and Penetration in Thick or Difficult to Penetrate Materials.....	153
7.2.4	Productivity .....	154
8	SIZING TECHNIQUES .....	155
8.1	Length and Height Sizing.....	155
8.1.1	Length Sizing .....	156
8.1.1.1	6dB Drop Length Sizing.....	156

8.1.1.2	6dB Drop Length Sizing Errors.....	158
8.1.2	dB Drop Through-Wall Height Sizing of Embedded Flaws .....	159
8.1.3	Tip Diffraction for Embedded Indications .....	161
8.1.4	Sizing Cluster Indications Such as Porosity.....	161
8.1.5	Tip Diffraction for Through-Wall Sizing of ID/OD-connected Cracks.....	162
8.1.6	Length and Height Sizing Comparisons with Various Methods–TFM, TOFD, PAUT 164	
9	FRACTURE MECHANICS FLAW CHARACTERIZATION.....	171
9.1	Introduction to Fracture Behavior .....	171
9.2	Overview of Fracture Mechanics .....	172
9.3	History of Fracture Mechanics .....	173
9.4	Two Main Categories of Fracture Mechanics .....	174
9.4.1	Summary .....	176
9.5	Application of Fracture Mechanics .....	176
9.5.1	Damage Tolerant Design.....	177
9.5.2	Planning for Inspection Using These Damage Tolerance Principles .....	178
9.6	ASME Code Margins and Safety .....	180
9.7	Flaw Evaluation Procedures Using Fracture Mechanics.....	180
9.7.1	Steps in the ASME BPVC Section XI Flaw Evaluation Procedure .....	181
9.8	Acceptance Criteria Examples .....	183
9.9	Applying the Acceptance Criteria Tables and Using Interpolation.....	187
9.9.1	Linear Interpolation.....	189
10	APPLICATIONS .....	193
10.1	In-service Inspections: FMC Techniques for High Temperature Hydrogen Attack Assessment.....	193
10.1.1	Problem Definition .....	193
10.1.2	Solution .....	194
10.1.3	Array Probes Design and Optimization.....	194
10.1.4	FMC Capabilities Validation.....	199
10.1.4.1	Samples Selection and Preparation .....	199
10.1.4.2	Experimental Setups.....	200
10.1.4.3	Distance Calibration.....	200
10.1.4.4	Amplitude Fidelity .....	201
10.1.4.5	Sensitivity and Resolution.....	202
10.1.4.6	Investigation of Samples with Machined Flaw .....	204
10.1.4.7	Investigation of Samples with Synthetic HTHA Damage.....	207
10.1.4.8	Investigation of Samples Removed from Service (Progressive Validation) .....	211
10.1.5	Conclusions .....	226
10.2	FMC/TFM Based Inspection of Small-Diameter Components for FAC Damage.....	226
10.2.1	Summary .....	226
10.2.2	Background .....	226
10.2.3	Feeder Pipes .....	227
10.2.4	Degradation Mechanism.....	227
10.2.5	Component Description.....	228
10.2.6	Inspection Specification Requirements .....	229
10.2.7	Complicating Factors .....	230
10.2.8	Overview .....	232
10.2.9	Separation of Tasks .....	232

10.2.10 Training .....	232
10.2.11 Equipment .....	233
10.2.12 Software .....	234
10.2.13 Calibration.....	234
10.2.14 Data Acquisition Process.....	235
10.2.15 Recording .....	236
10.2.16 Data Acquisition Procedure.....	236
10.2.17 Data Analysis Process .....	238
10.2.18 Data Analysis Procedure .....	241
10.2.19 Results .....	241
10.2.20 Discussion .....	243
10.2.21 Further Developments .....	246
10.2.22 Conclusions .....	246
10.3 Crack Growth Monitoring with PAUT and TFM.....	247
10.3.1 Introduction .....	247
10.3.2 Approach .....	247
10.3.3 Description of the UT Setup.....	249
10.3.4 Results .....	250
10.3.5 Analysis.....	250
10.3.6 Conclusions and Next Steps.....	256
10.4 Weld Examination-Introduction .....	257
10.4.1.1Procedures .....	257
10.4.2 Equipment .....	258
10.4.2.1Instruments .....	258
10.4.2.2Probes .....	258
10.4.2.3Wedges .....	258
10.4.3 Getting Started.....	258
10.4.4 Scan Plan.....	259
10.4.4.1Search units .....	260
10.4.4.2Image Paths .....	260
10.4.5 Equipment Set-Up.....	261
10.4.5.1Image Grid Density .....	261
10.4.5.2TFM Frame Size.....	262
10.4.5.3Grouping.....	262
10.4.6 Scanning/Data Collection.....	263
10.4.6.1Encoding.....	264
10.4.6.2Weld Examination Scan Strategy.....	265
10.4.6.3Artifacts.....	265
10.4.7 Evaluation.....	266
10.4.7.1Data Views .....	266
10.4.7.2Detection .....	267
10.4.7.3Characterization .....	267
10.4.8 Examples .....	269
References .....	275
Appendix A: FMC-TFM Data of Internal Surface (ID), External Surface (OD) and Mid-Wall Types of Defects Represented by Notches .....	278
Appendix B: TFM Data Presentation and Flaws Sizing.....	303

**LIST OF FIGURES AND TABLES**

Figure 1-1: Period Repair Work on a Riveted Seam ..... 1

Figure 1-2: The Steamship Sultana ..... 2

Library of Congress, Prints & Photographs Division, Civil War Photographs, LC-DIG-ppmsca-34001 ..... 2

Figure 1-3: Policeman Next to Another Failed Boiler ..... 2

Figure 1-4: The Before and After of the Grover Shoe Factory in Brockton, Massachusetts ..... 3

Figure 1-5: Static Screen Shot from the Applus IWEX System..... 4

Figure 2-1: Firing Pattern and Resulting Matrix for FMC ..... 7

Table 2-1: Breakdown of the FMC signal data as represented on images ..... 8

Figure 2-2: Example of Redundant Pairs ..... 10

Figure 2-3: Firing Pattern and Resulting Matrix for HMC ..... 11

Figure 2-4: Firing Pattern and Resulting Sparse Acquisition of 1:2, 1:4, and 1:8 ..... 11

Figure 2-5: Example of a Possible SMC with 1:2 Sparsity ..... 12

Figure 2-6: Schematic of a Side-by-Side Pitch Catch Configuration..... 13

Figure 2-7: Wave Propagation Path for a Transmit-Receive Pair to a Specific Pixel ..... 16

Figure 2-8: TFM being constructed from a single transmit and receive pair. Note that as it progresses, each individual pixel has a set of delays and an intensity reported for its location. .... 17

Figure 2-9: The Cumulative TFM (lower right) becomes a compilation of all T&R pairs. This example is only four T&R pairs. .... 18

Figure 2-10: We have progressed from the previous cumulative TFM of 4 pairs to 410 pairs (left) or about 10% complete. For this component, a set of side drilled holes have formed. In the image to the right, which is 2,048 pairs or about 50% complete, you can further see the effects of the summation process by witnessing that the large “swath” of noise in the image has begun to clear up. .... 18

Figure 2-11: The final image at 100% (all 4,096 pairs) completed. It is important to consider the order of magnitude with which we have progressed through these images. We started with a single pair assigning data to every pixel, then went to 4 pairs, then 410 pairs, then 2,048, then finished at 4,096 pairs. (1) ..... 19

Figure 2-12: Example of How Mode Nomenclature Works. .... 21

Figure 2-13: Schematic of Some Common Reconstruction Modes ..... 21

Figure 2-14: Examples illustrating the advantages of different reconstruction modes in detection of certain flaws ..... 22

Figure 2-15: (a) and (b) Position of the pixel in the TFM frame; (c) and (d) acoustic field simulation using the function of beam spread dedicated to the pixels in (a) and (b), respectively ..... 23

Figure 2-16: Coverage that can be obtained with (a) standard phased array sectorial sweep and (b) TFM in TT-TT mode..... 24

Figure 2-17: Valid location for a TFM frame reconstructed using T-T and TT-TT modes ..... 24

Figure 2-18: Inappropriate TFM frame location for TT-TT reconstruction mode ..... 25

Figure 2-19: Inappropriate TFM frame location for T-T reconstruction mode ..... 25

Figure 2-20: Examples of the Expected Response from Self-tandem Modes ..... 26

Figure 2-21: An example illustrating the inefficient spatial coherence of the TFM trajectories for a specimen with different thickness than the nominal value used for image reconstruction. In a.) the actual and input thickness is the same, in b.) the actual thickness is less than the input thickness, in c.) the actual thickness is greater than the input thickness. The delays remain the same..... 26

Figure 2-22: Maps of the amplitude envelope computed using the TFM on the three samples of different thicknesses, using: (a) 20 mm (nominal), (b) 18 mm, (-10%), and (c) 22 mm (+10%) wall thickness samples. (Courtesy of Olympus NDT Canada INC.) [Painchaud-



April, G., Badeau, N. and Lepage, B., 2018, April. Total focusing method (TFM) robustness to material deviations. In AIP Conference Proceedings (Vol. 1949, No. 1, p. 200007). AIP Publishing LLC.] ..... 27

Figure 2-23: The dependency that the self-tandem modes, T-TT, and TT-TTT, in this case, rely upon having an accurate thickness value for the delay calculation ..... 28

Figure 2-24: Inaccuracy in signal digitalization and Amplitude Fidelity for signal digitized at a frequency of 5 points per wavelength..... 29

Figure 2-25: Inaccuracy in signal digitization and Amplitude Fidelity for signal digitized at a frequency of 2 points per wavelength..... 29

Figure 2-26: Principal parameters of a TFM frame..... 30

Figure 2-27: (a) Signal amplitude distribution on the lateral axis as a result on the interaction between the beam at its minimum waist with a point scatterer and (b) Representation of the (rectified) amplitude TFM image of a hypothetical point scatterer using a common large bandwidth pulsed signal spanning  $1.5\lambda$  in length. The minimal structure to sample in amplitude is the  $\lambda/2$  oscillation [TFM Grid Resolution by Olympus Scientific Solutions Americas] ..... 32

Figure 2-28: Impact of the pixel size of the TFM image on the reliability and fidelity of TFM results ..... 33

Figure 2-29: Impact of pixel size used for TFM image reconstruction on the signal amplitude of an SDH. The signal amplitude changes with the TFM pixel size from (a) 87.1% FSH for  $\lambda/6$ , to (b) 42.6% FSH for  $\lambda/3$ , and finally to (c) 8.7% FSH for  $\lambda$ ..... 34

Figure 2-30: A schematic of the parameters required to define the region of interest in TFM configuration ..... 35

Figure 2-31: Schematic of the welded joint specimen for scenarios A and B..... 36

Figure 2-32: Acoustic paths and corresponding reconstruction modes for optimal detection of under evaluation flaws..... 36

Figure 2-33: Different TFM modes required to extend the coverage..... 37

Figure 2-34: Schematic of the applied grid ..... 37

Figure 2-35: (a) Simulated acoustic field and (b) ray tracing results for a void located in the weld material..... 37

Figure 2-36: (a) Simulated acoustic field and (b) ray tracing results for a toe crack ..... 38

Figure 2-37: (a) Simulated acoustic field and (b) ray tracing results for a toe crack using T-T..... 38

Figure 2-38: (a) Simulated acoustic field and (b) ray tracing results for a toe crack using TT-TT..... 39

Figure 2-39: (a) Simulated acoustic field and (b) ray tracing results for an incomplete penetration ... 39

Figure 2-40: Examples of time signals: (a) A-scan, (b) electrocardiogram (ECG)–(c) piece of music ..... 40

Figure 2-41: Time (b) and frequency (c) representation of a piece of music signal (a) ..... 41

Figure 2-42: Time (a) and frequency (b) representation of an A-scan ..... 42

Figure 2-43: Workflow of a filtering process in the frequency domain: Fourier transform of the noisy signal (a)–Multiplication of the spectrum with the transfer function of the filter (b)–Inverse Fourier transform of the filtered spectrum (c)..... 43

Figure 2-44: Time representation of a noisy A-Scan (a) and a filtered A-Scan (b). In this example the SNR of the filtered signal  $x'(t)$  is 6 dB higher than the SNR of the noisy signal  $x(t)$ .. 43

Figure 2-46: Temporal A-Scan (a) and its spectrum (absolute value of the Fourier transform obtained thanks to a FFT and for positive frequencies only) (b)..... 44

Figure 2-47: FFT feature on the Olympus-MX2 ..... 44

Figure 2-48: Example of a zero-mean A-scan (blue) and its envelope (red)..... 45

Figure 2-49: (a) Rectified signal (A-scan) (blue) and estimated envelope of the same A-scan (red)– (b) Details showing corresponding errors of both maximum amplitude and time position estimation of the maximum amplitude ..... 46

Figure 2-50: Example of TFM images of SDH: with rectified (absolute value) TFM (a)–with TFM envelope (b). Consequently, the occurrence of having several maxima is a challenge for estimating accurately the position of the maximum value of an indication within TFM images. This issue is illustrated in Figure 2-51. This point justifies having an interest in the construction of the envelope, in the specific case of TFM images..... 47

Figure 2-51: TFM images of a defect (SDH) showing a gap in the vertical position estimation of the maxima amplitude. (a) In-phase TFM–(b) Quadrature TFM–(c) Envelope TFM..... 47

Figure 2-52: Examples of an ID connected crack. TFM image on the left with envelope and on the right without envelope..... 48

Figure 2-53: Examples of a slag indication. TFM image on the left with envelope and on the right without envelope. .... 48

Figure 2-54: Transfer function of a Hilbert transform. (a) Modulus–(b) Phase ..... 50

Figure 2-55: Pure sine signal spectrum. (a) cosine—(b) sine..... 51

Figure 2-56: Detail of the In-phase signal  $x_1(t)$ (original A-scan, cf. Figure 2-42) (blue), quadrature component  $x_1(t)$  obtained thanks to a Hilbert transform (green), and the envelope  $A(t)$  (red). ..... 52

Figure 2-57: Computation of the envelope TFM from two FMCs in quadrature..... 53

Figure 2-58: (a) Modulus of the In-phase signal spectrum – (b) filtering function – (c) Modulus of the analytical signal spectrum ..... 54

Figure 2-59: Example of an impulse response for a type III generalized linear phase discrete Hilbert transformer of order 20..... 55

Figure 2-60: Implementation of the TFM envelope computation (a) In the frequency domain–(b) In the time domain..... 55

Figure 3-1: Reproduced from NUREG CR 3625-Busse 1984 ..... 57

Figure 3-2: Reproduced from NUREG CR 3625–Busse 1984..... 57

Figure 3-3: Reproduced from NUREG CR 3625–Busse 1984..... 58

Figure 3-4: Reproduced from NUREG CR 3625–Busse 1984..... 59

Figure 3-5: Principle of VSA. Array elements are excited with a delay lay to produce the intended wavefront, as if coming from a virtual source..... 59

Figure 3-6: On the left, a seismic shot record. On the right, ultrasonic NDT data displayed in the way customary in seismic exploration..... 61

Figure 3-7: Part of Figure 4.8 from thesis Niels Pörtzgen, 2007..... 63

Figure 3-8: Example of an IWEX image combining multiple modes ..... 63

Figure 3-9: Example of a typical IWEX image showing expanded color scale..... 64

Figure 3-10: Example of multiple modes / views, including a 3D image ..... 64

Figure 3-11: Generic Imaging Process for Iterative TFM..... 66

Figure 3-12: An example of an edge detection process identifying leading and trailing edges of a TFM image. The image itself has been removed to enable view of the detected edges.... 67

Figure 3-13: Block diagram of a generic Adaptive TFM process. The diagram also shows inputs to the main portion of the adaptive loop..... 69

Figure 3-14: Framework for a distributed parameter model of a hypothetical configuration ..... 70

Figure 3-15: Cauchy tensor depicting tensile and shear vectors associated with a unit volume. Right–matrix representation of Cauchy tensor..... 71

Figure 3-16: Examples of phase slowness curves, left–isotropic materials where the velocity remains constant irrespective of direction, right–anisotropic where velocity varies with direction..... 72

Figure 3-17: Phase and Group velocity vectors plotted on a slowness curve. The magnitude of the change has been exaggerated for the purpose of illustration..... 73

Figure 3-18: Sample, left with normal beam A scan response center. Note the phases remain consistent in each multiple. .... 74



Figure 3-19: Sample, left, A scan response center. Note the phase of the initial response is the same as Figure 3-18, whereas the phase is changed in subsequent signals. This behavior is indicative of anisotropy. .... 74

Figure 3-20: Examples of solution condition ..... 75

Figure 3-21: Plane waves generated for three different angles ..... 76

Figure 3-22: comparison of FMC/TFM image (top right) to PWI image (bottom right) for PWI setup with 6 plane wave angles (left) ..... 77

Figure 3-23: Screen shot comparison of classic TFM vs PWI next to microetch from the component. .... 78

Figure 3-24: A comparison of TFM, STF, and standard PA ..... 79

Figure 3-25: A schematic of the (a) STF, (b) LTF, and (c) CTF sweep..... 79

Figure 3-26: FMC scanning sequence ..... 81

Figure 3-27: TFM beam summed to generate a pixel from the 1st to the 64th element..... 82

Figure 3-28: Data acquisition and the generation of TFM image for a specific pixel..... 83

Figure 3-29: TFM image generation principle ..... 83

Figure 3-30: Index setup..... 84

Figure 3-31: Depth setup..... 85

Figure 3-32: Resolution setup for index and depth ..... 85

Figure 3-33: Toe crack. TFMi image on the right (2T-3T-4T) and sectorial scan on the left..... 87

Figure 3-34: Sectorial scan, TFM images (2T-5T) and TFMi image for a sequence of side drilled holes vertically aligned..... 87

Figure 3-35: TFMi image on the left and side view of a sample with a crack ..... 88

Figure 3-36: DAS Algorithm (above), and DAS with Phase Information Applied Post Hilbert Transform (below)..... 89

Figure 3-37: Shows statistical approach with randomized process and the variance difference of coherence vs. non-coherence areas..... 89

Figure 3-38: Shows high variance in coherence and non-coherence areas for noise to indication discrimination..... 90

Figure 3-39: The entire hook crack can be seen with only the TT-TT group on the left in PCI, where two groups are needed with conventional TFM (TT-T and TT-TT) on the left. The crack can be sized using the tip diffraction. .... 91

Figure 3-40: Shows High Temperature Hydrogen Attack (HTHA) PCI data on the left, and conventional amplitude based TFM on the right..... 92

Figure 3-41: Shows Creep Damage PCI data on the left, and conventional amplitude based TFM on the right..... 92

Figure 4-1: Schematic architecture of an FPGA (top) vs and GPU (bottom) based system ..... 95

Figure 4-2: Timeline showing the progression of GPUs..... 96

Table 4-1: Comparative Chart of FPGA and GPU Processors..... 97

Figure 4-3: Examples of wheel type encoders..... 98

Figure 4-4: Some examples of Semi-automated (chain) scanners, and the use of a laser guided system (bottom right) ..... 99

Figure 4-5: Examples of a fully automated scanner ..... 100

Figure 4-6: Examples of an elbow scanner (left), and a paintbrush scanner (right)..... 101

Figure 5-1: Direct (a) and inverse (b) piezoelectric effect. The most common transduction mechanism used in ultrasonic transducers for industrial, medical, and commercial ultrasound applications. .... 103

Figure 5-2: Various types of ultrasonic transducers that can be found in industrial NDT, including (a) single element contact transducers, (b) bespoke transducer design for turbine disk inspection, and (c) high temperature, wedge mount linear arrays for weld inspection .... 103

Figure 5-3: Basic transducer constructional elements for industrial single (a) and dual (b) element piezoelectric transducers. .... 104

Figure 5-4: Schematic representation of piezocomposite material in a) 2-2 connectivity and b) 1-3 connectivity ..... 106

Figure 5-5: Schematic view of linear array geometry showing electronic control over a sub aperture of the array which allows electronic control of the beam (steering, focusing and scanning). Elevation performance is fixed by the frequency and aperture size and potential addition of a focusing lens..... 107

Figure 5-6: Basic constructional elements of the acoustic stack of a linear array. A complete transducer would additionally have a transducer case and micro-coaxial cable/connector assembly. .... 108

Figure 5-7: 840 element 1.5D array (420 electrical connections) showing cable assembly with four, 128 channel cable assemblies with IPEX connectors..... 109

Figure 5-8: 2D matrix array. The secondary axis of beam control allows electronic manipulation of the beam in three dimensions: azimuth, elevation, and depth at the expense of increased channel count and system complexity. .... 110

Figure 5-9: Taxonomy for matrix arrays showing the increased control over the elevation plane that can be achieved in tradeoff to increasing channel count and system complexity. .... 110

Figure 5-10: Common array geometries used in non-destructive testing applications..... 111

Figure 5-11: Field II/Matlab beam simulation from a 5MHz, 12.7mm diameter ultrasonic transducer radiating into water. Sound intensity is indicated by the color scale in relative units ..... 113

Figure 5-12: Modeled sound field of a flat ultrasonic transducer, showing the intensity fluctuations in the near field transitioning to a smoothly varying beam at and beyond the Near Field Distance,  $N$ . .... 114

Figure 5-13: -6dB spot size ( $E_x$ ) and -3dB depth of field ( $E_z$ ) for flat and focused circular transducers..... 116

Table 5-1: Approximate formulas for -6dB spot size for flat and focused oscillators, narrow band approximation..... 116

Figure 5-14: Graphical representation of valid, marginal, and invalid element contributions due to the limitations of element beam divergence ..... 117

Figure 5-15: Schematic representation of beam divergence half angle..... 118

Figure 5-16: One way (free field) and two way (pulse echo) response for an array element two wavelengths in size ( $D/\lambda=2$ )..... 118

Figure 5-17: -6dB divergence half angle for element size in wavelengths (pulse echo)..... 119

Figure 5-18: B-scan view of a  $\varnothing$  1 mm SDH Standard using a 5 MHz linear array, 64 elements, LW wedge: Standard phased array (right) compared to FMC/Sectorial Total Focusing (STF) method (center) and FMC/Total Focusing Method (TFM) (right). Note that for standard PA, the targets are only in focus at a single depth. .... 120

Figure 5-19: B-scan view of a  $\varnothing$  1 mm SDH Standard using a 5 MHz linear array, 64 elements, LW wedge with varying aperture size. Note the reduction in resolution that corresponds with decreasing aperture size with corresponding increase in the effective lateral beam size..... 120

Figure 5-20: Example of probe and wedge configuration with consequent near field area and the region of interest on 25mm thick carbon steel weld..... 121

Figure 5-21: Beam divergence plots for element sizes of a)  $0.5\lambda$  b)  $1.0\lambda$  and c)  $4.0$  ..... 122

Figure 5-22: CIVA simulations of direct-contact imaging, contrasting the results of TFM using 0.5, 1, and 1.5 wavelength elements, with and without angle limitation. (a)-(c) processed using a Conventional TFM algorithm, (d)-(f) processed with angle limits (cone filter) of 30, 30, and 19.5 degrees, respectively. Results obtained using the following arrays: (a), (d) 64 element/0.63mm pitch ( $0.5\lambda$ ), (b), (e) 32 element/1.26mm pitch ( $1\lambda$ ) and (c), (f) 21 element/1.89 mm ( $1.5\lambda$ ) pitch..... 123

Table 5-2: Computations of achievable resolution based on element size, beam divergence and resulting focal ratio and focusing effect. ....	123
Figure 5-23: Schematic representation of critical parameters for linear scanning and sectorial scanning FMC/TFM.....	125
Figure 5-24: Simulations of cross-sectional beam profile at focal point of flat and elevation focused linear arrays. Ideal “circular” beam profile has equal sizing capability in both the active and passive plane. More commonly, the beam profile is elliptical, having non-uniform sizing and resolution capability. ....	129
Figure 5-25: Simulations of varying beam spot size for flat and elevation focused linear arrays. The ultrasonic beam is only truly in focus when both the azimuth and elevation are focused. Variation in imaging performance will be seen due to the variation in elevation spot size for flaws that are smaller than the beam spot due to Area-Amplitude. ....	129
Figure 6-1: Coarse grain (left) compared to isotropic material (right) with L0 immersion.....	132
Figure 6-2: Fields radiated by the 45 T-wave transducer in isotropic (left) and anisotropic (right) specimens .....	132
Figure 6-3: Beam of phased array transducer focused on weld prep .....	133
Figure 6-4: E=0.13mm .....	133
Figure 6-5: E=0.26mm .....	133
Figure 6-6: Mode Identification (Mode ID) .....	134
Figure 6-7: Example of a modeling simulation using the immersion technique.....	134
Figure 6-8: 45-degree L wave is shown on the left and 45 degree T wave is shown on right .....	135
Figure 6-9: Chart of flaw tilt vs. amplitude.....	135
Figure 6-10: B-scan 3D model for transverse 45 degree (T45) refracted angle interacting with from left to right: 0°, -5° and -10° flaw tilt .....	136
Figure 6-11: Raw results of the FMC simulation.....	137
Figure 6-12: Comparison of 3D iso-surfaces (left column) and YZ section (right column) images after TFM reconstruction without (first row) and with (second row) 'envelope signal ' as the computation option.....	137
Figure 6-13: 3D view of inspection setup with backwall breaking planar flaw .....	138
Figure 6-14: TT-T reconstruction.....	138
Figure 6-15: L-L reconstruction .....	138
Figure 6-16: T-T reconstruction.....	138
Figure 6-17: LL-L reconstruction.....	138
Figure 6-18: Inspection for Lack of Fusion 1 .....	139
Figure 6-19: T-T wave type.....	139
Figure 6-20: TT-TT wave type.....	139
Figure 6-21: Far field directivity pattern of a 3mm pitch element in Rexolite at 5 MHz.....	141
Figure 6-22: TFM inspection of a root crack in T-T mode .....	142
Figure 6-23: TFM inspection of a root crack in TT-T mode.....	142
Figure 6-24: a) Longitudinal scanner mounted on the ERW pipe sample, along with TFM flaw detector device showing the stacked vertical lack of fusions located inside the weld line. The flaws span about 25.4mm long over the pipe axis. b) Scan plan representing the weld and curvature of sample.....	144
Figure 6-25: The modeling for planar defect “heatmaps” computed for (a) the TT-T and (b) TT-TTT mode of propagations.....	145
Figure 6-26: TFM image on the stacked lack of fusion flaws for (a) the TT-T and (b) TT-TTT. The gain is adjusted to equalize the maximum amplitude.....	146
Figure 7-1: ID connected crack detection comparison between PAUT and TT-TT TFM .....	147
Figure 7-2: OD connected crack detection comparison between PAUT and TT-TT TFM.....	148
Figure 7-3: ID connected crack detection comparison between PAUT and TT-T TFM.....	148
Figure 7-4: OD connected crack detection comparison between PAUT and TT-TTT TFM .....	148

Figure 7-5: PAUT detection of SDH at different depths.....	149
Figure 7-6: TFM L-L mode detection of SDH at different depths.....	150
Figure 7-7: Detection of vertically stacked SDH comparison between PAUT and TFM L-L mode of propagation.....	151
Figure 7-8: Detection of link between blisters with TFM.....	151
Figure 7-9: Detection of shallow SDH comparison between PAUT and TFM L-L mode of propagation.....	152
Figure 7-10: Lack of fusion detection comparison between TFM TT-TT and TT-T modes .....	152
Figure 7-11: Vertical notch detection comparison with a TT-T mode of propagation: accurate velocity vs. 2.5% velocity input error.....	153
Figure 7-12: SNR difference at the detection of a flat bottom hole (FBH) between a 32 element Linear PAUT scan and TFM L-L mode.....	154
Figure 8-1: Measurement Tools–Cursors.....	155
Figure 8-2: Principles of 6dB Drop length sizing of discontinuities larger than the beam diameter .	156
Figure 8-3: Example of LOF 6dB Drop length sizing.....	157
Figure 8-4: Principles of 6dB Drop length sizing of discontinuities smaller than the beam diameter .....	157
Figure 8-5: Example of slag indication length using maximum amplitude sizing technique.....	158
Figure 8-6: Example of ID HAZ crack indication length using maximum amplitude sizing technique .....	159
Figure 8-7: Example of dB Drop Through-Wall Height Sizing technique .....	160
Figure 8-8: Through-Wall Height Sizing of LOF using Tip Diffraction technique.....	161
Figure 8-9: Through-Wall Height Sizing of Porosity cluster using Tip Diffraction technique.....	162
Figure 8-10: Through-Wall Height Sizing of cracks using Tip Diffraction technique: ID connected crack on 1 in. thick specimen. T-T image path. Red reference cursor on ID surface, green measurement cursor on deepest crack tip. D(m-r) reading of 0.485 in. shows through-wall height of crack. ....	163
Figure 8-11: Through-Wall Height Sizing of cracks using Tip Diffraction technique: OD connected crack on 1 in. thick specimen. TT-TT image path. Red reference cursor on OD surface, green measurement cursor on deepest crack tip. D(m-r) reading of 0.813 in. shows through-wall height of crack. ....	163
Figure 8-12: Weld Joint Geometry for 1 in. (25 mm) Samples.....	164
Figure 8-13: Flaw Sample Manufacturer’s Record of Sizing Tolerances .....	164
Table 8-1: A flaw sizing comparison between multiple methods .....	164
Figure 8-14: Images of Indication # 1–Lack of Sidewall Fusion: (a) TFM–T-T mode, (b) TOFD Non-Parallel Scan, (c) PAUT Sectorial Scan.....	165
Figure 8-15: Images of Indication # 2–ID Crack: (a) TFM-T-T mode, (b) TOFD Non-Parallel Scan, (c) PAUT Sectorial Scan .....	166
Figure 8-16: Images of Indication # 3 Porosity: (a) TFM T-T mode, (b) TOFD Non- Parallel Scan, (c) PAUT Sectorial Scan .....	167
Figure 8-17: Images of Indication # 4 Slag: (a) TFM T-T mode, (b) TOFD Non-Parallel Scan, (c) PAUT Sectorial Scan.....	168
Figure 8-18: TFM Images of OD-Connected Crack .....	169
Figure 8-19: TFM Images of ID-Connected Crack.....	169
Figure 8-20: TFM Images of Slag.....	170
Figure 8-21: TFM Images of LOF-Far Side Bevel-Height Sizing using Tip Signals .....	170
Figure 9-1: Load vs. Displacement from Testing of a Brittle and Ductile Material .....	171
Table 9-1: Strength of Materials vs Fracture Mechanics Method.....	172
Figure 9-2: The Three Elements Related to Component Fracture.....	172
Figure 9-3: Catastrophic Failure of a Liberty Ship During World War 2 .....	173
Figure 9-4: Pellini’s Fracture Analysis Diagram (FAD).....	174

Figure 9-5: The Two Types of Fracture Mechanics Methods .....	175
Figure 9-6: The Three Modes of Cracking.....	175
Figure 9-7: Illustration of Analysis of Flaws as a Function of Time.....	177
Figure 9-8: Stepwise process for Damage Tolerant Design .....	178
Figure 9-9: ISI Sequence.....	182
Figure 9-10: Flaw Evaluation Procedure.....	183
Figure 9-11: From ASME B31.3-2022 .....	184
Figure 9-12: From ASME BPVC Section VII-2021 .....	185
Figure 9-13: From ASME BPVC Section XI-2021.....	187
Figure 9-14: Depiction of surface or subsurface flaw proximity rules from ASME B31.3-2022.....	188
Figure 9-15: The aspect ratio column in red.....	189
Figure 9-16: Example of When Interpolation May be Needed .....	190
Figure 9-17: Interpolation Graph for Aspect Ratio (typical) where X=Aspect Ratio and Y=Acceptance Limit .....	191
Figure 9-18: Example of interpolating for thickness.....	191
Figure 9-19: Interpolation Graph for Thickness (typical) Where X=Thickness and Y=Acceptance Limit .....	192
Table 10-1: Natural focal spot sizes and near field for optimized 10 MHz, 64 elements, linear array probe with aperture 150 mm <sup>2</sup> .....	195
Table 10-2: Specifications summary for the probes: central frequency, aperture and near field at -6dB .....	196
Figure 10-1: Beam visualization at selected depth: (a) normal beam; (b) angle beam .....	196
Table 10-3: Beam sizes of 10 MHz, 64 elements, linear array probe at depth 25mm: (a) Longitudinal Wave, no Wedge; (b) Shear Wave, Rexolite Wedge .....	197
Figure 10-2: 10 MHz shear wave beam interactions—PAUT (left) and FMC/TFM T-T (right): (a) cluster of six SDHs; (b) notch .....	198
Table 10-4: Vessels material and process parameters .....	199
Figure 10-3: Calibrations: (a) normal beam (L-wave)—flexible wedge setup and L-L distance calibration imaging without TCG; (b) angle beam (S/T-wave)—flexible wedge setup and T-T distance calibration imaging without TCG; (c) angle beam (S/T-wave)—solid wedge setup, FMC/TFM T-T and PAUT SW distance calibration imaging with TCG. ....	200
Figure 10-4: Amplitude fidelity: (a) setup and pseudo A-scans; (b) T-T path/mode RoI; (c) failed T-T with RoI 30x25mm (width x height); (d) passed T-T with RoI 25x25mm (width x height).....	201
Table 10-5: Pixel Size and Resolution/Wavelength Ratio for selected RoI.....	203
Figure 10-5: Scanning plans and typical C-, B-, D- views.....	203
Figure 10-6: FMC/TFM 3D imaging of carbon steel bar with machined flaws.....	204
Figure 10-7: Example of micro-machined clustered flaws: (a) picture; (b) skew 90 TFM imaging; (c) skew 270 TFM imaging .....	205
Table 10-6: Clusters and SDHs height measurements using 10 MHz T-T path/mode.....	206
Table 10-7: SDHs vertical separation measurements using 10 MHz T-T path/mode.....	207
Figure 10-8: FMC/TFM LL imaging: (a) 15MHz imaging of non-damage block—pseudo A scan (top left), single plane B-scan (top right), single plane D-scan (bottom); (b) 10MHz projected C-scan of damage block; (c) 7.5MHz projected C-scan of damage block; (d) 5MHz projected C-scan of damage block; (e) 10MHz split screen imaging of selected indication: projected C-scan (left top), single plane B-scan (top right), single plane D-scan (bottom right), pseudo A-scan (bottom left).....	208
Figure 10-9: Optical microscopy and SEM imaging of accelerated HTHA damage: (a) ~100X; as-polished; fissures forming relatively large micro crack; (b) ~100X; as-polished; fissures forming small micro crack; (c) ~5000X; Nital Etchant; SEM photograph of damage feature showing grain boundary void formation and some early stages of coalescence of	



voids in the periphery of the main feature; (d) ~5000X; Nital Etchant; SEM photograph of damage feature showing severe dissolution of grain boundaries and some early stage of single void formation. .... 210

Figure 10-10: Setup for fully automated PAUT and FMC/TFM: (a) depentanizer reboiler channel; (b) zinc oxide drum ..... 212

Figure 10-11: 10 MHz T-T FMC/TFM and PAUT techniques imaging of HTHA weld damage: (a) linear probe C-scan and identification of the indications; (b) linear probe split screen views of indication #2; (c) indication of potential HTHA damage detected in the breaking areas using matrix probe and S-scan at skew-10° ..... 213

Figure 10-12: Weld damage validation using optical metallography and SEM: (a) root cracking (~20X, Nital etched); (b) stepwise macro cracking (~40X, Nital etched); (c) blisters (~40X, Nital etched); (d) voids along grain boundaries (~2,000X, Nital etched-left; ~20,000X, Nital etched-right); (e) stress-related micro cracking (~1,000X, Nital etched). .... 214

Figure 10-13: Imaging of Indication #10.1a.1 and #10.1a.2: (a) projected PAUT straight beam C-Scans comparison; (b) PAUT straight beam and FMC/TFM ATF M LL B-Scans comparison; (c) comparison of PAUT S-Scans and FMC/TFM T-T B-scans using shear wave techniques..... 216

Figure 10-14: Metallographic and CT Images for Indications 10.1a.1 and 10.1a.2: (a) cutting plan; (b) x10, Indications 10.1a.1 and 10.1a.2; (c) Magnification x50, close up view of Indication 10.1a.1; (d) x50, close up view of Indication 10.1a.2; (e) CT images of Indication 10.1a.2 from 2 to 10mm below the polished surface of the mount. .... 218

Table 10-8: Height and width measurements of Indication#10.1a.1 ..... 220

Figure 10-15: Drum south section FMC/TFM imaging and HTHA validation: (a) localized and through wall distribution; (b) base material coupon cutting plan with C-scan overlay; (c) 3D imaging of blister-like damage; (d) optical metallography of linking voids merging into blisters, ~80X; As-Polished; (e) SEM validation of early stage HTHA volumetric damage, ~5,000X; Nital etched..... 221

Figure 10-16: Drum north section FMC/TFM imaging and HTHA validation: (a) raster C-scan imaging of possible HTHA damage—localized and through wall distribution; (b) visual validation of typical blister bulging; (c) line scan imaging of possible blistering with sharp crack-like edges; (d) optical metallography of blistering with sharp crack-like edges, ~50X, As-Polished; (e) SEM of non-metallic inclusions and evidence of early stage HTHA damage of void formation and voids coalescence, ~5000X, Nital etched. . 224

Figure 10-17: Primary Heat Transport piping arrangement between the steam generators and the fuel channels..... 227

Figure 10-18: Example showing the typical congestion of the feeder pipes..... 227

Figure 10-19: Example of FAC adjacent to the downstream weld toe..... 228

Figure 10-20: Inspection regions for welded fitting feeder configurations..... 230

Figure 10-21: Platform Operator clad in PPE at the Reactor Face work location. The radiation shielding canopy is absent in this view. .... 231

Figure 10-22: A view of the reactor face work platform with a shield canopy installed ..... 231

Table 10-9: Training Requirements..... 232

Figure 10-23: (right) Instrument cart with MicroPulse and Vault Interface Module (manipulator and peripheral electronics module), (left) couplant reservoir and calibration stand. .... 233

Figure 10-24: Manipulator for 2 1/2 inch NPS fittings installed on a mock-up..... 233

Figure 10-25: Manipulator for 2 inch NPS fittings ..... 233

Figure 10-26: Transducer for both 2 and 2 1/2 NPS sized manipulators. The transducer fires tangentially to the inspection surface with the sound redirected via a mirror. .... 233

Figure 10-27: Typical screen presentation of the developed software ..... 234

Figure 10-28: Example of the custom calibration block ..... 234

Figure 10-29: Manipulator arms.....	235
Figure 10-30: Example of a typical inspection record .....	237
Figure 10-31: Example of a typical inspection record (cont.) .....	238
Figure 10-32: TFM image of the Outside Diameter (OD) surface.....	238
Figure 10-33: Image showing the trace outline to define the OD surface.....	239
Figure 10-34: The TFM image of the interior .....	239
Figure 10-35: Plotting of the ID interface .....	240
Figure 10-36: Evaluation revealing the minimum thickness.....	240
Figure 10-37: Plotting of the ID and OD interface in a 3D model.....	240
Figure 10-38: Minor inclusion from fabrication welding.....	242
Figure 10-39: Image(s) result in an accurate visualization of the component.....	242
Figure 10-40: Section of an ex-service feeder demonstrating step erosion at the weld root. Flow is right to left in this image. ....	242
Figure 10-41: Example of the MIT result for a case where both the exterior and interior surfaces are independently and rapidly changing in profile. The hub is on the right, weld center and intrados of the fitting is on the left of the image.....	243
Figure 10-42: 3D image of a fitting-to-fitting weld color coded for thickness. Note the areas in black are outside the range of color coding for thickness. ....	244
Figure 10-43: 3D image of a 2 1/2 inch fitting to fitting weld color coded for thickness.....	244
Figure 10-44: Color-coded 3D representation of a 2 inch feeder fitting to fitting joint.....	244
Figure 10-45: Rotation of the 3D model .....	244
Figure 10-46: Grey scale 3D model vs an actual photo of the component.....	245
Figure 10-47: OD imaged profiles vs the actual component.....	246
Figure 10-48: Illustration of a conventional SENB test specimen geometry .....	248
Figure 10-49: Fatigue test setup on a servo-hydraulic test machine using an MTS clip gage .....	248
Figure 10-50: The phased array ultrasonic technique setup to monitor the notch.....	249
Table 10-10: Periodic Crack Measurement Values Using Various Measurement Techniques.....	250
Figure 10-51: TFM images (left – T-T Mode, right – TT-T Mode), Number of Cycles = 0 .....	250
Figure 10-52: PAUT image (Sectorial Scan), Number of Cycles = 0 .....	251
Figure 10-53: TFM images (left–T-T Mode, right–TT-T Mode), Number of Cycles = 44914 .....	251
Figure 10-54: PAUT image (Sectorial Scan), Number of Cycles = 44914.....	251
Figure 10-55: TFM images (left–T-T Mode, right–TT-T Mode), Number of Cycles = 66953 .....	252
Figure 10-56: PAUT image (Sectorial Scan), Number of Cycles = 66953 .....	252
Figure 10-57: TFM images (left–T-T Mode, right–TT-T Mode), Number of Cycles = 109833 .....	252
Figure 10-58: PAUT image (Sectorial Scan), Number of Cycles = 109833 .....	253
Figure 10-59: TFM images (left–T-T Mode, right–TT-T Mode), Number of Cycles = 129476 .....	253
Figure 10-60: PAUT image (Sectorial Scan), Number of Cycles = 129476.....	253
Figure 10-61: TFM images (left–T-T Mode, right–TT-T Mode), Number of Cycles = 150378 .....	254
Figure 10-62: PAUT image (Sectorial Scan), Number of Cycles = 150378.....	254
Figure 10-63: Graphical representation of fatigue crack growth measured using each technique.....	254
Table 10-11: Post-test Measurements .....	255
Figure 10-64: Image of Sample 17279-4-13 used for detailed crack measurement.....	255
Table 10-12: Comparison between the four different crack measurement techniques in this study ..	256
Figure 10-65: SENB sample showing fatigue crack and corresponding FMC/TFM image of the crack .....	256
Table 10-13: Example of Essential and Non-essential variables.....	257
Figure 10-66: Wedge Measurements.....	258
Figure 10-67: Considering variables .....	259
Figure 10-68: Example of acoustic simulation for FMC/TFM scan planning. Image clearly shows the probe needs to be moved forward to achieve coverage of the weld root/I.D. HAZ, and in this way acoustic simulation proceeds much like the use of Ray Tracing.....	259

Figure 10-69: LOF and the response from differing image paths. From Left to right 2T Direct, 4T indirect, and Time Extended 2T .....	260
Figure 10-70: Example of the Influence an incorrect thickness parameter has on the signal response of an I.D notch.....	261
Figure 10-71: Example of the influence an incorrect velocity parameter has on signal response. 5Mhz, n=64, P=0.6mm, T-T direct, $\lambda/7$ , SDH @ 0.8 in. deep .....	261
Table 10-14: General example of scan speed vs grid density for standard TFM. 5Mhz x 32-element probe. Changes to parameters such as PRF, algorithms and many others will affect results.....	262
Figure 10-72: A clear change is seen from $\lambda/2$ to $\lambda/5$ , but less from $\lambda/5$ to $\lambda/7$ . 1/64th SDH, 5Mhz, n=64, p= 0.6 mm, L-L image path, Envelope on, 1.57 in. index x 2.26 in. depth TFM frame.....	262
Figure 10-73: Image path verification on through wall slot in the ASME BPVC Section V calibration block. Satisfying the ASME requirements may require multiple image paths. ....	263
Figure 10-74: Examples of encoded scanning and data collection techniques.....	264
Figure 10-75: Example of data drop-out .....	264
Figure 10-76: Example of typical scan layout.....	265
Figure 10-77: Example of Artifacts.....	265
Figure 10-78: Data View Schematic .....	266
Figure 10-79: Measurement of Signal width. Note: Synthetic A-scans are produced from plotting the summed amplitudes in the image axis selected. Therefore, higher grid resolutions will produce higher resolution synthetic A-scans.....	267
Figure 10-80: Example of Rise and Fall.....	268
Table 10-15: Key to flaws shown in Figure 10-81 and Figure 10-82 .....	269
Figure 10-81: Weld scanned from both sides with 0.600 in. (15.2 mm) index position .....	270
Figure 10-82: Weld scanned from both sides with 1.800 in. (46 mm) index position .....	270
Figure 10-83: End view response from 0.5in. (13 mm) Single V, Sidewall LOF–270 side .....	271
Figure 10-84: End view response from 0.5in. (13 mm) Single V, Porosity–Center Line.....	271
Figure 10-85: End view response from 0.5in. (13 mm) Single V, Root Crack–90 side.....	272
Figure 10-86: End view response from 0.5in. (13 mm) Single V, OD HAZ crack–270 side .....	272
Figure 10-87: End view response from 0.5in (13 mm) Single V, Lack of Penetration–Center Line. ....	273
Figure 10-88: End view response from 0.5in. (13 mm) Single V, Slag–Center Line .....	273
Figure 10-89: End view response from 1 in. (25 mm) Double V, LOF–Bottom Bevel, 270 side.....	274
Figure 10-90: End view response from 1 in. (25 mm) Double V, Center Line Crack .....	274
Figure A-1: TFM T-T mode of 30% ID notches .....	279
Figure A-2: TFM T-T mode of 30% ID notches .....	280
Figure A-3: TFM T-T mode of 30% ID notches.....	281
Figure A-4: TFM T-T mode of 30% ID notches .....	282
Figure A-5: TFM T-T mode of 30% OD notches, spherical. Sound is sent towards the notch acute angles.....	283
Figure A-6: TFM T-T mode of 30% OD notches, spherical. Sound is sent towards the notch obtuse angles.....	284
Figure A-7: TFM T-T mode of 30% OD notches .....	285
Figure A-8: TFM T-T mode of 30% OD notches .....	286
Figure A-9: TFM TT-T, TT-TT & TT-TTT modes of 30% ID notches .....	287
Figure A-10: TFM TT-T, TT-TT & TT-TTT modes of 30% ID notches, spherical. Sound is sent towards the notch obtuse angles. ....	288
Figure A-11: TFM TT-T, TT-TT & TT-TTT modes of 30% ID notches .....	289
Figure A-12: TFM TT-T, TT-TT & TT-TTT modes of 30% ID notches .....	290
Figure A-13: TFM TT-T, TT-TT & TT-TTT modes of 30% OD notches.....	291



Figure A-14: TFM TT-T, TT-TT & TT-TTT modes of 30% OD notches.....	292
Figure A-15: TFM TT-T, TT-TT & TT-TTT modes of 30% OD notches.....	293
Figure A-16: TFM TT-T, TT-TT & TT-TTT modes of 30% OD notches.....	294
Figure A-17: TFM T-T, TT-T, TT-TT & TT-TTT modes of 30% ID notches .....	295
Figure A-18: TFM T-T, TT-T, TT-TT & TT-TTT modes of 30% ID notches .....	296
Figure A-19: TFM T-T, TT-T, TT-TT & TT-TTT modes of 30% ID notches .....	297
Figure A-20: TFM T-T, TT-T, TT-TT & TT-TTT modes of 30% ID notches .....	298
Figure A-21: TFM T-T, TT-T, TT-TT & TT-TTT modes of 30% OD notches.....	299
Figure A-22: TFM T-T, TT-T, TT-TT & TT-TTT modes of 30% OD notches.....	300
Figure A-23: TFM T-T, TT-T, TT-TT & TT-TTT modes of 30% OD notches.....	301
Figure A-24: TFM T-T, TT-T, TT-TT & TT-TTT modes of 30% OD notches.....	302
Figure B-1: Instrumentation–Olympus X3.....	303
Figure B-2: Ultrasonic Setup.....	303
Figure B-3: Weld Configuration .....	304
Figure B-4: Display Configuration.....	304
Figure B-5: Sample U587.....	305
Figure B-6: Sample U587–Flaw 1, T-T–Depth=4.66 mm/Height=4.66 mm.....	305
Figure B-7: Sample U587–Flaw 2, TT-T–Depth=25.4 mm/Height=4.75 mm.....	306
Figure B-8: Sample U587–Flaw 2, T-T–Depth=25.4 mm/Height=4.75 mm.....	307
Figure B-9: Sample U587–Flaw 3, TT-TT–Depth=8.60 mm/Height=4.00 mm .....	308
Figure B-10: Sample U585.....	309
Figure B-11: Sample U585–Flaw 1, TT-T–Depth=25.4 mm/Height=5.36 mm.....	309
Figure B-12: Sample U585–Flaw 1, T-T–Depth=25.4 mm/Height=4.86 mm .....	310
Figure B-13: Sample U585–Flaw 2, T-T–Depth=25.4 mm/Height=3.13 mm .....	311
Figure B-14: Sample U585–Flaw 2, TT-TT–Depth=25.4 mm/Height=4.54 mm .....	312
Figure B-15: Sample U585–Flaw 3, TT-TT–Depth=3.54 mm/Height=3.54 mm .....	313
Figure B-16: Sample UT1639 .....	314
Figure B-17: Sample UT1639–Flaw 1, TT-TT–Depth=2.45 mm/Height=2.45 mm.....	314
Figure B-18: Sample UT1639–Flaw 2, TT-TT–Depth=20.95 mm/Height=2.40 mm.....	315
Figure B-19: Sample UT1639–Flaw 3, TT-TT–Depth=25.4 mm/Height=3.41 mm.....	316
Figure B-20: Sample UT1632 .....	317
Figure B-21: Sample UT1632–Flaw 1, TT-TT–Depth=2.73 mm/Height=2.73 mm.....	317
Figure B-22: Sample UT1632–Flaw 2, TT-TT–Depth=25.4 mm/Height=4.11 mm.....	318
Figure B-23: Sample UT1632–Flaw 3, TT-TT–Depth=9.68 mm/Height=3.52 mm.....	319
Figure B-24: Sample UT6164 .....	320
Figure B-25: Sample UT6164–Flaw 15, TT-TT–Depth=4.39 mm/Height=2.68 mm .....	320
Figure B-26: Sample UT6164–Flaw 15, TT-T–Depth=4.95 mm/Height=3.64 mm.....	321
Figure B-27: Sample UT6164–Flaw 30, TT-TT–Depth=4.50 mm/Height=3.56 mm .....	322
Figure B-28: Sample UT6161 .....	323
Figure B-29: Sample UT6161–Flaw 37, TT-TT–Depth=5.53 mm/Height=2.48 mm.....	323
Figure B-30: Sample UT 6151 .....	324
Figure B-31: Sample UT 6151–Flaw 37, TT-TT–Depth=5.52 mm/Height=2.02 mm.....	324
Figure B-32: Sample UT 6151, Unreported flaw .....	325
Figure B-33: Sample UT6154 .....	326
Figure B-34: Sample UT6154–Flaw 15, TT-T–Depth=4.95 mm/Height=3.61 mm.....	326
Figure B-35: Sample UT6154–Flaw 15, TT-T–Depth=4.72 mm/Height=4.72 mm .....	327
Figure B-36: Sample UT6154–Flaw 30, TT-TT–Depth=5.02 mm/Height=5.02 mm .....	328
Figure B-37: Sample UT6159 .....	329
Figure B-38: Sample UT6159–Flaw 18, T-T–Depth=3.89 mm/Height=3.89 mm .....	329
Figure B-39: Sample UT6159–Flaw 19, T-T–Depth=15.0 mm/Height=3.29 mm .....	330
Figure B-40: Sample UT6159–Flaw 19, TT-TT–Depth=15.0 mm/Height = 4.76 mm .....	331

Figure B-41: Sample UT 1813-Flaw 1, TT-TT–Depth=3.55 mm/Height = 3.55 mm ..... 332  
Figure B-42: Sample UT 1813-Flaw 2, TFM–Depth=19.1 mm/Height = 3.03 mm ..... 333  
Figure B-43: Sample UT1814-Flaw 2, TFM–Depth=19.1 mm/Height = 2.83 mm ..... 334  
Table B-1: Sizing..... 335

ASMENORMDOC.COM : Click to view the full PDF of ASME PTB-15 2023

## ACKNOWLEDGEMENTS

Upon the publication of the 2019 Edition of the ASME BPVC Section V, rules were established for Full Matrix Capture (FMC) in Article 4, Mandatory Appendix XI. This took an exceptional group of volunteers who came together and were able to dedicate time and establish processes which would allow us to finish an exceedingly challenging task in less than half the normal time.

Recognizing that we had provided a great service to industry for an emerging technology, we understood that to be truly successful, more was needed. It was obvious that there was strong interest for FMC. However, apprehension also took hold. Besides having a set of rules in the Code, a better understanding of the technology would further promote its use, and most importantly prevent a repeat of some of the mistakes of the past.

While some of us moved on after the publication of the Code rules, others remained, and soon, others would join us in the endeavor to bring this training manual to light. It cannot go without being said that only through the expertise of volunteers, and selfless sacrifice, being that of a great deal of time and dedication, would this work even be possible. The expense, let alone assembling this much talent, for the purpose of publishing a training manual such as this would otherwise have been impossible. Indeed, this was truly an exceptional group of individuals.

We also recognize that by writing this training manual, a precedent was set for ASME BPVC Section V. We would like to thank ASME for this opportunity, and hope that others will follow. Education is paramount.

### **The Authors:**

Paul Hayes (Chair) – Sinewave Solutions  
Emilie Peloquin (Vice Chair) – Evident Scientific  
Dr. James Barshinger – Sensor Networks Inc.  
Timothy Greisbach – Structural Integrity Associates (Ret.)  
Ray ten Grotenhuis – Ontario Power Generation  
William Lindo – Mistras  
Dr. Mark Lozev – BP (Ret.)  
Michael Monnette – Eddyfi Technologies  
Renato Nogueira – Sonatest  
Daniel Richard – Zetec  
Erica Schumacher – EXTENDE  
Oleg Volf – TWI  
Shane Walton – University of Ultrasonics  
Dr. Casper Wassink – Eddyfi Technologies

### **Contributing Authors:**

Adri van den Biggelaar – RTD  
Johann Catty - CETIM  
Dr. George Connolly – EPRI  
Jimmy Ellis – Jimmy Ellis LLC  
Dr. Lars Horchens – RTD  
Dr. Richard “Rick” Jacobs - PNNL  
Dr. Alain LeDuff – Evident Scientific  
Dr. Neils Portzgen – RTD  
Carlton R. M. Ramcharran – ASME

## FOREWORD

Established in 1880, ASME is a professional not-for-profit organization with more than 100,000 members promoting the art, science, and practice of mechanical and multidisciplinary engineering and allied sciences. ASME develops codes and standards that enhance public safety, and ASME provides lifelong learning and technical exchange opportunities benefiting the engineering and technology community. Visit [www.asme.org](http://www.asme.org) for more information.

ASME ST-LLC is a not-for-profit limited liability company, with ASME as the sole member, formed in 2004 to carry out work related to new and developing technologies. ASME ST-LLC's mission includes meeting the needs of industry and government by providing new standards-related products and services, which advance the application of emerging and newly commercialized science and technology and provides the research and technology development needed to establish and maintain the technical relevance of codes and standards. Visit <http://asmestllc.org/> for more information.

ASMENORMDOC.COM : Click to view the full PDF of ASME PTB-15-2023

## 1 HISTORY

### 1.1 ASME History

ASME has been around for more than 140 years, starting with the first meeting in the spring of 1880 in New York. As ASME was born during the industrial revolution, the meeting was largely attended by prominent industrialists of the time. The intention was to provide a forum for discussion and collaboration to better serve the needs of engineers and designers. The history of ASME cannot be appreciated without mentioning some of the consequences from the industrial revolution, two of which are boiler explosions and the need for standardization. Safety and standardization are still the main vision and mission for ASME.

The industrial revolution was made possible by the application of steam power as an energy source. In fact, the advent of steam power quickly became the industrializing nations' dominant power source. For example, the use of steam power increased from just 5% to 80% of the total power in the United States over a 20-year span in the mid-1800's. Today, steam energy (i.e., steam-driven turbines) still supplies 80% of the world's electricity.

When water converts to steam it expands ~1600 times in volume, which can generate enormous pressures. The use of steam to drive machinery was discovered to be a vast improvement over existing water mills, windmills, and even beast-of-burden power. However, early boilers from this period commonly suffered from catastrophic failures (i.e., explosions), mainly due to poor materials, poor design, and poor maintenance.

The earliest boilers were made of small wrought iron plates that were riveted together, but other materials such as copper were also commonly used. Quality improved with the use of rolled steel plates, but construction consisted of gusseted or slip-joint designs with rivets (see Figure 1-1). Acetylene was not discovered until 1836, and “conventional welding,” as it is presently known, was not developed until 1881. Repairs made to boilers were left up to “best practice,” which meant there were no standards of methods or quality.

**Figure 1-1: Period Repair Work on a Riveted Seam**

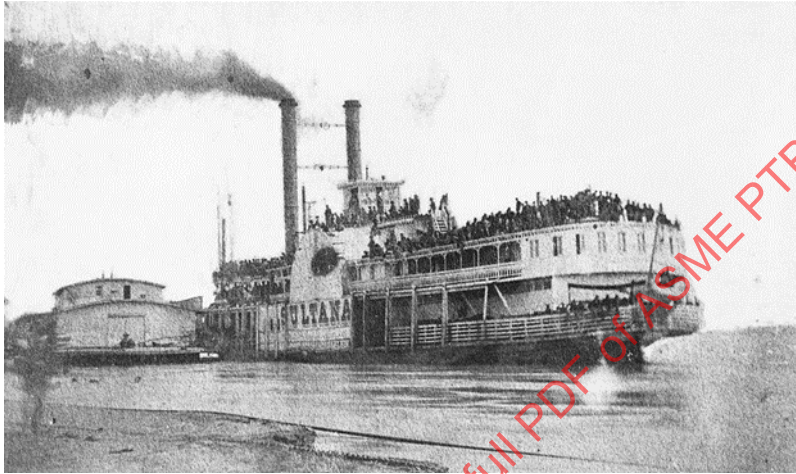


Image Courtesy of Sinewave Solutions



In 1865, a boiler explosion on the Steamship Sultana (shown in Figure 1-2) resulted in 1,500 to 1,800 casualties, representing the single largest loss of life due to a boiler explosion in U.S. history. The exact number of fatalities is unknown, but it is known that one of the four boilers on the ship had a recent repair. A resulting over-pressure situation caused that boiler to explode, triggering two other boilers to explode at the same time. In spite of incremental improvements to boiler design and manufacture, 1,900 separate boiler explosions were recorded between 1898 and 1903, resulting in the deaths of 1,200 people in the U.S. alone.

**Figure 1-2: The Steamship Sultana**



Library of Congress, Prints & Photographs Division, Civil War Photographs, LC-DIG-ppmsca-34001

**Figure 1-3: Policeman Next to Another Failed Boiler**



The manufacturing of boilers did improve over time, but equally significant was when the standardization of operating and maintaining boilers finally came to acceptance. A notable boiler explosion that helped facilitate standardization occurred at the Grover Shoe factory in Brockton, Massachusetts. In 1905, a boiler explosion killed 58 people and injured 150, leveling the building (see Figure 1-4). The public, insurance companies, and politicians were fed up with the regularity at which such explosions occurred. A new governor demanded prompt action, and in 1907 a common set of rules requiring inspection, maintenance, and safe operation was written into Massachusetts law. Ohio followed suit in 1911. These laws would influence, and eventually become, the first ASME Boiler Code, published in 1915.

**Figure 1-4: The Before and After of the Grover Shoe Factory in Brockton, Massachusetts**



Standardization of components and fittings across an industry was another need that sprang from catastrophes of the era. The great Baltimore fire of 1904 exemplified the need for standardization. When regional firefighters arrived from Philadelphia, Washington D.C., New York, and other surrounding areas to help battle the blaze, there was little they could do because their hoses were of a different manufacture and could not couple to the hydrants in the city. At that time, no national standards existed for firefighting equipment. Thus, the necessity of standardization came to light and continues to be the cornerstone of ASME.

The need for standardization of materials, construction methods, maintenance, inspection, and repairs has only grown across our global economy and touches almost every aspect of our lives. From the first published boiler code to the over 600 current ASME Codes and Standards, the members of ASME have strived to improve safety, conformance, and communication. Stakeholders, including manufacturers, end users, engineers, governments, and suppliers, work together to ensure the Codes and Standards will assure the safest possible outcomes.

## 1.2 ASME and FMC

In 2013, Applus RTD came to an ASME Code Week meeting to demonstrate some of their new equipment. The system looked like a fully automated phased array system, but the difference became evident as the data were collected. The system generated a real-time three-dimensional (3D) view of a welded large-bore pipe using Inverse Wave Extrapolation (IWEX), which is one of several processing forms for Full Matrix Capture (FMC). The system was not very fast, but the process it used and the amount of data it processed to generate the real-time 3D images were impressive. A screen shot from the IWEX system is shown in Figure 1-5.

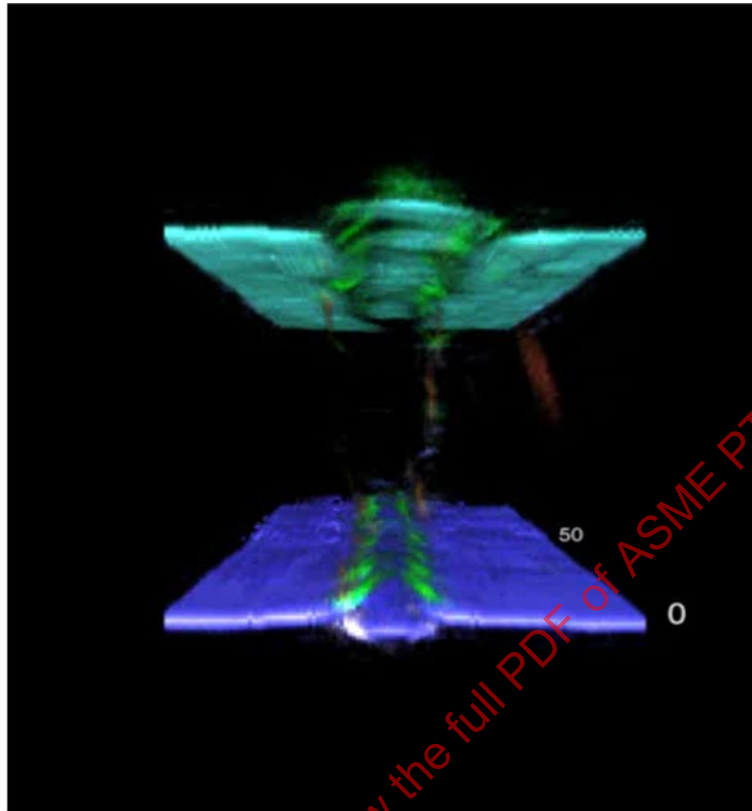
**Figure 1-5: Static Screen Shot from the Applus IWEX System**

Image Courtesy of APPLUS

ASME took note and having passed the rules for phased array a couple of years prior, they were interested in the technology and what it would bring to the future. A small handful of FMC specialists began showing up to the Code Week meetings and joined the Working Group Ultrasonic Testing (UT) meetings. This is the committee that is responsible for ASME BPVC Section V - 2019, Article 4.

Because the committee was focused almost entirely on phased array, a decision was made to create another committee dedicated to advanced UT. This new committee would be dedicated only to the rules for phased array and time of flight diffraction (ToFD). Since FMC was also an advanced technique, the people who came to the meetings specifically for FMC also joined the committee.

Splitting up the meetings and creating a new committee alleviated the demands of the Working Group, and more focus was given to the advanced techniques. Still, with all the work concentrated on phased array, little time was allotted for FMC. In spite of this, some writing was produced to form up what FMC should look like, and interest in the subject was gaining momentum. Also at this time, a portable FMC instrument had just been released to the industry, and interest in FMC from Code users was increasing.

By the late fall of 2016, interest in FMC had increased dramatically, as well as the associated increased attendance at the committee meetings. To address the situation, ASME again decided to split the Advanced UT committee, and the Task Group for FMC was formed as an official committee. With the full support of ASME and a group of extremely dedicated and knowledgeable people, work began. The first dedicated meeting took place in February 2017.

The publication deadline for the 2017 edition of the Code had just passed, so a full two years remained until the next publication cycle, which would translate to about 1.5 years for work to be accomplished. It was decided from the beginning that the 2019 edition would be the goal for publication. To achieve



this, the group had to work fast. Attendance fluctuated but generally hovered around 20 people, with as many as 40 interested parties and visitors in attendance. The committee was a well-rounded group of representatives from instrument manufacturers, fossil fuel interests, academics, service providers, utility companies, research labs, and practitioners, to name a few.

To achieve the goal of a 2019 publication, the committee adopted the use of E-meeting platforms. This approach enabled them to hold interim meetings between the usual Code Week meetings, allowing the committee to meet twice as often. In fact, all in-person meetings were accompanied by an E-meeting, which enabled the committee to reach out further and engage with international members. Also, live demonstrations of various FMC equipment and processes were held during in-person meetings, stimulating interest and comments. These approaches were not standard protocol for ASME at the time, but they produced results and gained ASME support.

The committee also had the advantage of the previous work on phased array and learned from some of the mistakes. One lesson learned was that the FMC Committee needed to provide more than just rules, but some guidance for the user. Consequently, not only were the rules of Mandatory Appendix XI written, but Nonmandatory Appendix F was also offered to provide background information.

Writing either of the two appendices within the short timeframe would normally be considered an accomplishment. However, finishing both appendices before the 2019 deadline is a testament to the knowledge and dedication of the people who were part of the FMC task group, many of whom continue as members to write this manual.

### 1.3 History of FMC and TFM

The full matrix referred to in Full Matrix Capture (FMC) consists of data from all transmit-receive element combinations and represents all information that could theoretically be collected with an array transducer. This information, once collected, is available for processing with many different algorithms. The Total Focusing Method (TFM) has emerged as the most intuitive and most common algorithm used. In this section, the history of development of these techniques in nondestructive testing (NDT) will be reviewed.

The first use of array transducers in NDT dates to 1968, just one year after the first prototype system was built for medical purposes (McNab and Campbell, 1987). These systems were used to create an ultrasonic beam, essentially emulating a monolithic transducer. This type of measurement typically presents a B-scan image to mimic the mechanical scanning of a single-element transducer. However, much more information beyond that of a single element transducer is available when other ultrasonic paths through the material are also considered. For example, the transmitting and receiving locations do not have to be the same.

Both FMC and TFM were developed independently in several places. Using these ideas for practical purposes became possible only in the early 2000s due to electronics advancements. It is also unsurprising that their development was virtually simultaneous. In preparation of this chapter, the early implementers were contacted, and the early intentions, victories, and setbacks were discussed.

In the UK, seminal work was performed in the group led by Paul Wilcox and Bruce Drinkwater at Bristol University and the group steered by Peter Cawley at Imperial College. FMC had been used in the PhD work of Paul Wilcox (1998) at Imperial College using an electromagnetic acoustic transducer (EMAT) circular array for generating Lamb waves in large structures, aimed at condition monitoring. At Bristol university, this practice was extended to more common piezoelectric arrays and eventually resulted in what is considered as the seminal paper on TFM (Holmes, 2005).

In Germany, the ideas for FMC and TFM were first presented for NDT by the group of Karl-Joerg Langenberg at Kassel university in the 1990s, using a crossover between NDT and geophysics. Development of a system was performed at Fraunhofer Institute for Nondestructive Testing (IZFP) in Saarbrücken with important contributions from Andrey Bulavinov and Krishnan Mohan Reddy. Here, the first application used EMAT transducers to generate Lamb Waves for inspection of coated pipes

(Bulavinov et al. 2002). In 2004, the research was extended to common transducers, resulting in a Sampling Phased Array (Von Bernus et al. 2006).

In the Netherlands, the ideas of FMC and TFM were first presented by Maarten Lorenz in 1993, again with a strong link to geophysics. These ideas were used by Delft University of Technology and RTD, to develop the IWEX algorithm. The first application was testing of pipeline girth welds (Portzgen, 2004). Eventually, IWEX was the first implementation of FMC to be commercially offered as a service and formally qualified as an inspection solution (Van der Ent et al. 2017).

In France, the developments were picked up in a joint industry program originating at CEA. This program resulted in two companies, M2M and TPAC, offering early field-deployable equipment. The M2M Gekko was the first commercially available system to perform real-time TFM.

The first bottleneck encountered with FMC was that most array controllers were multiplexed (many still are) and not all array elements are available simultaneously. A group of active elements is multiplexed over a large set of elements, e.g., 16 active elements on a 64-element array. The practical implication is that to collect a full matrix, each element must be fired several times. In the absence of dedicated driver software, even the allocation of each element in the matrix may need to be done individually, leading to very time-consuming data collection. For this reason, FMC needed a new generation of equipment, which reached the market around 2014.

The second bottleneck was the lack of computer power for processing the amount of data in a full matrix. It was realized very early that for field deployable NDT, a real time image would be needed to compete with conventional ultrasonic phased array systems. Commercial electronics offered two different solutions, a field programmable gate array (FPGA) (field programmable gate array) or a graphics processing unit (GPU) (graphics processing unit), both using parallel computing. The release of the GeForce 8800 series graphics cards in May 2007 offered massive parallel computing for gaming but also found immediate application to FMC.

Finally, it is important to mention that, as with many other NDT techniques, FMC and TFM were initially thought to be a magic solution to everything. The idea is alluring that technology exists to use diffraction signals to generate real-time tomography by the TFM algorithm, but it is not practically feasible currently. FMC/TFM is still an ultrasonic technique and adheres to the laws and limitations of physics. The early implementers encountered this after being asked to first solve inspection problems for which no solution yet existed. Examples of this were the testing of castings, for which other ultrasonic techniques were unsuccessful, and the testing of components with very challenging geometries made with additive manufacturing. Obviously, this slowed acceptance of a new technology like FMC/TFM, as solving these “impossible” problems was naturally more difficult. Consequently, a lot of time and energy was wasted, generating a high possibility of disappointment.

The initial excitement about the technology and high expectations about the possible industrial breakthrough of quantitative 3D imaging have also been tempered by the very conservative and inertial market. It is known from literature that NDT is one of the slowest industrial activities to innovate (Wassink, 2012). It is the impression of the early researchers contacted for this book that, after all these years, only part of the possibilities of FMC/TFM are used.

## 1.4 Equivalence of Early Developments

It has been shown that the early developments in FMC/TFM are equivalent, except for the way the amplitude information is processed (Wilcox, 2012). The phase information is the same in all cases and results from the path taken by the ultrasound from transmitter to target to receiver. In the amplitude weighing, several assumptions may be made on the ultrasonic wave propagation and characteristics of scatterers. These differences will be further explained in the theoretical parts of this book. At this point it is sufficient to state that the early implementers consider the differences to be small. [1] – [8]

## 2 FMC-TFM

### 2.1 Full Matrix Capture (FMC)

FMC is a data-acquisition process. Each array element is sequentially used as a single emitter and all array elements are used as receivers, creating a matrix of A-scan data. FMC has the advantage of being able to acquire all possible interactions between every pulsing and receiving element, enabling multiple ways of reconstructing images.

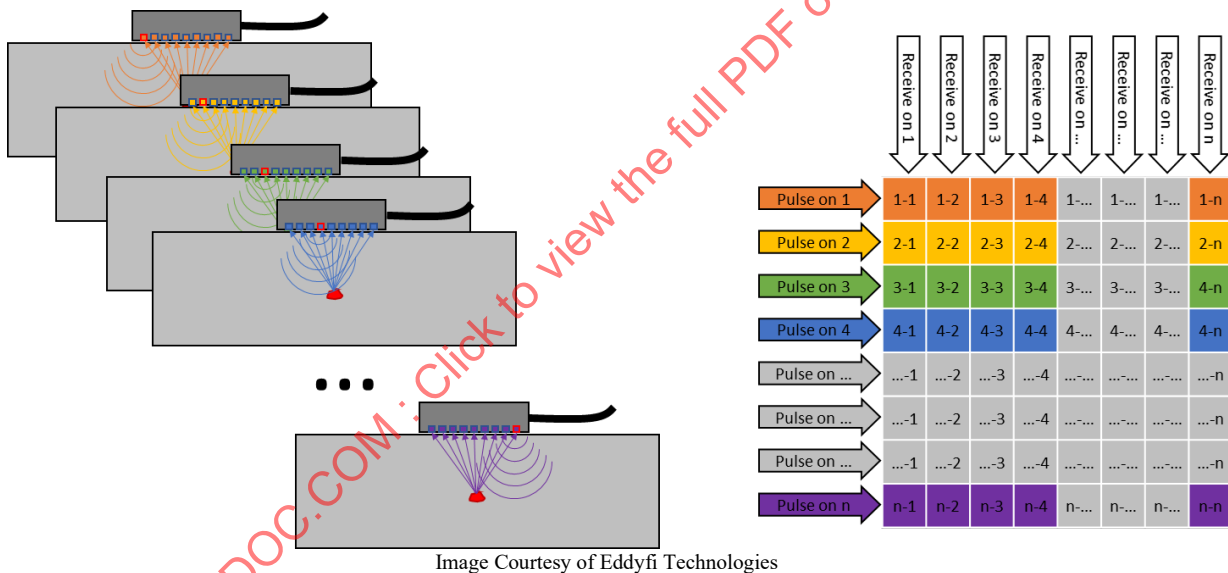
#### 2.1.1 Principle for Firing and Data Collection

FMC consists in capturing and recording A-scan signals from every transmitter-receiver pair in the array:

Each element of the aperture is pulsed (fired), in sequence, one by one. For every element pulsed, each receiving element collects an individual waveform.

The name Full Matrix Capture originates from the fact that it is possible to conceptualize every acquired waveform in a matrix shape. Pulsing elements are rows and receiving elements are columns. Such a data acquisition matrix is sometimes referred to as an FMC frame.

Figure 2-1: Firing Pattern and Resulting Matrix for FMC



From the individual waveform signals gathered (A-scans) during the FMC process, it is possible to generate imaging for improved algorithms such as Total Focusing Method (TFM).

#### 2.1.2 FMC Signal Characteristics

Elementary waveforms gathered by the FMC function are usually not designed to be used and interpreted by a human directly. While using every available signal from an FMC frame enables a computer (or device) to generate interesting images, a single individual elementary waveform is not very useful.

In some respects, FMC data is similar to Magnetic Resonance Imaging (MRI) used in the medical field. In both cases, numerous smaller pieces of information are collected, yet individually they are difficult to use. However, a computer can assemble them in collaboration to generate an image.

The difficulty in interpreting a raw FMC signal directly is usually due to the physics with which the method was used to collect it. Each of the elements are fired individually, resulting in a very wide and

non-focused beam which covers a large portion of the component under inspection. Interaction with every potential flaw, geometry, or other reflector, sends a signal back to multiple receiving elements, which then, in turn, will collect all the information into a single elementary signal (A-scan). The produced elementary A-scan from a single pulsing-receiving element pair includes echoes for every single reflector, without any notion of location or angle.

Additionally, elementary A-scan signals gathered by FMC will have similar characteristics. This enables them to be used later for image creation.

FMC data is always collected in RF mode. No rectification can be used because the image reconstruction algorithm requires phase information to compute constructive and destructive interference (summation).

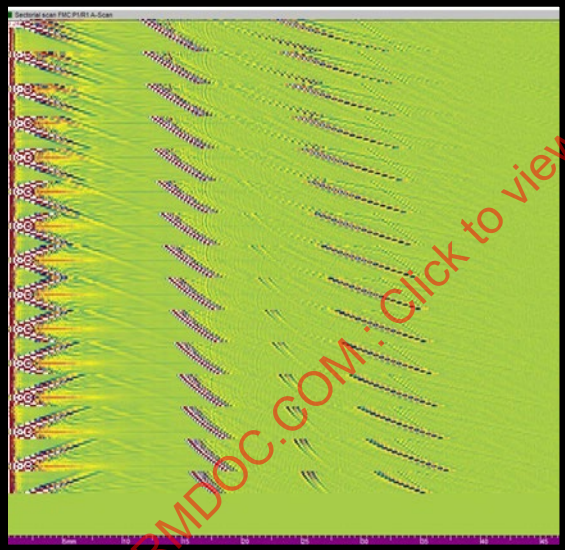
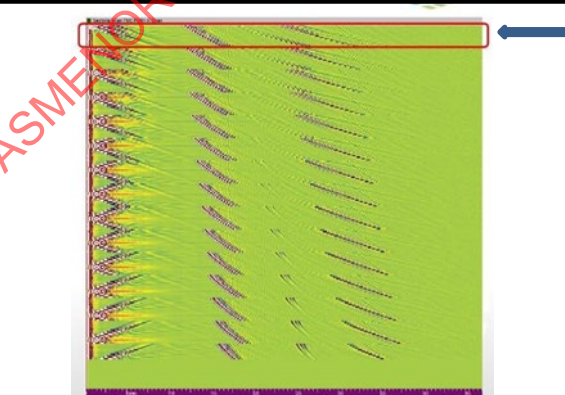
The digitizing frequency is usually high, generally at or above 100 MHz. Sample resolution is crucial for proper delay forming during image reconstruction. For this same reason, the signal is also typically not compressed.

High amplitude fidelity and very low noise is required because the signal from individual elements can be very weak.

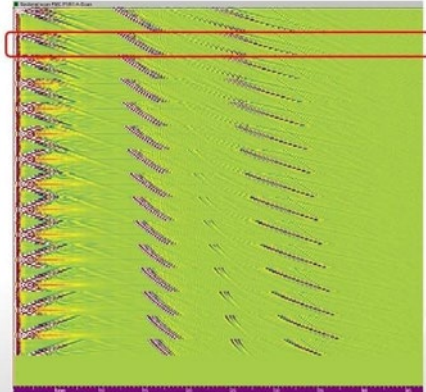
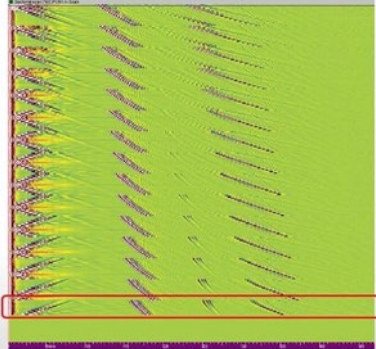
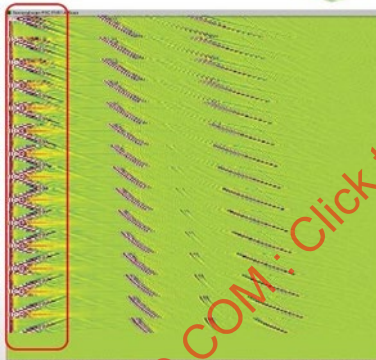
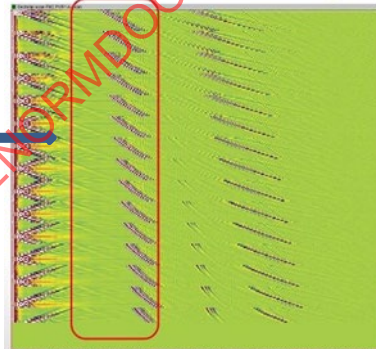
No smoothing is used. Smoothing is done only on a rectified signal, which is not possible on the RF elementary waveform.

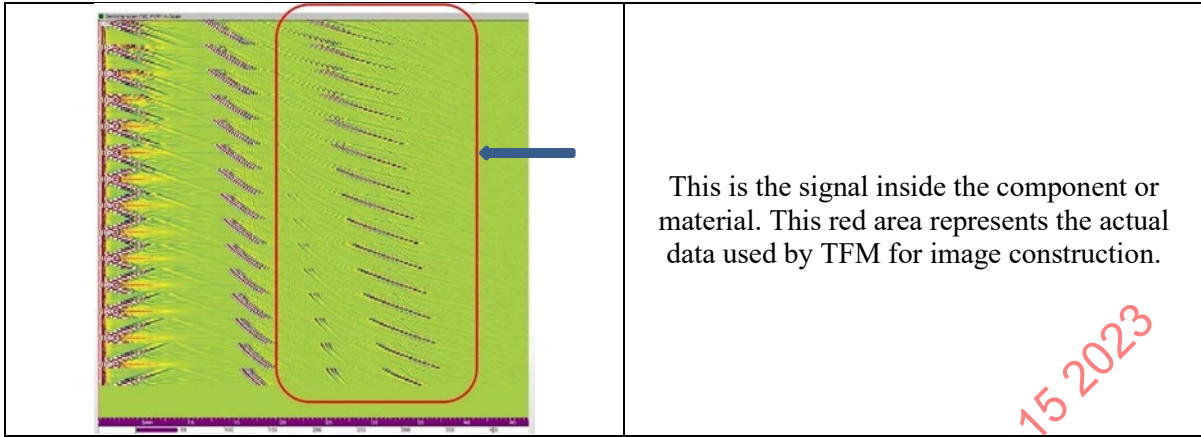
### 2.1.3 Typical FMC Signal Explained

Table 2-1: Breakdown of the FMC signal data as represented on images

	<p>This is an example of a 16-element probe and the raw FMC data that is displayed on the acquisition device's display screen. This information is not useful in this form without the underlying explanations of what the colored marks mean.</p>
	<p>In the highlighted red rectangle, the figure shows element 1 firing; receiving is then performed on elements 1 to 16.</p>



	<p>In the red area, now element 2 is firing; receiving with elements 1 to 16.</p>
	<p>Here the red area shows element 16 firing; receiving with elements 1 to 16 (elements 3 to 15 have also gone through this sequence).</p>
	<p>The red area demonstrates the initial bang from the probe onto the wedge.</p>
	<p>This is the signal inside the wedge, demonstrating the interface between the wedge and the component (or material).</p>



This is the signal inside the component or material. This red area represents the actual data used by TFM for image construction.

Courtesy of Eddyfi Technologies

## 2.1.4 Alternative Firing and Data Collection Methods

### 2.1.4.1 Half Matrix Capture

HMC is a variation of the FMC method that voluntarily drops some of the collected elementary A-Scans, to achieve greater imaging speed and reduce the file size of collected raw data.

With FMC, all elements are used to pulse and to receive. This results in a large amount of data that needs to be processed or stored. Out of this complete set of firing and receiving element pairs, under some conditions, some pairs would be redundant, and are equivalent in acoustic path, signal response and other characteristics (See Figure 2-2 and the following example). The performance increase with HMC is accomplished by voluntarily dropping elementary signals from one of the pulsing-receiving element pairs that would contain redundant data with the other pair in the collection matrix. When using HMC, nearly half of the FMC firing pattern can be deleted without showing a negative impact.

Example: The redundant pairs of elements occur on pulse echo probes, when the pulsing and receiving element are inverted in another pair. For example, firing element 1 and receiving on element 20 is equivalent in path and signal to firing on element 20 and receiving on element 1. In this situation, any echo seen from one of the pairs will also be seen by the equivalent element pair, at the same time of flight, and with the same amplitude.

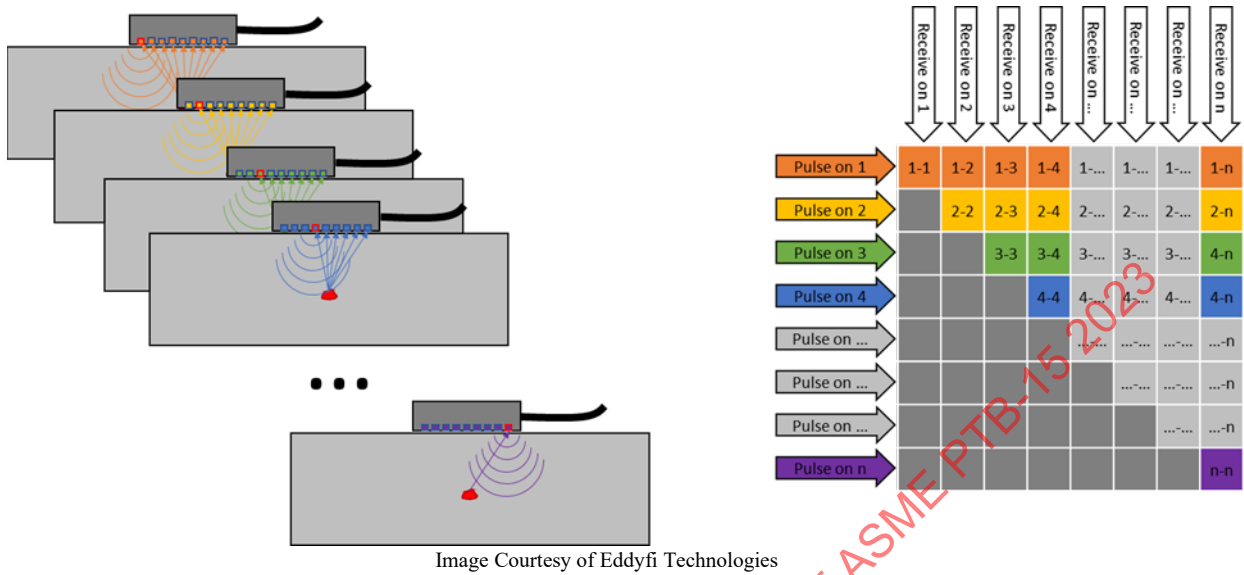
**Figure 2-2: Example of Redundant Pairs**



Image Courtesy of Eddyfi Technologies

Filtering out these redundant combinations allows a reduction in the amount of required data stored in the acquisition matrix, reducing the amount of data roughly by a factor of 2. More precisely, with FMC data, the number of elementary signals is  $n^2$ , whereas for HMC, the total number of elementary signals is  $(n^2+2)/2$ . (Figure 2-3).

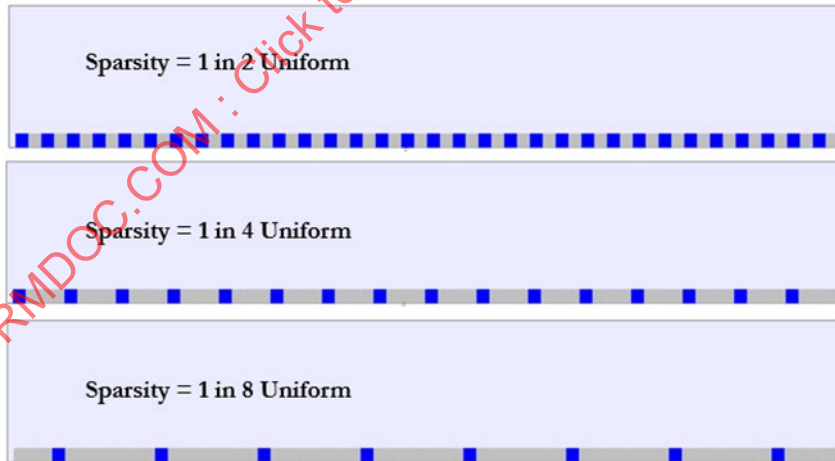
Figure 2-3: Firing Pattern and Resulting Matrix for HMC



### 2.1.4.2 Sparse Acquisition

In its simplest form, Sparse data acquisition reduces the number of active elements to Pulse, thereby reducing the number of iterations and creating less data to be calculated. This reduction can be achieved by only pulsing a limited number of elements in a traditional array probe. Reception can still be performed on all elements, just like FMC, or by deactivating some elements in the acquisition. Sparse Array TFM can use the same algorithm(s) as classical TFM reconstruction.

Figure 2-4: Firing Pattern and Resulting Sparse Acquisition of 1:2, 1:4, and 1:8



Courtesy of Kenneth Shane Walton-University of Ultrasonics

Figure 2-5: Example of a Possible SMC with 1:2 Sparsity

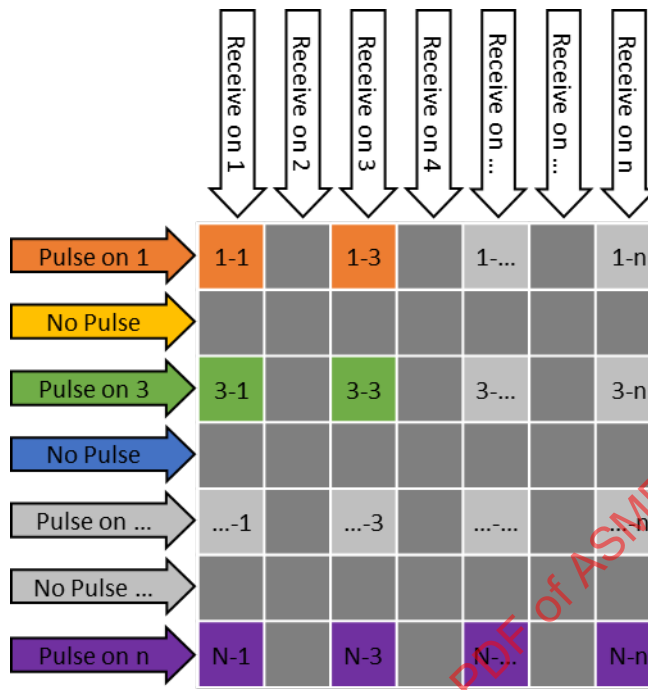


Image Courtesy of Eddyfi Technologies

**Advantages:**

Less data is collected for raw elementary signals. Therefore, less storage space is needed (If all raw data signals were to be saved).

Less data collected for raw elementary signals also means less data to transfer and to compute during image processing. This enables faster computation time and faster inspection speeds.

**Limitations/Conditions:**

Having less data overall could reduce resolution or degrade signal-to-noise-ratio (SNR), as compared to a complete FMC acquisition. The operator should be aware of the trade-off between speed and image quality.

**2.1.5 FMC Processes Using Different TR Methods**

**2.1.5.1 Different Methods**

For the FMC data acquisition, many UT configurations can be used such as pulse echo, pitch catch, through transmission, self-tandem, etc. Even a single-element conventional probe (see Synthetic Aperture Focusing Technique (SAFT) Chapter 3) can collect FMC data. Each configuration method has its own unique attributes and limitations.

**2.1.5.2 Pulse Echo**

The pulse echo configuration, using an array, is the most common method encountered in the field. In pulse echo, every element is used to pulse and to receive. All transmit-receive pairs belong to the same array.

Consequently, some pairs are equivalent in acoustic path, signal response, and other characteristics. In other words, when the pulsing and receiving elements are inverted, any echo seen from one of the pairs will also be seen by the equivalent element pair (e.g., transmit element #1 and receive on element #20 is an equivalent acoustic path as transmit on element #20, and receive on #1. (See Figure 2-2). Pulse



echo makes it possible to acquire the data using HMC instead of FMC. Nearly half of the FMC firing pattern can be deleted without negative impact to create the HMC frame. As mentioned previously, this equates to faster acquisition times.

### 2.1.5.3 FMC-TFM for Pitch/Catch

In the pitch catch configuration, each element of the transmit-receive pair belongs to a different array. These may be side-by-side, as shown in Figure 3-6, or they may be completely separated and opposing each other, like a ToFD setup. In other words, each element of the transmitter array (transducer a) is fired individually, and in sequence. For each element pulsed, every element of the receiver array (transducer b) collects the individual waveforms. Therefore, each transmit-receive pair has its own acoustic path and signal response, which makes each waveform specific within the FMC matrix. The image reconstruction, or TFM, remains the same as the pitch/catch configuration.

Figure 2-6: Schematic of a Side-by-Side Pitch Catch Configuration

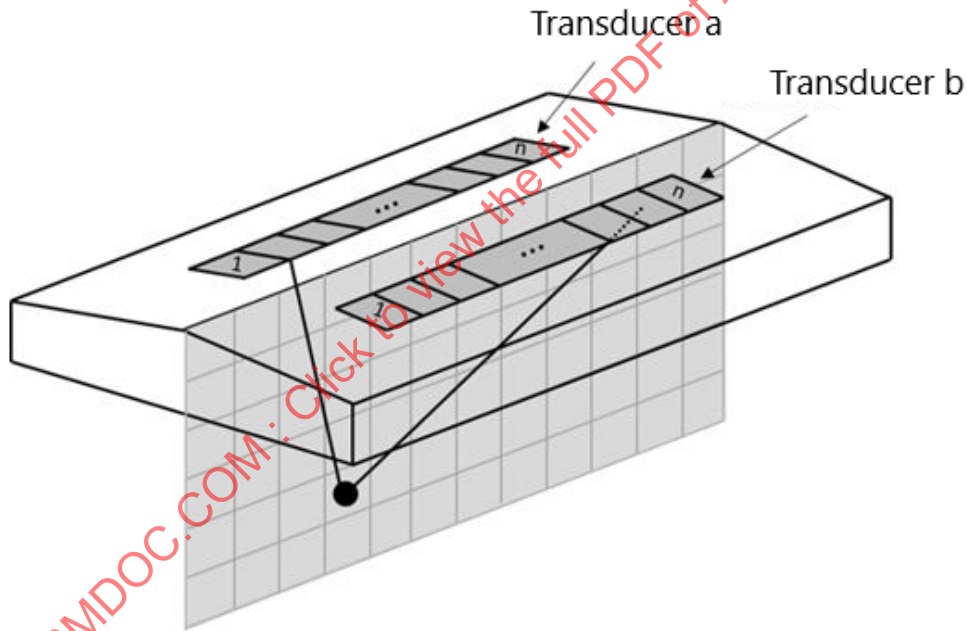


Image Courtesy of Eddyfi Technologies

### 2.1.5.4 Considerations

In all configurations, the applied delays are a function of several parameters including the pixel's distance from the array elements, the ultrasound velocity in the material, the wave type, the reconstruction mode, the presence/absence of a wedge, etc. The component configuration itself may not readily lend itself to a particular configuration. It is also important to remember that even though the acoustic paths theoretically cover the entire TFM frame, and are often drawn this way, the laws of physics will still apply, preventing any coverage beyond the maximum beam spread range.

## 2.1.6 FMC Data Size and Storage

### 2.1.6.1 The Full Data Set

As we have seen a full FMC data set is a compilation of every element in an array transmitting, and in return also receiving, from all other elements being fired (including itself), such that every combination of all the elements produces an A-scan. This process can generate a huge number of A-scans for any given probe size, and only at that search unit position (FMC frame). The formula for the number of A-scans within a given frame is  $n^2$  elements.

For Example:

For a 32-element array—Each element will be pulsed once for a total of 32 times. For every element pulsed, 32 will receive and generate an elementary A-scan. Therefore, in a single frame there will be 32 X 32 elementary A-scans created, or 1,024 in total. With a 64-element probe there will be 4,096 elementary A-scans generated.

- Keep in mind that this is for a single frame. If you are collecting a frame every 1 mm or so along the length of a weld, this can generate an enormous amount of data in a very short distance.
- To understand this further, and as a means of determining storage space needs or rather examination file sizes, there are a couple more points to consider.

### 2.1.6.2 A-Scan Sample Count for Time Base Range

Each elementary A-scan needs to cover a range long enough to image the full area of interest, usually on the order of several  $\mu\text{s}$  of data. The A-scan range must be long enough to cover the full area of interest and with every potential wave mode that is expected to be used for image reconstruction by the TFM function.

For Example:

A mild steel component 25 mm thick, being imaged using shear waves in T-T and TT-TT (half-skip and full skip) and roughly assuming refracted angles around 55SW, we can expect an A-scan range of around 54.5  $\mu\text{s}$ . The math would look like this:

$$2 * ((\text{depth} / \cos(\text{refracted angle}) * \text{number of legs}) / \text{sound velocity})$$

Or,

$$2 * ((25 \text{ mm} / \cos(55) * 2 \text{ legs}) / 3.2 \text{ mm}/\mu\text{s}) = 54.5 \mu\text{s}$$

**NOTE:** The previous example does not consider the wedge material, or to a lesser extent any system delay that would further increase the time base range. A good sanity check would use a calibration block to verify coverage. Additionally, because the wave mode and area of interest (FMC grid) can be manipulated in post-processing, it is usually good practice to collect a longer time base range to ensure image reconstruction capability.

### 2.1.6.3 A-Scan Sample Size (Actual)

Using a high digitizing frequency will sum to several thousand samples per A-scan. For example, at a 100MHz digitizing frequency, traveling a distance of 54.5  $\mu\text{s}$  will produce 5,450 samples per A-scan.

Every sample of the elementary A-scan requires multiple bits to be stored. This is also dependent on the hardware digitizer used. A standardized package of bits, called Bytes, is 8 bits per Byte. A digitizer producing 8 bits of amplitude would then be stored in a Byte. While a digitizer producing 9-16 bits of amplitude would be stored in 2 Bytes.

To estimate the file size, we can evaluate the storage size of a single FMC frame. We again must use some assumptions to get us in the ballpark:

Given a 64-element probe, and assuming 80  $\mu\text{s}$  elementary A-scan range (having sufficient extra time base to account for the wedge, system delay, etc.), and using a 16-bit digitizer.

We obtain:

4,096 elementary A-Scans (array of 64 \* 64 elements)

8,000 samples per A-Scan (80  $\mu\text{s}$  \* 100MHz digitizing frequency)

FMC frame data size = 4,096 \* 8,000 \* 2 = 64 MB

Again, this frame size would be for each probe location along a scan axis. When a full component is inspected, this size must be multiplied by the total number of probe firing positions (frames) along the scan axis.

For example, to scan a typical 12-inch pipe with standard resolution, huge files are produced and look something like this.

(12in. \* 3.1416/0.039in. (1 mm) scan resolution) \* 64 MB = ~62 GB

## 2.1.7 FMC Data Storage

### 2.1.7.1 Size

It becomes apparent that FMC not only can generate large amounts of data, but moving this many data can slow down exam times. There are many things to consider, including the type of instrument being used, and how it is configured (see Chapter 3 on Equipment). This is also the reason for the above-mentioned data collection schemes (HMC, Sparse), and why they are used.

The storage of large file sizes, and the processing speeds, are becoming more efficient and less expensive to perform as technologies continue to progress. Although storing large files is possible, it is not necessary for most examinations. If the user is required to store the raw FMC data for specific application needs (e.g., to change the inspection parameters such as mode of propagation, frequencies, filters, etc.) this can be done after the examination has been completed. In certain cases, the user should be vigilant in the selection of equipment as some may not provide a means to store the FMC data files. Typically, only the TFM generated images are all that is required to achieve an examination. However, user defined applications, research, academia, or for future algorithm development, may need to consider this variable. Once a full matrix of data has been stored, any post processing algorithm can be applied to it. Additionally, because an FMC data set is considered to have collected all possible transmit and receive combinations from an array over an area, it contains all possible information for that area, and is considered “future proof”.

## 2.2 Total Focusing Method (TFM)

### 2.2.1 TFM General

This section describes the basics for TFM reconstruction. Although there are many different types of TFMs, this section only describes what is considered “classical TFM”. The data can also be acquired or processed through other techniques, some of which are described in this book, such as those described in Chapter 3. Once present in the FMC matrix, the elementary A-scans can be processed using any available TFM imaging algorithms, and/or signal processing (e.g., Fourier, Hilbert, etc.) to reconstruct an intelligible image of the region of interest. The TFM image reconstruction can occur in real time during data collection (live image) or be processed during later analysis (post-processed image).

TFM describes any group of algorithms that employs a summation process for each pixel within the grid to generate the image. The name “total focusing method” originated from the fact that each point calculated in the grid is intended to be perfectly focused. It is important to understand the focusing

effects are synthetically formed through processing the data and are not physically focused beams. TFM algorithms can be applied to multiple FMC data collection schemes and probe configurations, including pulse echo, pitch catch, tandem, and self-tandem.

### 2.2.2 Principle for Data Reconstruction

There are also several types of beamformer schemes. The most common of which is referred to as Delay and Sum (DAS). DAS processing techniques have been used in various industries such as medical, communications, radar, photo-acoustics, etc., for many years prior to NDE. DAS is derived simply from what it does, and although there are other more sophisticated algorithms that can be applied (such as Migration, see Chapter 3.3 IWEX) DAS is easy to implement and very reliable.

For the TFM algorithm, a grid containing individual pixels is overlaid upon the region of interest (ROI). The algorithm creates delays for each T&R pair and summation (from all pairs) for every pixel within the grid. To do so, each pixel is treated as an independent data point for which the delay is calculated based on the total time of flight required for the ultrasonic wave propagation from the transmitter to a pixel coordinate and then back to the receiver. Figure 2-7 shows the wave propagation path for a transmit-receive pair to an individual pixel. Each transmit and receive pair will report a reflector along an elliptical arc. In Figure 2-7 the pixel located at  $X_p, Z_p$  lies along this arc, and therefore has information that will contribute to the summation and the overall image. This information will be in the form of an elementary A-scan. In this figure, anything outside the arc is essentially a zero net for the summation. Other T/R pairs will generate a similar arc but have a slightly different orientation. This is due to the other pairs having a different location within the array and therefore different delays. The other pairs will also have information at this pixel. The process then generates a summation of all pairs (elementary A-scans) and assigns an intensity for this pixel. After all T/R pairs across all pixels have been summed, then we have an image.

Figure 2-7: Wave Propagation Path for a Transmit-Receive Pair to a Specific Pixel

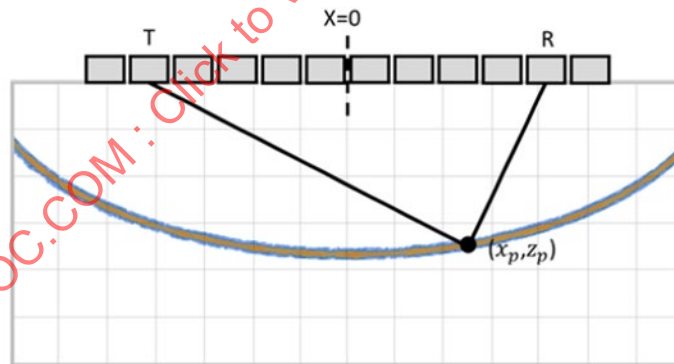


Image Courtesy of Sinewave Solutions

Each elementary A-scan generated from the FMC data (every transmit-receive pair) is applied to the summation process. This coherent summation is applied to the pixel of interest and generates the intensity information at that pixel. This process is repeated for every pixel in the grid. Every pixel then has a dedicated position (delays), with a calculated intensity through the summation process, thus generating the final image.

This process is shown in Figure 2-8 through Figure 2-11 and illustrates an example of delays being calculated within the grid and the summation of the A-scans to provide an intensity in the final TFM image.

**Figure 2-8: TFM being constructed from a single transmit and receive pair. Note that as it progresses, each individual pixel has a set of delays and an intensity reported for its location.**

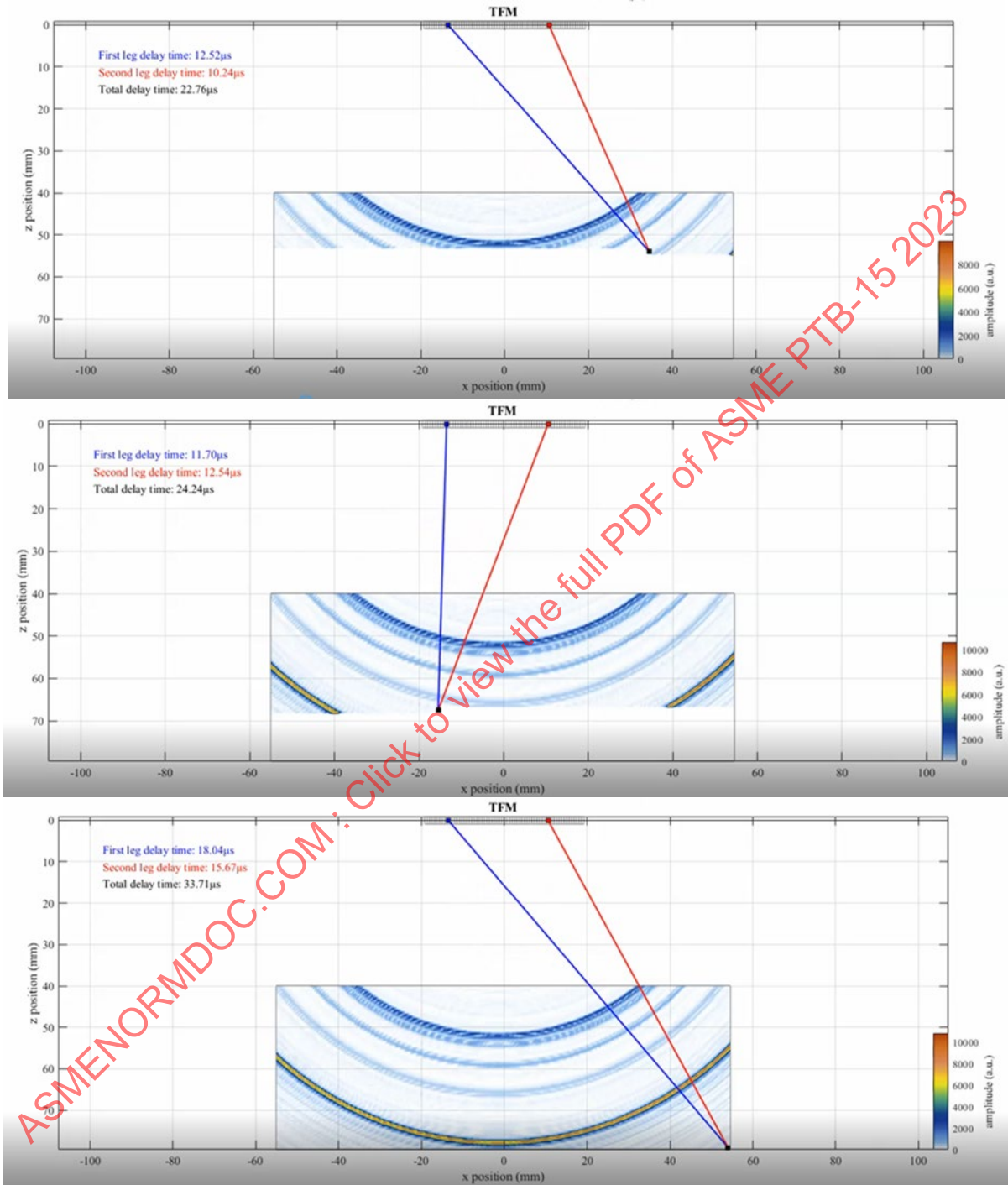


Image Courtesy of EPRI



**Figure 2-9: The Cumulative TFM (lower right) becomes a compilation of all T&R pairs. This example is only four T&R pairs.**

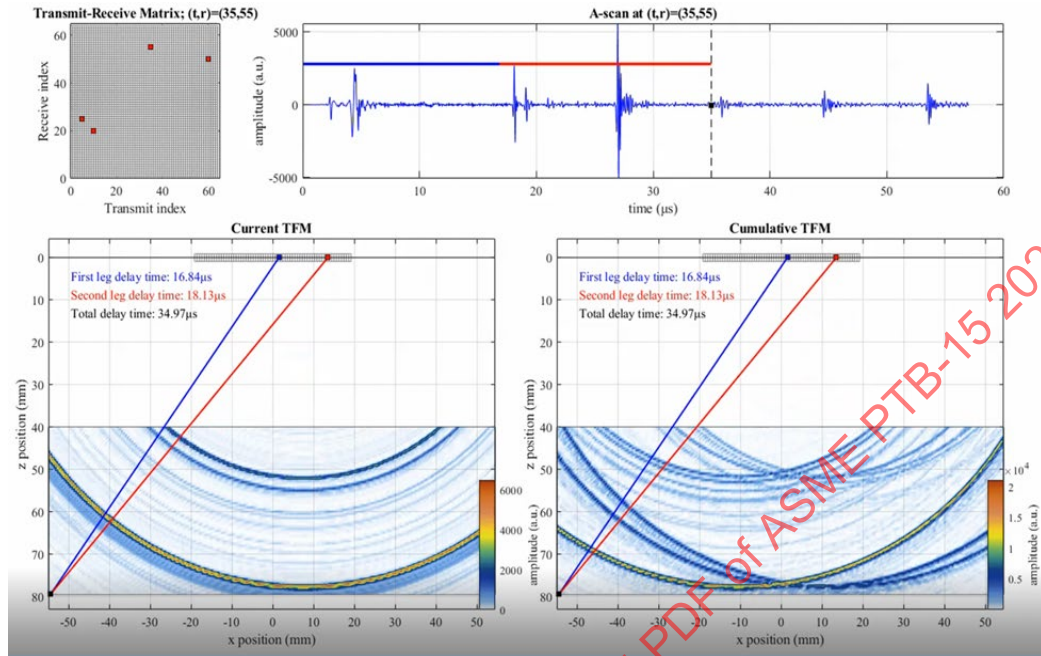


Image Courtesy of EPRI

**Figure 2-10: We have progressed from the previous cumulative TFM of 4 pairs to 410 pairs (left) or about 10% complete. For this component, a set of side drilled holes have formed. In the image to the right, which is 2,048 pairs or about 50% complete, you can further see the effects of the summation process by witnessing that the large “swath” of noise in the image has begun to clear up.**

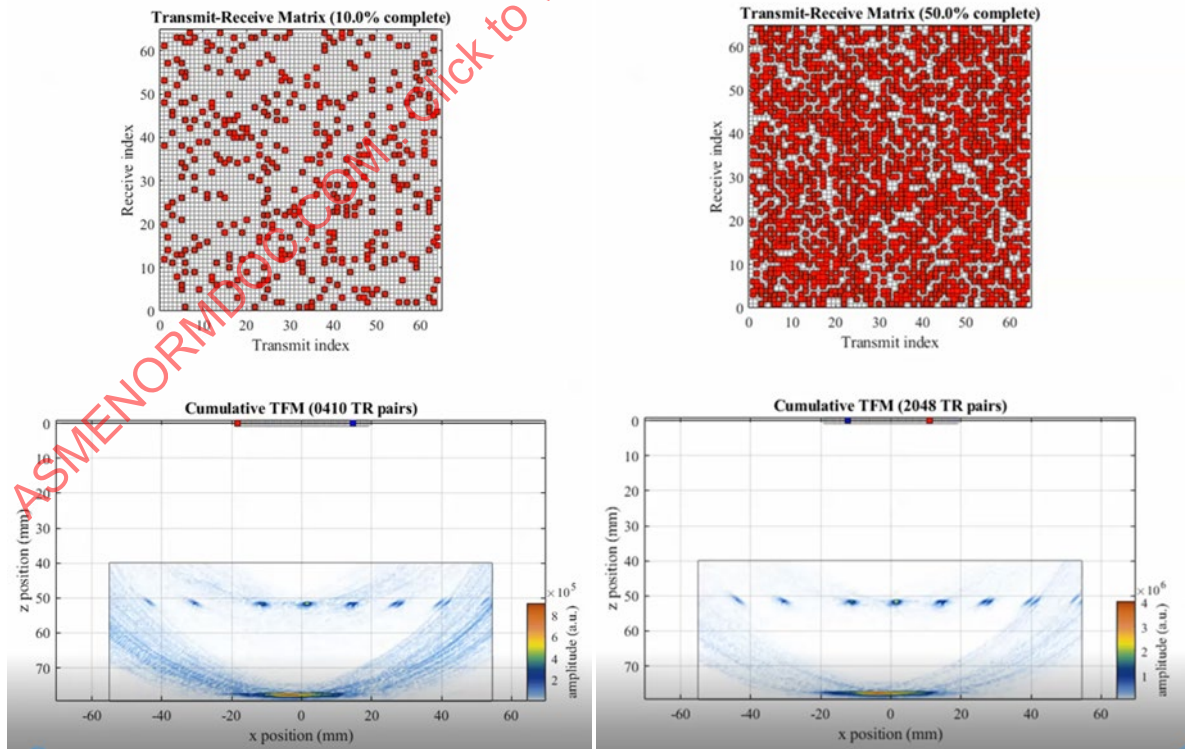
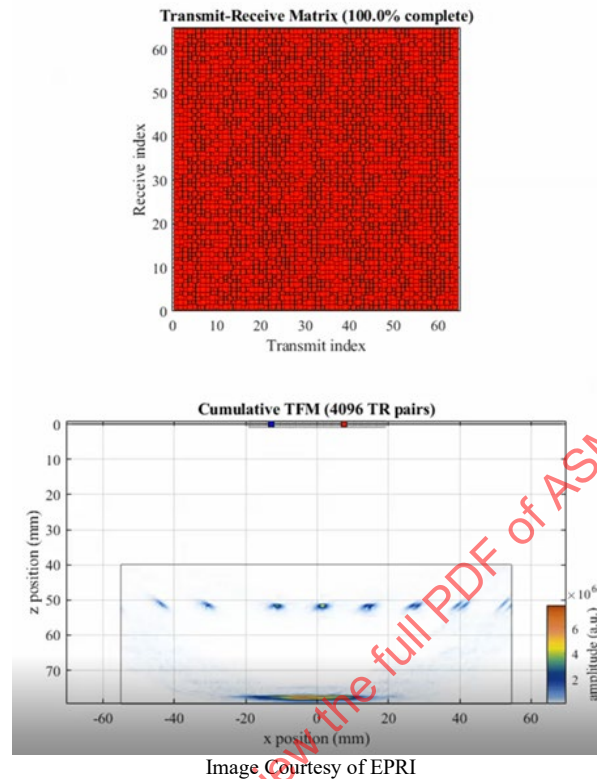


Image Courtesy of EPRI

**Figure 2-11: The final image at 100% (all 4,096 pairs) completed. It is important to consider the order of magnitude with which we have progressed through these images. We started with a single pair assigning data to every pixel, then went to 4 pairs, then 410 pairs, then 2,048, then finished at 4,096 pairs. (1)**



### 2.2.2.1 B-Scan

It is important to point out that the final TFM image may look like a familiar B-scan, but it is not. A B-scan is produced from stacking A-scans, typically derived by individual beam and angles using time vs. amplitude (Time Domain signals). The TFM image grid resides in the same plane, but it is not constructed in this manner. No angle dependent information exists to derive a reflector's location. The TFM image, after the summation process, displays an intensity at every pixel within the grid, whereas a B-scan displays amplitude along a beam. (2)

### 2.2.2.2 A Note on TFM and Noise

For all the beautiful images it can create, FMC-TFM is extremely noisy. Figure 2-10 and Figure 2-11 display noise as a “swath-like arc” that depletes in the image as the process continues until completion. This is obviously due to more T/R pairs reporting nothing of interest at these pixels, than those that are reporting something, and the summation process is reducing the noise. Yet, even in the final image the noise is still present and observable. The reason for this is because these images are built solely from the elementary A-scans, with no other processing involved. Typically, images would not be built from the raw conventional A-scan form without some other type of processing involved.

At this point, other processing schemes such as a Fourier transform, or a Hilbert transform, for example, would be applied to the “raw” elementary A-scans of the FMC data. These treated signals are often referred to as the “analytical” wave form. The processes that create the analytic wave form—not simply a summation of the conventional A-scan—that more effectively suppresses the spurious signals and provides the enhanced resolution that makes TFM images look so good. At the end of this chapter there is a section describing the Fourier and Hilbert transform processes in more detail.

## 2.3 Wave Type, Reconstruction Mode

### 2.3.1 Naming Conventions

It is important to understand what a reconstruction mode, path, beam, and ray tracing all mean when conversing about FMC-TFM.

#### 2.3.1.1 Reconstruction Mode

Commonly referred to as a “mode”, a reconstruction mode is the same as an ultrasonic mode of propagation, transverse or longitudinal. However, in the realm of FMC/TFM it refers to the actual acoustic paths desired for the TFM to calculate all pixel intensities. This is described in greater detail in the following sections.

#### 2.3.1.2 Path

An individual path is a subcomponent of a mode and is not a beam. It is the singular calculation of the sound travel to an individual pixel and often depicted by ray tracing, even though there is no ray, or beam, involved. The number of paths possible within a mode would be the same as the number of pixels in the grid.

#### 2.3.1.3 Beam

When conversing about ultrasonics, it is customary to use the word “beam”, especially when describing what the sound is doing within a given component. For TFM this would be incorrect, as the only beam(s) that occur is on the front end during the FMC. Those are sound beams. TFM is a calculation of individual paths performed on FMC data.

#### 2.3.1.4 The Problem with Ray Tracing

When ray tracing is used in TFM, it is often used to describe a reconstruction mode or a path. This representation is correct in a general sense, but often leads to the misconception of generating beams. In fact, no other logical way to draw and represent a mode or path exists.

### 2.3.2 TFM Modes

As with any ultrasonic inspection technique, it is possible to use longitudinal and transverse wave modes with TFM. In other words, by applying different amounts of delay to compensate for velocity in transmission and in reception, the use of multiple acoustic wave modes can be created and the TFM image reconstructed. Therefore, the image reconstruction mode, by convention, is described by using the mode of the acoustic waves of each path segment (leg). The description consists of a certain number of letters separated by a hyphen, and is explained as follows:

**T** represents transverse wave mode (Shear wave)

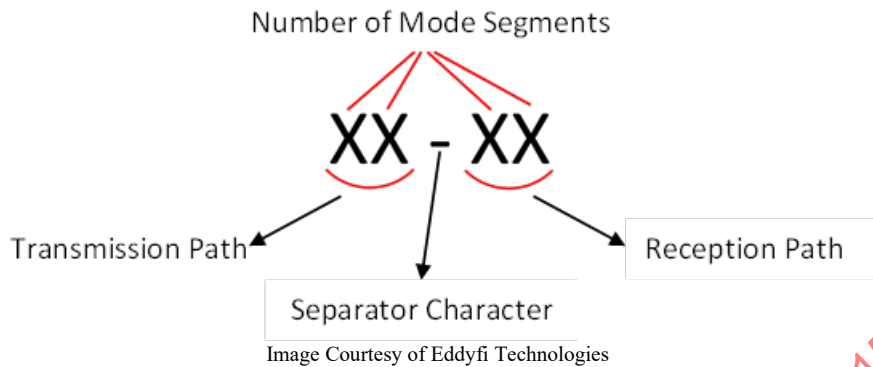
**L** represents longitudinal wave mode (Compression wave)

The **hyphen** is used to separate the whole acoustic path into two parts:

- Before the separator character (hyphen): The signal from the transmitter array to target location (Transmission path)
- After the separator character (hyphen): The signal after the target location toward the receiving element. (Reception path)

The number of letters on the left side of the separator character represents the number of legs from the transmitting element to the target location. Similarly, the number of letters on the right side of the separator character represents the number of legs from the target location to the receiving element.

**Figure 2-12: Example of How Mode Nomenclature Works.**

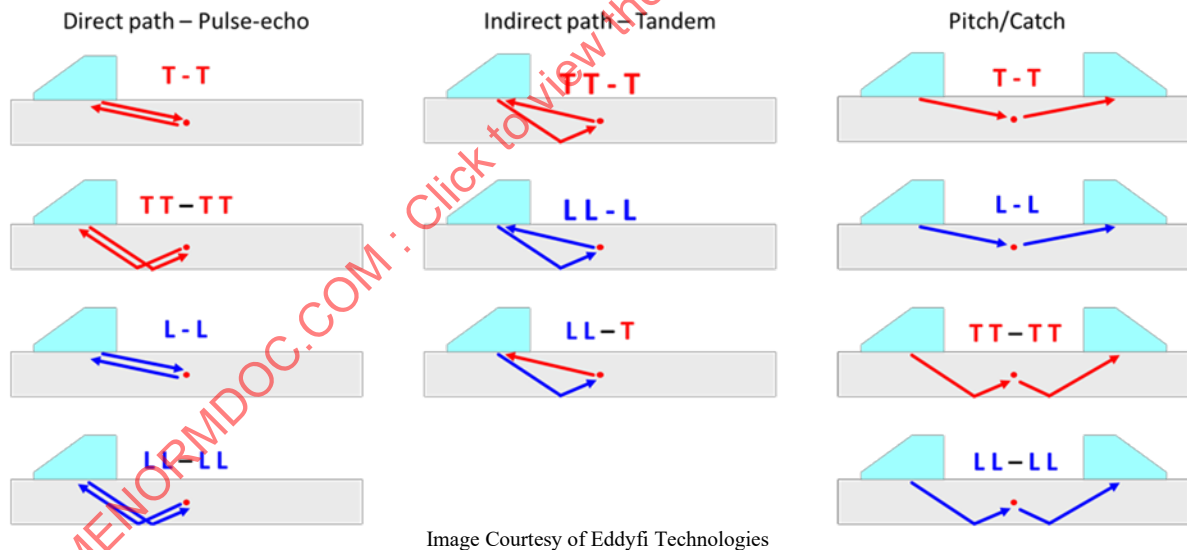


This notation, along with the probe configuration, can be used to fully describe the inspection configuration, such as:

- Pulse-echo direct, or T-T
- Pulse-echo after skip, or TT-TT
- Pitch-catch, or L-L
- Tandem LL-T

Figure 2-13 illustrates the operation of several common reconstruction modes as well as their definition. The T wave mode orientation is shown in red, while the L is shown in blue.

**Figure 2-13: Schematic of Some Common Reconstruction Modes**



Many more reconstruction modes are possible and are used depending on the specimen's geometry, the flaw type, its location, and the probe's configuration. Some modes are very similar to each other such as TT-T and T-TT. Multimode (any combination of T and L) is also possible. This provides a very large number of combinations that are available for use.

It should also be noted that, as in any ultrasonic technique, appropriate acoustic wave modes should be used to reliably detect, accurately size different types of flaws and simultaneously obtain full coverage for the ROI. Depending on the flaw of interest, its potential characteristics, and location. The user should select the appropriate reconstruction mode making it possible to receive a signal back from the flaw of interest.

### 2.3.3 Some Flaw Strategies

Figure 2-14 illustrates some examples of preferred reconstruction modes for certain flaws. Actual examples of flaw interactions with different modes can be found in the back of this book in Appendix A.

**Figure 2-14: Examples illustrating the advantages of different reconstruction modes in detection of certain flaws**

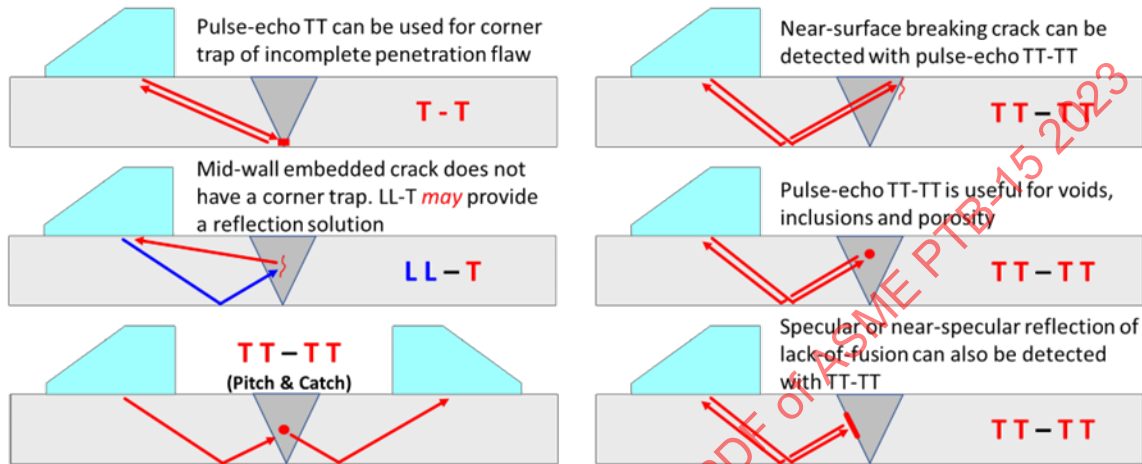


Image Courtesy of Eddyfi Technologies

### 2.3.4 Beam Spread Considerations

Multiple reconstruction modes are also generally required to obtain complete coverage, especially for weld examinations. It is possible to apply multiple reconstruction modes to the same FMC/HMC frame to create different images of the inspection zone. The presence of acoustic waves must be physically possible in the selected image frame, considering the probe/wedge configuration and the location of the image frame related to the probe position.

With standard phased array UT, the ultrasonic beams are limited to the amount of steering that can be applied. The limitation of the FMC frame becomes a function of the beam spread from a single element within the array. The area outside of the beam spread can still be computed, but the sound energy will not necessarily cover the expected area of the frame past the maximum beam spread angle, or an angle chosen as the cut-off point (e.g., -6Db). This may lead to a situation where pixels could contain data unrelated to the actual location.

$$\sin\theta = 1.2 \frac{V}{DF}$$

Where:

V: sound velocity in medium

D: element diameter

F: frequency



Figure 2-15 illustrates a 64-element 5MHz linear array probe mounted on a SW55 wedge in a direct mode pulse-echo configuration.

**Figure 2-15: (a) and (b) Position of the pixel in the TFM frame; (c) and (d) acoustic field simulation using the function of beam spread dedicated to the pixels in (a) and (b), respectively**

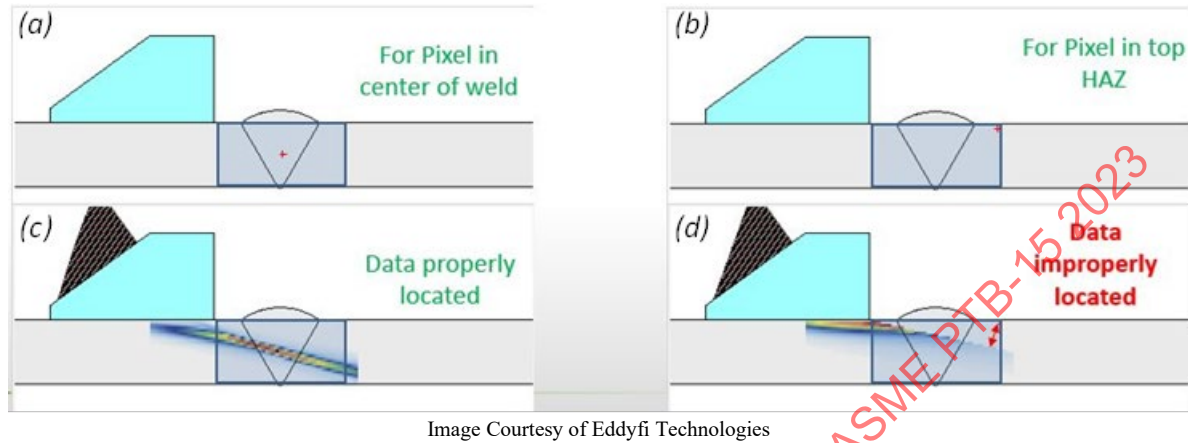


Image Courtesy of Eddyfi Technologies

In Figure 2-15(a), the data will be properly located within the frame due to the proper probe and wedge's configuration relative to the grid. However, for the pixel in Figure 2-15(b), the dedicated focal point will not be able to be accurately imaged due to the limitations imposed by maximum beam spread. Consequently, the data in this pixel will not be representative of its actual position.

Therefore, the following points should be considered when preparing a TFM configuration and defining the frame parameters:

Know the capabilities of the array being used for the FMC. (See Chapter 5 for array considerations).

Maximum coverage is a function of the beam spread from the single element within the aperture.

Past the maximum beam spread angle, the frame can still be computed, but if the reconstruction mode cannot physically cover the expected area it may lead to situations where pixels may contain data related to a different location.

The number and type of reconstruction modes must be considered to achieve complete coverage.

Ensure that the FMC has enough range for the types of TFM to be applied.

Figure 2-16 illustrates the results of beam simulations for a standard phased array sectorial sweep (beams) and a TFM frame reconstructed in the TT-TT mode. The simulations were performed using the following configuration:

Thin V-bevel weld, T = 37.5 mm

Linear array 5 MHz, 32 el.

55SW wedge

32 elements aperture

5 to 85 degrees SW (for standard PA)

TT-TT reconstruction mode (for TFM)

**Figure 2-16: Coverage that can be obtained with (a) standard phased array sectorial sweep and (b) TFM in TT-TT mode.**

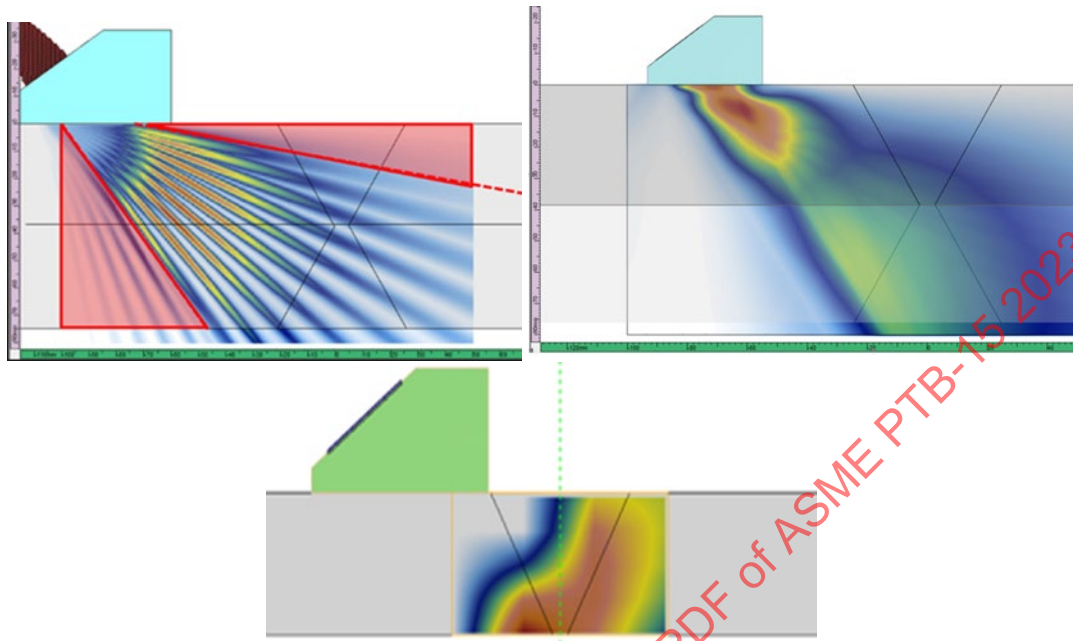


Image Courtesy of Eddyfi Technologies/Evident Scientific, Inc.

**Note:** The uppermost images are beam/sound field simulations. The lower TFM image simulation is not. The colors in the lower TFM image depict the degree of response that should be attainable within the frame. This modeling tool is further described in Chapter 3.

If a given pixel of the TFM frame is covered by the field of the pulsing element and the field of the receiving element, potential for detection exists (actual detection is still dependent on flaw orientation, nature of the flaw, amplitude level, noise level, etc.). Multiple possible TFM frame locations can be selected. Figure 2-17 illustrates using multiple modes to achieve coverage. Valid data for every pixel within the ROI can be computed using either mode, or both modes in combination.

**Figure 2-17: Valid location for a TFM frame reconstructed using T-T and TT-TT modes**

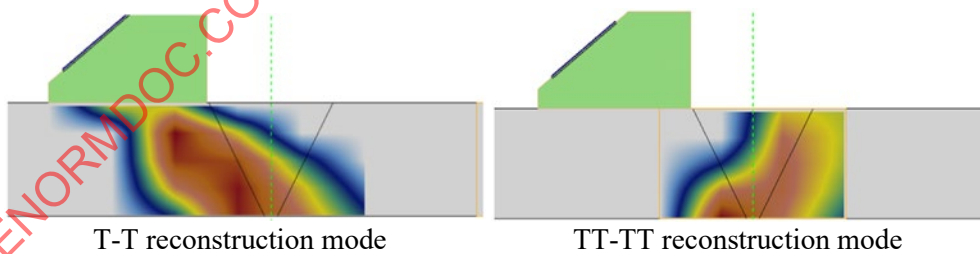


Image Courtesy of Evident Scientific, Inc.

To illustrate this further, the location of the red-colored box in Figure 2-18 is considered inappropriate for TT-TT reconstruction mode since:

The frame is not within the transverse wave field, and nothing can be detected using the transverse wave mode.

A possible longitudinal wave field exists in that location (not simulated and shown in Figure 2-18) that may detect some reflectors (e.g., back-wall).

Anything seen by L-waves will be plotted using the transverse wave velocity because the mode is configured as a transverse wave mode (TT-TT), so the plotted depth of such indications will be incorrect.

**Figure 2-18: Inappropriate TFM frame location for TT-TT reconstruction mode**

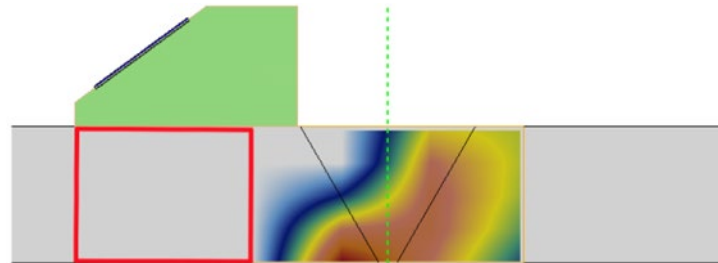


Image Courtesy of Evident Scientific, Inc.

When a T-T TFM frame is only used for reconstruction at the location displayed by the red-colored box in Figure 2-19:

A large portion of the frame is within the optimal transverse wave field and will generate responses from potential flaws or discontinuities in this location.

The upper-right portion will have a very weak response, compared to the average of the frame, as the amplitude drop in that area is not linear.

**Figure 2-19: Inappropriate TFM frame location for T-T reconstruction mode**

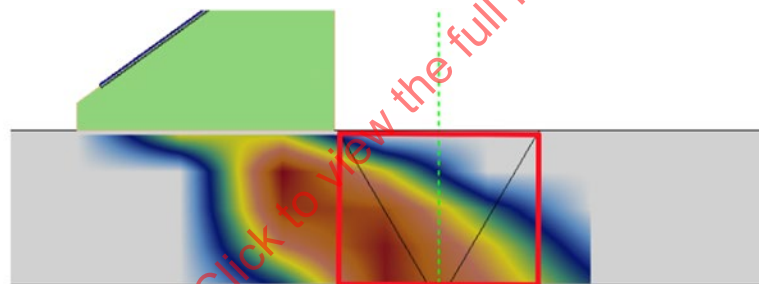


Image Courtesy of Evident Scientific, Inc.

### 2.3.5 Self-Tandem Modes

Discussion so far has looked at 2T and 4T modes because they are probably the most used. Again, seemingly countless numbers of combinations exist for modes, each having their own attributes, and the self-tandem modes are worth mentioning. These self-tandem modes, due to their paths and directivity, especially when coming out of a wedge, seem to do particularly well on vertical or near-vertical flaws. The best example of this would be a lack of fusion in the bevel of a narrow groove weld, K-groove, etc., or any almost vertical flaw. The self-tandem modes can be finicky but are necessary.

While it is easy to understand, from the images above, how a 2T mode (T-T) would be the most ideal for ID connected flaws and mid-wall flaws within reach, the 4T (TT-TT) mode should work well for an OD connected flaw and some mid-wall flaws. The 2T and 4T modes will not catch everything. Figure 2-20 shows the expected response(s) from the self-tandem modes individually and in combination.

Figure 2-20: Examples of the Expected Response from Self-tandem Modes

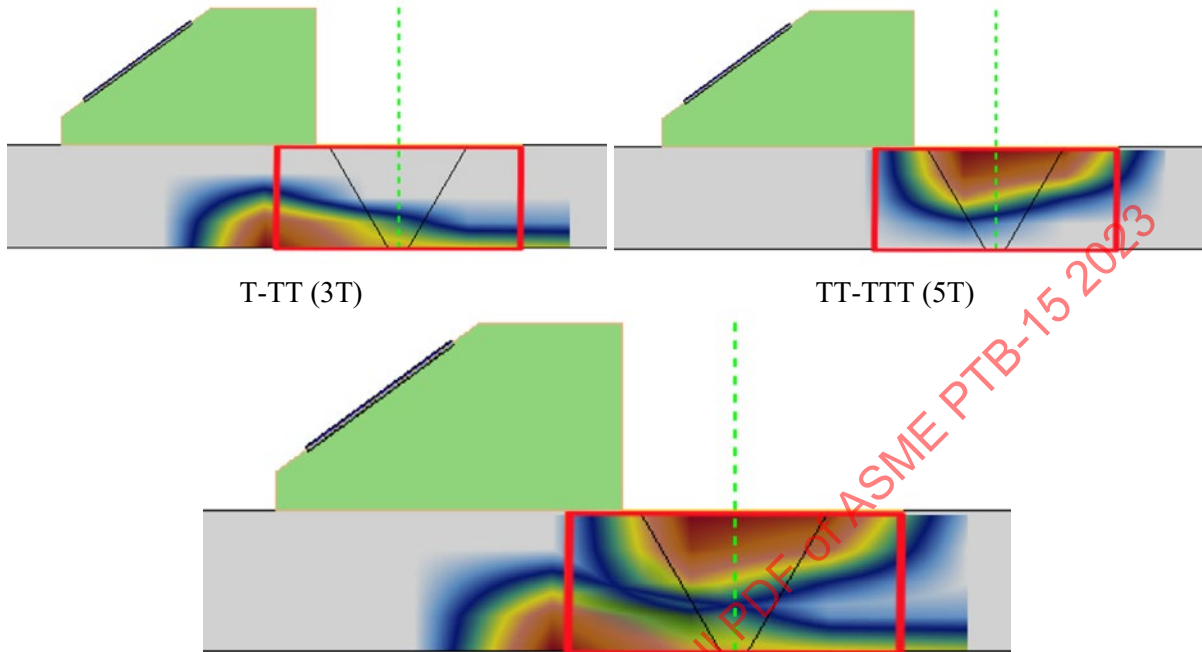


Image Courtesy of Evident Scientific, Inc.

### 2.3.6 Effects of Thickness

All TFM reconstruction modes are built from calculations (algorithms). When using modes that require a skip or rebound off a component's surface, having a correct thickness, and to a lesser extent velocity, for the component is essential. This is especially true for the "odd" numbered modes, also referred to as self-tandem, (i.e., 3T (T-TT), and 5T (TT-TTT)) as they seem to be the most affected by this. Figure 2-21 displays how easily the difference between the actual thickness and input thickness can throw the calculation off.

Figure 2-21: An example illustrating the inefficient spatial coherence of the TFM trajectories for a specimen with different thickness than the nominal value used for image reconstruction. In a.) the actual and input thickness is the same, in b.) the actual thickness is less than the input thickness, in c.) the actual thickness is greater than the input thickness. The delays remain the same.

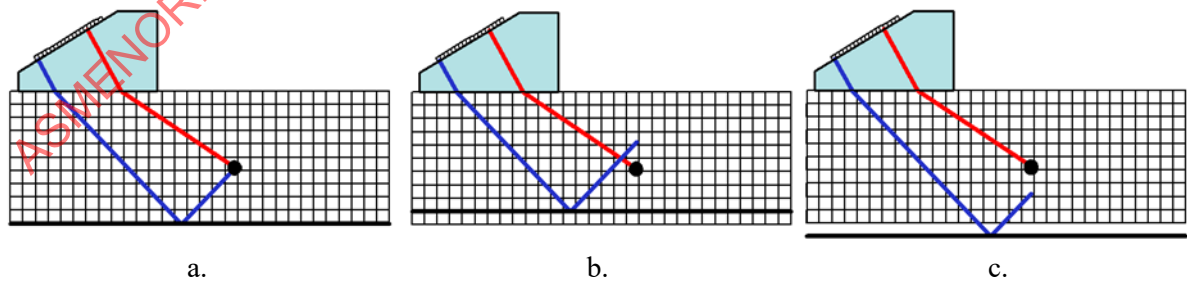


Image Courtesy of Sinewave Solutions

Because the length of the acoustic path is a function of the specimen's thickness, the exact value of the thickness should be known and considered for image reconstruction. Any difference between the nominal thickness of the specimen with its actual thickness will cause an erroneous delay calculation and hence inefficient focusing (delay) and a degradation of the image. Figure 2-22 demonstrates a configuration in which the specimen's actual thickness is less than, and greater than, its nominal value of the specimen shown. The delays are calculated based on the nominal thickness value (from instrument/user input) to focus the acoustic paths on a specific pixel. Meanwhile, the actual thickness will cause a difference in the delay calculation. Because the delay calculation relies on a rebound from the back wall, if the difference between the actual vs. nominal (input) thickness is great enough, the image will be degraded and possibly unusable.

In a study by Painchaud-April et al., the impact of  $\pm 10\%$  thickness difference on the amplitude of a side drilled hole (SDH) indication in a TFM self-tandem configuration was evaluated. The FMC data was acquired on three different specimens possessing (a) 20 mm, (b) 18 mm (-10%), and (c) 22 mm (+10%) wall thickness. Images were reconstructed using the self-tandem configuration of the nominal part (20 mm wall thickness) in all cases. The results for the (b) and (c) data set showed a signal amplitude drop of -9 and -8 dB, respectively, as compared to maximum signal amplitude of the (a) data set. See Figure 2-22.

**Figure 2-22: Maps of the amplitude envelope computed using the TFM on the three samples of different thicknesses, using: (a) 20 mm (nominal), (b) 18 mm, (-10%), and (c) 22 mm (+10%) wall thickness samples. (Courtesy of Olympus NDT Canada INC.) [Painchaud-April, G., Badeau, N. and Lepage, B., 2018, April. Total focusing method (TFM) robustness to material deviations. In AIP Conference Proceedings (Vol. 1949, No. 1, p. 200007). AIP Publishing LLC.]**

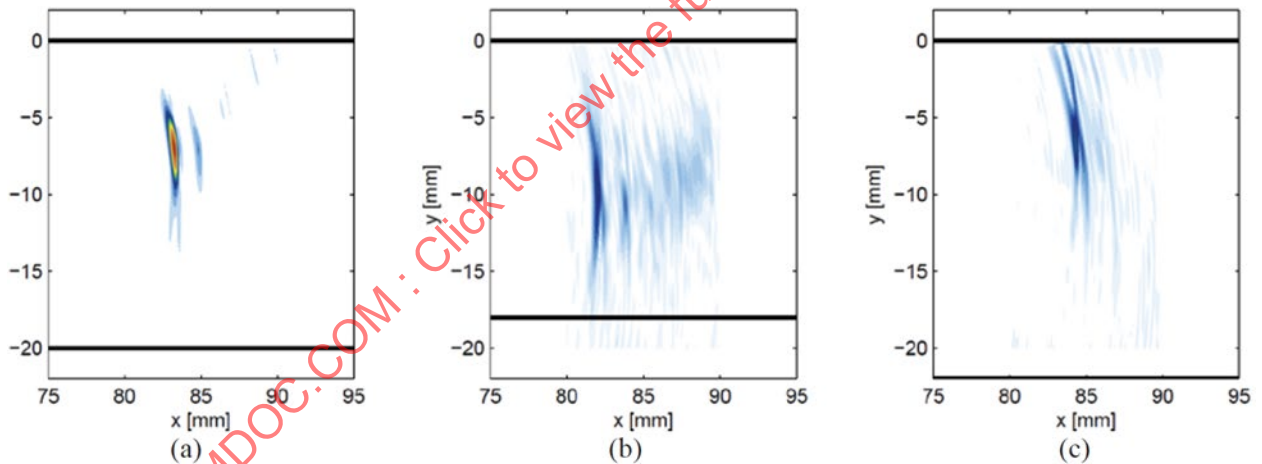


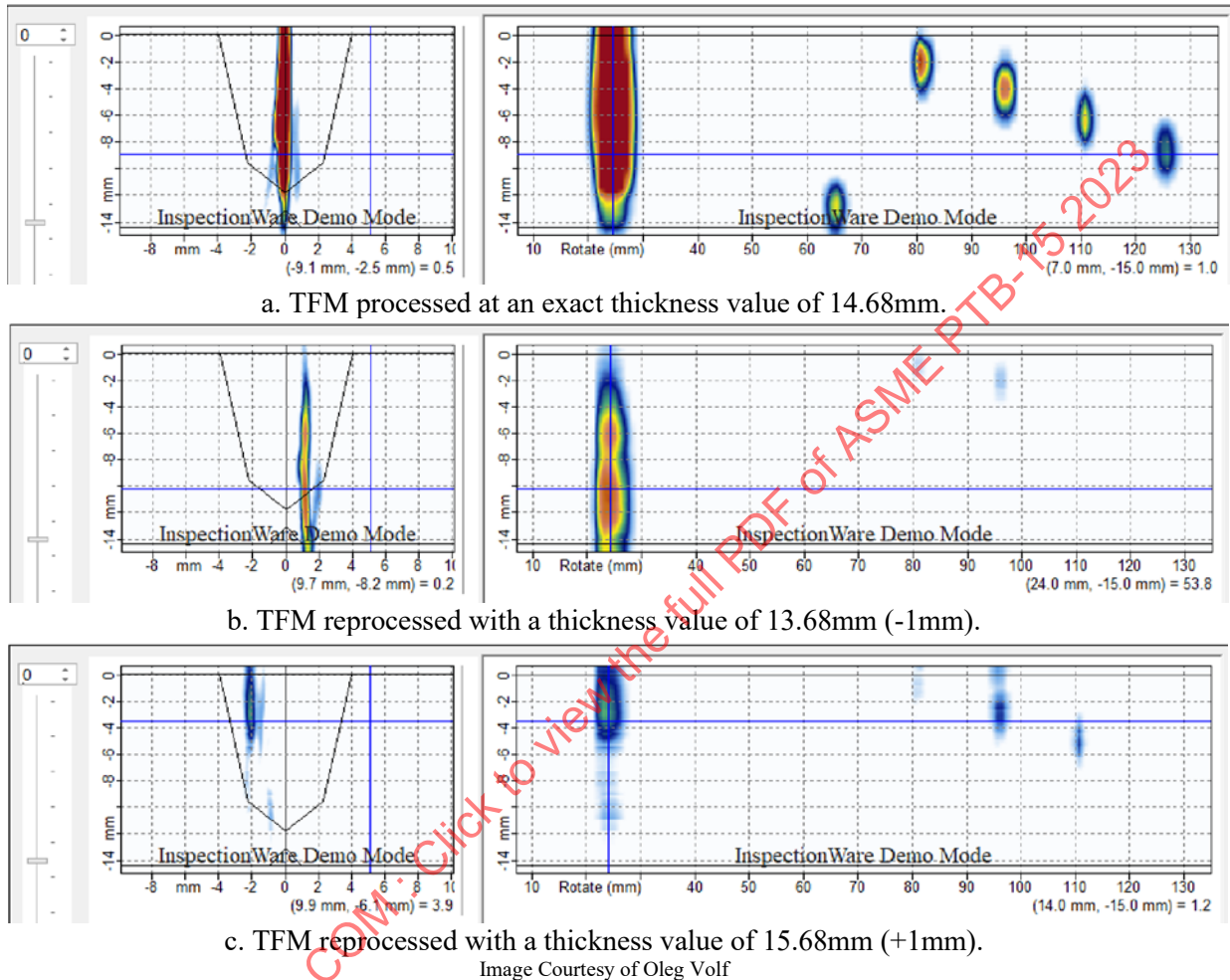
Image Courtesy of Evident Scientific, Inc.

In all three images, a similar color palette of linear scale from white to red is used, and the signals are normalized based on the maximum found on the (a) case. The back wall position is illustrated by horizontal black lines. In addition to the maximum amplitude drop for the (b) and (c) cases, the distribution of the signals has also changed.



In Figure 2-23, another case study is depicted using an aluminum calibration block having various reflectors and a known thickness of exactly 14.68mm.

**Figure 2-23: The dependency that the self-tandem modes, T-TT, and TT-TTT, in this case, rely upon having an accurate thickness value for the delay calculation**



## 2.4 Amplitude Fidelity

In general, amplitude fidelity is the preservation of analog signal information when converted to digital. Many things can adversely affect retaining amplitude fidelity, but the two main aspects are signal processing and grid resolution.

### 2.4.1 Amplitude Fidelity in Signal Processing

When performing most ultrasonic examinations, compliance with codes generally requires that the digitizing frequency be at least 5 times the nominal probe frequency. This is based on the Nyquist Theorem, or Sampling Theorem, used in numeric processing. For FMC/TFM, the amplitude fidelity requirement ensures that the amplitude of an indication remains true within 2 dB of its expected nominal value. Very often, with modern equipment the digitizing frequency is even higher at ~100 MHz. Achieving amplitude fidelity within 0.1 dB of its analog value is entirely possible.

To explain this concept further, in the following we see that the digitizing frequency is 5 times the probe frequency (as an example, on the propagation axis x, between 1.0 and 2.0  $\lambda$  units, there are five

digitalization points). This means that the space between any two digitalization points is  $1/5$  of the wavelength, or  $\lambda/5$ .

The maximum possible amplitude falls between two digitalization points. The exact amplitude height is unknown because it occurs within an unsampled portion of the waveform.

In a best-case scenario, digitalization points coincide with the maximum amplitude, and in such circumstances, an accurate measurement is obtained. A more accurate measurement may be obtained by increasing the number of digitalization points, even though there will still be some loss, it will be less. A worst-case scenario would be the maximum amplitude falls in the middle of two digitalization points, resulting in the maximum inaccuracy.

As depicted in Figure 2-24, if the space between two samples (or digitalization points) is  $\lambda/5$ , in a worst-case scenario, the measured amplitude is still within 2 dB of the nominal analog value.

**Figure 2-24: Inaccuracy in signal digitalization and Amplitude Fidelity for signal digitized at a frequency of 5 points per wavelength**

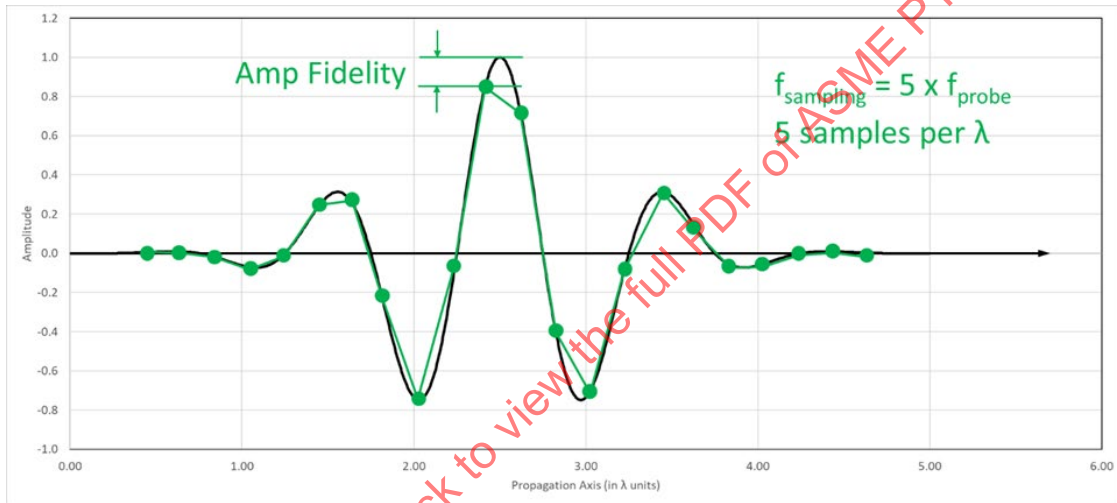


Image Courtesy of Eddyfi Technologies

Figure 2-25 illustrates a potential situation where less digitization points are used, resulting in a larger amplitude infidelity.

**Figure 2-25: Inaccuracy in signal digitization and Amplitude Fidelity for signal digitized at a frequency of 2 points per wavelength**

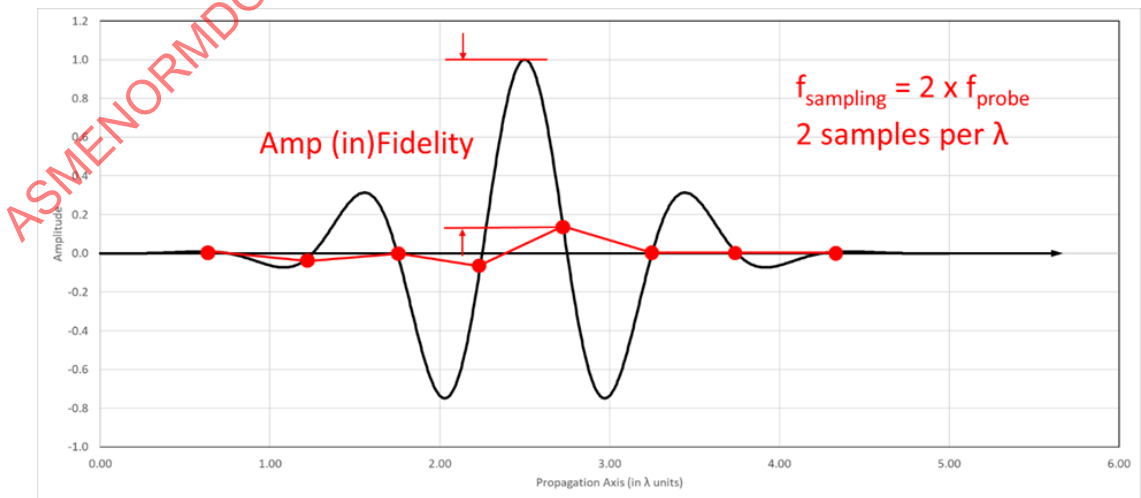


Image Courtesy of Eddyfi Technologies

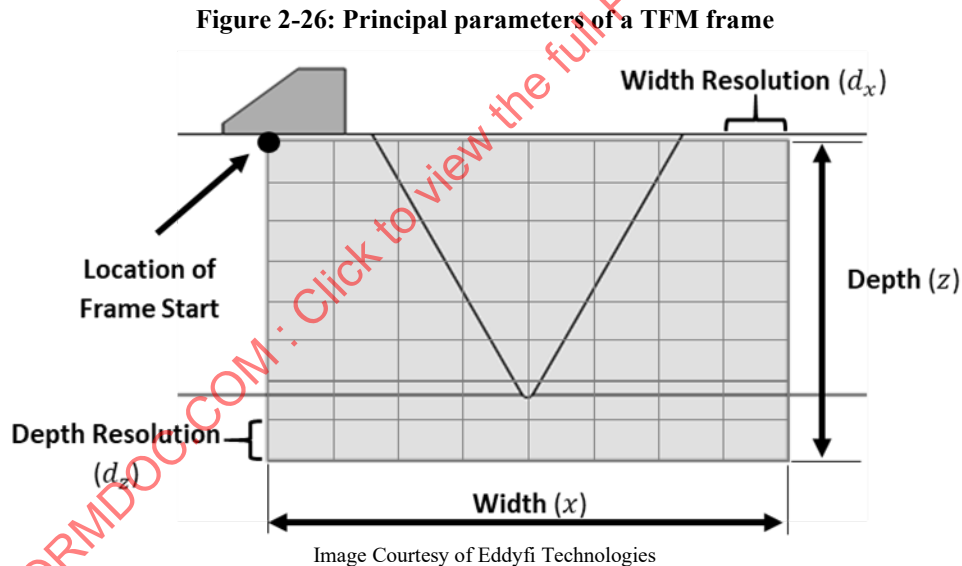
The actual position of a point over a signal is random and not predictable, and therefore, the worst condition should be assumed.

In general, it can be stated that the greater the number of digitalization points, the lower the theoretical maximum error.  $\lambda/5$  may not always be the solution for every scenario; some examinations may require more (e.g.,  $\lambda/6$ ,  $\lambda/7$ ) and some maybe even less. The trade off with signal processing is between the acceptable amount of error and the number of digitalization points. This can be limited by the processing capacity of the acquisition unit.

#### 2.4.2 Grid Construction

As previously discussed, TFM is a processing method using FMC collected data to generate an image from a predefined grid of pixels (Figure 2-26), where each pixel is computed using a dedicated intensity summation and therefore said to be focalized (synthetically) at the pixel's position. For each pixel in the grid, the TFM algorithm uses the complete probe aperture, creates appropriate delays, and performs a summation of the elementary A-scans that creates an area (grid) of pixels having a defined resolution and focus at all distances. Typically, this results in a better definition and localization of defects in all areas of the frame, due to the dispersion of energy sent in all directions, within the component.

TFM algorithms also provide the possibility of reconstructing the image using direct, indirect, and mode-converted paths in any feasible combination. Therefore, besides the frame location, size and resolution, the user should also consider the reconstruction mode to finalize the definition of a TFM setup.



Complete coverage and various defect types may require multiple reconstruction modes as well as different common probe configurations, such as pulse-echo, pitch & catch, tandem and self-tandem. Ultimately, in the analysis phase the TFM images, which are obtained from different configurations and reconstruction modes, can be merged to enhance detection and sizing capability. (See TFMi in Chapter 3)

Advantages:

The TFM algorithm has a reduced dead zone (near field) in the top section of the frame, due to the size of the individual elements, and accordingly, an increased likelihood of detection for flaws close to the scanning surface. This again is a result of the summation from multiple transmit-receive paths over larger interface areas.

Every pixel of the TFM image is synthetically focused. This can lead to optimal resolution in all points of a well-conditioned frame and consequently more accurate flaw characterization.

As compared to Phased Array Ultrasonic Testing (PAUT), setting up the TFM frame has fewer parameters that are required to be defined (e.g., focusing and beam steering parameters are not required).

Limitations:

Pixel size must be smaller than  $\lambda/5$ , which can lead to large pixel counts for thick materials and a large amount of processing.

Because each pixel is being generated by summation from all available A-scans, its angle information is not readily accessible. The concept of detection angle for indications is not valid in TFM.

### 2.4.3 TFM Grid Resolution

Amplitude fidelity can also be influenced by the TFM grid construction from the FMC data.

In respect to the TFM image reconstruction mode, the pixel size must be small enough to have at least 5 pixels per wavelength ( $\lambda/5$ ).

- (a) In the best-case scenario, the waves propagate in a direction that is parallel with the principal axes of the TFM grid. Consequently, the measurement of signal digitization remains valid because the minimum grid pitch is limited by the wavelength (velocity/central frequency) of the ultrasonic beam. Therefore, with a TFM grid pitch of  $\lambda/5$ , the maximum amplitude of the signal is detected within the -2 dB tolerance.
- (b) In the worst-case scenario, the sound propagation direction crosses the diagonal of the TFM grid. In such a case, the  $\lambda/5$  value for the TFM grid pitch would still be considered as an optimal value. The reason can be described by the fact that for a point scatterer (a scatterer having a minimum size), the -6 dB width of the detected amplitude distribution, on the beam's lateral axis, can be considered in the same order of magnitude as the minimum beam waist size, which is approximately equal to  $\lambda$ , as represented in Figure 2-27. Therefore, with a TFM grid pitch of  $\lambda/5$ , the maximum recorded amplitude of a point scatterer would still be above 90 % of its maximum signal amplitude [TFM Grid Resolution by Olympus Scientific Solutions Americas].

Previous sections of this chapter discussed using a conical beam shape having a large amount of beam spread (typical) coming from a small element. Of the two scenarios, para. (a) would be the least likely, and any grid density considerations should be given for para. (b) above. It is also worth noting that when using modern equipment, the ability to generate a very dense grid is readily available. There is, however, a point of diminishing returns as well as a tradeoff for processing times.

As examples, a 512 x 512 grid is equal to 262,144 pixels, and a 1,086 x 1,086 is about 1.2 million pixels, and so on. The user must consider things like the physical size of the ROI vs. resolution as well as what is tolerable for the actual visible representation and detection capabilities. A 512 x 512 grid covering an ROI of 0.5 in. of material is different from a 512 x 512 grid covering 2.0 in. of the same material. This is why we need to pay attention to the wavelength, ( $\lambda = v/f$ ). As a rule of thumb and a good place to start, is to set a grid spacing having a minimum of approximately 20% of the wavelength.

A major benefit of TFM is the improved image resolution, and the subsequent gain in the quality and the accuracy of the inspection image. However, TFM requires more attention given to the selection of probe frequency and the wave type, and again, the availability of high-resolution grids. The TFM resolution refers to the number of pixels (pixel count) used to reconstruct the image, and it can be configured during the image reconstruction process. For example, if a grid of 512 columns and 512 rows is used to reconstruct the image, the TFM frame will have a resolution of 512 x 512. Once the FMC data are available, the user can reconstruct the TFM image using the resolution of interest. It is possible to use the same FMC data to reconstruct multiple TFM images possessing different degrees of resolution.

As stated previously, for each pixel in the TFM frame, an image intensity from the summation of all pairs, in transmission and reception, is tuned for the center of the pixel. Therefore, increasing the TFM resolution to achieve a higher image quality comes at the expense of a higher amount of computation.

**Figure 2-27: (a) Signal amplitude distribution on the lateral axis as a result on the interaction between the beam at its minimum waist with a point scatterer and (b) Representation of the (rectified) amplitude TFM image of a hypothetical point scatterer using a common large bandwidth pulsed signal spanning  $1.5\lambda$  in length. The minimal structure to sample in amplitude is the  $\lambda/2$  oscillation [TFM Grid Resolution by Olympus Scientific Solutions Americas]**

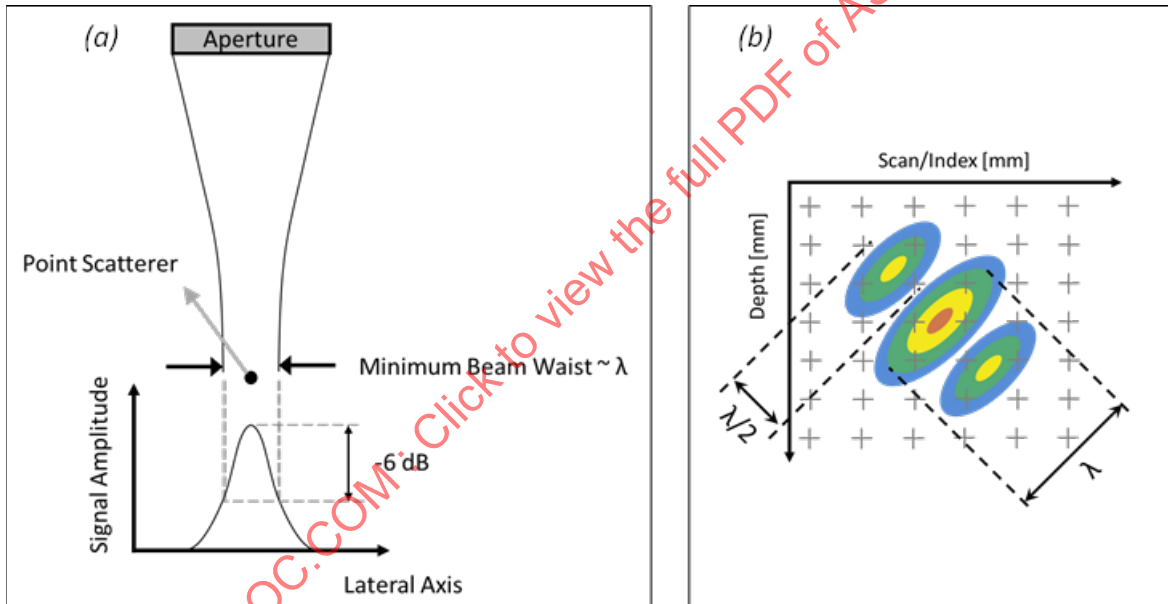
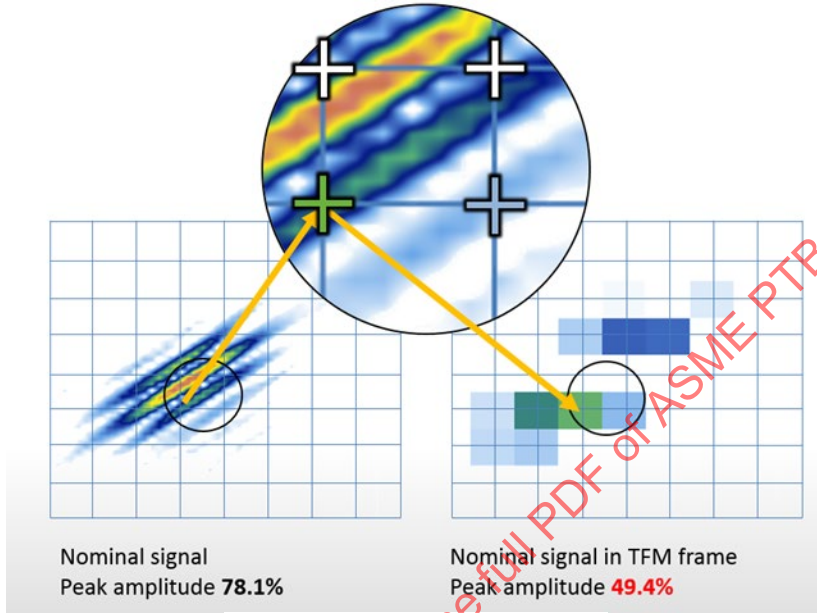


Image Courtesy of Evident Scientific, Inc.



If the  $\lambda/5$  grid pitch condition is not, or cannot be, respected, the results can lead to incomplete and/or missing information in the TFM image, which in turn makes the data unusable. Figure 2-28 provides an example illustrating the importance of pixel size in the reliability and fidelity of the reconstructed TFM image.

**Figure 2-28: Impact of the pixel size of the TFM image on the reliability and fidelity of TFM results**



The importance of respecting the number of pixels (through  $\lambda/5$  as a minimum) can determine whether the detection is **reliable**, **unreliable**, or even result in **no flaw detection**. Figure 2-29 provides an example illustrating the importance of the pixel size used for the reconstruction of the TFM image on the reliability of flaw detection. In this example, a 64-element linear array of 5 MHz on a 55LW wedge is used on a carbon steel calibration block containing 0.039in (1 mm) side drilled holes.

**Figure 2-29: Impact of pixel size used for TFM image reconstruction on the signal amplitude of an SDH. The signal amplitude changes with the TFM pixel size from (a) 87.1% FSH for  $\lambda/6$ , to (b) 42.6% FSH for  $\lambda/3$ , and finally to (c) 8.7% FSH for  $\lambda$ .**

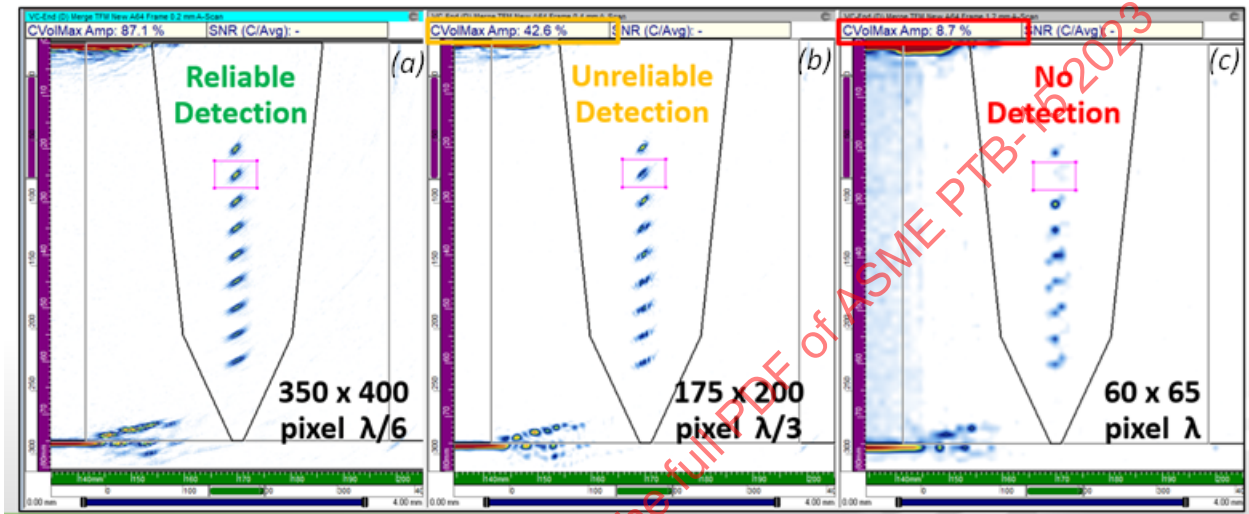


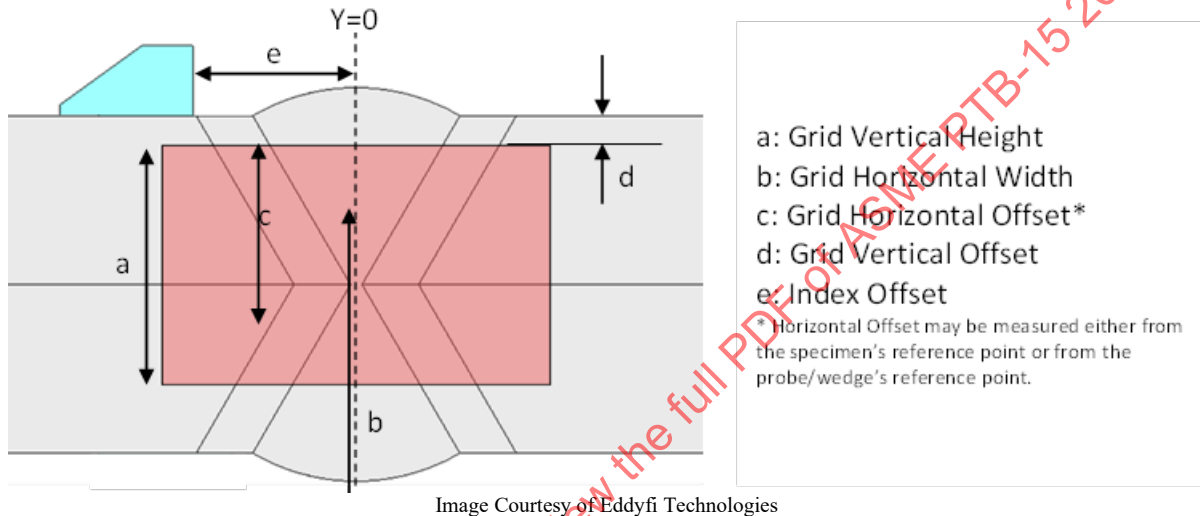
Image Courtesy of Eddyfi Technologies

## 2.5 Scan Plan

When using TFM technology, tools like ray tracing and acoustic field simulation play an important role in the design of the inspection procedure and scan plan. Most considerations for standard phased array scan plan designs can be directly applied to a TFM scan plan design. These considerations, to a lesser extent, include probe and wedge selection as well as the calculations performed to determine the optimal probe location, and in the case of Plane Wave Imaging (PWI) or Sectoral Total Focusing (STF), sometimes beam angles. In the TFM configuration, because the image information is formed in a synthetic manner, pixel by pixel, the reflectors are not insonified by real angle beams but rather by the contribution of individual elements whose acoustic field covers the reflector's position. This fact is valid for transmission and reception sequences. Therefore, a wider range of what would normally be angles will contribute to the formation of the signal generated by a reflector in the TFM image. The capability of the detection will be improved, with a "more-shots-at-the-goal" approach. However, the directivity of signals will still play an important role in the design of a proper scan plan for the TFM configuration. In short, consideration of the reflector's orientation is crucial when selecting the mode of propagation. The more perpendicular the sound is to the reflector, the better.

As stated by most codes, the preparation of scan plans to examine a specimen should be performed based on a methodology that is repeatable and standardized. In addition to the parameters that are covered in the standard PAUT scan plans, such as required examination volume coverage representation, specimen geometry, number of scan lines, and probe/wedge location, other key parameters for TFM configuration, such as image reconstruction paths and image grid density, should also be included. Compared to the standard PAUT configuration, different parameters are used to define the region of interest for TFM, see Figure 2-30.

**Figure 2-30: A schematic of the parameters required to define the region of interest in TFM configuration**



The examination volume, particularly for welds, will be as defined by a code or standard. The horizontal width of the TFM grid must be defined respecting the recommended volume coverage. For example, for a welded joint, the width and height of the grid should encompass, as a minimum, the weld and the heat affected zone (HAZ).

Naturally, the horizontal and vertical offset values, which define the position of the TFM grid, are related to the reference datum of the search unit, and the component.

The offset in the index axis defines the position of the probe/wedge as related to the index reference of the specimen. To define an optimal index offset, various parameters including the volume to be covered, the acoustic field distribution in the region of interest, and geometrical restrictions (e.g., weld cap width) must be considered.

It is essential to use acoustic field simulation and ray tracing tools to make sure that the defined grid is within the optimal acoustic field such that potential indications can be detected within the selected grid, index offset, and image reconstruction mode.

To illustrate the importance of ray tracing and acoustic field simulations, a scan plan scenario will be presented and evaluated in the following section. Note: the probe offset will be set as close as possible to the weld cap.

### 2.5.1 Defining the Specimen and the Probe

The following component in Figure 2-31 will be used:

**Figure 2-31: Schematic of the welded joint specimen for scenarios A and B**

- Carbon steel - plate butt weld
- Thickness 17.5mm
- V-bevel (30 degrees)

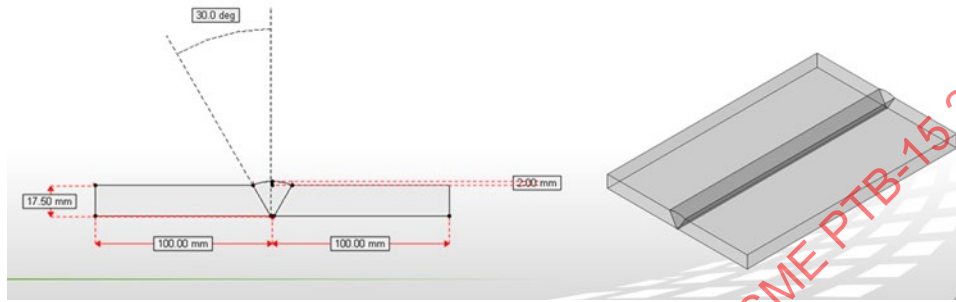


Image Courtesy of Eddyfi Technologies

The probe/wedge is as follows:

A 5-MHz array possessing the following characteristics:

- 32 elements
- Pitch 0.6mm
- Width 15.0 mm

A 55SW wedge possessing 55-degree SW nominal refracted angle (in steel)

### 2.5.2 Scan Plan for Specific Flaws

In both scenarios, the scan plan is created to detect the following flaws, shown in Figure 2-32:

Incomplete penetration

Toe crack (surface breaking)

Volumetric flaws: void, porosity, slag inclusion

Lack-of-fusion in the bevel

The inspection modes T-T and TT-TT should be sufficient to cover the weld area and the adjacent HAZ (heat-affected zone). NOTE: no single mode will detect all flaws! It is important to have a detailed understanding of the weld joint being examined. A determination of the correct modes to use for an exam must be made. For a general understanding, examples of different modes vs. flaws can be found in Appendix A.

**Figure 2-32: Acoustic paths and corresponding reconstruction modes for optimal detection of under evaluation flaws**

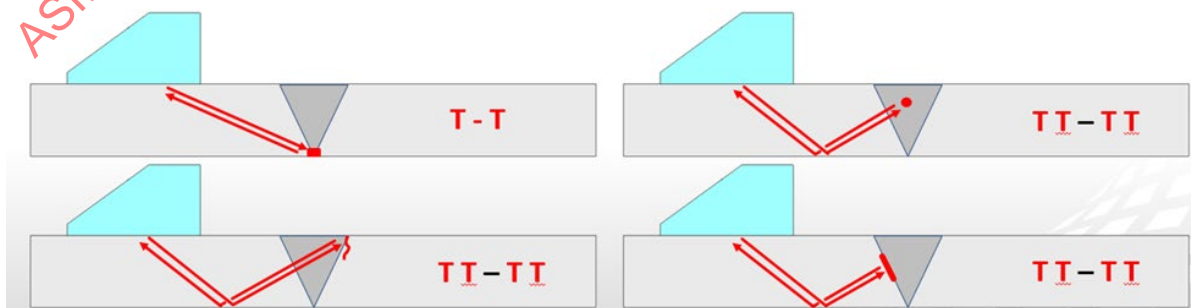
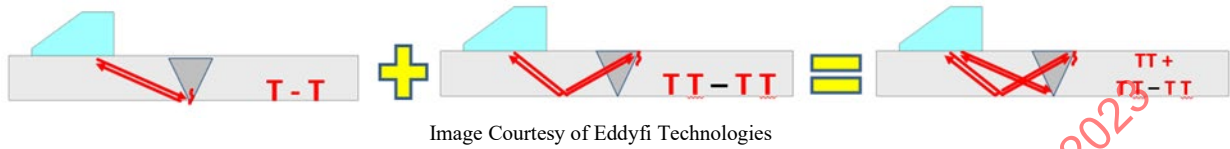


Image Courtesy of Eddyfi Technologies

### 2.5.3 Locating the TFM Grid

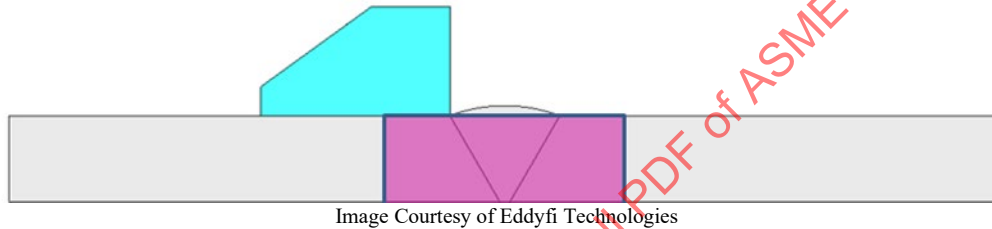
Different TFM grid locations and modes can be combined to extend coverage, as shown in Figure 2-33:

Figure 2-33: Different TFM modes required to extend the coverage



### 2.5.4 Scan Plan Design

Figure 2-34: Schematic of the applied grid



Here, the probe/wedge assembly is placed on the specimen so that the wedge's front face is as close as possible to the weld cap.

In this section, simulations and ray tracing are provided to answer the following questions:

Is this a good scan plan for the situation?

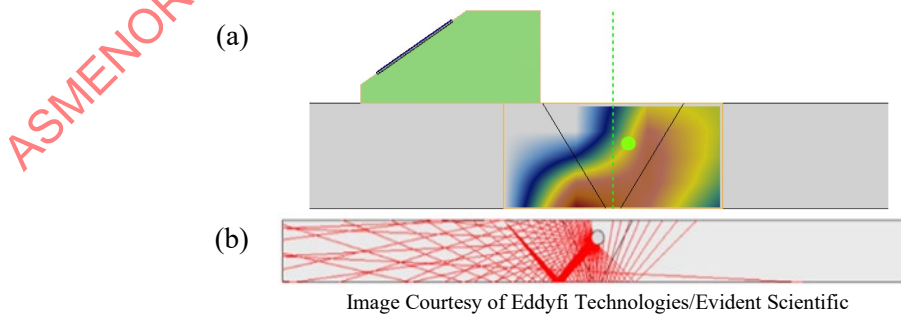
Will every flaw be detected?

What can be improved?

#### 2.5.4.1 Volumetric Flaw (Void) in TT-TT Mode

According to the beam simulation result, depicted in Figure 2-35, the acoustic field of the TT-TT mode provides a partial coverage of weld volume. The ray tracing results show a great amount of reflection at the flaw's surface with most of the acoustic energy returning to the probe/wedge contact area. In such a case, it is likely that the flaws are detected.

Figure 2-35: (a) Simulated acoustic field and (b) ray tracing results for a void located in the weld material

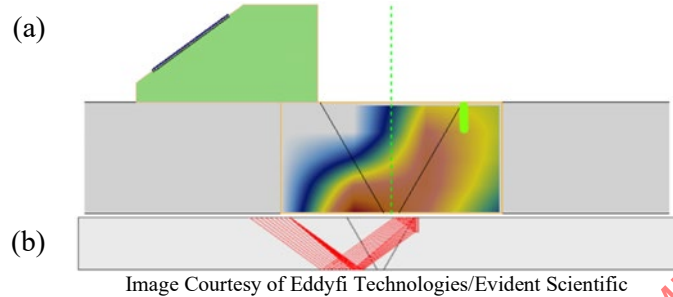




### 2.5.4.2 Toe Crack in TT-TT Mode

As depicted in Figure 2-36 (a), the reflector, representing the toe crack, is completely within the simulated acoustic field of the T-T mode. In addition, the ray tracing results show that the incident beam is reflected by the toe crack, and a significant number of reflected beams return to the probe/wedge contact area. In such a case, it is likely that the toe crack is detected.

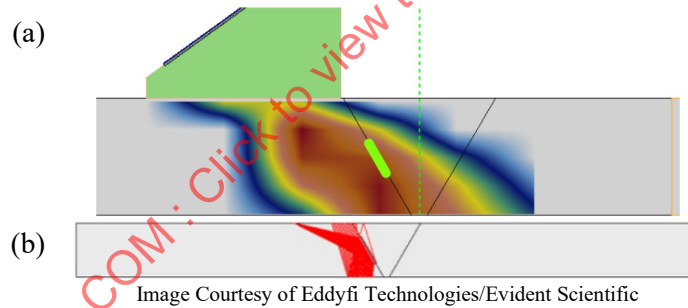
**Figure 2-36: (a) Simulated acoustic field and (b) ray tracing results for a toe crack**



### 2.5.4.3 Lack of Fusion T-T Mode

According to the beam simulation result, depicted in Figure 2-37 (a), the reflector is within the acoustic field of the T-T mode. However, as illustrated in Figure 2-37 (b), the ray tracing results show that no acoustic energy is reflected to the probe along the direct path to the reflector. In addition, the reflected acoustic energy does not return to the probe area and hence no signal is expected from the reflector.

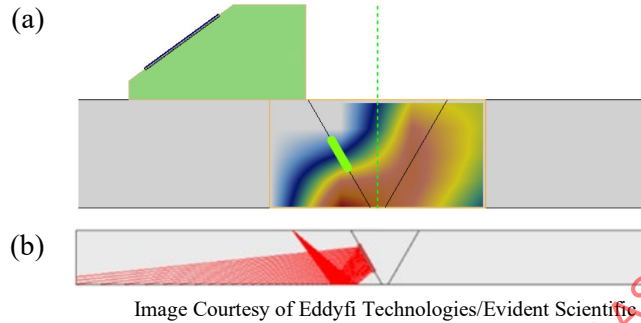
**Figure 2-37: (a) Simulated acoustic field and (b) ray tracing results for a toe crack using T-T**



#### 2.5.4.4 TT-TT Mode

According to the beam simulation result, depicted in Figure 2-38 (a), the reflector is partially covered by the acoustic field of the TT-TT mode. However, as illustrated in Figure 2-38 (b), the ray tracing results show that no acoustic energy is reflected to the probe along the rebound path. In addition, the reflected acoustic energy does not return to the probe area and hence no signal is expected from the reflector.

**Figure 2-38: (a) Simulated acoustic field and (b) ray tracing results for a toe crack using TT-TT**

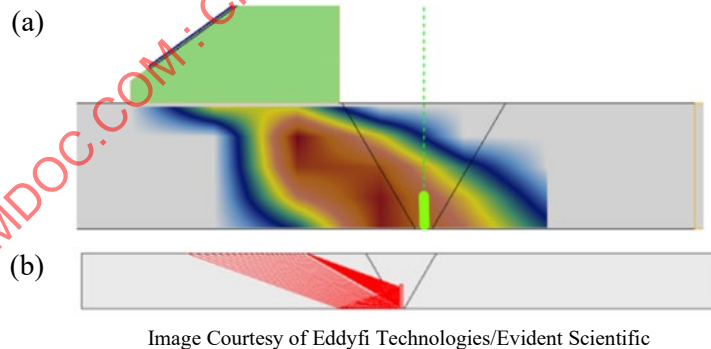


Therefore, it can be concluded that the detection of the lack of fusion is not likely in this scenario because no signal is expected from the specular reflection, either in the T-T or in the TT-TT mode.

#### 2.5.4.5 Incomplete Penetration in T-T

As depicted in Figure 2-39 (a), the reflector, representing incomplete penetration, is completely within the simulated acoustic field of the T-T mode. In addition, the ray tracing results show that the incident beam is reflected by the incomplete penetration and a significant number of reflected beams returns the probe/wedge contact area. In such a case, it is likely that the incomplete penetration is detected.

**Figure 2-39: (a) Simulated acoustic field and (b) ray tracing results for an incomplete penetration**



#### 2.5.4.6 Conclusion

In this scenario, complete volume coverage of the weld and the heat affected zone is not achievable with a single mode. Using a combination of T-T and TT-TT modes is required for exam volume coverage.

The toe crack is within the acoustic field and the geometry allows the acoustic energy to reflect back to the receiving elements of the probe.

The lack of fusion is most likely not detected in this scenario because with the TT-TT mode the area of the flaw is only marginally covered within the acoustic field. In the T-T mode, the lack of fusion is

fully covered by the acoustic field, but most importantly, the geometry of the flaw does not allow the acoustic energy to reflect back to the probe, for either mode.

For the incomplete penetration, the detection is likely since the reflector is insonified with the acoustic field and, considering the geometry, the reflected ultrasound beam returns to the probe.

A complete volume coverage of the weld and the heat affected zone could be achievable using a single offset position. However, the lack of fusion flaw was missed with the 2T and 4T modes. The change in the probe's physical location would improve the detectability of this flaw and possibly with the same coverage. If the probe were set further back away from the weld, it is likely the 4T mode would have detected this flaw, but this cannot be guaranteed due to flaw orientation. Exactly how much offset to use is a matter for simulations and ray tracing.

This section was used for the sole purpose of presenting the effects of probe position and the importance of developing a scan plan. Other modes, including self-tandem, are available for the user and may better serve against specific flaws and weld joint geometries. Please see Appendix A for more examples.

## 2.6 Fourier and Hilbert Transforms

### 2.6.1 Time vs. Frequency Representation of Signals (Fourier Transform)

The most natural way to display a signal is in the time domain. This mode of representation, also called chronogram, describes the evolution of a quantity  $x$ , usually of a physical kind, such as an electric voltage or an acoustic pressure for example, as a function of a variable that is time  $t$  expressed in seconds (s). Figure 2-40 shows three examples of time signals: an A-scan (a), an electrocardiogram (ECG) (b), and a piece of music (c).

Figure 2-40: Examples of time signals: (a) A-scan, (b) electrocardiogram (ECG)–(c) piece of music

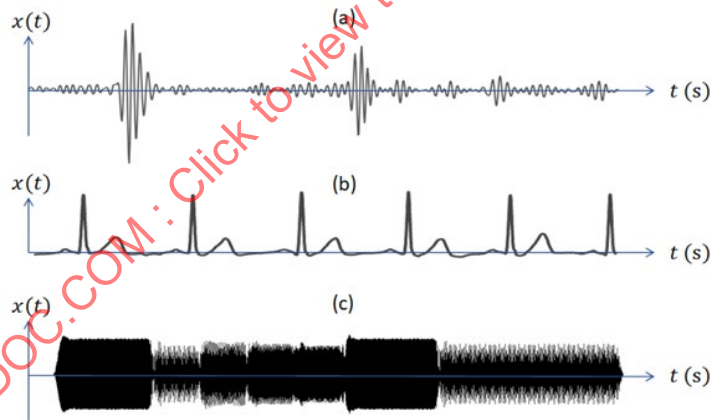


Image Courtesy of Evident Scientific, Inc.

#### 2.6.1.1 Frequency representation of signals

Another way of describing signals is to represent them in the frequency domain. In this mode of representation, the variable is no longer time, but frequency. Frequency is the number of occurrences of a repeating event per unit of time and is expressed in Hertz (Hz), which is equal to one per second (1/s) or also one event per second. For example, if a heart beats 120 times for one minute (60 s), its frequency is equal to  $120/60 = 2$  Hertz ( $F_H=2$  Hz). In the same manner, a musical note, an A for example, corresponds to 440 beats per second, i.e.,  $F_A=440$  Hz.

The widely adopted mathematical tool that allows the conversion from the time mode to the frequency mode of a signal is the Fourier Transform (FT) formalized by Equation 1:

$$x(t) \text{ FT} \leftrightarrow X(f) \quad (1)$$

FT can also be used to highlight the frequency properties of some signals. This can be illustrated by using the example of the piece of music in Figure 2-40 (c). Figure 2-41 illustrates the principle of using a FT to identify the various frequencies in the music piece, i.e., the notes. The music score shown in Figure 2-41 (a) is a sort of time-frequency representation of a musical signal. It gives a symbolic representation of a melody (here a minute from Bach). As a musician read the partition from the left to the right, the horizontal axis is the time. The vertical axis represents, for its part, the frequency of each note, here 8 notes D-G-A-B-C-D-G-G, in that order, for 5 different frequencies (392 Hz for G, 440 Hz for A, 493 Hz for B, 523 Hz for C, and 587 Hz for D). Figure 2-41 (b) shows the time representation of the musical signal, the signal if it was transmitted to a speaker via a power amplifier, for instance. Finally, Figure 2-41 (c) shows the frequency representation, also called spectrum, of the musical signal of the Figure 2-41 (b) obtained, thanks to the FT. All the notes present in the piece of music are identifiable thanks to the position of peaks in the spectrum centered on their respective frequencies. The differences in the heights of these peaks also reflect the difference in the total duration of each of the notes and thus the respective contribution of their energy to the signal.

Moreover, the FT of a real physical signal  $x(t)$  almost always leads to a complex result  $X(f)$ . But a complex signal can be described by two components, the modulus and the phase. For the sake of simplicity, only the modulus of the FT,  $|X(f)|$ , is shown in this example and is enough to identify the various frequencies.

It may be confusing to notice that the temporal representation of a signal requires positive and negative frequencies. This is related to the intrinsic nature of the FT, the theoretical demonstration of which is beyond the scope of this document. Nevertheless, it is important to remember that these negative frequencies have no physical existence, which explains why they are almost never shown on dedicated equipment, such as spectrum analyzers, for example. However, these negative frequencies play an important role in the calculation of the Hilbert transform, the principle of which is explained in the following paragraph.

Figure 2-41: Time (b) and frequency (c) representation of a piece of music signal (a)

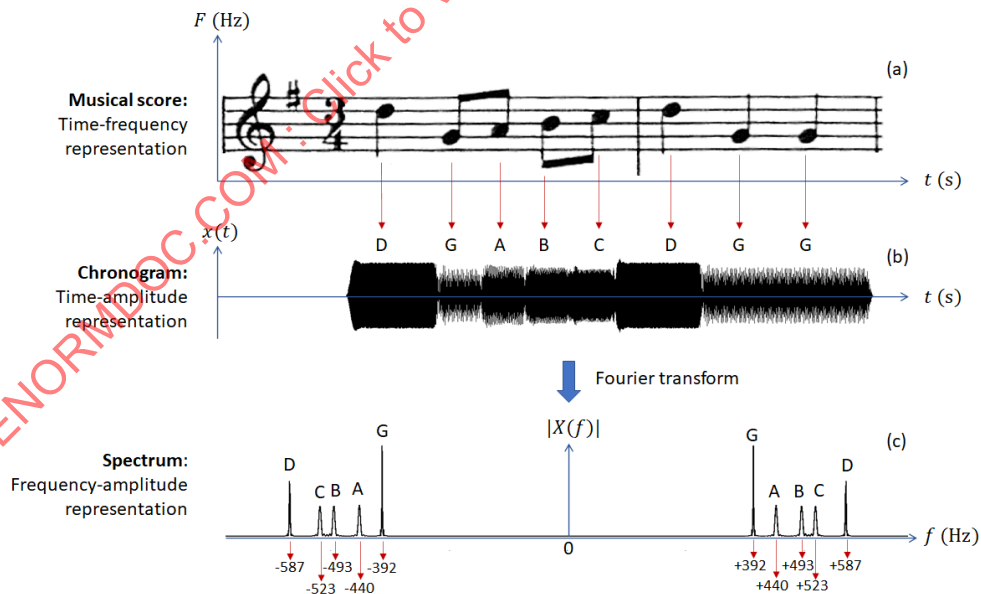


Image Courtesy of Evident Scientific, Inc.

### 2.6.1.2 Frequency Representation of A-scan

Figure 2-42 illustrates the principle of frequency description of signals applied to an A-scan. The FT computation of the A-Scan signal  $x(t)$  leads to the spectrum  $X(f)$  from which it is possible to identify some characteristics of the signal such as the central frequency, here of the order of 5 MHz, which corresponds to the central frequency of the probe used to obtain this A-Scan, as well as the frequency width, also called bandwidth, which depends on the characteristic of the probe and, to a lesser extent, on the nature of the excitation signal. The identified central frequency could be retrieved directly from the temporal oscillations seen on the time signal, thus illustrating the duality of temporal and frequency representations.

It is now possible to use the FT to introduce the notion of Hilbert transform which is used to estimate the envelope of an A-scan.

Figure 2-42: Time (a) and frequency (b) representation of an A-scan

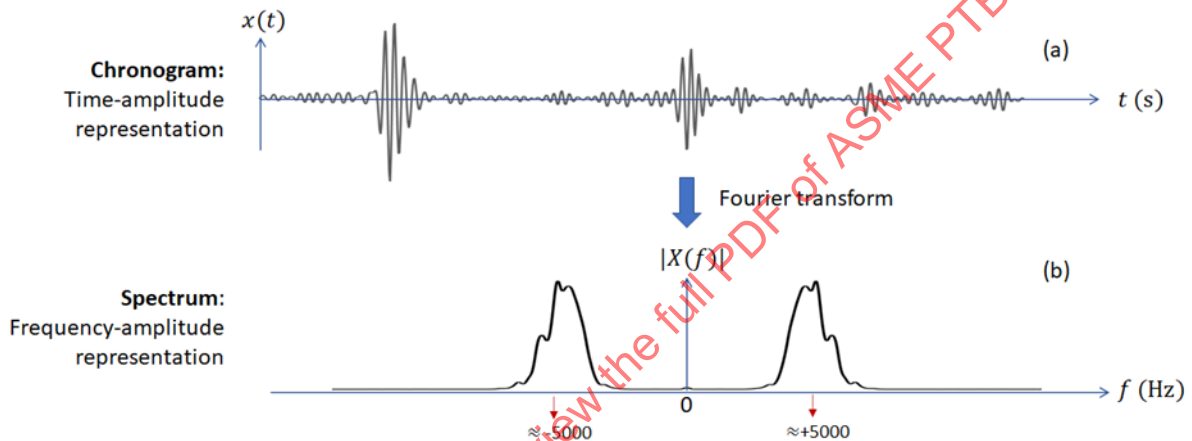


Image Courtesy of Evident Scientific, Inc.

### 2.6.1.3 Examples in NDT

The frequency representation of signals, and the Fourier transform that is associated with it, can be useful for signal processing. Two examples illustrate this point:

#### 2.6.1.4 Example #1: Signal Filtering

This kind of process can be performed directly in the time domain thanks to a convolution operation between the signal to be filtered,  $x(t)$ , and the impulse response of a bandpass filter,  $h(t)$ , and leads to the filtered signal  $x'(t)$ . This process enables lowering the noise that is present in the signal, or in other words, increasing the Signal-to-Noise Ratio (SNR), for example.

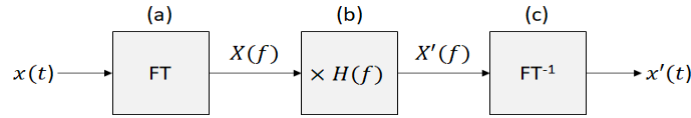
Considering the time-frequency duality, this filtering operation can be performed in an equivalent way in the frequency domain thanks to the multiplication of  $X(f)$ , the spectrum of the noisy signal  $x(t)$ , by  $H(f)$  the transfer function of the bandpass filter. This operation is given by Equation 1:

$$X'(f) = X(f) \times H(f) \quad (1)$$

where  $H(f)$  is the Fourier transform of  $h(t)$ . Then the filtered signal,  $x'(t)$ , can be retrieved thanks to the inverse Fourier transform of  $X'(f)$ . Figure 2-43 summarizes this filtering process in the frequency domain.



**Figure 2-43: Workflow of a filtering process in the frequency domain: Fourier transform of the noisy signal (a)–Multiplication of the spectrum with the transfer function of the filter (b)–Inverse Fourier transform of the filtered spectrum (c)**



As an example, Figure 2-44 shows a noisy A-Scan (a) and the filtered A-scan (b) obtained after applying the filtering procedure in the frequency domain as described in Figure 2-43. In this example, the SNR of the obtained filtered A-Scan is 6 dB higher than the SNR of the noisy A-Scan.

The Figure 2-45 illustrates all the filtering procedure:  $X(f)$ , the spectrum of the noisy A-Scan  $x(t)$  is multiplied by  $H(f)$ , the transfer function of a bandpass filter to obtain  $X'(f)$ , the spectrum of the filtered A-Scan. An inverse Fourier transform allows then to find  $x'(t)$ , the filtered A-Scan in the time domain.

**Figure 2-44: Time representation of a noisy A-Scan (a) and a filtered A-Scan (b). In this example the SNR of the filtered signal  $x'(t)$  is 6 dB higher than the SNR of the noisy signal  $x(t)$**

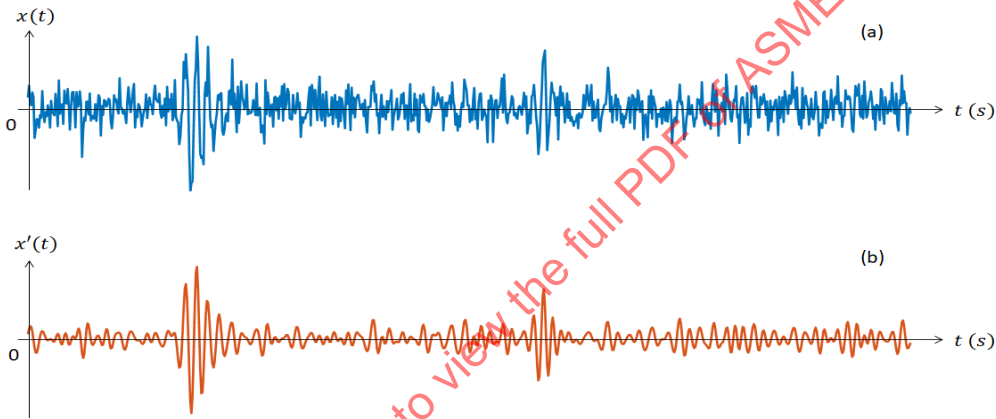


Image Courtesy of Evident Scientific, Inc.

**Figure 2-45: Frequency representation of the filtering process:  $X(f)$ , the spectrum of the noisy A-Scan of Figure 2-44(a), is multiplied by  $H(f)$ , the transfer function of a bandpass filter centered on the central frequency of  $X(f)$ , with a bandwidth  $BW$  (a). The result is  $X'(f)$ , the spectrum of the filtered A-Scan (b).**

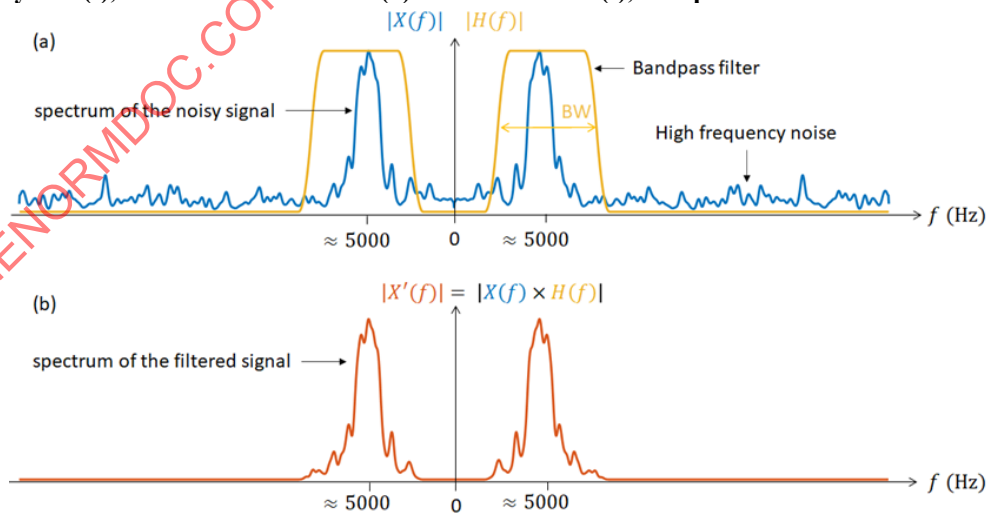


Image Courtesy of Evident Scientific, Inc.

2.6.1.5 Example #2: Probe bandwidth checking

Figure 2-46: Temporal A-Scan (a) and its spectrum (absolute value of the Fourier transform obtained thanks to a FFT and for positive frequencies only) (b)

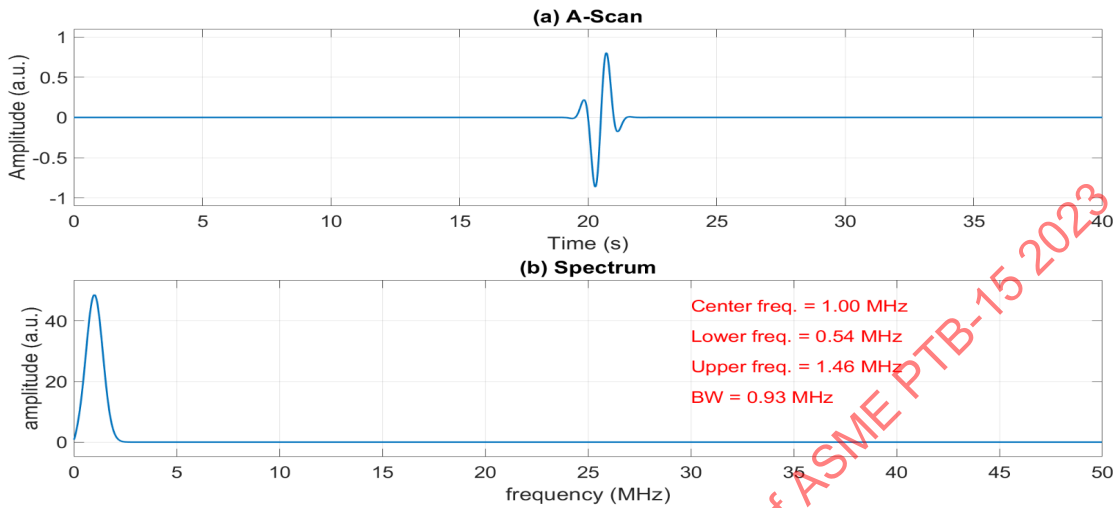


Image Courtesy of Evident Scientific, Inc.

Figure 2-47: FFT feature on the Olympus-MX2



Image Courtesy of Evident Scientific, Inc.

## 2.6.2 Hilbert Transform

### 2.6.2.1 What is a Hilbert Transform?

The Hilbert transform (HT) is a concept that demands a strong mathematical background, in particular the notion of an analytical signal, which is the complex representation (model) of signals and their spectrum. However, it is possible to have a more intuitive approach to this mathematical notion that will allow us to see its relevance in the context of signal processing in ultrasonic NDT and in TFM imaging.

The idea of a Hilbert transform can be applied to the time and frequency domains, which are the two main representations of signals. There are many different uses for performing a Hilbert transform, especially in the telecommunications field where this concept has been widely used for years. This chapter uses the example of constructing an envelope in ultrasonics for NDE.

### 2.6.2.2 How Can Hilbert Transform be Used in NDT?

In NDT, Hilbert transform can be used to get the envelope of a signal, such as an A-scan. The A-scan signals encountered in NDT have the necessary narrow-band properties to be processed with a Hilbert transform. The next paragraph will try to give an intuitive approach to this concept.

### 2.6.2.3 What is the Envelope of a Signal?

In a general way, the envelope of an oscillating signal (or narrow-band signal) is a smooth curve, also called an instantaneous amplitude, outlining its extrema (maximum peaks). Under some assumptions (e.g., no phase inversion, zero-mean narrow-band signal) it might be possible to make a rough estimate of this envelope by tracing its temporal trajectory with a pencil, connecting successively the local maximum peaks of the A-scan signal as illustrated in Figure 2-48. This work, which of course cannot be done by hand, can then be carried out by an automatic procedure using the Hilbert transform. This will be explained in the next paragraph.

Figure 2-48: Example of a zero-mean A-scan (blue) and its envelope (red)

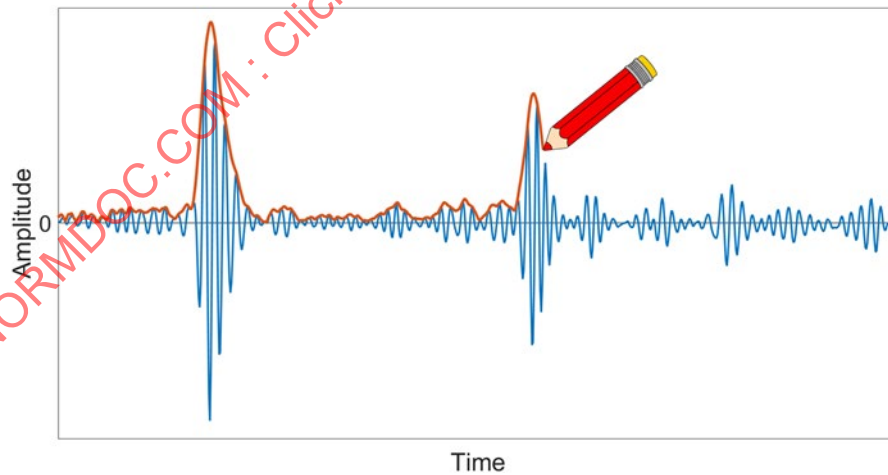


Image Courtesy of Evident Scientific, Inc.

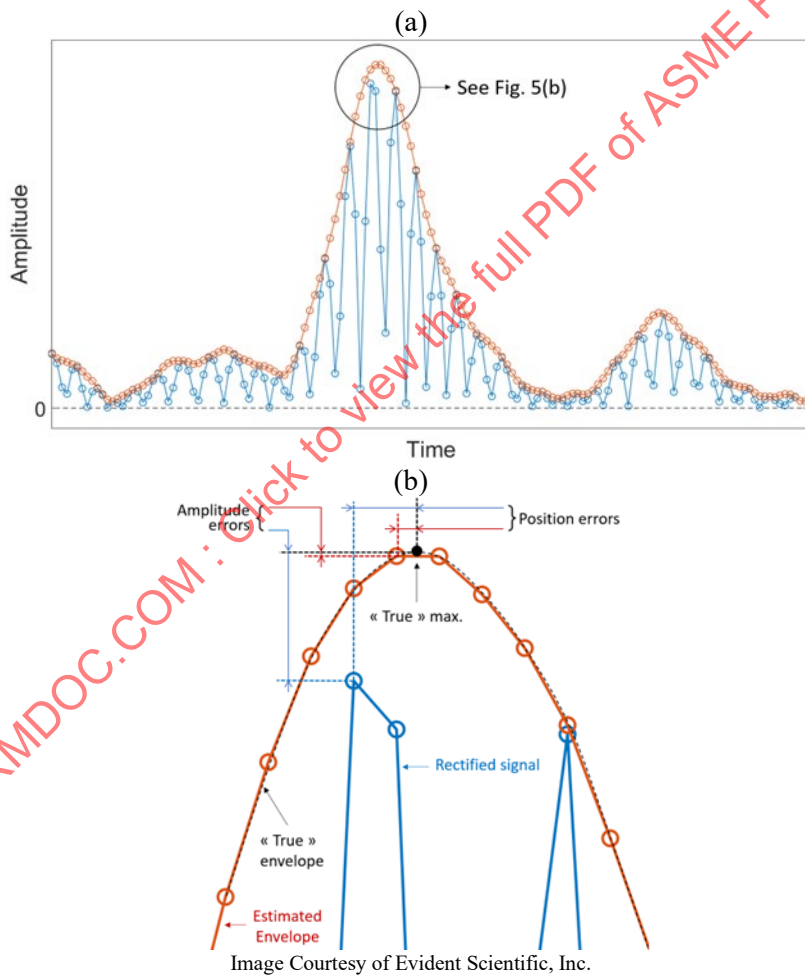
### 2.6.2.4 Why Represent an A-Scan Signal with its Envelope Rather Than in an RF Form?

The previous explanations were given with the assumption of continuous or analogue signals. In practice, and to be digitally processed, signals are sampled, i.e., they are represented by a series of samples collected at the sampling rate.

Figure 2-49 illustrates the advantage of conducting estimates of the maximum value of an indication on an A-scan as well as the temporal position of this maximum using the signal envelope instead of the rectified version. The reason for this is that the amplitude and position of a local maximum, of the rectified signal, is a function of the initial phase  $\phi_0$ , which is not the case for the envelope that is not dependent on this parameter. Estimation from the rectified signal usually leads to an under-estimation of the maximum amplitude and a bias in its position estimation. This can lead to inaccuracies when measuring thickness, for example.

One way to overcome this problem of inaccuracy would be to increase the sampling rate at the expense of greater algorithmic complexity (greater memory depth required, faster electronics, etc.). An alternative approach to improving amplitude fidelity is to apply the estimates from the envelope of the A-scan signal obtained using a Hilbert transform.

**Figure 2-49: (a) Rectified signal (A-scan) (blue) and estimated envelope of the same A-scan (red)–(b) Details showing corresponding errors of both maximum amplitude and time position estimation of the maximum amplitude**



A similar issue is encountered in the case of TFM images. As an example, Figure 2-50 shows two TFM images of the same side-drilled hole (SDH) obtained with strictly positive amplitude values and signal oscillation (i.e., rectified TFM) (Figure 2-50(a)) and with the TFM envelope applied (Figure 2-50(b)). The same defect leads to the observation of several local maximums on the rectified version but only one maximum in the case of the envelope image.

**Figure 2-50: Example of TFM images of SDH: with rectified (absolute value) TFM (a)–with TFM envelope (b). Consequently, the occurrence of having several maxima is a challenge for estimating accurately the position of the maximum value of an indication within TFM images. This issue is illustrated in Figure 2-51. This point justifies having an interest in the construction of the envelope, in the specific case of TFM images.**

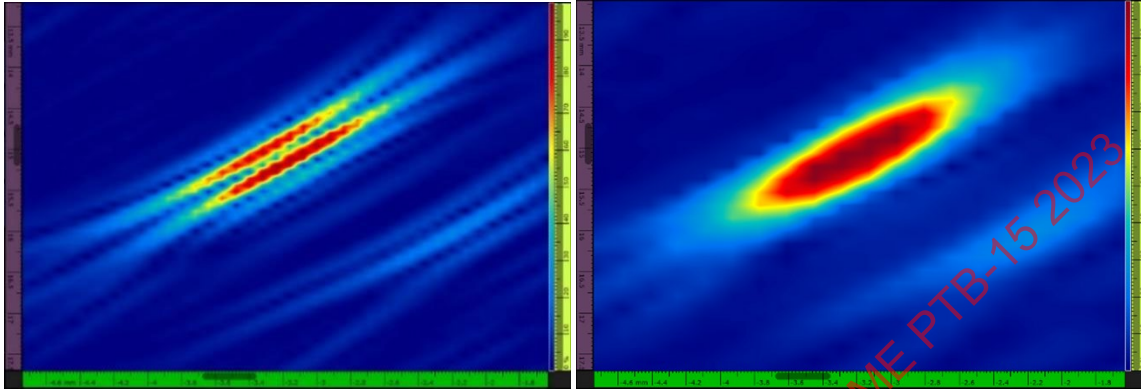


**Figure 2-51: TFM images of a defect (SDH) showing a gap in the vertical position estimation of the maxima amplitude. (a) In-phase TFM–(b) Quadrature TFM–(c) Envelope TFM**

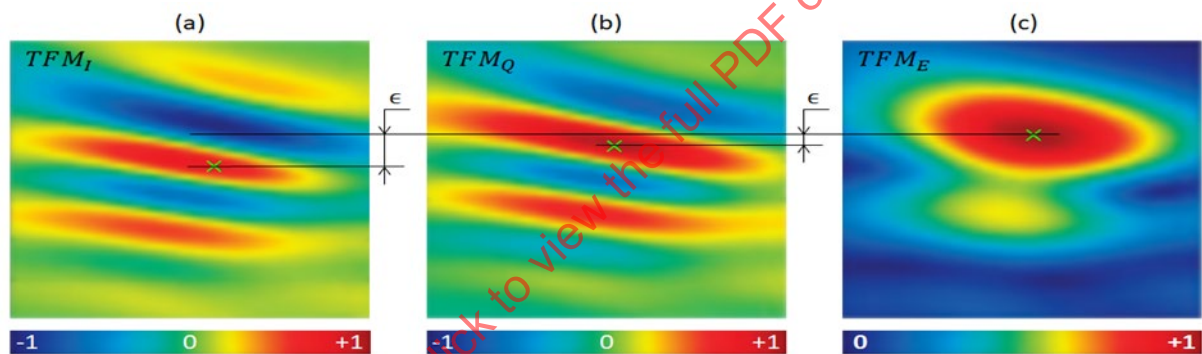


Image Courtesy of Evident Scientific, Inc.

Another benefit of using the envelope is to mask the oscillations that are present in the A-scan and in the TFM reconstructed images. These oscillations do not provide any relevant information on the defects that we are trying to identify and image. They are largely due to the frequency characteristics of the probe, i.e., the central frequency and bandwidth as well as the nature of the excitation signals. These are parameters that are totally independent of the nature of the defects found in the part being inspected.

Removing these oscillations enables a better interpretation of the TFM image. On the one hand, it avoids the ambiguity of a rectified indication for which the presence of several local maxima can be interpreted as a spatial succession of several defects while only one true defect is present in the part. For example, the TFM shown in Figure 2-50 (a) might be interpreted as two defects being imaged while only one SDH is present in the part. This allows us to concentrate on the analysis of the defects from the envelope only. This leads to a more accurate estimation of the position and amplitude, as previously demonstrated, without losing any relevant information. Figure 2-52 and Figure 2-53 further illustrate two examples of indications with and without the envelope.



Figure 2-52: Examples of an ID connected crack. TFM image on the left with envelope and on the right without envelope.

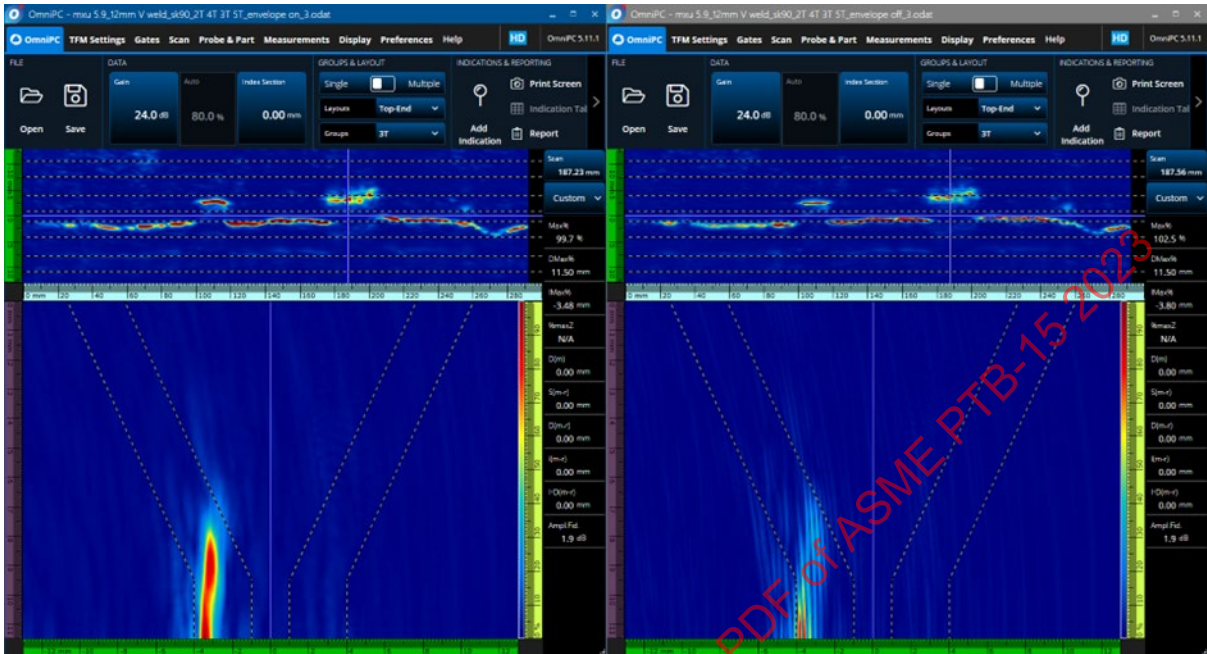


Image Courtesy of Evident Scientific, Inc.

Figure 2-53: Examples of a slag indication. TFM image on the left with envelope and on the right without envelope.

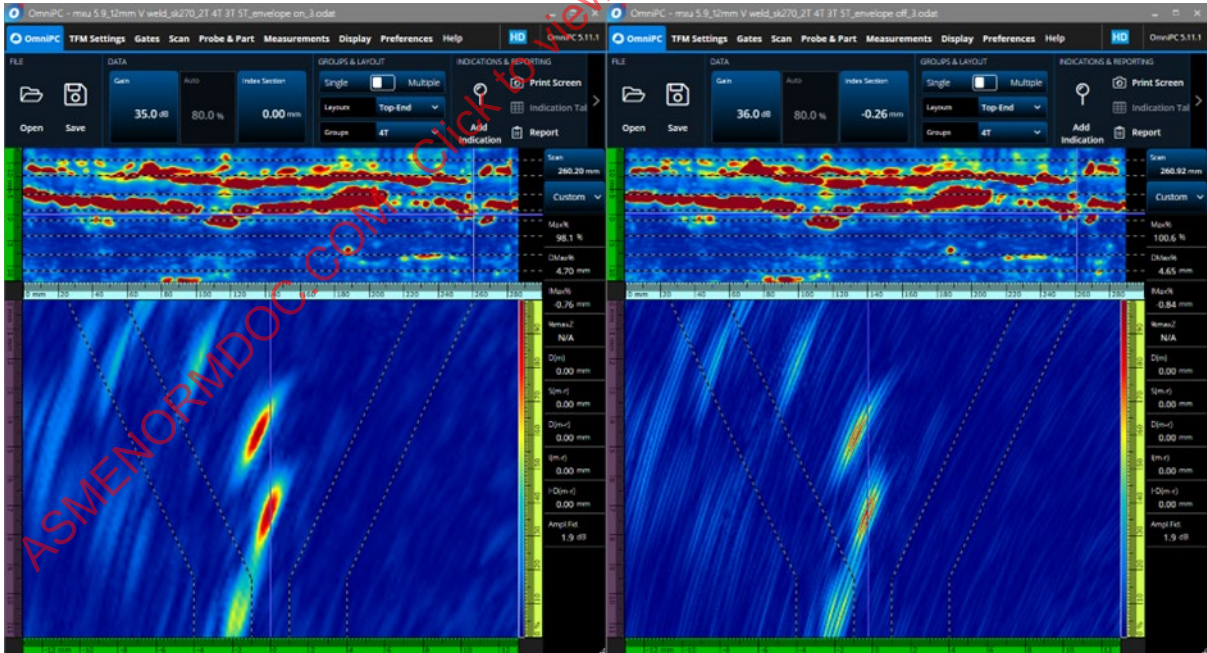


Image Courtesy of Evident Scientific, Inc.

### 2.6.2.5 Conclusions

The key points of using the envelope and the Hilbert transform for TFM image forming are as follows:

A Hilbert transform is a mathematical operator that shifts the phase of an A-scan signal  $x_Q(t) = A(t) \cdot \cos \phi(t)$  by  $-\pi/2$  radians ( $-90^\circ$ ) resulting to quadrature signal  $x_Q(t) = A(t) \cdot \sin \phi(t)$  ;

From  $x_I(t)$  and  $x_Q(t)$  it is possible to estimate the envelope  $A(t)$  of the A-scan from the simple trigonometric expression  $A(t) \approx \sqrt{x_I^2(t) + x_Q^2(t)}$  ;

The calculation of the Hilbert transform can be done either in the time domain with a Finite Impulse Response (FIR) filter or in the frequency domain with a Fourier Transform.

No information is lost by the Hilbert transform. Only the amplitude information is retained to reconstruct the envelope TFM. The phase is not used because it does not constitute relevant information.

Working from the envelope of a signal rather than its rectified version, for example, is profitable on two main aspects:

- This allows hiding the signal oscillations that do not provide relevant information to the formation of the images. These oscillations are not related to the defects we are trying to identify but to the intrinsic characteristics of the probe, essentially the central frequency and the bandwidth, and to a lesser extent to the nature of the excitation signals. No relevant information related to the defect itself is lost using only the envelope.
- The sampling rate required to achieve the same amplitude fidelity is much lower when working from the signal envelope than from the rectified signal.

In contrast to these advantages, the envelope calculation requires more computation and increases the algorithmic complexity of the TFM image reconstruction.

### 2.6.2.6 The Hilbert Transform is a Mathematical Function

This chapter would not be complete without including the following mathematics. It is important to understand that mathematics is a universal language that allows scientists and engineers to communicate. Once you work with math long enough, you start to understand that the various equations are actually tools. Just like a lathe, or mill, they do specific things, and just like tools, once you know and understand what they do, you can reach out to them for specific jobs and hopefully not hurt yourself.

In the frequency domain, the signal  $x(t)$  is represented by its Fourier transform (FT)  $X(f)$ . The Hilbert transform of  $x(t)$  is then like a filtering process expressed as:

$$X(f) HT \rightarrow H(f) \cdot X(f) \quad (2)$$

with

$$H(f) = -j \cdot \text{sgn}(f) \quad (3)$$

This is the transfer function of the Hilbert transform.

In Equation 3,  $\text{sgn}$  is the signum function that derives the sign of. As shown in Figure 2-54, a Hilbert transform can therefore be seen as an all-pass filter. An all-pass filter is a signal processing filter that passes all frequencies equally in gain (cf. Figure 2-40 (a)) but changes the phase relationship among various frequencies (cf. Figure 2-40 (b)).

**Figure 2-54: Transfer function of a Hilbert transform. (a) Modulus–(b) Phase**

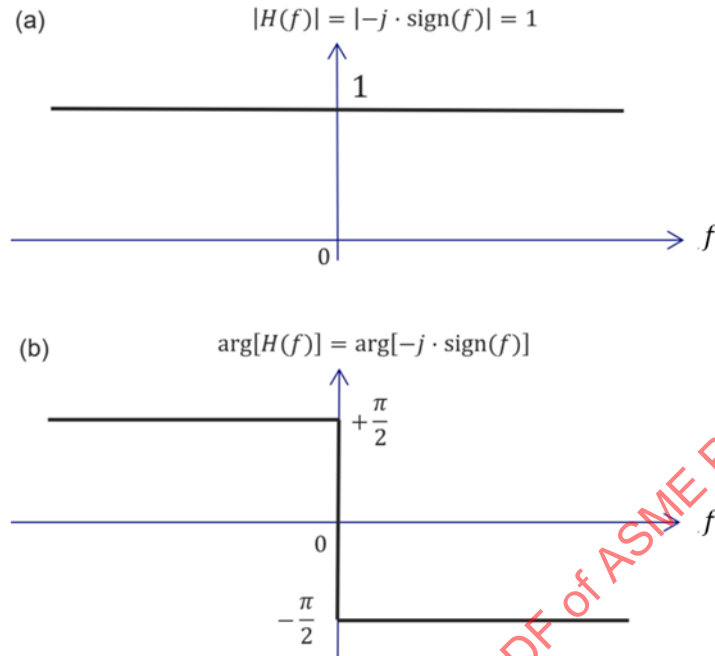


Image Courtesy of Evident Scientific, Inc.

Considering the principle of time-frequency duality, the Hilbert transform of a signal  $x(t)$  can be seen in the time domain as the convolution operation:

$$x(t) \text{ HT} \rightarrow (h * x)(t) \tag{4}$$

where  $h(t)$  is the impulse response obtained from the inverse Fourier transform of the transfer function  $H(f)$  and  $*$  is the convolution operator. This impulse response can be approximated by a linear FIR filter to implement a Hilbert transform in the time domain directly.

### 2.6.2.7 Where the Hilbert Transform May Be Used

The Hilbert transform is a mathematical tool widely used in signal analysis, particularly in the field of telecommunications. Within this domain it is often helpful to give a complex representation of narrow-band signals, i.e., with a very narrow spectrum (i.e., in Fourier space).

Then, we shall then try to associate a signal  $x_I(t)$  with its quadrature counterpart, i.e., out of phase by  $-\pi/2$  radians ( $-90^\circ$ ),  $x_Q(t)$  to form the complex signal:

$$x_a(t) = x_I(t) + jx_Q(t). \tag{5}$$

$x_a(t)$  is known as the analytical signal associated with the In-phase signal  $x_I(t)$ .

As an example, to illustrate this point in a simple manner, it is possible to use a pure sine signal of frequency  $f_0$ :

$$x_I(t) = \cos(2\pi f_0 t) \tag{6}$$

The spectrum of this signal, shown in Figure 3-41 (a), is the sum of two direct pulses centered on the frequencies  $+f_0$  and  $-f_0$ . This signal is thus narrow band. The quadrature complement of  $x_I(t)$ , i.e., out of phase by  $-\pi/2$  radians, is therefore:

$$x_Q(t) = \cos \cos \left( 2\pi f_0 t - \frac{\pi}{2} \right) = \sin(2\pi f_0 t) \tag{7}$$

$x_I(t)$  and  $x_Q(t)$  can be combined to form the analytical signal:

$$x_a(t) = \cos(2\pi f_0 t) + j \cdot \sin(2\pi f_0 t) = e^{j2\pi f_0 t} \tag{8}$$

It turns out that the signal  $x_Q(t)$  (Equation 7) can be obtained using the Hilbert transform of the signal  $x_I(t)$ :

$$x_I(t) TH \rightarrow x_Q(t). \quad (9)$$

Indeed, the representation of the signal  $x_I(t)$  in the frequency domain (see Figure 3-55(a)) is obtained by the Fourier transform  $X_I(f)$ :

$$X_I(f) = \frac{1}{2} \cdot \delta(f + f_0) + \frac{1}{2} \cdot \delta(f - f_0). \quad (10)$$

According to Equation 1, the Hilbert transform of  $X_I(f)$ , expressed in the frequency domain, is given by:

$$X_Q(f) = H(f) \cdot X_I(f) \quad (11)$$

$$X_Q(f) = -j \cdot \text{sgn}(f) \cdot \frac{1}{2} \cdot \delta(f + f_0) - j \cdot \text{sgn}(f) \cdot \frac{1}{2} \cdot \delta(f - f_0) \quad (12)$$

$$X_Q(f) = \frac{1}{2j} \cdot \delta(f - f_0) - \frac{1}{2j} \cdot \delta(f + f_0). \quad (13)$$

Equation 13 is precisely the Fourier transform of the sine signal  $x_Q(t)$  (Figure 2-55(b)).

Finally, the Hilbert transform may be seen as an operator that enables narrow-band signals to be shifted in phase by  $-\pi/2$  radians. The following paragraphs will demonstrate the value of calculating the signal envelope in the context of NDT.

**Figure 2-55: Pure sine signal spectrum. (a) cosine—(b) sine**

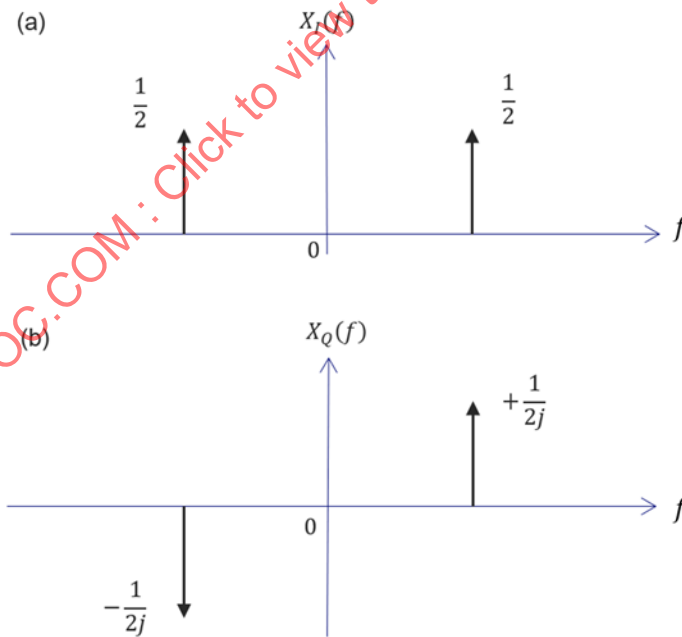


Image Courtesy of Evident Scientific, Inc.

### 2.6.2.8 How the Hilbert Transform Can Be Used to Extract the Envelope of a Signal

The A-scan shown in Figure 2-42 is an oscillating signal, i.e., a narrow-band signal (also called a quasi-sinusoidal signal). It can be modeled with the mathematical expression:

$$x_I(t) = A(t) \cdot \cos(2\pi f_0 t + \varphi_0) \quad (14)$$

where  $f_0$  is the central frequency,  $\varphi_0$  the phase at time  $t=0$ , and  $A(t)$  the instantaneous amplitude, i.e., the envelope. It is therefore possible to identify the argument of the sinusoidal function as the instantaneous phase of the A-scan signal:

$$\phi(t) = 2\pi f_0 t + \varphi_0. \quad (15)$$

However, it is not possible to recover the envelope  $A(t)$  directly from  $x_I(t)$ .

On the same principle as for a pure sinusoidal signal, and because  $x_I(t)$  is still a narrow-band signal, its Hilbert transform leads to a  $-\pi/2$  phase-shifted (quadrature) version which an approximation is given by:

$$x_Q(t) \approx A(t) \cdot \sin(2\pi f_0 t + \varphi_0). \quad (16)$$

**Figure 2-56: Detail of the In-phase signal  $x_I(t)$  (original A-scan, cf. Figure 2-42) (blue), quadrature component  $x_Q(t)$  obtained thanks to a Hilbert transform (green), and the envelope  $A(t)$  (red).**

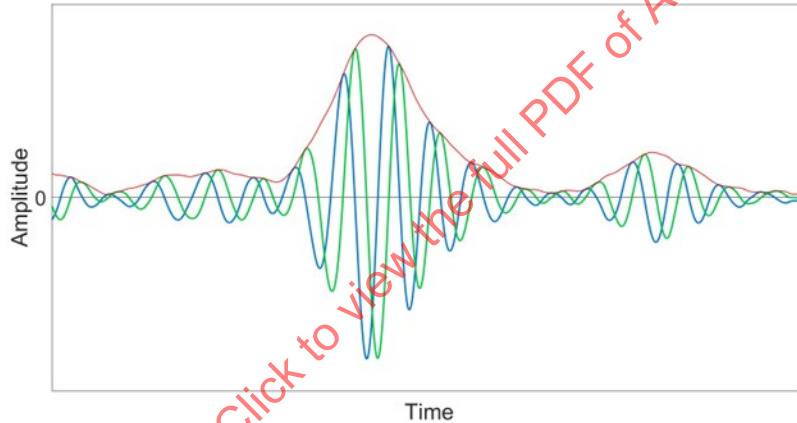


Image Courtesy of Evident Scientific, Inc.

Figure 2-56 shows both  $x_I(t)$  and  $x_Q(t)$ , and the envelope  $A(t)$ .

From Equations 17 and 18, an estimation  $\hat{A}(t)$  of the envelope  $A(t)$  can be calculated with the expressions:

$$\begin{aligned} \hat{A}(t) \approx A(t) &= \sqrt{x_I^2(t) + x_Q^2(t)} \\ &= \sqrt{[A(t) \cdot \cos(2\pi f_0 t + \varphi_0)]^2 + [A(t) \cdot \sin(2\pi f_0 t + \varphi_0)]^2}, \quad (17) \end{aligned}$$

$$\hat{A}(t) \approx A(t) \cdot \sqrt{[\cos(2\pi f_0 t + \varphi_0)]^2 + [\sin(2\pi f_0 t + \varphi_0)]^2}. \quad (18)$$

remembering the trigonometric identity  $\sqrt{(\cos \alpha)^2 + (\sin \alpha)^2} = 1$ . It can be noted that a Hilbert transform allows to extract not only the envelope  $A(t)$  of an A-scan, but also, its instantaneous phase  $\phi(t)$  thanks to the expression:

$$\phi(t) \approx \text{atan} \left[ \frac{x_Q(t)}{x_I(t)} \right] \quad (19)$$

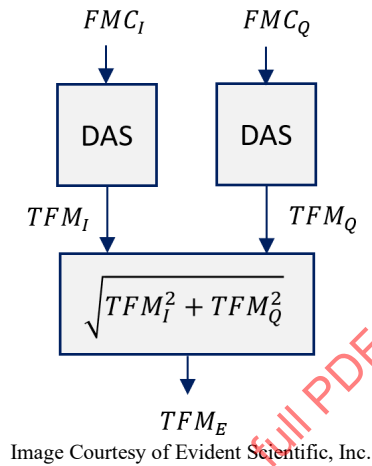
The latter is especially important for Phase Coherence Imaging in TFM, for example.



### 2.6.2.9 How the Hilbert Transform Can Be Used for TFM Reconstruction

Any TFM image reconstruction scheme using an envelope adopts the same principle as above. Each A-scan that composes the raw FMC (in-phase FMC,  $FMC_I$ ) is then phase shifted by  $-\pi/2$  radians and leads to the quadrature  $FMC_Q$ . The Delay and Sum (DAS) algorithm, which allows the reconstruction of a TFM, is then applied successively to the two quadrature FMCs to form two TFMs, also in quadrature, i.e.,  $TFM_I$  and  $TFM_Q$ . It is then possible to recover the enveloped TFM,  $TFM_E$ , from  $TFM_I$  and  $TFM_Q$ , as shown in Figure 2-57.

Figure 2-57: Computation of the envelope TFM from two FMCs in quadrature



Note: Another alternative way to compute the TFM with envelope would be to use directly the 2D Rietz transform from  $TFM_I$ . However, the corresponding algorithm leads to a high complexity and is not generally used.

### 2.6.2.10 Computing a Hilbert Transform

Two main ways can be used to compute the Hilbert transform: In the frequency domain and in the time domain thanks to a FIR filter that can approximate a Hilbert transform.

In the frequency domain the Hilbert transform can be computed directly from Equation 1. However, in TFM imaging, it is not the result of the Hilbert transform as such that is of interest, but rather the estimation of the envelope. The latter is derived by calculating the modulus of the analytical signal, of which the quadrature component (obtained from the Hilbert transform of the In-phase component) is only one element.

However, the analytical signal can be calculated directly in the frequency domain. It can be shown that  $X_a(f)$ , the spectrum of the analytical signal  $x_a(t)$ , associated with the signal  $x_I(t)$ , is the one-sided form (i.e., for which all components at negative frequencies are equal to zero) of  $X_I(f)$ . The spectrum of the signal  $x_I(t)$ , as stated by equation 19:

$$X_a(f) = 2 \cdot \epsilon(f) \cdot X_I(f) \quad (20)$$

Figure 2-58 illustrates the principle of cancelling the spectral components at negative frequency of a signal  $X_I(f)$  to produce its analytical version  $X_a(f)$ .

**Figure 2-58: (a) Modulus of the In-phase signal spectrum – (b) filtering function – (c) Modulus of the analytical signal spectrum**

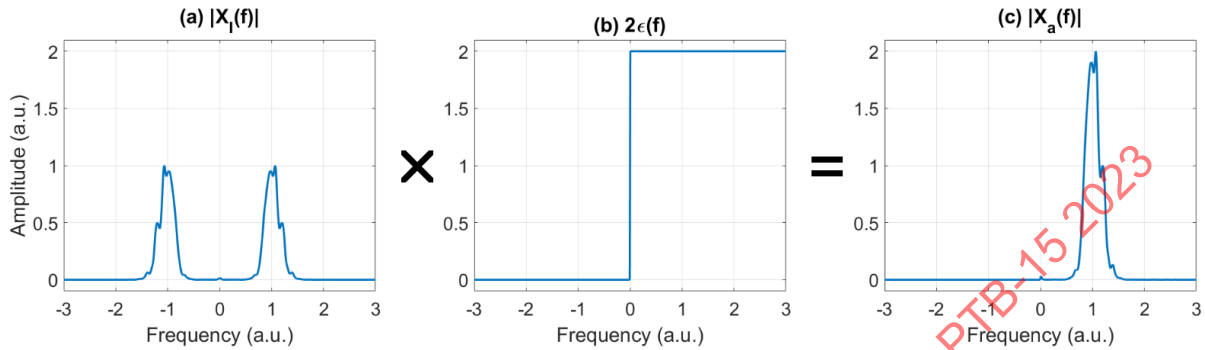


Image Courtesy of Evident Scientific, Inc.

From an operational point of view, the calculation of the envelope of a TFM image,  $TFM_E$ , from the FMC can be summed up in the operations illustrated in Figure 2-60 (a).

It is also possible to calculate a time-domain Hilbert transform from the ideal impulse response  $h(t)$  of the transfer function of  $H(f)$  given by Equation 21. As  $h(t)$  and  $H(f)$  being related by the Fourier transform and its inverse:

$$h(t) \text{ FT } \leftrightarrow H(f) \tag{21}$$

The quadrature component,  $x_Q(t)$  is then obtained by a convolution operation described by Equation 22 It is expressed as:

$$x_Q(t) = (h * x_I)(t) \tag{22}$$

After sampling, an approximation of  $h(t)$  can be obtained thanks to a digital Finite Impulse Response (FIR) filter. As an example, Figure 2-59 shows this impulse response for a type III generalized linear phase discrete Hilbert transformer of order 20 (i.e., 21 coefficients). In such approximation a  $+\pi/2$  phase shift, needed to obtain the quadrature component from the In-phase component, is exactly realized.

Figure 2-60 (b) illustrates, in a functional way, the implementation of the computation of the envelope of the TFM envelope from the FMC.

For more details on how to synthesize an FIR filter for the Hilbert transform approximation in the time domain, it is suggested to consult the reference by Oppenheim and Shafer [9], [10] [11]

Figure 2-59: Example of an impulse response for a type III generalized linear phase discrete Hilbert transformer of order 20

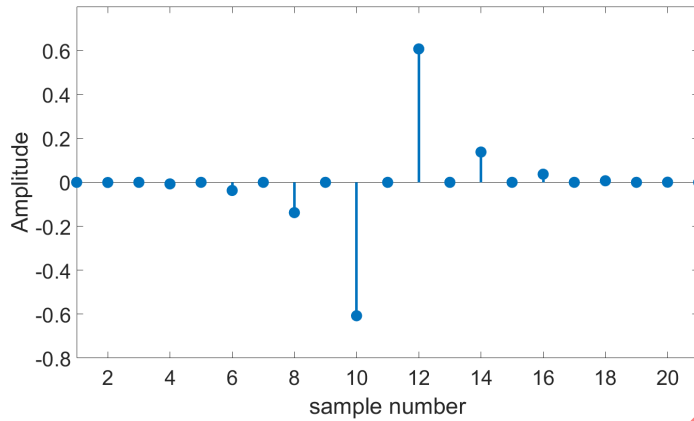
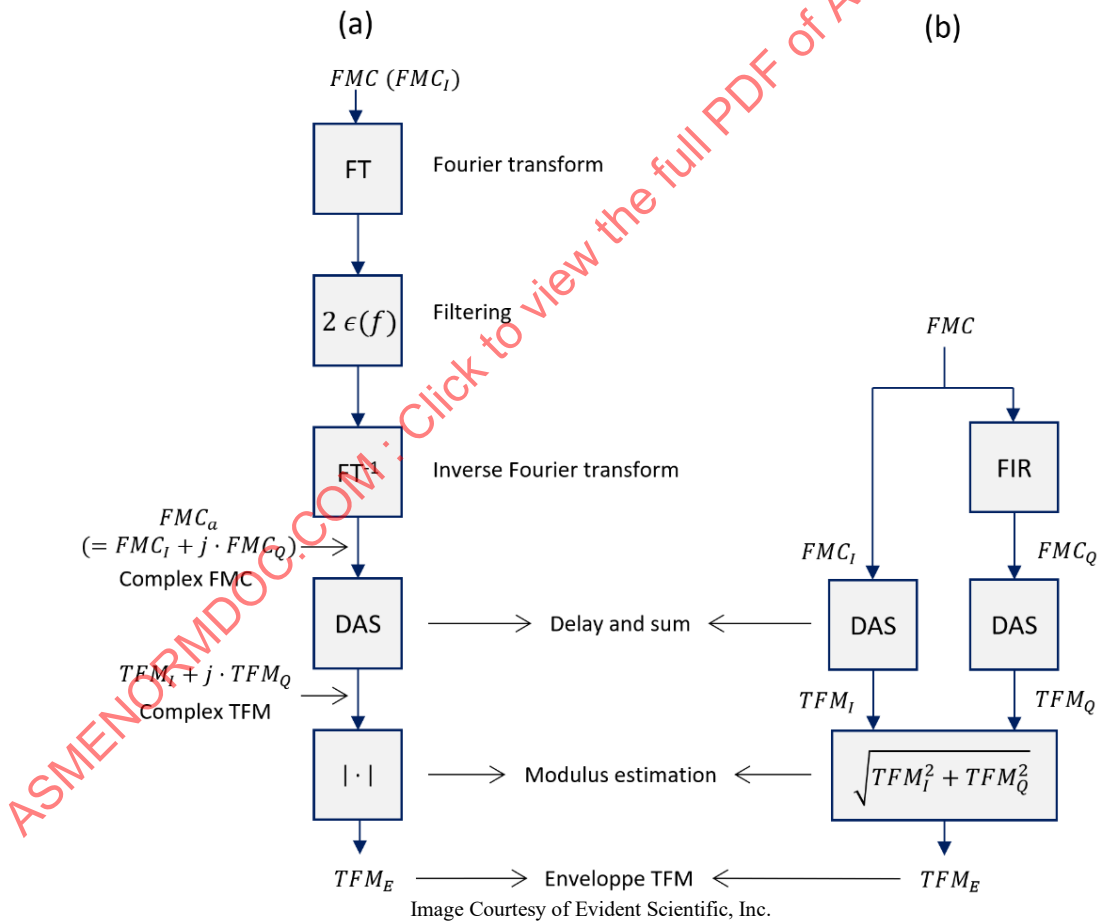


Image Courtesy of Evident Scientific, Inc.

Figure 2-60: Implementation of the TFM envelope computation (a) In the frequency domain–(b) In the time domain



### 3 TFMS

#### 3.1 Synthetic Aperture Focusing Technique

The NDE technology known as Synthetic Aperture Focusing Technique (SAFT) comes from radar technology of the late 1960's. Some of the earliest work was being done in the early to mid-1970's (Fredrickson 1974). Later SAFT technology was studied by the US Government as a possible way to inspect the heavy walled nuclear reactor vessels. The following was compiled from NUREG papers (NUREG CR 3625-Busse 1984, NUREGCR4583V2-Doctor 1987, NUREGCR5075-Hall 1988) and is a public record.

##### 3.1.1 Data Collection

Several data collection schemes can work with SAFT processing, some of which are not so different from the techniques we use today in what would be considered more "modern" FMC methods. Notably, at the time, there were 3 main data collection techniques described. Each has their own pros and cons. They were Plane Wave, Zero Offset, and Complete Data Set. Additionally, the early work explored different pulse echo, pitch catch, dual, and tandem techniques, using either immersion or direct contact. All of which can produce the required data. Because there are so many different data collection techniques, for the purpose of this manual we will only consider one of the older more "unique to SAFT" data collection methods. Zero Offset uses a single element transducer in pitch-catch.

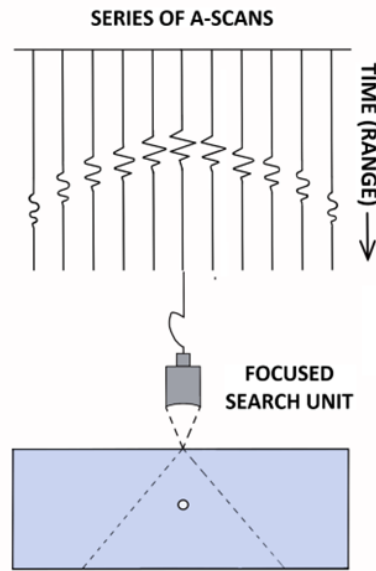
The title, Synthetic Aperture Focusing Technique, is very descriptive of the process. The image the user desires to create would require a large enough aperture that it would be impossible, or at least improbable, to accomplish. Instead, the user will employ a much smaller aperture to construct, or otherwise "synthetically" create a larger one.

To describe this technique, let's start with an analogy using radar. If one was wanting to take an aerial survey of a section of land that was 100KM<sup>2</sup>, disregarding modern satellite technology of course, one would load radar equipment onto an airplane, and fly a back-and-forth pattern across the landscape. The radar would transmit and receive signals at predetermined intervals, which in turn would produce a series of "shots" or pictures in a grid like fashion. The individual shots could then be assembled into a larger map, which would represent the entire 100KM<sup>2</sup> area, and therefore create a large enough aperture, synthetically.

The above analogy is the most basic formation of a synthetic aperture and is no different from how we accomplish it in NDE. The NDE user would select a single element transducer, using transmit and receive in pulse-echo, and then follow a predetermined grid, using encoders for location and to pulse on position, across the surface of the component. A focus would also be applied, by lens or firing sequence, such that the sound will be focused, at the entry surface of the component, or otherwise having a defocusing effect within the part. The firing pattern itself would be established depending upon things like component geometry, desired lateral resolution, predicted flaw size, and so on.

As depicted in Figure 3-1, the search unit is scanned over the surface of the object. A series of A-scans are recorded for each position of the search unit. Each point like reflector produces a collection of echoes within the recorded A-scans. This collection lies on a hyperbolic curve, the apex of which is entirely dependent upon the depth of the point like reflector. The relationship of the curve to the actual depth of the reflector within the component makes it possible to reconstruct an image from the raw data.

Figure 3-1: Reproduced from NUREG CR 3625-Busse 1984



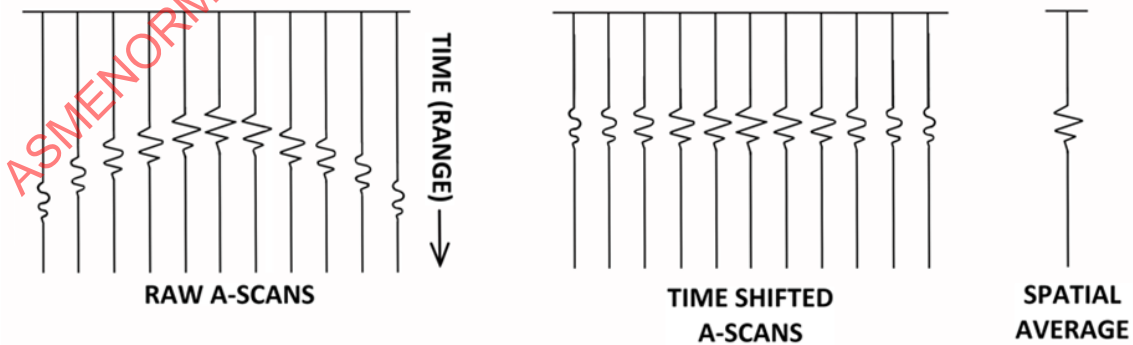
U.S. Nuclear Regulatory Commission NUREG CR-3625

### 3.1.2 Post Processing

After all the data has been collected, of which any given technique (e.g., dual, pitch catch, angle, tandem etc.) may be used, all the A-scans then must be processed by sorting, comparing, averaging, transforming, reassembling, etc., to generate an image of the component. This is a job for an algorithm. We have already covered what an algorithm is previously in this book, but to reiterate, it is simply an iterative quarry to the data and often described by a mathematical expression. A simple procedure, with specific steps, to provide the desired result of constructing the image.

The hyperbolic curve is predictable given the component velocity, and the depth of the indication. The actual depth of the reflector being equal to the apex of this curve (Figure 3-1). Being predictable, the curve can also be corrected by time shifting the A-scans, and then a summation takes place to create a coherent point of data. Assemble all the points of data together, and you have built the image. Figure 3-2 is a visual representation of the process.

Figure 3-2: Reproduced from NUREG CR 3625-Busse 1984



U.S. Nuclear Regulatory Commission NUREG CR-3625

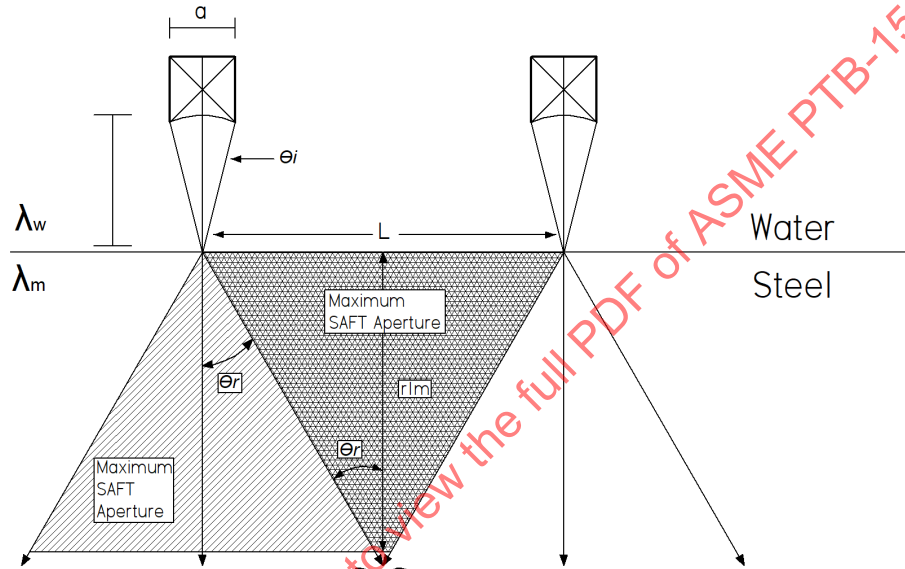
### 3.1.3 Resolution

As with any imaging system comprised of a series of components, the weakest link will dominate the systems resolution. For SAFT, there are two main elements that determine resolution: 1) The synthetic focused aperture (scanning resolution) and 2) the transducer or probe (beamspread). Figure 3-3 provides the illustration.

$$\text{SAFT Lateral Resolution} = \frac{(\lambda_m)(r_{1m})}{2L}$$

$$\text{Probe Lateral Resolution} = 1.22 \frac{(\lambda_w)f}{a}$$

Figure 3-3: Reproduced from NUREG CR 3625–Busse 1984



U.S. Nuclear Regulatory Commission NUREG CR-3625

Because the flaws have a greater depth, it is possible the SAFT resolution could become larger than the probe resolution, therefore the SAFT resolution determines the system resolution. For shallow flaws the probe resolution dominates the lateral resolution. By equating the above formulas, we can determine the depth at which the crossover occurs in the component. This is the  $r_{1m}$ .

$$R_{1m} = 2.44 \left( \frac{\lambda_m}{\lambda_w} \right) \left( \frac{a}{f} \right) L \quad (23)$$

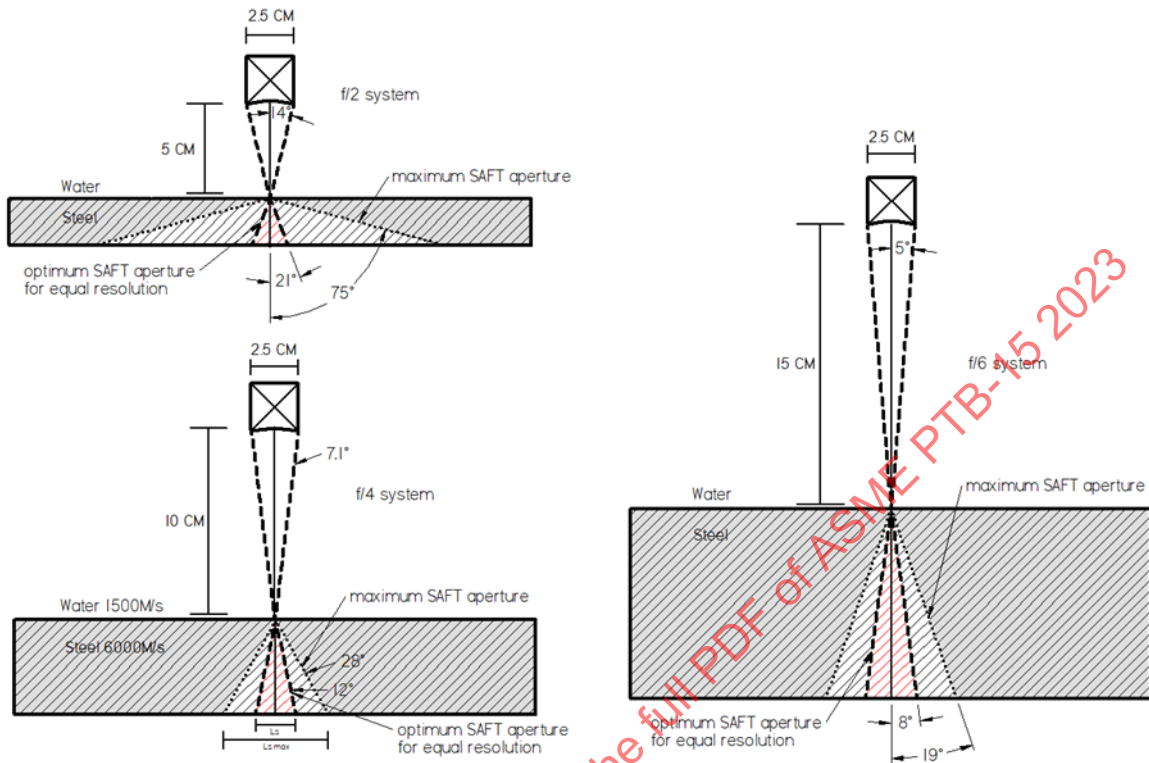
This can also be expressed in terms of the half-angle by the following equation, which is further reduced to:  $\theta_r = 12^\circ$

$$\tan \theta_r = \frac{1}{4.88} \left( \frac{\lambda_w}{\lambda_m} \right) \left( \frac{a}{f} \right) \quad (24)$$

Figure 3-4 depicts the use of different focal systems  $f_2$ ,  $f_4$ , and  $f_6$  in an immersion system.  $f_4$  provides greater detail to coincide with Equation 24. All are focused on the component surface, therefore producing a divergent (defocusing) effect within the component.



Figure 3-4: Reproduced from NUREG CR 3625–Busse 1984



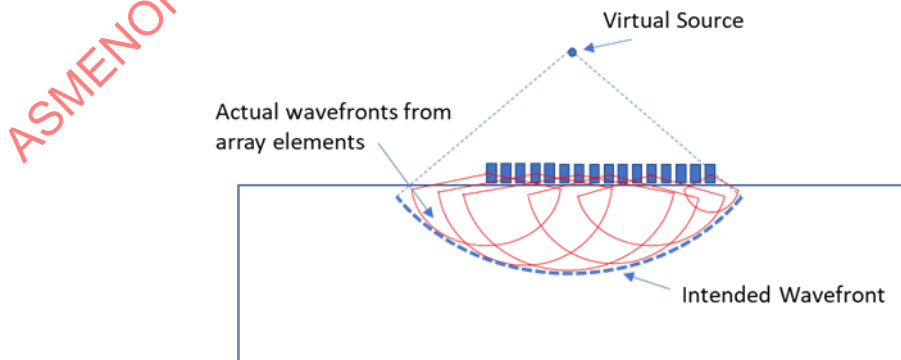
U.S. Nuclear Regulatory Commission NUREG CR-3625

### 3.2 Virtual Source Aperture

Virtual Source Aperture (VSA) is an acquisition scheme that has been derived from medical imaging and is related to Synthetic Aperture Focusing Technique (SAFT). Medical imaging borrowed technology from radar and sonar applications in its development. In its best-known implementations, it is a close relative to PWI.

The basic principle is that an ultrasonic array is transmitting to produce a wavefront that is shaped as if it is coming from a point source behind the array (Figure 3-5). Reception is done with the TFM imaging scheme.

Figure 3-5: Principle of VSA. Array elements are excited with a delay lay to produce the intended wavefront, as if coming from a virtual source.



As mentioned in the first paragraph, VSA was developed as an addition to SAFT. SAFT, in its simplest form, consist of a single element transmitting, in combination with detection at multiple locations, to produce an image with a higher resolution, with an increasing number of receiver locations. The SAFT image is produced in post-processing. FMC/TFM can be considered a generalization of SAFT where transmission is now performed using an array, and reception is performed with the same array (in fact, one of the early names for FMC/TFM was multi-SAFT).

With VSA, the elements in an array are pulsed to produce a wavefront as if it had occurred from a point some distance behind the array. This is typically repeated from several virtual source points. In this way, the imaging path can still be considered to be from a point like source and received by a point like receptor. The TFM imaging scheme can be used unaltered in this way. The benefit is that multiple elements will be firing, increasing the transmission energy, and thus increasing the signal-to-noise ratio. In NDT, this is especially important for the inspection of thick or scattering materials, like austenitic components. The image resolution will depend on the number of firings and how the virtual source points are located.

When applied, VSA and PWI are very similar, as a virtual source point at a large distance will produce a wave front that approaches a planar shape. The advantages and disadvantages are also very similar. Advantages are a larger SNR and less transmissions, resulting in faster inspection and a reduction in the amount of data. The image resolution approaches basic FMC/TFM. VSA also comes with disadvantages. As all elements of the array are fired according to a delay lay, this results in a larger dead-zone compared FMC where only one element is fired, as data collection is not effective while elements are firing. Additionally, VSA is less omni-directional than FMC, and thus more sensitive to defect orientation. In complex situations more virtual source points will be needed because of this. [12]

### **3.3 Migration and Inverse Wave Extrapolation (IWEX), crossover between NDT and Geophysics**

#### **3.3.1 History of Migration in Geophysics**

Migration is a term that originates from geophysics and seismic exploration. In that field, it refers to the various processes that can be used to translate the information in a time-domain signal (an A-scan in NDT, which is called a shot-record in seismic exploration) into geometric information. It is not entirely clear where the term migration comes from. One explanation is that it refers to finding the location to where oil migrates (at the top of the oil reservoir), such that the place where drilling should take place can be identified, i.e., finding the highest point of the subsurface layer in which oil is expected. Recorded indications are moved from the position where they were originally detected to a corrected position with respect to the detected underground geometries such as layers, faults, and salt domes.

Some of the idiosyncrasies of migration-based NDT methods are a result of the fact that geophysicists are solving a different problem than NDT scientists. Geophysicists necessarily start with much less knowledge about the nature of the object they are investigating. They commonly do not know beforehand the location of the subsurface boundary layers and the propagation speed of the acoustic waves. These properties must be estimated from the measurements. In general, the model of the subsurface is assumed to consist of layers. Early processing was often done by layer. Additionally, the boundaries between layers are assumed to be diffuse rather than abrupt, with the consequence that sound is more likely to be scattered at the boundaries than reflected. Finally, a geophysics problem is always three-dimensional, whereas NDT use 2D models. As a result of the nature of the problem the geophysicist is trying to solve, the formulation of theories tends to be more fundamental and mathematical than what we are used to in NDT (excluding the exceptional case).

Migration was proposed as early as 1921. Seminal contributions were made by:

Frank Rieber in the 1930s, who made predictions of received signals based on model of the subsurface, assumed diffraction signals (the result is conceptually comparable to the TOFD B-scan image), and constructed array receivers for directional reception of indications (conceptually comparable to S-scan Phased Array reception).

Mendel Hagedoorn in the 1950s, who used geometric models for predicting the location of subsurface features (conceptually comparable to using a hyperbolic cursor in TOFD) and contracting received signal curves into their proper point of origin (conceptually comparable to SAFT). This was later expanded to the Kirchhoff method, which is based on Huygens principle (the same on which Phased Array instruments are based).

Jon Claerbout in the 1970s, who made the first rigorous mathematical formulation for using the wave equation for imaging. Downward and upward waves are independently modelled and coupled by something called “the imaging condition”. In essence, a computer model is used for calculating the wave form traveling through the material, taking into account the subsurface geometries already detected in the information received up to the point where the wave has travelled.

Another conceptual step was made when wave propagation models were Fourier transformed into the frequency-space domain by Bob Stolt, which made digital processing of complex 3D data much more efficient. This developed into wavenumber-space and frequency-wavenumber algorithms, comparable to the wavenumber algorithm in NDT.

Seismic exploration has been more than a few conceptual steps ahead of ultrasonic NDT. Considering that there are some similarities to the two disciplines—both try to find features in materials with the use of acoustic waves—it is only logical that a crossover from seismic exploration to NDT has happened several times. These crossovers have been called migration approaches, taking their name from the field in geophysics. Migration refers to an evolving field of nearly 100 years, but it is impossible to pinpoint a distinct single migration theory in NDT, and we must go by examples.

**Figure 3-6: On the left, a seismic shot record. On the right, ultrasonic NDT data displayed in the way customary in seismic exploration**

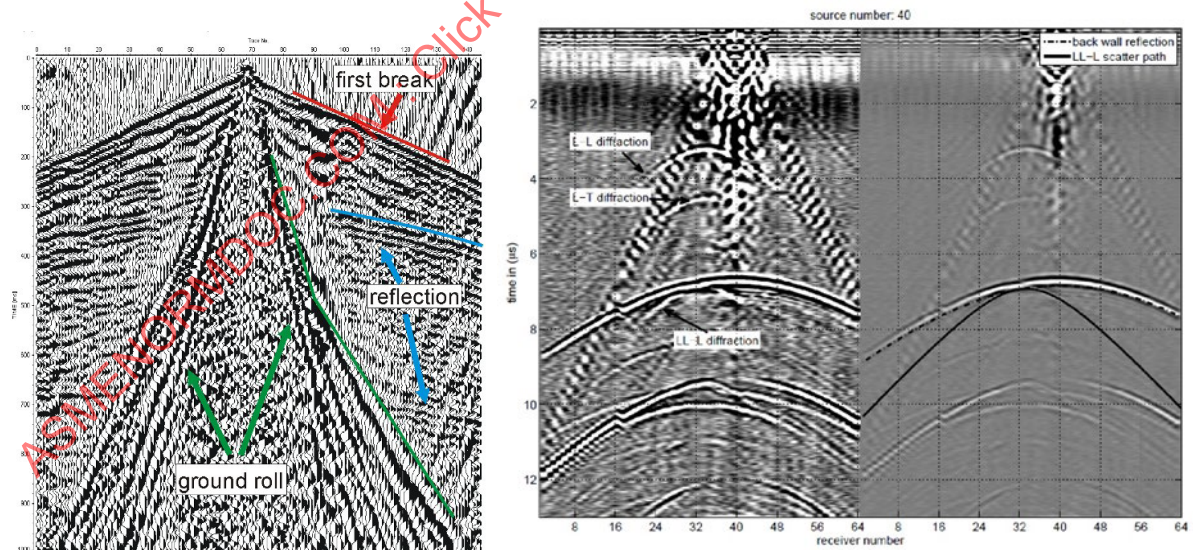


Image Courtesy of Niels Portzgen

### 3.3.2 Examples of crossover between geophysics and NDT

One of the most influential groups in geophysics is the Delphi consortium located at Delft University of Technology in the Netherlands. Its founder, Guus Berkhout, did not work only in Geophysics; he

also supervised a handful of PhDs in NDT. Naturally, these made use of the conceptual lead of Geophysics, but did so with the disadvantage of not having equipment for NDT with the same lead. Maarten Lorenz, in his 1994 thesis, expanded the concept of SAFT into what he called multi-SAFT. He moved a two-probe SAFT arrangement and collected a full matrix of data manually. In the process he made the full mathematical description of what we now know as multi-mode TFM.

Niels Pörtzgen expanded on the work of Lorenz, updating it for the next generation of geophysics algorithms (in the wavenumber domain) and with the benefit of an array controller. This work became the IWEX algorithm in NDT. The cross-over between NDT and geophysics in Delft is continuing, with work on guided waves tomography performed by Arno Volker.

This is far from the only example of a cross-over between Geophysics and NDT. The group of Karl-Joerg Langenberg at Kassel university in Germany worked on Kirchhoff migration in NDT in the 1990s. Ewen Carcreff, at Le Mans university, referred to the work of Bob Stolt, which resulted in a 2014 PhD thesis. Sabine Mueller et al. at BAM in Berlin similarly referred to Geophysics papers in their backpropagation approach. Other examples can be found elsewhere.

Geophysics is not the only cross-over discipline for NDT. NDT also used knowledge out of sonar and radar research (SAFT), particle physics (TOFD and Born scattering), as well as medical ultrasound.

### 3.3.3 Difference Between Basic FMC-TFM and IWEX

In discussing the difference between IWEX and basic FMC/TFM, it must be realized that both were modified multiple times after their introduction in literature. The IWEX algorithm is derived from the full wave equation using the Born approximation (without taking multiple scattering into account), whereas TFM is derived as an extension of existing concepts for focusing as applied for phased array inspection. The resulting image has been shown by Wilcox to have the same phase information, but slightly different amplitude because of the differences in the coefficients used. For practical purposes, the two approaches can be considered equivalent. Some authors have reported that migration-based algorithms have a better resolution and contrast than basic TFM (Carcreff 2016 and Hunter 2008).

To explain IWEX in detail we need to start with the wave equation (Pörtzgen, 2007). In NDT, a single A-scan represents a measurement of a reflected wave field in a single location, caused by a secondary source, such as a defect. According to fundamental wave theory, a source (e.g., a defect) can be reconstructed from measurements of the entire wave field. Wave fields can be extrapolated forward in time and space. For example, the wave field caused by a stone thrown into the water can be predicted later in time by extrapolating measurements earlier in time. The result would be a weaker and bigger circular wave field further away from the position where the stone was thrown into the water (i.e., the source location).

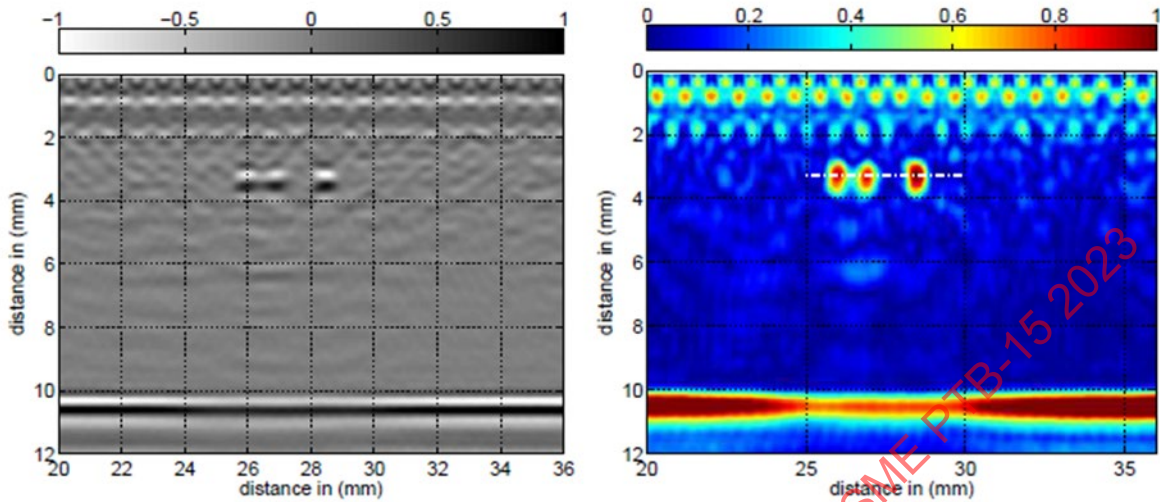
The opposite is also possible. The wave field can be extrapolated to positions where the wave field passed earlier in time than when the measurements were taken. This process is called backward or inverse wave field extrapolation. The result is a stronger wave field closer to the source. With this process, all propagation effects can be eliminated so that the wave field converges at the location of the source and at the time when the source was activated. Propagation effects from the source to the imaging point, and from the imaging point to the receiver are removed using the Rayleigh II integral. If the source was a secondary source, the strength of the inversely extrapolated wave field equals the reflectivity of the secondary source multiplied by the incident wave field. By taking these propagation and reflectivity effects into account in the imaging, the image is composed more correctly with respect to the amplitudes in the image.

### 3.3.4 Data Displays Used for IWEX

Depending on the algorithms used and processing, the image can be displayed including phase information (typically in grey scale, similar to a TOFD image) or using the envelope (typically in color scale, similar to a phased array image).



Figure 3-7: Part of Figure 4.8 from thesis Niels Pörtzgen, 2007



(a) The L-L image of the three bore holes

(b) The envelope of the L-L image from figure a

Image Courtesy of Niels Pörtzgen

An attempt to combine multiple image modes into one display used different colors for the different image paths, while the amplitude is shown as brightness (intensity) (Deleye et al. WCNDT 2012).

Figure 3-8: Example of an IWEX image combining multiple modes

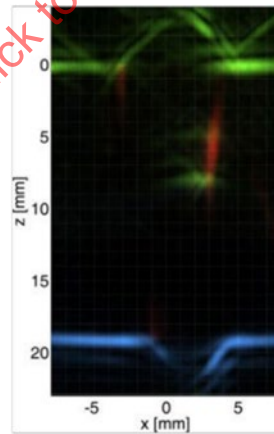


Image Courtesy of APPLUS

The color scale was expanded with a grey scale (from light grey to black) to improve the visibility and contrast of low signals just above the noise level, with a visible separation between signals below and above a given threshold e.g., at 20% amplitude (Hörchens et al. ECNDT 2018).

**Figure 3-9: Example of a typical IWEX image showing expanded color scale**

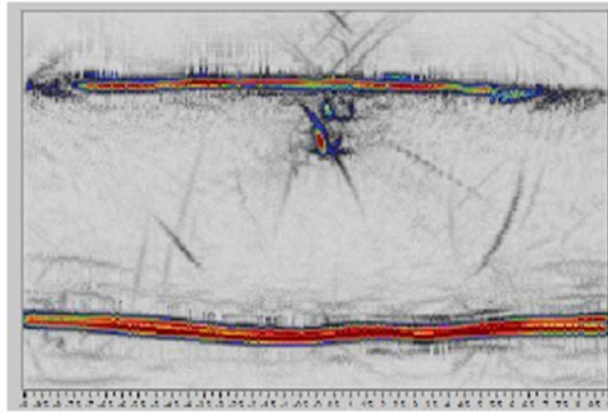


Image Courtesy of APPLUS

In addition to the IWEX images in the plane under the probe(s) the data can also be presented in different views along the scan direction to support the evaluation of the data. These views are constructed from the same three-dimensional dataset e.g., top view, side view and selections like strip charts (cap, volume, root). A three-dimensional view can also be constructed.

**Figure 3-10: Example of multiple modes / views, including a 3D image**

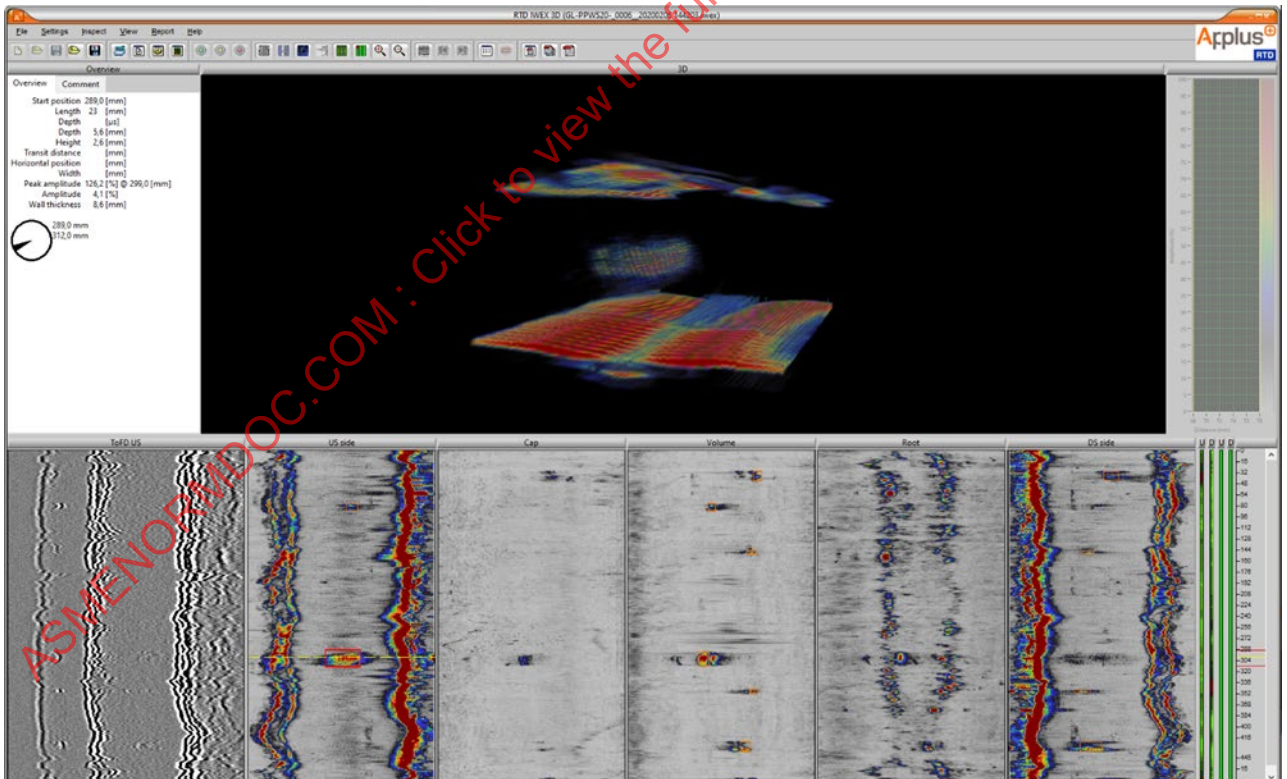


Image Courtesy of APPLUS



### 3.3.5 Electronics Hardware

Instead of focusing individual beams at each grid point, TFM and IWEX use A-scan data collected for all transmitter-receiver combinations (FMC). This results in significant amounts of data to be collected and processed. Originally the data transfer and processing were limited so the processing had to be performed off-line. IWEX dedicated electronics hardware was designed to facilitate real-time parallel processing of all receiver channels into an image format (patented) without the need to transfer the A-scan data to the computer. This also facilitated the simultaneous creation of images for multiple image paths from the same FMC data. Further developments and improvements on processing and processing speed are ongoing.

## 3.4 Iterative TFM

Recent advances in TFM beam forming strategies have resulted in new, powerful capabilities. Areas addressed by these developments include accommodation of a variable inspection geometry and inspection of anisotropic materials by detection and correction of the effects of anisotropy. Systems manufacturers and research institutions have labelled both as “Adaptive” TFM. The problem then arises that these are two different applications requiring two different solutions. Applying the same label to two different processes will inevitably lead to confusion and mistakes. To prevent this problem, a realignment of descriptors for the two processes.

With reference to the body of knowledge that defines the study of Control Systems, it is appropriate to apply the term “Adaptive” to the ability to address changes in material property, i.e., solutions to anisotropic material inspection. It is recommended to use the term “Iterative” in place of the term Adaptive when discussing solutions addressing variable inspection geometry. Thus, the process of Iterative TFM is described in the following section.

Conventional FMC-TFM operates under implicit assumptions that the inspection interface surface is smooth, regular, and flat with respect to the inspection plane. These assumptions enable contact mode testing, most often with an angled contact wedge, and the ability to define the transit time from each element to each node or pixel in the inspection volume. Real time imaging of the inspection volume is possible when applying these assumptions. As the characteristics of the interface surface depart from the assumed conditions, the quality of the TFM image will degrade to the point where effective inspection capability is no longer possible. Iterative TFM may be a solution in these cases.

Iterative TFM is the term used to describe the variant of the TFM beamformer where the TFM algorithm is applied sequentially two or more times to form the image of the inspection volume. Iterative TFM can be effective where:

The interface surface is irregular or otherwise unknown. Examples of this case can include as-welded surfaces, repairs, and formed products.

The interface surface geometry varies over the length of the inspection region. Examples of this include fittings and other complex surfaces developed via various processes.

The interior surface and the interface surface are nonparallel in the region of the inspection. This situation can occur on conical inspection geometries, tapers, and castings or eroded surfaces.

Inspection of articles containing two or more materials.

The iterative TFM process can be applied to any refractive or reflective surface. The generic iterative algorithm process is found in Figure 3-11.

**Figure 3-11: Generic Imaging Process for Iterative TFM**

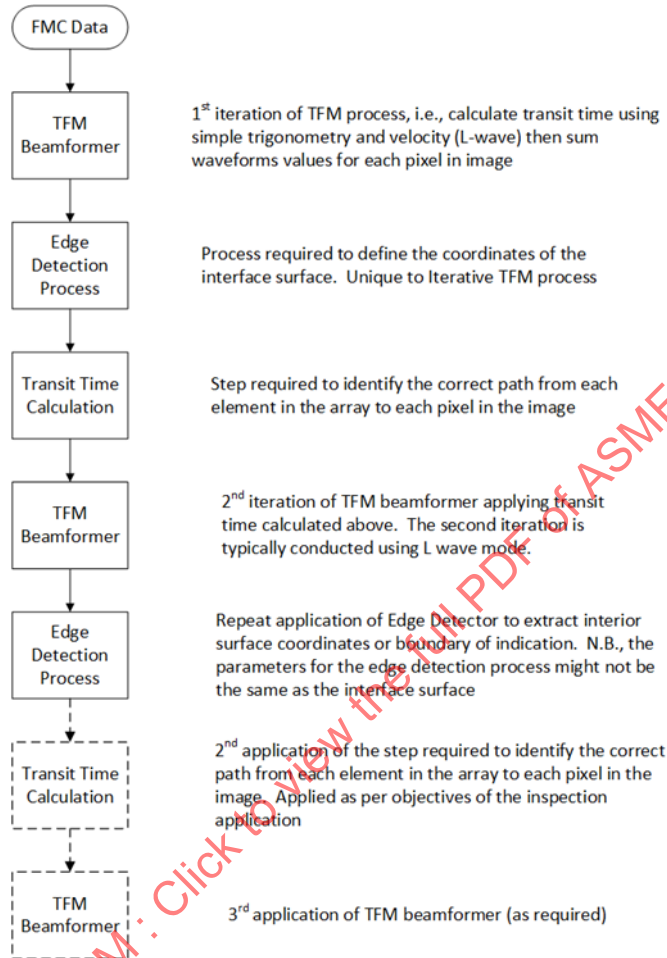


Image Courtesy of Ontario Power Generation, Inc.

In the case of the irregular interface surface, data is usually collected in immersion mode or, less frequently, with compliant wedges. In these applications, the first iteration of the TFM beamformer creates an image of the interface surface. A surface detection algorithm is then applied to define the coordinates of the interface surface. Edge detection algorithms are an extensively developed body of knowledge. Many texts are available to explore this area in detail. Various algorithms can be used such as peak detection, threshold, phase congruency, Sobel and Prewitt, and Laplacian of Gaussian (LoG), to list a few. A frequently used algorithm is the Canny edge detector. The majority of edge detection methods will identify the leading and trailing edges of the signal envelope, see Figure 3-12. Because the trailing edge is not significant in this application, it is easily dispensed by using some ‘wrapper logic’ in the analysis code.

**Figure 3-12: An example of an edge detection process identifying leading and trailing edges of a TFM image. The image itself has been removed to enable view of the detected edges.**

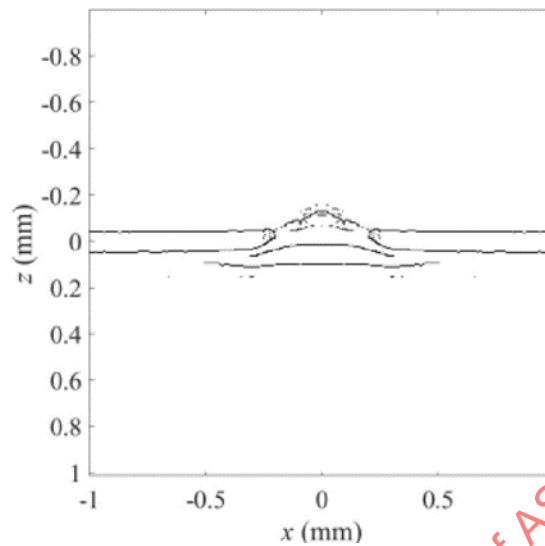


Image Courtesy of Ontario Power Generation, Inc.

The Canny algorithm is a general-purpose detector that is robust and stable with respect to image noise and amplitude fluctuations. The Canny detector identifies the inflection point on the leading edge of the signal envelope. The detected point on the surface corresponds to the maximum slope of the envelope leading edge. The inflection point will be stable with respect to envelop amplitude fluctuations. It is very important to establish the relationship of the inflection point to the time base calibration of the system. This is usually achieved by establishing the offset between the chosen reference point on the signal (departure from baseline or signal peak) and the inflection point of the signal envelope leading edge. The relationship is typically represented as a calibration parameter.

The coordinates extracted by the detector are used in the process of solving for the transit time in the next iteration of the TFM beamformer. The longitudinal wave velocity is used in this calculation, because it is the direct longitudinal wave artefacts that arrive first.

Solving for the transit time can be conducted in either of two ways. The first is the application of Snell's Law based on the local geometry (as determined from the extracted coordinates). The second method is the application of the Fermat Principle. The Fermat Principle states the true path from an emitter through an interface to a specified point in the second media is the one that transits in the least time. The problem then becomes solving for the shortest transit time. This is done by sequentially solving the transit time to each point in the interface in the region of interest and then to the point in the second media. A curve fit is applied through the transit times calculated and the minimum is identified. The minimum may reside between two of the transit time values calculated. Consequently, the true point would be located on the interface between the two corresponding points explicitly calculated.

The Snell's Law method is computationally fast, but it suffers from sensitivity to error or uncertainty in the coordinates of the detected surface. The Fermat Principle is computationally intensive (slower), but it is much less sensitive to noise and can provide greater accuracy when evaluating the flight time to a given pixel in the imaging region. The Snell's Law method works well when the image of the interface surface can be relied upon to be smooth with low noise. The Fermat Principle can accommodate surface roughness or other disturbances such as air bubbles in the interface image.

Regardless of the method used to determine transit time, a second iteration of the TFM beamformer is used to image the region beyond the interface. This completes the second iteration cycle.

In principle, a third and fourth iteration can be implemented following the steps described above. These iterations can use shear wave velocity in place of longitudinal wave velocity or could use the coordinates of the interior surface to solve the transit time for indirect (reflected) modes. In practice, however, the FMC data set will include artefacts in a variety of wave modes and interactions. The artefacts are often imaged as spurious indications or combined to reduce the overall signal-to-noise ratio in the image. Other issues may arise because the fidelity of the image construction is also a function of the errors in the previous iteration. Errors can rapidly accumulate iteration over iteration, limiting the practicality of using several iterations. The user should assess the image quality when applying more than two iterations.

The case where the interface surface is flat, smooth, and regular while the interior surface is unknown and/or variable is easier to address. The first iteration of the TFM beamformer images the interior region inclusive of the interior surface. The edge detection algorithm then identifies the coordinates of the interior. The user has the option of using the Fermat Principle or simple geometry to determine the correct flight time to a pixel in the search region. The choice is influenced by the quality of the interior image and returned interior coordinates. The second iteration of the TFM beamformer can apply longitudinal wave velocity when imaging via indirect paths or Shear wave velocity when searching for indications sensitive to mode conversion. The same caution should be applied as in the previous case, that is, spurious indications can be imaged via other wave mode interactions. Confirmation of indications should be obtained via direct longitudinal wave imaging where possible.

### 3.5 Adaptive TFM—A Framework

At times, some confusion exists between the terms Adaptive TFM and Iterative TFM. Adaptive TFM is differentiated from Iterative TFM in the following way. Fundamentally, Adaptive TFM alters an established model of a material based on information derived from the FMC data set before applying TFM beamforming, whereas Iterative TFM applies separate cycles of the TFM beamformer to identify and accommodate changes in specimen geometry. The changes in geometry may be located at both reflective and refractive interfaces.

TFM beamforming capabilities are challenged when applied to anisotropic materials. The difficulties arise from two principal conditions. The first is the velocity dependency with respect to the path taken to the reflector. Summation under these conditions leads to poor reconstruction of the reflector image. The second is the difference between group and phase velocities that can arise in anisotropic materials. Differences in group and phase velocities result in the signal phase no longer coherent with the group. The TFM beamformer relies upon summation of the analytic waveform enabled by the Hilbert transform. The assumption underlying TFM is the phase always remains coherent with the group transmission. If the signal phase varies within the group envelope, the TFM signal summation will provide poor performance.

Adaptive TFM is useful when the material longitudinal and shear wave velocities are not known to the required degree of accuracy and/or are variable with respect to location and time within the specimen. This situation describes the challenge imposed by materials where anisotropy is induced by environmental factors (heat, temperature gradients, molecular uptake, radiation, etc.) and stress.

#### 3.5.1 Basic Process

Adaptive TFM is implemented as follows:

1. Acquire the FMC data set.
2. Evaluate the FMC data set for parameters associated with material properties.
3. Associate the identified parameters with a model of the material.
4. Update the distributed parameter model.
5. Apply the TFM beamformer.

A diagram of the Adaptive TFM process is found in Figure 3-13. This diagram shows inputs to the Path Dependent Adaptation – Material Anisotropy Distribution Model loop. Principal inputs are obtained from the Metallurgical Study–Christoffel Matrix segments and the Signal Analysis segment. These segments are described in the following section.

The FMC data set can be acquired in conventional methods such as contact testing or local immersion testing. Nothing unique exists in the data collection process for Adaptive TFM to distinguish it from conventional approaches to FMC/TFM. Selection of transducer parameters may, however, be influenced by the material model developed to describe the inspection region.

**Figure 3-13: Block diagram of a generic Adaptive TFM process. The diagram also shows inputs to the main portion of the adaptive loop.**

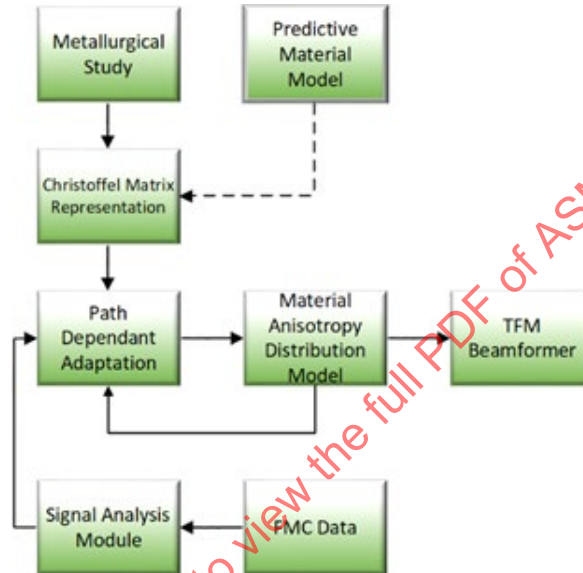


Image Courtesy of Ontario Power Generation, Inc.

### 3.5.2 Metallurgical Study

A detailed metallurgical study of the material(s) to be inspected is required before a suitable model can be developed. The objectives of the study are twofold: The first is to establish the range of velocity with respect to direction for the material beginning with its nominal state to the fully anisotropic state. This requirement applies to Longitudinal and Shear wave modes. The second objective is to determine the direction and rate or change of anisotropy (gradient) with respect to the sample's geometry. The gradient and potential changes in gradient anticipated over service life are inputs to the model. Alternatively, if the properties over the range of states have been determined based on other efforts, then a predictive or statistical model of the material can be applied in lieu of a metallurgical study.

### 3.5.3 Material Anisotropy Distribution Model

A model of the material velocity parameters is a central element of Adaptive TFM. A distributed parameter model is developed based on the maximum gradient of anisotropic characteristics identified in the metallurgical study. The model cell size is determined by the step that would induce a change at the detection threshold assuming the cell is in the region of the maximum gradient. The cell attributes are the key parameters obtained as solutions from the Christoffel matrix (discussed as follows).

Anisotropic properties can arise from the operating environment by the introduction of a foreign species into the matrix of the target material. The concentration of foreign species can vary over time with exposure and can similarly vary in distance along the target component. Anisotropic behavior may propagate over time to eventually reach a state of equilibrium. Similarly, the anisotropic gradients can vary over time with exposure to the same environmental factors. The model is required to accommodate the range of anisotropy from the initial state to the maximally anisotropic state. The size and the spacing of the cells in the model will be determined based on the gradients in anisotropic properties. Figure 3-14 presents a hypothetical configuration for a model of a weld sensitized and exposed to anisotropy inducing species.

**Figure 3-14: Framework for a distributed parameter model of a hypothetical configuration**

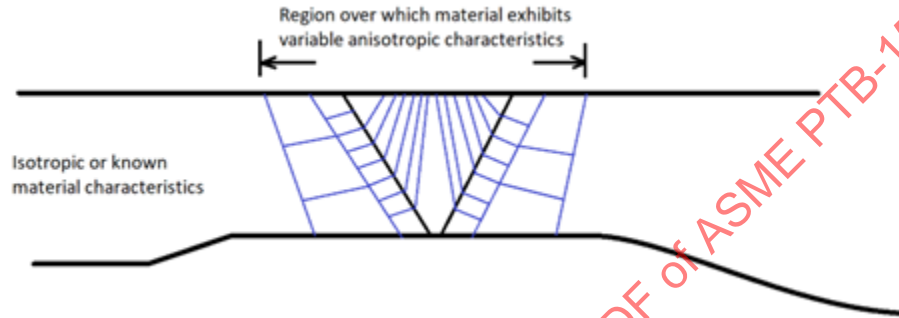


Image Courtesy of Ontario Power Generation, Inc.

### 3.5.4 Material Properties and Wave Propagation in an Elastic Media

The general form of the elastic wave equation is:

$$V^2 \frac{\partial^2 \varphi}{\partial x^2} = \frac{\partial^2 \varphi}{\partial t^2}$$

Furthermore, it can be shown that the material characteristics are related to wave propagation by:

$$E/\rho \frac{\partial^2 \varphi}{\partial x^2} = \frac{\partial^2 \varphi}{\partial t^2}$$

Or

$$G/\rho \frac{\partial^2 \varphi}{\partial x^2} = \frac{\partial^2 \varphi}{\partial t^2}$$

Where:

E is the Tensile modulus

G is the Shear modulus

$\rho$  is the material density

The following relationships are established based on the previous equations:

$$V_L = \sqrt{(E/\rho)}$$

and

$$V_S = \sqrt{(G/\rho)}$$

Where:

$V_L$  and  $V_S$  are the Longitudinal and Shear phase velocities, respectively. When the material properties are constant with respect to direction, i.e., isotropic, the phase velocity is the same as the group velocity.

In practice, the velocity measured is typically within a range of:

$$0.995 < V_n < 1.005$$



Processing methods, heat treatments, marginal changes in alloy content, etc., often account for a nominal variation in velocity.

### 3.5.5 Cauchy Tensor, Christoffel Matrix, and Key Velocity Parameters

The Cauchy tensor or Cauchy matrix is an effective tool to represent the distribution of the mechanical properties of the material. Based on the information derived from the metallurgical study, a representation of the material can be expressed in the form of the Cauchy tensor; see Figure 3-15. In the case of isotropic materials, the material properties are constant with respect to the direction. The Tensile modulus values are all equal, i.e.,  $T_1 = T_2 = T_3$  and the Shear modulus values are all equal, i.e.,  $S_{12} = S_{21} = S_{13} = S_{31} = S_{23} = S_{32}$ . In the case of anisotropic materials, in general  $T_1 \neq T_2 \neq T_3$  and  $S_{12} \neq S_{21} \neq S_{13} \neq S_{31} \neq S_{23} \neq S_{32}$ .

Because the relationship between the moduli and corresponding velocities has been established, it is possible to derive a representation for the Longitudinal and Shear velocities as a function the Tensile and Shear moduli values of the material. In the case of the Shear wave, we need to also account for the polarization for each Shear wave vector. The resultant representation is constructed in a notation known as the Christoffel matrix. The inspection plane is not necessarily aligned with the principal axis of the Christoffel matrix and may be displaced by an arbitrary angle to the basis of the Christoffel matrix. As the material properties evolve with increased exposure to anisotropy inducing species, the Christoffel representation will change in a similar manner. In other words, the Christoffel matrix represents one state of the material properties.

**Figure 3-15: Cauchy tensor depicting tensile and shear vectors associated with a unit volume. Right-matrix representation of Cauchy tensor**

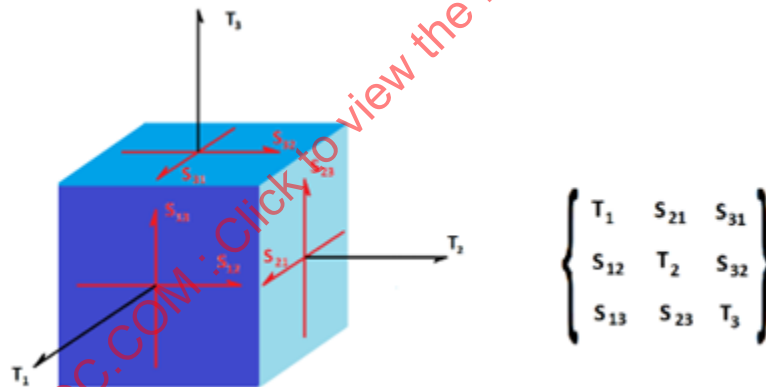


Image Courtesy of Ontario Power Generation, Inc.

### 3.5.6 The Slowness Surface, Slowness Curves

Slowness surfaces and their corresponding slowness curves are an effective means to visualize phase and group vectors. Phase slowness is defined and the reciprocal of phase velocity. The faster wave mode is closer to the origin than the slower wave mode. Wave slowness can be plotted as a 3-dimensional volume. These 3-dimensional shapes are known as slowness surfaces and can take on a variety of shapes, generally modifications of ellipsoids and spheroids and in unique situations can fold in on themselves. Slowness curves represent the phase velocities for a plane passing through a slowness surface. Nominally, the planes are on the primary axis of the coordinate system i.e., the XY, XZ and YZ planes.

**Figure 3-16: Examples of phase slowness curves, left–isotropic materials where the velocity remains constant irrespective of direction, right–anisotropic where velocity varies with direction**

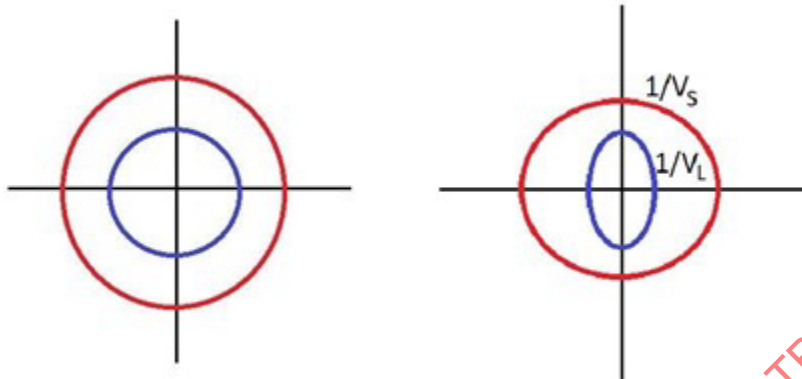


Image Courtesy of Ontario Power Generation, Inc.

### 3.5.7 Group velocity and Phase velocity

There are four parameters that need to be determined when addressing anisotropic materials. These are:

- The phase vector
- The phase velocity
- The group vector
- The group velocity

The phase vector is an independent variable representing a direction through the material. The group vector is the Curl of the phase velocity, with the direction normal to the phased velocity slowness curve. In practice, the phase vector represents the direction of wave propagation, and the group vector represents the orientation of the wave front. Based on expansion of the Elastic Wave equation in two dimensions, the phase velocity within the media can be expressed as:

$$V_p = \omega/k$$

Where:

$\omega$  is the angular frequency expressed in radians/s,

$k$  is the wave number vector expressed in radians/m

This relation holds for both the Longitudinal and Shear wave modes when the vector quantity  $k$ .

The group velocity is defined as:

$$V_g = \vec{\nabla} \omega$$

The vectors and magnitudes for both phase and group can be visualized when plotted on a slowness curve as found in Figure 3-17.

**Figure 3-17: Phase and Group velocity vectors plotted on a slowness curve. The magnitude of the change has been exaggerated for the purpose of illustration.**

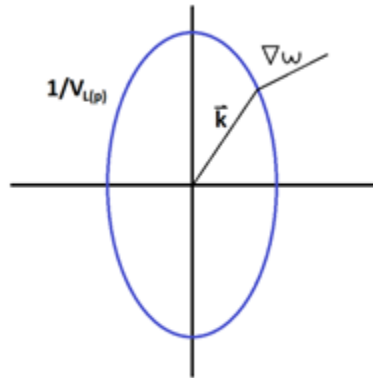


Image Courtesy of Ontario Power Generation, Inc.

### 3.5.8 Detection of Anisotropic Characteristics

In most situations, it is the group velocity that is observed in the UT data acquired by the inspection system. The group and phase velocities are equal when the material is isotropic (within a given plane) or at the maxima and minima of the phase velocity. These conditions are known as stationary points. Under conditions where the phase velocity is not at a maxima or minima, the difference in phase velocity versus group velocity is observed as a shift in the signal phase with respect to the group. The detection of anisotropy is dependent upon the nature of the effect and is specific to the material. In some materials it may be the shear component that is most affected, yet in other materials it may be the longitudinal mode that is influenced. The detection strategy should isolate the most sensitive mode to obtain reliable estimates of material anisotropy.

Longitudinal group velocity measurements are typically obtained via autocorrelation techniques spanning a known distance. These measurements provide group velocity and phase vector direction information. Similarly, shear wave group velocity can be measured relative to longitudinal group velocity along the same path via autocorrelation, provided that no phase alteration occurs relative to the group.

The velocity ratio between the longitudinal and shear wave modes can be used to enhance the sensitivity of anisotropic property detection relative to detection of change in one constituent velocity. The situation where the tensile and shear moduli change in opposite directions is common. These occurrences have a corresponding effect on longitudinal and shear wave velocities. Changes in properties are more readily detected when monitoring the ratio between the two modes.

Another avenue to evaluate the localized changes in wave propagation properties is to detect and measure the amount of phase displacement within the group. A reference signal and target signal are chosen, and a Fourier transform is applied. The difference in the weighted phase component of the two signals provides the angle between the phase vector and the group vector. The phase velocity relative to the group velocity can also be calculated.

**Figure 3-18: Sample, left with normal beam A scan response center. Note the phases remain consistent in each multiple.**



Image Courtesy of Ontario Power Generation, Inc.

Figure 3-18 shows a hydride, anisotropic sample on the left and the resulting A scan in immersion mode. Note after the interface signal, the first reflection is the reference signal. All other echoes following have the same phase-group relationship as the reference signal.

**Figure 3-19: Sample, left, A scan response center. Note the phase of the initial response is the same as Figure 3-18, whereas the phase is changed in subsequent signals. This behavior is indicative of anisotropy.**



Image Courtesy of Ontario Power Generation, Inc.

Figure 3-19 shows the same scan file, but the A scan at the center represents a pitch-catch configuration. The scan contains L-L signals as well as L-S signals. Note on the reference signal the first L-L reflection retains the same phase-group relationship as found in Figure 3-18, but subsequent L-S signals demonstrate a marked change in phase-group relationship.

### 3.5.9 Path Dependent Adaptation Process

Results from the detection process for a given cell are applied in an equality with the corresponding variables in the Christoffel matrices, e.g., L wave phase vector, L wave group velocity, group to phase vector angle, etc. The Eigen vector solution identifies the orientation of the Christoffel matrix applicable to that cell as well as the state corresponding to the degree of anisotropy developed. Each application will have different degrees of freedom arising from the material properties. Due to symmetry in the Christoffel matrix, more than one potential solution may be valid for the cell. Further evaluation (input) is necessary to resolve conditions where symmetry is encountered.

### 3.5.10 Model Evolution

The process begins at a location on the inspection sample that is assumed to have known properties i.e., nominal material characteristics. The model is updated or adapted by evaluating the unknown cell immediately adjacent to the known region(s). The process solves for the orientations and magnitudes of the phase and group velocity and vectors in the cell in question, assuming a wave form transiting through both known regions(s) and the unknown cell. Note that a single measurement is insufficient to enable the determination of parameter values. More than one point on the slowness surface could provide a valid solution. The solution must be constrained by providing a separate estimate of complementary parameters and/or from an independent path through the same cell. This evaluation can be derived from the same wave mode transiting at an angle that is separated in direction from the first, or via a complementary wave mode when the relationship between the two wave modes is known. As the cell is evaluated and found to have characteristics corresponding to the known region, then the cell is subsumed into the known region and the model is deprecated. Where a cell is distinct from the known region, the model is updated to the parameter values determined in the Path Dependent Adaptation process.

The cell adjacent to the one that has been resolved is evaluated next. The process repeats using parameters from the base material and the resolved cell, combined with parameters obtained from the FMC data set to determine the properties of the new cell. If the cell parameters are unique, the cell is retained as an individual entity. If the parameters correspond to adjacent material, then the cell is subsumed into the neighboring adjacent structure. In this manner, the model progresses from a fine structure containing many small cells into a structure with fewer but larger cells. The behavior of merging cells mimics annealing in materials when exposed to high heat.

### 3.5.11 Degrees of Freedom

As described above, several independent paths through the cell under consideration are needed to identify parameters linked to material characteristics. Paths are considered independent when they do not traverse parallel or near parallel vectors, or of different modes; see Figure 3-20. This requirement places constraints upon the transducer pitch–array size, the specimen geometry, scanning pattern, and any scanning constraints that may be encountered. If the material properties are highly sensitive to direction for all wave modes, or if the range of anisotropic behavior from base state to full anisotropy is significant, then the number of degrees of freedom to resolve the various states will increase. The extent to which the number of degrees of freedom will vary according to the application.

**Figure 3-20: Examples of solution condition**

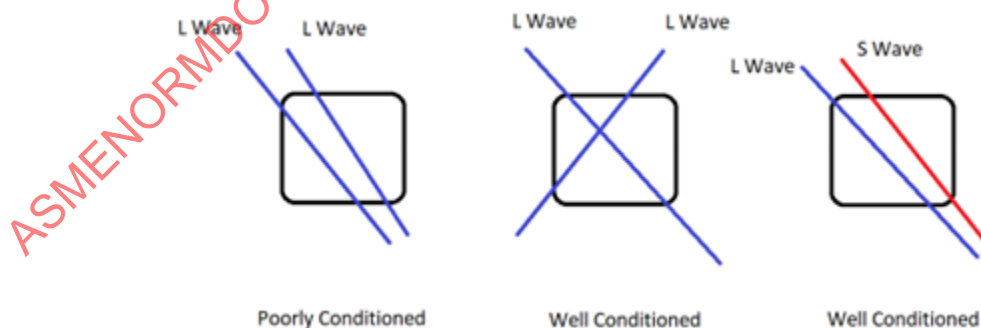


Image Courtesy of Ontario Power Generation, Inc.

Figure 3-20 demonstrates the concept of well-conditioned solutions versus a poorly conditioned solution.



### 3.5.12 TFM Process

Under Adaptive TFM, the TFM process remains largely intact, relative to conventional TFM processes. Transit time through each of the cells is governed by the group velocity for the vectors under evaluation. The correct path is the one that conforms to the Fermat principle, i.e., the minimum transit time. When the group and phase velocities are not equal, phase displacement relative to group will occur. The difference between the phase and group velocity must be accounted for and compensated prior to summation for any pixel where signals transit through this type of cell. Failure to do so will result in various phase displacements summed, resulting in poor imaging performance.

## 3.6 PWI-ML

### 3.6.1 Plane Wave Imaging

Plane Wave Imaging (PWI) is an acquisition scheme that has been derived from medical ultrasound. In the medical field it is not just used as an acquisition scheme, but has other processes associated with it, for example, time reversal methods. The medical field used algorithms from geophysics (Stolt migration, see the migration section) in the development. In the medical field PWI has been thoroughly validated. In the transition to NDT the main issue to be solved was testing through the material interface, which has been done for planar and complex material surfaces.

The main reason for transferring PWI to NDT applications are to overcome two well-known disadvantages of the FMC acquisition scheme: (1) Due to acquiring all pulser-receiver combination, the data acquisition may be very time consuming, and (2) Due to pulsing one element at a time, very limited energy is introduced into the material, making the testing of noisy or attenuative materials difficult.

The acquisition consists of firing all the elements of the array simultaneously along several angles, like a sectorial scan, while all the elements are received individually. The delay law is calculated to result in a plane wave for PWI, compared to a spherical wave for FMC. A TFM is then performed the same way as with FMC/TFM, providing improved productivity while keeping the optimum spatial resolution that we know with TFM.

**Figure 3-21: Plane waves generated for three different angles**

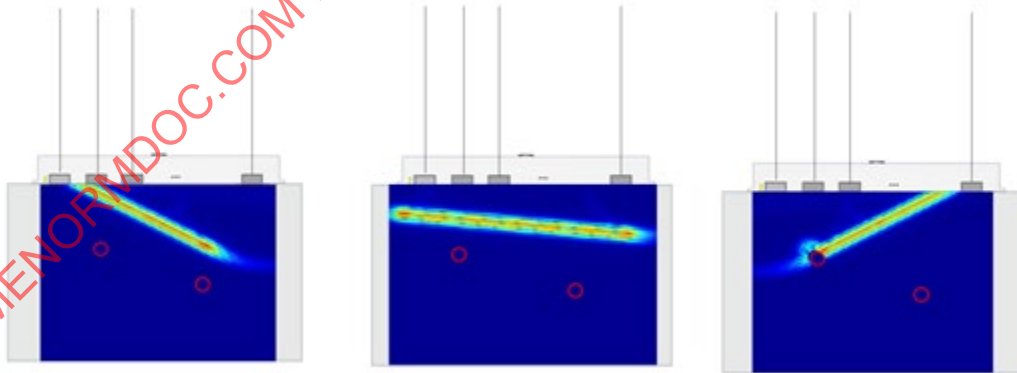


Image Courtesy of Eddyfi Technologies

At the end of the PWI data acquisition process, the resulting matrix contains  $M \times N$  elementary A-scans compared to  $N \times N$  for FMC, where  $M$  is the number of angles and  $N$  is the number of elements. Of course, the idea here is to have  $M$  angles as small as possible to improve productivity while maintaining an image with sufficient resolution and sensitivity.

PWI looks very similar to a sectorial scan for PAUT. The user defines the minimum, maximum angles and the angle step. In case of weld testing, the low angles are used to inspect the bevel and volume of the weld after a rebound off the backwall, while the high angles are used to inspect the root of the weld. People familiar with PAUT inspection can use PWI right away, and there is no need to worry about where to focus the energy as TFM will focus everywhere within the region of interest.

For practical situations, between 6 and 10 different plane wave angles already give an image quality that is comparable to FMC/TFM. This may result in an increase in scan speed of 3 to 10 times, and greatly reduce computational demands. For more challenging applications more angles may be needed.

**Figure 3-22: comparison of FMC/TFM image (top right) to PWI image (bottom right) for PWI setup with 6 plane wave angles (left)**

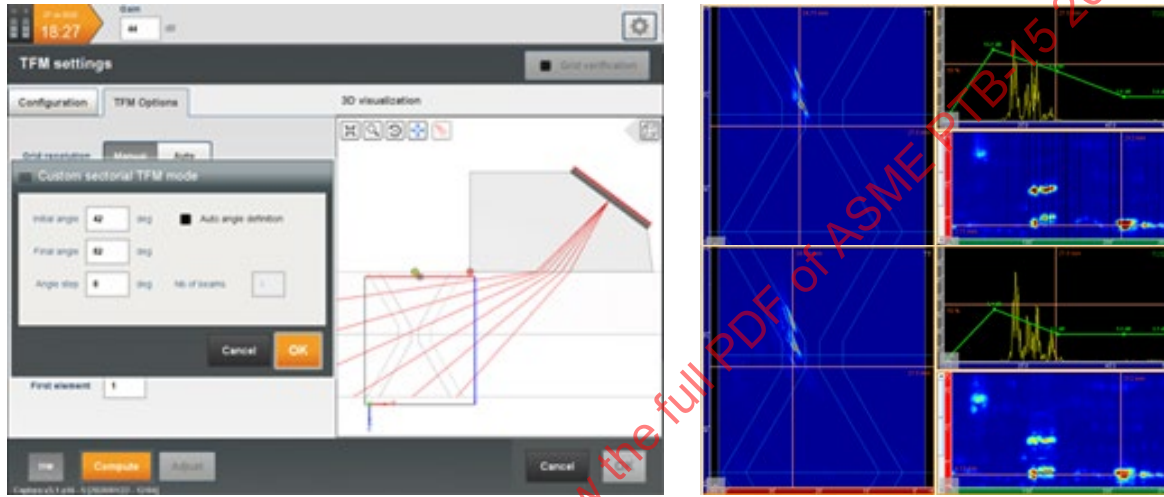


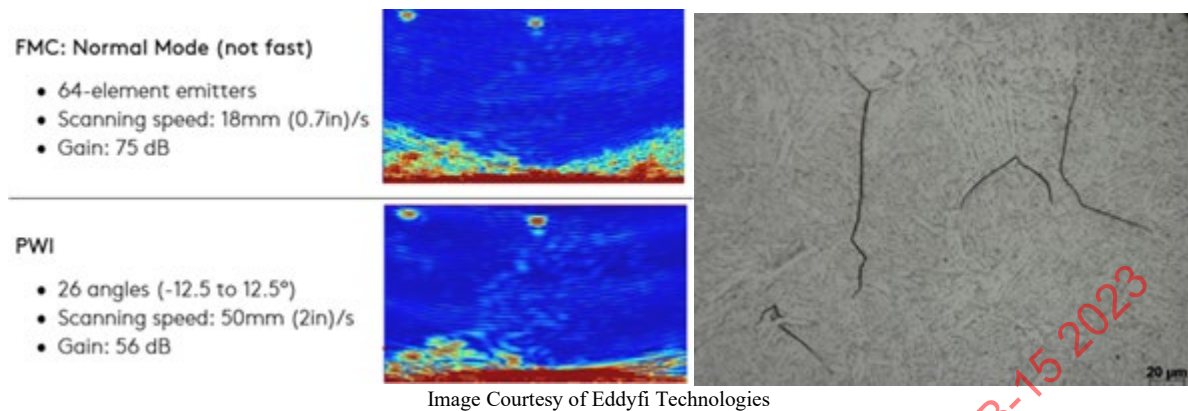
Image Courtesy of Eddyfi Technologies

In Figure 3-22, the top image shows the results obtained with the FMC/TFM and the bottom image with the PWI/TFM. The results are identical: all three defects (root crack, toe crack and crack along the fusion face) are detected. Missing frames on the C-scan of the FMC/TFM data are a result of the difficulty in moving the probe at a steady 16 mm (0.63 in) per second.

By reducing the number of excitations, PWI drastically reduces the amount of data if one wishes to record the  $M \times N$  elementary signals. For the 508 mm (20 in) pipe and the six angles mentioned before, the amount of data would decrease by a factor of 10.

Another advantage of PWI is the potential increase in sensitivity. When performing FMC/TFM, we fire each element individually. While the reconstruction process uses the full 64 elements, the excitation of only one element may not be enough while inspecting thick structures and/or noisy materials. In the case of PWI, we fire all the elements at the same time, sending more energy into the part. The overall energy level, thus sensitivity, depends on the number of angles used during the PWI/TFM process.

As an example, we compared FMC//TFM to PWI/TFM for an HTHA inspection. We used a sample that contains microcracks along the inner diameter (ID) surface; a micrograph of that surface is shown in the following figures. The micrograph was taken along the backwall of the sample. The setups used for comparison are summarized in the following table, together with the TFM images obtained for the FMC (top) and PWI (bottom), respectively. We used a 64L10-G2 probe (pitch 0.3 mm/0.01 in) with a TFM that contains 92 Kpixels.

**Figure 3-23: Screen shot comparison of classic TFM vs PWI next to microetch from the component.**

Again, the TFM images obtained from FMC and PWI data acquisition are similar, except for the gain used for PWI, which is about 20 dB less, providing better a Signal-to-Noise Ratio (SNR). The strong signal along the backwall (bottom left corner in the PWI image) is due to the HTHA visible in the micrograph. For that position, FMC/TFM leads to some diffraction patterns that cover the indications, making it difficult to see the HTHA. Micro-cracking is propagating inside the thickness of the material in the PWI image. The improved sensitivity allows the detection of smaller indications. Productivity is also improved for that configuration because 2 to 3 times fewer excitations were used.

PWI also comes with disadvantage. As all elements of the array are fired sequentially according to a delay lay, this results in a larger dead zone compared FMC where only one element is fired, as data collection is not effective while elements are firing. Additionally, PWI is less omni-directional than FMC and more sensitive to defect orientation. In complex situations, more plane wave angles will be needed because of this. [13] [14] [15]

### 3.7 Sectorial Total Focusing

#### 3.7.1 STF, LTF, CTF Processes (Techniques but not Methods)

This section describes the Sectorial Total Focusing (STF), Linear Total focusing (LTF), and Compound Total Focusing (CTF) processing techniques in which a frame containing a sweep of A-scans is used in contrast to the rectangular TFM frame comprising of pixels.

STF is a processing technique that uses FMC collected data to generate a sectorial sweep of A-scans, where each sample of every A-scan is fully focalized. The TFM function is used to compute the signal, but instead of organizing the results in a grid of pixels, the resulting image is organized as a series of beam angles and samples along those beams, mimicking the appearance of an S-Scan (Azimuthal sweep). A comparison of TFM, STF and regular PA is shown in Figure 3-24.

**Figure 3-24: A comparison of TFM, STF, and standard PA**

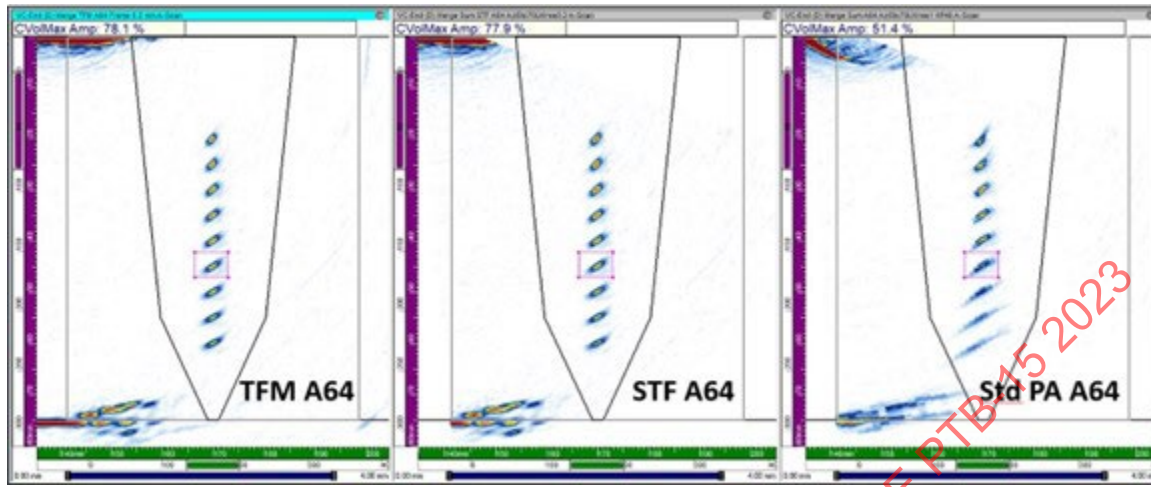


Image Courtesy of Eddyfi Technology

LTF is a processing technique that uses FMC collected data to generate a linear sweep of A-scans, where each sample of every A-scan is fully focalized. The TFM function is used to compute the signal, but instead of organizing the results in a grid of pixels, the resulting image is organized as a series of beams having a constant angle, but varying aperture, and sampling along those beams, mimicking the appearance of an L-Scan (Linear sweep).

CTF is a processing technique that uses FMC collected data to generate a compound sweep of A-scans, where each sample of every A-scan is fully focalized. As with STF and LTF, the TFM is used to generate the CTF image, which organizes the resulting data in a varying angle and aperture set of beams. The results mimic the appearance of a compound sweep.

A schematic of the techniques is shown in Figure 3-25.

**Figure 3-25: A schematic of the (a) STF, (b) LTF, and (c) CTF sweep**

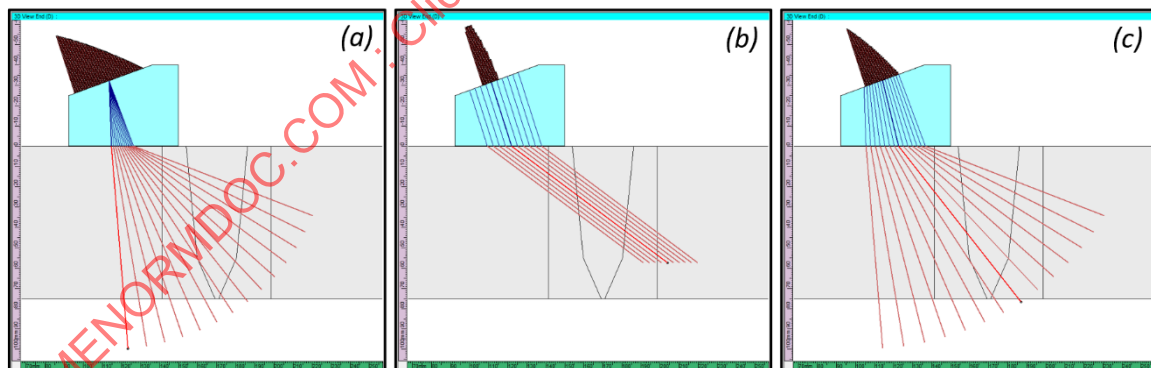


Image Courtesy of Eddyfi Technology

Advantages:

The total probe aperture can be used in the STF algorithm, which results in a focusing capability very similar to TFM, while in the LTF and CTF algorithms partial probe aperture is used.

An unprocessed A-scan is recorded for each beam (which is similar to the Sector scan View composed of A-scans of swept beams), while the TFM image is composed of columns of pixels.

The motion of the target reflector of an A-scan is similar between STF, LTF and CTF to standard PA.

The indication signal changes as the probe are moved similarly to PA, in contrast to TFM, where the synthetic vertical A-scan does not originate from the probe.

For the same depth of coverage, the sample count of STF, LTF, and CTF is smaller than that of TFM frames, which is equal to number of pixels in the width axis multiplied by number of pixels in the depth axis, allowing for higher scan speeds using the former frames. For STF, LTF, and CTF the pixel count is equal to the number of samples in the A-scan multiplied by the number of beams.

In contrast to TFM, the concept of the detection angle for detected indications is valid for STF, LTF, and CTF configurations because a sweep of real A-scans is used to reconstruct the image in the later configurations.

Limitations:

Beam angle parameters need to be defined when creating a STF, LTF, or CTF setup.

The rectangular TFM frame can provide extended volume coverage as compared to the sectorial, linear, or compound coverage area.

When to use:

In some circumstances where the user desires to benefit from the advantages of advanced focusing techniques, the use of STF, LTF, and CTF configurations (totally focused sweep of A-scans) is preferred to TFM. These circumstances include (but are not limited to):

When it is required to migrate from standard PA to advanced focusing techniques, using STF, LTF and CTF configurations allows for fewer modifications to the existing procedure parameters.

When the application requires the use of Fast Fourier Transform (FFT) technique, TFM cannot be used because the synthetic A-scans is not made of regularly spaced sampled on a time scale, and thus FFT will not yield meaningful results. In such a case, real A-scans of STF, LTF, and CTF frames will make it possible to benefit from advanced focusing techniques and to appropriately apply FFT.

When it is required to ensure the users retain their training, the similarity of STF, LTF, and CTF configurations to standard PA (e.g., in terms of A-scans, detection angle, indication shape) allows for such an action.

## 3.8 TFMi™

### 3.8.1 Terminology

Total Focusing Method intermode (TFMi™) is an advanced ultrasonic inspection technique that is based on the data-acquisition process of Full Matrix Capture (FMC). The data acquisition process basically records every A-scan into a matrix, which are generated by pulsing every phased array element within a probe and receiving the backscattered echoes on all other array elements. The FMC matrix saves all the A-scans generated by the interactions between every pulsing and receiving element. This technique enables the image's reconstruction in multiple ways. More precisely, the intermode factor enables the image reconstruction to combine up to four FMC matrices that are generated by different wave propagation modes.

In another words, A-scans are collected from every combination of transmitting and receiving elements across a specified range, in which every element of an array probe is individually pulsed to generate sound that is received on every element, including the transmitter. The A-scans are then stored in an FMC matrix. The inspector would select n elements, forming a synthetic aperture, distributed across one or more arrays. The matrix with the data would therefore contain n x n A-scans, having in total n transmitting elements and n receiving elements.



FMC has the advantage of being able to acquire all possible interactions between every pulsing and receiving element, enabling multiple ways of reconstructing images. Figure 3-26 shows the FMC scan along each element into the probe.

Figure 3-26: FMC scanning sequence

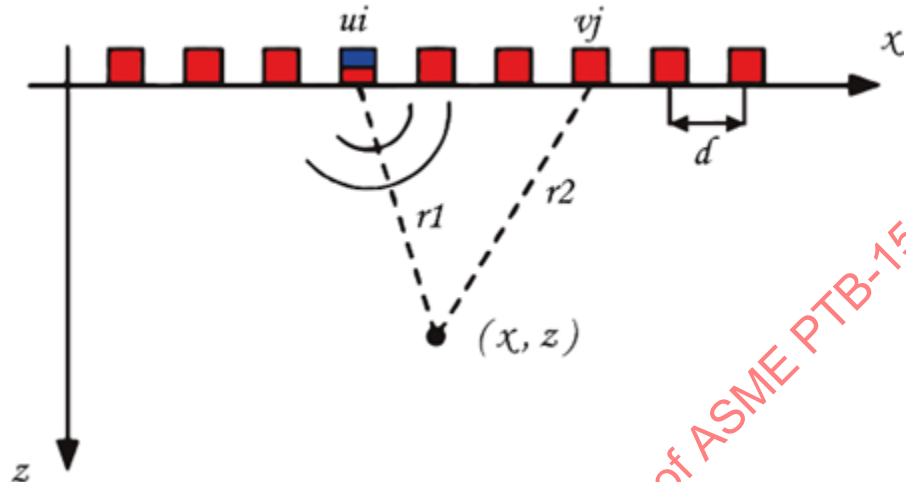


Image Courtesy from Sonatest

### 3.8.2 FMC Acquisition Characteristics

Sound wave emissions are made by a single punctual source with no steering or focusing on the transmission. As a result, there is lower transmitting energy when compared to phased array transmitting (16 to 32 elements). In reception, the receiving elements collect raw A-scans with disregard to information about the steering angle and focusing. From this, the instrument is ready to build any propagation mode of TFM frames. There are more received A-scans than phased array, but they typically show the same level of noise.

There are other FMC alternatives for data acquisition such as:

HMC: half matrix capture

SMC: sparse matrix capture

DMC: diagonal matrix capture

And others

For the basic 64-element FMC scan, a single TFM frame requires 4,096 A-scans. Figure 3-27 displays the process of building up the FCM matrix through a 64 elements probe, data acquisition, and the subsequent generation of a TFM image.



Figure 3-27: TFM beam summed to generate a pixel from the 1st to the 64th element

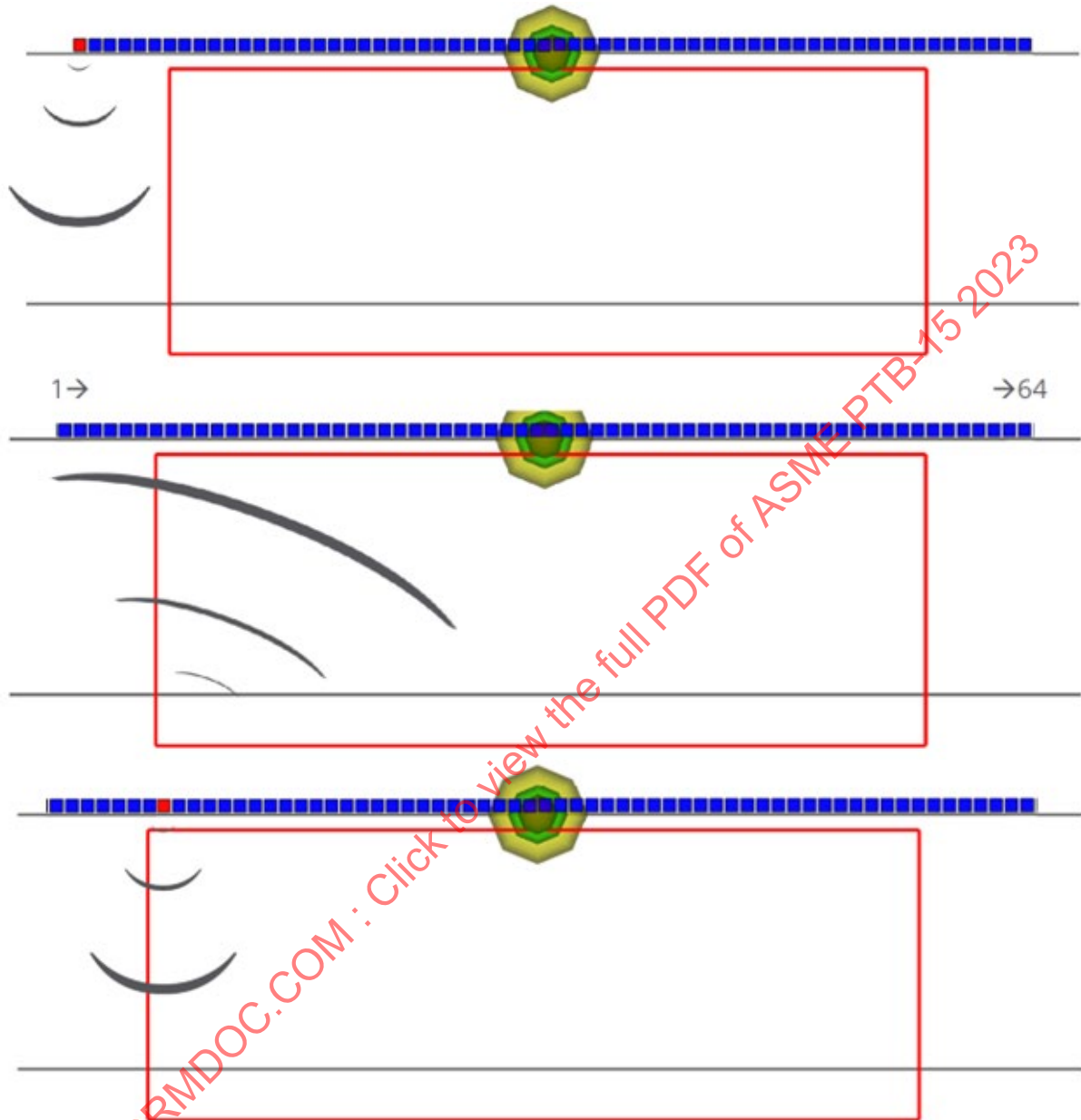


Image Courtesy from Sonatest

Find the predefined travel path for one pixel (x, z).

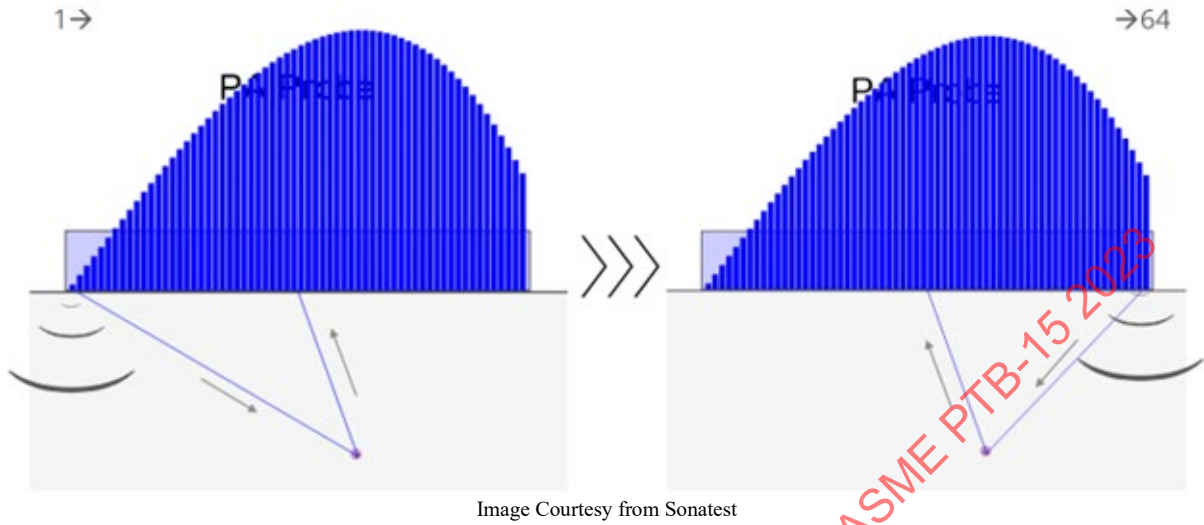
Sum all receiving elements.

Repeat the previous steps for all 64 transmitting elements.

Repeat the same procedure for every single pixel inside the Region of Interest (ROI).

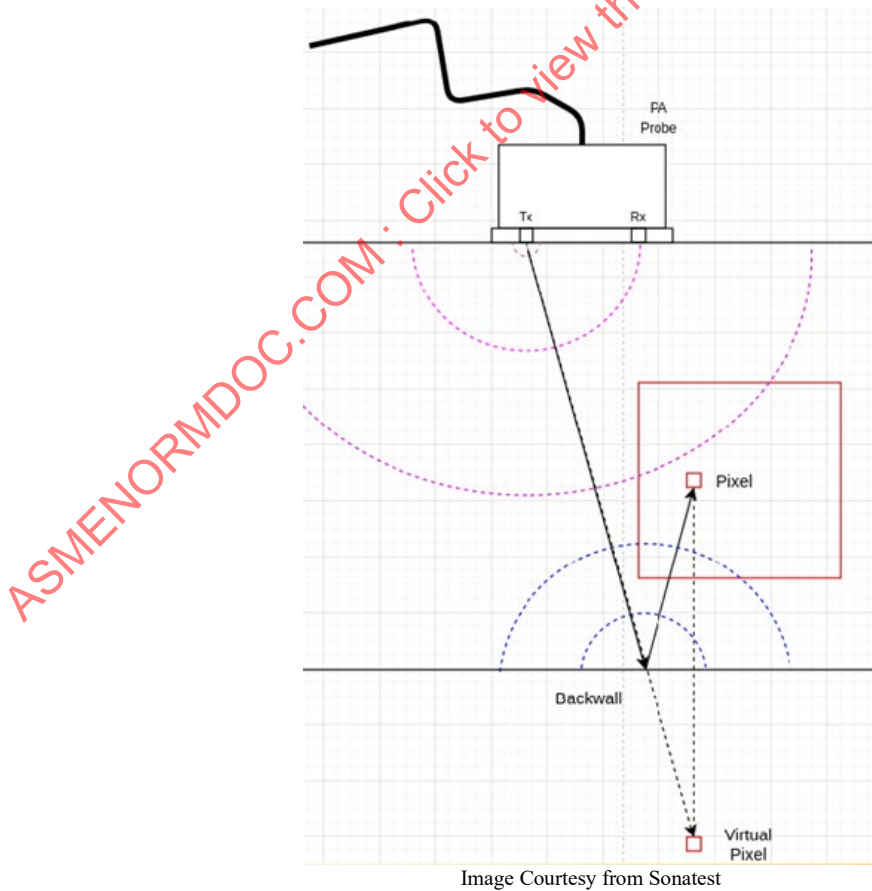
Figure 3-28 illustrates graphically how the image generation works in accordance with every single “TFM Beam”. The omnidirectional transmitting wave will reach a specific pixel at a specific position within the Region of Interest. All pixels are sampled for each propagation mode set to generate the corresponding associated image.

**Figure 3-28: Data acquisition and the generation of TFM image for a specific pixel**



Once the TFM acquisition is made as a function of a propagation mode, a TFM image is generated from an array of pixels. This image is rectangular and is built by sampling multiple A-scans data (synthetic A-Scan). The image color palette is typically from 0 to 200% FSH in range and shows no negative value.

**Figure 3-29: TFM image generation principle**



### 3.8.3 Propagation Modes

A propagation mode can be separated into a series of paths, also called legs, each of which is delimited by reflected points or by an interface point. Each leg is then associated with a certain velocity, called a propagation velocity. This mode is either said to be transversal (T) or longitudinal (L). Consequently, the propagation mode names are “L-L”, “T-T” or “L-TT”, etc. It means that direct, indirect, and reflection paths define the trajectory of the propagation mode. As a reminder, on TFM the focus is on the reception legs.

### 3.8.4 Region of Interest

The region of interest (ROI) is set in terms of the following parameters:

Propagation mode  
Index  
Depth  
Resolution  
Image sensitivity

The ROI is the “region” a user sets to extract A-scans from which to build the FMC, and then later the corresponding image for that zone of interest.

The propagation mode must be set as a function of the defect that users are expecting to detect, as a function of the manufacturing process, and as a reference to the procedure/standard. Depending on the geometry/shape and size of the defects, some propagation modes are more suitable for the detection of some defects in comparison to others. On the journey to improve the probability of detection, TFMi has been developed to allow the user to set up and view 4 propagation modes simultaneously. It will combine, through a mathematical operator, all FMCs from the propagation modes set, and then generate an image resulting from this combination.

Index is the parameter relative to horizontal orientation in the ROI. In other words, it can be considered as like the width of the ROI because the user has predetermined the starting and ending point (minimum and maximum) in terms of a dimension. Index can be located anywhere within the part, within reason. However, when it gets bigger, it will also have a direct influence in terms of whole processing time.

Figure 3-30: Index setup

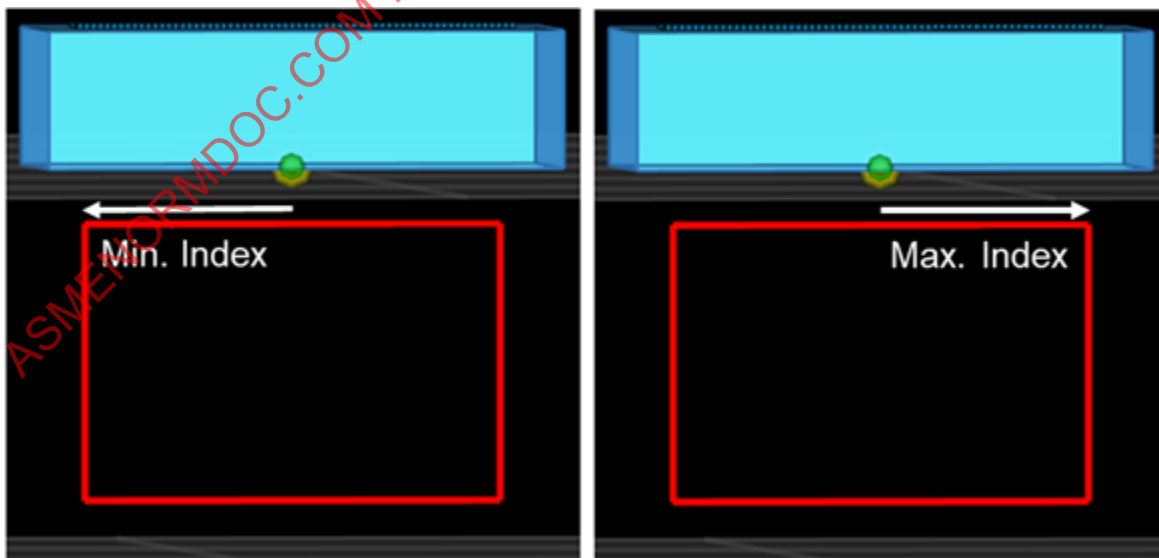


Image Courtesy from Sonatest

Depth is the parameter relative to vertical orientation because it sets the height of the ROI. Just as on the index dimension, the user must set the start and end point (minimum and maximum). Axis orientation in this case increases from the surface (0) into the part and as far as the thickness increases. However, the maximum height does not need to be limited to the nominal thickness of the part. Under some circumstances this may be desirable. For direct incidence modes (T-T, L-L, L-T) it is possible to set the ROI's depth thicker than that of the actual component. This feature is very useful for corrosion mapping assessment where in most cases there is a significant variation in the back wall echoes.

Figure 3-31: Depth setup

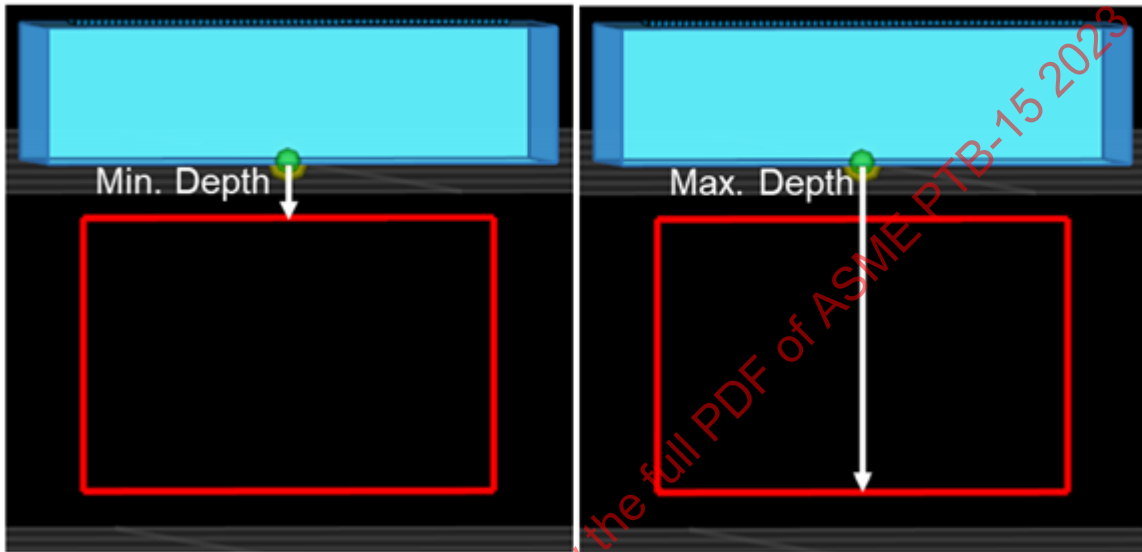


Image Courtesy from Sonatest

Resolution is related to the resolution of the image that it is going to be generated by TFM. Typically, TFM resolution is 0.1 x 0.1mm. However, the user can set different resolutions in both, or either, axis (depth and index) if necessary. With respect to increasing the image resolution (smaller values) the quality of TFM image will certainly improve, to a point, but it will also negatively affect the scanning speed.

Figure 3-32: Resolution setup for index and depth

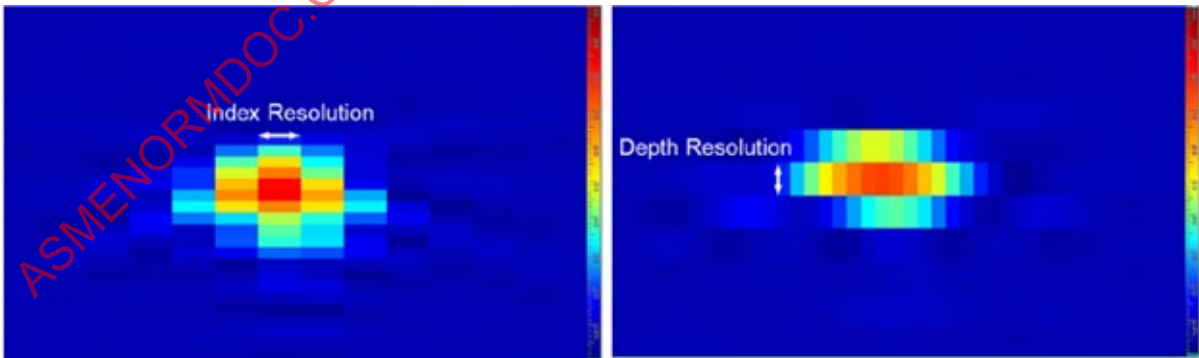


Image Courtesy from Sonatest

### 3.8.5 Image Sensitivity

The pixel amplitude height is not necessarily proportional as it would be for conventional and phased array UT. This means that by adding 6dB to a scanning it will not correspond to the same increment within the image. This behavior can be explained by two reasons:

Some elements can be already saturated (over 200% FSH; TFM amplitude ranges from 0 to 200% full screen height).

Some elements are close to 0% FSH and their amplitude will not improve, even when a major gain is applied to the scanning.

In addition, TFM scan amplitude can drop by having a ROI with a very low resolution as well. This means that under some circumstances, narrow echoes can vanish as TFM resolution decreases.

### 3.8.6 TFMi

TFMi (Total Focusing Method Intermode) is a feature that was developed to improve TFM capabilities. In most instruments available in the market, a user can run multiple single-propagation modes at the time. Therefore, the user must cerebrally combine the contribution of every single mode to generate the TFM image. With the help of TFMi, the user can combine the contribution of up to 4 different propagation modes to generate the TFM image. To make this possible, the user can select the most suitable propagation modes according to the above-mentioned part specificities, and then by selecting a mathematical operator, generate a TFMi image as a result of the contribution of every single propagation mode that has been selected.

There are two mathematical operators available on TFMi: “Product”, and “Keep max”. These mathematical operators are applied to FMC matrices for all selected propagation modes. The user must select one mathematical operator at a time, but they can be switched back and forth at any time.

Each mathematical operator applies a different action into the FMC matrix. They are described as follows:

**Product:** This multiplies every single element (echo amplitude) of all FMC matrices of every propagation mode that has been selected. Therefore, the TFMi image is the result of this multiplication among the elements through the FMC matrices.

**Keep max:** This takes the highest amplitude (echo amplitude) among every single element through the FMC matrices from the propagation modes that have been selected. Therefore, the TFMi image is the resulting selection from the highest amplitudes through the FMC matrices.

These mathematical operators can lead to different results in terms of TFMi image, even when the same propagation modes are selected. The “product” operator will proportionally enhance (increase) the amplitude within the TFMi image for those propagation modes that show non-zero amplitude. Zero amplitude elements on FCM matrices will no longer contribute to image generation. On the other hand, elements having a very high amplitude will greatly contribute to image generation.

The “keep max” operator will generate the TFMi image from the combination of the highest single contribution from every element through all FMC matrices, according to the propagation modes that have been selected. In this case, the TFMi image will be generated because of the highest amplitude from every pixel within the FMC matrices.

Figure 3-33 shows an example of a TFMi image. It compares, side by side, a sectorial scan and a TFMi image for a toe crack detected in a sample.



Figure 3-33: Toe crack. TFMi image on the right (2T-3T-4T) and sectorial scan on the left

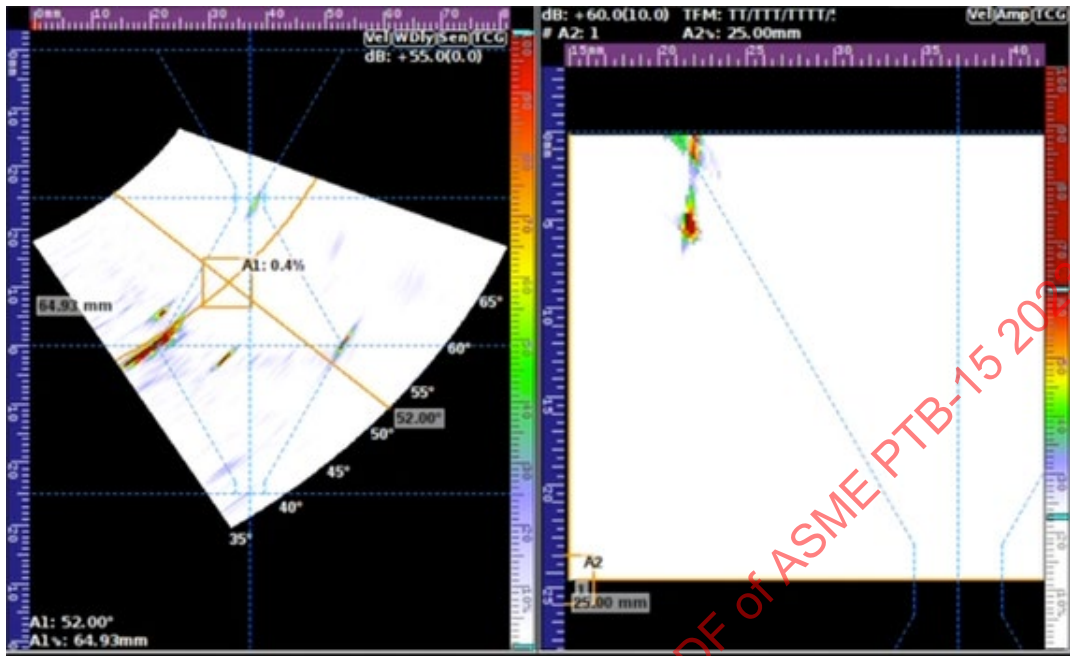


Image Courtesy from Sonatest

Another example is shown in Figure 3-34. It represents a sequence of multiple propagation modes (2T to 5T), the TFMi image, and a traditional PA image applied to the inspection of stacked side drilled holes in a standard block. One can identify the results of every single propagation mode and their individual contributions for the final image on TFMi. In addition, it is even more evident that the TFMi image is represented with a higher level of image fidelity for the shape/geometry of the side drilled holes, when compared to the typical sectorial scan of phased array.

Figure 3-34: Sectorial scan, TFM images (2T-5T) and TFMi image for a sequence of side drilled holes vertically aligned.

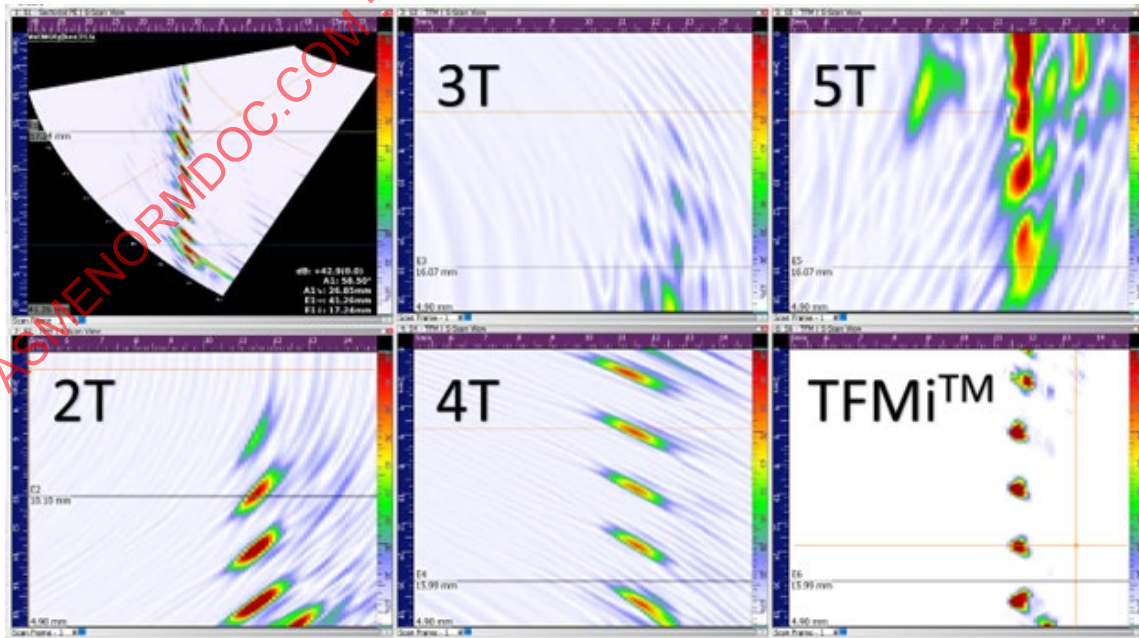


Image Courtesy from Sonatest



Figure 3-35 depicts a TFMi image of a vertical crack in a sample, and the side view (macroetch) of the sample. It is interesting to see how close the TFMi image is to the real crack, when one looks at its shape and geometry.

**Figure 3-35: TFMi image on the left and side view of a sample with a crack**



Image Courtesy from Sonatest

### 3.8.7 Advantages of TFMi

Ultrasound Phased Array represented a big improvement for detecting defects when compared to conventional ultrasonic inspection. Today, with TFM, the capability of inspection has moved to a higher level in terms of defect visualization and representation. Real life defects can exhibit very complicated geometries, shapes, orientations, and locations. TFM has arrived to bring the users a very powerful tool, enabling them to characterize defects by using multiple approaches in terms of propagation modes. The most favorable of which, in terms of incidence, would likely be unknown at the time of examination.

TFMi makes TFM even better because it enables the users to combine multiple propagation modes, according to their specific needs, to generate an image that represents, with a high level of fidelity, a defect (shape, location, and orientation). Consequently, the user(s) can accurately assess a defect in terms of an image, instead of an amplitude-based evaluation.

### 3.9 Phase Coherence Imaging

Although TFM enables easier image interpretation than conventional phased array inspection techniques, the use of a single element in transmission during acquisition can result in images with a poor signal-to-noise ratio (SNR). This low SNR is due to poor acoustic penetration, typically occurring in thicker components or components made with highly attenuative materials. However, this can also be affected by diffraction (transmitter element, receiver element, scatterers); transmission/reflection coefficients at interfaces; geometric attenuation of signal; inhomogeneities scattering losses; absorption/friction losses, and more.

To improve the SNR and remove the difficulties in achieving accurate distance amplitude correction (DAC) or Time Corrected Gain (TCG) calibrations in FMC acquisitions, researchers have started to look at the Phase Coherence Imaging (PCI) technique.

### 3.9.1 What is PCI?

Phase Coherence is a TFM imaging algorithm that uses only the phase information of the FMC data and ignores the amplitude information. Discounting the amplitude information from the acquired A-scans enables the generation of images that are solely based on signal coherence.

**Figure 3-36: DAS Algorithm (above), and DAS with Phase Information Applied Post Hilbert Transform (below).**

$$I_{TFM}(x, z) = \left| \sum_{k,l} \hat{a}_{kl}(\tau_{kl}(x, z)) \right|$$

$$= \left| \sum_{k,l} \underbrace{|a_{kl}(\tau_{kl}(x, z))|}_{\text{Amplitude}} \cdot e^{i\phi_{kl}(\tau_{kl}(x, z))} \right|$$

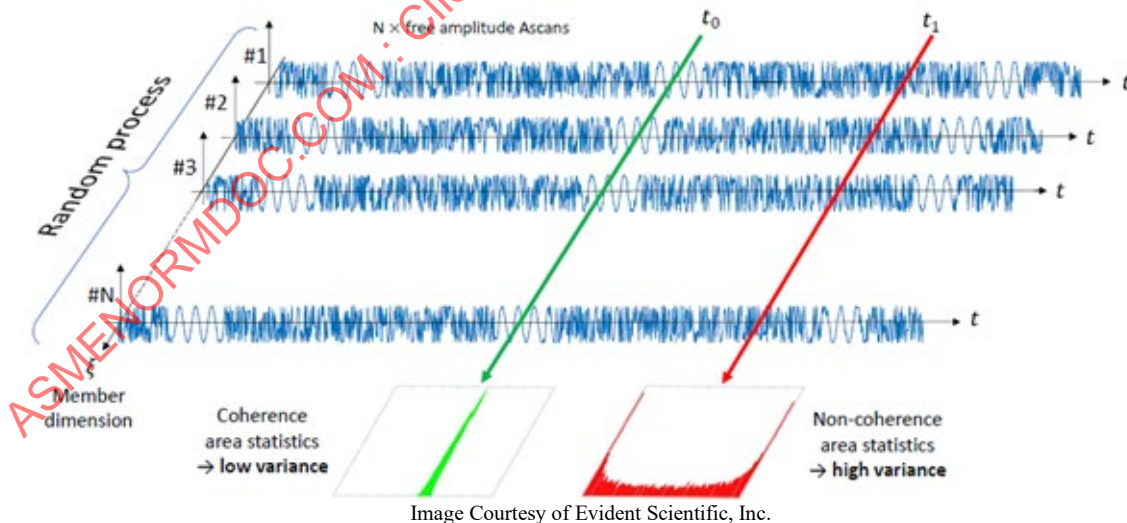
Amplitude Phase

Image Courtesy of Evident Scientific, Inc.

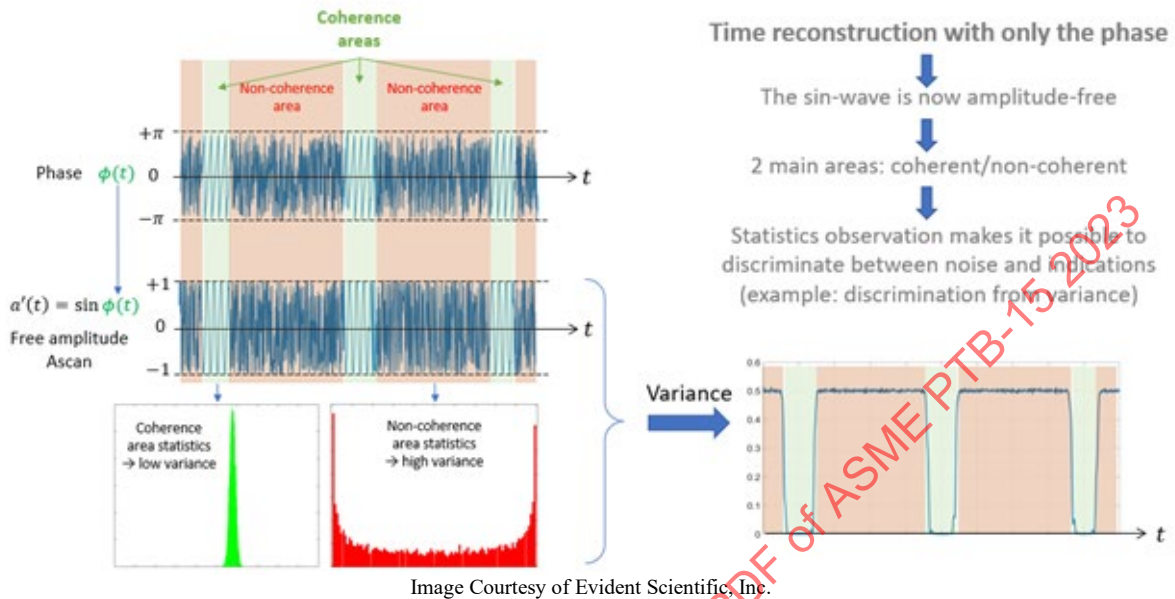
The first formula represents conventional TFM with Delay and Sum (DAS) summation of the delayed amplitude signals. The second formula represents the Analytic signal, once a Hilbert Transform is applied, to express the phase portion of the signals. (The Hilbert Transform is explained in greater detail in this chapter.)

Phase Coherence uses a statistical approach to identify defects. Figure 3-37 illustrates a randomized process where “N” can represent a large number of A-Scans, typical of an FMC acquisition. The noise areas will generate a much larger phase variance as depicted on the red histogram. Whereas the relevant coherent signal will repeat in a constant way, creating a defined and consistent signal phase distribution (seen on the green histogram).

**Figure 3-37: Shows statistical approach with randomized process and the variance difference of coherence vs. non-coherence areas**



**Figure 3-38: Shows high variance in coherence and non-coherence areas for noise to indication discrimination**



Looking at only the phase information enables flaw detection with signal amplitudes that would otherwise be considered incoherent noise in an amplitude based TFM image. Because material attenuation does not affect the phase of the signal, non-amplitude TFM performance can be greatly improved in thick or highly attenuative material inspection applications, or in noisy materials.

Phase Coherence Imaging is not based on the signal amplitude of a reflector, but instead on phase, so it is also virtually impossible to saturate the signal. This results in a more consistent and repeatable inspection. It also limits inducing human error with a time corrected gain or a gain adjusted signal, as gain is no longer needed to enable detection. In other words, the recorded signal only flags what is highly repeated in the coherence, and not on the strength of the returning signal to the probe. The magenta color represented as 100% on the color palette means that a high number of A-scans have considered this area coherent (or not-randomized noise) where the white, gray area has shown more variance in the signal. It is important to understand that the colors no longer represent an amplitude response as they normally would when using phased array or standard TFM.

PCI also does not require perfect perpendicularity with the indications to detect them, it is often found that fewer TFM groups or probe positions will be typically needed to perform the same inspection as compared to standard TFM. Figure 3-39 illustrates a hook crack in an Electric Resistance Weld (ERW) welded pipe. The PCI results on the left are capable of not only imaging the full length of the flaw using a single TT-TT mode of propagation, but also depicting an accurate depth and the connection to the inside diameter of the component. By contrast, two TFM groups are needed on the right, with conventional TFM, to image the flaw in its entirety.

**Figure 3-39: The entire hook crack can be seen with only the TT-TT group on the left in PCI, where two groups are needed with conventional TFM (TT-T and TT-TT) on the left. The crack can be sized using the tip diffraction.**

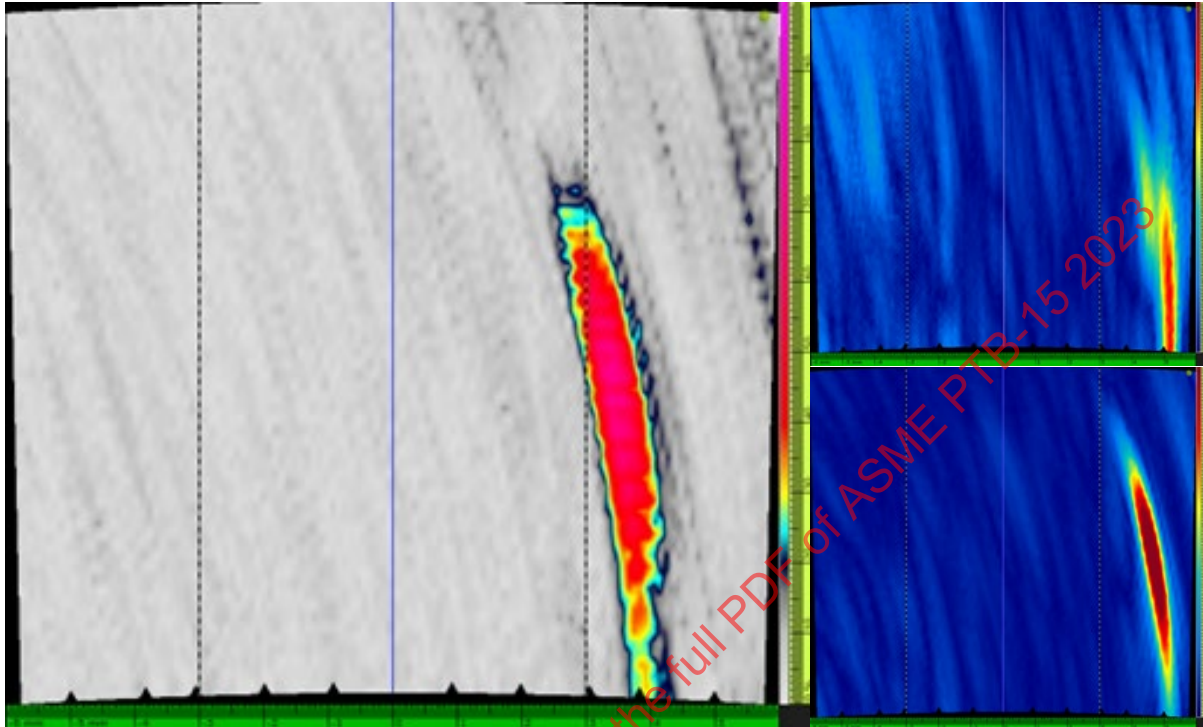


Image Courtesy of Evident Scientific, Inc.

### 3.9.2 Interpreting PCI data

Because the final PCI images are generated using the phase information, rather than the amplitude, the same analysis techniques cannot always be used. One key feature of phase coherence imaging is how different types of indications are imaged. Large and flat reflectors, which are considered specular reflectors, do not return a highly coherent signal to all the probe elements. The opposite being smaller reflectors that generally do not return a high amplitude response, which will tend to diffract the ultrasound waves. This produces a highly coherent signal to the majority of the probe.

The resulting effect is that smaller defects and crack tips are highlighted without being lost in the high amplitude signal from the other, larger defects. It is also easier to size these small defects because the tip diffractions will create a “hotspot”, having a maximum coherence level that is located directly at the crack tip. This is similar to the time-of-flight diffraction (TOFD) technique, where the cursors are used with the phase inversion to size defects. With PCI the cursors can be placed on the maximum values of these “hot spots” to accurately size cracks and other defects. This method also works for defects such as lack of fusion or porosity.

For these same reasons, additional details about defects can be seen using PCI. For example, it can also be difficult with amplitude-based techniques to identify if the defect is connected to the component surface. With PCI, each artifact, within a defect (crack direction changes, secondary tips, sharp artifacts, or corners), will return a coherent signal. This produces significantly more detail about the shape and form of the defect. For these types of defects, PCI can be an excellent tool for detection and sizing where damage mechanisms such as HTHA, SCC, H<sub>2</sub>S, or other small crack defects could be present.



Because amplitude has no effect on the final image, the sound distribution in the part is less of a consideration. Even if only a weak signal remains, the phase information can still be evaluated. This has two advantages compared to conventional TFM. The first is that the coherence level of the same defect will vary less throughout the entire TFM zone than that of the amplitude. The second advantage is a resulting technique that requires less preparation before an inspection. It also makes it easier to interpret the final images, and can make defects that were previously difficult, or impossible to see, obvious.

**Figure 3-40: Shows High Temperature Hydrogen Attack (HTHA) PCI data on the left, and conventional amplitude based TFM on the right**

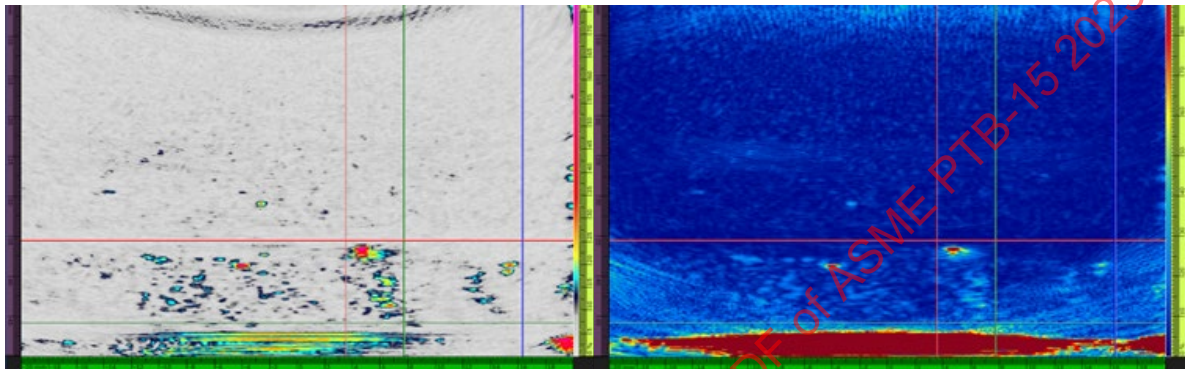


Image Courtesy of Evident Scientific, Inc.

**Figure 3-41: Shows Creep Damage PCI data on the left, and conventional amplitude based TFM on the right**

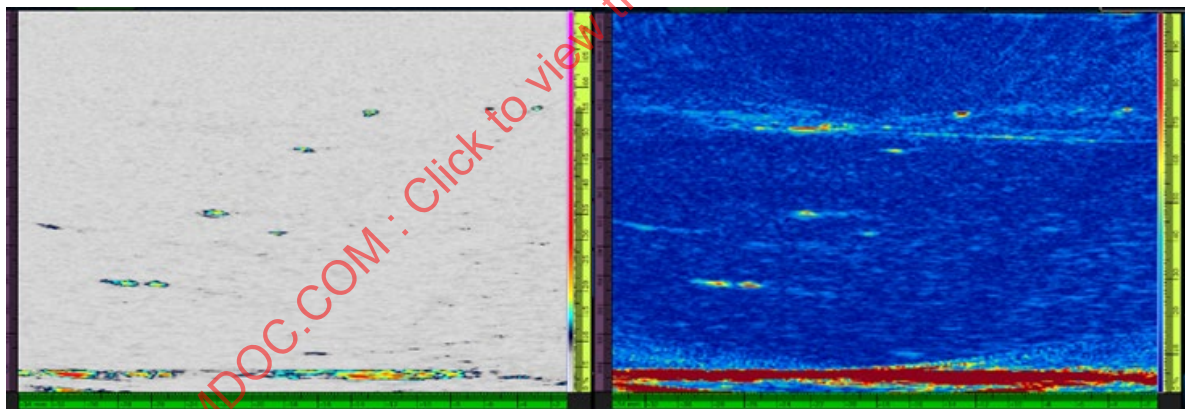


Image Courtesy of Evident Scientific, Inc.

As seen in Figure 3-40 and Figure 3-41, the smaller scatterers are better detected with the phase technique (PCI) than with the amplitude-based technique (TFM). Additionally, the signal-to-noise ratio has been greatly improved.

### 3.9.3 Conclusion

PCI can be beneficial for attenuative materials, thick components, or small intergranular diffractive damage mechanisms. It also limits human errors occurring in common inspections and can potentially increase the speed of acquisition, due to using fewer groups. PCI can also be extremely sensitive to small reflectors and provide accurate sizing using a tip diffraction technique, all while having the added benefit of a visual 2D representation of the flaw, for easier characterization.

## 4 INSTRUMENTS

### Hardware

#### 4.1 Hardware Challenges

In this section the issues of designing an FMC system are described. After sketching the challenge posed by the amount of data and calculations needed for making an image, some possibilities for dealing with the challenge are described. These are then further developed into system architectures. Finally, some of the additional requirements of more advanced algorithms are discussed.

##### 4.1.1 The Challenge Posed by FMC

The main challenge posed by processing FMC data is the full matrix. All combinations of transmitter and receiver elements of an array are collected during FMC, resulting in a large amount of data.

Consider the amount of data from a 64-element probe: the full matrix will have  $64 \times 64 = 4,096$  A-scans for each probe position. The amount of data generated for each full matrix, assuming an A-scan length of  $100 \mu\text{s}$ , a digitization rate of 100 MHz, and two bytes (16 bits) for storing the amplitude for each sample is:

$$4,096 \text{ A-scans} \times 100 \mu\text{s} \times 100 \text{ samples}/\mu\text{s} \times 2 \text{ Bytes} = 82 \text{ MB}$$

For example, a 1 m scan acquired at 1 mm increments would generate an 82 GB data set. Only a few years ago this would have been too big for storage on personal computers.

Knowing the size of the data set, we can now calculate the data acquisition rate. Assuming a 20 mm/s scan speed, the scan would take 50 seconds to complete, and the data rate would be  $82 \text{ GB}/50 \text{ seconds} = 1.6 \text{ GB/s}$ . A very fast network is required to sustain this amount of data over a network link. Typical ethernet cable only supports 100 Mb/s. Even inside a computer it is a challenge to deal with such acquisition rates.

##### 4.1.2 TFM Image Data Rate

Imagine the FMC data would be reconstructed into a  $512 \times 512$ -pixel image, i.e., 256k pixels. If we again use two bytes for storing the amplitude, the resulting image size is:

$$256\text{k pixels} \times 2 \text{ bytes} = 512 \text{ Kbytes}$$

The data acquired for the same 1 m scan length would be:

$$512 \text{ kB} \times 1000 \text{ mm} = 512 \text{ MB}$$

The data rate for images only is:

$$512 \text{ MB}/50\text{s} = 10.2 \text{ MB/s}$$

This is a much more manageable data rate.

##### 4.1.3 The TFM Calculation Challenge

For the TFM algorithm, the time-of-flight from each pixel to each imaging point must be calculated:  $256\text{k} \times 64 \text{ elements} = 16 \text{ million time-of-flight values}$ . This number can be reduced by half by realizing that, due to reciprocity, the TOF value for  $n$  transmitting elements and  $m$  receiving elements is  $n \times m$ , the same as  $m \times n$  if the acoustic path is the same in emission and reception.

For calculation of the image, the amplitude value for the appropriate time of flight needs to be collected for each of the 4,096 A-scans for each pixel of the full matrix. These 4,096 values are then added together. This requires 16 million address and sum operations. A standard computer CPU would not be able to process the data fast enough; thus, the calculations are almost always done in specialized processing structures like GPUs or FPGAs.



Assume that collecting each of the 16 million values takes 100 CPU clock cycles. This is roughly equivalent to the access time of basic memory of a computer, while accessing the hard disk takes longer and accessing specialized memory, like cache, is faster. The total time for collecting the amplitude values for the image for a 3 GHz processor would be:

$$16M \times 100 \text{ cycles}/3\text{GHz} \approx 0.5\text{s}$$

Imaging the whole weld from the example above would take about 500 seconds, or 8.3 minutes, for shoveling data around only. This is only an estimate, as actual times will depend strongly on how data is handled (hard disk, memory, etc.).

Real-time imaging should display at least 20 images per second (the scan rate), which is 10 times faster than the calculation shown above. Only electronic chips specialized in real time, or quasi real time, processing large volumes of data in parallel can achieve the required computation time. The TFM processing is a simple summation conducted over and over for hundreds of thousands of pixels, and these pixels can be independently managed.

Currently, the only chips programmable and flexible enough for the specific and relatively small NDT market (compared to Gaming or High Frequency Trading, for example) are:

FPGA acronym of “Field Programmable Gate Arrays”

GPU acronym of “Graphics Processing Unit”

A combination of both

Figure 4-1 shows a schematic overview of the system architecture of an FPGA and a GPU based system.

#### 4.1.4 FPGA Performance

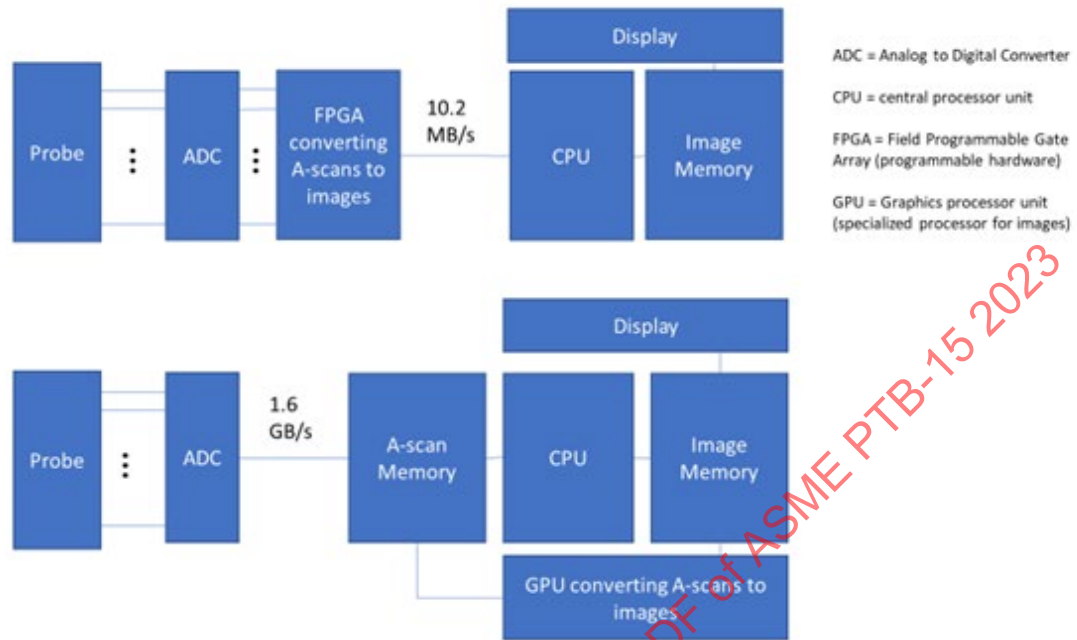
In an FPGA, many of these calculations can be done on board and in parallel with data collection. The time-of-flight values can be calculated prior to scanning, and the treatment of each A-scan could be done in parallel, depending on the architecture of the code in the FPGA. As an FPGA is programmable electronics rather than a computer, the process itself is also much faster.

As an example of FPGA performance, the “IWEX” FMC system (Applus RTD) processes over 10 different TFM imaging paths in parallel at a refresh rate of 60 Hz. This is over 300 times faster than the example shown above. The main challenge is to manage the FPGA memory and the memory accesses to DDR, which can slow down the processing of big images. The FPGA memory and the processing clock speeds continue to increase.

#### 4.1.5 GPU Performance

A GPU-based system uses a processor that is optimized for making images and runs in parallel. GPU performance improves every year. Typical GPUs in 2020 have around 2000 parallel processing units, and this might double for the next generation in 2021. The performance in terms of screen refresh rate is ultimately higher than that of an FPGA solution. The main bottleneck is that the data must be transferred to the GPU before the calculation can be done. Thus, the GPU-based system can be limited by data transfer rates and file sizes, as described above.

**Figure 4-1: Schematic architecture of an FPGA (top) vs and GPU (bottom) based system**



#### 4.1.6 FPGA/GPU Comparison

Advantages of FPGAs:

“Really real time”, usually faster if the memory of the FPGA can manage a larger number of computation kernels (i.e., pixels)

Necessary to have at the digitizing/processing buffering level for GPU anyway

Simpler cabling/networking solutions

Disadvantage of FPGAs:

Much more difficult and time consuming to program than GPUs

Evolving less quickly than GPUs

Less specialized for image processing

Raw A-scan data must be discarded to gain the advantage in data transfer speed

Advantages of GPUs

Flexibility and coding speed: much easier to adapt to a new algorithm than FPGAs

The GPU processing power increases every year, but the code doesn’t need to be partially or totally re-written at every generation, as TFM speed increases accordingly.

Easier to accommodate storing the raw data and post-processing with advanced algorithms

Disadvantages of GPUs:

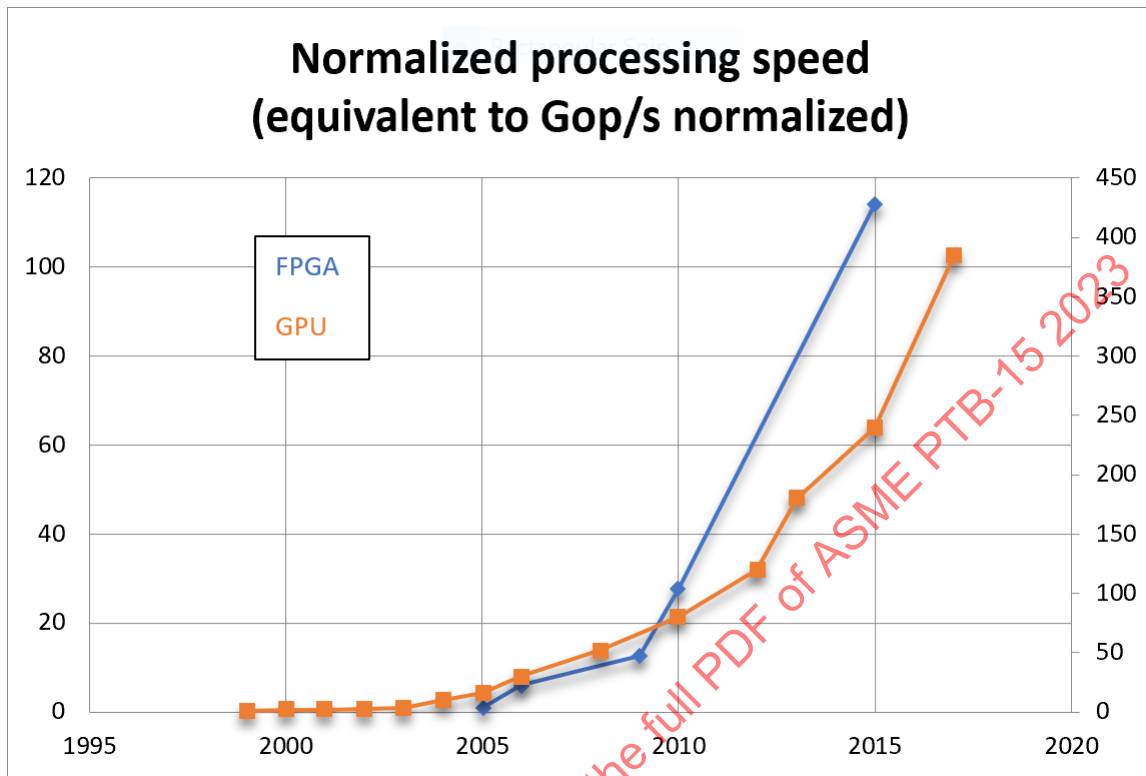
GPUs are not “real time”. Element signals must be digitized, eventually processed, buffered, and then transferred to the GPU. An FPGA is usually required to manage that.

The high data throughput bottleneck of FMC must be managed

Energy consumption is higher than FPGAs

In terms of pure processing speed, FPGAs and GPUs are extremely difficult to compare, but some references in the following timeline have tried to compare both chips [16] [17]:

Figure 4-2: Timeline showing the progression of GPUs



#### 4.1.7 Adaptive and Iterative TFM

These TFM processes pose different challenges, especially when performed in real time. Here, the challenge is in calculation of the Time of Flight (ToF) values for the TFM calculations. In the examples used above, there are 16 million ToF values. In ATFM, we would want to adjust these values based on information in the A-scans or the images to enhance the final image. This could be a single pass or an iterative process.

TFM paths are usually calculated using Fermat's principle, basically trying to find the shortest path between two points for given values of the sound velocity between those points. The issue is that most NDT applications have at least two media with different sound velocities, such as in the wedge or immersion medium versus the material to be examined. Finding the correct path(s) is compounded by the fact that the wave mode in both media might be different, e.g., compression waves in the immersion medium and shear waves in the material to be examined. A further complication is that the interface between both media might not be straight, at a fixed angle, or continuous. For each ATFM application, the conditions must be worked out, and the optimal scheme for calculating the ToF values are determined. A sizable amount of literature exists about the ways to find the shortest path of ultrasonic waves.

It may be readily understood that some of these calculations may become complex and take a lot of time or processing power.

**Table 4-1: Comparative Chart of FPGA and GPU Processors**

	FPGA	GPU
Speed	“Real time” data processing	Not real time, and may require an FPGA for data transfer to and from the GPU
Hardware/Implementation	Simpler cabling and networking, lower energy consumption	Higher energy consumption
Programmability	Difficult to program	Easier to adapt new algorithms, algorithms are forward compatible with new generations GPUs
Data Handling	Raw A-scan data must be discarded	All data can be retained, specialized for image processing

## 4.2 Deployment Schemes/Scanning Equipment

### 4.2.1 Introduction

FMC/TFM is no different than any other ultrasonic technique with regards to deployment. There are numerous, different schemes for delivering sound into the component. In general, these can be lumped into four different categories as defined in the ASME Sec. V Code. Arguments can be made against one being better than the other, but there are many considerations to be made when selecting any type of scanning equipment, and different advantages and limitations to each.

### 4.2.2 Manual Scanning

Manual scanning (ASME): “A technique of ultrasonic examination performed with search units that are manipulated by hand, without data being collected.” Quite simply put, this is having a probe literally in hand, with no scanning mechanism involved.

Some of the advantages to this are:

Unlimited resolution. Being able to manipulate the search unit in any orientation, skew angle, back and forth across a weld, etc., can be a benefit, especially when sizing flaws. Having a live action view on the screen and the ability to move the search unit everywhere can reveal unique components exhibited by an indication. These may or may not otherwise be available in a dataset.

The least expensive and easiest of all.

Some of the limitations are:

Manual scanning is operator dependent. Rate of movement, total surface coverage, or any amount of overlap is difficult to achieve, or especially prove.

There is no data recorded for future analysis or record keeping.

### 4.2.3 Nonautomated Scanner

Nonautomated scanner (ASME): “A scanner operated without a mechanical means of holding an index or search-unit offset position. Nonautomated scanners are propelled manually by the operator and have no means of holding or maintaining probe position once released.” These are your typical string type (potentiometer or “string pot”), or small wheel type encoders. Typically, they are just affixed to the search unit in some manner. See Figure 4-3.

**Advantages:**

These are simplistic and easy to use.  
Good for small jobs, bench-top work in a lab, etc.  
Generally, the least expensive option.

**Limitations:**

Data collection is only along a single axis. Different offsets or scan lines, when required, are generally stitched together with software, or not at all.  
Can be a challenge to maintain reliable contact and steady speed.  
Some type of external guidance (e.g., magnetic strip) is recommended to keep the data from wandering as they have no means to mechanically maintain search unit position.

**Figure 4-3: Examples of wheel type encoders**

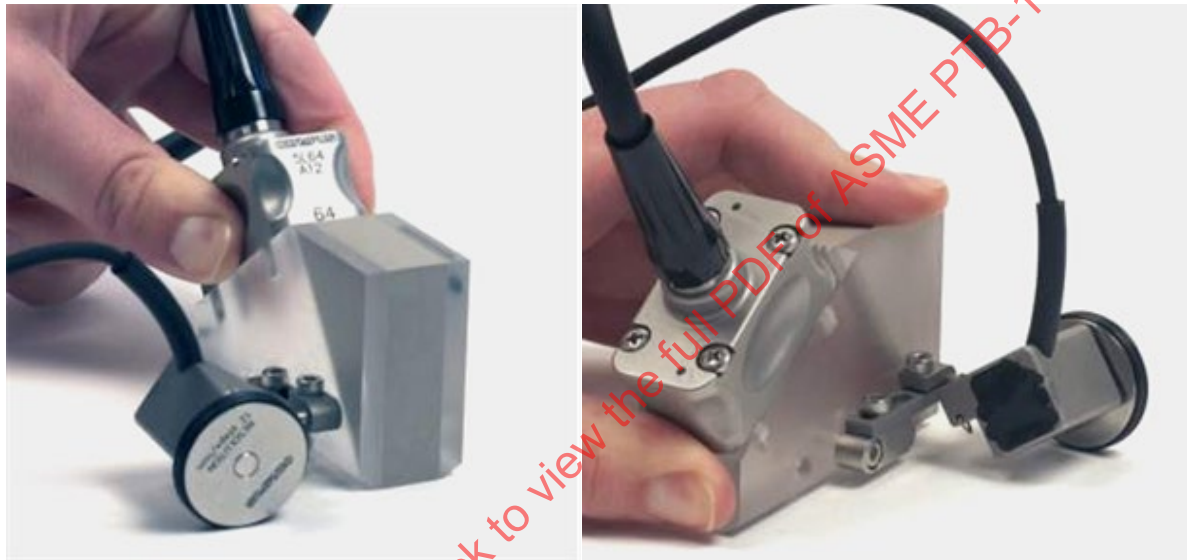


Image Courtesy of Evident Scientific, Inc.

**4.2.4 Semi-automated Scanner:**

Semi-automated scanner (ASME): “A manually adjustable scanner that has mechanical means to maintain an index of the search unit while maintaining the search-unit offset position, but which must still be propelled manually by the operator. This scanner does have mechanical means to retain its position while attached to the component once released by the operator.” This is probably the most common type of scanner encountered in the field. There are many different configurations, and they are usually employed for weld exams as well as area scanning for corrosion. From simplistic, to complex, to highly configurable modular designs there is a semi-automated scanner for almost every occasion. They usually have some type of guidance like a roller chain, track, or even gearing. The important differentiator is that they have some type of guidance but are still manually propelled. See Figure 4-4.

**Advantages:**

Some are configurable for different applications.  
Most, if not all, modern portable instruments have the corresponding encoder inputs and software for these. Essentially making them “plug and play”.  
Are generally easy to use.  
Can collect good data in two axis, especially when a guiding device is set.

**Limitations:**

Moderately expensive to expensive.



They can be larger and require more space to operate. Some scan limitations are to be expected in the field.

Are still propelled by hand, which lends some capability to the technician.

May require an additional technician to control both scanner and acquisition unit.

**Figure 4-4: Some examples of Semi-automated (chain) scanners, and the use of a laser guided system (bottom right)**



Image Courtesy of Evident Scientific, Inc.

#### 4.2.5 Fully Automated Scanner

Automated scanner (ASME): “A fully mechanized scanner that, after being attached to the component, maintains an index and the offset position of the search unit. The scanner is manipulated by an independent motor controller and requires no manual handling during operation.” These scanners can range from the old industry standard pipe scanner, which is very simplistic, reliable, and rugged, to state-of-the-art robotics with laser or optical guidance systems. Some are custom builds used only with specific hardware, while others, although typically requiring a motion control system, are built to be flexible between different instruments. See Figure 4-5.

Advantages:

When set up and running properly, they can collect data very consistently and repeatedly.

Depending on the application, some are built to access spaces humans cannot occupy, and “Driving” to a location, then scanning remotely, is appealing.

Some are submersible.

Limitations:

Often the most expensive option.

Longer set up times.

Due to the complexity of some of these, additional training will be required. Due to their size, and depending on the application, scanning limitations can be expected in the field.

**Figure 4-5: Examples of a fully automated scanner**



#### 4.2.6 Application Specific

It is worth noting that some scanners only perform a specific function or are only configured for a specific type of component. Although these can also be categorized with the above, they are otherwise considered niche. Some are specialized to perform area exams on elbows, others are specific for examining nozzle to shell welds, others are purpose built for small diameter boiler tube exams, and still others act like a paint brush that can move in any direction reporting coverage in real time. See Figure 4-6 for examples.

**Figure 4-6: Examples of an elbow scanner (left), and a paintbrush scanner (right)**



Image Courtesy of Evident Scientific, Inc.

#### 4.2.7 Conclusion

Any type of configuration or complexity, it would seem, has already been solved. Even though some great tools have been made over the years to provide better ultrasonic data and keep the operators safe, there is so much more to come given recent advancements with robotics and drones. When considering a scanner, the inspector must keep in mind the application they will be using it on. Scanners can be versatile, or niche to a specific application. They can ease the inspection process or add mechanical complexity to the project.

ASMENORMDOC.COM : Click to view the full PDF of ASME PTB-15 2023

## 5 ARRAYS

### Transducer Considerations for Full Matrix Capture

#### 5.1 Abstract

This chapter gives an overview of ultrasonic transducers, their construction, and application to Total Focusing Method/Full Matrix Capture. The chapter begins with the basic construction and operation of transducers, initially reviewing conventional single and dual element transducer construction, and then progressing to arrays. Basic transducer beam modeling is then covered, and the usefulness of these models with respect to array elements and array apertures is discussed. Finally, array selection for FMC/TFM is discussed.

#### 5.2 Basic Overview of Ultrasonic Transducers and Their Construction

##### 5.2.1 What is a Transducer?

The dictionary definition of a transducer is a device that converts variations in a physical quantity, such as pressure or brightness, into an electrical signal, or vice versa. In the case of ultrasonic transducers, these specialized devices convert a detected pressure wave into voltage and inversely convert a voltage pulse from an instrument into a transmitted pressure wave.

While there are several different transduction mechanisms that can be used for ultrasonic transducers, including piezoelectric, electromagnetic (including Lorentz force and magnetostriction), and capacitive, this chapter only considers the piezoelectric device, which is the most widely used for transducer arrays. These transducers contain a piezoelectric element (or array of elements), that performs the task of converting physical pressure into electrical voltage and vice versa.

##### 5.2.2 The Piezoelectric Effect

The piezoelectric effect is a physical phenomenon observable in certain materials where an electric charge is generated in response to an applied mechanical stress. The word piezoelectric means “electricity resulting from pressure and latent heat” and is derived from the Greek piezein, which means to squeeze or press, and piezo, which is Greek for “push”. This conversion of stress/pressure to charge/voltage is referred to as the direct piezoelectric effect (Figure 5-1a).

The piezoelectric effect is reversible, i.e., materials exhibiting the direct piezoelectric effect (the generation of electricity when stress is applied) also exhibit the inverse effect (the generation of stress when an electric field is applied); see Figure 5-1b. Thus, an ultrasonic transducer constructed with a piezoelectric material can be used as a transmitter and a receiver.



**Figure 5-1: Direct (a) and inverse (b) piezoelectric effect. The most common transduction mechanism used in ultrasonic transducers for industrial, medical, and commercial ultrasound applications.**

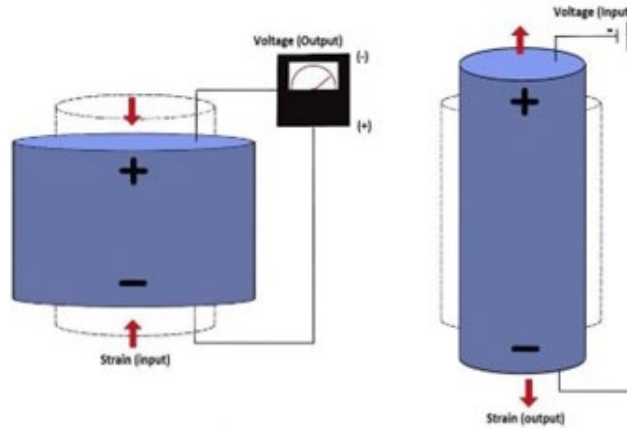


Image Courtesy of Sinewave Solutions

Piezoelectric materials are widely used in industrial, scientific, medical and commercial applications. Examples of industrial devices include those used for the production and detection of sound (and ultrasound), generation of high voltages, electronic frequency generation and micro-actuation. Piezoelectricity is also the basis of some scientific instruments such as scanning tunneling microscopes (STM), atomic force microscopes (AFM) and transducers in acoustic microscopes. Commercial applications include spark ignition sources for cigarette lighters or gas grills, transducers for fish finders, actuators for fuel injectors, and transducers for object detection and distance measurement, to name a few.

There are many natural and synthetic materials that exhibit the piezoelectric effect. While natural materials, including quartz crystals, were initially used as transduction materials for ultrasonic transducers, most transducers constructed today use a variety of synthetic materials due to their superior properties. Synthetic materials that are commonly used in industrial ultrasonic transducers include various formulations of lead zirconate titanate (PZT), lead metaniobate, and lithium niobate crystals.

Composite materials formed of PZT ceramic and polymer epoxy are also now common and offer improved performance for certain applications. Piezo-composites are widely used in industrial array transducers due to their superior ultrasonic properties and ease of manufacturing.

### 5.2.3 Types of Transducers

There are many types of ultrasonic transducers found in industrial nondestructive testing (NDT), including devices that are used in direct contact with components, in a water immersion bath, and specialized transducers that are fabricated to conform to very specific part or array geometries. A small sampling of industrial transducers is shown in Figure 5-2.

**Figure 5-2: Various types of ultrasonic transducers that can be found in industrial NDT, including (a) single element contact transducers, (b) bespoke transducer design for turbine disk inspection, and (c) high temperature, wedge mount linear arrays for weld inspection**

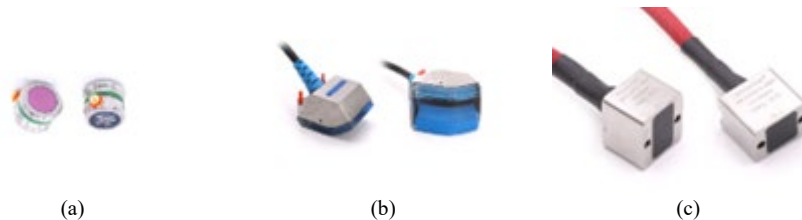


Image Courtesy of Sensor Network Inc.



In general, industrial parts have widely varying geometries, inspection requirements and physical properties, which in turn require a diverse range of ultrasonic transducers. Transducer parameters include type (direct contact, wedge mount, immersion), overall size and shape, individual element size, frequency, number of elements, cabling, and electrical connections (e.g., connector type, number of connections, pinout, etc.).

#### 5.2.4 Basic Construction

Figure 5-3 exhibits the basic constructional elements of two common types of piezoelectric ultrasonic transducers: single element and dual element.

**Figure 5-3: Basic transducer constructional elements for industrial single (a) and dual (b) element piezoelectric transducers.**

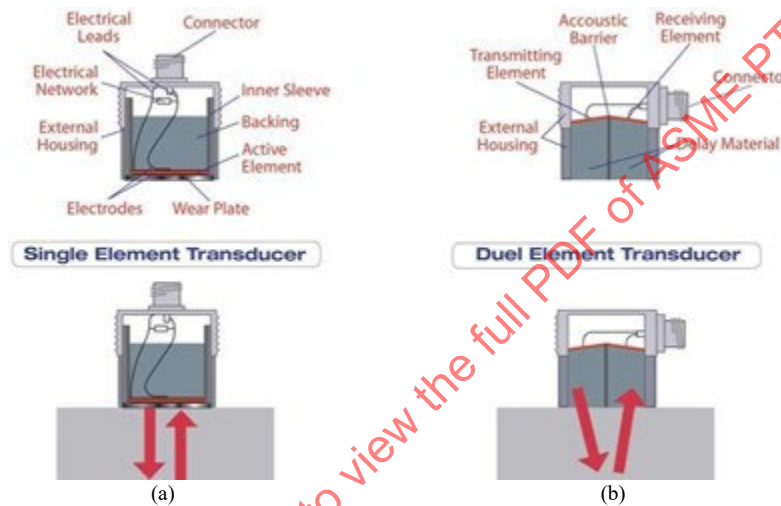


Image Courtesy of Evident Scientific, Inc.

Turning first to the basic acoustic components of the single element transducer, the “acoustic stack” consists of the piezoelectric material (including electrodes), front matching layer(s) or wear face, and backing material. The components and materials in the acoustic stack are primarily responsible for the performance of the transducer, including parameters such as frequency, gain, pulse duration, and bandwidth. The transducer designer can choose from several different components and/or materials to tailor the performance of the transducer. The electrical characteristics of the transducer are also dependent on the acoustic stack, and careful material selection is important to electrically impedance match the transducer to the instrumentation.

**Active Element/Resonance Frequency:** Ultrasonic transducers for NDT are most often constructed as resonant devices, having a natural frequency response that is typically in the frequency range of 0.5MHz to 20MHz (MHz: millions of cycles per second!). In most designs, the piezoelectric material vibrates at twice the natural frequency of the element thickness, thus the element is sized to be one half ( $\frac{1}{2}$ ) wavelength in thickness to produce the desired resonant frequency. As an example, for a 5MHz transducer, the thickness of a piezocomposite element is around 0.3 mm (0.012 in.).

Most typically, the piezoelectric material chosen can include any of several formulations of lead zirconate titanate (PZT) as offered by a variety of ceramic manufacturers. Generally, these materials and their specific model designations can be equated to various “Navy” types as defined by the United States Navy for sonar applications (Navy type II, IV, V), etc. Material properties vary widely and can be chosen for a variety of reasons, including desired bandwidth and electrical impedance matching. Lead metaniobate (for high resolution), lithium niobate (high frequency or high temperature), and PZT composites (general purpose and high sensitivity) are also commonly used transducer elements. High

dielectric materials of the PZT 5H type is usually used for array transducers to improve electrical impedance matching.

**Electrodes:** Electrodes are applied to the front and back surface of the piezoelectric material to transmit charge to and from the ceramic. Solid ceramics are often plated with thick-film silver electrodes for lower frequency elements, while sputtered electrodes are used for higher (>10MHz) ceramics.

Electroless copper or nickel plating as well as sputter-deposited plating are commonly used on piezocomposite elements.

**Front matching layer/wear face:** A front matching layer is placed on the front (operational) side of the ceramic to provide acoustic impedance matching, protection, and a wear surface (for contact transducer type). Usually, an epoxy compound is used for immersion or wedge mounted probes for improved acoustic impedance matching to those materials. Alumina ceramic provides a hard, wear resistant surface that is common for contact probes. From an impedance matching perspective, the acoustic impedance of the matching layer is chosen to be in between the impedance of the element and the impedance of the transmitted material (water, plastic, steel) to provide optimum energy transmission. The thickness of the layer is typically chosen to be in the range one quarter ( $\frac{1}{4}$ ) wavelength in thickness. Multiple matching layers are also sometimes used to further improve sound transmission.

**Backing:** A backing material is applied to the rear face of the ceramic to suppress unwanted vibrations of the ceramic (ringing) and to provide mechanical structure to the transducer. The acoustic impedance (analogous to mechanical stiffness) can be tailored to achieve the desired acoustic response of the transducer. Higher impedance, “heavy” backings are used to create short duration pulses or “broadband” transducers. Backings for transducers containing solid piezo ceramics are often made of epoxy loaded heavily with tungsten powder to achieve an acoustic impedance greater than 10 MRayls. Backings for piezocomposites are often epoxies loaded with various metal oxide powders, as they only need to achieve an acoustic impedance of 3-7 MRayls. The unit of measure of characteristic acoustic impedance is the Rayl, named after Lord Raleigh. It is calculated by multiplying the density of a material with its ultrasonic velocity ( $Z=\rho C$ ). Typical values (in MRayl) include Steel: 45, Water: 1.5, Air: 0.0004, Plexiglas: 3.2, PZT 5H: 34, Piezocomposite: 6-15.

**Electrical leads:** The electrical leads provide the electrical connection between the active element and the electrical connector and usually consist of fine-gauge copper wire. Fine ribbon wire is usually used at the element as it can be sandwiched between the backing, element and face layers without creating an excessively thick glue joint that would degrade the performance of the transducer.

**Electrical Connector:** Electrical connections to ultrasonic transducers are usually made with coaxial cables due to the relatively high frequencies involved; thus, the electrical connector is usually a coaxial type of connector. Connector types such as BNC, 10-32/ “microdot”, Lemo (push-pull), and UHF are all commonly used. Sometimes, a coaxial cable is constructed to be integral to the transducer and the connectors are applied to the end of the cable.

**Electrical Network:** The electrical network is also commonly referred to as “tuning” and is used for a variety of reasons including altering the bandwidth or frequency response of the transducer, matching electrical impedance between the active element and the transducer cabling and system, and altering the amplitude of the signal (also referred to as transducer “gain” or “sensitivity”). The tuning network often consists of one or more inductors, resistors, or transformers.

**Inner Sleeve:** The inner sleeve of a transducer provides some acoustic isolation between the acoustic stack and the external housing so that sound is not transmitted into the housing causing unwanted or “parasitic” echoes in the transducer response. It is also a structural element of the transducer.

**External Housing:** The external housing of the transducer provides the overall physical package of the transducer and is typically constructed of stainless steel. It often has attachment points such as bolt holes or threads that are used for holding the transducer as well as to attach the transducer to polymer wedges.

Dual element transducers: Dual element transducers (Figure 5-3 b) have some additional constructional elements. A dual element transducer separates the transmit and receive elements, rather than using the same element for both transmit and receive. This is done primarily to increase the near surface resolution of the transducer so that small, near surface reflections are not swamped by the otherwise large direct reflection of the surface as found with single element probes. These transducers use a delay line between the transmitting and receiving elements to delay the initial system pulse response from the ultrasonic reflections from the material. The delay lines are usually a plastic material or graphite for high temperature probes. An acoustic barrier, usually consisting of cork-rubber, is used to acoustically isolate the transmit and receive sides of the transducer.

### 5.2.5 Piezocomposite

As already mentioned in this chapter, piezocomposite materials are one of the options for the “active element” in an ultrasonic transducer. Because of the somewhat unique construction and properties that are achievable with piezocomposites, they are often used as the active elements for industrial transducer arrays and thus warrant extra discussion as follows. Additionally, piezocomposite elements can provide improved sensitivity and increased bandwidth—both advantageous for many NDT applications.

Connectivity: A piezocomposite material is a composite consisting of a piezoelectric ceramic (most often lead zirconate titanate (PZT) ceramic) and a polymer (usually epoxy). These composites can be constructed in various forms but two most commonly used for ultrasonic transducers are shown in Figure 5-4. The “connectivity” of the composite is defined to describe the physical connection of the ceramic and polymer, respectively. In the case of 2-2 composite (Figure 5-4 a), the ceramic and polymer phases are connected/continuous in two dimensions. In the case of 1-3 composite (Figure 5-4 b), the 1-3 designation describes a material with ceramic/ “1” direction connectivity in a single direction and epoxy/ “3” direction connectivity in three directions. Most “composite” transducers for NDT use some variety of 1-3 composite. Medical arrays frequently use 2-2 composite as well as 1-3 varieties.

Figure 5-4: Schematic representation of piezocomposite material in a) 2-2 connectivity and b) 1-3 connectivity

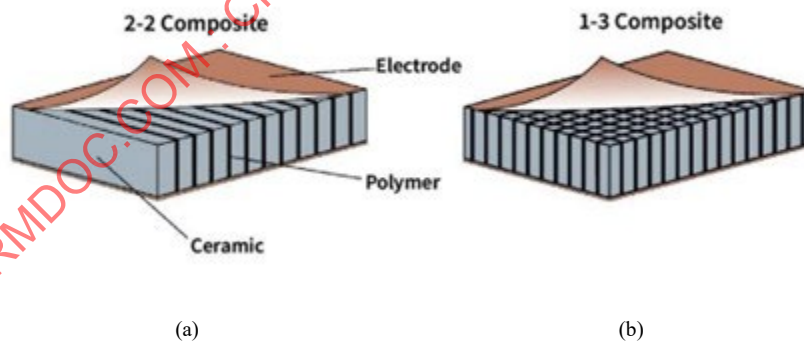


Image Courtesy of Sinewave Solutions

Volume Fraction: The volume fraction (VF) of the composite denotes the percentage of ceramic material to polymer. A 100% VF denotes solid ceramic, while a 0% VF denotes 100% polymer. The typical range of VF is 30% to 80%, as it has the best properties. Volume fraction is tailored by the designer to alter the acoustic impedance, electrical impedance, and sometimes the mechanical flexibility of the material.

Advantages: Advantages of piezocomposites are that they are readily tailored, have high electromechanical coupling efficiency, have lower acoustic impedance that allows improved impedance matching to water or plastic, have broad bandwidth/low mechanical quality factor, are mechanically flexible (easily allowing curved or focused elements), and can be segmented into arrays

by electrode patterning. The thickness-mode electro-mechanical coupling ( $K_t$ ) of the composite exceeds the  $K_t$  (0.4-0.5) of the base ceramic, approaching the value of the rod-mode  $K_t$  (0.7 to 0.8) of the ceramic. Effective acoustic impedance of typical 1-3 piezocomposite is often in the range of 6-15 MRayls as opposed to that of the raw PZT (30-40 MRayls) and provides an improved impedance match to materials such as water for immersion transducers and plastic for wedge mount transducer.

### 5.3 Transducer Arrays

Generally, an array is any transducer that has multiple elements within a single mechanical housing. With respect to their use in nondestructive testing transducer arrays are multi-element transducers that have 16–128 (or more) small, approximately 0.25-5 wavelength elements, where signals from multiple or all elements are used to form a coherent beam using electrical manipulation such as delay and sum beamforming, indexing, and/or full matrix capture (FMC) and total focusing method (TFM).

#### 5.3.1 Linear Arrays

The linear array is perhaps the most common form used in industrial phased array testing, including TFM/FMC applications (Figure 5-5). This configuration allows electronic control of one plane of the transducer, as defined by the Azimuth and Depth axes. This plane could be further described/defined as the “active plane” of the transducer. On this plane, electronic control via conventional phased array and/or TFM/FMC processes can alter the steering angle, depth of focus, and position of the sound beam. The elevation direction/plane of the linear array transducer is static, and its beam characteristics are determined by the probe frequency, aperture size, and whether a focusing lens (or curvature) is present. This plane is often called the passive plane. In medical b-mode imaging, practitioners also refer to “slice thickness,” which describes the beam width parallel to the passive plane and thus the depth of the image slice.

When considering the selection of an array geometry, it is important to include the parameters that define both the active plane (pitch, # elements) and the passive plane (elevation width, focusing lens) to achieve optimum imaging results.

**Figure 5-5: Schematic view of linear array geometry showing electronic control over a sub aperture of the array which allows electronic control of the beam (steering, focusing and scanning). Elevation performance is fixed by the frequency and aperture size and potential addition of a focusing lens.**

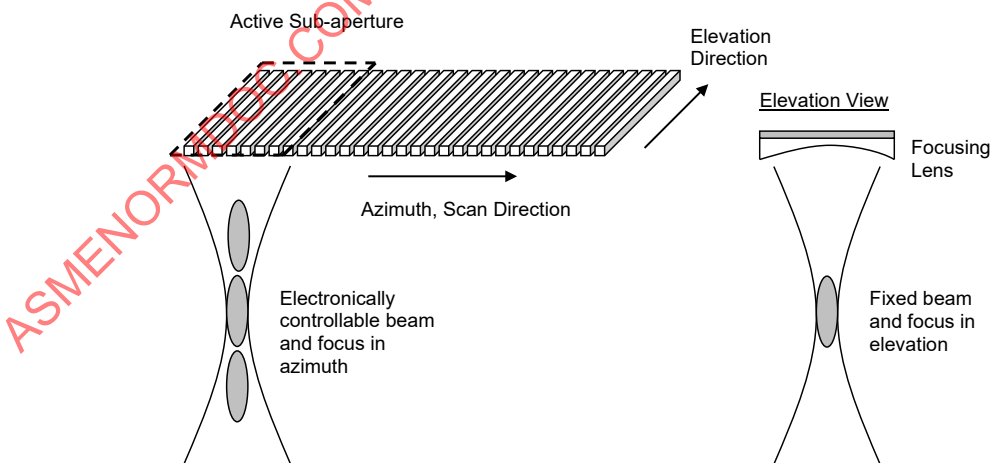


Image Courtesy of Sensor Network Inc.

**Figure 5-6: Basic constructional elements of the acoustic stack of a linear array. A complete transducer would additionally have a transducer case and micro-coaxial cable/connector assembly.**

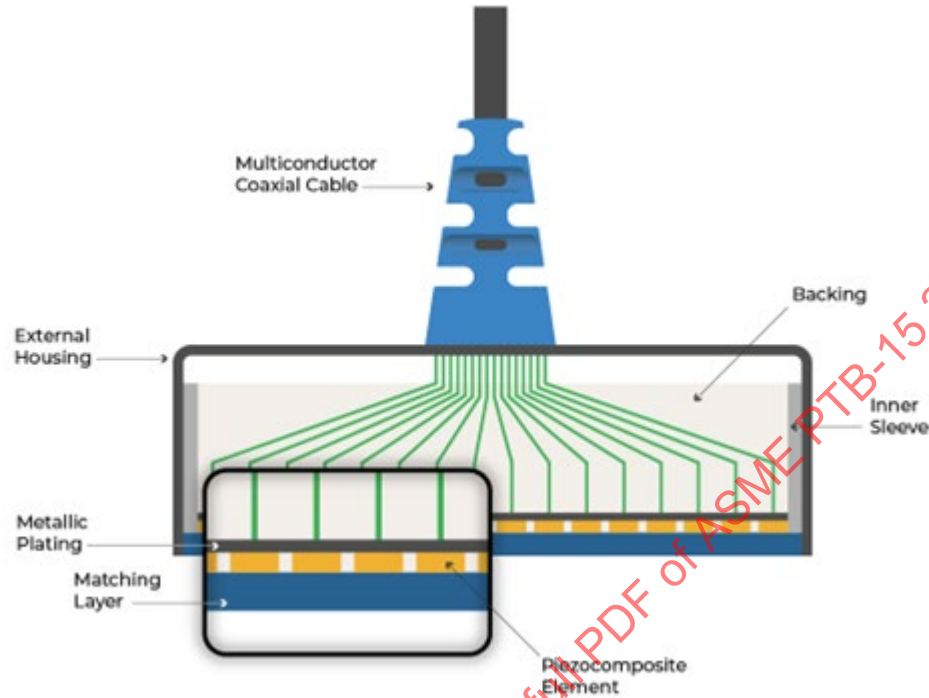


Image Courtesy of Sensor Network Inc.

### 5.3.2 Construction of Transducer Arrays

Figure 5-6 shows the basic constructional elements of the acoustic stack of a linear array. These elements are mostly the same as those found in single element transducers shown in Figure 5-3 (i.e., front matching layer, active element, backing, electrode, etc.).

The largest difference between single element transducers and arrays is the handling of the multiple electrical connections. Here, one micro-coaxial cable must be connected to each active element. While this can be done in many ways, intermediate rigid or flexible printed circuit boards are often used to make the connection between the array elements and the micro-coaxial cable.

Aside from the acoustic stack, constructional elements include the array case and the cable/connector assembly. Typically, arrays are provided with a “potted cable”, that is, the cable is integral to the array and does not disconnect from the array. This is due to the lack of suitable, miniature connectors to achieve the required tens to hundreds of connections that would be required. The instrument-end connector is chosen to mate to the appropriate system-specific connector. Sometimes, multiple cables and connectors are used for arrays with high element counts, for example an 840 element 1.5D array shown in Figure 5-7 having four cables/connectors.



**Figure 5-7: 840 element 1.5D array (420 electrical connections) showing cable assembly with four, 128 channel cable assemblies with IPEX connectors**



Image Courtesy of Sensor Network Inc.

### 5.3.3 Matrix Arrays

Generally, matrix arrays are those where the element pattern is segmented in two dimensions, resulting in an array that can achieve electronic control of the sound field in all three dimensions: azimuth, elevation, and depth (Figure 5-8).

In a traditional sense, the 2D array is one where the element pattern is placed in a rectilinear grid with equal pitch in azimuth and elevation directions. This allows equal steering and focusing performance on both azimuth and elevation planes but does so with a maximum amount of system channels. As an example, an  $11 \times 11$  element array requires 121 system channels and often yields a small aperture size when elements are sized to achieve good steering, thus possibly limiting the imaging performance of the array.

However, the requirements for steering and/or focusing on the elevation direction are often not as stringent as what is needed in the azimuth direction. This allows for alternative array patterns such as 1.25D, 1.5D, and 1.75D as shown in Figure 5-9, which give some amount of control over the elevation plane but with relaxed requirements on channel/element counts. Thus, for the channel count available, the array can potentially be designed with a more efficient use of those channels.

**Figure 5-8: 2D matrix array.** The secondary axis of beam control allows electronic manipulation of the beam in three dimensions: azimuth, elevation, and depth at the expense of increased channel count and system complexity.

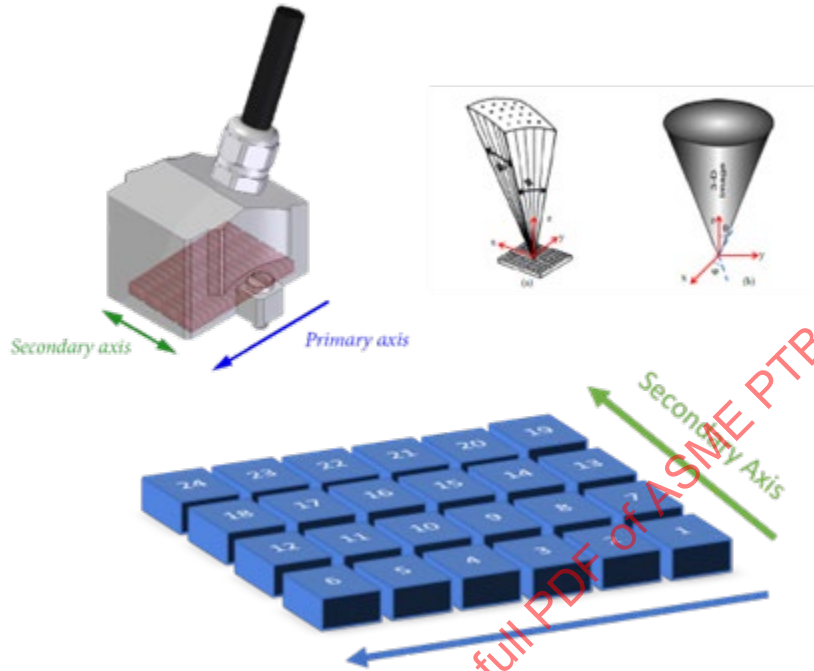


Image Courtesy of Eddyfi Technologies

**Figure 5-9: Taxonomy for matrix arrays** showing the increased control over the elevation plane that can be achieved in tradeoff to increasing channel count and system complexity.

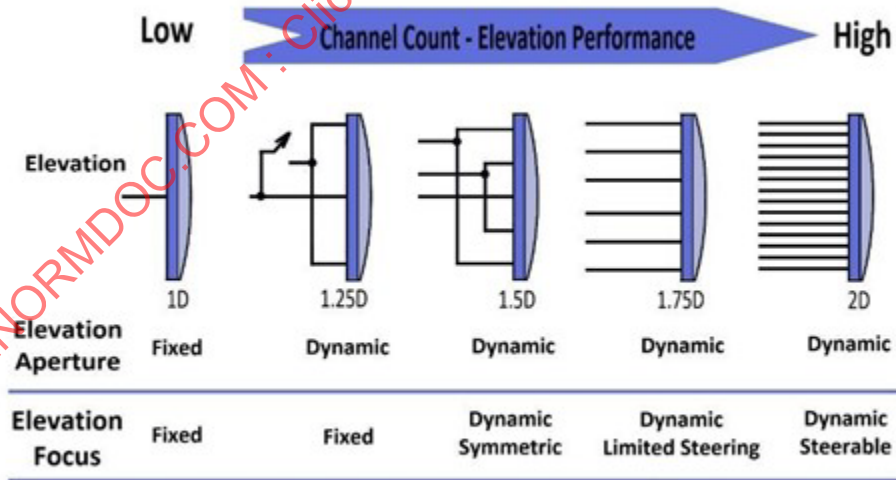


Image Courtesy of Sinewave Solutions

Figure 5-9 shows that transducer taxonomy in terms of the array elevation architecture and wiring. Elevation performance increases progressing from the 1D linear case (left) to the full 2D architecture (right) at the expense of system channels and complexity.

Moving from left to right in Figure 5-9, the 1.25D and 1.5D architectures are suitable when only focusing and/or aperture control is needed in the elevation plane. The 1.25D uses only one system channel for each elevation row and uses active switching in the probe head to increase or decrease the elevation width of the probe. While this architecture is somewhat common in medical imaging transducers, it is not typically used in industrial transducers because manufacturers have not adopted the incorporation of active electronics into the probes themselves. Beam steering in the elevation plane is not possible with this architecture.

The 1.5D architecture takes advantage of symmetry when only focusing is needed in the elevation plane. Symmetric rows of elements are wired in pairs to system channels, allowing more efficient use of the system channels. Often, the elevation pitch is selected to be relatively large, and optionally a lens is used to pre-focus the beam. Phasing is used to adjust the focal depth in or out as needed. Beam steering in the elevation plane is not possible with this architecture.

The 1.75D architecture is distinguished from the full 2D architecture in that the pitch is selected to be relatively large so that only limited steering is available in the elevation plane. A lens may be used to pre-focus the beam. This architecture is commonly used in dual matrix arrays for nuclear inspection. Notably, the electronic steering capability of the array in the azimuth plane will greatly exceed the capability in the elevation plane where only limited beam steering is possible.

There are additional matrix array architectures including segmented annular, randomized, and sparse arrays that can achieve various performance goals.

**Figure 5-10: Common array geometries used in non-destructive testing applications**

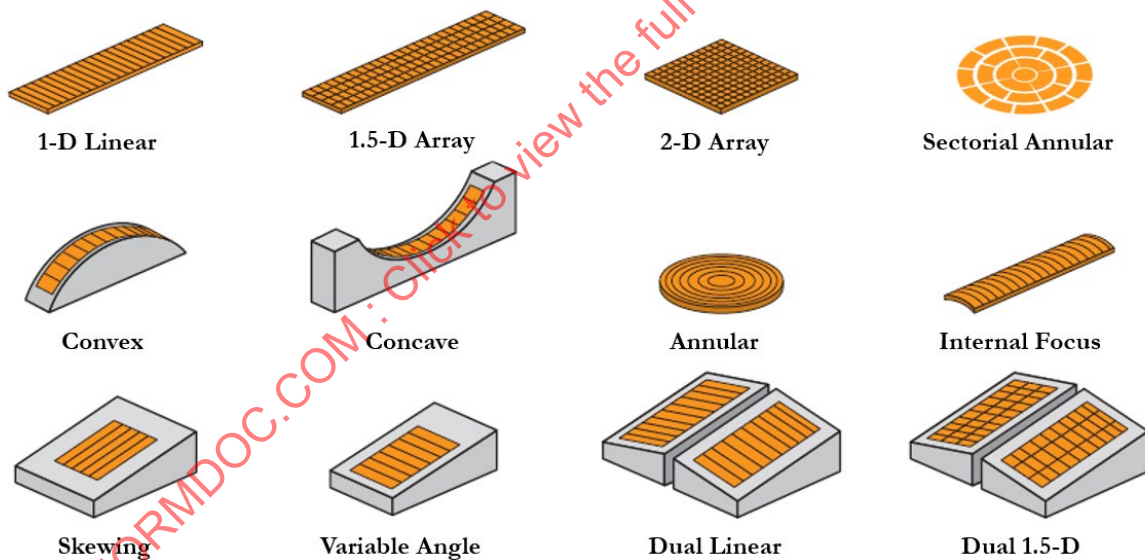


Image Courtesy of Sensor Network Inc.

#### 5.3.4 Common Configurations of Arrays Used in NDE

There are many different types of arrays that are commonly used in NDT applications. Some of these are simply variations of the basic linear array (variable angle) and others are significantly different in configuration and application (segmented annular for instance). Figure 5-10 shows many of the common configurations. For this discussion, a brief application with comments regarding the applicability of TFM/FMC is as follows:

**Linear:** As previously discussed, the linear array is segmented in one direction and allows one active imaging plane. It is the most used array geometry, and variants such as variable angle, skewing, and

dual linear configurations are also common. These arrays are commonly used and suitable for FMC/TFM for both linear and angular sweep imaging.

The 1.5D, 1.75D, and 2D Matrix: 1.5D, 1.75D, and 2D configurations add additional control over the elevation plane and allow focusing and steering (for 1.75D and 2D configurations) at the expense of additional element count and complexity; see additional discussion in “matrix arrays”. Because a significant benefit of FMC/TFM is the ability to achieve optimal focal properties over a large range of material depth, the fixed elevational beam characteristics of the linear array may be suboptimal, particularly when imaging thick sections and noisy materials. As such, matrix arrays can be used to overcome this deficiency.

Annular: The annular array is a configuration used to achieve control over the focal depth of the transducer. It is particularly useful when combined with dynamic depth focusing (DDF) to achieve an optimal focus over a large range of material. FMC/TFM does not achieve much if any advantage over DDF, so it would be unusual to pair an annular array with FMC.

Segmented Annular: The segmented annular geometry is often used to perform linear scanning with or without steering and focusing on cylindrical geometry when inspecting from the end view of the cylinder. The inspection of bolts for cracking is a common application, as well as inspection of riveted joints. FMC/TFM could be used in a cylindrical scanning application to increase focal resolution and depth of field.

Focused Linear: An elevation focus can be applied to a linear array by either curving the array in the elevation direction or adding a plano/concave or plano/convex lens to the array. Elevation focusing provides a tighter spot size in the elevation direction, thereby providing narrower “slice thickness” at the expense of a shorter depth of field. The smaller spot size achieved with elevation focus can improve the ability to detect small size defects and is suitable to use with TFM/FMC.

Linear Convex/Linear Concave: Curved linear arrays (CLA) are often used for phased array inspection of tubes and bars from the OD (concave) or ID (convex). Curved linear arrays are suitable for use with TFM, particularly if a large depth of field is required for the application. CLAs are often used in production environments where testing speed is critical. Therefore, an analysis would be required to determine if TFM would result in any gain in testing productivity.

Variable Angle: Variable angle is a variation of the linear array, using a wedge to pre-steer the nominal refracted angle of the beam in the component. The wedge is often externally supplied and attached to the array using machine screws. This has the advantage of replacing the wedge separately from the array. Arrays can also be fabricated with internal wedges. Variable angle scanning is common for inspecting welds, and TFM offers benefits of improved testing speed and improved imaging due to increased image density and improved focusing.

Skewing: Skewing is another variation of the linear array and is similar to variable angle in that a wedge is used to pre-steer the beam to a nominal refracted angle. However, in this case, the array elevation plane is parallel to the wedge angle and the azimuth plane is perpendicular to the wedge angle. Electronic steering of the beam then skews the refracted angle and is suitable for detecting and sizing off-axis cracking in welds. A larger linear array can also be placed in a similar position so that a linear scan can be accomplished in the skew direction. TFM could provide improved focusing and image formation in this application.

Dual Linear/Dual Matrix: Similar to the dual element of Figure 5-3, linear and matrix arrays can be configured in a dual approach, separating the transmit and receive elements. This approach is useful in improving near-surface resolution and decreasing backscattered noise. These transducers are commonly used for inspecting thick section cast stainless steel pipes and vessels found in nuclear power plants. As with the variable angle case, TFM can offer the benefit of improved resolution and possibly testing speed over the conventional phased array approach.

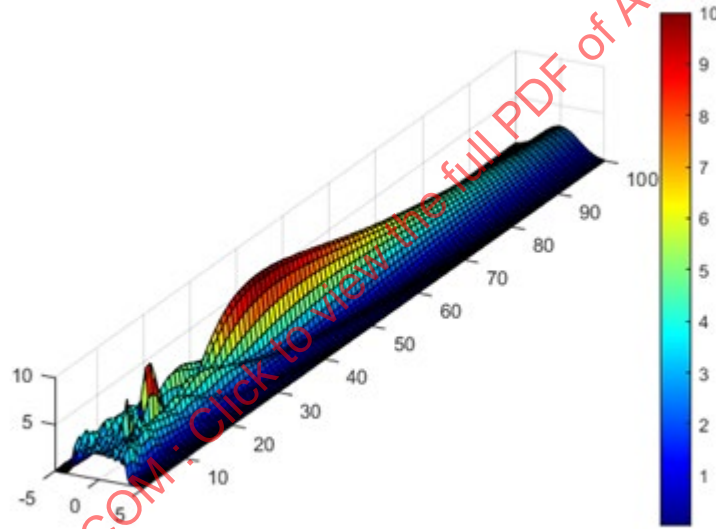
## 5.4 Transducer Sound Fields

This sub-chapter discusses basic beam models that enable quick calculation of many of the sound field parameters that can be used to describe the performance of the array elements and the array apertures. These models all derive from the approximation of a single frequency “continuous wave” source. While actual transducers used in NDE have considerable bandwidth, these models still offer a good approximation of performance and the beam parameters and can be readily computed without any special software. More sophisticated models are also available, as discussed in Chapter 6.

### 5.4.1 Basic Beam Modeling

Typical ultrasonic wavelengths are relatively large, in the range of millimeters, and are of a similar magnitude to the size of the transducer generating the sound field. Thus, the beams emanating from ultrasonic transducers cannot be treated as plane waves, and are more aptly described as diffraction patterns, having beam intensity that varies widely (Figure 5-11).

**Figure 5-11: Field II/Matlab beam simulation from a 5MHz, 12.7mm diameter ultrasonic transducer radiating into water. Sound intensity is indicated by the color scale in relative units**



Simulation from Field II.

(1) J.A. Jensen: Field: A Program for Simulating Ultrasound Systems, Paper presented at the 10th Nordic-Baltic Conference on Biomedical Imaging Published in Medical & Biological Engineering & Computing, pp. 351-353, Volume 34, Supplement 1, Part 1, 1996.

(2) J.A. Jensen and N. B. Svendsen: Calculation of pressure fields from arbitrarily shaped, apodized, and excited ultrasound transducers, IEEE Trans. Ultrason., Ferroelec., Freq. Contr., 39, pp. 262-267, 1992.

To calculate the beam intensity profile, single frequency “continuous wave” models treat the transducer as an infinite number of infinitesimal sources on the surface of the face of the transducer, each source radiating a semi-spherical wave into the propagation medium at a single frequency (Huygens’ principle). Mathematical integration sums all the contributions of these infinitesimal sources at each point in the acoustic beam and yields relatively simple formulas describing beam divergence, spot size, and depth of field.



### 5.4.2 Near Field Distance

The contributing waves from the infinitesimal sources on the surface of the transducer constructively and destructively interfere to create fluctuations of the beam intensity in the radiated field of the transducer. These effects are sometimes generally referred to as diffraction effects. This interference can create extreme fluctuations, particularly in the region near the transducer. This region of extreme fluctuation is referred to as the transducer near field or Fresnel zone.

Further from the transducer, the infinitesimal sources are too distant to destructively interfere, and the beam becomes more uniform, spreading like a spherical wave front. This region is referred to as the far field, or Fraunhofer zone. The on-axis transition point between the two zones is referred to as the near field distance,  $N$ , and is computed using Equation 25 for circular transducers.

$$N = \frac{D^2}{4\lambda} \quad (25)$$

$N$  = Near field distance

$D$  = Transducer diameter (or aperture width)

$\lambda$  = Ultrasonic wavelength (velocity/frequency)

Figure 5-12 depicts the near field and far field regions of a circular transducer along with the near field distance,  $N$ . Intensity fluctuations are due to the constructive and destructive interference that occurs within the near field and are depicted for both on axis and lateral beam profiles.

**Figure 5-12: Modeled sound field of a flat ultrasonic transducer, showing the intensity fluctuations in the near field transitioning to a smoothly varying beam at and beyond the Near Field Distance,  $N$ .**

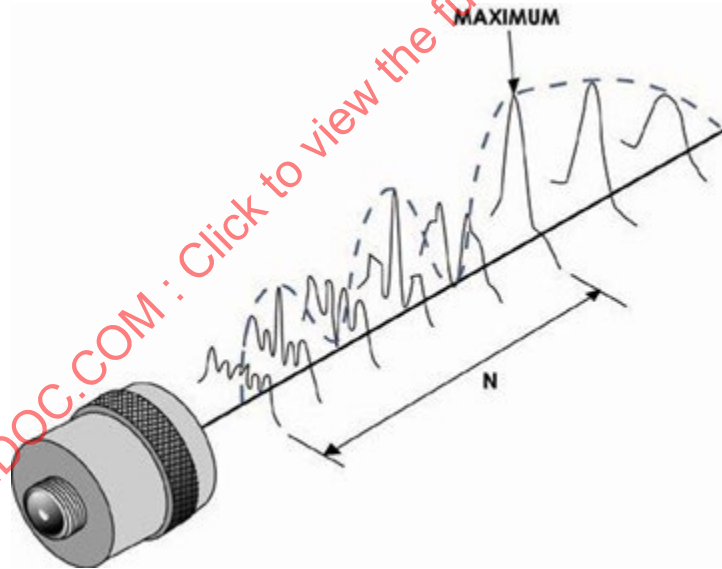


Image Courtesy of Evident Scientific, Inc.

The near field distance is an important parameter of a transducer aperture for several reasons. First, the near field distance is a point of natural focus for an unfocused (flat) transducer and can be an optimum region to perform inspection as it is the point of maximum beam intensity and lacks the extreme fluctuations that can occur within the near field. When considering the sound field of arrays, the passive axis/elevation plane is often flat and unfocused, so the region of natural elevation focus is at the near field distance. Minimum “slice thickness” will be obtained at the near field distance and within the -6dB depth of field surrounding the focal point. Secondly, when using focusing, either with a focusing lens or with phased array, it is only possible to focus within the near field where constructive and destructive interference can take place. Strong focusing can only be obtained within the region of approximately  $N/2$ . Weaker focusing can occur beyond  $N/2$  to the natural focal point at the near field

distance for a flat aperture. The array practitioner should be aware of the near field distance for the elevation (passive) and azimuth (active) planes to help understand what may be achieved in an inspection. The near field distance can be increased by increasing aperture size or by decreasing the ultrasonic wavelength (by increasing transducer frequency).

### 5.4.3 Focusing Flat and Curved Oscillators, Spot Size and Depth of Field

The modeling of focused apertures is important to understand the imaging capability of array apertures in both the active and passive planes. In the active imaging plane, conventional phased array beamforming as well as TFM/FMC processes create a focused beam electronically. The ability to achieve good resolution of defects depends upon the beam characteristics at the point of the defect. The largest advantage of FMC/TFM is that the beam can be focused everywhere on the active plane within the limit of the near field distance, improving resolution for targets that vary in distance from the array versus the fixed focal depth that is usually achieved with conventional phased array. To achieve strong focusing with phased array including TFM, it is still important that the imaging aperture produces a near field that is well beyond the desired focal point. Lateral beam width and depth of field are important parameters that can be calculated for a focused aperture, though with TFM, depth of field is somewhat irrelevant as the focal point is adjusted dynamically.

In the passive plane for linear arrays, a natural focus and depth of field is present, even without the presence of a focusing lens. As mentioned, the near field distance of a flat aperture is a natural focal point where the beam intensity is maximum, and the lateral beam width is minimum. The lateral spot size is easily approximated as 0.22 times the elevation width for rectangular apertures. The -6dB depth of field is approximately identical to the nearfield distance,  $N$ .

Figure 5-13 schematically shows the basic beam characteristics of flat and focused oscillators that are of most interest, the focal length,  $F$ , lateral spot size  $E_x$  and depth of field  $E_z$ . Often, it is necessary to make the calculation assuming that there are two propagation mediums, for instance in the case of immersion testing or when a transducer is placed on a wedge. Interestingly, this does not create a change in the beam diameter, but it does alter the depth of field and the location of the focal point. Table 5-1 shows the equations that can be used to calculate spot size for flat and focused apertures.

F-number: The equations of Figure 5-13 and Table 5-1 offer straight forward calculations of the beam characteristics for the active and passive imaging planes. The F-number, commonly used for optical lenses, is defined as the ratio of focal distance from the transducer,  $F$ , to the aperture size  $D$ . The lateral spot size is easily approximated as the sonic wavelength times the F-number of the aperture and is a useful way to quickly estimate the lateral image resolution capability of an aperture. In FMC/TFM, it is important to note that the F-number will change as the focal point moves away from the aperture (when  $F/D > 1$ ); therefore, shallower targets will potentially be more “in focus” than deeper targets. Constant F-number (also referred to as “constant angle”) imaging is possible with some systems where the number of elements used in the TFM pixel reconstruction are adjusted based on the distance from the transducer. Aperture size can then be increased with imaging depth to create a constant spot size and imaging resolution.

**Figure 5-13: -6dB spot size (Ex) and -3dB depth of field (Ez) for flat and focused circular transducers**

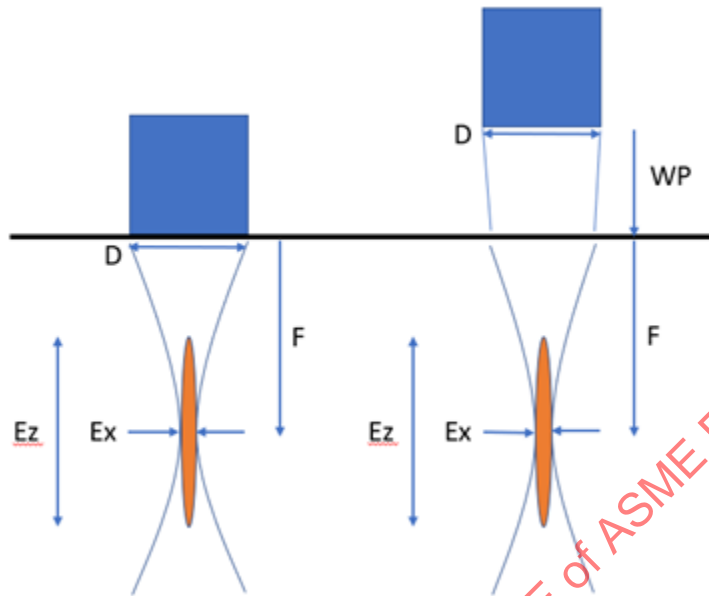


Image Courtesy of Sinewave Solutions

**Table 5-1: Approximate formulas for -6dB spot size for flat and focused oscillators, narrow band approximation**

	Direct Contact		With Standoff ( $F'=F+WP*(C_w/C)$ )	
	Ex (-6dB)	Ez (-3dB)	Ex (-6dB)	Ez (-3dB)
Focused Apertures	$1.03\lambda \left(\frac{F}{D}\right)$	$3.6\lambda \left(\frac{F}{D}\right)^2$	$1.03\lambda \left(\frac{F'}{D}\right)$	$3.6\lambda \left(\frac{F'}{D}\right)^2$
Un-focused @ Near-field (F=N)	0.26D	$\frac{D^2}{4\lambda}$	0.26D	$\frac{D^2}{4\lambda}$
Un-focused in Far-field	$1.03\lambda \left(\frac{z}{D}\right)$		$1.03\lambda \left(\frac{z}{D}\right)$	

Courtesy of Sensor Network Inc.

Ez = Axial depth of field (-3dB)

F = Focal length

$\lambda$  = Ultrasonic wavelength (velocity/frequency)

D = Element diameter/aperture size

z = Distance from transducer

F' = Adjusted focal length in second material (accounting for standoff)

WP = Water path/distance in water (or wedge path)

C = material velocity

Cw = water velocity (or wedge velocity)

## Notes:

1. The author has found these equations to be useful approximations of the beam behavior of focused and unfocused ultrasonic transducers. Technically, these equations are derived for circular apertures and while there are additional expressions for the rectangular apertures typically found in phased array, it is recommended that those looking for additional precision should seek the use of a broadband beam model rather than a more precise “approximate” expression.
2. According to H. T. O’Neil, “Theory of Focusing Radiators”, The Journal of the Acoustical Society of America 21, 516-526 (1949)
3. The expressions for transducers are written with the assumption that the focal length  $F$  is set within the material as is typical when operating a phased array. For the case where the focal length is set based on lens geometry and within the standoff material, the focal length within the material is:  $F=(F_w-WP)C_w/C$ .

#### 5.4.4 Beam Divergence/Array Element Performance

So far, the discussion regarding acoustic sound fields of transducers has focused on individual transducers or transducer apertures consisting of multiple array elements. However, it is equally important to consider the beam characteristics of individual array elements, particularly, their angular response or divergence.

Figure 5-14 depicts the TFM reconstruction of three image pixels in the active plane of a 32-element linear array transducer. The “steering range” of elements 1 and 8 are depicted as dashed lines in the image. Depending on the pixel being reconstructed, the portion of the element’s beam that is used in the reconstruction may or may not validly contribute to the reconstruction. In the case of Pixel 3 in the image, neither element 1 nor element 8 provide a valid contribution to the pixel reconstruction, in which case, summing the waveform data from those elements would only contribute noise to that pixel.

**Figure 5-14: Graphical representation of valid, marginal, and invalid element contributions due to the limitations of element beam divergence**

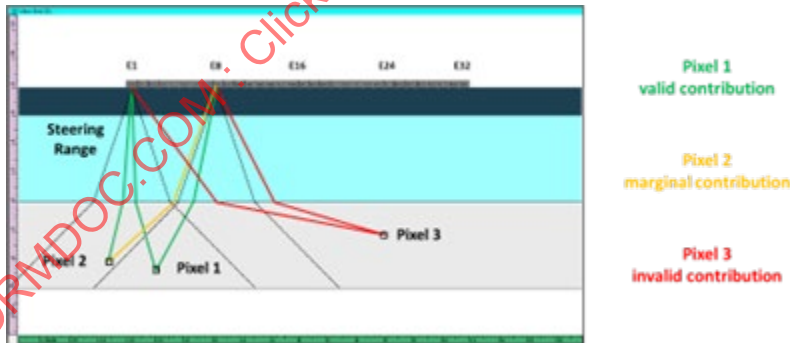


Image Courtesy of Eddyfi Technologies

The way to describe array element performance is through the beam divergence calculation, schematically shown in Figure 5-15. The divergence of rectangular elements is mathematically described by a sinc function, i.e.,  $\text{sinc}(x)=\sin(x)/x$ .

Figure 5-15: Schematic representation of beam divergence half angle.

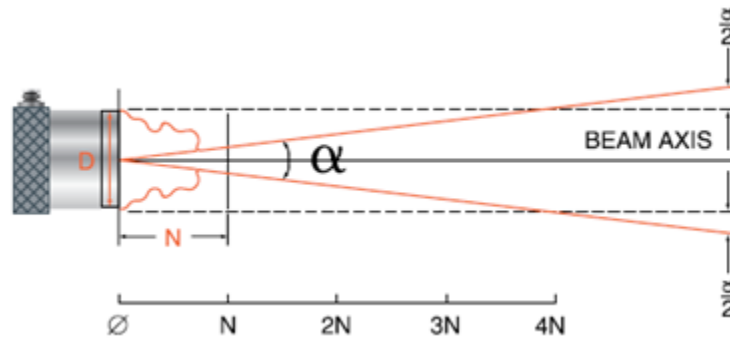


Image Courtesy of Evident Scientific, Inc.

$$\frac{\alpha}{2} = \left( K \frac{\lambda}{D} \right) \quad (26)$$

$\alpha/2$  = half angle beam divergence

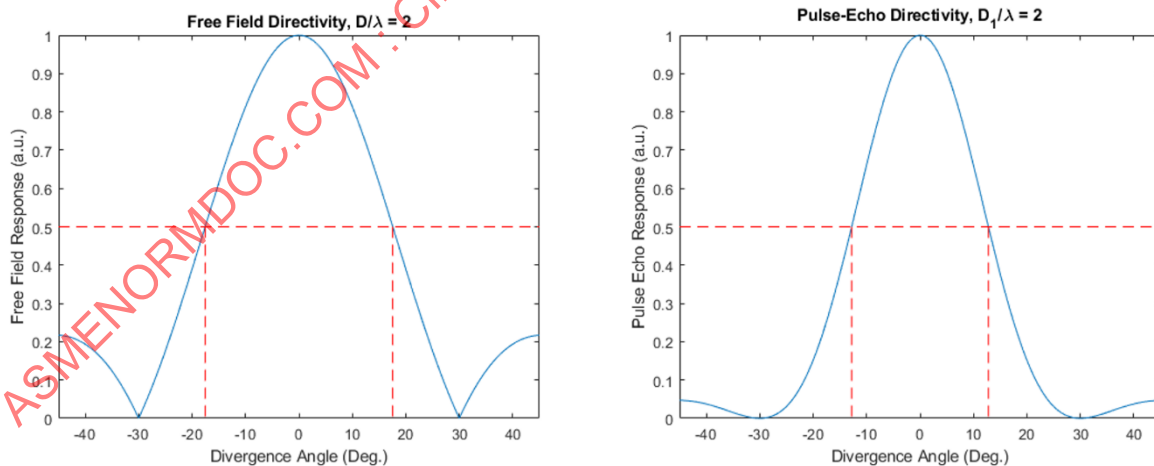
$\lambda$  = ultrasonic wavelength (velocity/frequency)

D = element width

K = 0.602 (one-way/free field) or 0.442 (two-way/pulse-echo)

From the perspective of array element performance, one typically looks at the pulse echo response, which is described by the function  $(\sin(x)/x)^2$  because the element is typically used to both transmit and receive. A useful rule of thumb to evaluate whether an element will contribute is to look at the -6dB pulse/echo divergence angle. Figure 5-16 graphically shows the one-way and two-way beam divergence for an array with a pitch that is two wavelengths in size. The red, dashed lines show the -6dB points.

Figure 5-16: One way (free field) and two way (pulse echo) response for an array element two wavelengths in size ( $D/\lambda=2$ )



Simulation from Field II.

(1) J.A. Jensen: Field: A Program for Simulating Ultrasound Systems, Paper presented at the 10th Nordic-Baltic Conference on Biomedical Imaging Published in Medical & Biological Engineering & Computing, pp. 351-353, Volume 34, Supplement 1, Part 1, 1996.

(2) J.A. Jensen and N. B. Svendsen: Calculation of pressure fields from arbitrarily shaped, apodized, and excited ultrasound transducers, IEEE Trans. Ultrason., Ferroelec., Freq. Contr., 39, pp. 262-267, 1992.

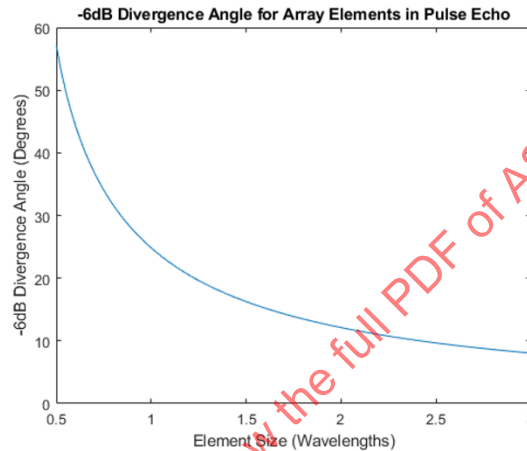


It is most convenient to consider array element size based on its comparison to the wavelength of the ultrasonic beam as computed from the transducer center frequency and the wave velocity in the propagation medium. This makes the computation universal, and the plotted results in these chapters will hold for various element sizes.

Ideally, the array element pitch should be chosen to be very small, on the order of 0.5 wavelengths. In this way, the element divergence is wide and lacks unwanted grating lobes. However, designing to 0.5 wavelength may result in an impractical solution as large amounts of steering are often not needed and a large number of system channels are required to create meaningfully large apertures.

Figure 5-17 displays the -6dB divergence angle as an element size in wavelengths. This provides a quick visual reference to evaluate array element steering performance.

**Figure 5-17: -6dB divergence half angle for element size in wavelengths (pulse echo)**



Simulation from Field II.

(1) J.A. Jensen: Field: A Program for Simulating Ultrasound Systems, Paper presented at the 10th Nordic-Baltic Conference on Biomedical Imaging Published in Medical & Biological Engineering & Computing, pp. 351-353, Volume 34, Supplement 1, Part 1, 1996.

(2) J.A. Jensen and N. B. Svendsen: Calculation of pressure fields from arbitrarily shaped, apodized, and excited ultrasound transducers, IEEE Trans. Ultrason., Ferroelec., Freq. Contr., 39, pp. 262-267, 1992.

## 5.5 Array Design for FMC

This sub-chapter focuses on strategies for choosing the array parameters of frequency, element pitch, elevational width, and number of elements/system channels to provide good performance in an FMC/TFM application.

We will concentrate on linear arrays in linear and sectorial imaging scenarios. The basic concepts introduced can be applied to more complex array geometries with commensurate complexity of analysis. Beam modeling becomes increasingly necessary when evaluating the tradeoffs for complex array geometries.

### 5.5.1 Goal of FMC/TFM Imaging

The typical goal of FMC/TFM is to inspect (image) a volume of material, where all of the volume inspected is tightly in focus. The parameters of the probe should be selected to enable this goal.

Perhaps the simplest way to highlight the goal of TFM is to contrast it with conventional phased array. While both methods aim to inspect volumes of material using electronic manipulation of a set of array elements, conventional phased array often achieves that goal with relatively small apertures and at a single focal length. The result is that when imaging a volume of material, for example a side drill hole block, only certain targets will appear in focus. Additionally, the reduced apertures typically involved

in standard PA (16 or 32 elements) limit the near field distance and perhaps the ability to achieve a tight focus in the entire volume of interest. While an overly tight focus in conventional PA limits the depth of field and can be problematic for volume imaging, TFM provides the ability to focus independently on each pixel of the image, thereby enabling the use of tight focal ratios that would be impractical with conventional phased array.

See Figure 5-18 and Figure 5-19 to contrast the differences between standard TFM, sectorial TFM, and standard phased array. Figure 5-18 contrasts the ability to focus “everywhere” in the volume as compared to a single focal point with standard phased array. Figure 5-19 contrasts the impact of aperture size. All else being equal, smaller apertures will reduce the focusing capability of the array.

**Figure 5-18: B-scan view of a Ø 1 mm SDH Standard using a 5 MHz linear array, 64 elements, LW wedge: Standard phased array (right) compared to FMC/Sectorial Total Focusing (STF) method (center) and FMC/Total Focusing Method (TFM) (left). Note that for standard PA, the targets are only in focus at a single depth.**

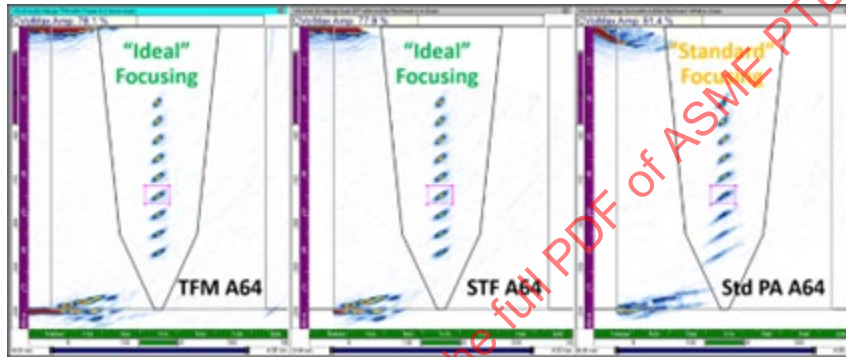


Image Courtesy of Eddyfi Technologies

**Figure 5-19: B-scan view of a Ø 1 mm SDH Standard using a 5 MHz linear array, 64 elements, LW wedge with varying aperture size. Note the reduction in resolution that corresponds with decreasing aperture size with corresponding increase in the effective lateral beam size.**

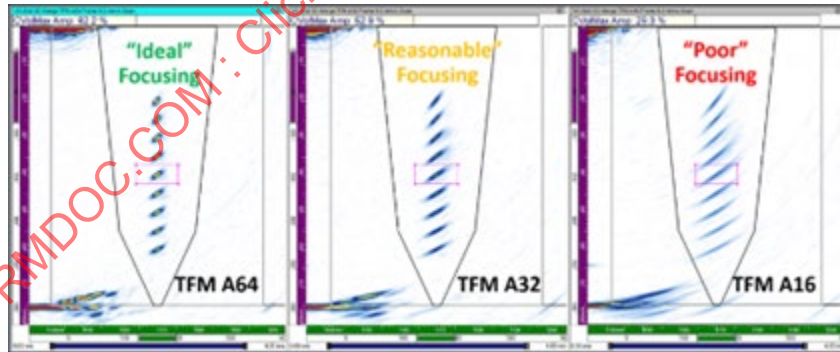


Image Courtesy of Eddyfi Technologies

### 5.5.2 Near Field Imaging

To achieve strong focusing on a volume of material, it is critical that the near field of the array is well beyond the region of interest for imaging so that strong focusing can be achieved. No beam shape improvement by focusing can be achieved at or beyond the near field distance (Figure 5-21). For a rectangular-shaped aperture, typical for linear phased array transducers, the nearfield distance is given by Equation 27.

$$N = 1.35 \frac{D^2}{4\lambda} \quad (27)$$

$N$  = Near field distance

$D$  = Transducer diameter (or aperture width)

$\lambda$  = Ultrasonic wavelength (velocity/frequency)

While there is no simple rule or equation that can yield the optimum positioning of the region of interest within the nearfield, when reconstructing an imaging point within approximately  $\frac{1}{2}$  of the nearfield, strong focusing will be achievable. As the focal distance moves from  $\frac{1}{2}$  to 1 time the nearfield distance, the focusing will be reduced to ultimately that of the equivalent, unfocused, flat oscillator. The equations in Table 5-1 can be used to estimate the lateral spot size achievable for a given array aperture or modeling can be used to further estimate the imaging performance.

With respect to TFM, the near field distance can be computed in terms of the relevant probe parameters of frequency ( $f$ ), system channel count ( $S$ ), element pitch ( $P$ ), and material velocity ( $C$ ) as follows:

$$N = 1.35 \frac{f(SP)^2}{4C} \quad (28)$$

$N$  = near field distance

$f$  = transducer frequency

$S$  = system channel count

$P$  = element pitch

$C$  = material velocity

Figure 5-20 shows a ray traced example of weld inspection using sectorial TFM (or sectorial phased array) and the relative relationship between the region of interest for imaging vs the positioning of the near field distance. Given this example, one could expect strong focusing on the region of interest nearest to the probe, while further from the probe, the imaging performance might degrade as it approaches the near field distance. Changes in probe pitch, frequency, or number of imaging channels could be used to push the nearfield point further beyond the region of interest may be required to achieve stronger focusing over the entire area.

**Figure 5-20: Example of probe and wedge configuration with consequent near field area and the region of interest on 25mm thick carbon steel weld**

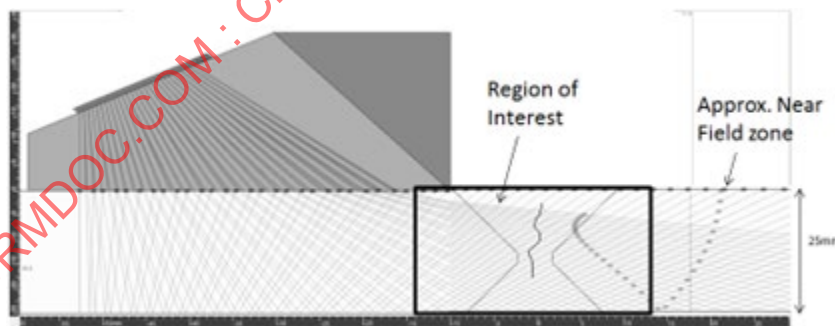


Image Courtesy of APPLUS

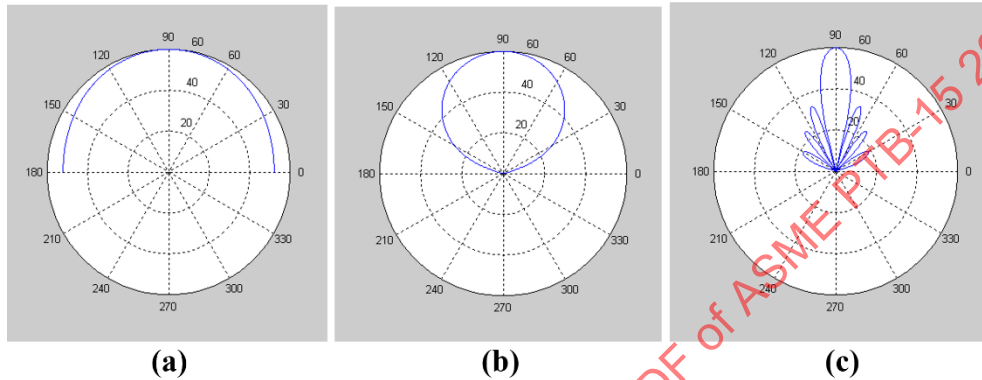
### 5.5.3 Angle Limitation/Constant Focal Ratio (F/D)

One half wavelength element are often recommended for FMC/TFM due to the broad beam divergence and lack of grating lobes that could be present in the image due to spatial aliasing. However, for linear scanning applications in particular,  $\frac{1}{2}$  wavelength elements can result in a relatively small probe footprint, particularly with respect to typical TFM instrument channel counts of 32 or 64 elements. Wilcox et al. studies the use of greater than  $\frac{1}{2}$  wavelength elements and concludes that the approach is conservative for linear scanning applications. The use of larger elements offers increased probe footprints at the expense of potential image artifacts due to special aliasing. Instrument algorithms can

counteract the generation of artifacts when reconstructing image pixels by selecting or deselecting the elements contributing to the reconstruction based on whether they will meaningfully contribute based on the ray angle and the element beam divergence (Figure 5-14).

Figure 5-21 shows a comparison of the beam divergence plots for  $\frac{1}{2}$ , 1.0, and 4.0 wavelength elements. The clear benefit of the  $\frac{1}{2}$  wavelength element is that there is no necessary consideration of the ray angle. Any angle within  $\pm 180$  degrees is acceptable. The useful angle range narrows considerably for the  $1.0\lambda$  and  $4.0\lambda$  elements.

**Figure 5-21: Beam divergence plots for element sizes of a)  $0.5\lambda$  b)  $1.0\lambda$  and c)  $4.0\lambda$**



Simulation from Field II.

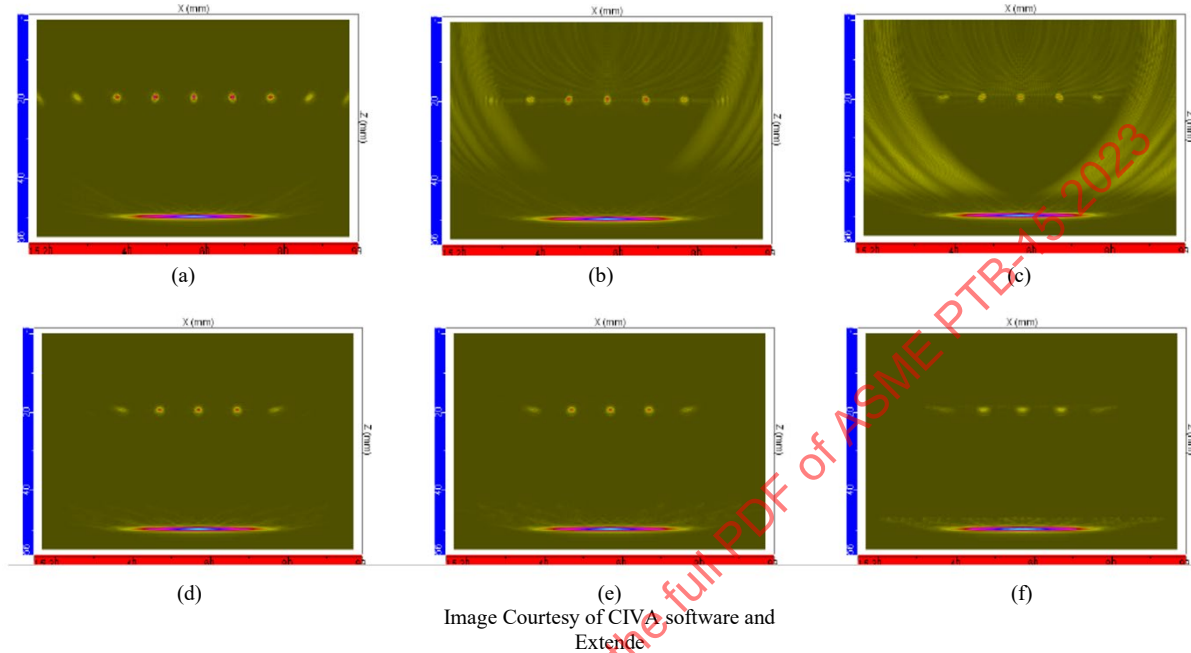
(1) J.A. Jensen: Field: A Program for Simulating Ultrasound Systems, Paper presented at the 10th Nordic-Baltic Conference on Biomedical Imaging Published in Medical & Biological Engineering & Computing, pp. 351-353, Volume 34, Supplement 1, Part 1, 1996.

(2) J.A. Jensen and N. B. Svendsen: Calculation of pressure fields from arbitrarily shaped, apodized, and excited ultrasound transducers, IEEE Trans. Ultrason., Ferroelec., Freq. Contr., 39, pp. 262-267, 1992.

Large elements can help achieve the combined TFM goal of strong focusing with maximal scan width. An additional goal may be to reduce the cost of the electronics and transducers, as increasing the channel count, for example from 32 to 64, dramatically increases the instrument cost, and to a lesser extent also increases the transducer cost.

Figure 5-22 shows a comparison between three arrays with varying pitch to illustrate the effect on TFM imaging. From left to right in the image are represented the following arrays/results: 64 element, 0.63 mm pitch ( $0.5\lambda$ ); 32 element, 1.26 mm pitch ( $1\lambda$ ); and 21 element, 1.89 mm pitch ( $1.5\lambda$ ). Note that the same physical array was used for the comparison but was spatially down sampled to create three effectively different arrays. In the case of the top row of images, no angle limitation is used to limit the imaging artifacts due to spatial aliasing. Conversely, in the bottom row, angle limitation was applied, effectively removing the imaging artifacts while preserving the image quality on the side drilled holes.

**Figure 5-22: CIVA simulations of direct-contact imaging, contrasting the results of TFM using 0.5, 1, and 1.5 wavelength elements, with and without angle limitation. (a)-(c) processed using a Conventional TFM algorithm, (d)-(f) processed with angle limits (cone filter) of 30, 30, and 19.5 degrees, respectively. Results obtained using the following arrays: (a), (d) 64 element/0.63mm pitch ( $0.5\lambda$ ), (b), (e) 32 element/1.26mm pitch ( $1\lambda$ ) and (c), (f) 21 element/1.89 mm ( $1.5\lambda$ ) pitch.**



The strategy of using greater than  $\frac{1}{2}$  wavelength elements can be evaluated by calculating their beam directivity and potential contribution to improving the lateral resolution through focusing. Table 5-2 computes the -6dB half angle beam divergence value for various element sizes, computing: 1) the maximum focal ratio that can be achieved without excessive imaging artifacts due to grating lobes and 2) resultant potential lateral resolution in wavelengths. While it is convenient that  $\frac{1}{2}$  wavelength elements reduce the potential for imaging artifacts, the table highlights that the achievable focal ratios will not substantially increase lateral resolution, which is diffraction limited at approximately one times the wavelength at best. This is further evidenced in Figure 5-22 where effectively larger element pitches are shown to achieve similar imaging performance as compared to the  $\frac{1}{2}$  wavelength case as long as angle limitation is used to prevent unwanted artifacts in the image due to grating lobes.

**Table 5-2: Computations of achievable resolution based on element size, beam divergence and resulting focal ratio and focusing effect.**

Element Size (Wavelengths)	Half Angle Divergence (Degrees)	Possible Focal Ratio (F/D)	Potential Lateral Resolution (Wavelengths)*
0.5	62.2	0.3	0.2
0.6	47.5	0.5	0.4
0.7	39.2	0.6	0.5
0.8	33.6	0.8	0.7
0.9	29.4	0.9	0.8
1	26.2	1.0	0.9
1.1	23.7	1.1	1.0

Courtesy of Sensor Network Inc.



\* Lateral resolution is limited to approximately one wavelength in the material so the use of less than  $F/D=1.0$  focal ratios though enabled by sub wavelength elements yield diminishing returns from an imaging perspective except for the convenience of not requiring angle (F-number) limitation.

#### 5.5.4 Selection of Array Parameters (Active Plane)

The inter-related FMC parameters must be considered for the active plane: probe frequency, element pitch, and number of system channels. Selection of these parameters dictates imaging performance based on computations such as near field distance, aperture size/scanning width, focal ratio, and spot size. Probe frequency is usually the first parameter selected, as the probe pitch is set based on the resultant wavelength in the test object.

##### 5.5.4.1 Frequency

The operational frequency of the array is tremendously important to defect detection and imaging performance and is mainly governed by the application from a defect detection perspective. Once the array frequency is chosen, the other active plane array parameters are set based on the resulting wavelength in the test piece, particularly the array pitch and resultant aperture based on available system channels.

The considerations for frequency are generally as follows:

- a. If goal is to maximize SNR (where noise is due to microstructure) then there is a sweet spot – increasing frequency will initially increase SNR because when the microstructural noise is dominated by single scattering, a smaller the focal spot (i.e., higher frequency) means fewer grains contribute to noise at each point in the image. At some point, SNR starts to degrade again as multiple scattering starts to dominate and the noise increases.
- b. If goal is to maximize resolution, high frequency is better (up to the onset of multiple scattering), but there is a potential conflict if associated reduction in array element pitch reduces the size of array aperture because the total number of array elements is constrained.

Importantly, the frequency (wavelength), element pitch, and system channel count dictate the nearfield distance as already discussed, which is critical to achieving a strong focusing ability.

It is always useful to consider non-TFM inspection results prior to selecting probe frequency, as TFM is a method primarily for improving the focusing over a volume of material. To the extent that conventional or conventional phased arrays have already successfully been used for inspecting a test object, the probe frequency can be nominally carried over to a similar TFM inspection.

Generally, adjusting the array frequency results in the following advantages/disadvantages.

Advantages of choosing a higher frequency:

Improved defect detection: Higher frequency can improve defect detection because the minimum resolvable defect is on the order of the ultrasonic wavelength in the material. (Until the onset of multiple scattering)

Improved lateral resolution: The lateral spot size decreases for increasing frequency.

Increased near field depth: Focusing can only be achieved within the near field that is increased with higher frequency. However, to the extent that higher frequency reduces element pitch, increased system channels would also be needed to overcome the reduction in aperture.

Disadvantages:

Attenuation and/or scattering increases with increasing frequency and can result in an inability to detect defects, particularly as increased attenuation is often associated with increased noise caused by backscatter from material grain boundaries. (See point a. above for discussion on single vs. multiple scattering.)

For a given element size, beam divergence is reduced, perhaps limiting the useful angular imaging range and/or can cause limits on ability to achieve focus.

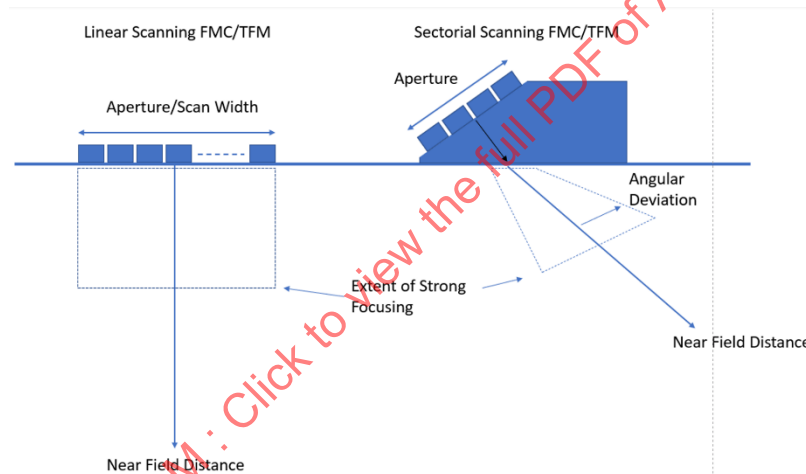
Element sizes are generally smaller, resulting in smaller apertures and/or the need for increased system channels.

#### 5.5.4.2 Pitch/System Channels

The array pitch defines the aperture size based on the number of system channels available and thus further dictates the array scanning width (for linear scanning applications) and the imaging performance (based on the near field distance and resultant focal ratio and spot size). For sectorial imaging FMC, the array pitch also dictates the amount of angular range over which an element can usefully contribute to the image reconstruction.

Typically, the element pitch is first chosen based on the frequency of the array and resultant wavelength in the material. Generally, half wavelength elements are the starting recommendation due to their broad angular directivity (Figure 5-21) and resulting lack of potential imaging artifacts. If this approach yields an aperture that is too small (unacceptably small scan width or near field distance), then a larger element pitch of up to one wavelength should be evaluated as long as the angle limitation is supported in the TFM/FMC algorithm. For linear scanning applications, one wavelength elements are likely preferable.

**Figure 5-23: Schematic representation of critical parameters for linear scanning and sectorial scanning FMC/TFM**



Simulation from Field II.

(1) J.A. Jensen: Field; A Program for Simulating Ultrasound Systems, Paper presented at the 10th Nordic-Baltic Conference on Biomedical Imaging Published in Medical & Biological Engineering & Computing, pp. 351-353, Volume 34, Supplement 1, Part 1, 1996.

(2) J.A. Jensen and N. B. Svendsen: Calculation of pressure fields from arbitrarily shaped, apodized, and excited ultrasound transducers, IEEE Trans. Ultrason., Ferroelec., Freq. Contr., 39, pp. 262-267, 1992.

Once the active aperture is calculated, important parameters such as the scan width and near field distance can be computed. Notably, the near field distance for the aperture should be sufficiently large such that the imaging reconstruction is within 50% or less for strong focusing to occur. Adjustments to element pitch or system channel count can be done to adjust aperture/scan width and nearfield distance.

For sectorial imaging FMC, the angular deviation should also be considered. If elements are half wavelength in size, then there is no particular concern. If larger elements are selected, then the half angle divergence formulas should be evaluated to ensure that the entire range of angles is within the -6dB half angle at worst case. Elements greater than the wavelength can also produce grating lobes with resulting imaging artifacts that may cause degradation in imaging performance.

At maximum imaging depth, it is also useful to consider the focal ratio ( $F/D$ ) and estimate the lateral beam spot size (Table 5-1).  $F/D$  values less than or equal to one will achieve strong and uniform focusing as the lateral resolution will be approximately one wavelength.

### 5.5.4.3 Algorithms for Setting Active and Passive Plane Parameters

The following are recommendations for a structured way of deciding on the active and passive plane parameters of linear arrays for TFM/FMC. Two algorithms are presented for setting the active plane parameters for the cases of linear imaging and sectorial imaging. The algorithms differ slightly as there is a difference in the goals of the inspection and therefore the desired characteristics. In linear imaging, generally a larger electronic scan width is desirable to minimize the number of mechanical scans required to cover an area. Scan width can only be improved with an increase in system channels and/or array pitch. Alternatively, sectorial TFM achieves area coverage through steering capability. Probe width based on system channels and/or probe pitch is still important to extend the nearfield beyond the imaging area, but there is a secondary concern of maintaining sufficient beam steering capability.

The recommended algorithms begin by setting the probe frequency, which can be established based on known inspection characteristics. The pitch is then recommended based on the wavelength—1.0 wavelengths for the linear scanning application to improve scan widths and 0.5 wavelengths for sectorial imaging. Increasing the pitch beyond these recommendations may be necessary to achieve the desired nearfield depth and scan width but may introduce imaging artifacts. Even with 1.0 wavelength elements, angle limiting should be used to reduce artifacts due to special aliasing.

Beam modeling is also a tool that can be used to verify the design results prior to array construction. Basic continuous wave models can be used to quickly compute parameters such as element divergence, near field distance and beam widths. More sophisticated modeling software such as CIVA can be used, particularly when evaluating difficult tradeoffs.

Finally, an algorithm for determining passive plane parameters is also presented as the passive plane plays an important (and sometimes overlooked) role in defect detection, sizing and imaging performance.

### 5.5.4.4 Linear Imaging FMC

Generally, the goal of linear imaging TFM/FMC is 1) to create a strong focus over an entire imaging volume of material with sufficient resolution to detect the desired material defects and 2) to achieve a sufficient scan width for a single pass inspection, or alternatively to minimize the number of mechanical passes over the material. The following algorithm will assist in setting the active plane probe parameters of frequency, pitch, and number of system channels. Often, the number of system channels is limited and therefore requires the tradeoff of increasing element pitch, which in turn may require a reduction in probe frequency. Angle limitation in the TFM algorithm can be used to counteract some imaging artifacts that can otherwise be created by using a larger than ideal element pitch.

Linear Scanning Algorithm:

Step 1: Establish basic inputs

Number of system channels (actual number available or desired number)

Material velocity (5900 m/s for carbon steel)

Maximum desired imaging depth

Desired scan width (single pass)

Step 2: Set probe frequency

Set frequency based on material and defect considerations

Compute wavelength ( $\lambda = \text{Material Velocity} / \text{Frequency}$ )

Step 3: Computations for  $1.0\lambda$  elements

Probe pitch ( $\text{Pitch} = 1.0 * \lambda$ )

Aperture width (# System Channels X Pitch)

Near field =  $1.35 * (\text{Aperture Width})^2 / (4 * \lambda)$

Compute approximate lateral beam width at maximum imaging depth  $B(-6\text{dB}) = \lambda[F/D]$

Step 4: Test results

Is aperture width  $\geq$  desired scan width?

Is nearfield  $\geq 2X$  Maximum imaging depth to achieve strong focusing?

Is beam width sufficiently small for desired detection and sizing?

Step 5: Decide/Iterate

Are step 4 results sufficient?

If yes, continue

If no:

If aperture width is too narrow, solve by either increasing probe pitch or increasing system channels.

If the nearfield is too short, increase the system channels or probe pitch.

If the beam width is too large, increase the probe pitch or increase frequency.

Step 6: Modeling

Perform beam modeling, if possible, particularly if evaluating difficult tradeoffs.

Step 7: Proceed to setting passive plane parameters.

#### 5.5.4.5 Sectorial Imaging FMC

Generally, the goal of sectorial imaging TFM/FMC is 1) to create a strong focus over an entire imaging volume of material with sufficient resolution to detect the desired material defects and 2) to have sufficient angular scan width without generation of imaging artifacts such as grating lobes. Ideally, one half wavelength element pitch allows for large angular coverage without the introduction of spurious imaging artifacts such as grating lobes however larger elements are often used to increase nearfield distance with a corresponding reduction in useable angular coverage. The following algorithm will assist in setting the active plane probe parameters of frequency, pitch and number of system channels.

Sectorial Scanning Algorithm:

Step 1: Establish basic inputs

Number of system channels (actual number available or desired number)

Material velocity (longitudinal or shear)

Maximum imaging depth

Longitudinal or shear wave imaging

Maximum angle deviation

(Normally a wedge is used to pre-steer the beam to a nominal angle for longitudinal or shear wave imaging. Angle deviation should be considered as the amount of deviation from the nominal angle.)

Step 2: Set probe frequency

Set Frequency

Compute Wavelength ( $\lambda = \text{Material Velocity} / \text{Frequency}$ ) (Compute wavelength based on the longitudinal or shear wave in the inspected material as appropriate)

Step 3: Computations for  $\frac{1}{2}$  wavelength elements

Pitch (Pitch =  $0.5 * \lambda$ )

Aperture width (# System Channels X Pitch)

Near Field =  $1.35 * (\text{Aperture Width})^2 / (4 * \lambda)$

Compute -6dB element divergence (if choosing  $> 0.5$  lambda elements)

Compute approximate lateral beam width at maximum imaging depth  $B(-6\text{dB}) = \lambda[F/D]$

Step 4: Test results

Is nearfield  $\geq 2X$  maximum imaging depth to achieve strong focusing?

Is beam width sufficiently small for desired detection and sizing?

Is divergence angle sufficient to cover desired angular scan range?

Step 5: Decide/Iterate

Are step 4 results sufficient?

If yes, continue

If no:

If the nearfield is too short, increase the system channels or probe pitch.

If the beam width is too large, increase the probe pitch or increase frequency.

If the angular coverage is too narrow, decrease the element pitch or decrease frequency.

Step 6: Modeling

Perform beam modeling if desired, particularly if one is trying to resolve difficult tradeoffs.

Step 7: Proceed to setting passive plane parameters.

### 5.5.5 Strategy for Setting Passive Plane Parameters

Setting the passive plane parameters is also important for imaging and defect sizing performance. It is common in phased array to have a non-uniform cross-sectional beam profile as the active (the azimuth-depth plane) is dynamically controlled while the passive (the elevation-depth) plane is usually passively controlled by the selection of frequency, elevation width, and potential use of a focusing lens (for linear arrays). This may create non-uniform detection and sizing capability with depth, even though the active plane is focused everywhere in the case of TFM/FMC. This is particularly apparent for flaws that are smaller than the beam width due to area-amplitude considerations or detection of small flaws in noisy materials.

Figure 5-24 shows an “ideal” circular cross sectional beam profile and a more typical elliptical beam profile. The ideal case is not necessarily a requirement of careful array design, but it is just used to highlight the fact that the active and passive planes are often significantly dissimilar and that the imaging performance can vary with depth (Figure 5-25) despite the use of FMC/TFM in the active plane.

Due to lack of active control in the elevation plane, it is usually necessary to make more compromises on performance. To contrast:

Circular/well controlled:

Necessary for most uniform detection and sizing with depth

Imaging small volumetric flaws in noisy material (i.e., titanium hard alpha)

More accurate defect sizing in elevation direction

Small beam, requires smaller scan index in elevation direction (impacting scan time and larger volume of collected data)

Elliptical/varying:

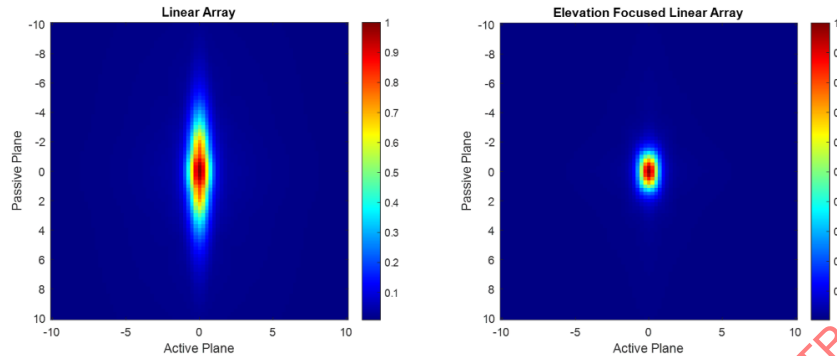
Larger beam allows larger scan index in elevation direction (faster scan time, less data)

For linear flaws, low impact to image and sizing performance. (lack of fusion, stringers)

Variation in detection and sizing performance for small defects



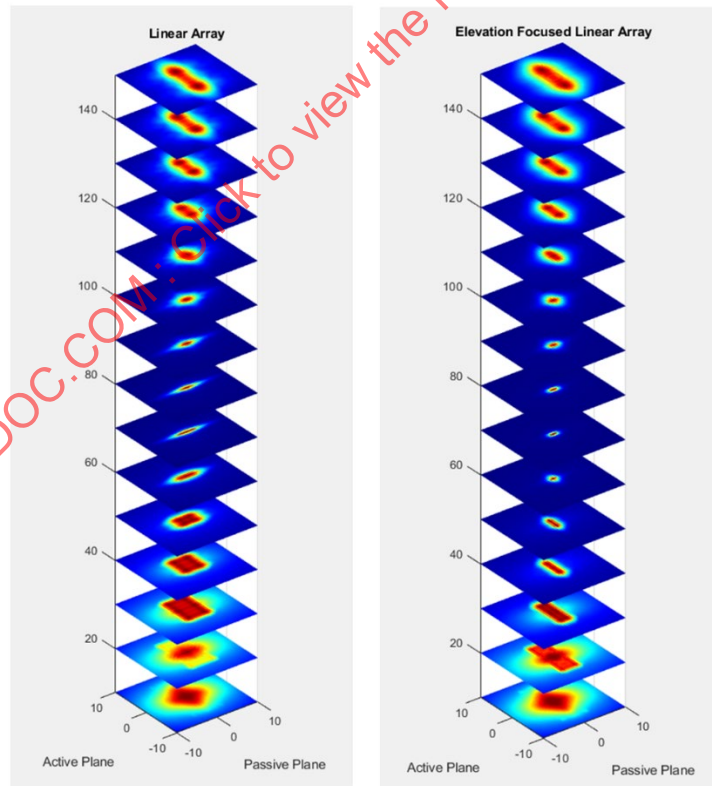
**Figure 5-24: Simulations of cross-sectional beam profile at focal point of flat and elevation focused linear arrays. Ideal “circular” beam profile has equal sizing capability in both the active and passive plane. More commonly, the beam profile is elliptical, having non-uniform sizing and resolution capability.**



Simulation from Field II.

- (1) J.A. Jensen: Field: A Program for Simulating Ultrasound Systems, Paper presented at the 10th Nordic-Baltic Conference on Biomedical Imaging Published in Medical & Biological Engineering & Computing, pp. 351-353, Volume 34, Supplement 1, Part 1, 1996.
- (2) J.A. Jensen and N. B. Svendsen: Calculation of pressure fields from arbitrarily shaped, apodized, and excited ultrasound transducers, IEEE Trans. Ultrason., Ferroelec., Freq. Contr., 39, pp. 262-267, 1992.

**Figure 5-25: Simulations of varying beam spot size for flat and elevation focused linear arrays. The ultrasonic beam is only truly in focus when both the azimuth and elevation are focused. Variation in imaging performance will be seen due to the variation in elevation spot size for flaws that are smaller than the beam spot due to Area-Amplitude.**



Simulation from Field II.

- (1) J.A. Jensen: Field: A Program for Simulating Ultrasound Systems, Paper presented at the 10th Nordic-Baltic Conference on Biomedical Imaging Published in Medical & Biological Engineering & Computing, pp. 351-353, Volume 34, Supplement 1, Part 1, 1996.
- (2) J.A. Jensen and N. B. Svendsen: Calculation of pressure fields from arbitrarily shaped, apodized, and excited ultrasound transducers, IEEE Trans. Ultrason., Ferroelec., Freq. Contr., 39, pp. 262-267, 1992.

Notably, by recognizing the impact of the passive plane on imaging performance, array design can be used to manage the passive plane spot size and can improve detection and sizing capabilities. The remainder of the chapter is used to address designing the passive plane for linear arrays. More complicated arrays with 1.25D to full 2D architecture can, of course, be used to provide active control in the elevation-depth plane if needed for a particular application.

### 5.5.6 Flat or Focused?

The parameters to be set for the passive axis of the probe include the elevation width and whether a focusing lens will be applied. Notably, the frequency has already been set based on the performance of the active plane. The passive plane (for linear arrays) can be treated as a static aperture with focal characteristics that can be computed based on the discussion in Chapter 5.3.

Generally speaking, the flat, unfocused aperture is the standard solution for much phased array inspection and should first be considered for FMC/TFM transducers as the goal of TFM is usually to provide a focused image over a relatively large depth of material. Static focused apertures, on the other hand, can be used to improve the detection and sizing performance in the passive plane of the transducers but need to be used carefully due to the corresponding reduction in depth of field. Other array geometries such as 1.25 – 2D arrays to achieve active control of the beam spot in the elevation direction of the array but with a large increase in the amount of system channels required, and increased expense and complexity of the array.

Some contrasting advantages and drawbacks of flat, static focused and active focused arrays are presented as follows.

Flat:

Longer depth of field consistent with FMC/TFM goal of focusing everywhere

Natural focus at near field distance. -6dB cross sectional beam profile approximately 0.25 times the elevation width.

Easy to implement for contact or wedge mount transducers

Larger area coverage in elevation scanning direction thus potential for faster scanning/reduced data collection

Beam profile will likely be much wider in the elevation/passive direction than the azimuth

Reduced sizing and detection capability, particularly for small flaws

Area–amplitude can vary detection performance over depth

Static Focused:

Smaller beam profile in elevation direction yields improved detection performance, particularly for small flaws and/or grainy materials.

Improved sizing capability in the elevation/passive scan direction

Reduced depth of field lessens the amount of material that can be inspected with the beam in focus.

Reduced beam width in the elevation/passive scan direction requires smaller scan index and potential increase in scan time and amount of data collected.

Potentially more complicated to implement in contact or wedge mount applications

Active Focused:

Focus at all depths with a consistent beam profile

Large increase in required system channels to achieve an aperture of sufficient size to produce focused beams

A general recommendation is to first consider using an unfocussed aperture. This produces a lateral beam spot to  $\sim 1/4$  times the aperture width at the near field distance. This natural focus occurs at the near field point and the focal depth of field is also approximately equivalent to the near field distance. Ideally, the aperture size should position the near field point on the center of the region of interest in the part to take advantage of this natural focal point.

If the flat aperture is not able to provide sufficient detection or sizing performance, then focusing can be used to improve detection and sizing in elevation direction. Focusing can be done by lens or by curved ceramic. Focal ratio dictates improvement in lateral beam width at expense of shorter depth of field. Standard rules for focusing apply—and the elevation width needs to be sufficient so that the focal point is within  $\frac{1}{2}$  nearfield distance. The lateral beam spot size and depth of field can be approximated per the equations in Table 5-1.

## 5.6 Transducer Standards

Transducer standards are also worth mentioning as they offer a standard method of defining and testing the performance of transducers. Several common standards for single element and array transducers are worth reviewing:

ASTM E1065: Standard Practice for Evaluating Characteristics of Ultrasonic Search Units

ASTM E2904: Standard Practice for Characterization and Verification of Phased Array Probes

EN/ISO 22232-2:2020: Non-destructive testing—Characterization and verification of ultrasonic test equipment—Part 2: Probes

EN/ISO 18563-2: Non-destructive testing—Characterization and verification of ultrasonic phased array equipment—Part 2: Probes

## 5.7 Conclusions and Recommendations

The authors hope that the information presented above has been informative and helpful with respect to the selection of the array parameters for TFM/FMC. [18] [31]

Even though there are only a few seemingly basic parameters to be selected (i.e., frequency, pitch, number elements, elevation width, and elevation focus), their combination results in a large variation in sound field performance. Often, an iterative approach coupled with modeling is required to truly optimize an inspection. Nonetheless, the following recommendations are an attempt to summarize and distill the previous chapter into a simpler set of recommendations.

Set the frequency of the array first. Use previous results with conventional inspections or standard PAUT inspections as an indicator of what frequency will likely work in the application.

For sectorial imaging TFM, set the array pitch to be equal to one half ( $\frac{1}{2}$ ) wavelength. For linear imaging TFM, set the array pitch equal to one wavelength if the instrumentation has the ability to limit the acceptance angle of the elements (angle limiting).

Calculate the near field distance of the aperture and confirm that the region of interest is within  $\frac{1}{2}$  of the near field distance to ensure strong focusing.

Size the elevation for a flat/non-focused aperture to place the near field distance approximately in the center of the region of interest to take advantage of the natural focal point.

If detection and/or sizing is a challenge (for example looking for small flaws in grainy material), consider adding a focusing lens to the elevation, though carefully consider the reduction in depth of field.

Use sound field models to estimate the results, including either elementary beam models as presented in this chapter, or the more sophisticated models presented in Chapter 6.

## 6 MODELING

### 6.1 General benefits of weld simulation

#### 6.1.1 Effects of Material on Inspection Results

When setting up a PAUT inspection, the wave type and angles, their corresponding delay laws, and the material shear and longitudinal velocities are entered into the ultrasonic flaw detector. When delay laws are calculated by a flaw detector, it assumes the angle and material velocity remain constant. With many welds, this is an erroneous assumption. Simulation of anisotropy, grain structure and the base metal to weld interface can demonstrate significant scatter and distortion of the sound beam when compared to the sound beam through a uniform isotropic material. Take for instance, the scatter shown in the coarse grain material compared to isotropic and the distortion of the transverse 45-degree sound beam in anisotropic stainless steel compared to in isotropic carbon steel.

Figure 6-1: Coarse grain (left) compared to isotropic material (right) with 1.0 immersion

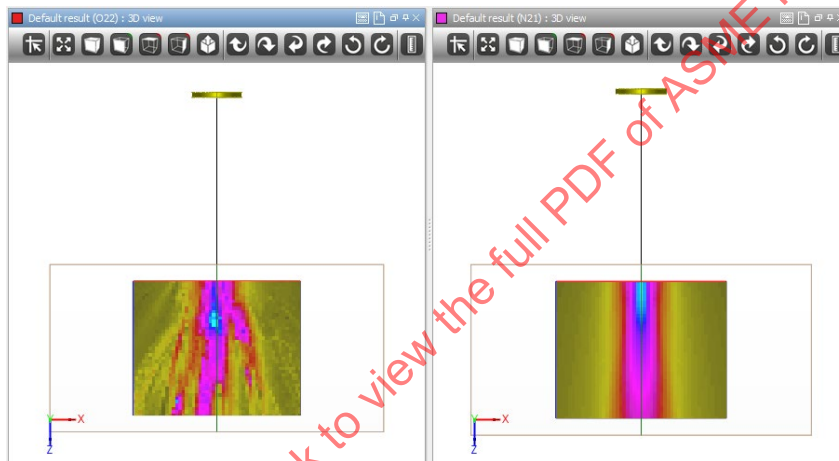


Image Courtesy of CIVA software and Extende

Figure 6-2: Fields radiated by the 45 T-wave transducer in isotropic (left) and anisotropic (right) specimens

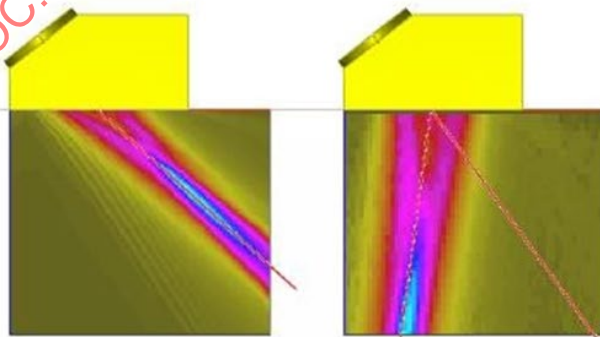


Image Courtesy of CIVA software and Extende

Simulation greatly assists in seeing where a probe actually focuses, and not just the angle or focal points that are desired. As shown in this image, this phased array transducer focusing on the area of the weld prep is not as precise as people may expect it to be.

**Figure 6-3: Beam of phased array transducer focused on weld prep**

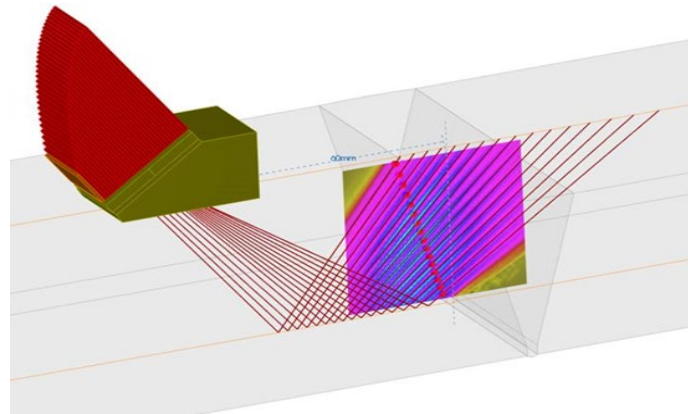


Image Courtesy of CIVA software and Extende

While beam simulation in zero degree FMC/TFM imaging is not as relevant as for standard UT inspection, simulation of the elementary beam from an element of the probe may help estimate its directivity as the sound travels in the part. By simulating the unfocused beam of an element, it is easier to visualize the insonified zone when one element is active in transmission. From simulation one can clearly see that the larger the element is, the more directive the beam and the narrower the beam spread. By modeling the unfocused beam, you can visualize the near field, which represents the optimum thickness range in which to use the FMC/TFM method for a zero degree inspection. This information can be used to optimize a probe at the design stage, or to choose the right one for the job at the inspection stage.

**Figure 6-4: E=0.13mm**

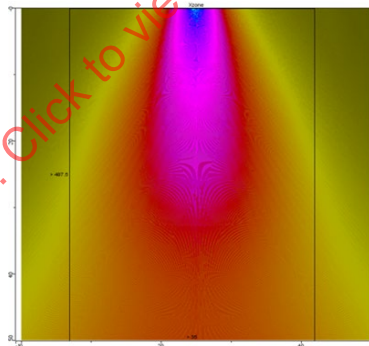


Image Courtesy of CIVA software and Extende

**Figure 6-5: E=0.26mm**

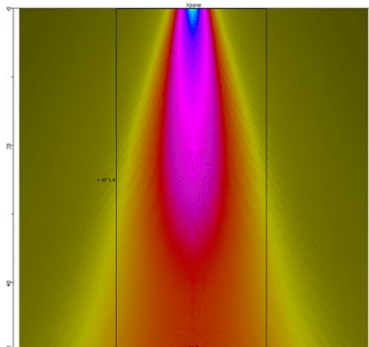


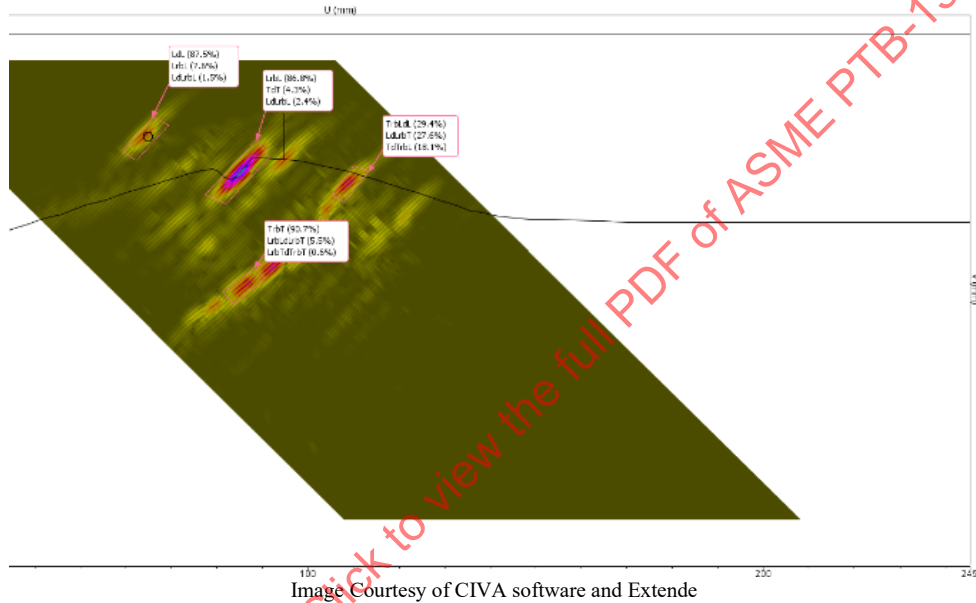
Image Courtesy of CIVA software and Extende



### 6.1.2 Better Understanding of Results via Simulation

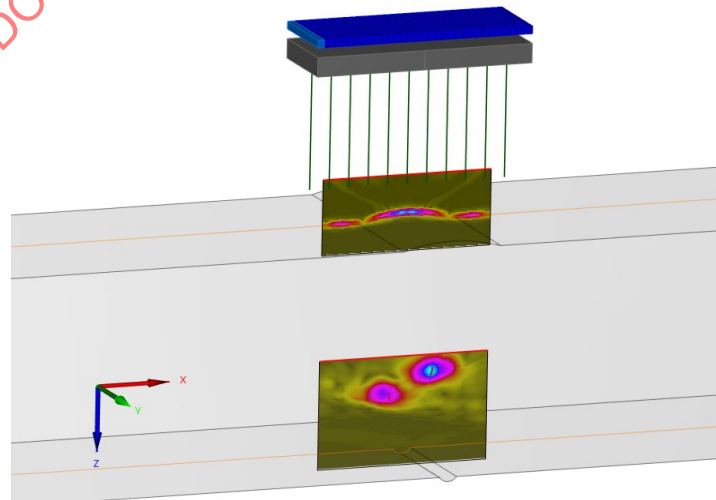
When simulating an inspection, the computer knows which surfaces are the test piece geometry and which are flaws. This makes it possible to use tools such as “mode identification” to identify the wave type and surfaces reflected that result in the B-scan image seen on the ultrasonic scope. In this image the reflection from the root convexity has a stronger signal than the reflection from either the side drilled hole or large planar flaw. Furthermore, the modes ID tells us that over 87% of the response from the SDH is from a longitudinal wave that directly reflects off the flaw, while 90% of the reflection that appear mostly outside the part is from a shear wave reflection directly off the back wall of the part. This information also becomes useful for future inspections to determine which modes will better interact with suspected flaws in the component.

**Figure 6-6: Mode Identification (Mode ID)**



The following image demonstrates the ability of this transducer in immersion to detect the top surface of the part as well as the two crack-like flaws within the weld.

**Figure 6-7: Example of a modeling simulation using the immersion technique**



By using modeling, it is possible to determine the optimal probe for the inspection. Factors that can easily be simulated include frequency, wave type, transducer size, and number of elements. In the following example showing PAUT simulation, it is clear that longitudinal waves penetrate this dissimilar metal weld better than shear waves.

**Figure 6-8: 45-degree L wave is shown on the left and 45 degree T wave is shown on right**



Image Courtesy of CIVA software and Extende

Simulation can also help estimate the effects of flaw orientation on the amplitude of detection. With modeling software, one can run a variation study evaluating the effects of different variables. In this example, the flaw orientation varied from -10 to +10 degrees, while the refraction angle (45°) and frequency of the probe remain constant. Figure 6-9 demonstrates the maximum amplitude occurring when the flaw is at 0 degree and the corner trap effect is the strongest.

**Figure 6-9: Chart of flaw tilt vs. amplitude**



Image Courtesy of CIVA software and Extende

**Figure 6-10: B-scan 3D model for transverse 45 degree (T45) refracted angle interacting with from left to right: 0°, -5° and -10° flaw tilt**

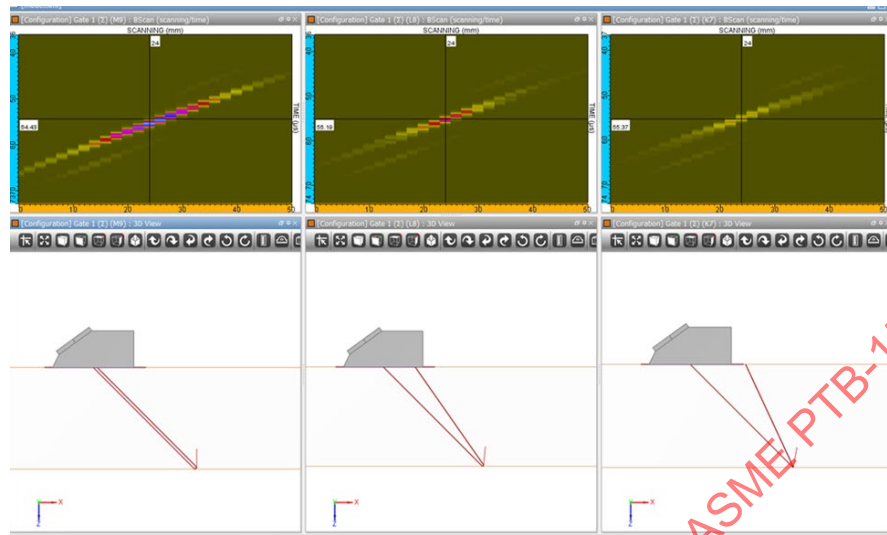


Image Courtesy of CIVA software and Extended

## 6.2 Inspection Simulation

With inspection simulation, key inspection parameters can be modeled on a computer to test the ability to detect (or not detect) flaws. In some simulation tools it is possible to vary the size, shape, orientation and position of a flaw to see how slight variations in values from what is expected can affect the ability to accurately detect and size flaws. It is also possible to see how slight variations in the setup, such as probe starting position and skew angle can greatly affect detectability of a flaw.

One area where simulation can be very helpful is to run variation studies. These can be aimed at aspects such as those described above but can also include variables such as variation in material properties that might be seen, for example temperature related changes in material velocity.

Another area where simulation is useful is to better understand experimental results. With experimental data, indications can be present that are from a variety of sources other than flaws such as geometric echoes, noise, and scatter off large grain. There is not always an easy way to know if you are looking at a response from a flaw or if there is some other source of the indication. With simulation it is possible to simulate the inspection on a flaw free part and see if the indication is present.

Different simulation tools can provide different ways to simulate results. It can be achieved by simulating an FMC acquisition (see Figure 6-11) and then post-process to obtain different TFM reconstruction (Figure 6-12), and determine which options work best for detection of the flaws that need to be detected. This option has a large file size, but it provides the most flexibility in regard to the TFM configurations that can be explored. The other and more common option models TFM images directly. This latter option can create a separate file for each configuration to be explored. These files can then be run as a batch. In some software it is possible to run a TFM configuration but store also the FMC containing all the elementary channels. When all channels are stored in addition to TFM images, it is then possible to explore other TFM modes in post-processing.

**Figure 6-11: Raw results of the FMC simulation**

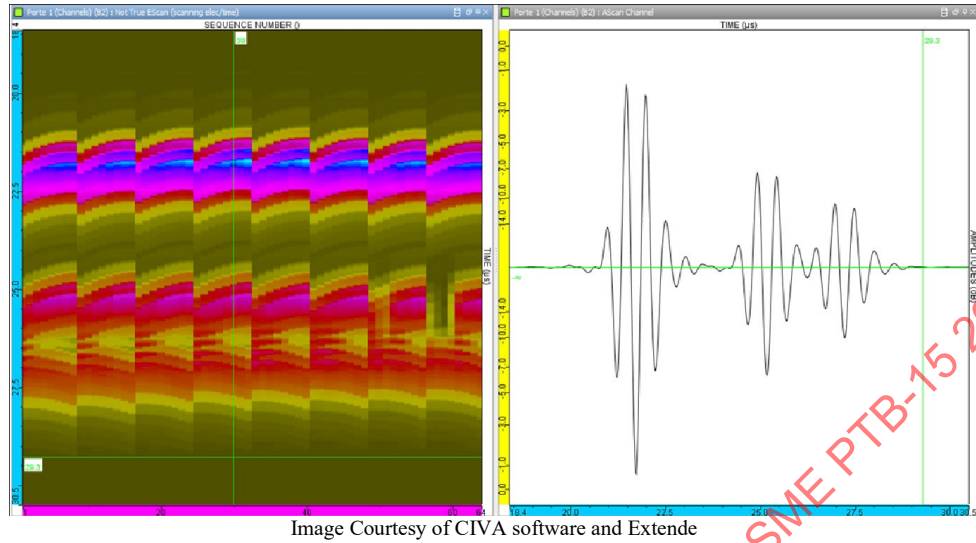
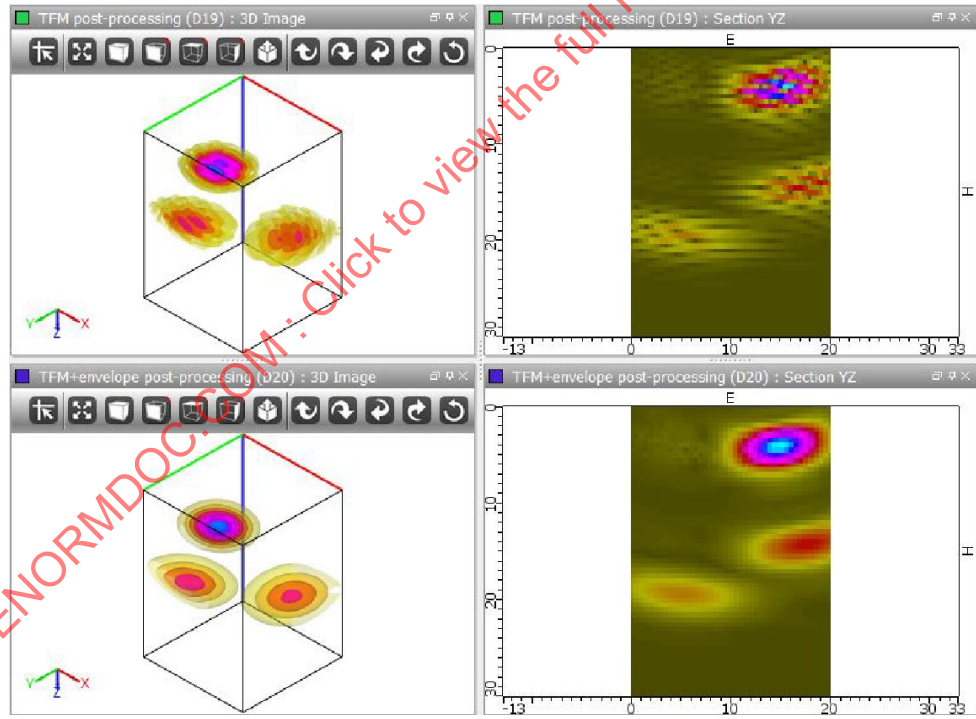


**Figure 6-12: Comparison of 3D iso-surfaces (left column) and YZ section (right column) images after TFM reconstruction without (first row) and with (second row) 'envelope signal' as the computation option.**



By simulating the reconstruction of different TFM modes of propagation, one can determine in advance which mode will best detect the flaws suspected in the material. The following example simulated the ability of a 64-element 5MHz transducer to detect a planar flaw represented in red to model a crack-like backwall surface breaking flaw. Four modes of propagation are evaluated: L-L, T-T, LL-L and TT-T.

It is possible to simulate addition modes, for example when mode conversion is present. In this case, using a TT-T reconstruction clearly shows the flaw, and shows the approximate shape and length of the flaw, whereas an L-L reconstruction only shows the corner trap and tip diffraction, as shown in Figure 6-15. The T-T reconstruction in Figure 6-16 only shows the corner trap, while the LL-L reconstruction in Figure 6-17 does not show the shape of the flaw as clearly as in TT-T mode.

**Figure 6-13: 3D view of inspection setup with backwall breaking planar flaw**

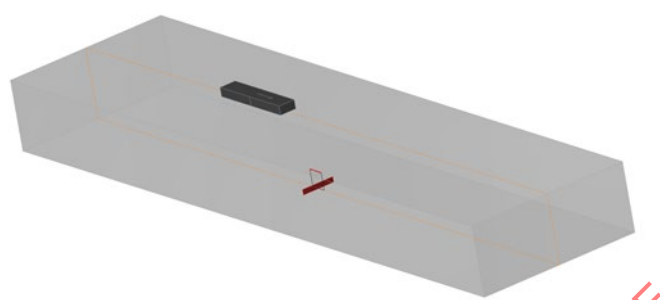


Image Courtesy of CIVA software and Extende

**Figure 6-14: TT-T reconstruction**

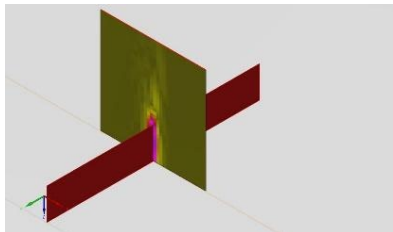


Image Courtesy of CIVA software and Extende

**Figure 6-15: L-L reconstruction**

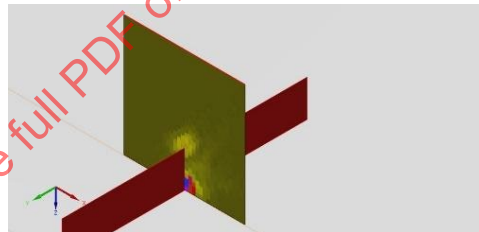


Image Courtesy of CIVA software and Extende

**Figure 6-16: T-T reconstruction**

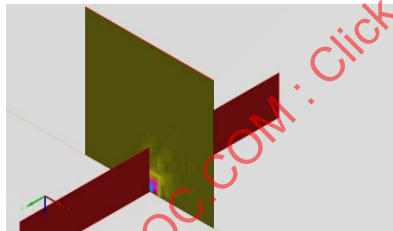


Image Courtesy of CIVA software and Extende

**Figure 6-17: LL-L reconstruction**

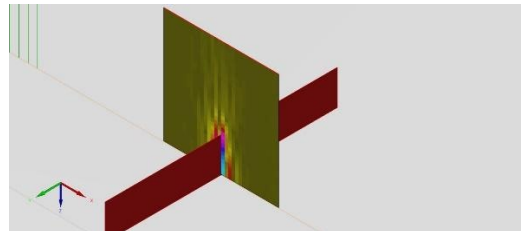


Image Courtesy of CIVA software and Extende

One of the types of weld defects that is important to detect is a lack of fusion along the weld prep. When access to the weld only permits inspection from one side, it can be difficult to detect with conventional UT, even when performing a sectorial scan with a PAUT transducer. Using TFM can provide for much better detection and sizing provided the correct wave type is used. The setup for such an inspection is shown in Figure 6-18, where a 64 element, 5MHz transducer on a 55-degree transverse wave wedge is used to detect the lack of fusion.



**Figure 6-18: Inspection for Lack of Fusion 1**

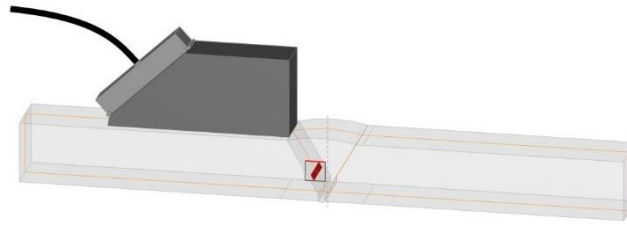


Image Courtesy of CIVA software and Extende

When comparing the response using T-T and TT-TT, the TT-TT provides a stronger response and clearer picture of the size and orientation of the flaw, as shown in Figure 6-19 and Figure 6-20.

**Figure 6-19: T-T wave type**

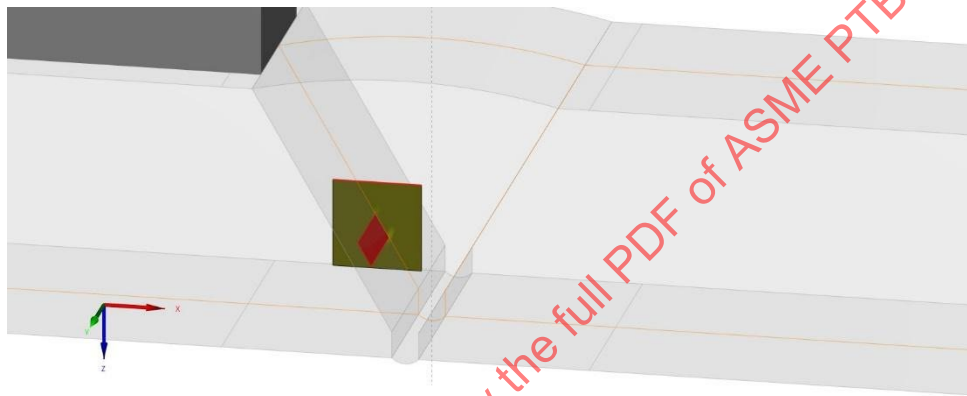


Image Courtesy of CIVA software and Extende

**Figure 6-20: TT-TT wave type**

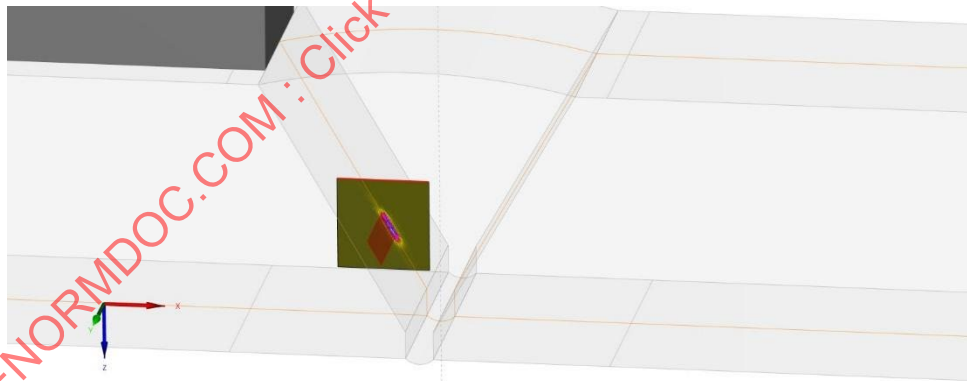


Image Courtesy of CIVA software and Extende

As demonstrated in the above examples, while the flaw shape is planar in both cases, the orientation and placement of the flaw, as well as the probe incident angle in the part greatly influence which wave mode will best detect the flaw. When running TFM simulations, the user must ensure that the expected range and location of the flaw are simulated so that the wave type that best detects and sizes the flaw over the range of situations that are likely to be seen is evaluated, and the most robust inspection option chosen, instead of the one that might work best for one scenario, but be so sensitive as to miss the flaw when slight variations in location and orientation are present. If there is more than one transducer being considered for the inspection, running a study of how each probe operates over the range of expected conditions can be advantageous in choosing the best one for the job.

### 6.3 Using Modeling for TFM Inspection

Although TFM applies delays in the transmission and reception processes to electronically focus at every pixel within the region of interest, the probability of detection of a potential defect and the imaging quality of the TFM inspection is still heavily dependent on the setup parameters of the scan plan. During the scan plan design process, the inspector needs to select the appropriate ultrasound probe, wedge, active aperture, and the proper TFM mode of propagation for the given inspection. Modeling is the most effective way at providing guidance for the selection of all the parameters stated above.

#### 6.3.1 Probe Selection

The first step of the scan plan design is to choose the appropriate ultrasound probe. Different probes may have different number of elements, width of elements, pitch spacing between elements, element elevation dimension, and resonance central frequency. In general, increasing the aperture size (number of elements multiplied by the pitch spacing) would improve the lateral resolution of the TFM image. From optics, it is well known that for a circular aperture, the minimum diffraction-limited separable distance between two objects is described by the equation:

$$x_{sep} \cong 1.22 \left( \frac{cL}{fD} \right) \quad (29)$$

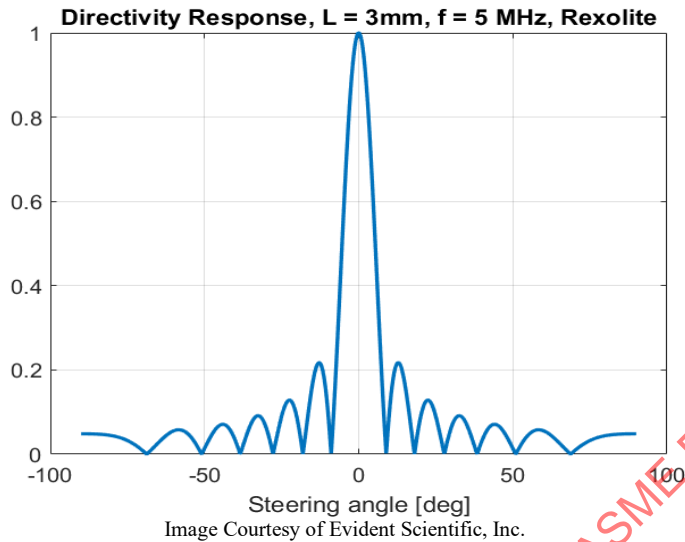
In Equation 29,  $c$  is the speed of light in the medium,  $L$  is the distance of the objects from the aperture,  $f$  is the light frequency and  $D$  is the aperture diameter. Although Equation 29 was originally derived for optics, the physics still applies for ultrasonic testing. From Equation 29 we see that increasing the aperture size decreases the minimum separable distance between two features and therefore improves lateral resolution.

However, having too large of an aperture can be a disadvantage when it comes to inspecting defects close to the top surface. Close to the face of an ultrasound probe, the amplitude and phase of the arriving wavefronts from different elements can be extremely incoherent. Simple electronic focusing without amplitude and phase compensation would lead to poor focus and/or low resultant acoustic intensity. For a same given defect depth, this effect would show more pronounced for larger apertures.

A related consideration to the aperture size is the size of the individual elements. The far-field directivity pattern of an element with a pitch  $p$  is given by the following formula:

$$directivity(\theta, \omega) = \text{sinc} \left( \frac{p\omega \cdot \sin(\theta)}{2c} \right) = \text{sinc} \left( \frac{p\pi \cdot \sin(\theta)}{\lambda} \right) \quad (30)$$

In Equation 30, the  $\text{sinc}(x)$  is defined as  $\sin(x)/x$  and  $\lambda$  refers to the wavelength in the propagation medium. Figure 6-21 shows the directivity pattern for a transducer with a 3 mm pitch travelling in Rexolite at the center frequency of 5 MHz.

**Figure 6-21: Far field directivity pattern of a 3mm pitch element in Rexolite at 5 MHz**

From Equation 30, we see that increasing the pitch of an element increases the term inside the “sinc ()” function. This has the effect of making the element more directional (weaker relative response when electronically steered at large angles).

Another important consideration for probe selection is the element center frequency. From Equation 29, a higher center frequency would lead to improved lateral resolution. From Equation 30, it can also be noted that increasing the center frequency makes the element more directional and is therefore less suitable for large electronic steering angles.

A third effect of increasing the center frequency is improved resolution along a beam propagation direction. The propagation direction resolution in TFM is limited by the duration of the ultrasound pulse produced by one element. High frequency transducers are typically designed to be highly damped and therefore have short durations. However, because acoustic attenuation increases with wave frequency, high frequency probes are not suitable for use in highly attenuative media and/or inspection of very thick samples. These parameters can be imaged using modeling tools, so the inspector can view the effect of the probe characteristic on the simulated beam for a given inspection.

### 6.3.2 Mode of Propagation Selection

A unique TFM imaging parameter that is not found in conventional PAUT imaging is the selection of modes of propagation. Modes of propagation, also known as Imaging Paths or Wave Sets, determine the speed of sound used to calculate the acoustic time of flight at each segment during transmission and reception. The transverse (shear) speed of sound in a material is always slower than its longitudinal wave speed of sound and therefore leads to a longer time of flight. Different speeds of sound also affect the refracted angles at each interface through Snell’s law:

$$\theta_2 = \left( \frac{c_2}{c_1} \sin \theta_1 \right) \quad (31)$$

In Equation 31, the  $c_1$  and  $c_2$  are the speeds of sound before and after the interface.  $\theta_1$  and  $\theta_2$  are respectively the incidence and refracted angles. From Equation 30, we see that a higher speed of sound in the second medium would lead to a larger refracted angle.

By changing the speed of sound used in the time-of-flight calculation, we effectively select the mode of propagation in each ray-traced segment used for the resultant TFM image. The convention of specifying modes of propagation is usually in the format “XX-YY”. Where XX indicates the wave modes in transmission and YY indicates the wave modes in reception.

As an example, the mode “TL-T” indicates there are two ray-traced segments in transmission and one segment in reception. The first “T” indicates the transverse (shear) speed of sound is used in the first segment of transmission; the second L indicates the longitudinal (compression) is used for the second segment of transmission (after a skip). Lastly, the only “T” in reception indicates the direct path is used in reception and the transverse speed of sound is used.

When the transmission modes are equal to the reception modes, the entire mode of propagation is called a direct or pulse-echo TFM inspection. Direct modes TFM inspections can be considered as analogous to conventional PAUT with the difference where every point in the region of interest is electronically focused. When the number of skips in transmission is different from the number of skips in reception, it is then called an indirect or self-tandem TFM inspection. Indirect or self-tandem inspections are unique to TFM and in some cases can lead to better representation of the true geometry of the defects. The selection of the right mode depends on the expected location and orientation of the potential defects. The following TFM images are obtained from the T-T and the TT-T mode of propagation for a root crack.

**Figure 6-22: TFM inspection of a root crack in T-T mode**

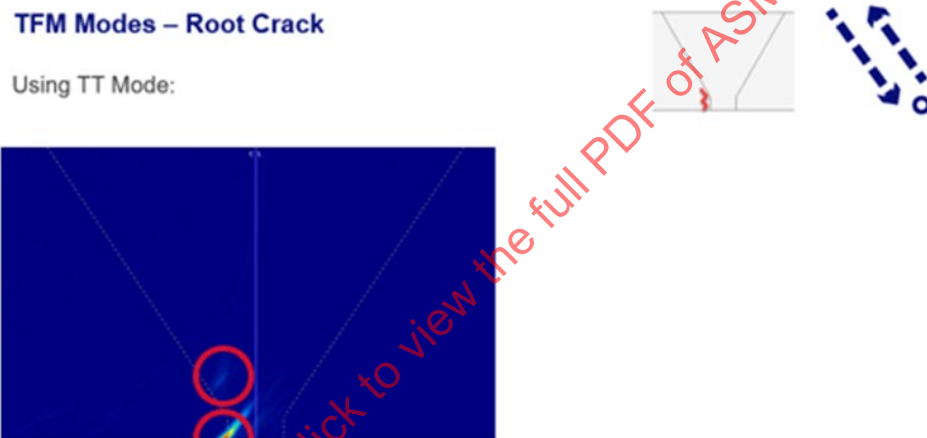


Image Courtesy of Evident Scientific, Inc.

**Figure 6-23: TFM inspection of a root crack in TT-T mode**

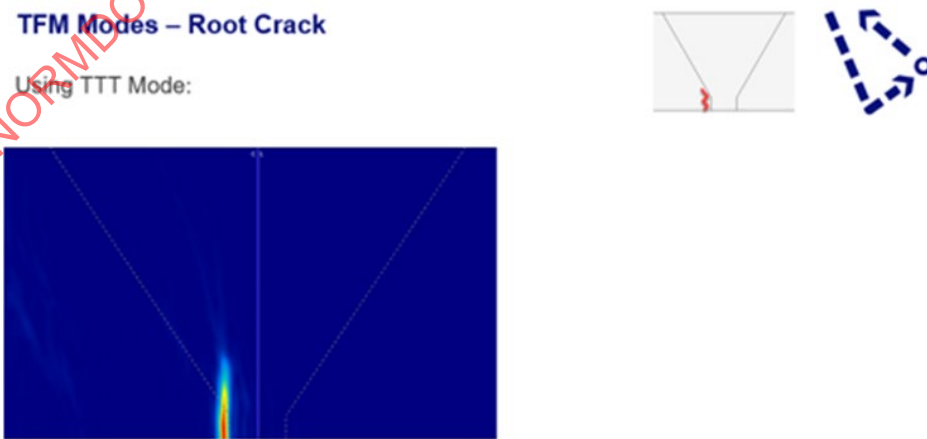


Image Courtesy of Evident Scientific, Inc.

From Figure 6-22 we see that the T-T inspection only shows a faint tip-diffracted echo and a stronger corner-trapped echo at the base of the root crack. In comparison, using the TT-T mode, one can see the true vertical geometry of the crack. The TT-T indirect mode is especially suited for imaging near vertical features near the bottom of a plate or the inner diameter of a pipe. This is because vertical features serve as a specular reflector, connecting the second segment of the transmission ray with the reception ray. However, it is important to keep in mind that a tightly curved geometry could alter the returning path considerably due to beam divergence at the skip. Modeling for different type and orientation of flaw will provide better guidance to determine which mode should be utilized during inspection. The importance of modeling for geometric changes like curvature will also be covered later on.

### 6.3.3 Modeling as TFM Scan Plan Assistance Tool

As examined in the previous section, scan plan parameters such as probe, active aperture, wedge, and mode selection can have significant influence on the quality of the resultant TFM image and on detection. As these scan plan parameters interact with each other, it is therefore very difficult to create an optimal scan plan without the use of a modeling tool. For this reason, some modeling tools have been created to help calculate the theoretical acoustic intensity for a selected TFM scan plan.

A semi analytical acoustic model that considers the effects of probe frequency, element directivity, aperture size, transmission/reception coefficients, geometric beam spread, material attenuation and the selection of a mode of propagation helps inspectors decide ahead of time which mode will be the right one for their inspection. In addition, these tools can calculate the acoustic intensity for directional and non-directional scatterers. A non-directional scatterer is often referred as volumetric, where the scattering coefficient is equal for all combinations of ray incidence and observation angles (ex: porosity), whereas directional scatterers are often referred as a linear indication (crack, lack of fusion, etc.). Different scatterers will require the use of different modes of propagation to be detected successfully. Modeling is crucial in determining the proper mode for the given scatterer. In addition to the type of scatterer, the user also needs to provide the expected orientation of potential indications to be able to make an educated selection.

For directional and non-directional scatterers, the modeling tool assumes there is a scatterer at every point within the region of interest. Consequently, the scan plan image demonstrates the spatial variation of acoustic intensity for the selected scatterer type. The inspector can use this information to optimize the position of the probe/wedge assembly. Some tools will offer modeling images that are self-normalized, therefore the maximum acoustic intensity before normalization is displayed as a sensitivity index. Using the sensitivity index, one can also compare the relative acoustic sensitivity across different modes of propagation.

### 6.3.4 Example of Modeling as TFM Scan Plan Assistance Tool on ERW pipe

A typical use of modeling is presented in the following section. A pipe with an electrical resistance weld (ERW) of 6.35mm (0.25 in.) carbon steel pipe sample presents a stacked lack of fusion flaw, Figure 6-24. The flaws are about 2mm deep, vertically oriented along the weld bevel of the 323mm (12.75 in.) diameter pipe. A 5L32 probe combined with a corresponding 55-degree shear wave wedge is mounted on a longitudinal weld scanner. The weld cap, accessible from the outer diameter surface, is leveled. In this applicative example, it is sought to obtain a TFM representation of the flaws that are closest to its anatomically correct layout.



**Figure 6-24: a) Longitudinal scanner mounted on the ERW pipe sample, along with TFM flow detector device showing the stacked vertical lack of fusions located inside the weld line. The flaws span about 25.4mm long over the pipe axis. b) Scan plan representing the weld and curvature of sample**

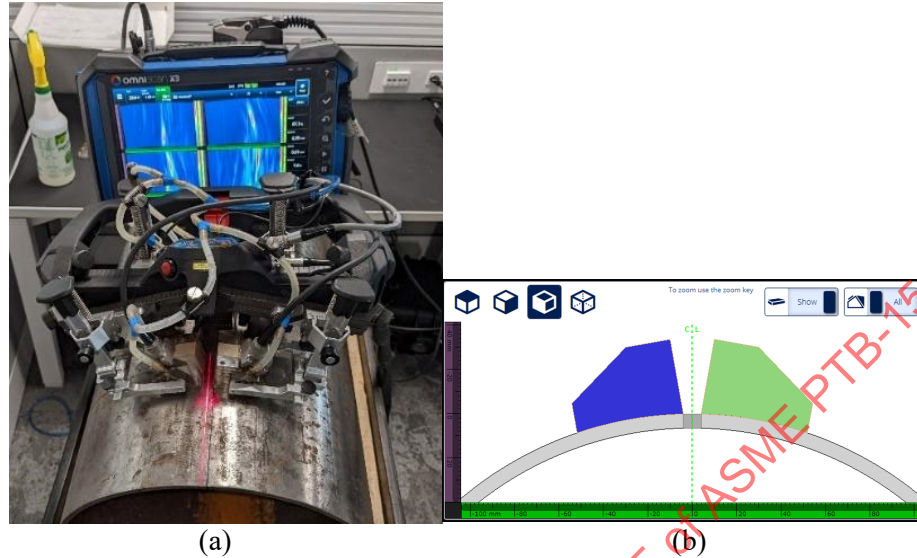


Image Courtesy of Evident Scientific, Inc.

First, the mode of propagation selection strategy is based on the a priori knowledge of the target flaw type acoustic response. Four modes of propagation were highlighted by the modeling tool and selected to be used simultaneously for this inspection. The direct T-T and TT-TT modes here are showing less interest because they are expected to produce weak diffractive echoes from the vertical flaws. The following example will address the TT-T (3T, shear wave self-tandem), and TT-TTT (5T, shear wave half skip going, single skip returning) modes of propagation that were selected as good candidates due to their likelihood to echo back to the probe through specular reflection at the face of vertical flaw. However, without modeling, it is still unclear how these modes of propagation would have provided an effective representation of the flaws under study.

In this configuration, the modeling was configured to produce the 32 elements aperture and expected TFM acoustic response from a planar flaw over the region of interest. Because the weld cap is leveled, the weld volume is accessible from the top of the part.

The modeling heatmaps are shown in Figure 6-25 for the TT-T and TT-TTT modes of propagation. An inspection of the maps reveals that the TT-TTT mode of propagation covers a larger area with strong amplitude in comparison with the TT-T mode of propagation. The TT-T is most sensitive directly under the wedge, and along an area near the internal diameter surface.

**Figure 6-25: The modeling for planar defect “heatmaps” computed for (a) the TT-T and (b) TT-TTT mode of propagations**

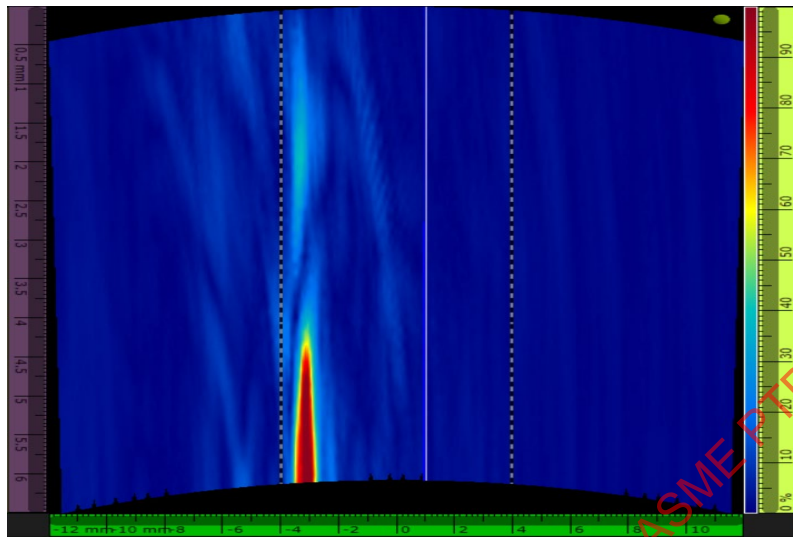


Image Courtesy of Evident Scientific, Inc.

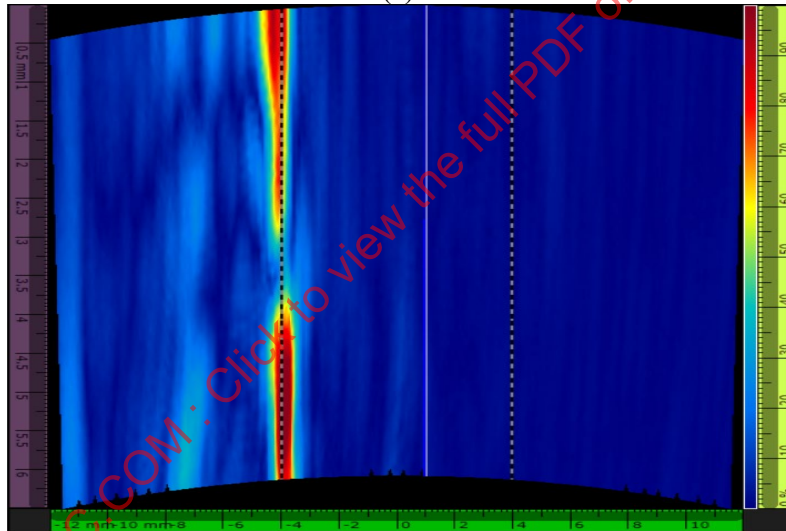
The sensitivity index provided in some modeling tools also highlights the maximum sensitivity value of a given mode of propagation. The sensitivity index for the TT-T and TT-TTT modes had similar values, so it is understood that the two modes of propagation may respond with a similar maximum amplitude. However, the corresponding high sensitivity regions do not necessarily overlap, as illustrated by the modeling heatmaps. The sensitivity index is especially useful at identifying early weak sensitivity from strong sensitivity modes of propagation.

The TFM images corresponding to TT-T and TT-TTT modes of propagation are presented in Figure 6-26. While the TT-T mode a) is effective at imaging the lower lack of fusion flaw, both segments of the flaw are well represented using b) the TT-TTT mode. This observation agrees with the prediction provided by the modeling heatmaps of Figure 6-25.

**Figure 6-26: TFM image on the stacked lack of fusion flaws for (a) the TT-T and (b) TT-TTT. The gain is adjusted to equalize the maximum amplitude.**



(a)



(b)

Image Courtesy of Evident Scientific, Inc.

The acoustic modeling tools are therefore useful to determine, at the scan plan stage, which mode of propagation is appropriate to inspect in each region of interest, and at the analysis stage, to interpret correctly the TFM image produced by the different mode of propagations. In the example above, the modeling heatmap predicted that the TT-TTT mode of propagation had a larger high-sensitivity region than the TT-T mode with respect to the vertical lack of fusions. The corresponding TFM images confirm the prediction: the TT-TTT mode of propagation perceives the flaw over its complete extent while the TT-T mode of propagation renders correctly only the lower lack of fusion, leaving the low amplitude echoes coming from the upper lack of fusion as structures to interpret with care. In this matter, the TT-TTT mode of propagation image best captures the actual layout of the flaw under investigation.

## 7 ADVANTAGES AND LIMITATIONS OF FMC/TFM VERSUS PAUT

### 7.1 Advantages

#### 7.1.1 Accurate Visualization

When using Phased Array (PAUT), the most used method (technique) of inspection is the Pulse-Echo (PE), where the same group of elements (active aperture) pulses and then receives the ultrasound. This makes for a simpler implementation and a more flexible use of the technology, but where the method excels at representing indications perpendicular to the ultrasound propagation path, it can be difficult to interpret off axis indications such as vertical reflectors. The traditional signature for a vertical crack with PAUT would be a strong corner trap signal and a shallower tip diffraction signal; these two signals may be confused for two separate indications to an untrained eye.

The so called Self-tandem mode is a Pitch-Catch PAUT technique and uses one aperture to pulse and a different one to receive. Self-tandem is less common and often dedicated to specialized applications. One of this method's key advantages is the detection and representation of vertical indications. The implementation of this technique remains more complex, however, as upfront calculations are required to determine the optimal probe position and which combination of elements to use for the detection of targeted indications.

The Total Focusing Method (TFM) offers the choice between Pulse-Echo and Pitch-Catch modes and uses the same principles as traditional PAUT when rebuilding the sound path from the raw Full Matrix Capture (FMC). Just like when applied in Phased Array, the Self-tandem technique requires more precision when defining the inspection scan plan because of all the trigonometry involved; parameters like material velocity and thickness are essential to achieve accuracy. TFM improves on PAUT by being able to reconstruct the indication from a tightly spaced grid of points instead of pre-determined beam paths, making the implementation of Pitch-Catch more accessible and bringing the benefits of the accurate, true-to-life, representation to a broader pool of operators.

Figure 7-1 and Figure 7-2 show examples of ID connected cracks and OD connected cracks being detected by PAUT S-scan and TFM using the Pulse-Echo method. In the case of TFM, the TT-TT mode has been used. Note that the flaws appear almost identically between PAUT and TFM.

**Figure 7-1: ID connected crack detection comparison between PAUT and TT-TT TFM**

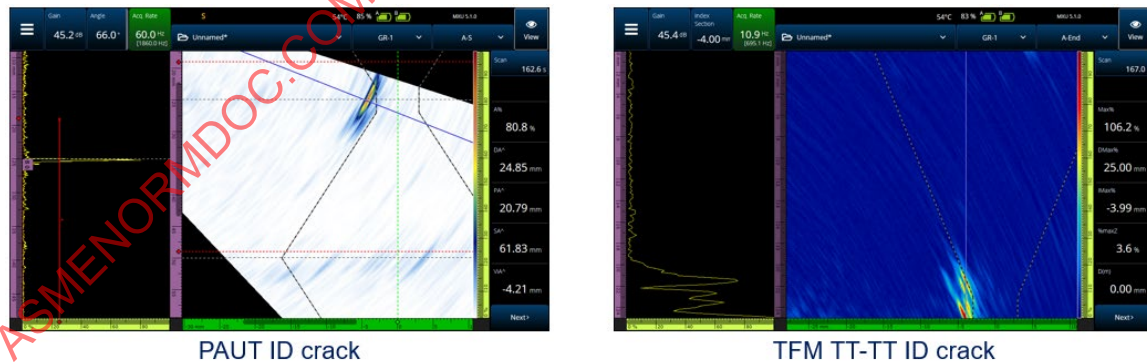


Image Courtesy of Evident Scientific, Inc.



**Figure 7-2: OD connected crack detection comparison between PAUT and TT-TT TFM**

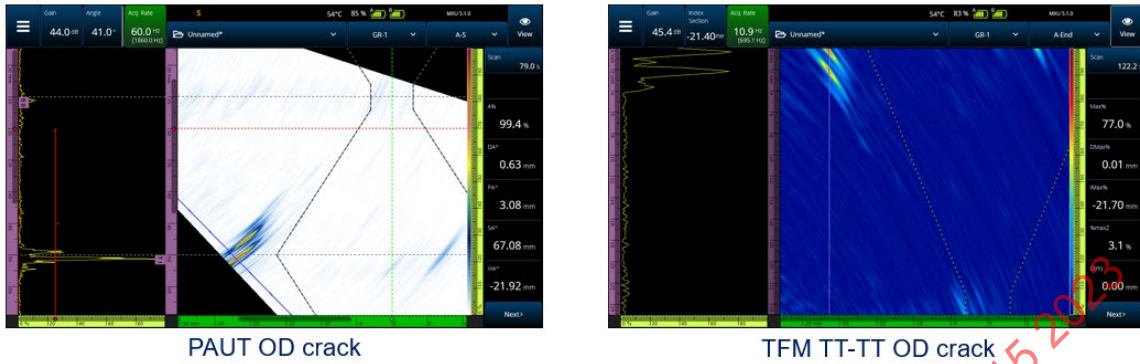


Image Courtesy of Evident Scientific, Inc.

The advantage of using Pitch-Catch, or the Self-Tandem mode, is in the representation of the flaw. The flaw will appear on the screen similarly to what a micrograph of the defect would provide. Figure 7-3 and Figure 7-4 show examples of the same ID connected cracks and OD connected cracks being detected by PAUT and TFM, but this time using the Pitch-Catch method. In the case of TFM, the TT-T and TT-TTT modes have been used. Note that the TFM now renders the ID and OD flaws as vertical and uninterrupted, as they are in the physical part.

**Figure 7-3: ID connected crack detection comparison between PAUT and TT-T TFM**

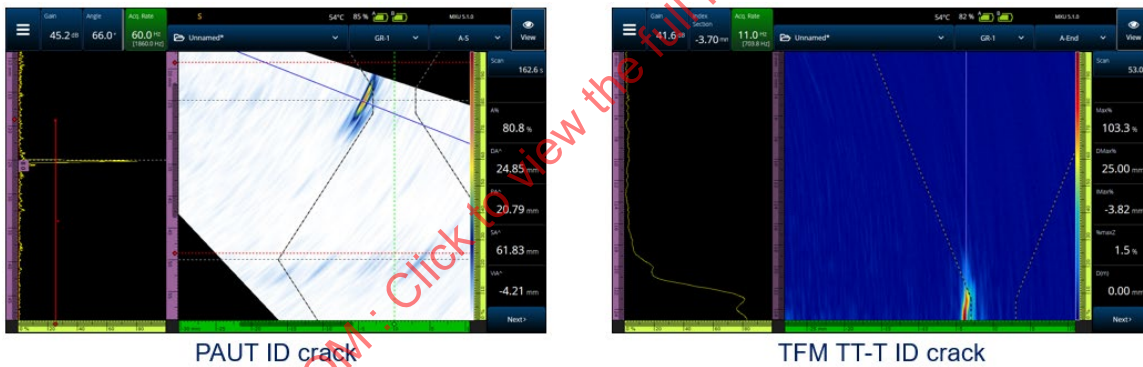


Image Courtesy of Evident Scientific, Inc.

**Figure 7-4: OD connected crack detection comparison between PAUT and TT-TTT TFM**

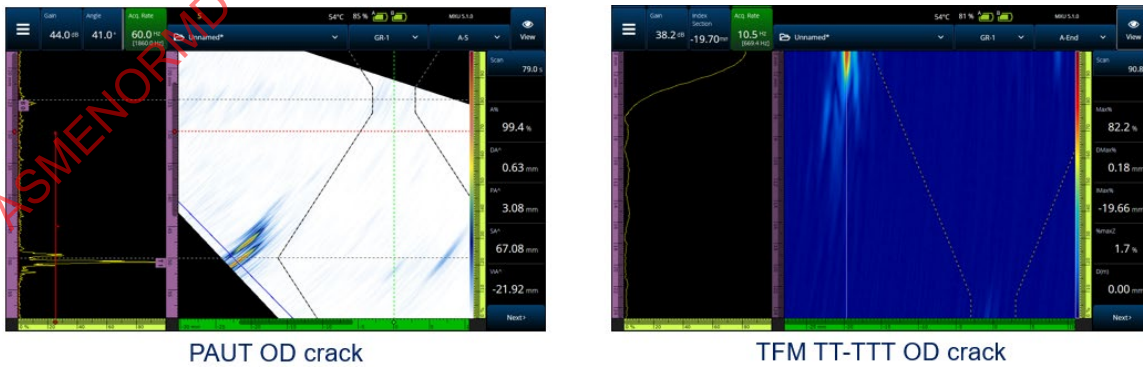


Image Courtesy of Evident Scientific, Inc.

### 7.1.2 Improved Resolution

The common advantage that brought FMC/TFM to the industry is the appeal of having the final image being focused at every pixel of the selected zone. The Delay and Sum (DAS) process is applied to all the A-scans, using the expected delays for a selected mode of propagation (i.e., T-T, TT-T, TT-TT, etc.) to a specific position in the defined TFM zone. In this way, every pixel of that zone is said to be optimally “focused”.

Of course, proper imaging and detection is still dependent on other factors like probe configuration, frequency, material attenuation, known thickness and geometry parameters, and proper mode selection. Outside the near-field region, focalization parameters have little to no effect on the measurement, this is true for both PAUT and TFM.

Theoretically, TFM can produce more appealing images, which is the driving force behind this technology. Another effect of being focused at all points is the reduction of geometrical echoes.

Figure 7-5 illustrates a Phased Array Linear scan and the response of 1mm side drilled holes (SDH) over a depth range of 55mm drilled in a calibration block. A 5MHz, 1mm pitch probe in direct acoustical contact with the block and focused to 37mm depth was used. At and around the focusing depth the resolution of the SDH is great, but as the detection gets further away from the focus depth, the resolution worsens, and the indications are less defined.

Figure 7-5: PAUT detection of SDH at different depths



Image Courtesy of Evident Scientific, Inc.



Figure 7-6 illustrates using the same probe with TFM and an L-L mode. The holes shape remains constant over the depth range.

Figure 7-6: TFM L-L mode detection of SDH at different depths



Image Courtesy of Evident Scientific, Inc.

### 7.1.3 Sound Propagation (dead zone)

With Conventional UT and PAUT inspections, if a large enough reflector is detected, the zone behind it remains unseen, similar to an object creating a shadow when pointed with a light source.

With TFM however, because the entire array of elements is used to receive and analyze data, we can see details we might have missed with PAUT. The way that the sound will propagate in an FMC/TFM inspection can be another benefit to the method. Because of its acquisition pattern, the spherical emission of a single transducer will flood the material with sound similar to a Time-of-Flight Diffraction (TOFD) technique. This spherical wave propagation can allow for detection of defects that would typically be blocked by other reflectors in a common PAUT technique where an individual front wave would be formed.

To illustrate this effect, Figure 7-7 is comparing a  $0^\circ$  PAUT inspection to a TFM L-L inspection. Note on the Phased Array inspection that the first SDH is detected and normalized to the reference amplitude, but subsequent SDH are either missed or detected only from the adverse echoes. On the right side, TFM detects the three stacked SDH with a good resolution.

**Figure 7-7: Detection of vertically stacked SDH comparison between PAUT and TFM L-L mode of propagation**



PAUT only showing the first SDH

TFM showing all 3 SDH

Image Courtesy of Evident Scientific, Inc.

Another advantage of the ultrasound propagation with TFM is the detection of vertical or inclined links between in-service induced by hydrogen damage so-called blisters. These links are difficult to confirm with PAUT because there are no solid surfaces perpendicular to the propagation of the ultrasound to reflect a strong signal. The multi-directional nature of TFM allows to confirm the link or no link between blisters, which can be the difference between benign damage and asset failure. Figure 7-8 illustrates step wise cracking and inclusions detected with TFM.

**Figure 7-8: Detection of link between blisters with TFM**

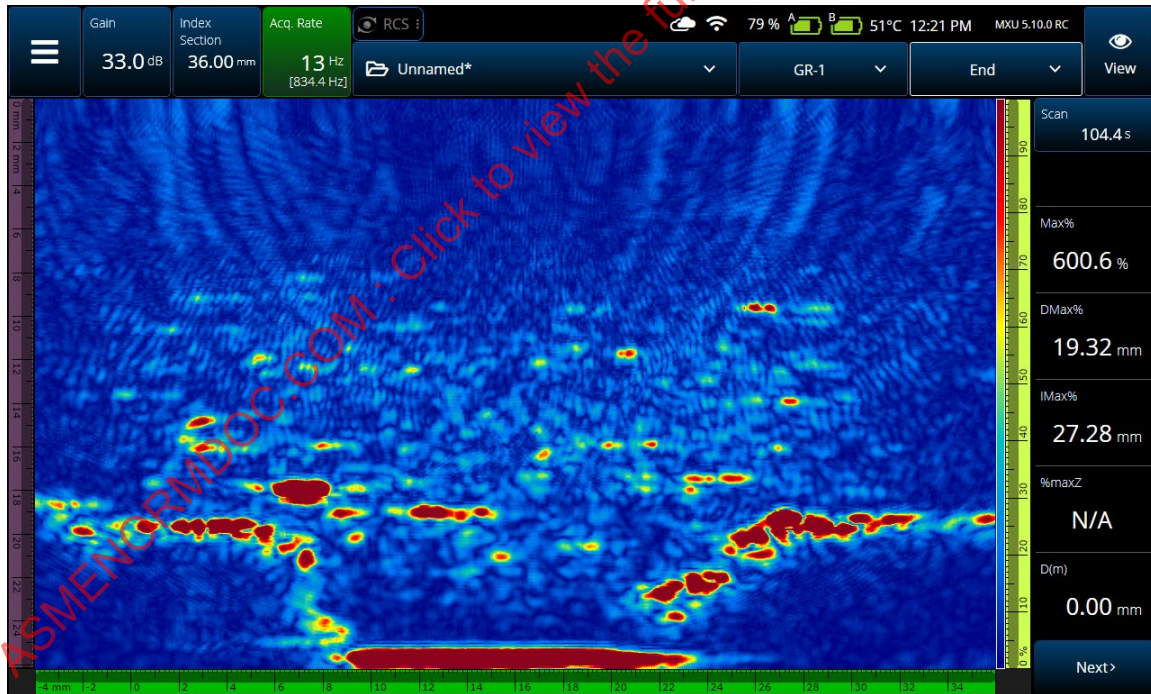


Image Courtesy of Evident Scientific, Inc.

### 7.1.4 Near Surface Resolution

Because of its firing sequence method (only one element firing at the time) the initial pulse, called the Main Bang, is considerably reduced as compared to PAUT. This interface noise reduction can provide a greater near surface resolution. This helps to isolate indications that are closer to the surface or show indications that may have otherwise been missed. Figure 7-9 shows a comparison of the series of SDH in an arc as detected by PAUT and TFM using a 5MHz 1mm pitch probe. On the left, the PAUT Linear scan resolves the 5mm deep SDH. Anything shallower is hidden by the Main Bang. On the middle screenshot, the same 5mm deep screenshot is resolved with the TFM L-L path (mode of propagation). Also, the next two SDH are shown compared to the PAUT scan where they are hidden by the first one. On the right, shallower SDHs at 2.5mm deep were detected when gain was increased. Note that because the detection happens in the ultrasonic constructive/destructive interference zone, the signal-to-noise ratio (SNR) is worse compared to deeper SDH.

**Figure 7-9: Detection of shallow SDH comparison between PAUT and TFM L-L mode of propagation**

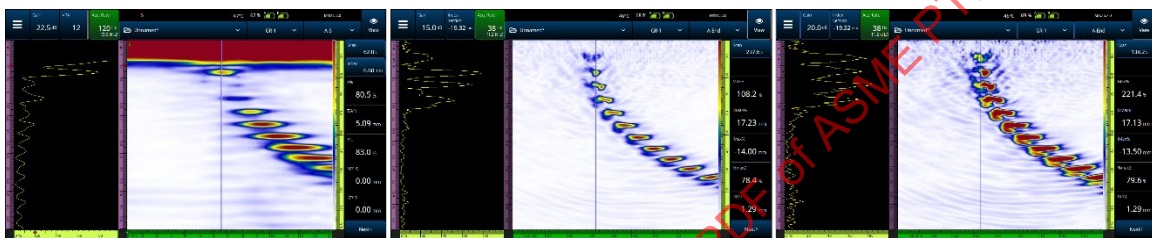


Image Courtesy of Evident Scientific, Inc.

## 7.2 Limitations

### 7.2.1 Selection of the Correct Mode of Propagation for the Type of Flaws

When using TFM during the inspection, the inspector must be mindful of the part geometry and thickness, the type of indications that are expected and their location and prepare the scan plan accordingly. Flaw detection and characterization capabilities are dependent on the selected mode of propagation. The physics remain the same, so when selecting a mode of propagation, the acquisition instrument will reconstruct the TFM data based on the selected ultrasound path or mode (Pulse-Echo, Self-Tandem, first leg, second leg, etc.).

Figure 7-10 illustrates the importance of planning and modeling: in this example, the same lack of fusion is observed with two different TFM modes of propagation. On the left, the Pulse-Echo TT-TT mode produces a strong reflection, and the lack of fusion is easily detected and characterized. However, on the right side, the indication is missed because the mode of propagation used is a Self-Tandem TT-T. The orientation would require for a Full-Skip Pulse-Echo inspection (TT-TT mode) and has been modeled before testing, the Self-Tandem inspection is not suited for this flaw location and orientation to obtain adequate perpendicularity of the sound with the flaw.

**Figure 7-10: Lack of fusion detection comparison between TFM TT-TT and TT-T modes**

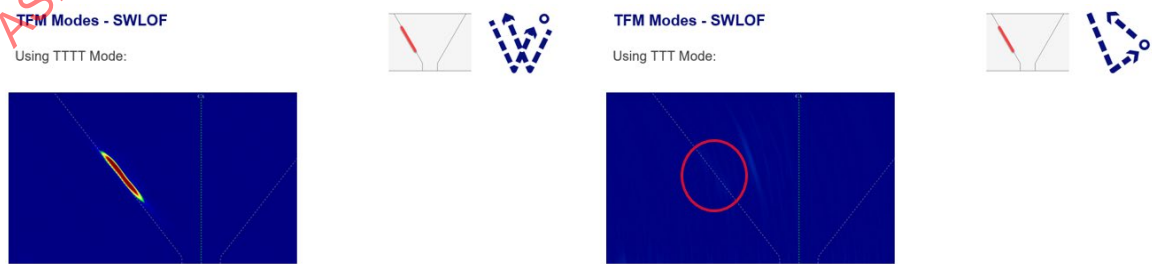


Image Courtesy of Evident Scientific, Inc.

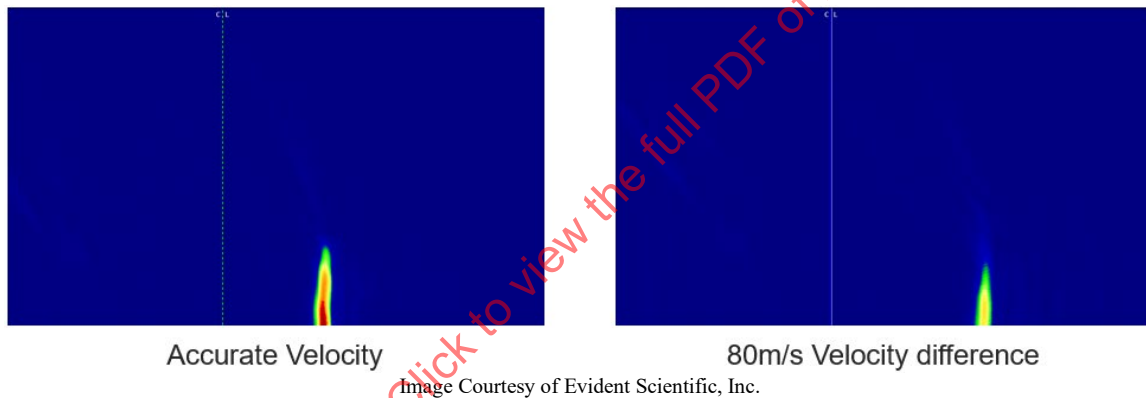
### 7.2.2 Part Geometry and Material Definition

Self-Tandem mode results are very sensitive to a part's thickness and geometry. An error in the time-of-flight calculation may lead to poor detection capabilities or no detection at all. Thickness or geometry (flat or curved surface) changes will affect the accuracy of the readings when skipping the ultrasound. An accuracy error in the thickness input results in inaccurate readings and a wrong indication severity assessment. The computation of the time of flight (TOF) relies heavily on the first and/or second skips. If the TOF is shorter than expected (material being thinner than the entered parameter), the indication can be entirely missed.

Care should be taken when examining welds of complex geometry like welds joining materials of unequal thickness, materials that are joined at an angle, nozzles, etc. These types of welds will introduce ultrasound skips and unpredictable mode conversion signals that must be considered during modeling and scan plan to produce the correct results. This is also true for Pulse-Echo modes.

Illustrated in Figure 7-11 is the detection variation of a notch between a TT-T mode with the correct material velocity and the same TT-T mode but a material velocity error of 2.5% (80m/s): the result is a loss in signal of 17.9 dB for this vertical notch.

**Figure 7-11: Vertical notch detection comparison with a TT-T mode of propagation: accurate velocity vs. 2.5% velocity input error**



### 7.2.3 Attenuation and Penetration in Thick or Difficult to Penetrate Materials

The classical FMC data collection uses one element of the PAUT probe at the time to send ultrasound in the material. This has multiple advantages as stated previously, but a limitation is that this data collection strategy does not produce ultrasound as strong as a PAUT wavefront that happens when combining the signal of multiple probe elements. The PAUT Wavefront, while being oriented in a single direction, provides better signal-to-noise ratio if enough elements are combined (large active aperture) for the inspection of thicker or harder to penetrate materials. Figure 7-12 shows the difference in SNR at the detection of a flat bottom hole (FBH) between a 32 element linear PAUT scan and TFM L-L mode. The sample used was a special hard to penetrate alloy, and the PAUT probe was 5MHz with a 1mm pitch. On the left, we can see that the PAUT SNR is superior to the TFM mode on the right.

**Figure 7-12: SNR difference at the detection of a flat bottom hole (FBH) between a 32 element Linear PAUT scan and TFM L-L mode**

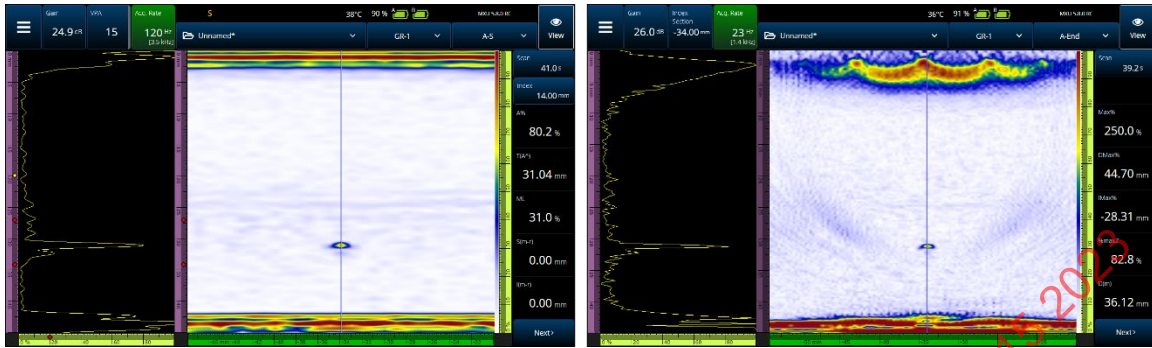


Image Courtesy of Evident Scientific, Inc.

### 7.2.4 Productivity

Depending on the number of elements and the number of laws to be generated, PAUT tends to be more productive because there are fewer transmission cycles for an equivalent inspection. Similar to the maximum scan speed, PAUT tends to also generate less data, hence smaller file size.

ASMENORMDOC.COM : Click to view the full PDF of ASME PTB-15-2023



## 8 SIZING TECHNIQUES

### 8.1 Length and Height Sizing

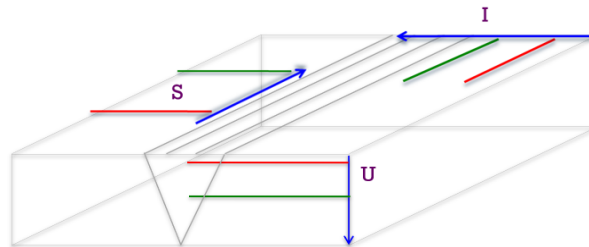
After an indication has been detected and the discontinuity type characterized, the next step in analysis is typically to perform a determination of sizing. The length and through-wall height of the indication will often dictate whether it is considered acceptable or rejectable. The rules for length and height sizing with FMC/TFM are consistent with those used in PAUT and conventional UT. Various dB drop methods (6-dB, 3-dB, etc.) for length sizing are still applicable with TFM. A 6-dB drop for sizing the through-wall height of embedded indications is also similar to what is used in PAUT, but due to the improved focusing that is possible with the technique, there is a potential for more accurate results. Crack tip-diffraction height sizing techniques work especially well with FMC and TFM, the crack tips can often be imaged with great resolution. Also, tip diffraction height sizing on embedded defects such as sidewall Lack of Fusion (LOF) works especially well due to the omnidirectional nature of the elementary A-scans, and the ability of the TFM process to reconstruct data in the area of interest.

The welding processes can have a great influence on the possible sizes of defects, and the examiner should always be familiar with these. For manual welding techniques such as Shielded Metal Arc Welding (SMAW) and Gas Tungsten Arc Welding (GTAW), the average weld deposit layer is approximately 0.120 in.– 0.160 in. (3.0 mm – 4.0 mm). For automated welding techniques such as Submerged Arc Welding (SAW), the weld layers will be about double that 0.240 in.– 0.320 in. (6.0 mm – 8.0 mm). That being said, the through-wall heights of indications such as sidewall LOF typically should not exceed one weld layer. On the other hand, clusters of porosity have the potential to be taller in through-wall size. Often, porosity will span multiple weld layers as the gases try to escape. Flaws in automated welding processes have the potential to be much larger than flaws in manual processes because their passes tend to be larger.

With FMC/TFM data, just as with PAUT, sizing is performed with a series of cursors that are attached to the different views and axes along the data (see Figure 8-1). These positional cursors are also tied to measurement readings. Useful measurement readings show the positions of the cursors, as well as the delta between cursors, which are used for lengths and heights. Length sizing is performed along the scan axis, usually found on the Top view (C-scan) and Side view (B-scan). Height sizing is performed on the Ultrasonic or Depth Axis, found on the Side and End views. Different equipment manufacturers have varying terminology for these tools, but the functionality is largely the same regardless of instrument.

Figure 8-1: Measurement Tools–Cursors

#### Measurement Tools - Cursors



- U – Ultrasonic (Depth) Axis- A-scan, End View, Side View (B-scan)
  - Flaw depth and height
- I – Index Axis- End View, Top View (C-scan)
  - Position of indication relative to weld centerline
- S – Scan Axis- Top View (C-scan) and Side View (B-scan)
  - Flaw start/ end and length

Courtesy of Kenneth Shane Walton-University of Ultrasonics

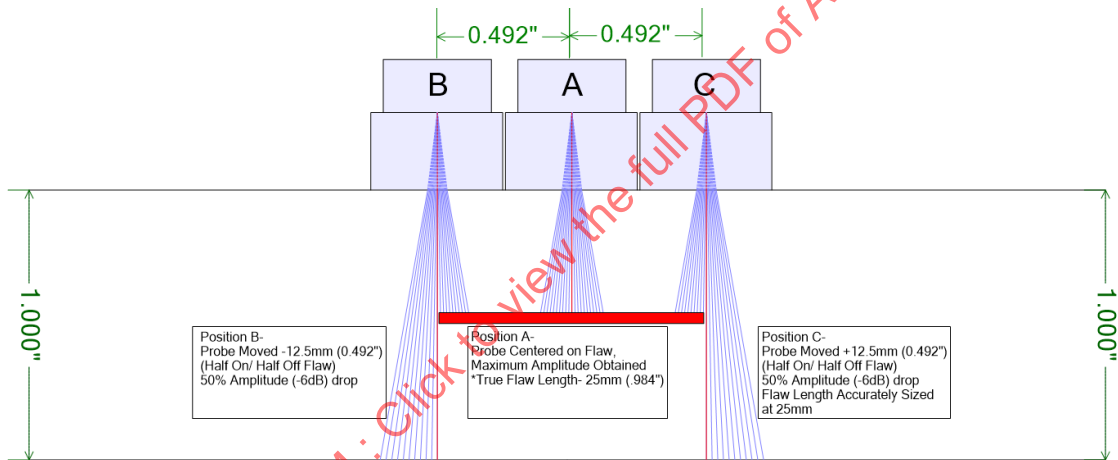
Sizing in length and height is never a one-size-fits-all task. Varying material types, thicknesses, geometries, transducer frequencies, etc. present specific challenges that must be addressed. Optimum sizing techniques should be developed and qualified using components with implanted flaws of known dimensions and orientations, representative of what may be encountered during the examination. For the sake of the current discussion, examples will be given on some of the more common approaches.

## 8.1.1 Length Sizing

### 8.1.1.1 6dB Drop Length Sizing

The concept of 6dB drop sizing works under the premise that when a UT beam is half-on and half-off of the edge of a discontinuity, the signal amplitude should drop 50% from the max amplitude that was shown on top of the flaw—Figure 8-2. A 50% reduction in amplitude is said to be a loss of 6dB. A decibel (dB) is nothing more than a comparison between two amplitudes or magnitudes. To place a beam  $\frac{1}{2}$  on and  $\frac{1}{2}$  off an indication, it is implied that the discontinuity must be at least the same size as the beam diameter, or larger.

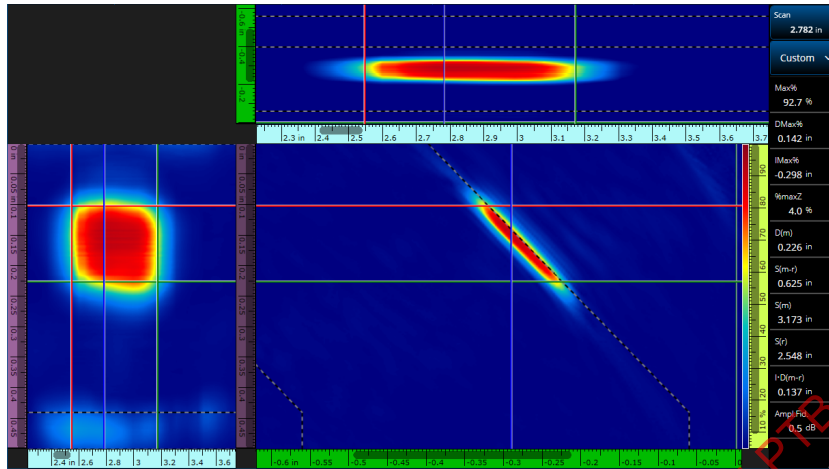
**Figure 8-2: Principles of 6dB Drop length sizing of discontinuities larger than the beam diameter**



Courtesy of Kenneth Shane Walton-University of Ultrasonics

A 6dB drop length sizing works best for smooth, continuous indications, larger than the beam diameter, such as the sidewall LOF shown in Figure 8-3. The LOF indication starts at 2.548 in. (64.8 mm) from datum, marked with the red S(r) reference cursor. The end of the indication is at 3.173 in. (80.6 mm), marked with the green S(m) measurement cursor, and the length was measured to be 0.625 in., shown by the S(m-r) reading. The maximum amplitude was near the middle of the indication, at 92% FSH. Cursors mark the left and right extents of the flaw where the amplitude dropped approximately 50% or 6dB. The top and side views were useful in determining the length of the flaw.

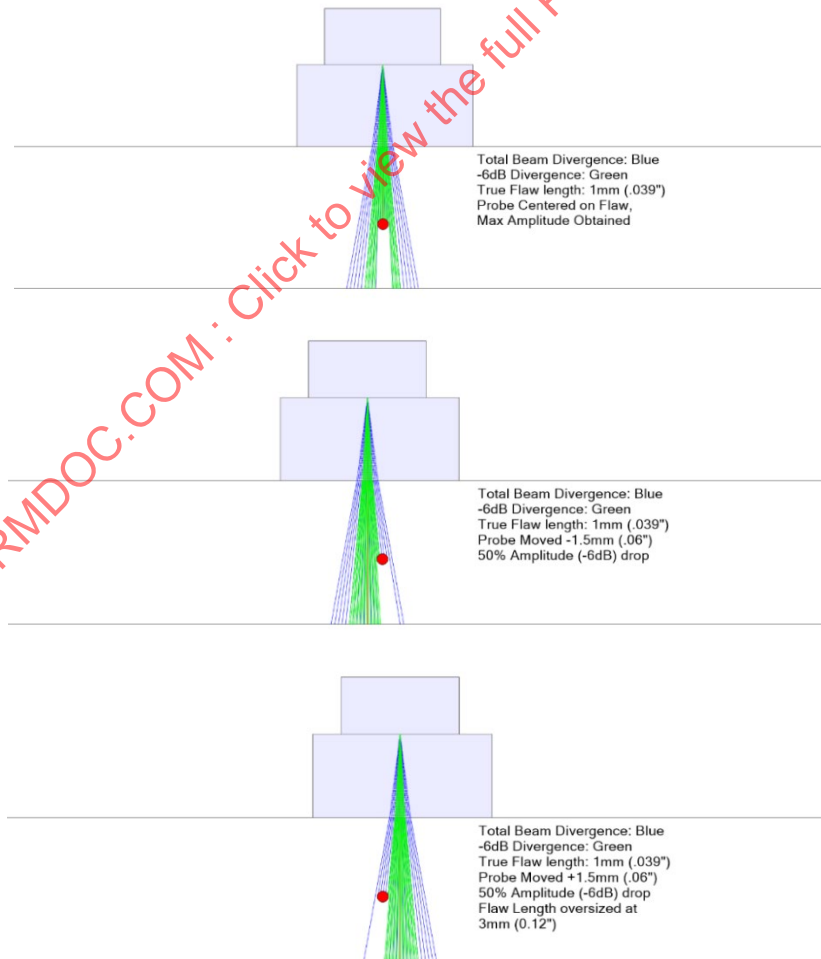
Figure 8-3: Example of LOF 6dB Drop length sizing



Courtesy of Kenneth Shane Walton-University of Ultrasonics

For discontinuities smaller than the beam diameter, 6dB drop techniques will only size the 6dB limits of the beam spread, and not the flaw itself, as depicted in Figure 8-4.

Figure 8-4: Principles of 6dB Drop length sizing of discontinuities smaller than the beam diameter



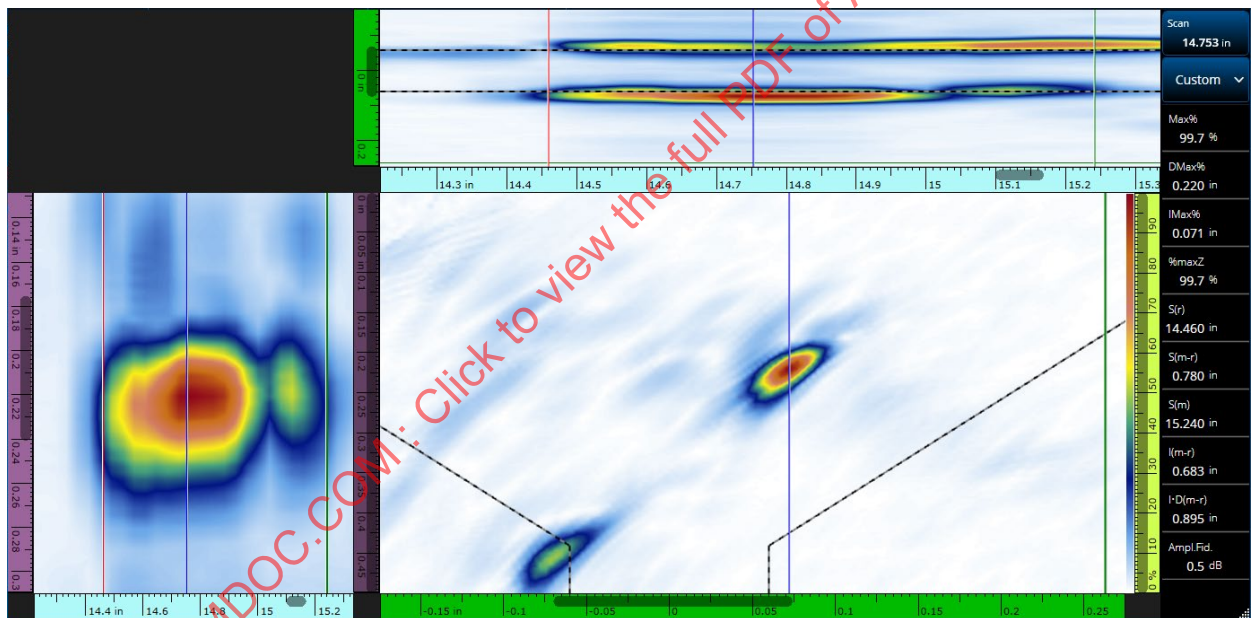
Courtesy of Kenneth Shane Walton-University of Ultrasonics

### 8.1.1.2 6dB Drop Length Sizing Errors

Typically, with FMC/TFM and PAUT, length sizing is performed using the lateral portion of the transducer, also known as the passive/mechanical/secondary axis. For a standard 1D linear array, lateral focusing is not possible, and the examiner is at the mercy of the passive aperture beam spread. This typically results in oversizing the length of the flaw. Curved internally focused arrays or passive-aperture focused wedges can help minimize this over-sizing error.

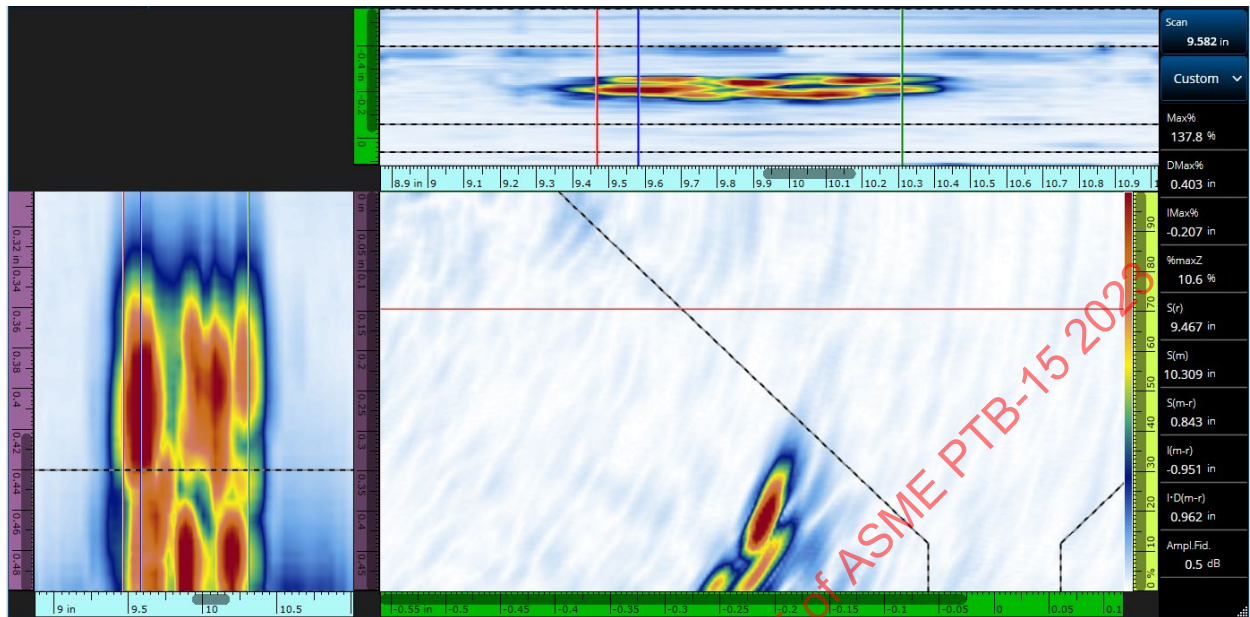
The 6dB drop method also assumes that the flaw indication has one solid reflecting surface, with the highest peak located near the center, as seen in Figure 8-3 above. This is often seen with the textbook indications found in training samples, but in real welds, flaws are often fractal and irregular. In these cases, it is sometimes more accurate to do a 6dB drop from one end of the indication, mark it with a cursor, and repeat on the other end of the indication to get the full length of the flaw. This approach is demonstrated for the slag indication example in Figure 8-5. The Top and Side views are both useful for this application. This approach is sometimes referred to as a maximum amplitude or last amplitude variation of a 6dB drop. The red S(r) reference cursor marks the indication start at 14.46 in. (367 mm), the green S(m) measurement cursor marks the indication end at 15.24 in. (387 mm), and S(m-r), the delta between the two cursors, representing the flaw length at 0.780 in. (19.8 mm).

Figure 8-5: Example of slag indication length using maximum amplitude sizing technique



Courtesy of Kenneth Shane Walton-University of Ultrasonics

A variation of the Maximum Amplitude length sizing technique is shown in Figure 8-6. In this example, an ID HAZ crack is considered. The peak of the last tip at either end of the crack was used as the measuring point, as opposed to a dB drop.

**Figure 8-6: Example of ID HAZ crack indication length using maximum amplitude sizing technique**

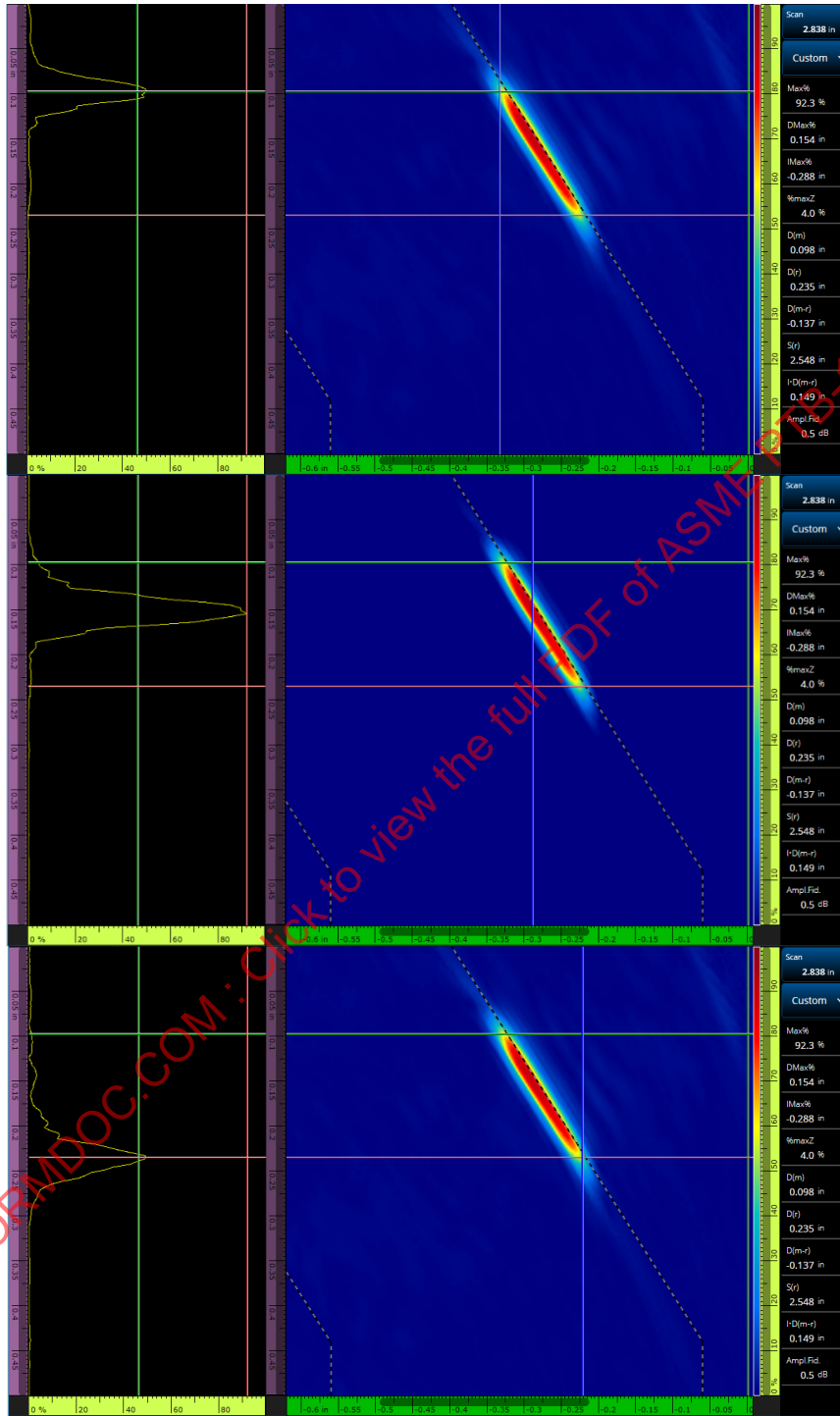
Courtesy of Kenneth Shane Walton-University of Ultrasonics

### 8.1.2 dB Drop Through-Wall Height Sizing of Embedded Flaws

Similar to length sizing, a dB drop technique can also be applied to assess the through-wall height of embedded flaws like sidewall LOF. The 6-dB drop method for through-wall height sizing of embedded defects is subject to errors due to aperture size vs. flaw size, frequency, amplitude, gain levels, etc. The 6-dB drop has a tendency to oversize flaws, especially small ones. Again, care should be taken to ensure the proper technique has been qualified on flaws with known dimensions. Small flaws have the tendency to be oversized due to beam divergence, so focusing at the flaw depth will often help mitigate this effect. Conventional PAUT could only be focused at one plane at a time, and often the technician is required to refocus at a flaw, with as many elements as possible to get optimum sizing with the smallest beam. FMC/TFM gives the benefit of being optimally focused at multiple places simultaneously, as long as it is within the capabilities of the array/wedge combination. So, with proper probe, wedge, and mode of propagation selection, sizing accuracy can be improved. An example of dB Drop Through-Wall Height Sizing of embedded sidewall LOF is shown in Figure 8-7. The green D(m) measurement cursor is placed at the top of the flaw, the red D(r) reference cursor is placed at the bottom of the flaw, and the reading D(m-r) shows the through wall height of 0.137 in. (3.5 mm) for the sidewall LOF.



Figure 8-7: Example of dB Drop Through-Wall Height Sizing technique

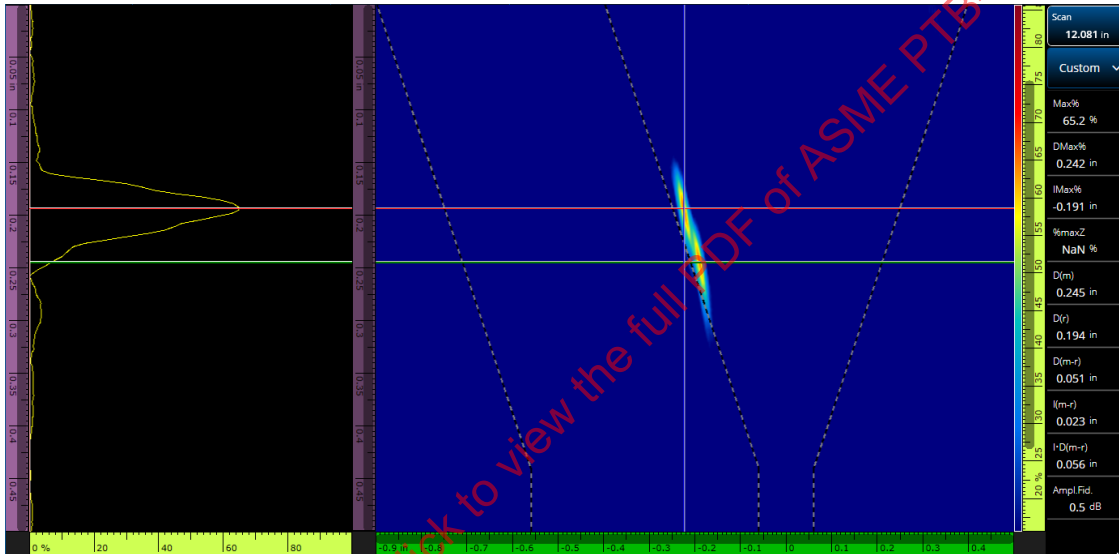


Courtesy of Kenneth Shane Walton-University of Ultrasonics

### 8.1.3 Tip Diffraction for Embedded Indications

Another method for sizing embedded flaws, such as sidewall LOF, is by using tip diffracted signals from the extremities. True diffraction occurs when waves pass a boundary and wrap around the edges of it, resulting in the signals we are familiar with in methods like TOFD. The tip diffraction that we see with pulse-echo UT usually results as a combination of true diffraction, reflection, and mode conversion. To generate tip-diffracted signals, we must impinge on the flaw at oblique, non-perpendicular angles. Diffraction typically generates signals with much lower amplitudes than the ones seen with the specular reflection that comes from perpendicular angles. An example of a sidewall LOF, with tip signals on the top and bottom is shown in Figure 8-8. The tip signals act as beacons, showing exactly where to take the measurements from, as opposed to relying on a dB drop. The through-wall height was measured to be approximately 0.051 in. (1.3 mm).

Figure 8-8: Through-Wall Height Sizing of LOF using Tip Diffraction technique

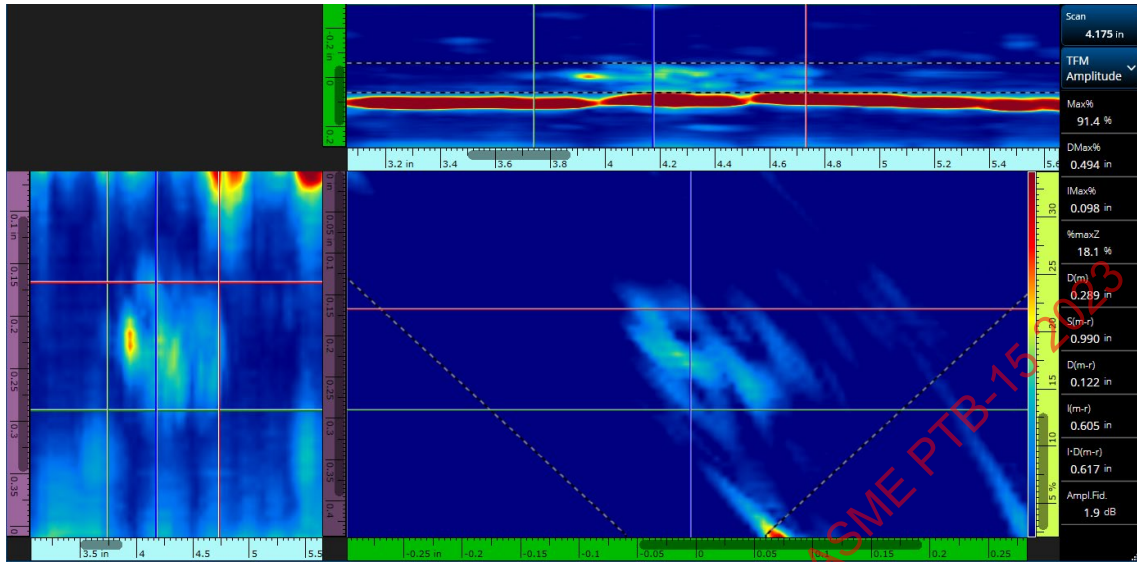


Courtesy of Kenneth Shane Walton-University of Ultrasonics

### 8.1.4 Sizing Cluster Indications Such as Porosity

On cluster porosity indications, the 6-dB drop is not always reliable, as amplitudes are typically very low and fluctuate rapidly along the indication. In Figure 8-9, the first and last discernible individual pores were used to find the flaw start, end, and length. For height, the upper and lower pores were used to find the top, bottom, and through-wall extent of the flaw. S(m-r) shows the flaw length at 0.990 in. (25.1 mm), and D(m-r) shows the through-wall height of 0.122 in. (3.0 mm).

**Figure 8-9: Through-Wall Height Sizing of Porosity cluster using Tip Diffraction technique**

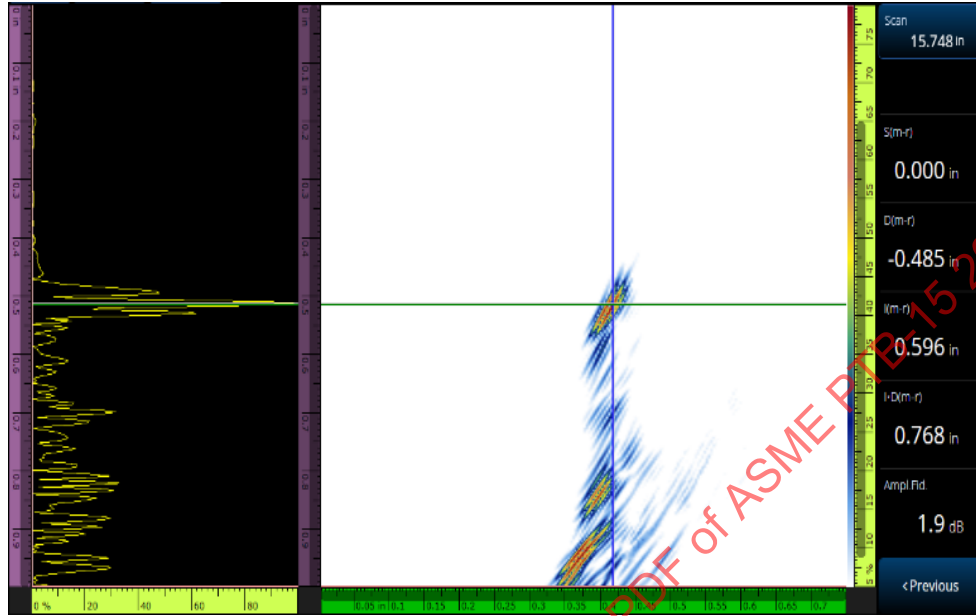


Courtesy of Kenneth Shane Walton-University of Ultrasonics

### 8.1.5 Tip Diffraction for Through-Wall Sizing of ID/OD-connected Cracks

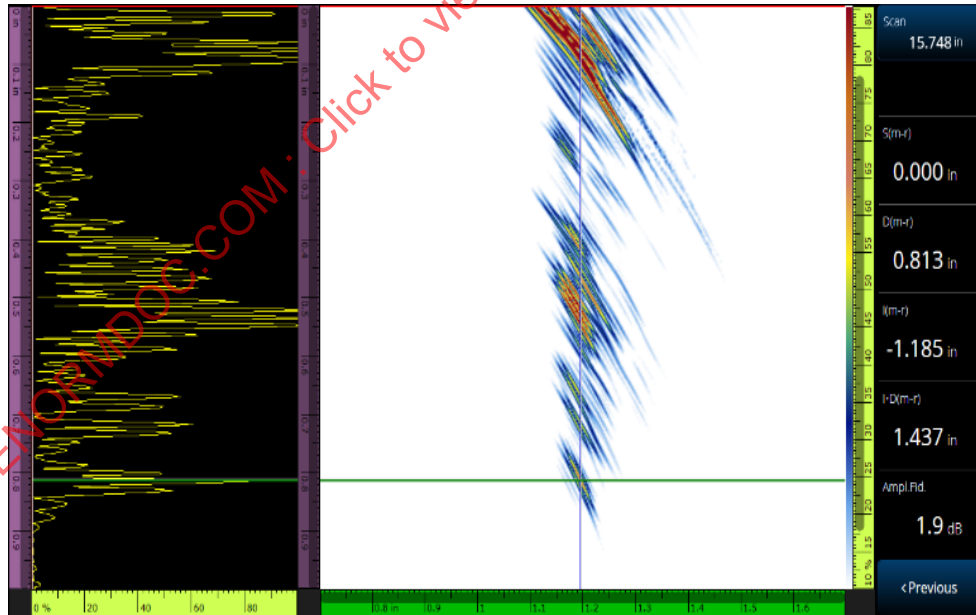
Early UT crack sizing methods employed a dB drop approach, which was not always reliable, as the crack tips provide much lower amplitude responses compared to the corner trap at the ID or OD surface. This led to the advent of TOFD and various tip-diffraction techniques using pulse-echo and dual element conventional UT transducers. With PAUT, tip-diffraction is typically the default method, and the same holds true with FMC/TFM. Figure 8-10 and Figure 8-11 show two crack examples. The first one is connected to the ID surface, and the second is connected to the OD surface of the sample. In both examples, the red reference cursor is placed on the depth that corresponds to the connection surface, and the green measurement cursor is placed in the deepest diffracted tip signal. The through-wall extents of the cracks are easily sized with this approach. The multitude of data views available with FMC/TFM often gives a macro or global view of the indication, allowing the examiner to see the flaw in its entirety.

**Figure 8-10: Through-Wall Height Sizing of cracks using Tip Diffraction technique: ID connected crack on 1 in. thick specimen. T-T image path. Red reference cursor on ID surface, green measurement cursor on deepest crack tip. D(m-r) reading of 0.485 in. shows through-wall height of crack.**



Courtesy of Kenneth Shane Walton-University of Ultrasonics

**Figure 8-11: Through-Wall Height Sizing of cracks using Tip Diffraction technique: OD connected crack on 1 in. thick specimen. TT-TT image path. Red reference cursor on OD surface, green measurement cursor on deepest crack tip. D(m-r) reading of 0.813 in. shows through-wall height of crack.**



Courtesy of Kenneth Shane Walton-University of Ultrasonics

**8.1.6 Length and Height Sizing Comparisons with Various Methods–TFM, TOFD, PAUT**

The sizing accuracy of TFM is comparable to the results obtained from more established UT methods such as PAUT and TOFD. Several one-inch thick carbon steel weld samples with 50/50 Double-V geometries (Figure 8-12) were scanned and the collected data was used for comparisons in the presented examples. The indications shown in the examples were in the bottom half of the weld zone. This ensured that the flaws were in the optimal focal zone of a TOFD setup with a PCS set to achieve a 2/3rd “T” focus, to eliminate the timing error and increase accuracy for that method. TOFD is often seen as a benchmark for through-wall sizing, so care was taken to optimize the results there. The TFM and PAUT techniques were also optimized in the region of interest.

**Figure 8-12: Weld Joint Geometry for 1 in. (25 mm) Samples**

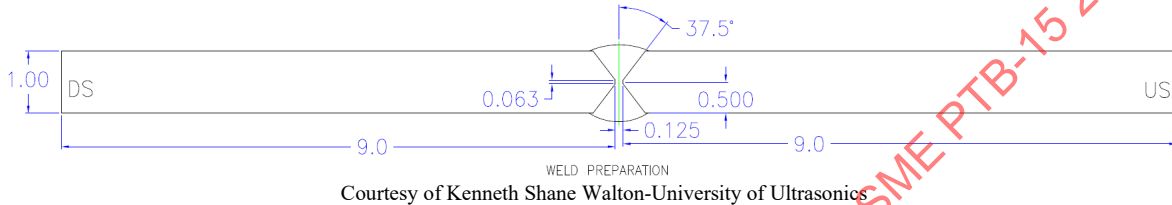


**Figure 8-13: Flaw Sample Manufacturer’s Record of Sizing Tolerances**

DEFECT TOLERANCES: LENGTH  $\pm 0.080''$   
 HEIGHT  $\pm 0.040''$  (SURFACE BREAKING)  
 $\pm 0.080''$  (MIDWALL)  
 TILT/SKEW  $\pm 5^\circ$   
 DIMENSIONAL TOLERANCES: .X $\pm 0.1''$ , X $\pm 0.020''$ , .XXX $\pm 0.005''$ , 0 $\pm 5^\circ$   
 (UNLESS OTHERWISE STATED)

Courtesy of Kenneth Shane Walton-University of Ultrasonics

**Table 8-1: A flaw sizing comparison between multiple methods**

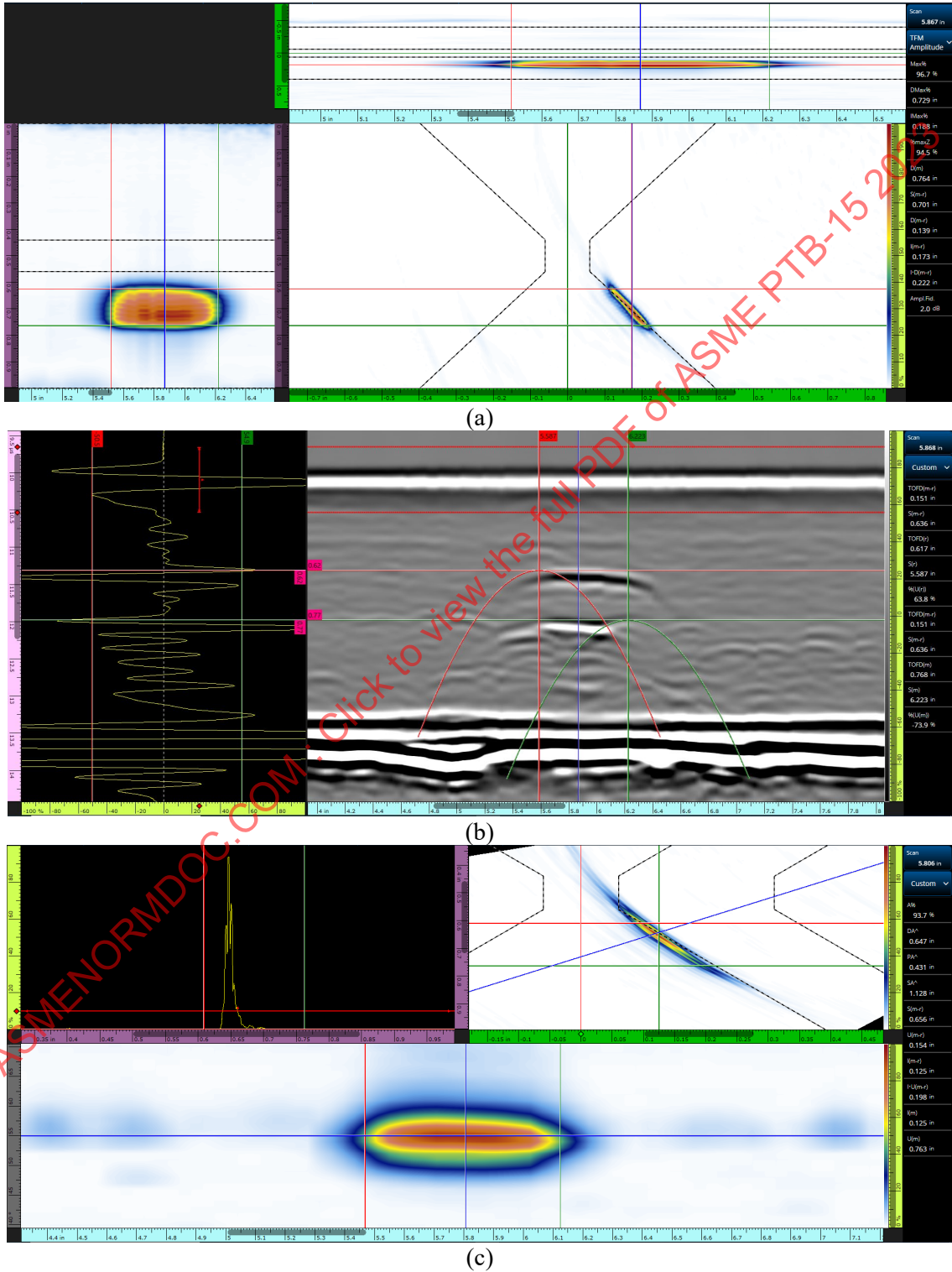
Flaw Length and Through-Wall Height Comparisons between TFM, PAUT, and TOFD				
Indication Description	1-DOF	2-ID Crack	3-Porosity	4-Slag
Documented Length	0.650 in.	0.825 in.	0.750 in.	0.650 in.
Documented Height	0.130 in.	0.260 in.	0.130 in.	0.100 in.
TFM Length	0.675 in.	0.837 in.	0.775 in.	0.649 in.
TFM Height	0.139 in.	0.281 in.	0.154 in.	0.082 in.
TOFD Length	0.636 in.	0.841 in.	0.764 in.	0.646 in.
TOFD Height	0.131 in.	0.260 in.	0.155 in.	0.089 in.
PAUT Length	0.656 in.	0.867 in.	0.783 in.	0.651 in.
PAUT Height	0.154 in.	0.281 in.	0.157 in.	0.093 in.

Courtesy of Kenneth Shane Walton-University of Ultrasonics



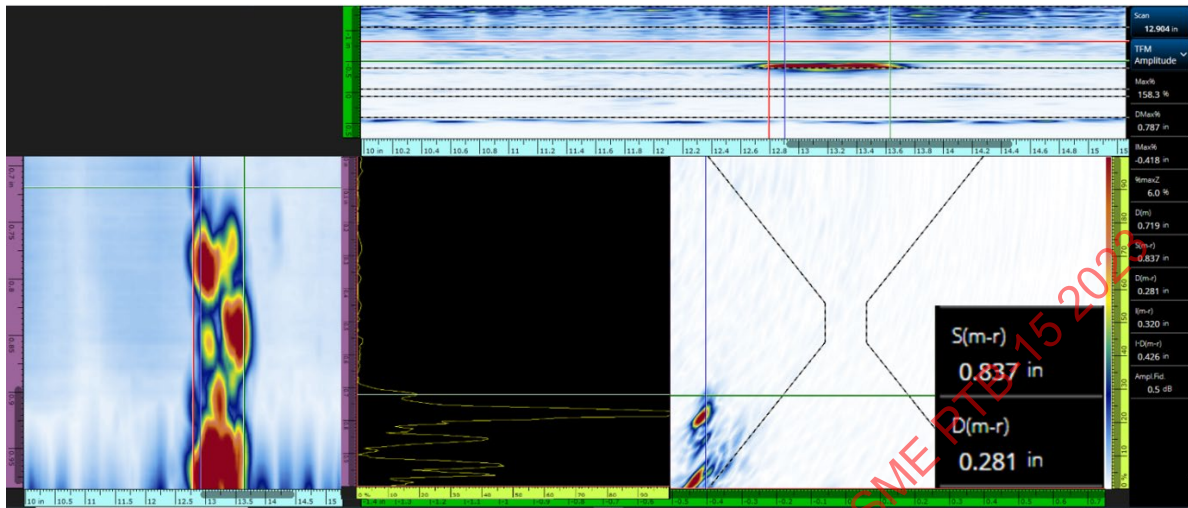
Figure 8-14, Figure 8-15, Figure 8-16, and Figure 8-17 show TFM, TOFD, and PAUT images of the scan data for each indication.

**Figure 8-14: Images of Indication # 1–Lack of Sidewall Fusion: (a) TFM–T-T mode, (b) TOFD Non-Parallel Scan, (c) PAUT Sectorial Scan**

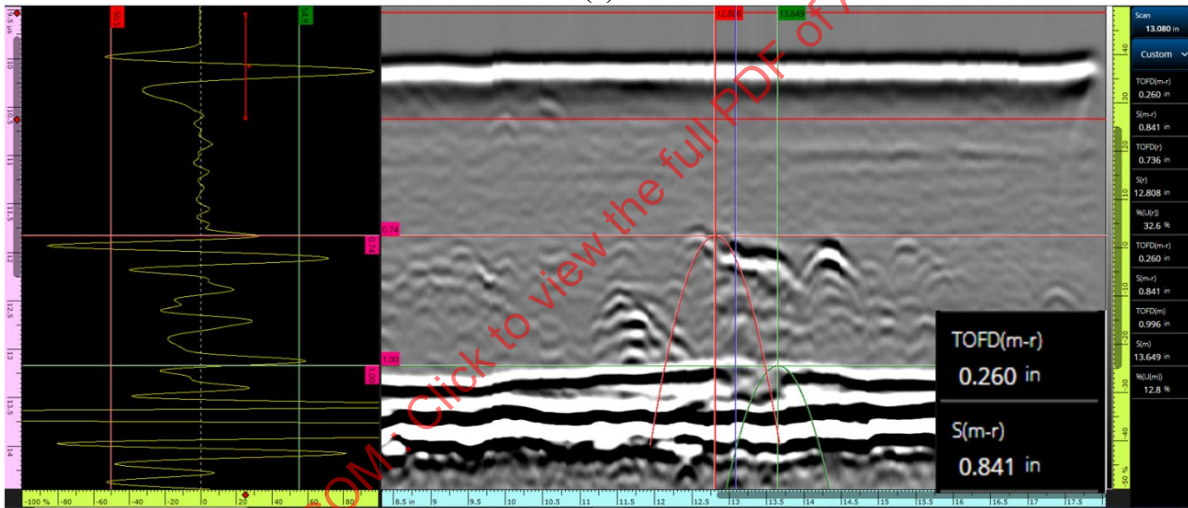


Courtesy of Kenneth Shane Walton-University of Ultrasonics

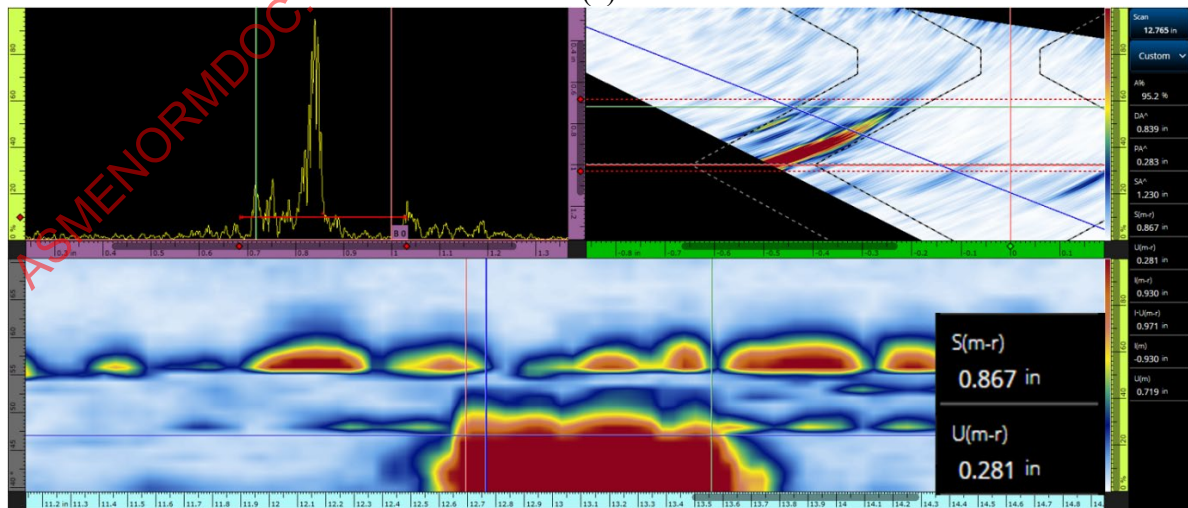
Figure 8-15: Images of Indication # 2-ID Crack: (a) TFM-T-T mode, (b) TOFD Non-Parallel Scan, (c) PAUT Sectorial Scan



(a)



(b)

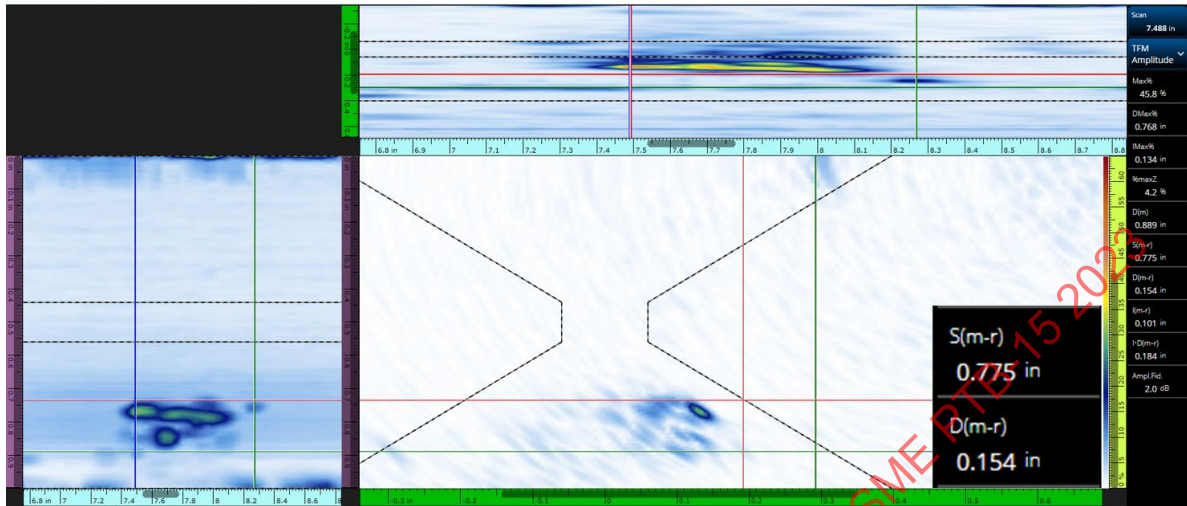


(c)

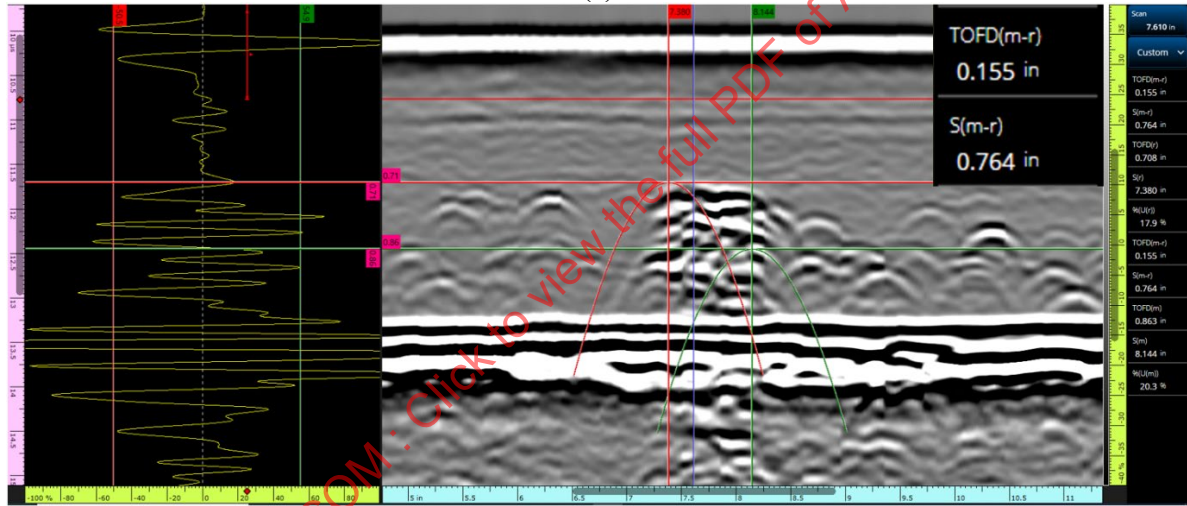
Courtesy of Kenneth Shane Walton-University of Ultrasonics



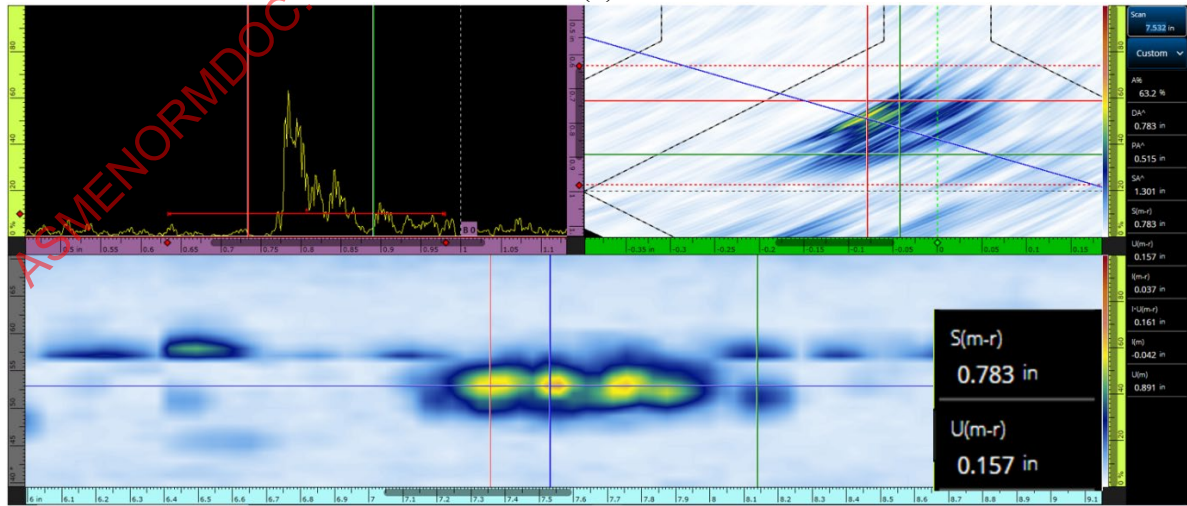
Figure 8-16: Images of Indication # 3 Porosity: (a) TFM T-T mode, (b) TOFD Non- Parallel Scan, (c) PAUT Sectorial Scan



(a)



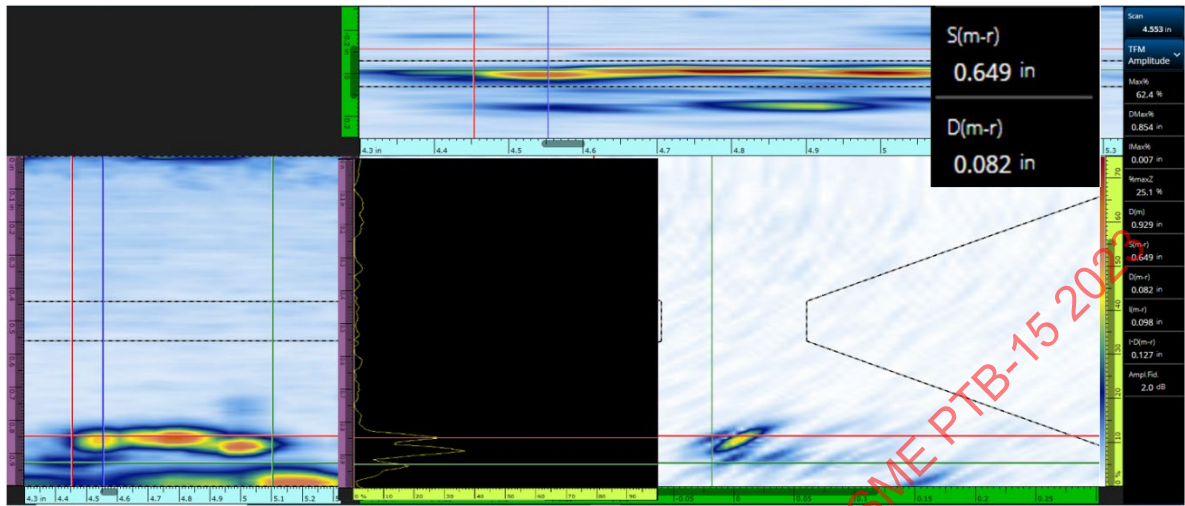
(b)



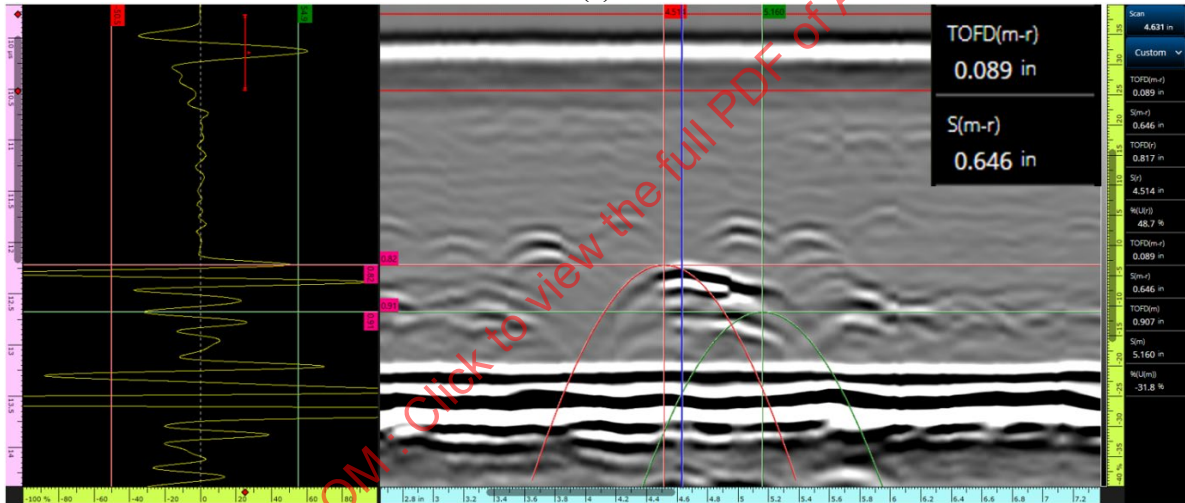
(c)

Courtesy of Kenneth Shane Walton-University of Ultrasonics

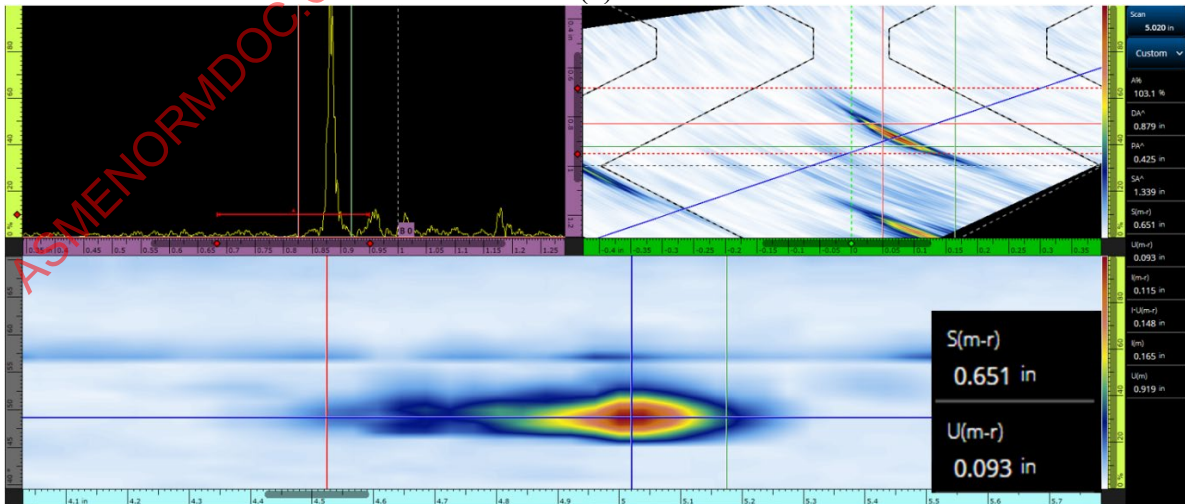
Figure 8-17: Images of Indication # 4 Slag: (a) TFM T-T mode, (b) TOFD Non-Parallel Scan, (c) PAUT Sectorial Scan



(a)



(b)

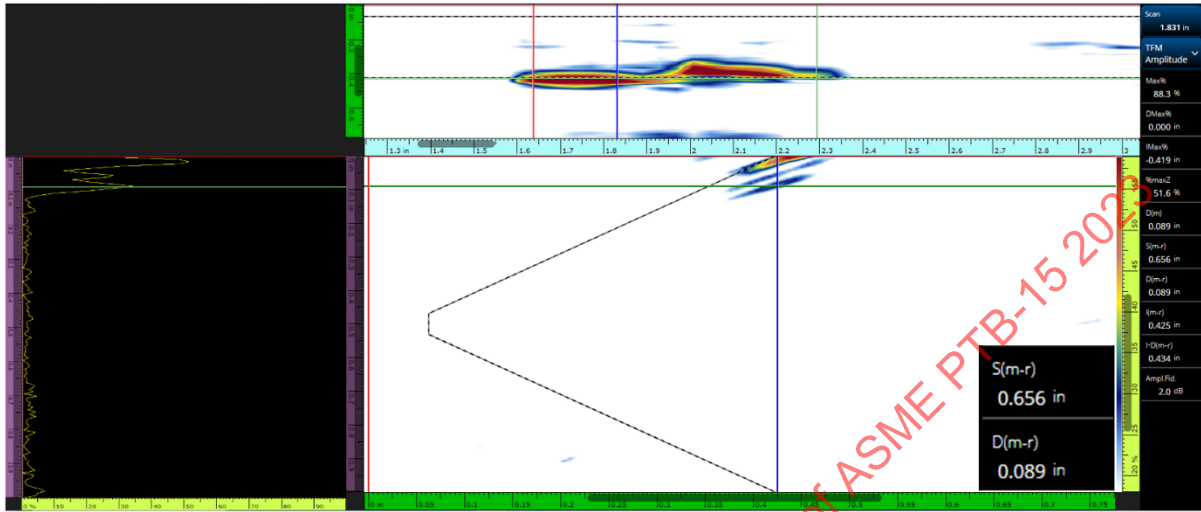


(c)

Courtesy of Kenneth Shane Walton-University of Ultrasonics

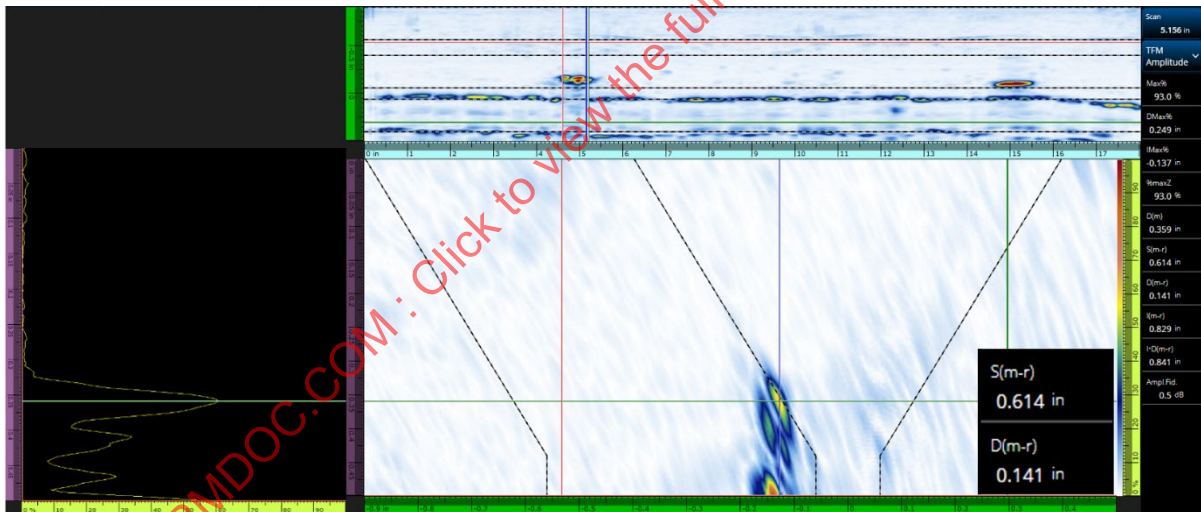
Additional TFM only sizing examples are shown in Figure 8-18, Figure 8-19, Figure 8-20, and Figure 8-21.

**Figure 8-18: TFM Images of OD-Connected Crack**



Courtesy of Kenneth Shane Walton-University of Ultrasonics

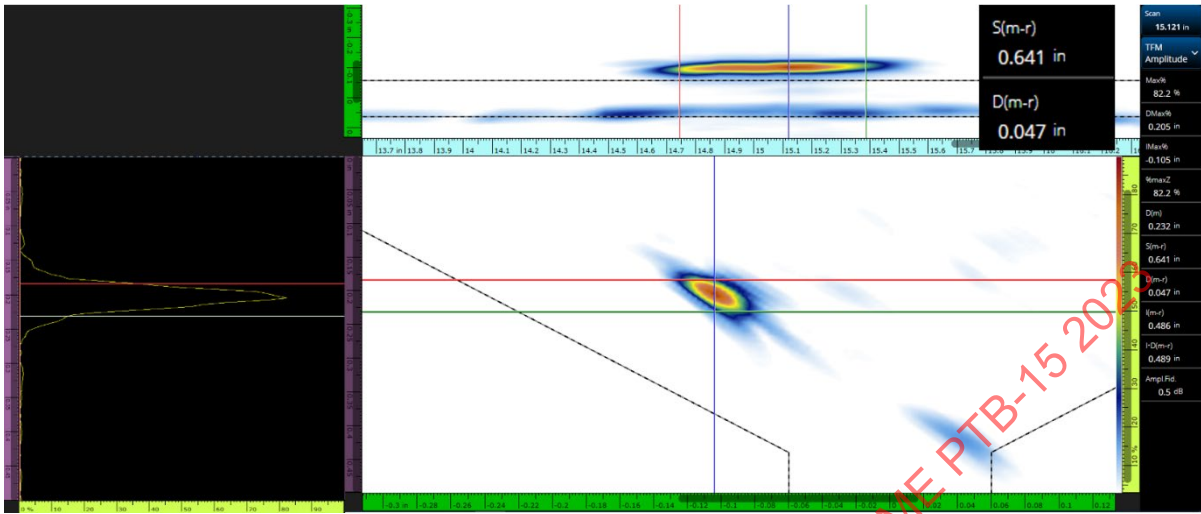
**Figure 8-19: TFM Images of ID-Connected Crack**



Courtesy of Kenneth Shane Walton-University of Ultrasonics

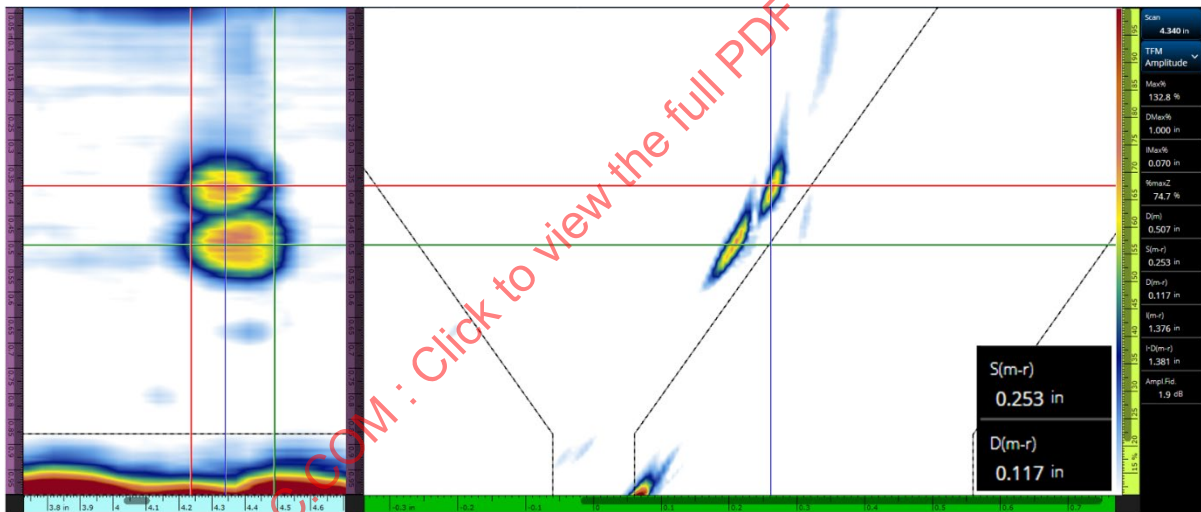


Figure 8-20: TFM Images of Slag



Courtesy of Kenneth Shane Walton-University of Ultrasonics

Figure 8-21: TFM Images of LOF-Far Side Bevel-Height Sizing using Tip Signals



Courtesy of Kenneth Shane Walton-University of Ultrasonics

## 9 FRACTURE MECHANICS FLAW CHARACTERIZATION

### 9.1 Introduction to Fracture Behavior

Knowing about the strength and load-carrying capability limits is essential for engineering structures, and in particular, pressure vessels and piping components. The strength of a material is normally associated with the point (or stress) at which the material no longer behaves in an elastic (or linear) manner, and the ultimate strength is that stress which causes failure. However, actual failure or fracture of a component can occur at stresses much lower than those strength values, depending on how much toughness or ductility the material exhibits before actual separation. The difference between a brittle (low toughness) material and a ductile (high toughness) material can be seen from the plot of tensile testing for load vs. displacement for two materials shown in Figure 9-1.

**Figure 9-1: Load vs. Displacement from Testing of a Brittle and Ductile Material**

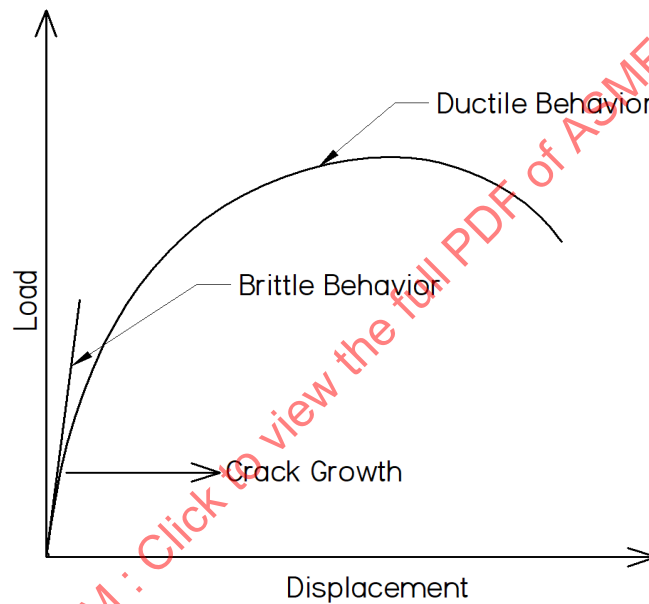


Image Courtesy of Sinewave Solutions

The actual point of fracture can either occur in a catastrophic brittle manner or after large amounts of ductile deformation and tearing, which would absorb much of the energy. Recognizing the difference and understanding the parameters that can cause the various types of failure, and building in safety margins to prevent such failures, is the task of the design engineers. Fracture mechanics is the means by which materials engineers can avoid the potential problems of unanticipated fracture by understanding the interrelationship between the applied loading of a structure, the environment (including temperature and potential chemically aggressive media), the presence of cracks (or crack-like defects), and the inherent material properties. The ASME Code has incorporated the standards and methods using the fracture mechanics tools and engineering practices to manage and avoid the failures or conditions leading to early retirement of these structures.

## 9.2 Overview of Fracture Mechanics

Fracture mechanics (FM) is an engineering discipline that answers the question: Is the material’s resistance to failure in the presence of a sharp crack greater than the stress-strain being applied by loading? Besides being used in design work, FM is applied in the analyses to predict and disposition the margin against failure of a component containing a flaw. Since flaws in a component can lead to premature failure or fracture, non-destructive examination (NDE) is used as a means to identify and characterize the presence of any flaws that could become critical and is a critical tool for the overall understanding and managing the structural integrity of the components. The methodology that is applied goes beyond the scope of this chapter. However, for the purpose of this chapter, it is important to realize that the presence of a flaw amplifies the stress to the material in its vicinity, and that could significantly reduce the load-carrying capability of the component.

Fracture mechanics considers the effects the flaw (i.e., cracks, or crack-like defects) has on the integrity of the component. The major premise for FM is that crack behavior in a structure can be predicted when the effect of several factors is known. Thus, establishing relationships between the different engineering criteria (e.g., materials, stresses and loading, operating requirements, flaws and their detectability) is the purpose for using the fracture mechanics method. The main objective of FM is the prevention of component failure, but it can also be applied to tailoring a complete component design, including NDE requirements.

There are typically two different approaches to the design and analysis of a component. The first being the traditional approach, which is the “strength of materials” concept. Basically, the engineer decides what the service life will be and builds according to that. Overbuilds would be more correct. ASME typically overbuilds components by 3.5 times what is needed, and sometimes more. This is a safety margin. With this approach to component design, failure will occur when the applied stresses exceed the material strength.

**Table 9-1: Strength of Materials vs Fracture Mechanics Method**

Strength of materials method	$\text{Stress} > \text{Material strength} = \text{Failure}$
Fracture Mechanics method	$\text{Stress} + \text{crack geometry} > \text{Material Fracture Toughness} = \text{Failure}$

Courtesy of Timothy Griesbach

The second method is the FM approach. The FM method recognizes that the presence of a crack (or defect) can reduce the load-carrying capability of a structure, and the target of a FM analysis is to examine the effects of the stresses and the material properties on the crack tip and is often depicted as a triangle as seen here:

**Figure 9-2: The Three Elements Related to Component Fracture**

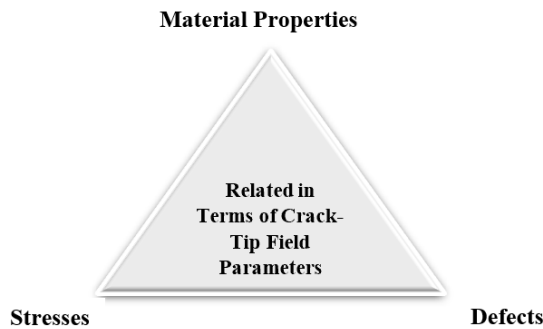


Image Courtesy of Sinewave Solutions

There are three outcomes that can typically happen that are dependent on many combinations of variables:

1. The flaw can grow, or a significant event may occur, resulting in failure of the component,
2. Depending on the stress level applied to the component, the flaw may mitigate itself, and stabilize or remain in a benign condition, or
3. The component is repaired or is to be retired or replaced in time so that the predicted useful life will outlive the flaw growth.

Therefore, monitoring the condition of a component or structure, and determining the margin and remaining component life, is a constant task defined by the procedures in the ASME Code and regulations that govern the safe and continued operation of the component. Fracture mechanics is just a tool to be used to perform these evaluations, but the knowledge of the design limits (stresses and cycles), material properties, environment and the presence or absence of flaws and defects relies on the inputs provided from other sources. Certainly, one of the key inputs to the FM analysis is the identification of the size (i.e., length), location, and depth of any flaws that may exist. Pre-service inspections should have eliminated any flaws or defects prior to going into operation, but flaws may initiate and propagate while in-service, and for this reason continued in-service inspection may be performed to detect such flaws. In addition, the material properties (including strength and toughness) could change because of aging effects, making the component more susceptible to one or more types of early failure.

It is important to note that FM is NOT what the UT technician does. NDE is “flaw characterization”. The technician locates and sizes flaws then applies the results to the accept/reject criteria within the various ASME tables. The tables themselves were derived using FM. The fracture mechanics evaluation occurs after a flaw has been detected and characterized following the UT examination.

### 9.3 History of Fracture Mechanics

The investigation into fracture behavior of large engineering structures began sometime after the first world war. Not much progress had been made until the second world war when approximately 25 percent of the all-welded U.S. Liberty ships experienced brittle fracture (as shown in Figure 9-3), especially during cold weather. A major inadequacy in the conventional design process became apparent: unstable fracture can occur at stress levels well below the design (elastic) limit when certain conditions exist (e.g., low service temperature and weld defects).

**Figure 9-3: Catastrophic Failure of a Liberty Ship During World War 2**

The image below shows the SS Schenectady tanker, one of the World War II Liberty Ships and one of the most iconic fracture failures. The Liberty ships all had a tendency to crack during cold weather and rough seas, and multiple ships were lost. Approximately half of the cracks initiated at the corners of the square hatch covers which acted as stress risers. The SS Schenectady split in two while sitting at dock. An understanding of fracture mechanics would have prevented these losses.



Image Source: [Wikimedia Commons](#)

Eventually, researchers at the Naval Research Laboratory developed materials tests and a general understanding of the principles of fracture-safe design. It became apparent that the ferritic steels being used would undergo a ductile-to-brittle transition behavior with decreasing temperature. This behavior could be measured as a material characteristic or parameter called the nil-ductility transition temperature, or NDT, as shown in the fracture analysis diagram (FAD) in Figure 9-4. [32]

Figure 9-4: Pellini's Fracture Analysis Diagram (FAD)

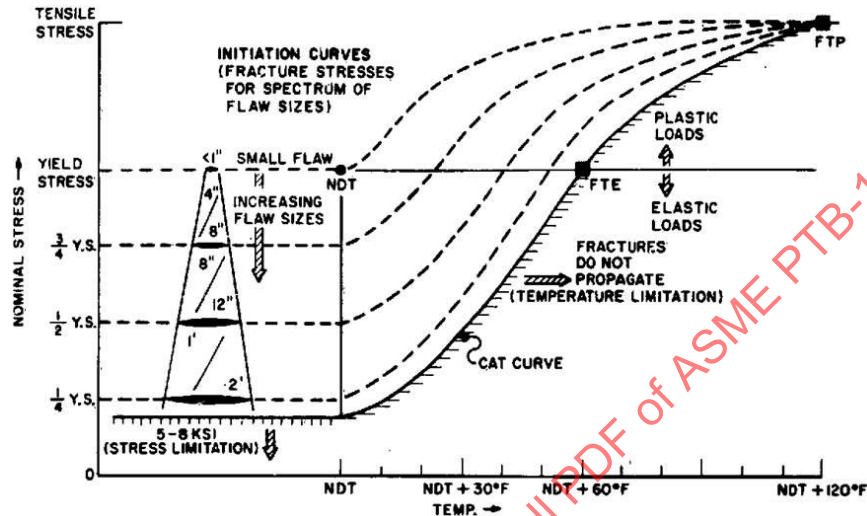


Image from the Naval Research Laboratory Report AD0402089 (report is in the public domain – Fig. 9)

The FAD relates operating stress to service temperature and to flaw sizes required for failure. It is indexed to the NDT temperature, defined as the highest temperature at which the material behaves in a predominantly brittle manner. The diagram further includes the Fracture Transition Elastic (FTE) point, defined as the upper limit for elastic fracture under yield stress levels for small flaws in relatively small thicknesses (e.g., 1-2 in.), and the Fracture Transition Plastic (FTP) which relates to failure after plastic overloading. At temperatures higher than the FTP, fracture can only occur by ductile tearing. Finally, the bounding Crack Arrest Temperature (CAT) defines the region that provides a conservative method for fracture-safe design based on dynamic crack arrest principles. Before the fracture mechanics concepts were fully developed, the FAD curve was used for fracture-proof design such as for small thickness components (e.g., 1-2 in.) the operating temperature should remain above  $NDT + 60^{\circ}F$ , and for larger thickness components (e.g., 6-12 in.) the operating temperature should remain above  $NDT + 120^{\circ}F$ . This was done to ensure that the component material properties remained ductile. It is important for the engineer to understand, from the FAD diagram, the relationship between temperature, flaw size, and component thickness to maintain a suitable safety margin for protection against failure.

#### 9.4 Two Main Categories of Fracture Mechanics

There are two main categories of FM: Linear Elastic Fracture Mechanics (LEFM) and Elastic Plastic Fracture Mechanics (EPFM). Linear Elastic Fracture Mechanics (LEFM) is the older and more highly developed of the two. LEFM considers the area immediately surrounding the crack tip as a very small area of plasticity (see Figure 9-5). EPFM is very similar to LEFM but uses a different parameter to characterize the stress-strain intensity at the region of the crack tip and can calculate a much larger area of plasticity at the crack tip. These two methods will be discussed in the following section.



**Figure 9-5: The Two Types of Fracture Mechanics Methods**

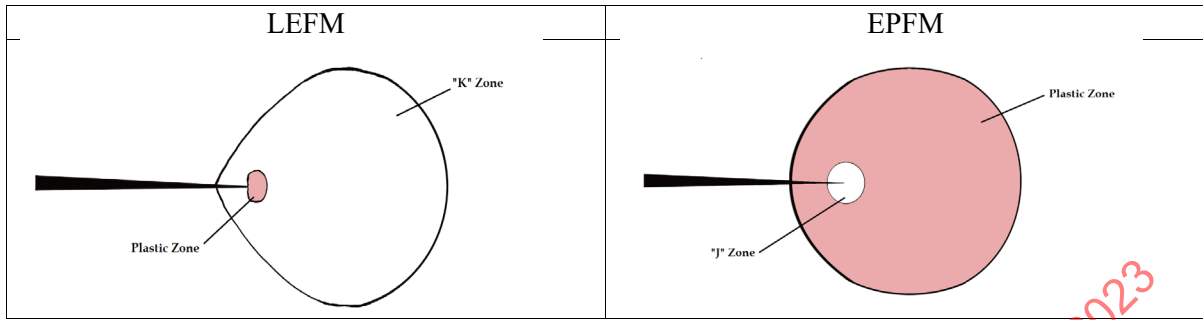


Image Courtesy of Sinewave Solutions

LEFM is used when material behavior is expected to be brittle. This includes items with heavy sections of high yield strength material, such as plates in reactor pressure vessels (RPVs). There are several variables that influence LEFM, some of which are: more brittle materials, low operating temperatures, component wall thickness (heavy), constraint on the structure, high rates of loading, etc. These are all conducive to generating a brittle fracture, but most importantly, with very little plastic deformation occurring.

LEFM is based on elastic analysis of the stresses in a relatively brittle structure that contains a sharp crack. The crack is expected to behave in a predictable manner until the applied loads exceed a certain calculated stress intensity value. The combination of the influencing factors is known as the crack driving force(s) and is denoted as “K”. Given a known crack size and component geometry, if a nominal load is continually increased, affecting the crack tip region, it will reach a critical level where the materials fracture resistance is exceeded. The crack will destabilize, and rapid fracture will occur. This critical value of “K” is termed “K<sub>1c</sub>”. When the stress intensity exceeds the calculated limiting value, the crack exhibits unpredictable growth, and a brittle failure of the structure occurs. For example, consider a glass rod and the way it would snap if it was bent too far. This is a brittle fracture. The intensity of the stress field in the area around the crack tip, or crack tip stress intensity factor, is usually based on a “Mode 1” (see Figure 9-6) method of cracking.

**Figure 9-6: The Three Modes of Cracking**

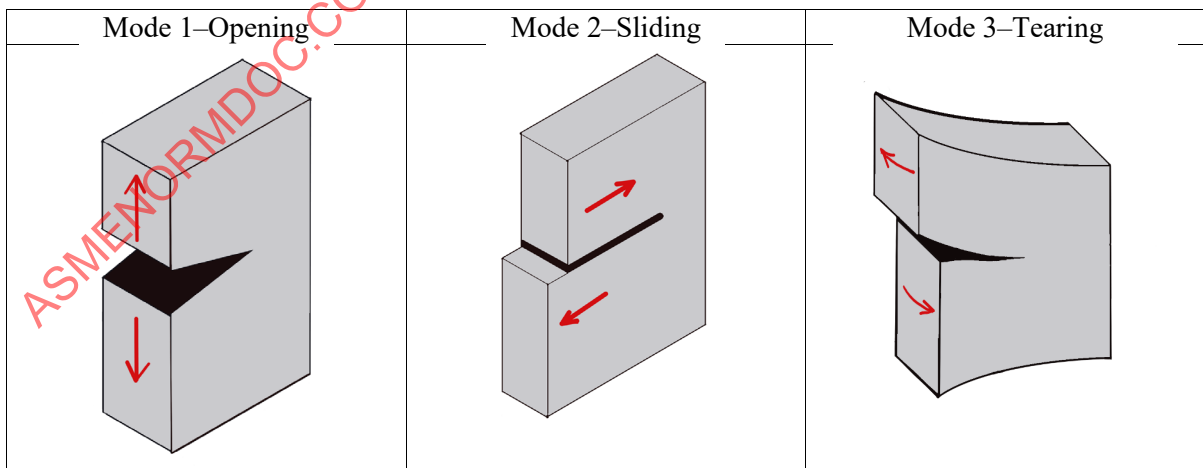


Image Courtesy of Sinewave Solutions

Elastic Plastic Fracture Mechanics (EPFM), which is very similar to LEFM, but uses a different parameter to characterize the stress-strain intensity at the region of the crack tip. This method can calculate a much larger area of plasticity at the crack tip. One limitation for LEFM that led to development of EPFM is the fact that austenitic stainless steels are much too tough of a material to apply the LEFM (i.e., brittle fracture) techniques. EPFM allows for calculations of margins against failure to apply to a wider range of materials, higher operating temperatures, essentially a more ductile fracture environment. This method has developed relatively rapidly and is gaining more and more acceptance in the engineering community.

EPFM analyses performed in the United States are based on the “J-Integral” concept. The basic difference between the J-Integral and the K used previously is that the J considers the intensity of the elastic-plastic stress field surrounding the crack tip, while K is purely elastic. EPFM’s major advantage is the ability to work under plastic loading and more ductile fracture conditions to assess safety margins. For example, consider breaking a clay bar. It will deform before it breaks, which is ductile fracture. This is applicable to thin sections of tough material, such as austenitic piping components or ferritic steel materials operating at high temperatures.

In EPFM there are four basic stages to crack growth.

1. At the first stage of ductile fracture, the crack tip is blunted because of loads on the crack.
2. Stresses reach some critical level of J and the crack begins to extend through the material thickness. This is expressed as “JIC”.
3. There is stable crack growth along a curve known as the J-R curve.
4. At a maximum load point the material ruptures by a rapid ductile tearing.

It should be noted that there is a third method of fracture mechanics: High Temperature Time Dependent Fracture Mechanics (HTTDFM). This more recent category uses a model that considers the whole cross section of a component to be fully under plastic loading conditions and applies itself to a more “creep” type of scenario where the stresses occur typically below the elastic limit. Such scenarios usually consist of statically loaded structures and at greater than half the melting point.

#### 9.4.1 Summary

Whether LEFM or EPFM methods are used, the intent of the analysis is to determine the crack driving conditions affecting the structure and the material’s response to those conditions. There is no known method of FM analysis that covers all possible material/ flaw conditions. Some LEFM concepts are applicable to EPFM and vice versa. The engineer performing the analysis is expected to use whatever works best for the conditions being analyzed.

It is important to remember that LEFM and EPFM are intended for different situations, and both have limitations. Fortunately, most relevant calculations have already been done and are available in the form of the ASME tables for acceptance criteria.

### 9.5 Application of Fracture Mechanics

The main objectives when using FM as a tool are to answer these basic questions:

What is the residual strength of the material for the expected loading environment (e.g., temperature, pressure and strain rate) as a function of crack size?

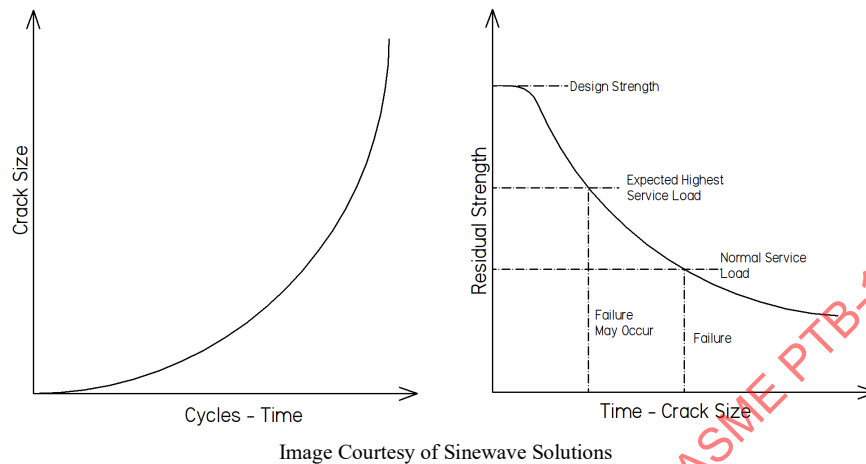
What is the critical crack size that could cause failure, and what is the “Margin”?

How long does it take a crack to grow from a certain initial crack size to the critical crack size?

The answer to these questions will determine whether the component can be returned to service, repaired, or replaced. If the margin against failure is sufficient for continued operation, a new inspection interval may be determined to assure no premature failure.

The relationship between crack size and residual strength, or determination of the time to failure if crack growth occurs, is the purpose for performing a FM analysis, as shown in Figure 9-7.

**Figure 9-7: Illustration of Analysis of Flaws as a Function of Time**



### 9.5.1 Damage Tolerant Design

Damage tolerant design, or safety by inspection, was developed as a design philosophy in the 1970s as an improvement on the fail-safe principle for structural components in the aerospace industry. A key element is the development of a comprehensive program of inspections to detect cracks before they can affect flight safety. Since its inception it has been applied successfully in many fields to manage the extension of cracks in structure through the application of the principles of fracture mechanics. An engineering structure is considered to be damage tolerant if a maintenance program has been implemented that will result in the detection and repair of accidental damage, corrosion, and fatigue cracking before such damage reduces the residual strength of the structure below an acceptable limit. In cases where a failure could be catastrophic, the principles have been adopted and codified in the ASME Code, the API Code, in military specifications, or in regulations intended to protect the public health and safety.

In ensuring the continued safe operation of the damage tolerant structure, inspection schedules are devised. This schedule is based on many criteria, including:

- Assumed initial condition of the structure (i.e., size and number of initial defects),
- Stresses in the structure (including cyclic stresses) that cause crack growth from the initial condition
- The geometry of the structure that intensifies or reduces the stresses on the crack tip,
- the ability of the material to withstand cracking due to stresses in the expected environment (i.e., strength and toughness),
- The largest crack size that the structure can endure before catastrophic failure,
- The likelihood that a particular inspection method will reveal (or miss) a crack,
- The criteria or acceptable level of risk for determining when a structure will fail.

These factors affect how long the structure may operate normally in the damaged condition before one or more inspection intervals has the opportunity to discover the damaged state and effect a repair. The interval between inspections must be selected with a certain minimum safety margin, and also must balance the expense of the inspections, the weight penalty of lowering fatigue stresses, and the opportunity costs associated with a structure being out of service for maintenance.

Therefore, damage tolerant design relies on the results of inspections and the application of fracture mechanics in the stepwise process shown in Figure 9-8.

**Figure 9-8: Stepwise process for Damage Tolerant Design**

1. Determine the size of initial defects  $a_0$ , NDI
2. Calculate the critical crack size  $a_c$  at which failure would occur  $\sigma\sqrt{\pi a_c} = K_{Ic}$
3. Integrate the fatigue crack growth equations to compute the number of load cycles for the crack to grow from initial size to the critical size

$$N = N_0 + \int_{a_0}^{a_c} \frac{da}{C(\Delta\sigma\sqrt{\pi a})^m}$$

4. Set inspection intervals

Image Courtesy of Sinewave Solutions

Once these fundamental principles have been established for the specific application, then the role of the inspector is to provide the necessary definition about the initial condition including sizes, location, and number of initial flaws or defects in the component. At every required inspection interval and after the inspection is performed, the process is repeated to establish whether the component is sound or how soon a repeat inspection is required.

When planning and preparing for an inspection of a system or component, it is important to recognize and consider the many possibilities that may arise. In the event that one or more indications are detected, what steps will be required to evaluate the indications in order to determine acceptability or unacceptability for the intended future operability?

### 9.5.2 Planning for Inspection Using These Damage Tolerance Principles

This section lists typical steps to be followed before, during, and after an inspection. If and when a fracture mechanics evaluation is required, the inspector and the inspection team are essential to achieving a successful disposition considering all the necessary information, such as:

1. What is the component and location(s) to be inspected?
2. Are these inspections required to meet specific ASME Code, licensing, or regulatory requirements? If Yes, follow the Code requirements. For example:
  - IWB-2000–Examination and Inspection
    - What are the Inspections
    - What is the Inspection Program
    - What is the Examination Categories
  - This Program defines the required inspections, inspection methods, examination volumes, acceptance standards and frequency of inspections
  - Assuming there are no “Unacceptable” indications, the reported results from the inspection will be used to justify continued operation for X number of remaining life years, or until the next planned inspection.

If the answer is No, then why are the inspections being performed? Is the inspection part of a preventive maintenance activity, or is there some other reason? Early detection and repair can avoid more serious problems later, but it is prudent to know what to look for and then to Be Prepared.

For all inspections, the planners must consider, what is the potential outcome if the results are “Acceptable” or “Unacceptable”?

3. What are the known (or suspected) degradation and failure mechanisms?
  - Excessive deformation (broken or missing parts?)
  - Ductile rupture
  - Crack initiation
    - Fatigue cracking
    - Stress corrosion cracking
  - Buckling
  - Erosion/Corrosion (e.g., surface pitting or loss of material)
  - Other types of cracks or defects
    - Weld defects
    - Fabrication flaws
    - Porosity (or voids) in castings or hydrogen flaking in forgings
    - Stringers or laminations in plate materials
4. Identify the appropriate inspection techniques, qualifications and reporting requirements. Are the inspection techniques properly calibrated to detect and size any relevant indications?
5. Prior to performing an ASME Code examination, the inspectors, the procedure, and the equipment must be qualified in accordance with the appropriate personnel qualification standards. For example:
  - ASME BPVC Section XI, Mandatory Appendix VII—Qualification of Nondestructive Examination Personnel for Ultrasonic Examination
  - ASME BPVC Section XI, Mandatory Appendix VIII—Performance Demonstration for Ultrasonic Examination Systems

Question: What is a relevant indication? Can you identify the acceptable/unacceptable condition?

For example, in many industries of high-volume, high-quality components, visual inspection is the primary QA test for acceptance (e.g., manufacturing, automotive parts, aerospace components, electronic circuits, casting foundries, etc.). The training of inspectors for these industries is to make sure they can identify and reject defective parts. In this case, the visual observation of a relevant indication is by definition an unacceptable condition (e.g., cracking at the leading edge of a jet turbine blade). The inspectors in these specific fields are trained to make that determination to accept or reject the part.

In the inspection of nuclear components, visual inspection is not the primary NDE technique because UT and other methods (e.g., FMC/TFM) may be used to characterize any relevant indications or relevant flaws that are detected before the final determination of acceptance or rejection. An indication detected during this examination is not automatically rejectable because, according to the ASME Code, an additional supplemental exam, corrective action, evaluation, or repair must be performed before the component is returned to service. In the inspection of safety-grade components (e.g., pressure vessels and piping), the inspector/technician is not qualified to make the determination whether an indication is acceptable or unacceptable. The inspector/technician is only responsible for performing the examination, detecting any relevant indications or flaws, accurately sizing those indications, and reporting the results of those exams.

If the size (i.e., depth and length) of planar flaws detected exceeds the Code allowables, then the inspection results will be used in an evaluation to determine continued operation for Y number of years (if justified by a Fracture Mechanics Analysis), or else the component must be repaired or replaced, or the plant component (or system) may be retired. If this is a new component, the defects may be the cause for rejection.



Here is a real-life case for consideration:

During the 10-year ISI examinations of the Doel 3 reactor pressure vessel and the Tihange 2 vessel in Belgium in 2012, the UT inspections showed 8,149 indications in Doel 3 and 2,035 indications in the Tihange 2 vessel.

What is the cause of these flaw indications?

Were they there from the beginning?

Is there any evolution in the size/number of these flaws?

How do these flaws influence the integrity of the pressure vessel?

Can the owner demonstrate the integrity of the vessel for continued operation?

What is the role of the inspection team in resolving these issues?

---

---

## 9.6 ASME Code Margins and Safety

The ASME BPVC Section VIII and Section III specifies safety margins for peak stresses during normal and accident conditions, and maximum number of cyclic stresses to prevent fatigue failures. All combinations of stresses (pressure, thermal, mechanical, etc.) are evaluated for the design conditions and life (years or expected cycle) for each component.

The Code provides standards and requirements to prevent against brittle (catastrophic) failure (such as standards for material selection).

The Code defines design stress limits with safety margins to prevent against overload.

The Code provides safety margins to prevent against ductile failure.

- Safety Factor = 3 for Level A (Normal) Conditions
- Safety Factor = 2.7 for Level B (Upset) Conditions
- Safety Factor = 2 for Level C (Emergency) Conditions
- Safety Factor = 1.4 for Level D (Faulted) Conditions

The Code defines safety margins (i.e., number of cycles) to prevent fatigue initiation.

Preservice and inservice inspections are performed to assure that safety margins are maintained. From a design perspective, no flaws or crack-like indications are permitted in new (or replacement) components.

Cracks that exceed a critical defect size will reduce the margin of safety and could lead to premature failure of the component. Fracture Mechanics is used to connect the relationship between strength of materials, loads or stresses, and the presence of flaws (or defects).

## 9.7 Flaw Evaluation Procedures Using Fracture Mechanics

The ASME BPVC Section XI provides procedures and rules to determine whether a component containing flaws is acceptable for continued operation.

ASME Code Philosophy:

1. Evaluate detected flaws against preservice inspection standards (Level 1).
  - a. IWB-3500
2. If IWB-3500 flaw acceptance limits are exceeded, evaluate detected flaws using Flaw Evaluation Procedures (Level 2) to show that:
  - a. ASME Code Margins are maintained considering crack propagation and it can be demonstrated that there is no brittle fracture using IWB-3600 standards and
    - i. There is a margin of 3.0 on stress for normal operation.
    - ii. There is a margin of 1.4 on stress for faulted conditions.

- iii. Cracks are acceptable if there is a factor of 10 on crack size for normal conditions.
- iv. Cracks are acceptable if there is a factor of 2 on crack size for faulted conditions.
- b. Cracks are acceptable for continued operation for a specific period of time, or until the next inspection is performed.

At this point it is important to determine to ask the question, “Run, Repair, or Replace?”

- 3. If the Level 2 procedures for acceptance are not successful, additional Fracture Mechanics analyses can be performed using Elastic-Plastic Fracture Mechanics (Level 3).
  - A detected flaw may be shown to be acceptable for a finite period of time considering depth and length of crack growth and the margins against ductile rupture to assure ASME Code margins.

Given the time and effort needed to perform a Level 2 or Level 3 analysis, the utility may decide whether it is more cost-effective (and timely) to perform the analyses or else repair or replace the component.

The outcome (and the ultimate decision) is highly dependent on the accuracy and reliability of the NDE results.

### 9.7.1 Steps in the ASME BPVC Section XI Flaw Evaluation Procedure

Figure 9-9 and Figure 9-10 describe the sequence of events which may lead to the need for a fracture mechanics evaluation of a flaw indicated during in-service inspection. Figure 9-9 indicates the general sequence of events, starting with the inspection program and ending with a flaw which may or may not satisfy the evaluation standards. If all detected flaws satisfy these standards, no additional evaluation is required. Unfortunately, experience has shown that flaws larger than those permitted in the standards may exist. When this happens, additional actions must be taken to disposition the flaw by one of these methods:

The flaw must be removed to the extent required to satisfy the acceptance standards, but without reduction in structural adequacy of the component (i.e., safety margin),

The flaw must be removed and repaired, as by a weld repair,

Evaluation of the flaw must be performed to confirm the structural adequacy for continued service, or

The component must be replaced.

Figure 9-10 describes the sequence in more detail for the evaluation of the flaw and indicates the possibility that such an evaluation will not be successful, in which case repair or replacement would be required.

Figure 9-9: ISI Sequence

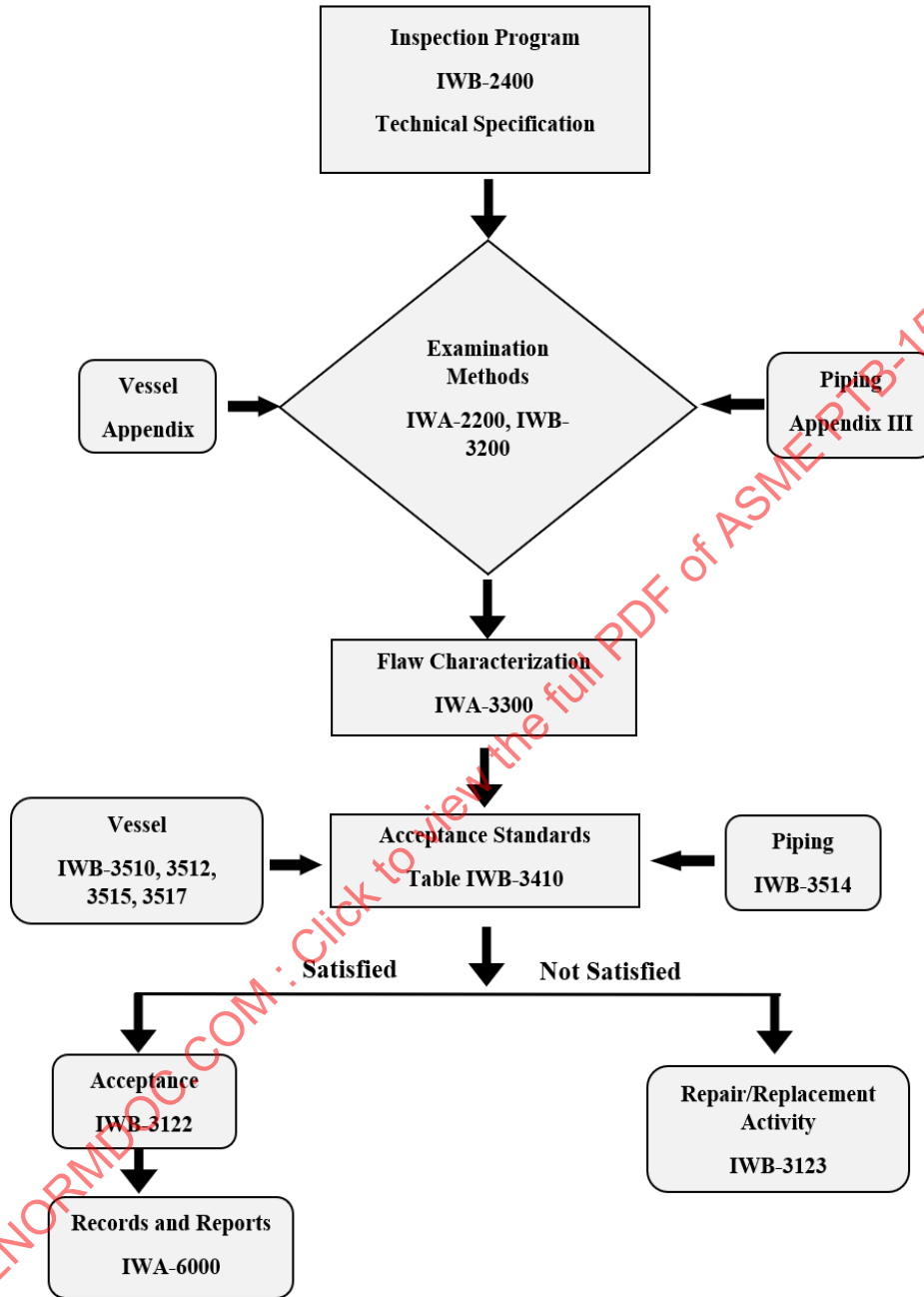


Image Courtesy of Sinewave Solutions

Figure 9-10: Flaw Evaluation Procedure

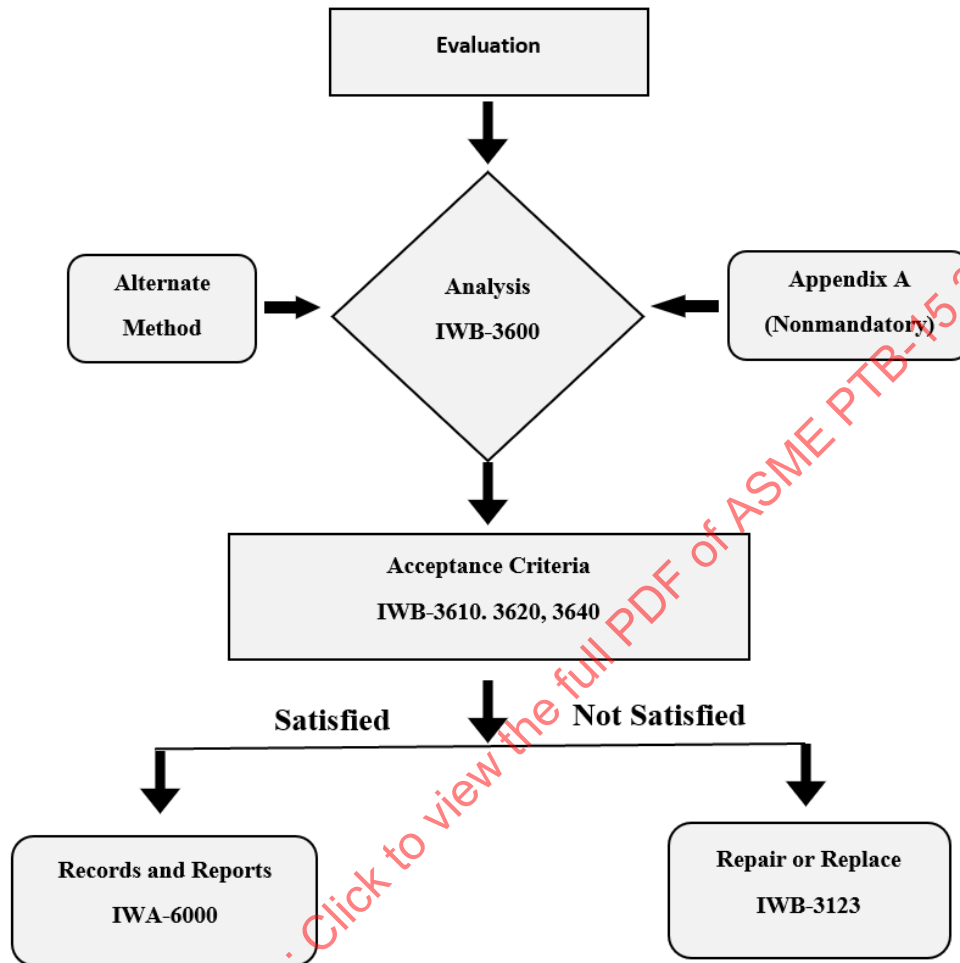


Image Courtesy of Sinewave Solutions

### 9.8 Acceptance Criteria Examples

The following examples are taken from three different Code books. They are ASME B31.3 Process Piping, ASME BPVC Section VIII Rules for Construction of Pressure Vessels, and ASME BPVC Section XI Rules for Inservice Inspection of Nuclear Power Plant Components.

The Code books provide drawings and acceptance criteria tables. However, the nomenclature, the component thickness ranges, and the maximum acceptance values of the books are all different. It is understandable that the different Code books would have different requirements for different types of service and especially when using different materials. In turn, this would naturally lead to different values within the tables. A practical example of a difference would be multiple flaws aligned through the volume of the weld. ASME BPVC Section VIII (vessels) and Section XI (inservice) go to great lengths to describe proximity rules for this, including additional steps, whereas the B31.3 does not. Even so, the process to disposition a flaw is all the same, and the Fracture Mechanics principles are the same.

Another question is why are the surface flaw and subsurface flaw criteria different? This is due to the force that is exerted from the flaw. A surface flaw is only considered as having one direction to grow, and a subsurface flaw has two. Therefore, any given aspect ratio for surface or subsurface will be different.

The following figures and tables illustrate the difference between the Code sections.

Figure 9-11: From ASME B31.3-2022

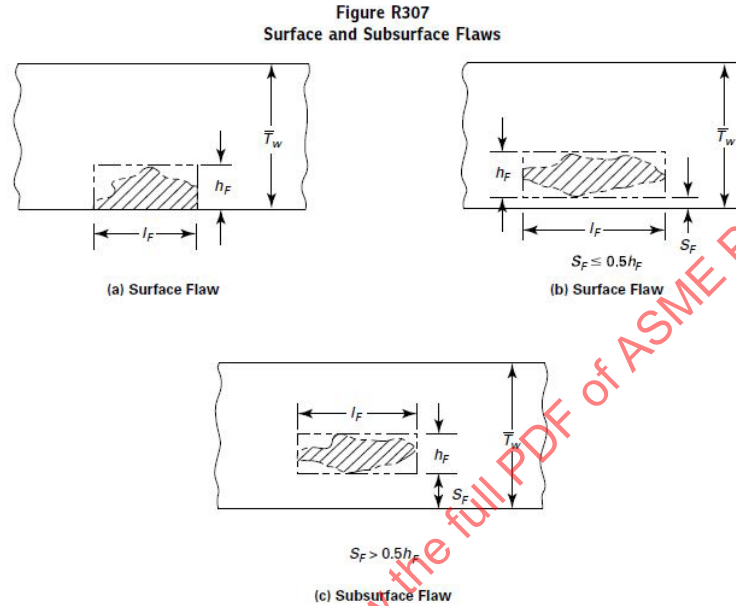


Table R308.1 Acceptance Criteria for Surface Flaws

Aspect Ratio, $h_F/l_F$	Maximum $h_F/\bar{T}_w$ for Nominal Weld Thickness	
	25 mm to 65 mm (1.0 in. to 2.5 in.)	100 mm to 300 mm (3.9 in. to 11.8 in.)
	0.00	0.031
0.05	0.033	0.020
0.10	0.036	0.022
0.15	0.041	0.025
0.20	0.047	0.028
0.25	0.055	0.033
0.30	0.064	0.038
0.35	0.074	0.044
0.40	0.083	0.050
0.45	0.085	0.051
0.50	0.087	0.052

GENERAL NOTES:

- (a) Aspect ratio ( $h_F/l_F$ ) used may be determined by rounding the calculated  $h_F/l_F$  down to the nearest 0.05 increment value within the column, or by linear interpolation.
- (b) For intermediate thickness  $\bar{T}_w$  [thicknesses greater than 65 mm (2.5 in.) and less than 100 mm (3.9 in.)], linear interpolation is permitted to obtain  $h_F/\bar{T}_w$  values. Otherwise, the lower values shall be used.

Table R308.2 Acceptance Criteria for Subsurface Flaws

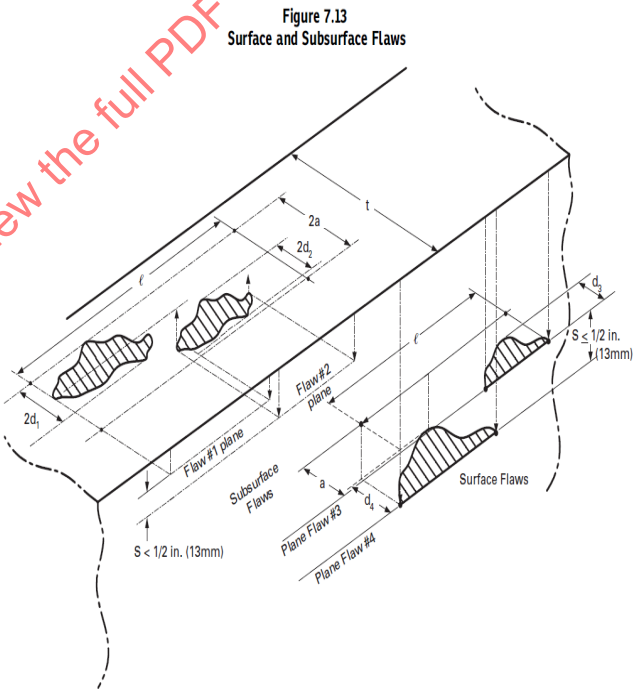
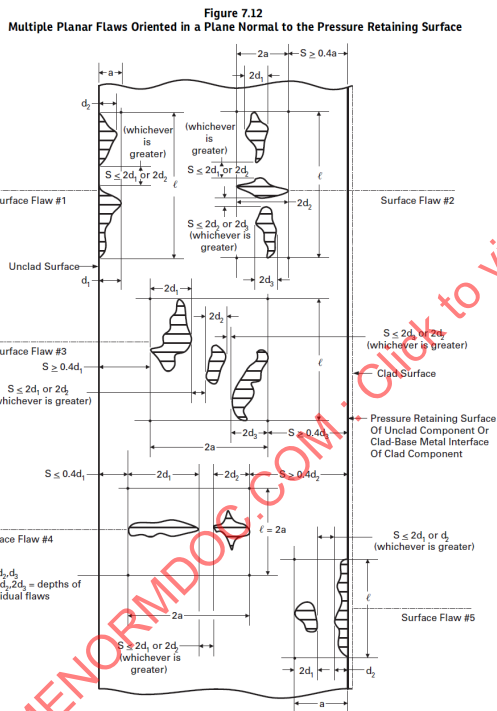
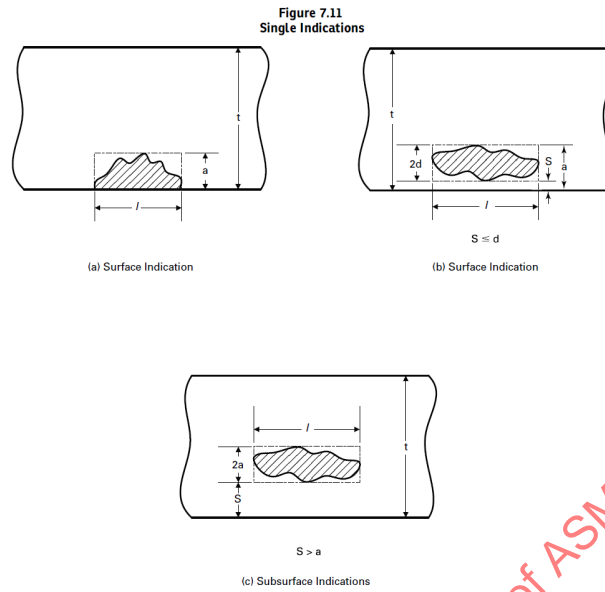
Aspect Ratio, $h_F/l_F$	Maximum $h_F/\bar{T}_w$ for Nominal Weld Thickness	
	25 mm to 65 mm (1.0 in. to 2.5 in.)	100 mm to 300 mm (3.9 in. to 11.8 in.)
	0.00	0.068
0.10	0.076	0.044
0.20	0.086	0.050
0.30	0.108	0.058
0.40	0.132	0.066
0.50	0.156	0.080
0.60	0.180	0.094
0.70	0.206	0.108
0.80	0.232	0.122
0.90	0.258	0.138
1.00	0.286	0.152

GENERAL NOTES:

- (a) Aspect ratio ( $h_F/l_F$ ) used may be determined by rounding the calculated  $h_F/l_F$  down to the nearest 0.10 increment value within the column, or by linear interpolation.
- (b) For intermediate thickness  $\bar{T}_w$  [thicknesses greater than 65 mm (2.5 in.) and less than 100 mm (3.9 in.)], linear interpolation is permitted to obtain  $h_F/\bar{T}_w$  values. Otherwise, the lower values shall be used.

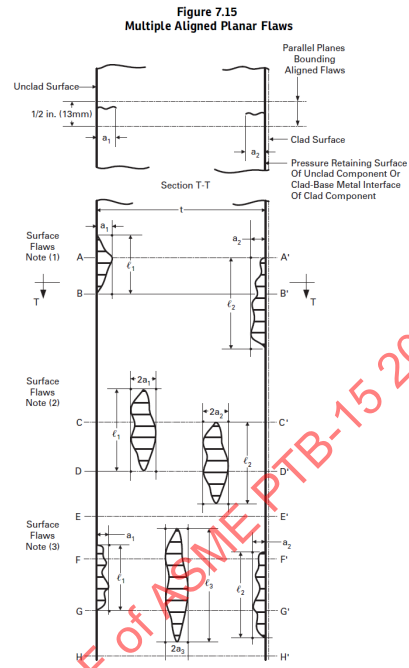
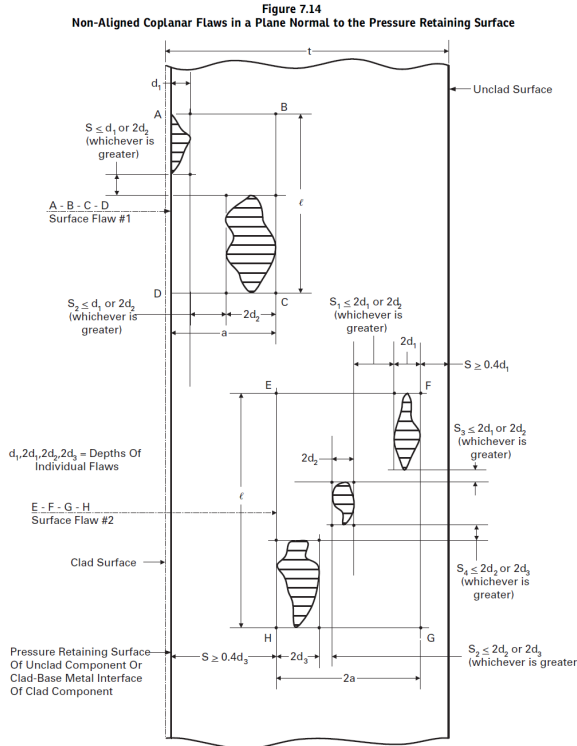


Figure 9-12: From ASME BPVC Section VII-2021



Click to view the full PDF of ASME PTB-15 2023

ASME NORMS.COM



NOTES:  
 (1) This illustration indicates two surface flaws. The first,  $a_1$ , is on the outer surface, and the second,  $a_2$ , is on the inner surface.  $[a_1 + a_2] \leq (a_1 + a_2)/2$  within planes A - A' and B - B'.  
 (2) This illustration indicates two subsurface flaws:  $[a_1 + a_2] \leq (a_1 + a_2)/2$  within planes C - C' and D - D'.  
 (3) This illustration indicates two surface flaws and one subsurface flaw.

**Table 7.9**  
**Flaw Acceptance Criteria for Welds With a Thickness Between 13 mm (1/2 in.) and Less Than 25 mm (1 in.)**

Flaw Type	$a/t$	$l$
Surface flaw	$\leq 0.087$	$\leq 6.4 \text{ mm } (1/4 \text{ in.})$
Subsurface flaw	$\leq 0.143$	$\leq 6.4 \text{ mm } (1/4 \text{ in.})$

GENERAL NOTES:  
 (a) The parameter  $t$  is the thickness of the weld excluding any allowable reinforcement, and the parameter  $l$  is the length of the flaw. For a butt weld joining two members having different thickness at the weld,  $t$  is the thinner of these two thicknesses. If a full penetration weld includes a fillet weld, then the thickness of the throat of the fillet weld shall be included in  $t$ .  
 (b) A subsurface indication shall be considered as a surface flaw if the separation ( $S$  in Figure 7.11) of the indication from the nearest surface of the component is equal to or less than half the through dimension [ $2d$  in Figure 7.11, Sketch (b)] of the subsurface indication.  
 (c) The acceptance limits specified here are based upon workmanship considerations and are not necessarily intended for use in evaluating flaws identified after the vessel has gone into service.  
 (d)  $a$  and  $l$  are as defined in 7.5.5.2.

**Table 7.10**  
**Flaw Acceptance Criteria for Welds With Thickness Between 25 mm (1 in.) and Less Than or Equal to 300 mm (12 in.)**

Flaw Aspect Ratio, $a/l$	25 mm (1 in.) $\leq t < 64$ mm (2 1/2 in.)		100 mm (4 in.) $\leq t \leq 300$ mm (12 in.)	
	Surface Flaw, $a/t$	Subsurface Flaw, $a/t$	Surface Flaw, $a/t$	Subsurface Flaw, $a/t$
0.00	0.031	0.034	0.019	0.020
0.05	0.033	0.038	0.020	0.022
0.10	0.036	0.043	0.022	0.025
0.15	0.041	0.054	0.025	0.029
0.20	0.047	0.066	0.028	0.034
0.25	0.055	0.078	0.033	0.040
0.30	0.064	0.090	0.038	0.047
0.35	0.074	0.103	0.044	0.054
0.40	0.083	0.116	0.050	0.061
0.45	0.085	0.129	0.051	0.069
0.50	0.087	0.143	0.052	0.076

GENERAL NOTES:  
 (a) The parameter  $t$  is the thickness of the weld excluding any allowable reinforcement, and the parameter  $l$  is the length of the flaw. For a butt weld joining two members having different thickness at the weld,  $t$  is the thinner of these two thicknesses. If a full penetration weld includes a fillet weld, then the thickness of the throat of the fillet weld shall be included in  $t$ .  
 (b) A subsurface indication shall be considered as a surface flaw if the separation ( $S$  in Figure 7.11) of the indication from the nearest surface of the component is equal to or less than half the through dimension [ $2d$  in Figure 7.11, Sketch (b)] of the subsurface indication.  
 (c) The acceptance limits specified here are based upon workmanship considerations and are not necessarily intended for use in evaluating flaws identified after the vessel has gone into service.  
 (d) For intermediate flaw aspect ratio  $a/l$  and thickness  $t$  [ $64 \text{ mm } (2 1/2 \text{ in.}) < t < 100 \text{ mm } (4 \text{ in.})$ ], linear interpolation is permissible.  
 (e) If the acceptance criteria in this table results in a flaw length,  $l$ , less than 6.4 mm (0.25 in.), a value of 6.4 mm (0.25 in.) may be used.  
 (f) For materials exceeding 655 MPa (95 ksi) ultimate tensile strength, the use of this table is limited to a thickness of 200 mm (8 in.).

Notice the different naming system. We see the letters  $H_f$ ,  $L_f$  for the B31 code, and “a”, and “l” for ASME BPVC Section VIII, however they both describe the same thing. This can lead to some confusion in an already unexplained process. There is also another proximity rule for ASME BPVC Section XI called “Y”.

Figure 9-13: From ASME BPVC Section XI-2021

Table IWB-3510-1 Allowable Planar Flaws Material: Ferritic steels that meet the requirements of NB-2331 and G-2110(b) of Section III						
Aspect Ratio, [Note (1)] $a/l$	Volumetric Examination Method, Nominal Wall Thickness, [Note (1)], [Note (2)] $t$ , in. (mm)					
	$2\frac{1}{2}$ (65) and less		4 (100) to 12 (300)		16 (400) and greater	
	Surface Flaw, [Note (5)] $a/t$ , %	Subsurface Flaw, [Note (3)], [Note (4)] $a/t$ , %	Surface Flaw [Note (5)], $a/t$ , %	Subsurface Flaw, [Note (3)], [Note (4)] $a/t$ , %	Surface Flaw, [Note (5)] $a/t$ , %	Subsurface Flaw, [Note (3)], [Note (4)] $a/t$ , %
0.0	3.1	$3.4Y^{1.00}$	1.9	$2.0Y^{1.00}$	1.4	$1.5Y^{1.00}$
0.05	3.3	$3.8Y^{0.96}$	2.0	$2.2Y^{0.90}$	1.5	$1.7Y^{0.91}$
0.10	3.6	$4.3Y^{0.72}$	2.2	$2.5Y^{0.69}$	1.7	$1.9Y^{0.69}$
0.15	4.1	$4.9Y^{0.48}$	2.5	$2.9Y^{0.47}$	1.9	$2.1Y^{0.43}$
0.20	4.7	$5.7Y^{0.50}$	2.8	$3.3Y^{0.47}$	2.1	$2.5Y^{0.45}$
0.25	5.5	$6.6Y^{0.65}$	3.3	$3.8Y^{0.61}$	2.5	$2.8Y^{0.57}$
0.30	6.4	$7.8Y^{0.84}$	3.8	$4.4Y^{0.77}$	2.9	$3.3Y^{0.75}$
0.35	7.4	$9.0Y^{0.99}$	4.4	$5.1Y^{0.93}$	3.3	$3.8Y^{0.90}$
0.40	8.3	$10.5Y^{1.00}$	5.0	$5.8Y^{1.00}$	3.8	$4.3Y^{1.00}$
0.45	8.5	$12.3Y^{1.00}$	5.1	$6.7Y^{1.00}$	3.9	$4.9Y^{1.00}$
0.50	8.7	$14.3Y^{1.00}$	5.2	$7.6Y^{1.00}$	4.0	$5.6Y^{1.00}$

NOTES:  
 (1) For intermediate flaw aspect ratios  $a/l$  and thickness  $t$ , linear interpolation is permissible. Refer to IWA-3200(b).  
 (2) Component thickness  $t$  is measured normal to the pressure-retaining surface of the component. Where the section thickness varies, the average thickness over the length of the planar flaw is the component thickness.  
 (3) The total depth of a subsurface flaw is  $2a$ .  
 (4)  $Y = [(S/t)/(a/t)]$  or  $(S/a)$ .  $Y$  is the flaw-to-surface proximity factor, and  $S$  is defined in IWA-3310 and IWA-3320. If  $S < 0.4d$ , the subsurface flaw is classified as a surface flaw. If  $Y > 1.0$ , use  $Y = 1.0$ .  
 (5) Applicable to flaws in surface region B-E shown in Figure IWB-2500-5 only if the maximum postulated defect of Section III Appendices, Nonmandatory Appendix G, G-2120, is justified. If a smaller defect is used, Refer to IWB-3410.2.

Remember that ASME BPVC Section XI is for in-service inspections, but the drawings provided are similar to those of ASME BPVC Section VIII. The tables are again different, and there is an additional “Y” factor considered for sub surface flaws. The reasoning for the “Y” factor is that a larger flaw near the surface would be more detrimental than a smaller one. To calculate the “Y” value it is simply  $S/a$ , and cannot exceed a value of 1.0, therefore any number larger than 1.0 is counted as 1.0. The “Y” value is then multiplied against the appropriate value in the  $a/t$  column. Also, in addition to the “Y” value, the resulting answer will then be multiplied by the given exponent value in the table.

By walking through the process, we can see that it is not as complicated as it would seem. Patience is required while working through the process, and regardless of the different nomenclature, symbols, or number of steps required the process for characterization is the same.

### 9.9 Applying the Acceptance Criteria Tables and Using Interpolation

For the purpose of this training, we will use a B31 code. This information comes from Appendix R of the B31.3 2018 edition. It is worth noting that the B31 is the simplest to use, and that other codes such as ASME Sec VIII, and Sec. XI are also easy to use, but are slightly different. While they are similar in overview, and the process is essentially the same, the acceptance criteria are different, and the process to arrive at the answers will be slightly more involved. Mainly this is due to the nature of the end product. From the first half of this chapter, we learned that the different fracture mechanics methods have different applications. Therefore, it makes sense that B31 piping is going to be different from ASME BPVC Section VIII pressure vessels, and both are going to be different from in-service

examinations contained in ASME BPVC Section XI. The end user needs to ensure they are using the right tables, and for the right Code.

Step 1 – Using the flaw dimension and location, determine if the flaw is surface, or subsurface. When multiple flaws are present, always start with the largest flaw.

A flaw is considered a Surface flaw if:

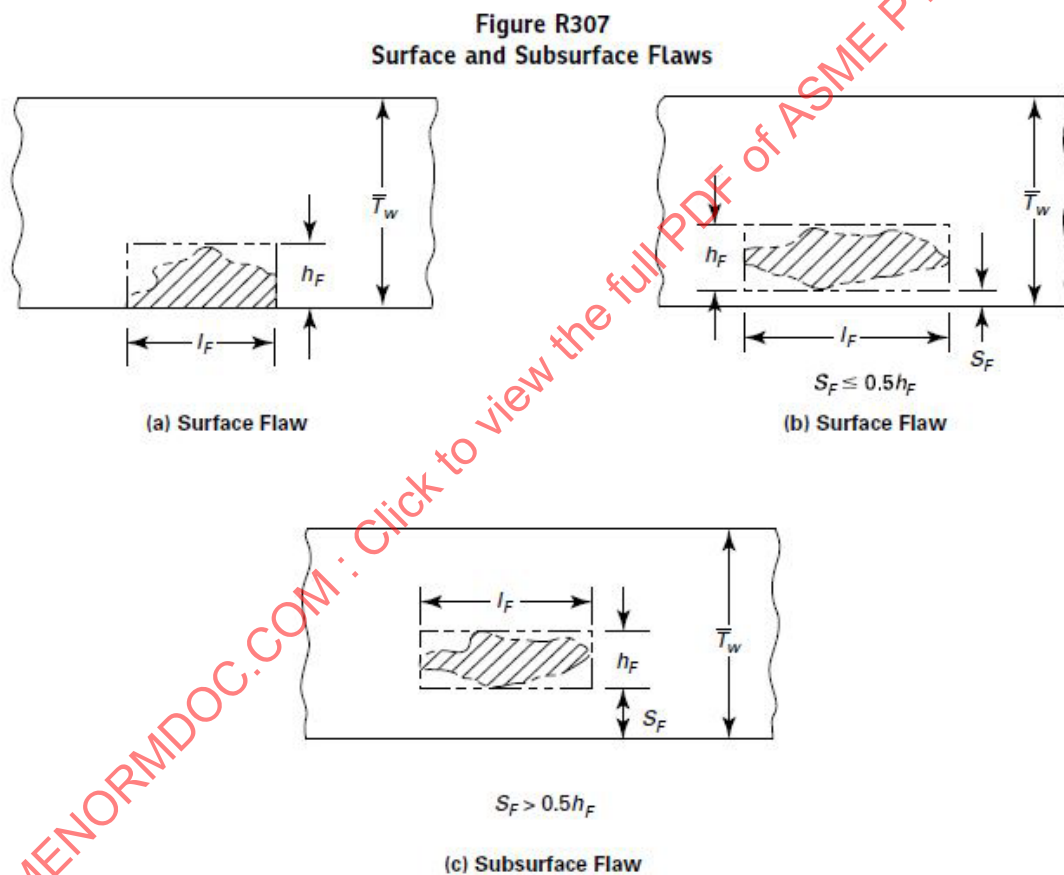
It is connected to the surface, OR

If the separation distance from the nearest surface is equal to or less than half the height of the flaw.  $S \leq 0.5h = \text{Surface}$

A flaw is considered a Subsurface flaw if:

The separation distance from the nearest surface is greater than half the height of the flaw.  $S > 0.5h = \text{Subsurface}$

Figure 9-14: Depiction of surface or subsurface flaw proximity rules from ASME B31.3-2022



NOTE: The dimension of the flaw(s) shall be determined by a rectangle that fully contains the area of the flaw(s), and the length shall be drawn parallel to the inside pressure retaining surface and the height of the flaw shall be drawn normal (perpendicular) to the inside pressure retaining surface.

Step 2 – Regardless of flaw height or aspect ratio, no flaw length shall exceed 4 times the nominal weld thickness (From B31.3).

Step 3 – Aspect ratio is the height of the flaw divided by the length of the flaw. For B31.3 this is denoted as  $H_f/L_f$ . Other codes may use different annotations, but it is the same thing. For this step simply divide the flaw height by the length.

Example:

Flaw height = 0.3 in.

Flaw length = 1 in.

Average weld thickness = 1.2 in. (will use this in the next step).

A flaw with a height of 0.3 in. divided by a length of 1.5 in. gives us an aspect ratio of 0.20 (0.3 in./1.5 in. = 0.20).

This establishes the aspect ratio for the flaw, and it corresponds to the left-hand column in the tables.

**Figure 9-15: The aspect ratio column in red**

Table R308.1 Acceptance Criteria for Surface Flaws			Table R308.2 Acceptance Criteria for Subsurface Flaws		
Aspect Ratio, $h_F/l_F$	Maximum $h_F/\bar{T}_w$ for Nominal Weld Thickness		Aspect Ratio, $h_F/l_F$	Maximum $h_F/\bar{T}_w$ for Nominal Weld Thickness	
	25 mm to 65 mm (1.0 in. to 2.5 in.)	100 mm to 300 mm (3.9 in. to 11.8 in.)		25 mm to 65 mm (1.0 in. to 2.5 in.)	100 mm to 300 mm (3.9 in. to 11.8 in.)
0.00	0.031	0.019	0.00	0.068	0.040
0.05	0.033	0.020	0.10	0.076	0.044
0.10	0.036	0.022	0.20	0.086	0.050
0.15	0.041	0.025	0.30	0.108	0.058
0.20	0.047	0.028	0.40	0.132	0.066
0.25	0.055	0.033	0.50	0.156	0.080
0.30	0.064	0.038	0.60	0.180	0.094
0.35	0.074	0.044	0.70	0.206	0.108
0.40	0.083	0.050	0.80	0.232	0.122
0.45	0.085	0.051	0.90	0.258	0.138
0.50	0.087	0.052	1.00	0.286	0.152

GENERAL NOTES:  
 (a) Aspect ratio ( $h_F/l_F$ ) used may be determined by rounding the calculated  $h_F/l_F$  down to the nearest 0.05 increment value within the column, or by linear interpolation.  
 (b) For intermediate thickness  $\bar{T}_w$  [thicknesses greater than 65 mm (2.5 in.) and less than 100 mm (3.9 in.)], linear interpolation is permitted to obtain  $h_F/\bar{T}_w$  values. Otherwise, the lower values shall be used.

Image Courtesy of Sinewave Solutions (Original Image from ASME B31.3 -2022)

Step 4 – Next, determine if the flaw is acceptable or rejectable, divide the flaw height by the nominal weld thickness. Then follow across the appropriate row for the flaws aspect ratio for the correct component thickness. If the number you have exceeds the number in the row, it is rejectable. The acceptance criteria column is a percentage of an allowable flaw height per given aspect ratio and lists the maximum value that is allowed.

Using the above example of a given aspect ratio of 0.20 we follow that row across to the column with the correct material thickness of 1.2 in. we will arrive at the following answer. Flaw height = 0.3 in./Weld T of 1.2 in. = 0.25. As you can see, this number far exceeds that of the table, and is therefore rejectable.

### 9.9.1 Linear Interpolation

In the previous example everything worked out great because we had an aspect ratio of 0.20 which was listed in the table. Chances are very likely that you will not have such a convenient number to work with. For example, you may have an aspect ratio of 0.33, which does not appear in either of the tables. The Code offers two ways to approach this (Read the “GENERAL NOTES” after the tables. In fact, always read the notes after any table).



**Figure 9-16: Example of When Interpolation May be Needed**

**Table R308.1 Acceptance Criteria for Surface Flaws**

Aspect Ratio, $h_F/l_F$	Maximum $h_F/\bar{T}_w$ for Nominal Weld Thickness	
	25 mm to 65 mm (1.0 in. to 2.5 in.)	100 mm to 300 mm (3.9 in. to 11.8 in.)
	0.00	0.031
0.05	0.033	0.020
0.10	0.036	0.022
0.15	0.041	0.025
0.20	0.047	0.028
0.25	0.055	0.033
0.30	0.064	0.038
<b>0.33</b> →	<b>???</b>	
0.35	0.074	0.044
0.40	0.083	0.050
0.45	0.085	0.051
0.50	0.087	0.052

**GENERAL NOTES:**

- (a) Aspect ratio ( $h_F/l_F$ ) used may be determined by rounding the calculated  $h_F/l_F$  down to the nearest 0.05 increment value within the column, or by linear interpolation.
- (b) For intermediate thickness  $\bar{T}_w$  [thicknesses greater than 65 mm (2.5 in.) and less than 100 mm (3.9 in.)], linear interpolation is permitted to obtain  $h_F/\bar{T}_w$  values. Otherwise, the lower values shall be used.

Image Courtesy of Sinewave Solutions (Original Image from ASME B31.3 -2022)

GENERAL NOTES: (a) The simplest way is to round the aspect ratio down (i.e., use lower value) to the nearest increment on the table. In our example of 0.33 you would select the row for 0.30 for the surface flaw table, and 0.30 for the subsurface table. Again, this is rounding down, and NOT rounding to the nearest number. For a ratio of 0.27, you would use 0.25 for surface flaws, and 0.20 for subsurface flaws.

The other option available is to use linear interpolation. Linear interpolation allows you to create those sections of the table that are not included in it. This may be a better option if you do not want to unfairly penalize the component. To see how this works, let's use the example above for surface flaws, having an aspect ratio of 0.33 in a 1.2 in. thick component. Knowing the actual aspect ratio of 0.33 and wanting to find the acceptance limit for this aspect ratio, we will use the surrounding values from the table and interpolate.

Locate the two aspect ratios that your "actual" aspect ratio value fits between. Using the immediate value(s) above and below your actual number. In this example 0.33 fits between 0.30 and 0.35 on the table (using the following equation, these will be our  $X_1$  and  $X_2$  values respectively).

Next, follow the rows across to obtain the two corresponding numbers from the  $H_f/T_w$  column. As you can see, we will land somewhere between 0.064 and 0.074 (for this equation these will be our  $Y_1$  and  $Y_2$  values).

Here is a common formula to accomplish interpolation:

$$Y = Y_1 + (X - X_1) \frac{Y_2 - Y_1}{X_2 - X_1}$$

An easy way to think about interpolation is to represent it in a simple X, Y graph as shown in Figure 9-17. In this case "X" represents the aspect ratio, and "Y" represents the acceptance criteria values.

**Figure 9-17: Interpolation Graph for Aspect Ratio (typical) where X=Aspect Ratio and Y=Acceptance Limit**

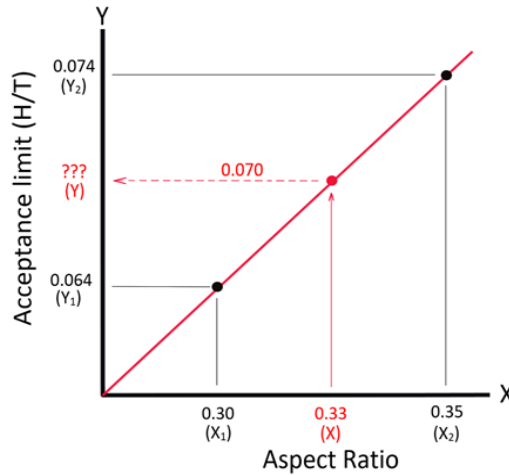


Image Courtesy of Sinewave Solutions

Also, from the GENERAL NOTES (b) you will notice that this same process can be applied to determine an acceptance value for a different thickness, when the component you are working on falls between the thickness ranges in the tables. Although, as with the example above you may have additional steps to create the acceptance values for an aspect ratio not included in the table (e.g., aspect ratio of 0.33) before you interpolate for the correct thickness.

**Figure 9-18: Example of interpolating for thickness**

**Table R308.1 Acceptance Criteria for Surface Flaws**

Aspect Ratio, $h_F/l_F$	Maximum $h_F/\bar{T}_w$ for Nominal Weld Thickness		
	25 mm to 65 mm (1.0 in. to 2.5 in.)	80 mm (3.2 in.)	100 mm to 300 mm (3.9 in. to 11.8 in.)
0.00	0.031		0.019
0.05	0.033		0.020
0.10	0.036		0.022
0.15	0.041		0.025
0.20	0.047		0.028
0.25	0.055		0.033
0.30	0.064	???	0.038
0.35	0.074		0.044
0.40	0.083		0.050
0.45	0.085		0.051
0.50	0.087		0.052

**GENERAL NOTES:**

- (a) Aspect ratio ( $h_F/l_F$ ) used may be determined by rounding the calculated  $h_F/l_F$  down to the nearest 0.05 increment value within the column, or by linear interpolation.
- (b) For intermediate thickness  $\bar{T}_w$  [thicknesses greater than 65 mm (2.5 in.) and less than 100 mm (3.9 in.)], linear interpolation is permitted to obtain  $h_F/\bar{T}_w$  values. Otherwise, the lower values shall be used.

Image Courtesy of Sinewave Solutions (Original Image from ASME B31.3 -2022)

As an example, the thickness ranges within the tables are limited. There is one column for 1.0 in. to 2.5 in., then the next column picks up at 3.9 in. to 11.8 in. The gap within the thickness range of the table is from 2.5 in. up to 3.9 in. There are no acceptance criteria provided in this range. Therefore, if you had a component that was 3.2 in. thick you would need to interpolate the table to include this thickness.

We will use the same simple process this time using an aspect ratio of 0.30, and instead of interpolating the acceptance criteria limit moving up and down the table vertically, we will be using the values going across the table columns horizontally. Please note that the X and Y direction in the graph has nothing to do with the direction you are interpolating within the tables, and is user defined. For the graph in Figure 9-19, we will simply replace “Aspect Ratio” values with known “Thickness” values.

**Figure 9-19: Interpolation Graph for Thickness (typical) Where X=Thickness and Y=Acceptance Limit**

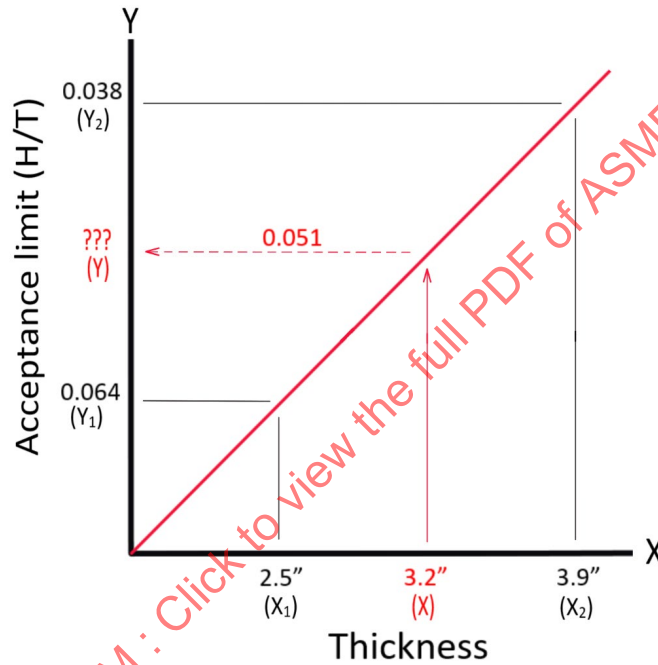


Image Courtesy of Sinewave Solutions

ASMENORMDOC.COM : Click to view the full PDF of ASME PTB-15-2023

## 10 APPLICATIONS

### 10.1 In-service Inspections: FMC Techniques for High Temperature Hydrogen Attack Assessment

#### 10.1.1 Problem Definition

High Temperature Hydrogen Attack (HTHA) is a localized complex damage phenomenon. HTHA occurs in welds, weld heat affected zones (HAZ), or base material in carbon and low alloy steels exposed to a high partial pressure of hydrogen at elevated temperature. HTHA is possible in hydrocarbon processing units, hydrogen producing units, synthetic gas units, ammonia plants under dry conditions, and in high pressure boiler tubes in wet environment. HTHA typically initiates near to the internal surface (ID) and the appearance includes:

Decarburization—surface and internal

Volumetric-Like damage—voids (methane bubbles), linking voids, disoriented micro cracking (fissures)

Blistering-like damage—bubbles accumulating in steel laminations near and parallel to internal diameter (ID) surface

Crack-Like damage—vertical or inclined cracks.

Detection, characterization, and sizing of HTHA is a challenging inspection task due to the complexity of the damage. API RP 941 past edition recommends many ultrasonic manual techniques developed in the 1980's-1990's (API 2016). These techniques have limitations, including operator variability.

Wang investigated and improved several historical techniques such as ultrasonic backscattering, frequency analysis, velocity ratio, and high-frequency shear wave (Wang 1999). Advanced Ultrasonic Backscattering Technique (AUBT) can detect HTHA damage at a depth of 10-20 percent wall thickness (Kallenberg and Munsterman 2002). Time-of-Flight Diffraction (TOFD) is an emerging screening technique for inspection of two side access welds (API 2016, ASME 2019). TOFD cannot detect HTHA damage at a depth of 10-12 percent wall thickness due to internal and external diameter dead zones limitations. TOFD can detect simulated HTHA in the weld HAZ, but with wavelength and imaging limitations it cannot distinguish HTHA microcracking damage from acceptable inclusions, slag, and porosity (Birring 2005). Regardless, TOFD has been applied for HTHA inspection applications (Krynicky et al. 2006).

The PAUT technique has been used for HTHA detection, characterization, and sizing (Birring 2005). Non-collinear wave mixing of ultrasonic waves has been applied to a test sample extracted from a retired pressure vessel exposed to hydrogen (McGovern et al. 2016). Full Matrix Capture/Total Focusing Method (FMC/TFM) and Adaptive Total Focusing Method (ATFM) ultrasonic techniques were first applied for enhanced HTHA detection, characterization, and sizing; a comparison of PAUT and FMC capabilities to detect HTHA damage was confirmed by metallography; TOFD to distinguish HTHA from metallurgical imperfections was confirmed; and novel principles for progressive validation and qualification using specimens extracted from service were proposed (Lozev et al. 2017). A UK HSE report reviews historical and new ultrasonic techniques for HTHA inspection, describes limitations of the techniques, and addresses ongoing efforts to codify the new techniques, evaluate inspection effectiveness, and provide training (Nageswaran 2018). PAUT, FMC/TFM, and TOFD techniques have been used for HTHA field inspections (Reverdy et al. 2018; Johnson et al. 2019; Neve et al. 2019).

PAUT and FMC/TFM techniques have been codified in ASME BPVC Section V - 2019 and API RP 941 Addendum 1 (ASME 2019; API 2020).

### 10.1.2 Solution

This application presents an approach for optimizing and evaluating the capabilities of codified ultrasonic array techniques for improved detection, characterization, and sizing of early stage HTHA in refining equipment. TOFD was not selected for this application because the characterization concerns and dead zones limitations prohibiting detection of early stages HTHA damage developed near to the ID surface. Ultrasonic modeling and simulation tools were used to design and optimize a set of linear and matrix array probes tailored for HTHA inspection. The predicted capabilities of the probes to detect and size HTHA damage smaller than 1mm (microscopic damage), utilized with PAUT sectorial scanning and FMC/TFM/ATFM longitudinal to longitudinal (L-L) and transverse to transverse (T-T) direct paths techniques were validated. Samples with micro machine flaws, synthetic HTHA and real HTHA damage were used. Ultrasonic array techniques results were compared with metallographic images and measurements.

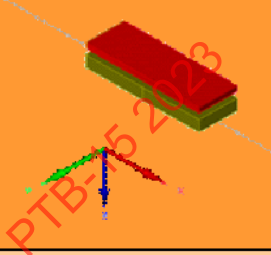
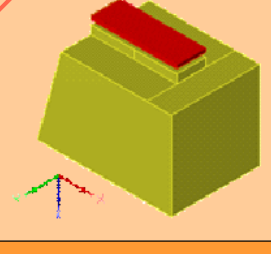
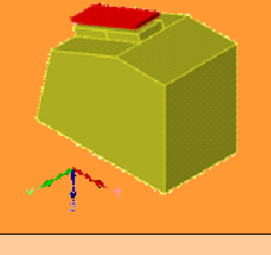
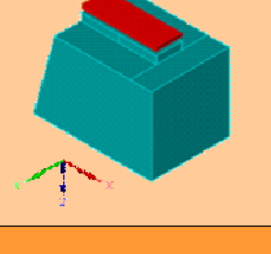

### 10.1.3 Array Probes Design and Optimization

The design of the probes and optimization of inspection procedures were based on a two-step approach applying semi-analytical tools and advanced software package for processing, imaging, and simulations (Lozev et al. 2005; Calmon et al. 2018). Ultrasonic modeling and simulation tools were used to design and optimize a set of linear and matrix array probes for improved detection, characterization, and sizing of HTHA damage. Array aperture was limited to 64 elements in linear (1x64) and matrix (4x16) arrangements with probe frequency from 5 to 10MHz.

In the first optimization step, called modeling, an unfocused (natural) beam profile for each probe was calculated, visualized, and used to determine the near field. Next, a profile for each beam focused on specific depth was calculated and beam cross sections were visualized. All beam calculations were performed for the following combinations of wedges: (1) normal beam with no wedge (hard face probe); (2) normal beam with solid, 1mm thick thermoplastic wedge; (3) normal beam with solid, 20-23mm thick Rexolite wedge; (4) normal beam with conformable (flexible) elastomer wedge filled with water, height 20mm; (5) angle beam with solid Rexolite wedge, height 14, 29 and 45mm, and (6) angle beam with conformable (flexible) elastomer wedge filled with water, height 14, 29 and 45mm. The natural focal spot was calculated and specified in three dimensions at -3 dB, -6 dB, and -9 dB levels from peak amplitude as shown in Table 10-1. This specification information assist operators to select the right probe for performing HTHA inspection only in the near field and to improve detection and characterization capabilities.



**Table 10-1: Natural focal spot sizes and near field for optimized 10 MHz, 64 elements, linear array probe with aperture 150 mm<sup>2</sup>**

Wedge	3D natural focal spot sizes at -3 dB, -6 dB and -9 dB			Near field (mm)	Associated depth at 55° in Carbon steel thickness (mm)	Probe/wedge combination 3D visualization
		X (mm)	Y (mm)			
Direct contact, hard face	-3 dB	12.3	11.4	35.4	198	
	-6 dB	15.4	17.5	194.3		
	-9 dB	17.8	23.4	286		
Rexolite wedge L0°, height 23mm	-3 dB	12.5	11.5	36.5	190	
	-6 dB	15.5	17.6	196.1		
	-9 dB	18	23.4	287.5		
Rexolite wedge SW55°, height 29mm	-3 dB	8.8	6.6	93.5	186	
	-6 dB	11.1	10	203		
	-9 dB	12.9	13.2	290.4		
Water wedge L0°, height 23mm	-3 dB	12.2	11.4	92.1	194	
	-6 dB	15.3	17.5	188.4		
	-9 dB	17.9	23.4	198.3		
Water wedge SW55°, height 29mm	-3 dB	7.5	4.9	100.1	145	
	-6 dB	9.4	7.4	137.8		
	-9 dB			168.4		
				204.6		

The central frequency, aperture, and near field for the developed set of linear and matrix probes are shown in Table 10-2. The near field represents the optimum thickness range for PAUT and FMC/TFM inspections in carbon and low alloyed steels.

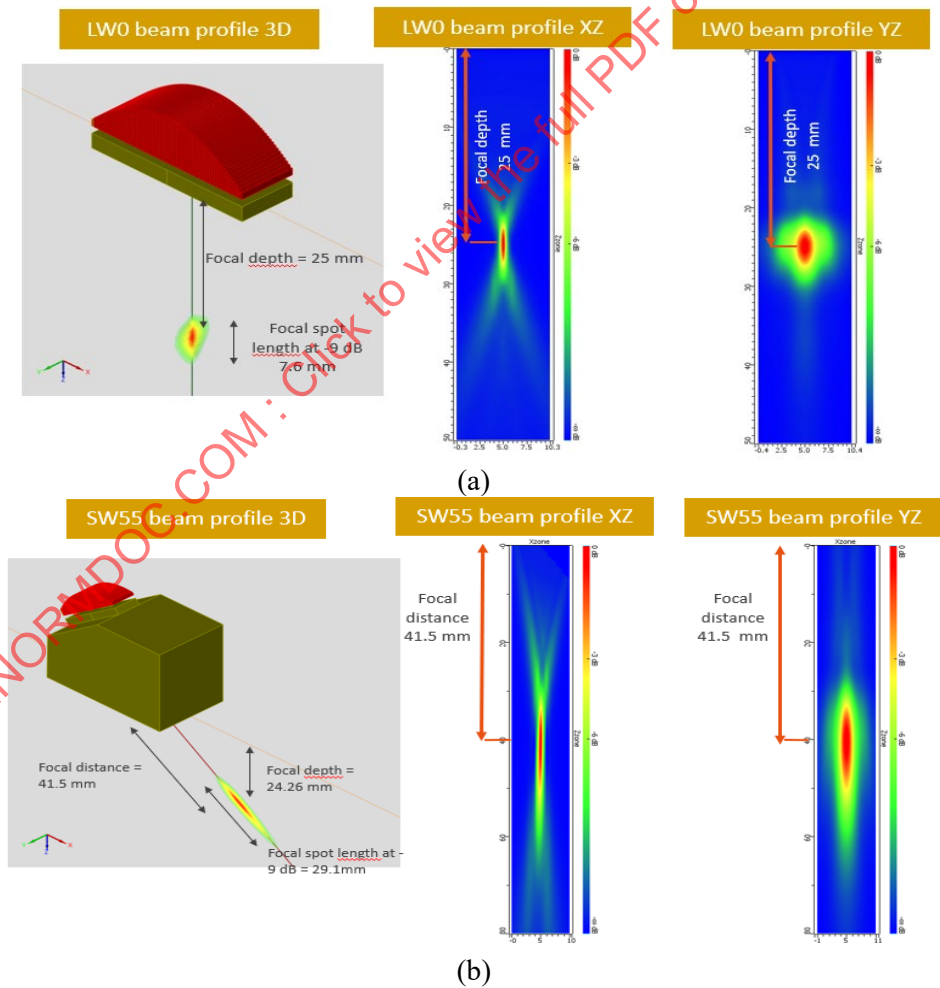
**Table 10-2: Specifications summary for the probes: central frequency, aperture and near field at -6dB**

Probe Central Frequency, MHz	Aperture, mm <sup>2</sup>		Near Field, mm (Normal Beam L-Wave, NO Wedge/Thermoplastic 1 mm Wedge)		Near Field, mm (Normal Beam L-Wave, 23/20 mm Height Resolite Wedge)		Near Field, mm (Normal Beam L-Wave, 23/20 mm Height water Wedge)		Near Field/Depth, mm (Angle Beam S/T-Wave, SW55° 45/29/14 mm Height Resolite Wedge)		Near Field/Depth, mm (Angle Beam S/T-Wave, SW55° 45/29/14 mm Height Water Wedge)	
	Linear, 1 x 64 elements	Matrix, 4 x 16 elements	Linear, 1 x 64 elements	Matrix, 4 x 16 elements	Linear, 1 x 64 elements	Matrix, 4 x 16 elements	Linear, 1 x 64 elements	Matrix, 4 x 16 elements	Linear, 1 x 64 elements	Matrix, 4 x 16 elements	Linear, 1 x 64 elements	Matrix, 4 x 16 elements
5	320	160	298	96	287	89	290	90	277/162	89/53	206/119	70/41
7.5	250	130	311	132	297	120	307	122	285/167	119/70	211/122	91/53
10	150	60	198	65	190	62	194	62	186/109	60/36	145/83	50/29

From Materials Evaluation, Vol. 78, No. 11: 1223–1238. Copyright © 2020 by The American Society for Nondestructive Testing Inc. Reprinted with permission.

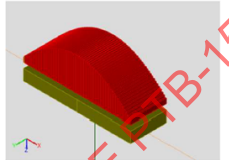
The 3D focused beam at selected depths were used to calculate the focal length (spot) and the beam size in two planes as shown in Figure 10-1 for a normal and angle beam probes.

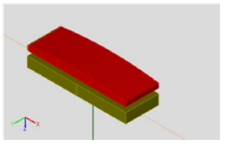
**Figure 10-1: Beam visualization at selected depth: (a) normal beam; (b) angle beam**



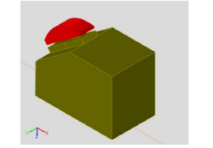
Focal spot sizes were then calculated for each probe and combinations of wedges at 25mm depth, and at the end of the near field as shown in Table 10-3. Focal spot sizes were calculated at -3dB, -6dB and -9dB. This specification information assists operators to select the right probe for performing HTHA inspection with a minimum spot size and to improve characterization and sizing capabilities.

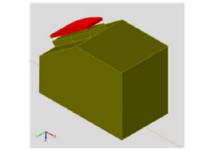
**Table 10-3: Beam sizes of 10 MHz, 64 elements, linear array probe at depth 25mm: (a) Longitudinal Wave, no Wedge; (b) Shear Wave, Rexolite Wedge**

Contact - No wedge - Focusing 25mm depth	3D focal spot sizes at -3 dB, -6 dB and -9 dB			Focal Depth (mm)	Associated depth at 55° in Carbon Steel (mm)	
	X (mm)	Y (mm)	Z (mm)			
-3 dB	0.4		4.4	25		
		1.9	4.4			
	0.7		6.2			
-6 dB		3.6	6.2			
	0.9		7.6			
-9 dB		5.3	7.6			

Contact - No wedge - Focusing near field limit distance (198 mm)	3D focal spot sizes at -3 dB, -6 dB and -9 dB			Focal Depth (mm)	Associated depth at 55° in Carbon Steel (mm)	
	X (mm)	Y (mm)	Z (mm)			
-3 dB	5.2		98.2	124		
		6.9	85.7			
-6 dB	7.7		132.2			
		9.9	130.2			
-9 dB	9.5		167.7			
		12.7	167.7			

(a)

Contact - Rexolite wedge SW55° - Focusing 25mm depth	3D focal spot sizes at -3 dB, -6 dB and -9 dB			Focal distance (mm)	Associated depth at 55° in Carbon Steel (mm)	
	X (mm)	Y (mm)	Z (mm)			
-3 dB	0.6		15.5	41.5	24.26	
		1.9	15.9			
-6 dB	1.1		22.5			
		2.9	23.1			
-9 dB	1.4		28.6			
		3.9	29.1			

Contact - Rexolite wedge SW55° - Focusing near field limit distance (277 mm)	3D focal spot sizes at -3 dB, -6 dB and -9 dB			Focal distance (mm)	Associated depth at 55° in Carbon Steel (mm)	
	X (mm)	Y (mm)	Z (mm)			
-3 dB	1.7		82.8	114	66.64	
		4	82.8			
-6 dB	8.2		181.9			
		5.9	130.9			
-9 dB	10.2		227.3			
		7.5	218			

(b)

From Materials Evaluation, Vol. 78, No. 11: 1223–1238. Copyright © 2020 by The American Society for Nondestructive Testing Inc. Reprinted with permission.

In the second optimization step, called simulation, the beam of each probe interacted with microscopic flaws virtually implanted in a 25mm thick double-V bevel carbon steel weld. The objective of the simulation was to define the capabilities of the probes utilized with both techniques to detect and size flaws smaller than 1mm. PAUT sectorial scan and FMC/TFM L-L and T-T techniques were simulated, and results were visualized in standard A-, B-, C-, D-, and S- views. The maximum amplitude difference in dB with respect to 2x10mm (diameter x length) reference Side Drill Hole (SDH) was recorded for the following flaws:

One cluster of 6 SDHs with 0.4mm (400 $\mu$ m) diameter in HAZ at ID surface simulating in-service HTHA volumetric damage (clustered linking voids and disoriented micro cracking)

Two notches with 0.4mm (400 $\mu$ m) height at top surface and bottom surface simulating in-service HTHA crack-like damage

Three Lack of Fusion (LOF) flaws with 0.4mm (400 $\mu$ m) height along the weld lines (top, middle and bottom) simulating fabrication flaws (metallurgical discontinuities).

Examples of beam interaction with simulated clusters of volumetric damage and crack-like damage for 10 MHz linear probe with solid Rexolite wedges are shown in Figure 10-2.

**Figure 10-2: 10 MHz shear wave beam interactions—PAUT (left) and FMC/TFM T-T (right): (a) cluster of six SDHs; (b) notch**

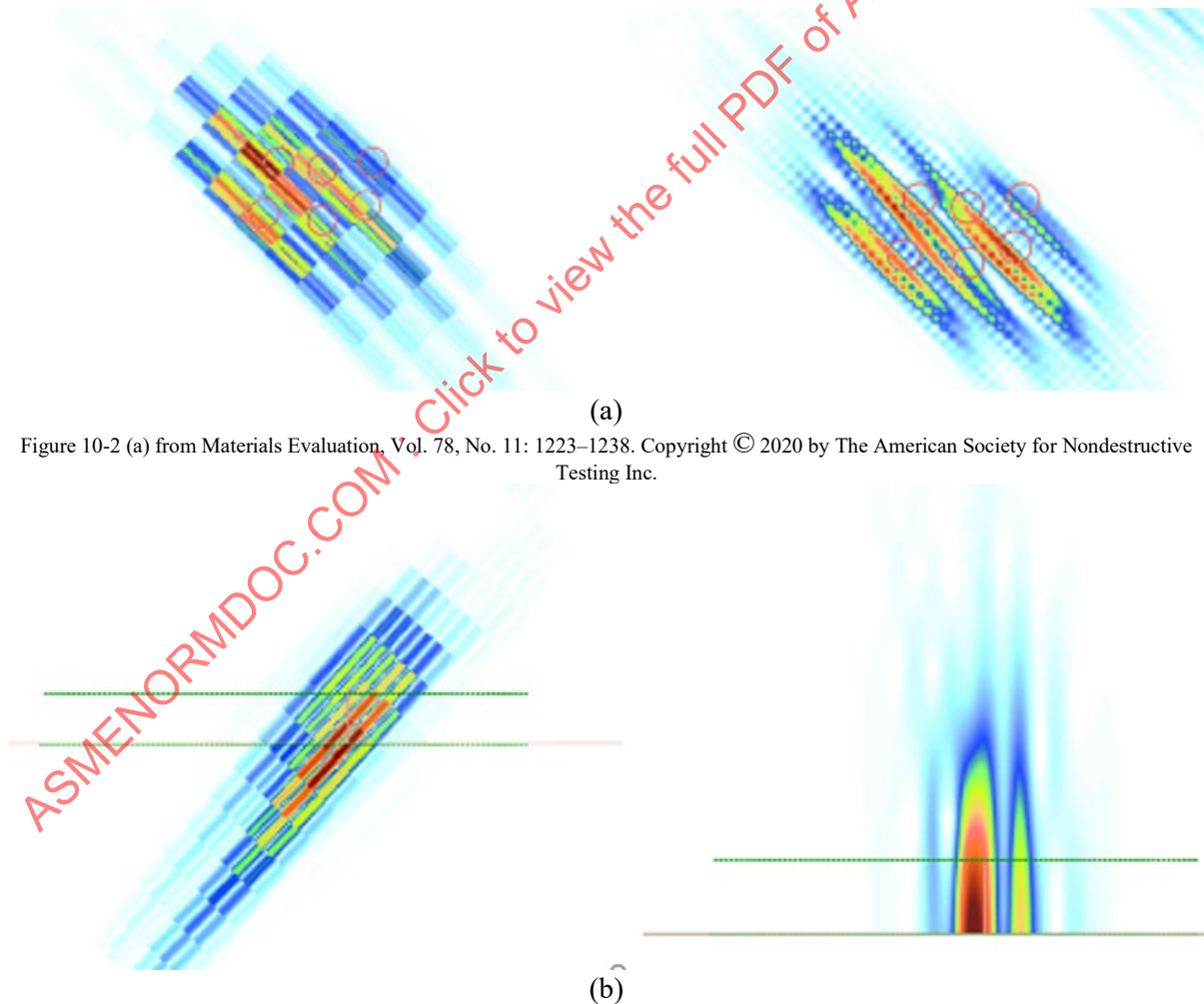


Figure 10-2 (a) from Materials Evaluation, Vol. 78, No. 11: 1223–1238. Copyright © 2020 by The American Society for Nondestructive Testing Inc.

Simulations predicted that HTHA micro damage is detectable only in the higher end of the investigated frequency range. Simulation results predicted that both PAUT and FMC/TFM 10 MHz techniques can

detect all damage, however the TFM/FMC technique was more precise at sizing micro indications including the height and separation SDH clusters. It was demonstrated that HTHA indications detected with higher frequency will be missing at the lower frequency range. Large macro HTHA damage may be detected and visualized using 5MHz techniques but the number of indications will be limited. For the notch, PAUT only detected the corner echo, and was not able to detect the tip, resulting in unreliable sizing. FMC/TFM detected the notch and revealed that TFM sizing is possible even when acquiring diffraction echoes is not probable. Regardless, the accuracy of sizing is dependent on the wavelength and array aperture.

#### 10.1.4 FMC Capabilities Validation

##### 10.1.4.1 Samples Selection and Preparation

The capabilities of ultrasonic array techniques were validated and qualified in three steps using a library of samples (1) with machined flaws, (2) with synthetic HTHA damage, and (3) removed from service during progressive validation and qualification.

Two carbon steel bars with micro-machined flaws were employed for the first validation step and the initial assessment of the techniques. Using micro-machined flawed samples allowed a comparison of ultrasonic findings with as-built dimensions without cutting the samples. 36 micro SDHs mimicking a volumetric damage were machined and grouped in three clusters. The height (diameter) of SDHs vary from 0.180 to 0.400 mm, SDHs vertical separations vary from 0.07 to 0.90 mm and overall cluster dimensions vary from 0.7 (length) x 1.3 (height) mm to 1.7 (length) x 3.0 (height) mm. Blister-like damage was represented by 6 shallow micro Flat Bottom Holes (FBH) with diameter and height (depth) less than 1mm. Crack-like indications were imitated by two step-wise flaws with height and length of the steps less than 1mm.

Two carbon steel blocks with synthetic HTHA damage were used in the second step. Initial block material was baseline tested using 15 MHz, 64 elements linear probe with FMC/TFM LL path technique. The baseline inspection verified that the material is free of micro/macro inclusions and laminations. Introducing synthetic damage in the validation samples permitted controlling the stage and spread of HTHA damage with less complexity. The samples were critical for optimizing the characterization capabilities of the techniques.

Samples from two vessels removed from service were investigated in the third step. The samples with in-service induced damage represent the unique HTHA morphology and localized manifestation at different stages and spreading across the components. These samples are very rare and difficult to collect. The samples with real HTHA damage were the most reliable source for assessing capabilities of the techniques before recommending widespread deployment in the field. Materials and process parameters of the vessels are presented in Table 10-4.

**Table 10-4: Vessels material and process parameters**

Vessel	Unit	Material	Wall Thickness, mm (in)	H2 Partial Pressure, MPa (psi)	Fluid Temperature, °C (°F)		Years in service
					In	Out	
Depentanizer reboiler channel	Hydro treater	C-0.5 Mo	14	1.5 (230)	400 (750)	385 (725)	53
Zinc oxide drum	Hydrogen plant	C-0.5 Mo	34	2.1 (337)	385 (725)	370 (700)	45

From Materials Evaluation, Vol. 78, No. 11: 1223–1238. Copyright © 2020 by The American Society for Nondestructive Testing Inc. Reprinted with permission.



Ten sections of a channel and eight large areas of a drum were selected for inspection. Multiple samples containing indications for potential HTHA damage were removed for destructive metallographic verification of the ultrasonic array findings. Precise EDM cuts and progressive grinding were used to validate the height and length extremes of the selected indications. Computed Tomography (CT) was used to verify the location and sizes of HTHA damage below the polished surface in the remnants of selected metallographic mounts.

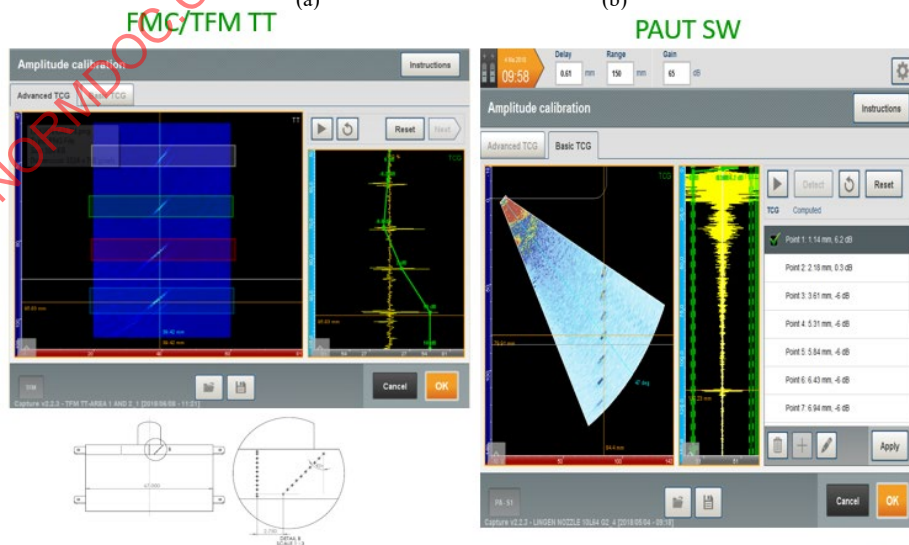
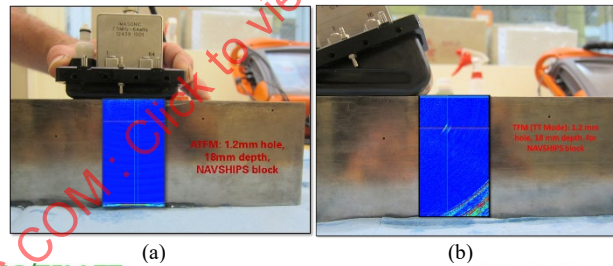
### 10.1.4.2 Experimental Setups

A battery powered, 64 channel, ultrasonic instrument with parallel architecture was used. The instrument was integrated with fully and semi-automated scanners for multiple array probe designs with solid wedges (Rexolite and Thermoplastic) and conformable (flexible) elastomer wedges filled with water. Normal beam L-wave array probes were used for inspection and damage verification on base material with all wedge designs, and on welds without removing the reinforcement (crown) with flexible wedge designs. Angle beam shear wave (SW) array probes were used for weld inspection and base material damage verification. The distance calibration, sensitivity, and amplitude fidelity check per ASME BPVC Section V - 2019 with and without Time-Corrected Gain (TCG) was completed on NAVSHIPS test block (AISI 1018 mild/low carbon steel), ASTM PAUT blocks, and SDHs fabricated in the test components.

### 10.1.4.3 Distance Calibration

Examples of calibrations using 1.2mm SDHs are shown in Figure 10-3.

**Figure 10-3: Calibrations: (a) normal beam (L-wave)–flexible wedge setup and L-L distance calibration imaging without TCG; (b) angle beam (S/T-wave)–flexible wedge setup and T-T distance calibration imaging without TCG; (c) angle beam (S/T-wave)–solid wedge setup, FMC/TFM T-T and PAUT SW distance calibration imaging with TCG.**



(c)

### 10.1.4.4 Amplitude Fidelity

The objective of the amplitude fidelity check was to prevent signal loss due to incorrect FMC/TFM properties, specifically grid density setting. The probe was positioned over the vertical row of 1mm diameter side drilled holes in the ASTM E2491 Phased Array Assessment Block. The probe was fixed on three different positions:

With the row of side drilled holes in the middle of the zone

With the row of side drilled holes approximately 2mm from the left edge of the zone

With the row of side drilled holes approximately 2mm from the right edge of the zone

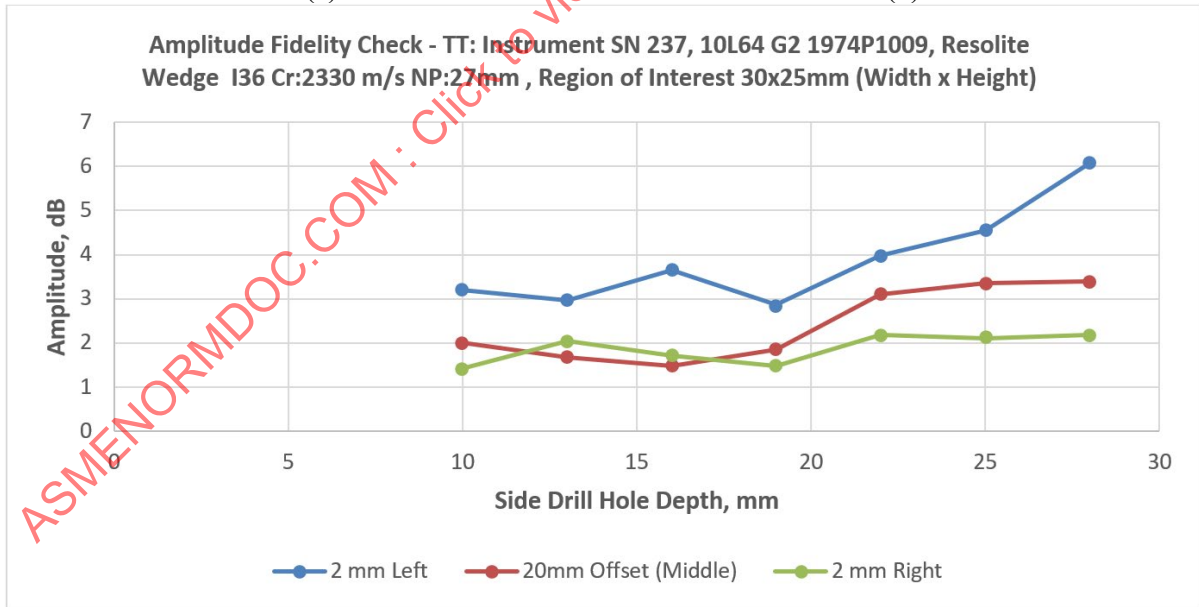
Examples of probe position and screen display for T-T path/mode, pseudo A-scans along a vertical line, and the ROI are shown in Figure 10-4.

**Figure 10-4: Amplitude fidelity: (a) setup and pseudo A-scans; (b) T-T path/mode ROI; (c) failed T-T with ROI 30x25mm (width x height); (d) passed T-T with ROI 25x25mm (width x height)**

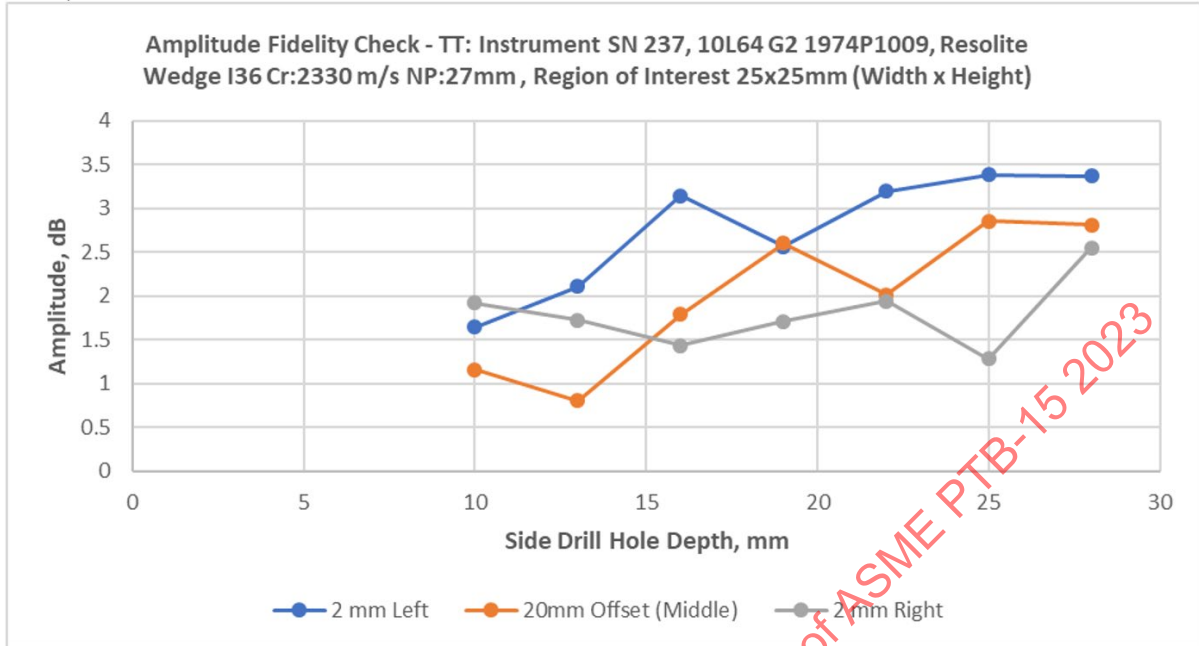


(a)

(b)



(c)



(d)

The side drilled hole with the highest amplitude was set to 80% screen height. The increment amount was calculated as 1/10 of the wavelength. Amplitude fidelity verification was completed in four steps for each of the three probe positions. The results were tabulated and AF for each side drilled hole was calculated as:

$$AF = 20 \log(\text{highest value}[\%]/\text{lowest value}[\%])$$

The procedure was considered successfully passed if AF values for each probe position were below 4dB (i.e.,  $\pm 2\text{db}$ ). Examples of failed and successfully passed AF verifications using 10 MHz, 64 elements linear array probe and grid increments 0.03mm ( $1/10 \lambda$ ) for T-T path/mode are shown in Figure 10-4(c) and Figure 10-4(d).

#### 10.1.4.5 Sensitivity and Resolution

A general rule of thumb for this application was that HTHA damage must be larger than one-half of the wavelength ( $\lambda$ ) to be detected and separated using at least one of the selected array techniques.

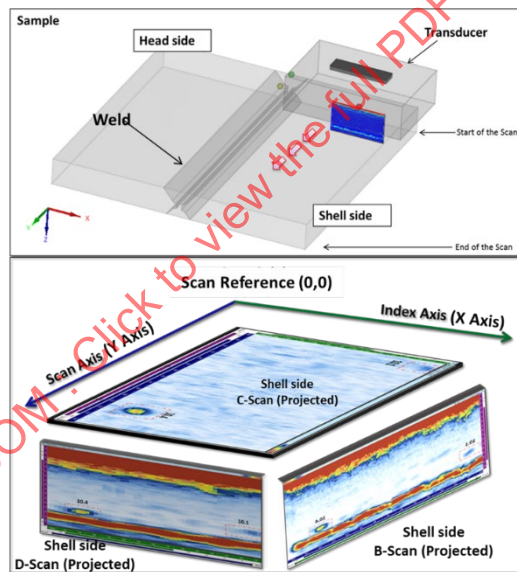
PAUT sensitivity and resolution were limited to half wavelength (for Carbon Steel, 10 MHz SW: 0.16mm/160 $\mu\text{m}$ ) and the focal spot size. Classical TFM sensitivity and resolution were limited to one-tenth of the wavelength and RoI grid's density (for Carbon Steel, 10 MHz SW, 497x497 grid points in 25x25mm RoI: 0.016mm/16 $\mu\text{m}$ ). Theoretical pixel size limit of  $0.28\lambda$  ( $\sim \lambda/3.6$ ) was used for calculations of pixel size and resolution (wavelength ratio) for selected RoI employed in this application. The pixel size and resolution/wavelength ratio for selected RoI are summarized in Table 10-5. For the desired mode (L or S/T) and frequency the highlighted in green and yellow RoI sizes are recommended for passing AF check. A wizard was developed for calculation of the right RoI using a similar approach and is integrated in the advanced software package.

**Table 10-5: Pixel Size and Resolution/Wavelength Ratio for selected RoI**

Probe Frequency, MHz	L-Wave Wavelength, mm ( $v = 5900\text{m/s}$ )	Theoretical pixel size limit ( $0.28\lambda$ ), mm	Resolution or Pixel Size, mm and (Resolution/Wavelength) Ratio							
			RoI 10x10mm 497x497	RoI 25x25mm 497x497	RoI 50x50mm 497x497	RoI 75x75mm 497x497	RoI 100x100mm 497x497	RoI 125x125mm 497x497	RoI 150x150mm 497x497	RoI 200x200mm 497x497
			pixel size = 0.02	pixel size = 0.05	pixel size = 0.10	pixel size = 0.15	pixel size = 0.20	pixel size = 0.25	pixel size = 0.30	pixel size = 0.40
5	1.18	0.33	0.02 $\lambda$	0.04 $\lambda$	0.09 $\lambda$	0.13 $\lambda$	0.17 $\lambda$	0.21 $\lambda$	0.26 $\lambda$	0.34 $\lambda$
7.5	0.79	0.22	0.03 $\lambda$	0.06 $\lambda$	0.13 $\lambda$	0.19 $\lambda$	0.26 $\lambda$	0.32 $\lambda$	0.38 $\lambda$	0.51 $\lambda$
10	0.59	0.16	0.03 $\lambda$	0.09 $\lambda$	0.17 $\lambda$	0.26 $\lambda$	0.34 $\lambda$	0.43 $\lambda$	0.51 $\lambda$	0.68 $\lambda$
Probe Frequency, MHz	SW/ T-Wave Wavelength, mm ( $v = 3240\text{m/s}$ )	Theoretical pixel size limit ( $0.28\lambda$ ), mm	Resolution or Pixel Size, mm and (Resolution/Wavelength) Ratio							
			RoI 10x10mm 497x497	RoI 25x25mm 497x497	RoI 50x50mm 497x497	RoI 75x75mm 497x497	RoI 100x100mm 497x497	RoI 125x125mm 497x497	RoI 150x150mm 497x497	RoI 200x200mm 497x497
			pixel size = 0.02	pixel size = 0.05	pixel size = 0.10	pixel size = 0.15	pixel size = 0.20	pixel size = 0.25	pixel size = 0.30	pixel size = 0.40
5	0.648	0.18	0.03 $\lambda$	0.08 $\lambda$	0.16 $\lambda$	0.23 $\lambda$	0.31 $\lambda$	0.39 $\lambda$	0.47 $\lambda$	0.62 $\lambda$
7.5	0.432	0.12	0.05 $\lambda$	0.12 $\lambda$	0.23 $\lambda$	0.35 $\lambda$	0.47 $\lambda$	0.58 $\lambda$	0.7 $\lambda$	0.93 $\lambda$
10	0.324	0.09	0.06 $\lambda$	0.16 $\lambda$	0.31 $\lambda$	0.47 $\lambda$	0.62 $\lambda$	0.78 $\lambda$	0.93 $\lambda$	1.24 $\lambda$

Line and/or raster scanning for data collection and typical C- (Top View), B- (T- or End View), D- (Side or Front View) scans were used for localization and sizing of HTHA damage—Figure 10-5. In addition, PAUT S- scan (view) and single plane TFM view were used for sizing verification. Data collection scans were performed at multiple frequencies and 12dB above the reference gain.

**Figure 10-5: Scanning plans and typical C-, B-, D- views**



The first step of the analysis was detection to i) identify the presence or absence of HTHA damage or metallurgical imperfections and ii) characterization. The analysis was performed at the reference gain or with reduced 3-6dB gain. Simulations predicted that HTHA micro damage is detectable only in the higher end of the investigated frequency range. The same HTHA indications will be missing at the lower frequency range. Large macro HTHA damage may be detected and visualized using 5MHz techniques, but the number of indications will be limited. When a mix of metallurgical imperfections and micro/macro HTHA damage was present multiple UT techniques, 3D visualization, and segmentation were used to improve the characterization process and differentiate HTHA damage from metallurgical imperfections.

The second step of the analysis was sizing. Tip diffraction technique was used for damage height sizing when the tip was detected and imaged. The 6dB or 3dB drop techniques were used for damage height sizing when the tip was not detected. The same techniques were used for length sizing.

The best results were achieved following these rules:

Use the highest practical frequency for a specific base material, weld, and wall thickness

Work in the near field (aperture and frequency dependent)

Use the smallest beam spot for PAUT (aperture and frequency dependent)

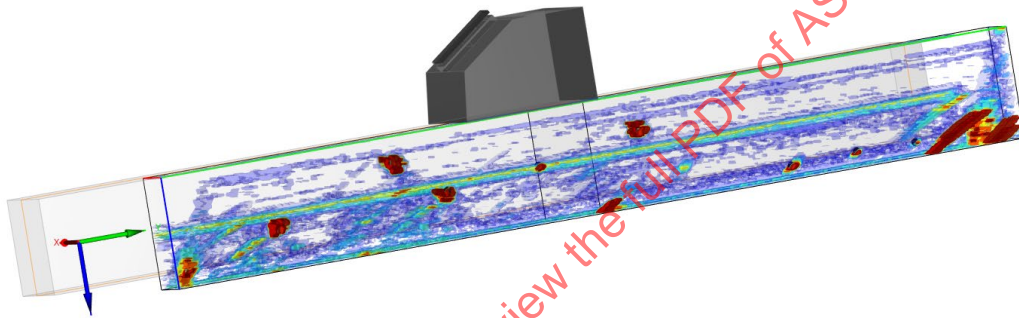
Use the highest density grid in RoI for FMC/TFM/ATFM (RoI size and number of pixels dependent).

#### 10.1.4.6 Investigation of Samples with Machined Flaw

The capabilities of PAUT sectorial scanning and FMC/TFM/ATFM (L-L and T-T paths) techniques were initially validated using samples with micro-machined flaws with known sizes and separation.

Two carbon steel bars with micro and macro machined flaws were used for the initial assessment of the techniques. 3D FMC/TFM T-T view of the bar and flaws is shown in Figure 10-6.

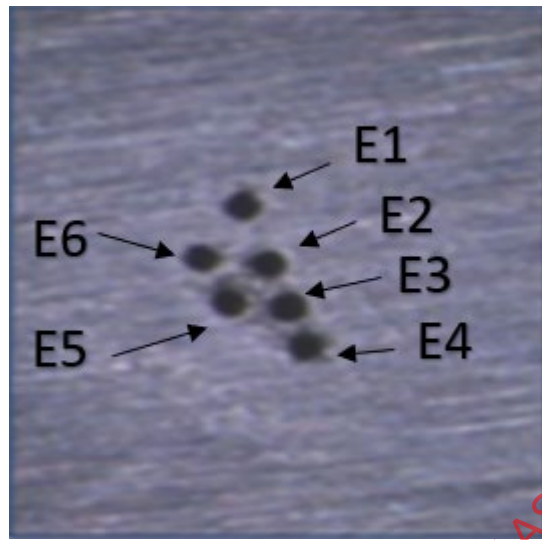
**Figure 10-6: FMC/TFM 3D imaging of carbon steel bar with machined flaws**



The 7.5 and 10 MHz FMC/TFM T-T techniques detected all 36 micro flaws, grouped in three clusters. Only 10 MHz FMC/TFM T-T technique separated all micro SDHs grouped in the clusters. A grid density of 256x256 pixels for two RoIs (25x25mm and 5x5mm) were investigated. A picture of cluster E is shown in Figure 10-7. Cluster E consists of the six smallest micro SDHs, with overall cluster dimensions 0.7 (length) x 1.3 (height) mm, height (diameter) of each SDH is 0.180 +/- 0.060mm and SDHs vertical separations vary from 0.07 to 0.90 mm. In the same figure, TFM imaging of the cluster from two directions (skew 90 and skew 270) are shown.

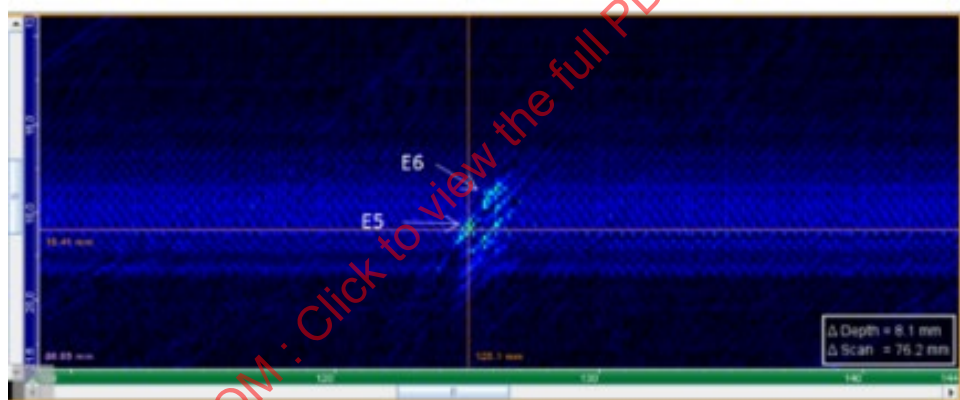


Figure 10-7: Example of micro-machined clustered flaws: (a) picture; (b) skew 90 TFM imaging; (c) skew 270 TFM imaging

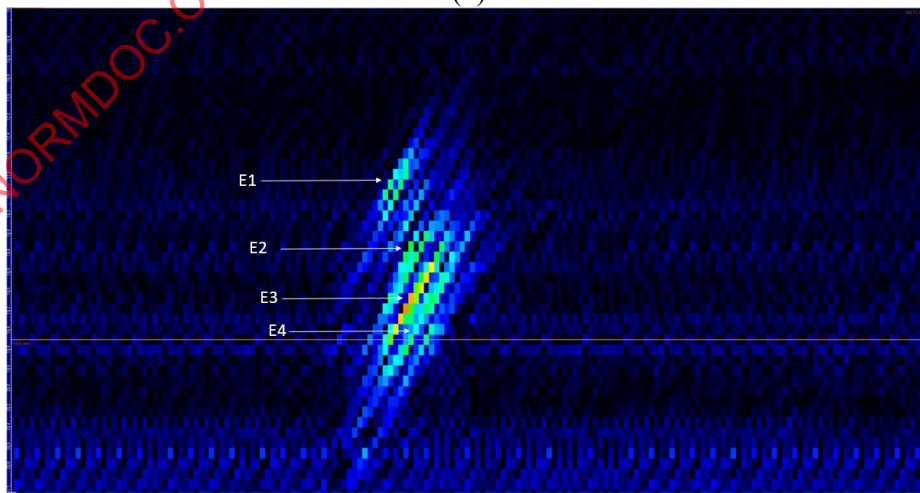


(a)

Figure 10-7 (a) from Materials Evaluation, Vol. 78, No. 11: 1223–1238. Copyright © 2020 by The American Society for Nondestructive Testing Inc. Reprinted with permission.



(b)



(c)

A comprehensive imaging analysis of the clusters and each SDH was performed for two RoIs. Absolute TFM measurements and errors for the height and vertical separations are summarized in Table 10-6 and Table 10-7.

**Table 10-6: Clusters and SDHs height measurements using 10 MHz T-T path/mode**

Indication	H-As Built, mm (As Built - optically measured vertical extend, height = diameter)	H-UT, mm (UT measured vertical extend /height = diameter)	RoI - 25x25mm		RoI - 5x5mm		
			$\Delta H, \text{ mm [Error = (UT measured vertical extend) - (As built)]}$	$\Delta H, \% ; \{\text{Error, \%} = [(UT \text{ measured vertical extend}) - (As built)] / As \text{ built } \times 100\}$	$\Delta H, \text{ mm [Error = (UT measured vertical extend) - (As built)]}$	$\Delta H, \% ; \{\text{Error, \%} = [(UT \text{ measured vertical extend}) - (As built)] / As \text{ built } \times 100\}$	
B (Cluster)	3.06	3.2	0.14	4.58%	3.3	0.24	7.84%
B1	0.4	0.8	0.4	100.00%	0.41	0.01	2.50%
B2	0.4	0.5	0.1	25.00%	0.42	0.02	5.00%
B3	0.4	0.4	0	0.00%	0.49	0.09	22.50%
B4	0.4	0.6	0.2	50.00%	0.53	0.13	32.50%
B5	0.4	0.5	0.1	25.00%	0.4	0	0.00%
B6	0.4	0.4	0	0.00%	0.5	0.1	25.00%
D (Cluster)	2.9	3.4	0.5	17.24%	2.8	-0.1	-3.45%
D1	0.24	0.5	0.26	108.33%	0.28	0.04	16.67%
D2	0.24	0.4	0.16	66.67%	0.35	0.11	45.83%
D3	0.24	0.3	0.06	25.00%	0.3	0.06	25.00%
D4	0.24	0.7	0.46	191.67%	0.44	0.2	83.33%
D5	0.24	0.3	0.06	25.00%	0.3	0.06	25.00%
D6	0.24	0.2	-0.04	-16.67%	0.35	0.11	45.83%
E (Cluster)	1.51	2.2	0.69	45.70%	1.8	0.29	19.21%
E1	0.18	0.3	0.12	66.67%	0.2	0.02	11.11%
E2	0.18	0.2	0.02	11.11%	0.19	0.01	5.56%
E3	0.18	0.4	0.22	122.22%	0.23	0.05	27.78%
E4	0.18	N/A	N/A	N/A	0.21	N/A	N/A
E5	0.18	0.2	0.02	11.11%	0.23	0.05	27.78%
E6	0.18	0.5	0.32	177.78%	0.19	0.01	5.56%

The clusters, simulating micro flaws concentrated in the vertical extend range from 1mm to 3mm, were oversized with up to 20% error when 5x5mm RoI was used and up to 50% when 25x25mm RoI was used. Single SDHs, simulating micro flaws in the range from 0.180 to 0.400mm (from 180 to 400µm) +/- 0.060mm (60µm) were oversized in an average with 20-50% error when 5x5mm RoI was used and in an average with 50-100% when 25x25mm RoI was used. The height measurements using 5x5mm RoI were very accurate as the spatial resolution was improved by the ROI pixel resolution; the height measurements using 25x25mm RoI were still acceptable considering the microscopic flaw size.

**Table 10-7: SDHs vertical separation measurements using 10 MHz T-T path/mode**

Vertical Separation (Through Wall Separation)	SH-As Built, mm (As Built - optically measured separation in vertical direction)	SH-UT, mm (UT measured separation in vertical direction)	$\Delta$ SH, mm [Error= (UT measured separation in vertical direction)- (As built	$\Delta$ SH, % ; {Error,% = [(UT measured vertical separation)-(As built)]/As built x100}	SH-UT, mm (UT measured separation in vertical direction)	$\Delta$ SH, mm [Error= (UT measured separation in vertical direction)- (As built	$\Delta$ SH, % ; {Error,% = [(UT measured vertical separation)-(As built)]/As built x100}
			RoI - 25x25mm			RoI - 5x5mm	
B1-B2	0.74	0.7	-0.04	-5.41%	0.8	0.06	8.11%
B2-B3	0.84	0.8	-0.04	-4.76%	0.9	0.06	7.14%
B3-B4	1.1	1	-0.1	-9.09%	1.1	0	0.00%
B5-B6	0.87	0.9	0.03	3.45%	0.8	-0.07	-8.05%
B6-B1	0.97	1	0.03	3.09%	0.9	-0.07	-7.22%
D1-D2	0.74	0.7	-0.04	-5.41%	0.8	0.06	8.11%
D2-D3	0.84	0.8	-0.04	-4.76%	0.8	-0.04	-4.76%
D3-D4	1.1	1.1	0	0.00%	1.1	0	0.00%
D5-D6	0.87	0.9	0.03	3.45%	0.9	0.03	3.45%
D6-D1	0.97	1	0.03	3.09%	0.8	-0.17	-17.53%
E1-E2	0.41	0.5	0.09	21.95%	0.4	-0.01	-2.44%
E2-E3	0.53	0.8	0.27	50.94%	0.6	0.07	13.21%
E3-E4	0.37	0.4	0.03	8.11%	0.4	0.03	8.11%
E5-E6	0.43	0.4	-0.03	-6.98%	0.5	0.07	16.28%
E6-E1	0.41	0.4	-0.01	-2.44%	0.5	0.09	21.95%

The errors for separation measurements were less than 20% using 5x5mm RoI and less than 50% using 25x25mm RoI. The vertical separation measurements using both RoI are very accurate for the range of 0.4-1.1mm as built separation.

A good agreement between the simulation predictions and TFM experimental sizing and separation measurements was demonstrated using samples with micro-machined flaws with known sizes and separation.

**10.1.4.7 Investigation of Samples with Synthetic HTHA Damage**

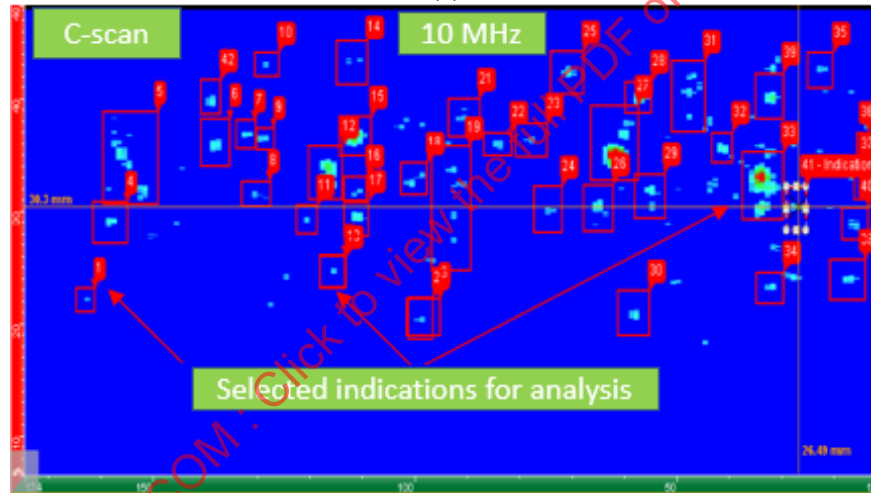
In the second investigation step, the capabilities of PAUT sectorial scanning and FMC/TFM/ATFM (L-L and T-T paths) techniques were validated using samples containing synthetic HTHA damage with controlled distribution and morphology.

Two carbon steel blocks with synthetic HTHA damage were used in the second step for assessing capabilities of the ultrasonic array techniques. Initial block material was baseline tested using 15 MHz, 64 elements linear probe with FMC/TFM LL path technique. The baseline inspection verified that the material is free of micro/macro inclusions and laminations. The baseline inspection results at selected single planes are shown in Figure 10-8 (a). The blocks were low frequency inspected using the array techniques after the synthetic HTHA damage was introduced. The best detection results were obtained using 10MHz linear and matrix probes, FMC/TFM technique in LL path/mode. 10MHz FMC/TFM projected C-scan is shown in Figure 10-8 (b). More than 100 micro and macro indications were identified (boxed). Only 30% of the indications were observed on projected C-scan created by using a lower frequency 7.5 MHz linear array probe (Figure 10-8 [c]) and only 10% of the indications were detected when using 5 MHz linear array probe (Figure 10-8 [d]). These images demonstrated the decrease in detectability and resolution at lower frequency and the potential increase of the sizing error.

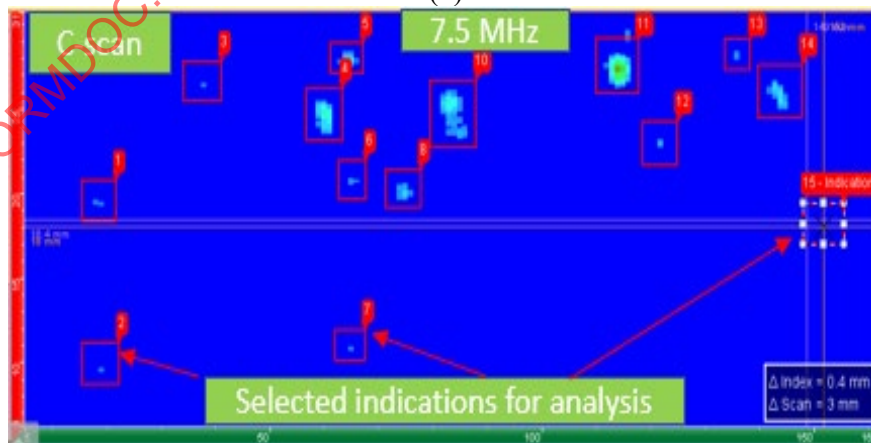
**Figure 10-8: FMC/TFM LL imaging: (a) 15MHz imaging of non-damage block–pseudo A scan (top left), single plane B-scan (top right), single plane D-scan (bottom); (b) 10MHz projected C-scan of damage block; (c) 7.5MHz projected C-scan of damage block; (d) 5MHz projected C-scan of damage block; (e) 10MHz split screen imaging of selected indication: projected C-scan (left top), single plane B-scan (top right), single plane D-scan (bottom right), pseudo A-scan (bottom left).**



(a)



(b)



(c)

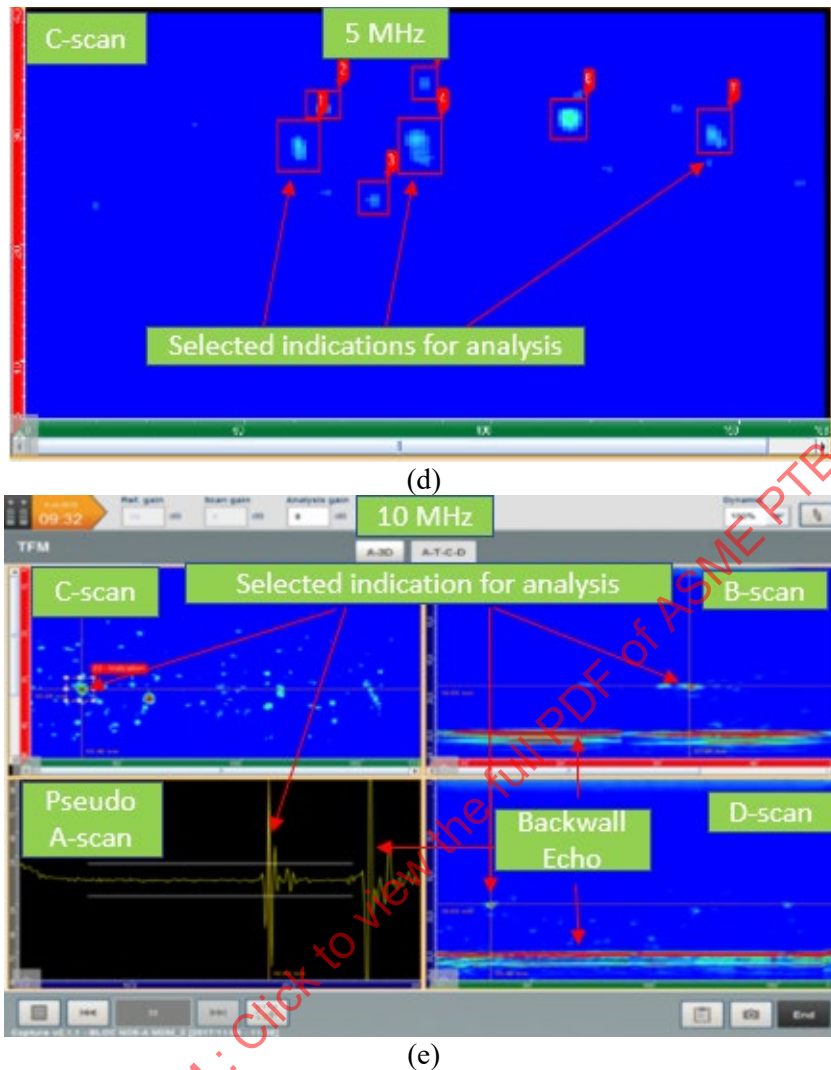


Figure 10-8 (b), (c), (d), (e) from Materials Evaluation, Vol. 78, No. 11: 1223–1238. Copyright © 2020 by The American Society for Nondestructive Testing Inc. Reprinted with permission.

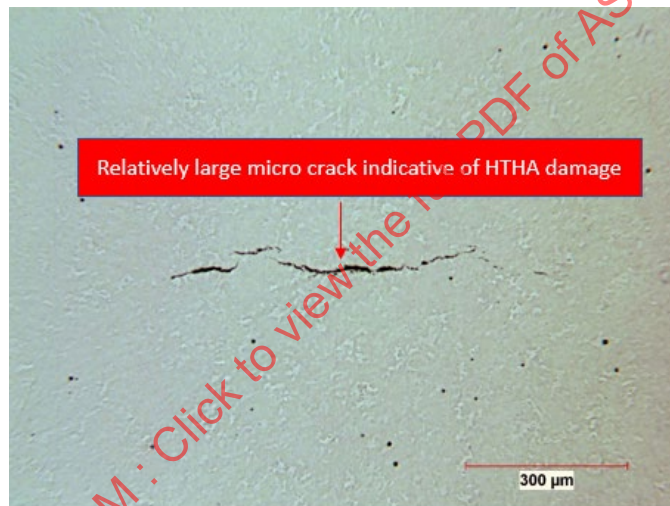
Figure 10-8 (e) illustrates a split screen analysis using C-scan, single plane B- and D-scan, and pseudo A-scan. One large indication of HTHA micro damage was selected for analysis and boxed in the projected top view image shown in the top-left corner of Figure 10-8 (e). The red color of the image indication is a sign of strong reflected and diffracted signals from the damage and was confirmed by pseudo A-scan (Figure 10-8 [e] bottom-left). The same indication is marked with a crossing of x/y measuring cursors in the single plane side view (Figure 10-8 [e] top-right) and front view (Figure 10-8 [e] bottom-right). This indication is relatively near to the hot surface of the block that was exposed to hydrogen. The estimated length of the indication in TFM front view was  $\sim 0.7\text{mm}$  ( $\sim 700\mu\text{m}$ ). Multiple small indications of HTHA volumetric damage were observed in both planes and are represented by light blue dots.

The presence and the length of  $\sim 0.7\text{mm}$  ( $\sim 700\mu\text{m}$ ) indication was validated at low magnification ( $\sim 100\text{X}$ , As-polished) using optical microscopy—Figure 10-9 (a). Optical microscopy at lower magnification in Figure 10-9 (b) displayed a smaller  $\sim 0.1\text{mm}$  ( $\sim 100\mu\text{m}$ ) fissure forming isolated microcrack below to the larger microcrack. The separation between these microcracks are larger than the pixel size and allows it to be visualized as isolated indications. Scanning Electron Microscopy (SEM) at higher magnification ( $\sim 5000\text{X}$ ) revealed damage features  $\sim 0.010\text{mm}$  ( $\sim 10\mu\text{m}$ ) showing grain

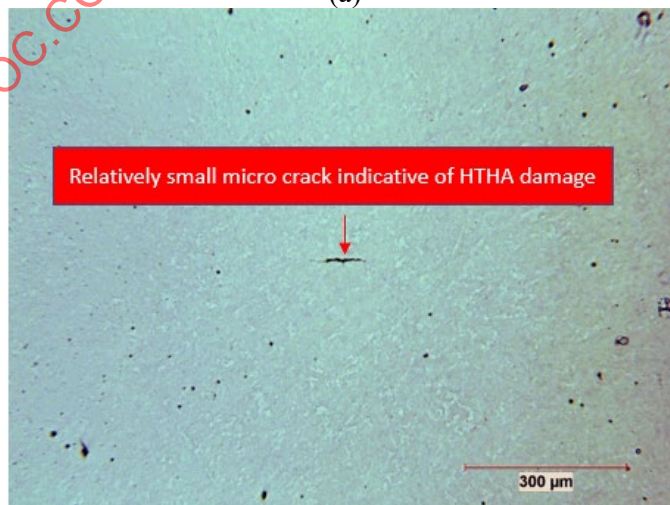


boundary void formation and some early stages of coalescence of voids in the periphery of the main feature—Figure 10-9 (c). No evidence was obtained to verify that any of the investigated techniques are capable to detect linking voids at one grain boundary or clustered linking voids in a small volume. If limited fissures start forming small micro crack in the clustered linking voids along 5-10 damaged grain boundaries the detectability probably is enhanced. This type of early stages volumetric damage is possibly visualized as a blue haze and cloudy area around internal large microcracks and macrocracks or adjacent to the bar surface exposed to the hydrogen (Figure 10-8 [e] right). This surface of the bar is acting as a backwall for ultrasound and is represented by the solid red line in the front and side view images. A damage feature showing severe dissolution of grain boundaries and some early stage of single sub-micron void formation are presented in Figure 10-9 [d]. Sub-micron void formations are not detectable by any of the techniques evaluated in this study.

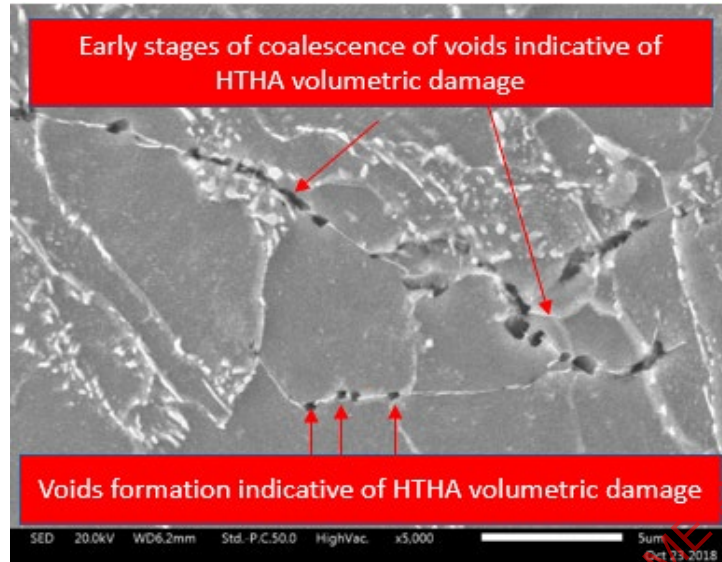
**Figure 10-9: Optical microscopy and SEM imaging of accelerated HTHA damage: (a) ~100X; as-polished; fissures forming relatively large micro crack; (b) ~100X; as-polished; fissures forming small micro crack; (c) ~5000X; Nital Etchant; SEM photograph of damage feature showing grain boundary void formation and some early stages of coalescence of voids in the periphery of the main feature; (d) ~5000X; Nital Etchant; SEM photograph of damage feature showing severe dissolution of grain boundaries and some early stage of single void formation.**



(a)

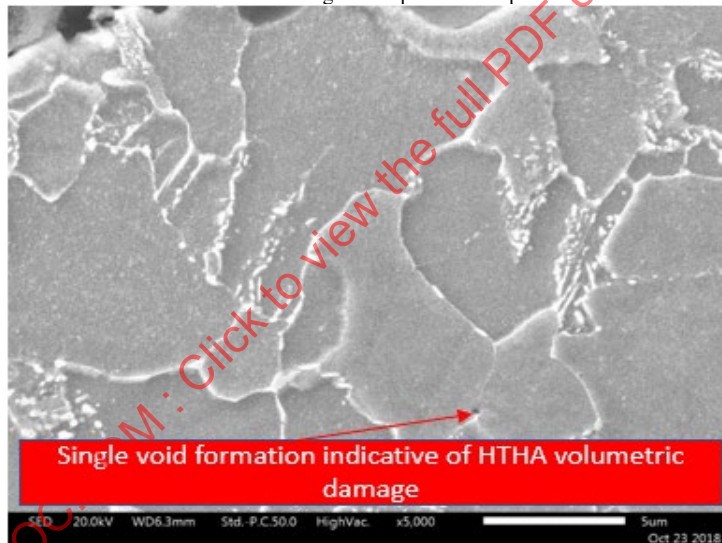


(b)



(c)

Figure 10-9 (a), (b), (c) from Materials Evaluation, Vol. 78, No. 11: 1223–1238. Copyright © 2020 by The American Society for Nondestructive Testing Inc. Reprinted with permission.



(d)

It was validated that 10 MHz FMC/TFM LL path technique can detect and size better synthetic HTHA damage oriented parallel to ID comparing with T-T path technique and lower frequency LL techniques.

#### 10.1.4.8 Investigation of Samples Removed from Service (Progressive Validation)

In the third investigation step, the capabilities of PAUT sectorial scanning and FMC/TFM/ATFM (L-L and T-T paths) techniques were assessed using samples removed from service with real, localized and complex HTHA damage at different stages and morphology.

The setups for fully automated PAUT and FMC/TFM of the vessels are shown in Figure 10-10.

**Figure 10-10: Setup for fully automated PAUT and FMC/TFM: (a) depentanizer reboiler channel; (b) zinc oxide drum**

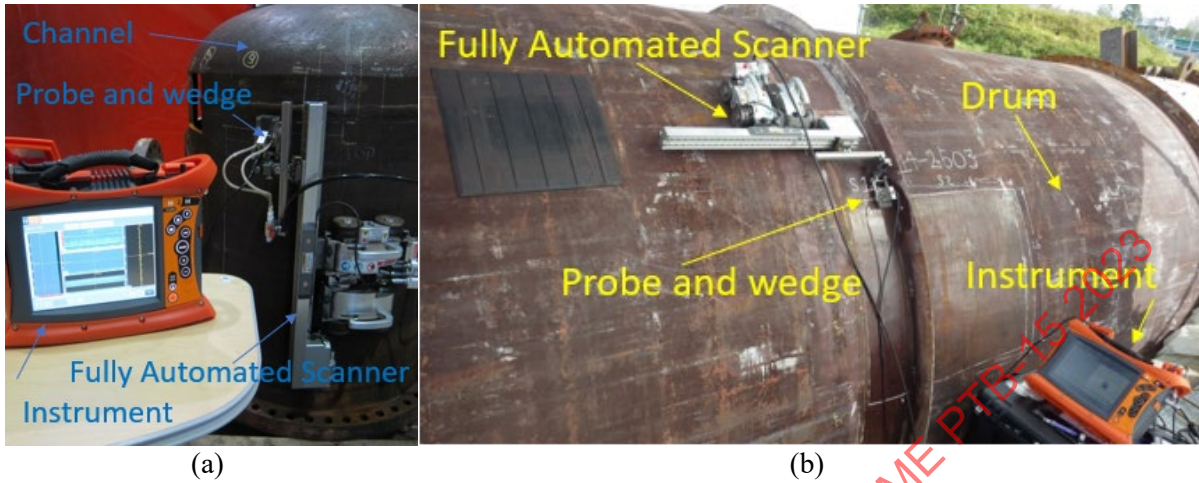


Figure 10-10 (b), from Materials Evaluation, Vol. 78, No. 11: 1223–1238. Copyright © 2020 by The American Society for Nondestructive Testing Inc. Reprinted with permission.

**Channel welds:**

Potential HTHA blistering, micro and macro cracking indications were detected in the channel welds using 10 MHz linear probe, FMC/TFM T-T technique. Multiple indications were detected in the HAZ of the most susceptible section of the shell to head circumferential weld. RoI width was extended to cover the HAZ of the weld at the head side.

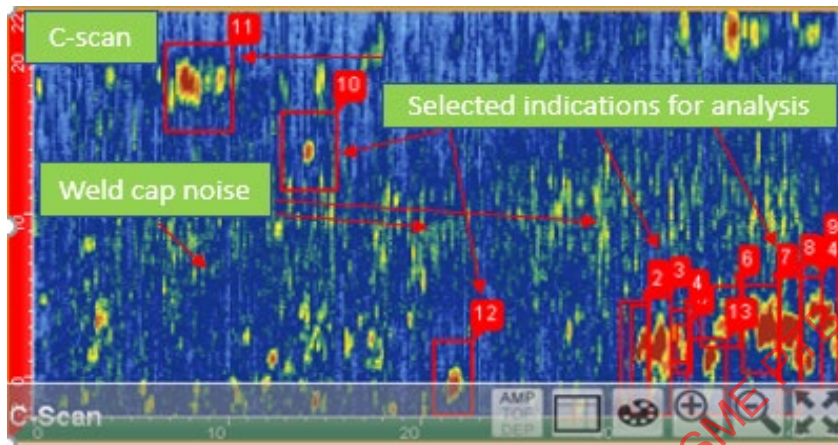
Similar micro and macro indications were observed on the head side, but the severity was lower compared to the shell side. The largest indications selected for a detailed analysis are shown in Figure 10-11 (a).

The analysis results for indication #2 (boxed in the right bottom corner of Figure 10-9 [a]) are shown in the split screen views of Figure 10-11 (b). B-scan image (Figure 10-11 [b] top-left) analysis displays a root crack with 5mm height representing 34% wall thickness (WT) damage. The intersections of the vertical and horizontal cursors on C-scan (Figure 10-11 [b] bottom-left), D- cumulative scan (Figure 10-11 [b] bottom-right) and D- scan single plane (Figure 10-11 [b] top-right) are showing the location of the same crack-like indication. The elongated red areas on the right side of C-scan and D-scans represent potentially breaking macro cracking at the root.

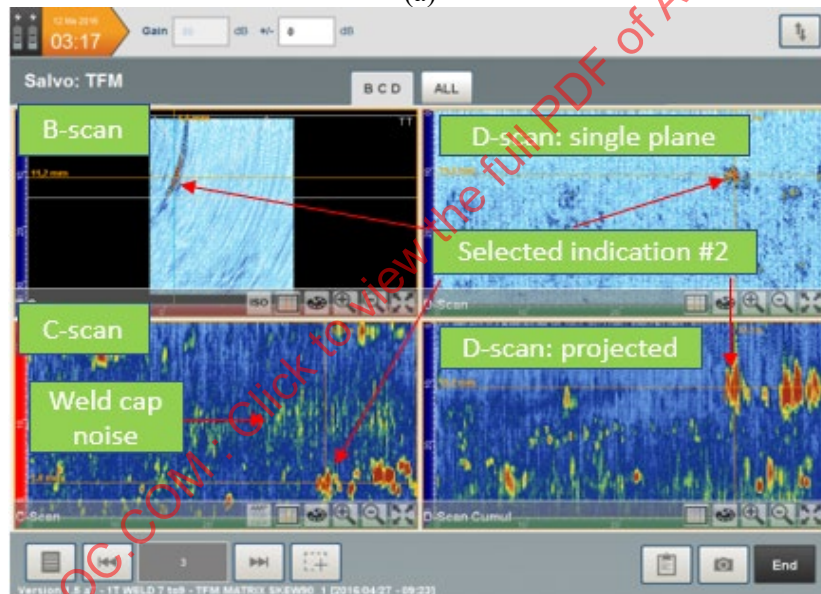
The clusters of blue dots in the single plane D-scan represent an early stage of HTHA damage. Indications of potential facets of HTHA damage was detected at skew  $-10^{\circ}$  in the breaking areas using matrix probe and S-scan—Figure 10-11 (c). The matrix probe results in the second focalization plane indicate that the root crack is potentially continuous.



**Figure 10-11: 10 MHz T-T FMC/TFM and PAUT techniques imaging of HTHA weld damage: (a) linear probe C-scan and identification of the indications; (b) linear probe split screen views of indication #2; (c) indication of potential HTHA damage detected in the breaking areas using matrix probe and S-scan at skew-10°**

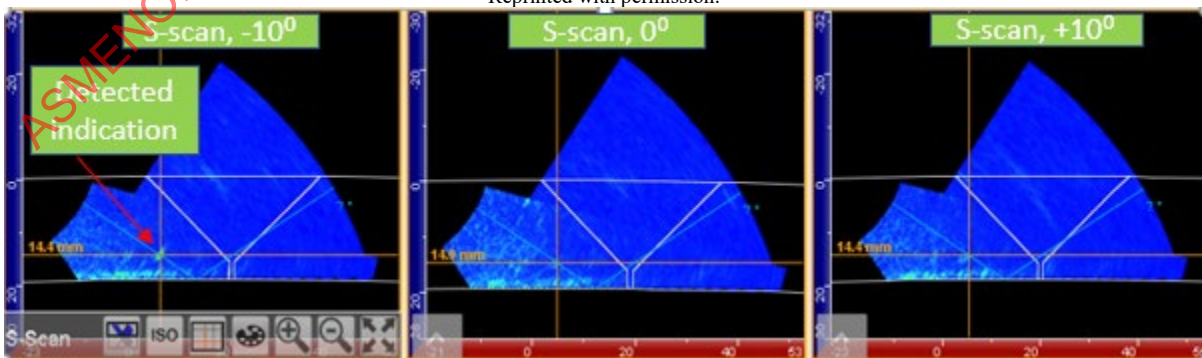


(a)



(b)

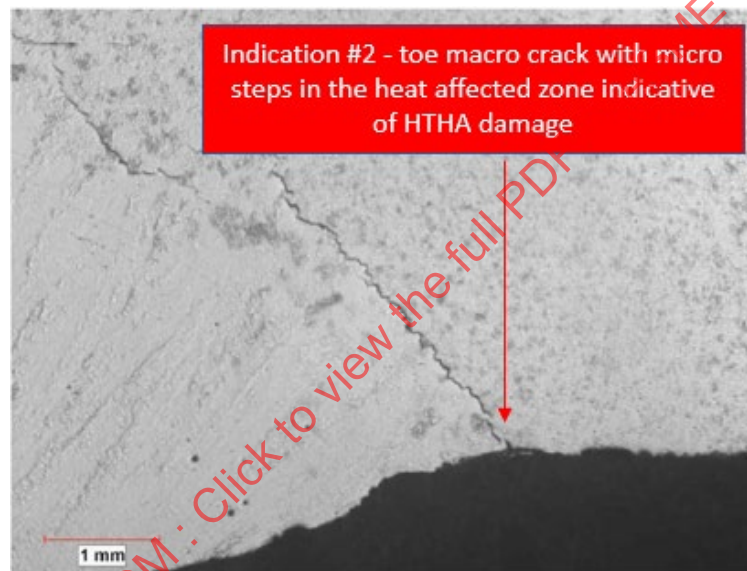
From Materials Evaluation, Vol. 78, No. 11: 1223–1238. Copyright © 2020 by The American Society for Nondestructive Testing Inc. Reprinted with permission.



(c)

The metallographic investigation verified the presence of root cracking, stepwise cracking and blistering with cracking edges. A cross-section image of the root crack is shown in Figure 10-12 (a). Optical metallography confirmed matrix probe findings that the crack in HAZ is a continuous macrocrack along the weld starting from indication #2 and finishing at the end of the scan. Macro stepwise cracking was observed in the base material adjacent to the root crack – Figure 10-12 (b). Microscopic and macro blistering with cracking edges was documented near to ID – Figure 10-12 (c). Voids and linked voids as an indication of volumetric HTHA damage were observed at the tips of the cracks and blisters at higher magnification – Figure 10-12 (d). Single sub-micron voids and sub-micron linking voids were not detected with any array techniques. Stress-related micro cracks were observed at the same magnification (Figure 10-12 [e]), but it was not possible to distinguish HTHA crack-like damage from stress-related micro cracking with ultrasonic techniques.

**Figure 10-12: Weld damage validation using optical metallography and SEM: (a) root cracking (~20X, Nital etched); (b) stepwise macro cracking (~40X, Nital etched); (c) blisters (~40X, Nital etched); (d) voids along grain boundaries (~2,000X, Nital etched-left; ~20,000X, Nital etched-right); (e) stress-related micro cracking (~1,000X, Nital etched).**



(a)



(b)



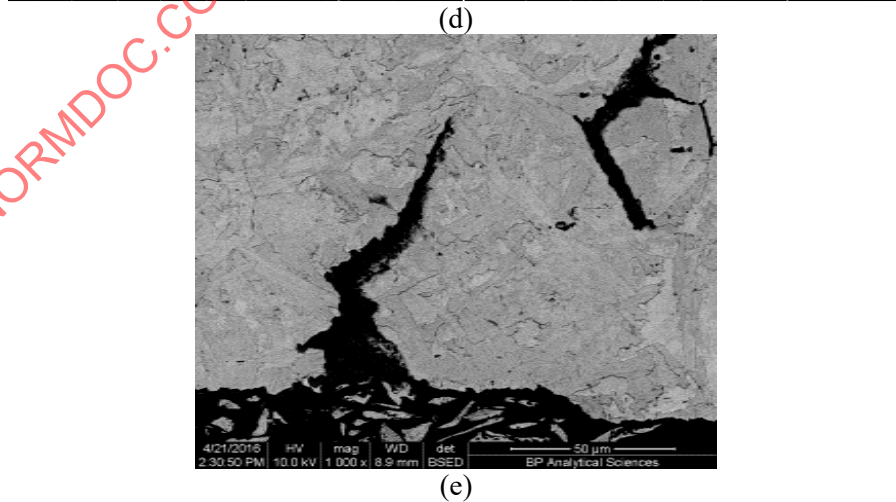
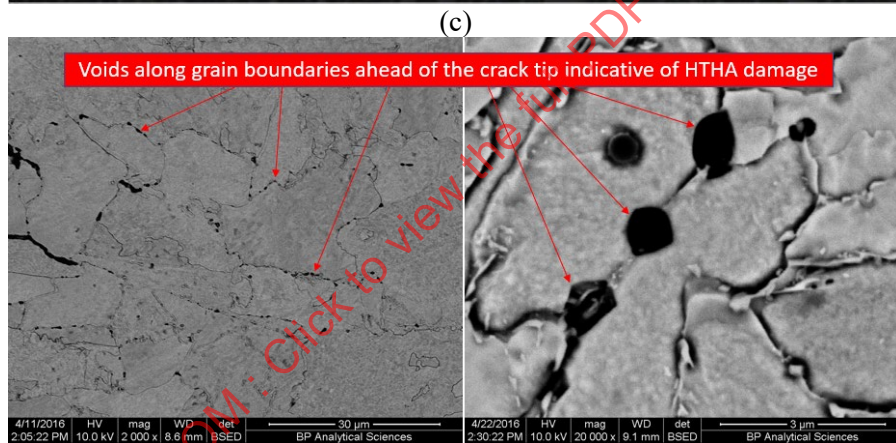
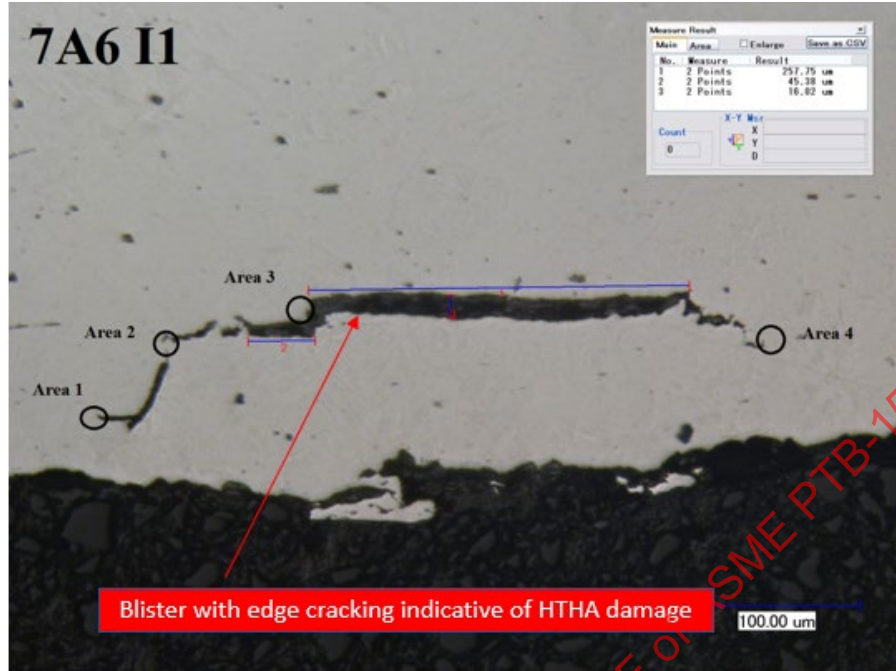


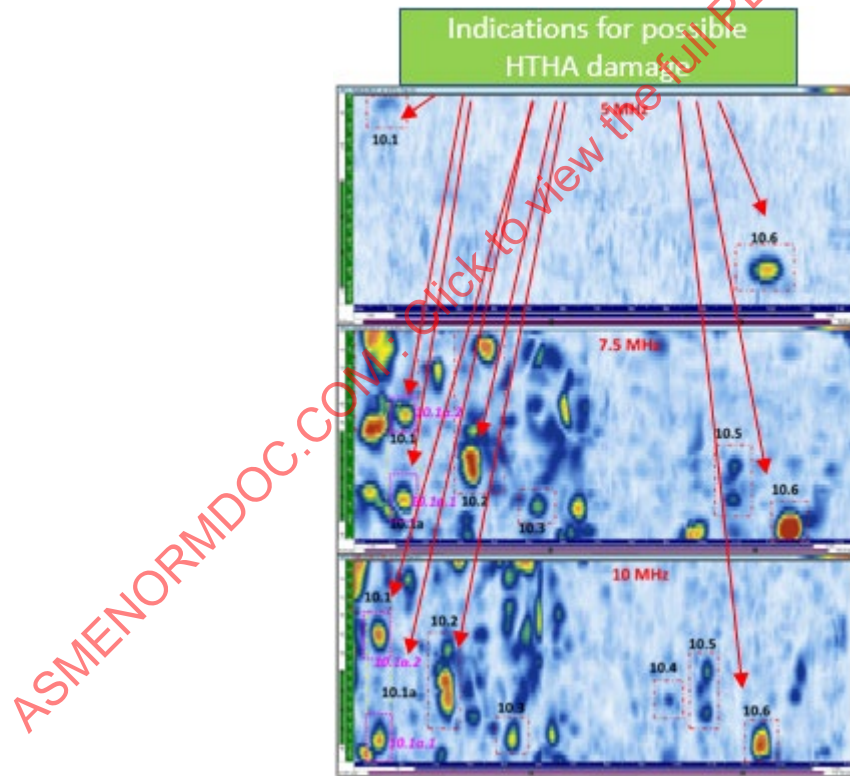
Figure 10-12 (a), (c), (d) from Materials Evaluation, Vol. 78, No. 11: 1223–1238. Copyright © 2020 by The American Society for Nondestructive Testing Inc. Reprinted with permission.

Channel base material:

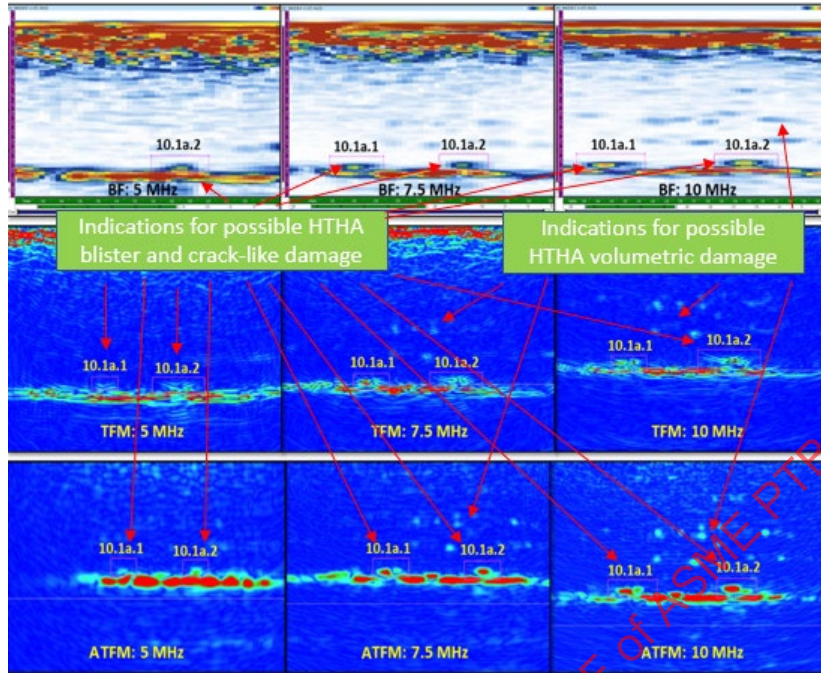
An example of identification (boxing) of the potential HTHA damage in C-scan projected views using PAUT 5-7.5-10 MHz straight beam techniques is illustrated in Figure 10-13 (a). A very small number of indications for potential damage were identified on 5 MHz C-scan compared to the relatively higher number of indications on 7.5 and 10 MHz C-scans.

Indications #10.1a.1 and 10.1a.2 were selected for detailed analysis and comparison using projected or single plain B-Scans. Figure 10-13 (b) illustrates the comparison of single plane B-Scans. The top row consists of the PAUT (BF) B-scan, the middle row FMC/TFM, and the bottom row FMC/ATFM imaging; the left column consists of 5MHz, the middle column 7.5MHz, and the right column 10MHz techniques imaging. The best detection and image resolution for indications 10.1a.1 and 10.1a.2 was achieved using 10 MHz FMC/ATFM LL technique—see bottom/right image of Figure 10-11 (b). A cluster of smaller and weaker indications were detected above both indications using the same technique. The 10 MHz PAUT SW, 7.5 MHz, and 10 MHz FMC/TFM T-T techniques confirmed the presence of both indications. PAUT S-scan images using two focal laws (groups) are shown in the top of Figure 10-13 (c). The first group was focused on the mid-wall (top-left) and the second group was focused on the bottom (top-right). The bottom row of Figure 10-13 (c) represents TFM technique images for both 7.5 MHz and 10 MHz transducers.

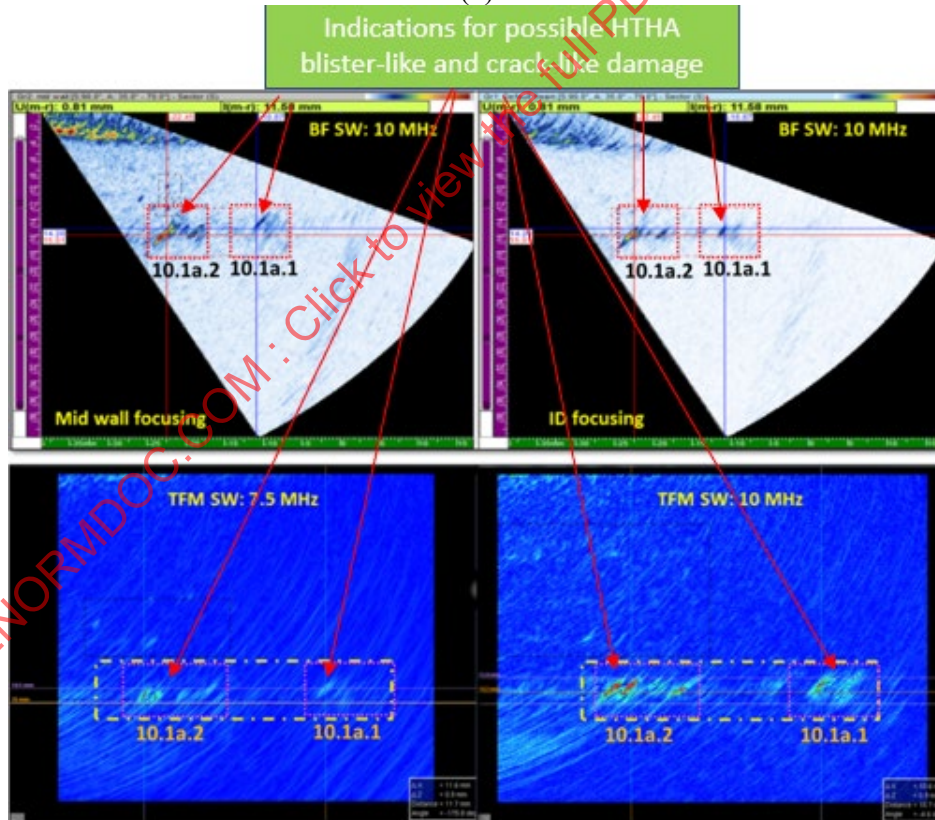
**Figure 10-13: Imaging of Indication #10.1a.1 and #10.1a.2: (a) projected PAUT straight beam C-Scans comparison; (b) PAUT straight beam and FMC/TFM.ATFM LL B-Scans comparison; (c) comparison of PAUT S-Scans and FMC/TFM T-T B-scans using shear wave techniques.**



(a)



(b)



(c)

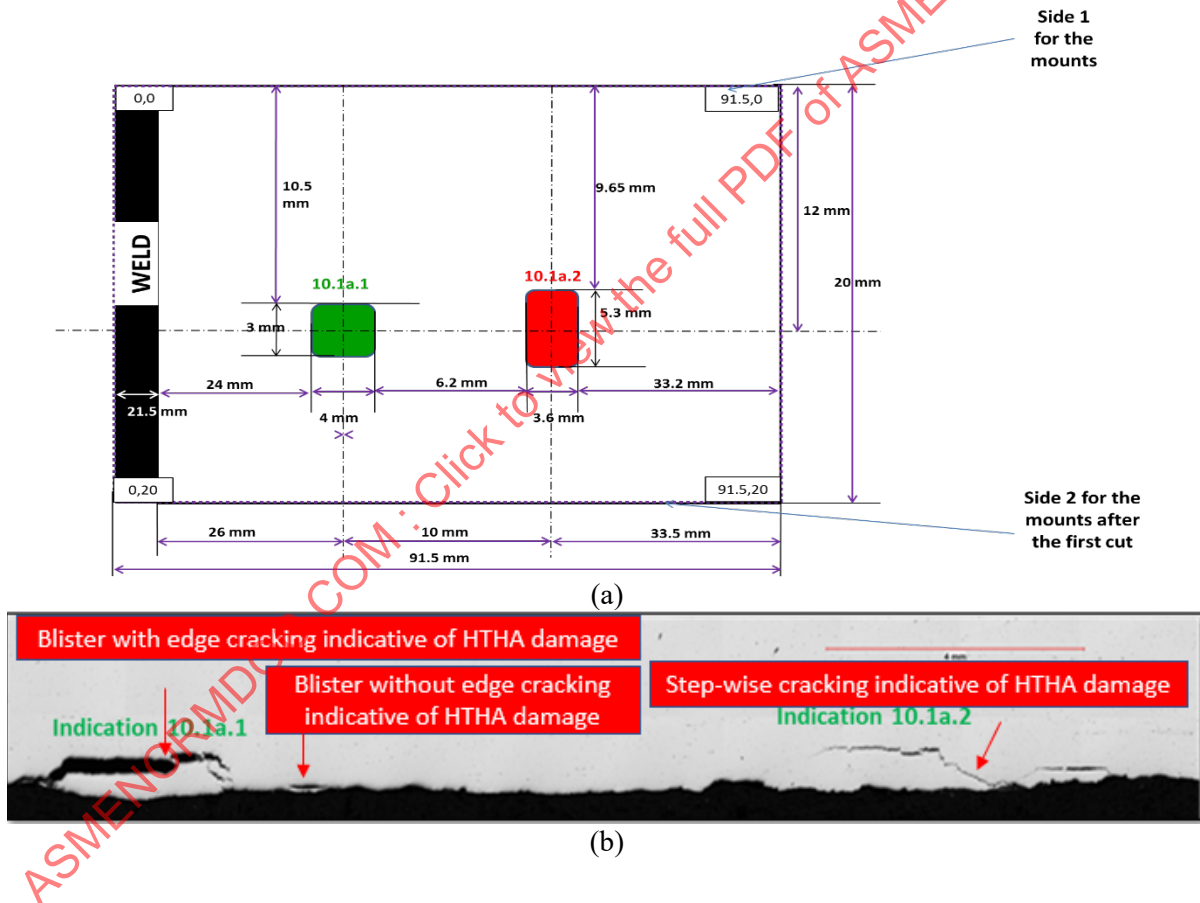
Figure 10-13 (b), (c) from Materials Evaluation, Vol. 78, No. 11: 1223–1238. Copyright © 2020 by The American Society for Nondestructive Testing Inc. Reprinted with permission.



The EDM cutting plan for three metallographic mounts preparation was developed and is shown in Figure 10-14 (a). To validate the locations and measure the width and height of indications #10.1a.1 and 10.1a.2, progressive grinding was performed from one side of each mount. During each grinding step, 0.5 mm of material was removed until the maximum height (depth) of the indication was obtained.

The metallographic images at lower (x10) and higher (x50) magnification for both indications are shown in Figure 10-14 (b-d). Enhanced detection and visualization capabilities of FMC/TFM and ATFM techniques at higher frequency were validated metallographically. Indications #10.1a.1 was classified as two micro blisters and 10.1a.2 as a stepwise micro crack. The complexity of the blistering morphology in the mount remnants was validated using Computed Tomography (CT). CT images of indication 10.1a.2 from 2 to 10mm below the front polished surface of the mount are shown in Figure 10-14 (e).

**Figure 10-14: Metallographic and CT Images for Indications 10.1a.1 and 10.1a.2: (a) cutting plan; (b) x10, Indications 10.1a.1 and 10.1a.2; (c) Magnification x50, close up view of Indication 10.1a.1; (d) x50, close up view of Indication 10.1a.2; (e) CT images of Indication 10.1a.2 from 2 to 10mm below the polished surface of the mount.**



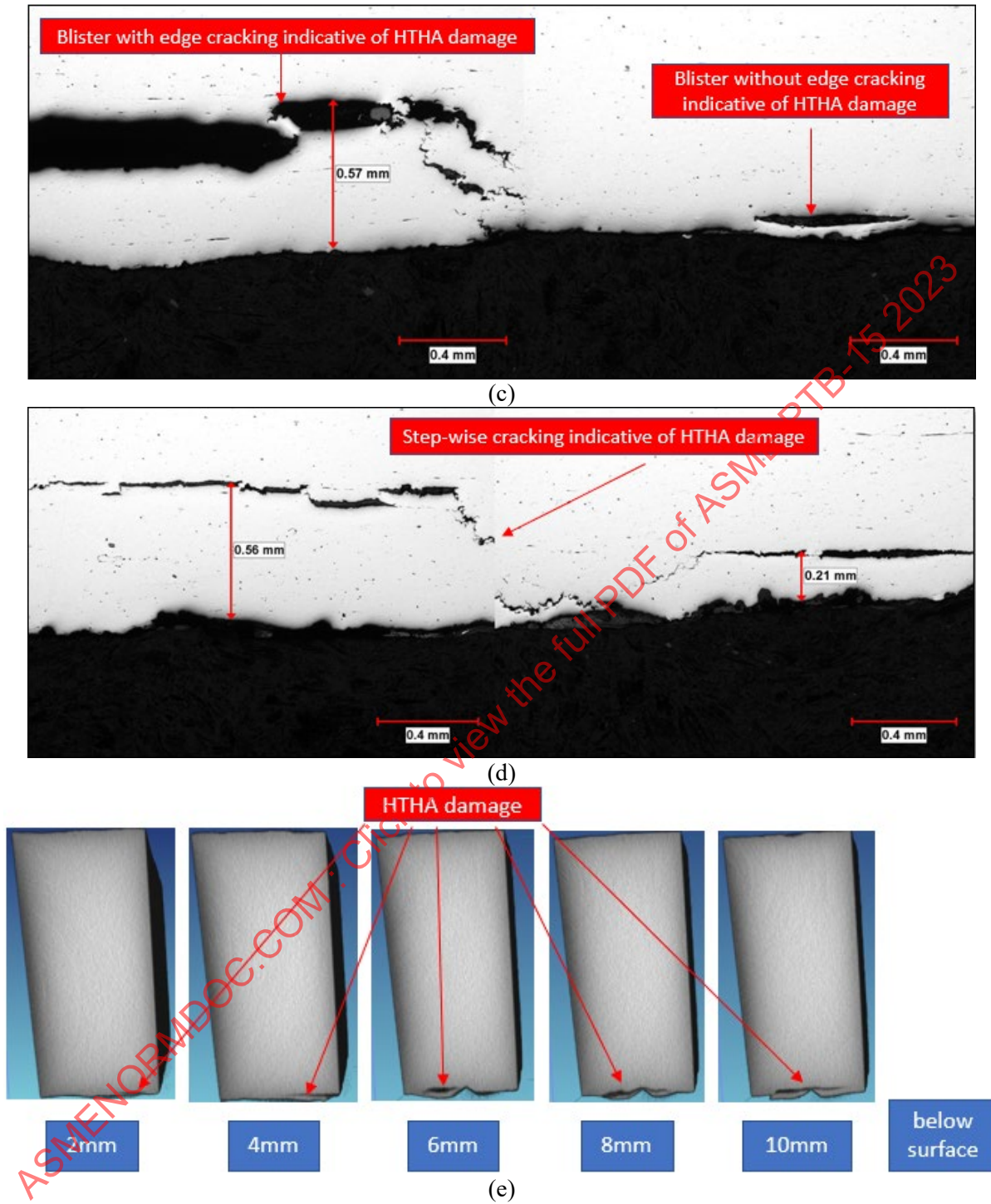


Figure 10-14 (b), (e) from Materials Evaluation, Vol. 78, No. 11: 1223–1238. Copyright © 2020 by The American Society for Nondestructive Testing Inc. Reprinted with permission.



The height and the width of the indications were measured from the metallographic images. A comparison of PAUT techniques results (longitudinal straight beam and angle shear wave beam) with FMC/TFM L-L, FMC/TFM T-T, FMC/ATFM L-L and metallographic measurements for Indication #10.1a.1 are shown in Table 10-8. RoI 10x10mm was used for FMC/TFM/ATFM techniques. A post processing tool called segmentation was applied to improve characterization and reduce the sizing inaccuracy. Better sizing results were demonstrated using high frequency FMC/TFM and FMC/ATFM techniques.

**Table 10-8: Height and width measurements of Indication#10.1a.1**

Frequency of the transducer	PAUT /TFM/ATFM	Height				Width			
		H <sub>Metallography</sub>	H <sub>BF/TFM</sub>	$\Delta H = H_{BF} - H_M$	$(\Delta H/H_M)*100$	W <sub>Metallography</sub>	W <sub>BF/TFM</sub>	$\Delta W = W_{BF} - W_M$	$(\Delta W/W_M)*100$
		mm	mm	mm	%	mm	mm	mm	%
LW-7.5 MHz	PAUT	0.57	1.00	0.43	75	2.4	4.6	2.2	91
LW-10 MHz		0.57	0.90	0.33	58	2.4	4.2	1.8	83
LW-5 MHz	TFM	0.57	0.90	0.33	58	2.4	4.0	1.6	67
LW-7.5 MHz		0.57	0.80	0.23	40	2.4	3.8	1.4	58
LW-10 MHz		0.57	0.70	0.13	23	2.4	3.3	0.9	38
LW-5 MHz	ATFM	0.57	0.80	0.23	40	2.4	3.8	1.4	58
LW-7.5 MHz		0.57	0.70	0.13	23	2.4	3.6	1.2	50
LW-10 MHz		0.57	0.60	0.03	5	2.4	2.9	0.5	21
SW-10 MHz	PAUT	0.57	0.90	0.33	58	2.4	4.0	1.6	67
SW-7.5 MHz	TFM	0.57	0.80	0.23	40	2.4	3.6	1.2	50
SW-10 MHz		0.57	0.70	0.13	23	2.4	3.2	0.8	33

From Materials Evaluation, Vol. 78, No. 11: 1223–1238. Copyright © 2020 by The American Society for Nondestructive Testing Inc. Reprinted with permission.

**Drum welds and base material:**

No signs of HTHA damage in the drum was reported using AUBT and TOFD during inspections of selected areas at risk. An area of scattered blistering, approximately 0.5 m x 0.5 m (20 in. x 20 in.), was detected visually during the following internal inspections.

The drum was removed from service and PAUT and FMC/TFM raster and line scans were completed in four shell locations (base material) and in two weld locations. No indications for crack-like HTHA damage was detected in the weld and HAZ. Metallography confirmed FMC/TFM findings that no crack-like HTHA damage is present in the weld and HAZ.

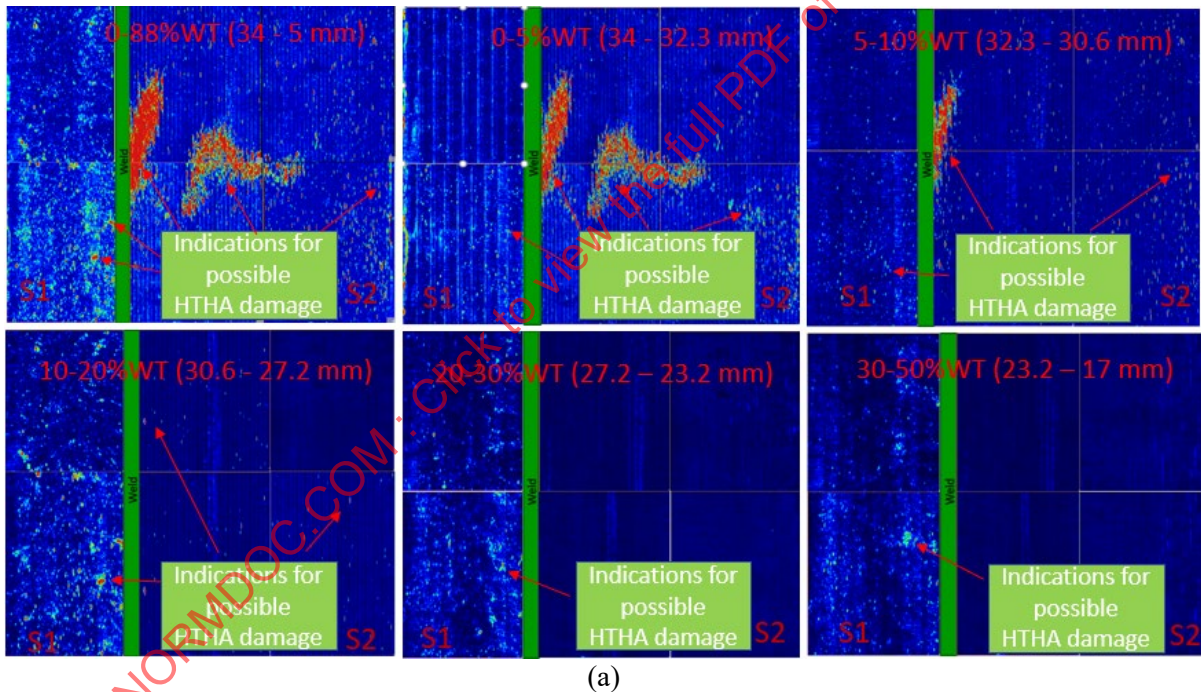
The 10 MHz, FMC/TFM LL C-scan data analysis revealed widely spread multiple indications of HTHA damage in the base material. In the south section of the drum the localized blister-like damage occurs in the base material and HAZ on both side of the welds. The localized nature of HTHA damage in one area of the south section and through wall distribution is shown in Figure 10-15 (a).

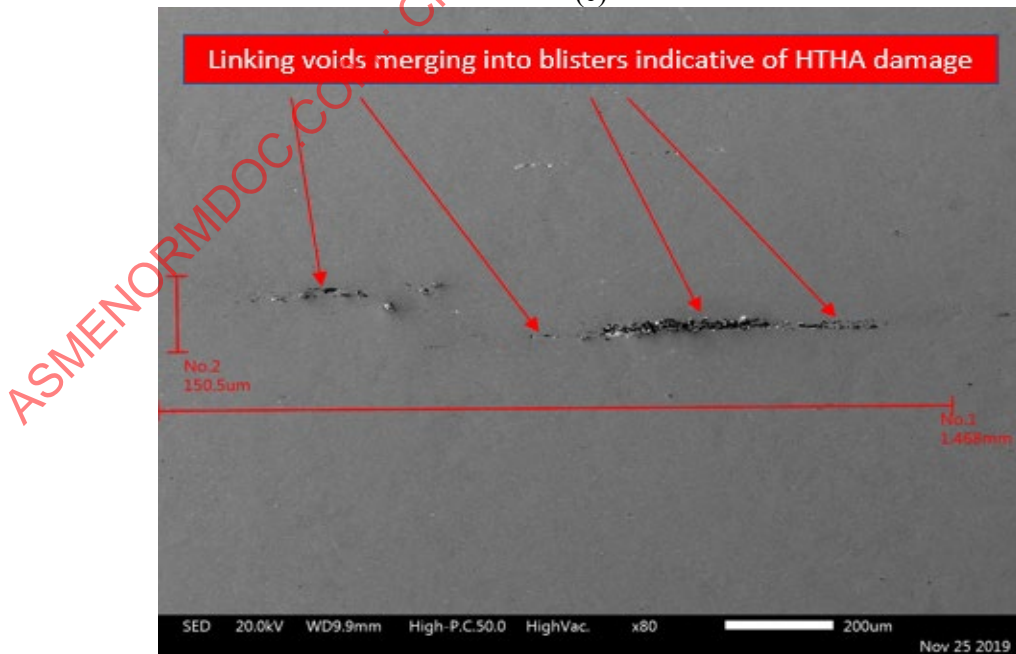
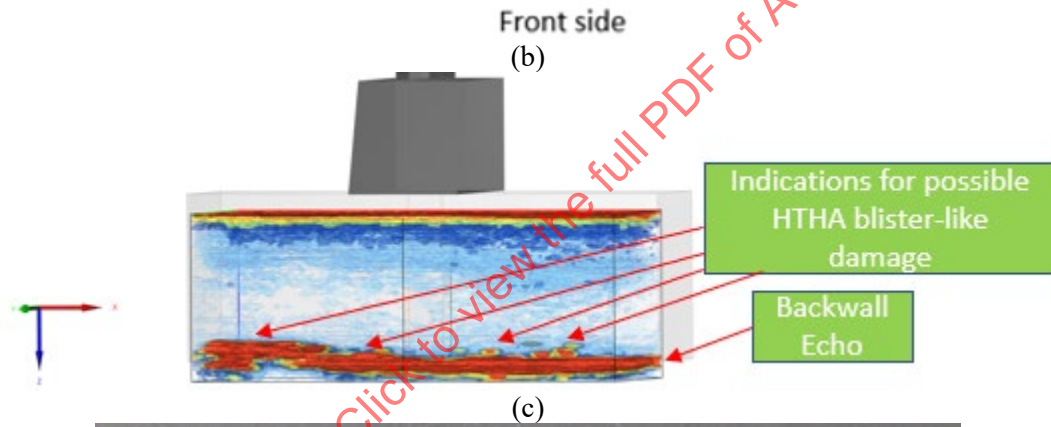
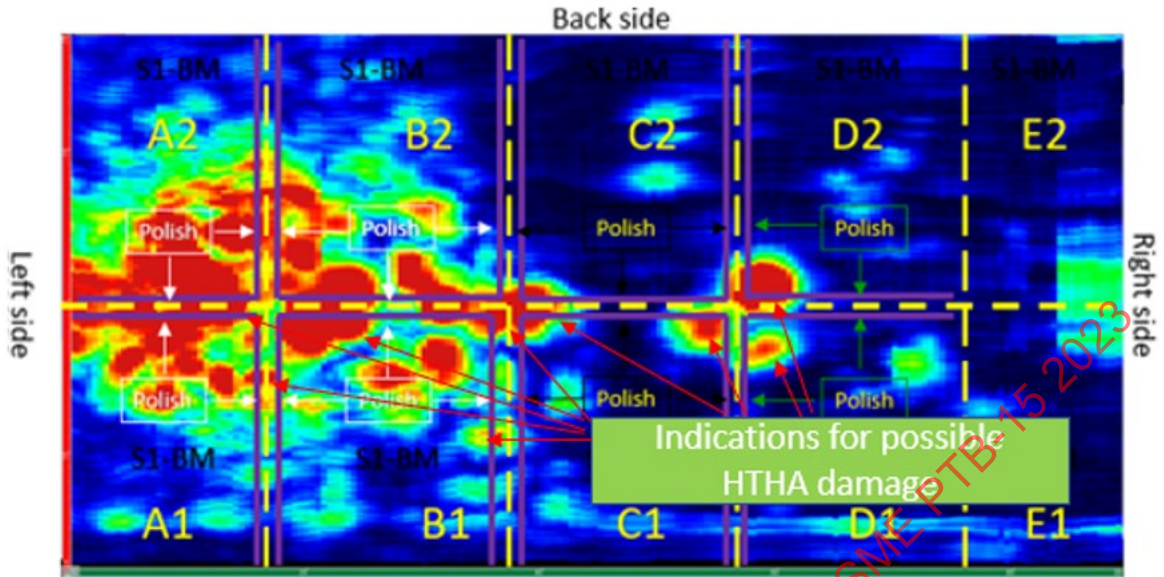
FMC/TFM raster C-scans, through wall thickness (WT) imaging and the analysis determined that predominantly HTHA damage in plate S1 is confined in less than 50% WT and for plate S2 is limited

in less than 20% WT. No indications for crack-like HTHA damage was detected in the weld and HAZ. One coupon containing the weld/HAZ and one coupon containing base material were extracted from the middle of the scanned area. One mount was prepared for verification of non-damage conditions of the weld. Metallography confirmed FMC/TFM findings that no crack-like HTHA damage is present in the weld and HAZ. Base material coupon was raster re-scan using the same FMC/TFM technique.

C-scan overlay of the base material coupon and the cutting plan for preparing of 10 mounts for metallographic and SEM investigations are shown in Figure 10-15 (b). 3D TFM visualization of the expected damage along B1/B2 cutting line and through wall distribution of blister-like damage is shown in Figure 10-15 (c). The separation of some damage observed in each side of mounts was less than 0.1mm (100µm). It was not possible to avoid ultrasonic interaction and the damage was not reported as separate indications. No substantial improvement in the indications reporting is observed when significantly lower that scanning gain was used for the analysis. An example for optical metallographic verification of micro and macro blistering is shown in Figure 10-15 (d). Figure 10-15 (e) is showing SEM image of voids formation and coalescence at an early stage.

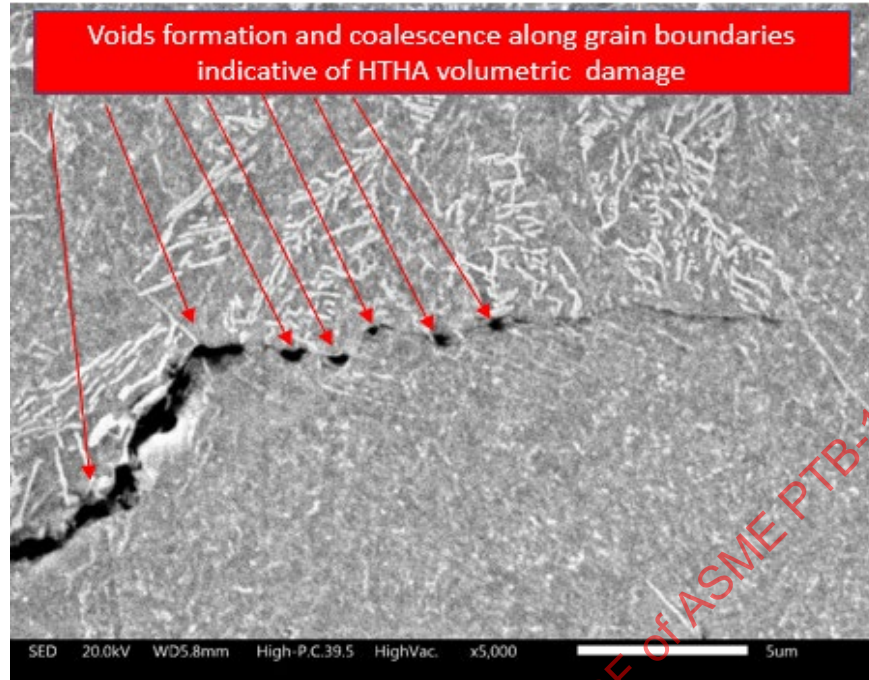
**Figure 10-15: Drum south section FMC/TFM imaging and HTHA validation: (a) localized and through wall distribution; (b) base material coupon cutting plan with C-scan overlay; (c) 3D imaging of blister-like damage; (d) optical metallography of linking voids merging into blisters, ~80X; As-Polished; (e) SEM validation of early stage HTHA volumetric damage, ~5,000X; Nital etched.**





(d)



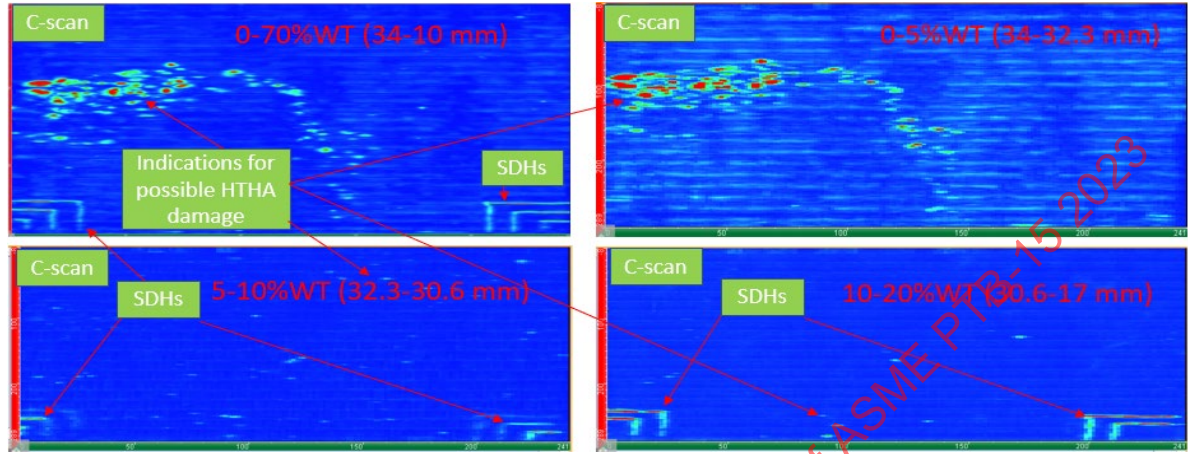


(e)

Figure 10-15 (a), (c), (d), (e) from Materials Evaluation, Vol. 78, No. 11: 1223-1238. Copyright © 2020 by The American Society for Nondestructive Testing Inc. Reprinted with permission.

The lower level of HTHA damage detected only in the base material of the north drum section is shown in Figure 10-16 (a). The damage appeared as a 'hockey stick' on FMC/TFM raster C-scan image. Ninety-five percent of the indications were very shallow and compacted in 5% through wall thickness. No indications were observed in a depth larger than 20%WT. Six sets of reference SDHs that were manufactured in the front side of plate are visualized at bottom of TFM images. A picture of visually observed scattered blistering (depth 1-3mm, length 2-12mm) is shown in Figure 10-16 (b). TFM line scan imaging (B- and D-scans) of the damage and a blister-like indication N2-7.1.2 (depth 5.4 mm, length 33.5mm) are shown in Figure 10-16 (c). Blister sizing based on 2D TFM multi-view imaging suggested 10-20% larger dimensions compared to measurements using a digital caliper. Reported larger TFM dimensions are due to bulging complexity and sharp blistering edges that were not contributing to the bulge visual appearance but subsidizing TFM imaging. An example of blister manifestation with sharp crack-like edges is shown in Figure 10-16 (d). SEM photograph revealing the presence of non-metallic inclusions and evidence of early stage HTHA damage of void formation and voids coalescence associated with the inclusion location ahead of the blister edges is shown in Figure 10-16 (e).

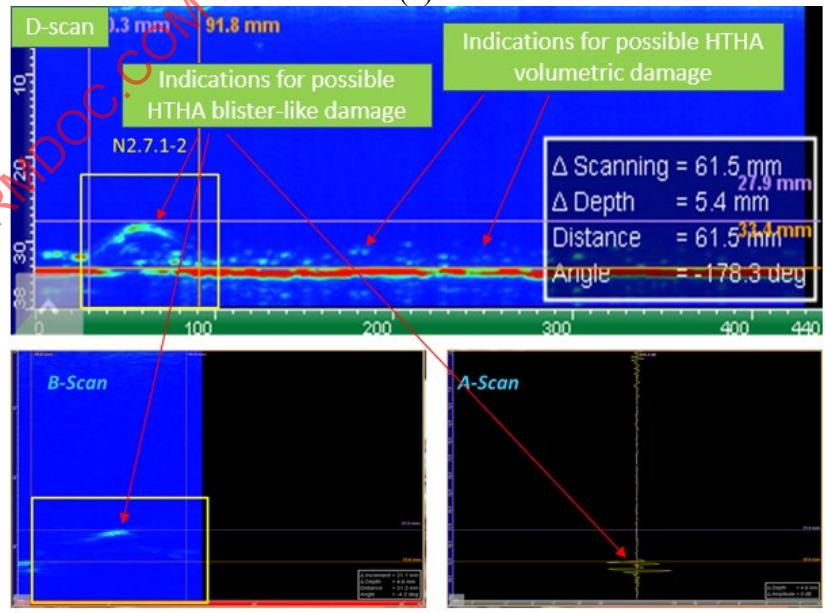
**Figure 10-16: Drum north section FMC/TFM imaging and HTHA validation: (a) raster C-scan imaging of possible HTHA damage—localized and through wall distribution; (b) visual validation of typical blister bulging; (c) line scan imaging of possible blistering with sharp crack-like edges; (d) optical metallography of blistering with sharp crack-like edges, ~50X, As-Polished; (e) SEM of non-metallic inclusions and evidence of early stage HTHA damage of void formation and voids coalescence, ~5000X, Nital etched.**



(a)

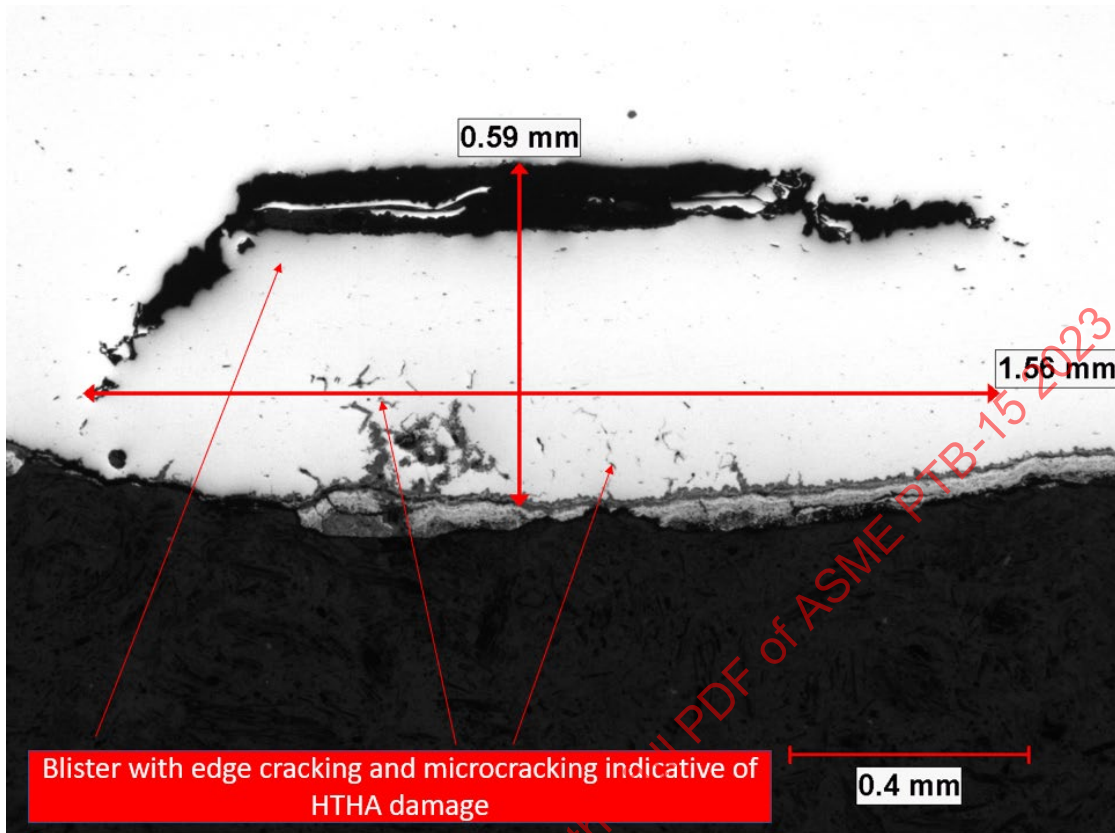


(b)

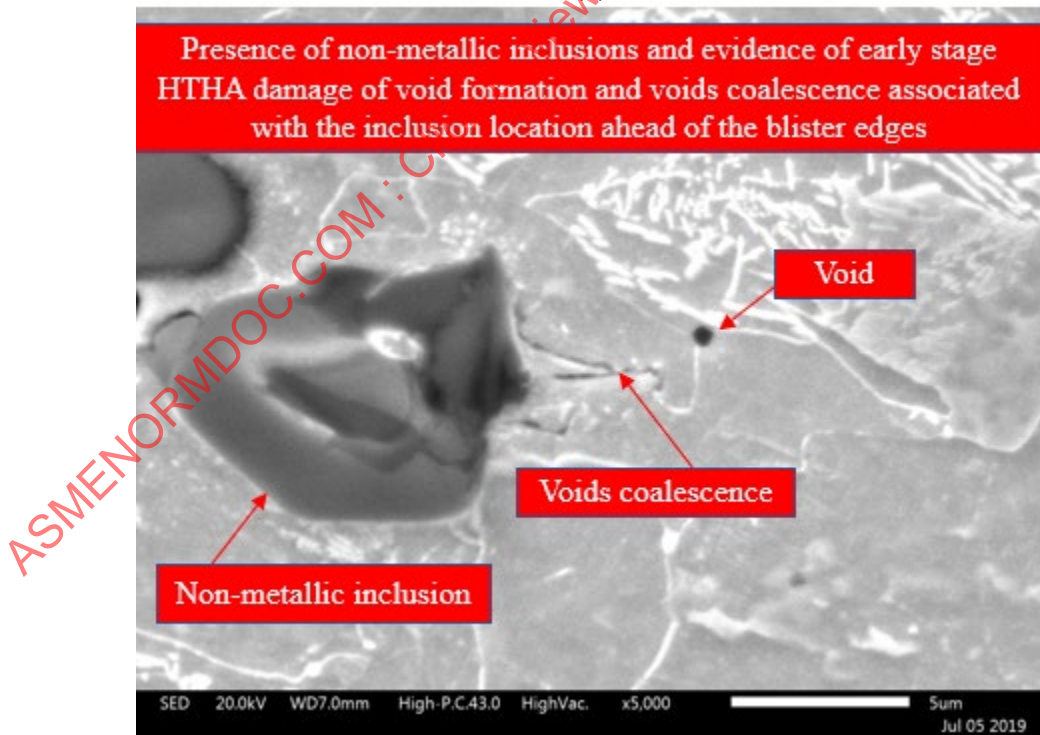


(c)





(d)



(e)

From Materials Evaluation, Vol. 78, No. 11: 1223–1238. Copyright © 2020 by The American Society for Nondestructive Testing Inc. Reprinted with permission.

It was validated that reliable detection, characterization, and sizing of in-service induced, localized, and complex HTHA damage can be achieved when multiple FMC/TFM/ATFM, L-L and T-T paths, and PAUT sectorial scan high frequency techniques are utilized.

### 10.1.5 Conclusions

This application has confirmed that optimized high frequency FMC/TFM and FMC/ATFM techniques are more reliable and offer some advantages over PAUT and TOFD for HTHA inspection:

- (a) Better than 0.2mm (200  $\mu\text{m}$ /0.008 in.) detection sensitivity for HTHA clustered volumetric damage, single blister, and crack-like indications and/or a combination of all of them. Less sensitive to the misorientation of the damage because FMC records all reflected, backscattered, and diffracted signals, and TFM image is created by summing multiple transmit-receive paths from all elements of the array.
- (b) Improved characterization as a result of the enhanced spatial resolution, e.g., the ability to resolve two or several closely spaced indications. When spaced apart larger than the grid ROI resolution, HTHA damage will be imaged better (without large arcs) and can be resolved.
- (c) Enhanced sizing resolution and more accurate sizing of HTHA clustered volumetric, blister and crack-like indications because all points or pixels defined by high resolution grid within the ROI can be focused during the imaging process using TFM.
- (d) Applying more effective ultrasonic techniques for detection, characterization, and sizing HTHA in early stages could improve confidence of Fitness for Service assessment. Damage growth could be monitored as a short-term mitigation strategy using frequent periodic inspections until the equipment is replaced.

The use of FMC/TFM and FMC/ATFM as primary techniques for more reliable early stage HTHA inspection is recommended. PAUT is recommended as backup for the primary techniques. TOFD is recommended only as secondary and screening technique since the dead zones and characterization limitations. [33] – [50]

## 10.2 FMC/TFM Based Inspection of Small-Diameter Components for FAC Damage

### 10.2.1 Summary

This section describes an FMC/TFM based inspection system developed for inspection of the welded joints of small diameter fittings for Flow Accelerated Corrosion (FAC). Unique aspects of this application include:

- Use of Immersion mode
- Implementation of a 2 iteration TFM beamformer
- Inspection of complex geometries

### 10.2.2 Background

The CANDU reactor design consists of a single large calandria vessel containing a heavy water moderator and mechanisms for reactivity control and shutdown. The vessel is horizontally oriented and axially intersected by many individual fuel channels. Depending upon the design, there can be anywhere from 370 to 480 channels within the calandria. Each channel acts as a separate pressure vessel containing the fuel bundles. Heavy water coolant is delivered from the inlet header to the fuel channel and returned to the outlet header by a network of tubes, collectively referred to as feeder pipes. The reactor design permits online refueling of the reactor at the cost of increased Primary Heat Transport piping network complexity. Figure 10-17 depicts the Primary Heat Transport piping arrangement for CANDU reactors.

**Figure 10-17: Primary Heat Transport piping arrangement between the steam generators and the fuel channels**

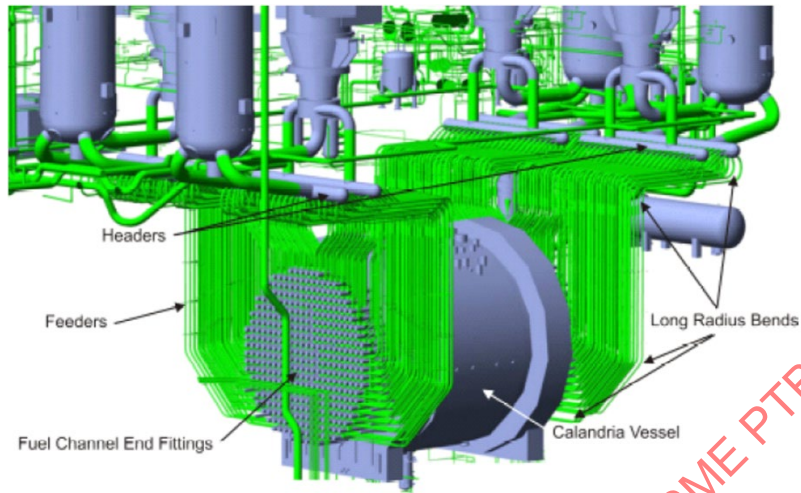


Image Courtesy of Ontario Power Generation, Inc.

### 10.2.3 Feeder Pipes

In most CANDU designs, the feeder pipes are ASME SA106 grade B or SA105 material carbon steel. The feeder pipes range from 4-inch nominal pipe size (NPS) to 1½ inch NPS. The length of the feeder pipes varies from 6 meters to over 30 meters. The diameter of the feeder pipes is varied to achieve the required flow rate while considering the pressure reduction induced by friction losses. Routing of the feeder pipes to their respective locations on the reactor face results in a range of nested configurations and constrained access options, such as shown in Figure 10-18.

### 10.2.4 Degradation Mechanism

**Figure 10-18: Example showing the typical congestion of the feeder pipes**

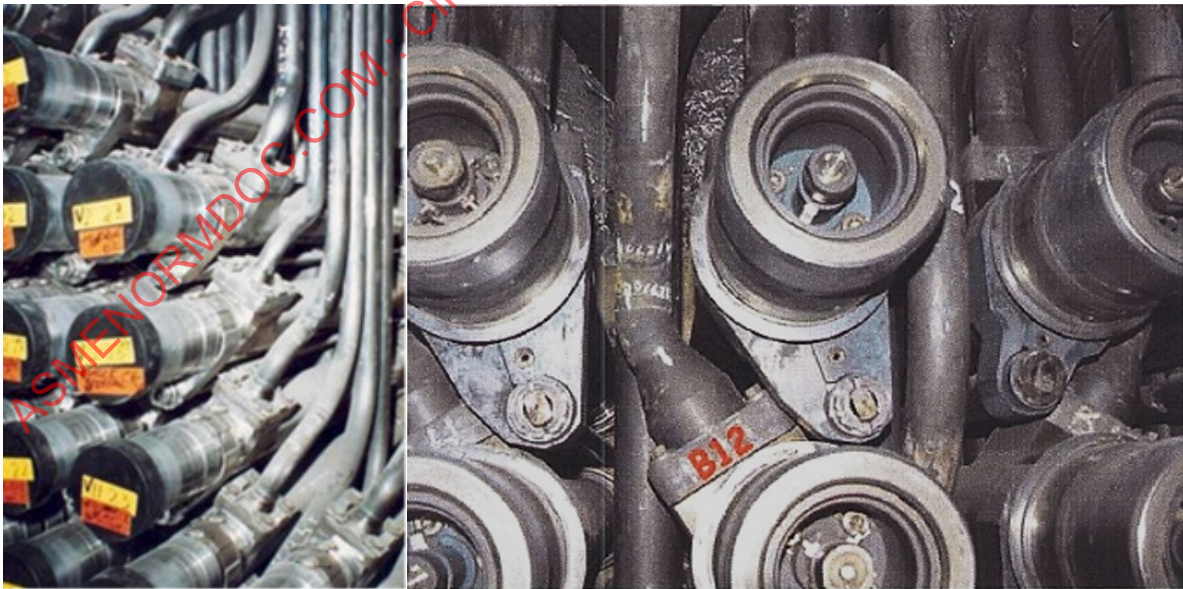


Image Courtesy of Ontario Power Generation, Inc.



Radiolysis of the heavy water coolant as it passes through the reactor core produces atomic oxygen and deuterium radicals. Some radicals recombine to form D<sub>2</sub>O (heavy water), but a portion stays in solution and presents a corrosion potential within the coolant. The heavy water, after having been heated by the fuel bundles and exiting the fuel channels, is unsaturated with iron oxide species. The oxygen radicals oxidize the interior surface of the feeder pipe; the sub-saturation of iron oxide promotes dissolution of the surface oxide layer into the flow. The flow rate unique to each channel enhances the transport of the iron oxide into the flow. As the flow absorbs iron oxide, it becomes saturated and reduces the corrosion potential. Consequently, the FAC is arrested after the first meter or so in the feeder pipe. In the steam generators, the coolant transfers heat to the secondary loop. As it cools, the solubility of iron oxide decreases, causing it to precipitate out of solution as magnetite. The cooled, saturated solution is then pumped to the reactor where heat transferred from the fuel bundles re-establishes the sub-saturation state in the heavy water.

Initially, it was believed the only area of concern for FAC attack was the extrados of the first bend/elbow due to flow impingement. Subsequent inspections encompassing the entire feeder bend identified high thinning rates at the entry to the intrados. This condition is partially explained by the presence of an adverse pressure gradient in the flow at the intrados, causing separation of the flow from the interior surface. Also discovered was a thinning trend at the beginning of the bend inspection. The design of the bend inspection tooling obstructs access to the region between scan start and the Grayloc® weld. An inspection tool was developed to examine this region. Results of these inspections confirmed the thinning trends in the intrados region and within the first 15 mm of the parent material adjacent the downstream weld toe. In some instances, the thinning exhibited trends extending under the weld cap material. Thinning artefacts are found adjacent the weld root on the downstream side of the fitting weld in Figure 10-19.

**Figure 10-19: Example of FAC adjacent to the downstream weld toe**

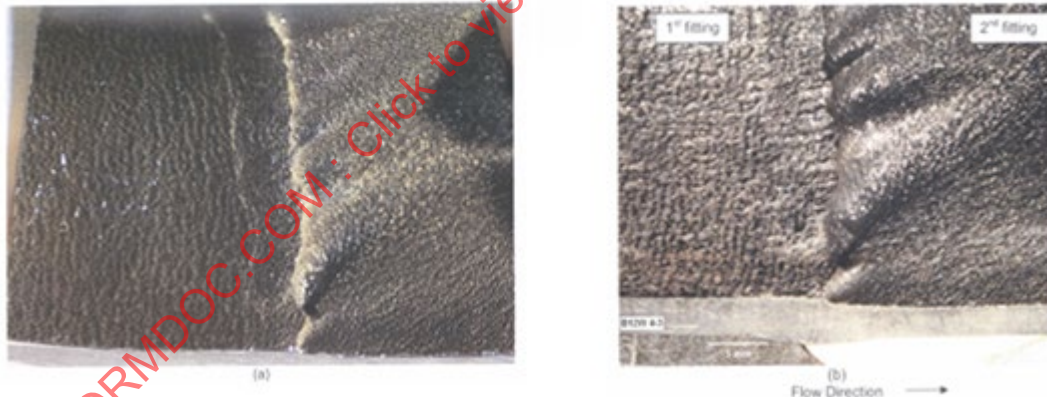


Image Courtesy of Ontario Power Generation, Inc.

### 10.2.5 Component Description

As described previously, the feeder material is either ASME SA106 grade B extruded pipe bent to the appropriate geometry or SA105 material hot-formed into fittings that are subsequently welded with other fittings into the required geometry. Deformation during bending process creates a variety of surface profiles cross sections including egg shaped, oval, cloverleaf, and occasionally circular. The outlet feeders are either 2 or 2½-inch schedule 80 NPS where FAC damage has been found. The feeder pipes terminate at the fuel channel and end with a Grayloc® fitting sized to the pipe diameter. The surface finish is as formed with the presence of ferrous oxide on the outlet feeders due to high temperature operation.

Welds to the Grayloc® hub are formed using automated GMAW methods. The weld prep is either Vee or U groove geometry, depending on station-to-station design differences. The weld caps produced by automated equipment tend to be smooth and are as formed. Welds between fittings are formed via manual SMAW techniques and may have multiple passes in the cap region. The weld caps on the manual welds have more pronounced ripples and higher cap heights relative to the automated welds.

The geometry of the feeder pipe joints is a function of their location on the reactor face to accommodate nesting of the feeder runs. Figure 11-20 shows the inspection areas for a typical feeder geometry. The permutations of pipe diameter, take-off angle, sweep angle, radius of bend, and compound bend configuration create a host of possible configurations; as a result, location specific tooling is impractical to deploy.

### 10.2.6 Inspection Specification Requirements

The Inspection Specification was originally developed to address widespread FAC in the extrados of the bends. As inspection results identified thinning in unanticipated regions, the Inspection Specification was extended to include these regions, often without modification. This extension had the unintended consequence that inspection requirements achievable in one region of the feeder were inappropriate to the task in another region. A specification for inspecting a region of gradual thinning was applied to regions containing abrupt geometry changes and highly localized thinning, see Figure 10-20. Lastly, the Inspection Specification was developed under the assumption that normal beam based technologies would be applied for the inspection. This assumption incorporates requirements that are germane to normal beam technologies but are not otherwise relevant to the measurement itself.

On its face, the concept of ‘thickness’ is intuitive. It is commonly understood to be the distance between two parallel, or nearly parallel, surfaces. The measurement reference is the local normal to the inspection surface. However, in context of the inspection specification applied to highly localized thinning while accommodating fitting and weld cap geometry changes, a thickness measurement relative to the normal is no longer meaningful. A generic definition for thickness was adopted as the distance between two surfaces regardless of the direction. This subtle change in definition has important consequences for the inspection technology.

One requirement from the Inspection Specification necessitates reporting coverage of not less than 90 percent of the inspection region. This requirement includes thickness measurements for material under the weld cap. As many UT practitioners are aware, inspection of material thickness through an as-formed weld cap is likely to lead to poor performance and inadequate results.

Other Inspection Specification requirements were difficult to implement, such as measuring a thickness variation greater than 0.06 mm from an adjacent location. This requirement is highly problematic in regions containing weld cap surfaces. Even relatively modest weld caps display thickness variation of at least 1 mm in a very short lateral displacement in either axial or circumferential directions. This requirement alone defined the need to provide a continuous surface profile throughout the inspection region.

The accuracy and precision of the derived measurement stipulated by the Inspection Specification is  $\pm 0.06$  mm and  $\pm 0.03$  mm, respectively. At these levels, fine surface features such as interior surface scalloping contribute to the measurement. The thickness measurement must also be reproducible.



### 10.2.7 Complicating Factors

Figure 10-20: Inspection regions for welded fitting feeder configurations

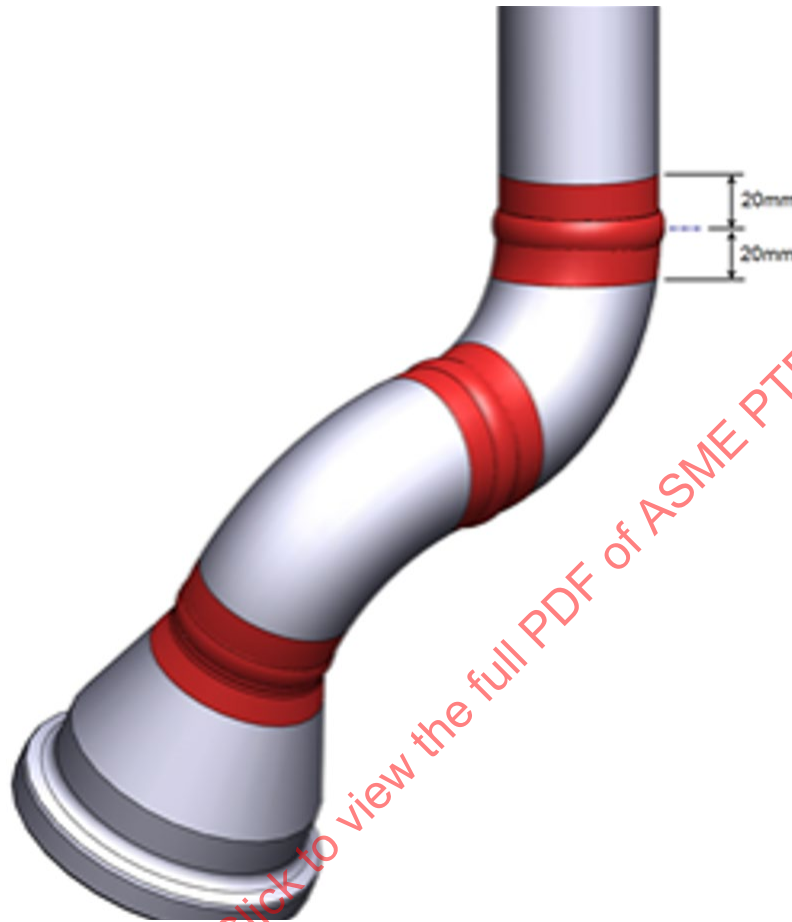


Image Courtesy of Ontario Power Generation, Inc.

Several factors complicate the required inspection.

**Work Location**—the operator is required to access the inspection location from a mobile platform installed in front of the reactor face. The location is recessed from the reactor face some 50 cm (19 inches). A radiation shielding canopy is placed between the operator and the reactor face, which further increases the reach distance (see Figure 10-22). Reaching into the inspection location results in poor ergonomic positioning of the operator.

Nesting of the pipe runs combined with the number of possible geometries creates obstructions that are often location specific. Portions of the inspection region can be accessed in one configuration but not in another. Access is obtained reaching into an aperture between four adjacent end fitting structures. This results in a condition where the inspection location can be seen or can be physically accessed. The act of accessing the location obstructs line of sight to the location.

Operator mobility, dexterity, and visual capability is impaired by PPE (see Figure 10-21). Multiple protective layers must be worn, including layers of gloves, all of which reduce range of motion and eliminate tactile sensation.

**Figure 10-21: Platform Operator clad in PPE at the Reactor Face work location. The radiation shielding canopy is absent in this view.**



Image Courtesy of Ontario Power Generation, Inc.

Geometry as found As noted previously, there are multiple unique geometries that are part of the feeder pipe designs. The variations are further compounded by manufacturing tolerances, as-installed deviations, and changes in positioning brought on by aging and plant operation. These variations increase the range of inspection geometry which in turn complicates the inspection task.

**Figure 10-22: A view of the reactor face work platform with a shield canopy installed**

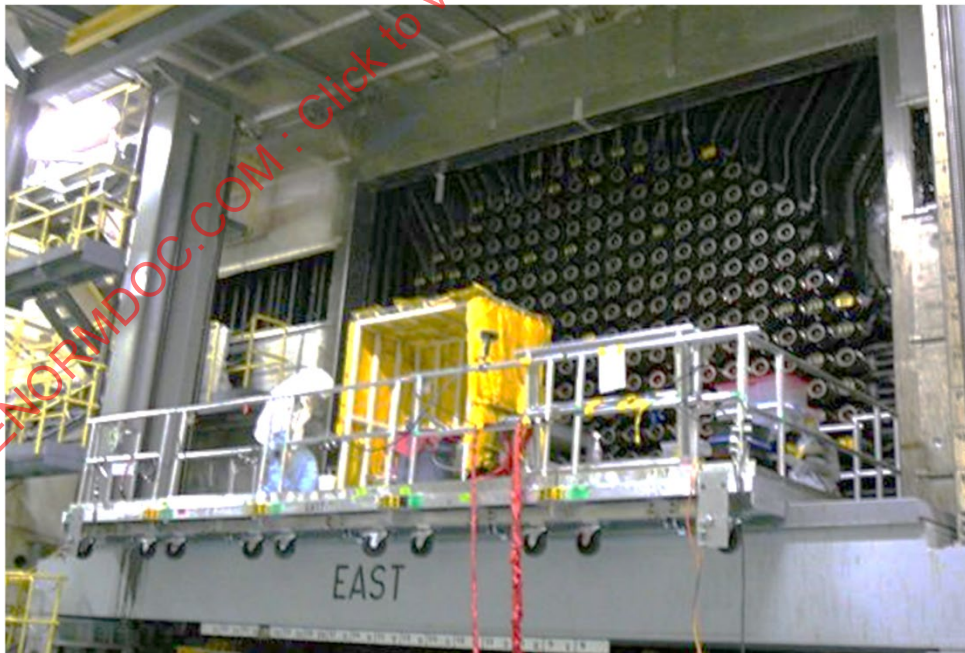


Image Courtesy of Ontario Power Generation, Inc.

**10.2.8 Overview**

Ontario Power Generation (OPG) has developed a unique approach to the inspection problem. The OPG approach combines FMC data acquisition principles, conducted in immersion mode, with a two stage iterative TFM beamformer. For the sake of brevity, this variant of FMC/TFM is referred to as the ‘Matrix Inspection Technique’ or MIT.

**10.2.9 Separation of Tasks**

FMC/TFM is founded on two independent processes: data acquisition and data analysis. For the feeder weld FAC application, OPG intentionally segregated the two processes so one group of inspectors could focus attention on the data acquisition task while another group addressed the analysis task. Separating the tasks is a strategy that is applied to other aspects of feeder inspection and is therefore consistent with conventional practice.

The choice to develop an immersion approach was based on Operating Experience (OPEX) with other inspection tools. Contact testing is problematic for feeder inspection. Immersion testing has clear benefits and limitations; however, for FMC applied to rapidly changing interface surface geometries, the benefits obtained via immersion outweigh the drawbacks.

**10.2.10 Training**

Training for feeder weld MIT is divided based upon function. The functions include Platform Operator, Acquisition Operator, Analysis Operator and Maintenance Technician. Training requirements are listed in hours in Table 10-9.

**Table 10-9: Training Requirements**

Training Environment	Task			
	Platform Operator	Acquisition Operator	Analysis Operator	Maintenance Technician
Classroom	11	25	30	20
Practical	25	50	45	35
Check out & Practical Eval.	4	5	5	5
Total	40	80	80	60
NDT Certification Required	No	Yes – Level II UT	Yes – Level II UT	Yes – Level II UT

Courtesy of Ontario Power Generation, Inc.

The classroom material addresses the following:

- System/component description
- Degradation mechanisms
- Inspection Specification
- Solutions based on established technologies
- FMC and TFM principles
- System hardware and software
- Applicable procedure
- Calibration, records, and quality metrics
- Troubleshooting

The practical component of the training addresses the following:

- Hardware (if any)

Software

Procedure steps and required forms

Calibrations, bench top exercises, and mock-up based exercises where applicable

Troubleshooting tasks

### 10.2.11 Equipment

The following instruments and devices are required to conduct the inspection:

Data acquisition instrument—Peak NDT, MicroPulse 5 PA or FMC; see Figure 10-24.

Instrumentation interface—Custom developed Vault Interface Module (VIM)

Transducer—Imasonic, custom developed 128 element, 7.5 MHz, 0.27 mm pitch linear array; see Figure 10-26

Manipulators—application specific for 2 and 2½ inch NPS fittings; see Figure 10-23 and Figure 10-25.

Calibration blocks—application specific for 2 and 2½ inch NPS fittings; see Figure 10-28.

Ancillary equipment—couplant pump, reservoir, IP switch, video cameras, addressable power bar.

**Figure 10-23: (right) Instrument cart with MicroPulse and Vault Interface Module (manipulator and peripheral electronics module), (left) couplant reservoir and calibration stand.**



Image Courtesy of Ontario Power Generation, Inc.

**Figure 10-24: Manipulator for 2 1/2 inch NPS fittings installed on a mock-up.**



Image Courtesy of Ontario Power Generation, Inc.

**Figure 10-25: Manipulator for 2 inch NPS fittings**

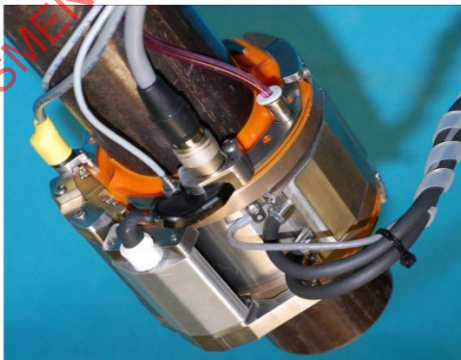


Image Courtesy of Ontario Power Generation, Inc.

**Figure 10-26: Transducer for both 2 and 2 1/2 NPS sized manipulators. The transducer fires tangentially to the inspection surface with the sound redirected via a mirror.**



Image Courtesy of Ontario Power Generation, Inc.



### 10.2.12 Software

Staff at Ontario Power Generation developed Neovision®, a software suite to perform both the acquisition and analysis tasks. The software is designed to present FMC UT data in a familiar and recognizable configuration while incorporating all essential features of conventional UT data acquisition. Several unique features have been introduced such as a floating interface gate and pre-trigger acquisition. The floating gate provides visual cues of the inspection geometry, enabling easy identification of features such as intrados, extrados, and weld cap. An example of one configuration for the acquisition window is found in Figure 10-27 (right). The pre-trigger acquisition permits the operator to observe conditions such as air bubbles on the interface and transducer-interface misalignment. The utility found in Figure 10-27 (left) enables the user to view any transmit/receive configuration in the FMC matrix.

Figure 10-27: Typical screen presentation of the developed software

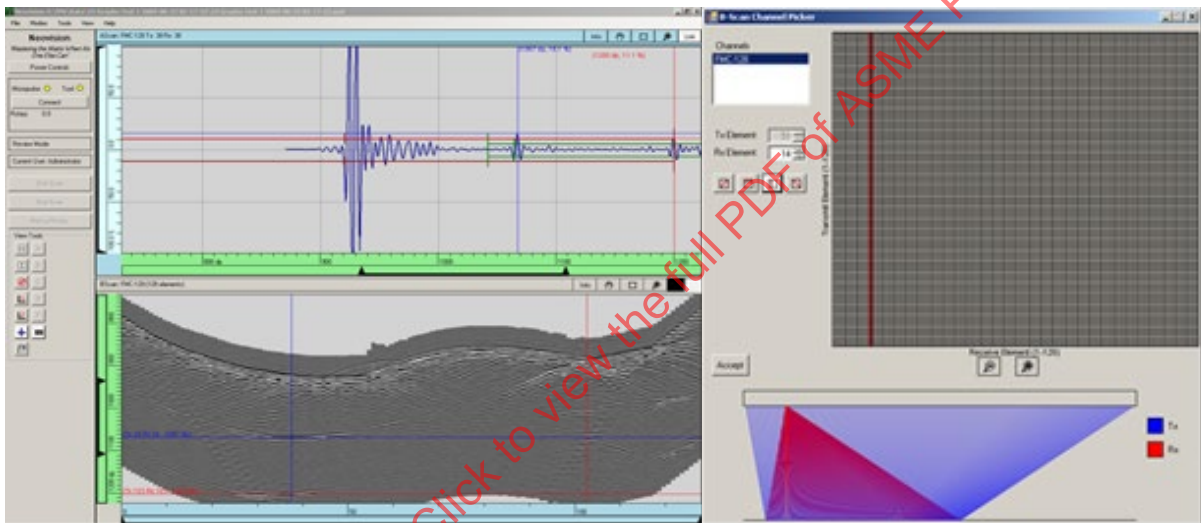


Image Courtesy of Ontario Power Generation, Inc.

### 10.2.13 Calibration

Figure 10-28: Example of the custom calibration block



Image Courtesy of Ontario Power Generation, Inc.



Calibration is performed at the beginning of the inspection campaign on all manipulator-transducer combinations on the inspection instrument. Parameters unique to each combination are recorded to a configuration file and are applied during the inspection activities. The calibration occurs in the radiological work area away from the inspection location where there are lower production pressures, lower radiation background, and working conditions more conducive to the detailed nature of the calibration task. At the inspection location, the calibration is verified at the beginning and end of the shift, every four hours, and upon change of equipment or Acquisition Operator. The calibration is considered valid provided key amplitude, linearity, accuracy, and repeatability criteria for the system are met.

The calibration verification is conducted on a custom calibration block that is mounted on a stand to which the manipulator is installed. Calibration verification checks a series of parameters including transducer delay, system time base linearity, system amplitude response, time corrected gain curves, manipulator positioning accuracy, and temperature sensor response. The calibration verification is a highly automated process that generates a report, the results of which are reviewed by a qualified acquisition operator. If the calibration verification fails for any reason, the operator applies corrective action and re-attempts the calibration. If a calibration verification cannot be successfully obtained, the situation is addressed by Acquisition Operator in conjunction with the inspection supervisor.

#### 10.2.14 Data Acquisition Process

Data are acquired in immersion mode; the manipulator is positioned encompassing the desired inspection region with the seals above and below the region. A multi-element 1D transducer, axially oriented, transmitting tangentially to the inspection surface is indexed circumferentially around the feeder inspected. The tangential beam is intercepted by an articulated acoustic mirror that redirects the beam to the inspection surface. The mirror is driven to optimize the amplitude of the interface signal obtained in a user defined window taken on the fitting material immediately adjacent the weld toe. This arrangement is necessary because the manipulator tracks a cylindrical path whereas the region inspected is essentially a section of a torus. The areas where the cylinder and the torus are parallel occur on the extrados and intrados of the torus. In all other areas the surfaces are not parallel. Consequently, the plane of the UT beam would intersect the inspection surface at an angle.

Figure 10-29: Manipulator arms

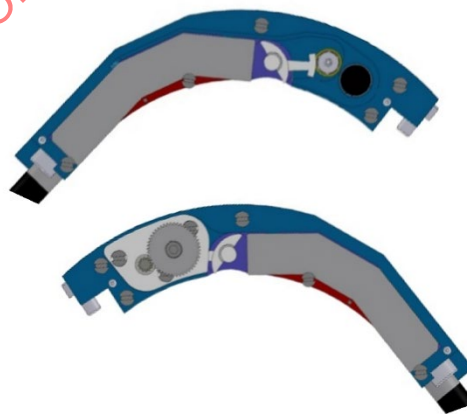


Image Courtesy of Ontario Power Generation, Inc.

When the interface signal in the region of interest has been optimized, the system acquires the FMC data frame for the region and then increments to the next location. The process repeats until the full circumference of the fitting joint has been inspected. The system acquires data with a step size of 0.5 mm. Coverage of the 245 mm circumference results in more than 500 FMC frames and a file approximately 6.5 Gigabyte for the 2½ inch feeder. Inspection of the 195 mm circumference results in 400 FMC frames and a file size of 5 Gigabyte for the 2 inch feeder. Scan times for the 2½ inch fittings are on the order of 9 minutes and 7 minutes for the 2 inch size.

### 10.2.15 Recording

The gain is set such that the interface signal from the parent material surface is 6 to 8 dB beyond saturation. This level of gain will typically result in an interior surface response in the range of 10 – 15% FSH. Experience has shown this gain setting is adequate to image the interior volume under the extremes of geometry encountered with welds and parent material. The entire FMC data set is retained. This choice was made to ensure full auditability of the inspection as well as keeping the option open for re-processing the data should new algorithms become available. Retaining the data set is useful from the perspective of providing the ability to investigate potential sources of artifacts generated in the TFM result.

### 10.2.16 Data Acquisition Procedure

The data acquisition instrumentation and associated peripherals are located in the reactor vault on a work platform installed on the fueling machine bridge. The instrument, manipulator, and peripherals are controlled by the Acquisition Operator from a remote trailer located outside the station building. The Acquisition Operator is responsible for setting the order of inspections, monitoring the UT data quality, recording the results for inspection activities and calibration verification tasks. The Platform Operator, located at the inspection work location, is responsible for identifying the inspection location, preparing the location for inspection activities, installation and removal of the inspection tooling, and monitoring the tooling for the duration of the inspection. The Acquisition Operator observes the general inspection work location via a series of cameras and video monitors. The Platform and Acquisition Operator communicate over headsets. This strategy is consistent with other feeder inspection systems and does not impose any unique burden.

The Acquisition Operator informs the Platform Operator of the location to be inspected. The Platform Operator identifies the appropriate location on the reactor face. The location is independently verified. The work platform is positioned to permit access to the identified location. The Platform Operator then examines the inspection location and, if accessible, prepares it for inspection by cleaning it of any debris. Any unusual constraints or clearance issues are reported to the Acquisition Operator. The Platform Operator then installs the manipulator over the intended inspection region. Cables are looped over the adjacent end fitting structure to reduce manipulator cable loads.

The Acquisition Operator then activates the couplant supply, initiates set-up, and monitors the interface signal. The Acquisition and Platform Operators work cooperatively to correct any couplant related UT issues. The Platform Operator optimizes the interface signal adjacent the weld toe and then initiates a coarse resolution test scan. The test scan is used to assess the correct positioning of the manipulator over the inspection region and discover potential issues such as obstruction, water column level, or air entrapment prior to committing to a full scan. Any issues identified in the test scan are corrected before the full scan is attempted.

Following the acquisition of a full scan, the Acquisition Operator evaluates the scan against several quality metrics and records the result in an inspection record—see Figure 10-30 and Figure 10-31. The file is saved and transferred for analysis. The inspection task then addresses the next inspection location.

Figure 10-30: Example of a typical inspection record

**ONTARIO POWER GENERATION** File Information: File per Results Co-ordinator's Instructions Internal Use Only I-FORM-50622 R003

**Inspection Record - Matrix Inspection Technique (MIT) Weld Area**

Station: PNGS A Unit: 4 Date: 21-Jan-14 Time: 10:35 AM  
 Face: East Feeder: P02E Weld: F1 Rescan: \_\_\_\_\_  
 Acquisition Operator: FAC Platform Operator: Uniform Thinning  
 Transducer Serial No.: B110 Manipulator Serial No.: 2.0 003  
 Vault Interface Module Serial No.: K-013/80-SN-ECN-002 Scan Type: Above  
 Micropulse Serial No.: 15030  
 Reference Tube Serial No.: \_\_\_\_\_ MIT 2.0 - 001  
 File Name: P4EP02F1A-IR Calibration File: FCAL-IN-006  
\* File name follows character structure outlined in 9.3.1 in Inspection Procedure (I-IP-30671-00001)  
 Scan Start: 0 Scan Length: 195

Data Quality Table					
Issue	Criteria	Pass	Fail	First	To
Probe Axis Alignment	No more than a cumulative total of 10% of the scan missing	<input checked="" type="checkbox"/>	<input type="checkbox"/>		
Air Bubbles	No appreciable reductions in interface or ID signal amplitude on pipe surface	<input checked="" type="checkbox"/>	<input type="checkbox"/>		
	No air bubbles found on transducer surface	<input checked="" type="checkbox"/>	<input type="checkbox"/>		
	For water column, air bubbles are not greater than 5 scan lines mis-triggered	<input checked="" type="checkbox"/>	<input type="checkbox"/>		
Air Pockets	Horizontal - Air pocket less than 5 consecutive scan lines	<input checked="" type="checkbox"/>	<input type="checkbox"/>		
	Vertical - less than 10 elements and no greater than 40 scan lines	<input checked="" type="checkbox"/>	<input type="checkbox"/>		
Signal Range Limits	Far- Sufficiently close to trigger Interface Gate, not to exceed 1300 DP	<input checked="" type="checkbox"/>	<input type="checkbox"/>		
Electrical Noise	Not to exceed 5% FSH if uncorrelated to 2% FSH if correlated	<input checked="" type="checkbox"/>	<input type="checkbox"/>		
Temperature Range	15 - 45 °C	<input checked="" type="checkbox"/>	<input type="checkbox"/>		
Missing- Dead Elements	No more than 13 total, and not greater than 3 adjacent	<input checked="" type="checkbox"/>	<input type="checkbox"/>		

Image Courtesy of Ontario Power Generation, Inc.

Figure 10-31: Example of a typical inspection record (cont.)

**ONTARIOPOWER GENERATION**

File Information:  
File per Results Co-ordinator's Instructions

Internal Use Only  
I-FORM-50622 R003

**Inspection Record - Feeder Weld Area Thickness Measurement Tool**

Data Quality Table					
Issue	Criteria	Pass	Fail	From	To
Interface Amplitude	Not exceeding 6 dB above 100% FSH on straight pipe sections or sufficient to reliably trigger interface gate on weld cap	<input checked="" type="checkbox"/>	<input type="checkbox"/>		
ID Signal Amplitude	Observable in electronic B-scan	<input checked="" type="checkbox"/>	<input type="checkbox"/>		
Inspection Coverage	Transducer centered axially over weld - subject to fitting geometry and obstructions	<input checked="" type="checkbox"/>	<input type="checkbox"/>		
	Full circumference scanned - subject to obstructions	<input checked="" type="checkbox"/>	<input type="checkbox"/>		
Start/ End Correspondance	Axial- Start & End UT features in same axial position +/- 1.0 mm	<input checked="" type="checkbox"/>	<input type="checkbox"/>		
	Radial Start & End UT features in same radial position 50 DP	<input checked="" type="checkbox"/>	<input type="checkbox"/>		

Restrictions/ Obstructions/ Comments:

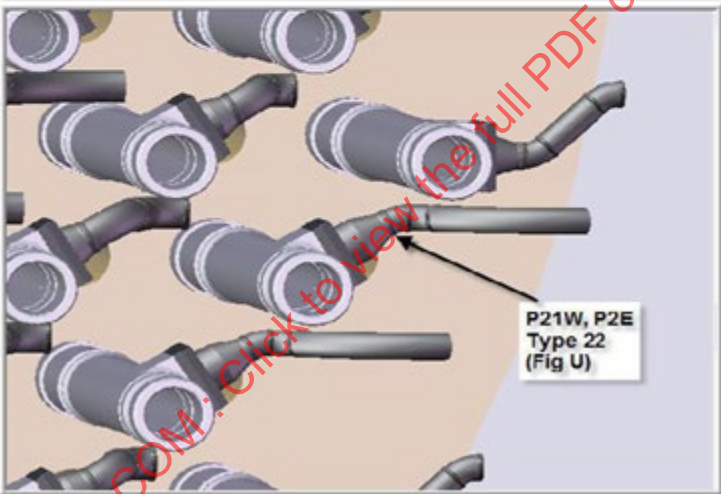


Image Courtesy of Ontario Power Generation, Inc.

### 10.2.17 Data Analysis Process

Data analysis is conducted using an iterative approach. The first step is to create a TFM image of the interface surface, see Figure 10-32. Key factors are optimization of the sub-aperture based on water path distance to the interface, correction for temperature-based velocity changes in the water path and selection of the contributing aperture based on maximum amplitude obtained for the pixel evaluated. All image formation is conducted using the direct L-L wave mode.

Figure 10-32: TFM image of the Outside Diameter (OD) surface

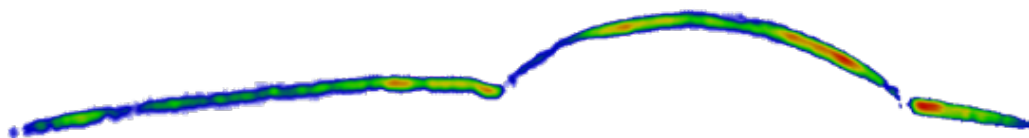


Image Courtesy of Ontario Power Generation, Inc.

The next step is to define the coordinates of the interface surface via a suitable edge detection method. A conventional approach would be to select the peak amplitude within the signal envelope attributed to the interface response. In this application, we apply a first order gradient-based technique known as the Canny edge detector. The Canny detector is stable and robust with respect to variation in envelope amplitude and to lesser degree, modulation; see Figure 10-33. Other edge detection strategies may be applied depending upon their suitability to the particular task. In this application, the location of the interface is measured to  $\pm 0.01$  mm. A review of field data and laboratory test suggests further improvement to the resolution may be possible, potentially to better than  $5 \mu\text{m}$ , however, this has not been pursued at this time.

**Figure 10-33: Image showing the trace outline to define the OD surface**

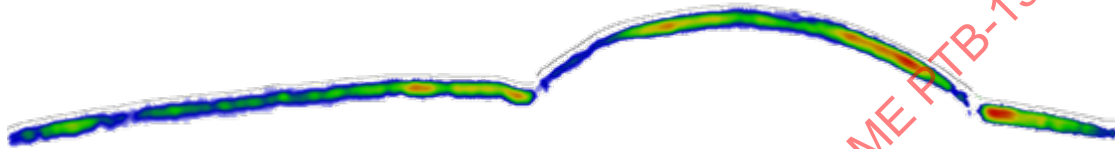


Image Courtesy of Ontario Power Generation, Inc.

When the coordinates of the interface surface have been determined, a second iteration of the TFM beamformer is applied. This iteration of the TFM beamformer employs the Fermat principle to determine transit time to the pixels in the imaging region rather than the more conventional Snell's Law. The Fermat principal results in a solution that is free from derivative based error and permits interpolation between points that have been explicitly solved. The TFM image of the interior volume is formed, and an enhanced resolution method is used to speed the image formation, beginning with a coarse resolution image, refining the resolution as amplitude of a suspect region increase and match the envelope for a valid reflector; see Figure 10-34. Time is not invested enhancing discrete speckles applying this approach.

**Figure 10-34: The TFM image of the interior**

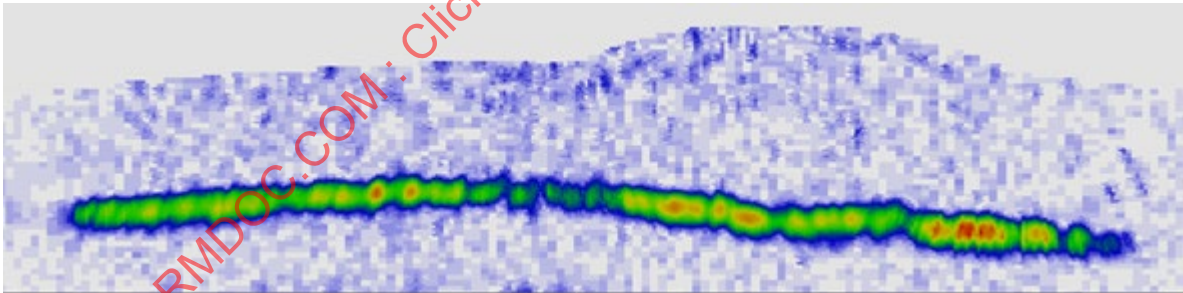


Image Courtesy of Ontario Power Generation, Inc.

A second application of the Canny edge detector defines the coordinates of the interior surface much in the same way as is done for the interface surface. However, the algorithm parameters have been altered to suit the characteristics of the interior waveform envelope; see Figure 10-35. It must be pointed out the Canny detector has been implemented to reject isolated bodies but rather to detect the continuous surface of the inspection zone ID. Transducer parameters and algorithm parameters must be linked through calibration. Parameter selection has been performed and verified during the development of the system. The resolution of the Canny detection algorithm has been set to  $0.025$  mm, that in combination with the interface resolution provides an overall measurement resolution of  $0.03$  mm.



**Figure 10-35: Plotting of the ID interface**

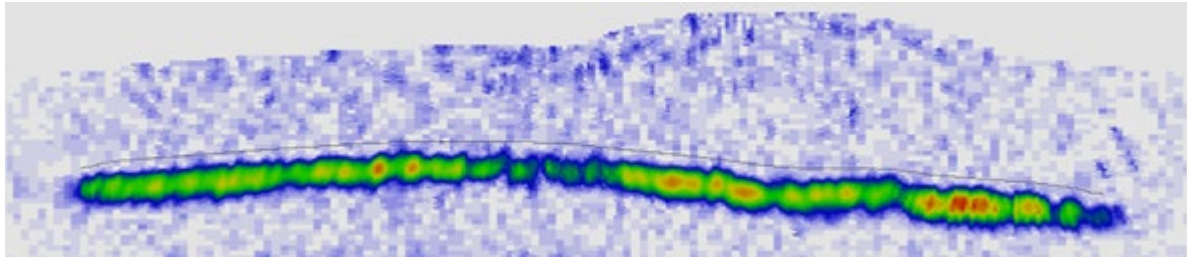


Image Courtesy of Ontario Power Generation, Inc.

For each TFM interface–interior volume coordinate pair, the minimum distance between the interface surface coordinates and the ID surface coordinates is evaluated and plotted, and the minimum thickness for that frame is identified; see Figure 10-36. This process is repeated for every FMC frame acquired. The interface and ID surface coordinates are plotted relative to the manipulator circumferential axis for all frames processed creating a 3D image of the inspection surfaces, a typical example is provided in Figure 10-37.

**Figure 10-36: Evaluation revealing the minimum thickness**

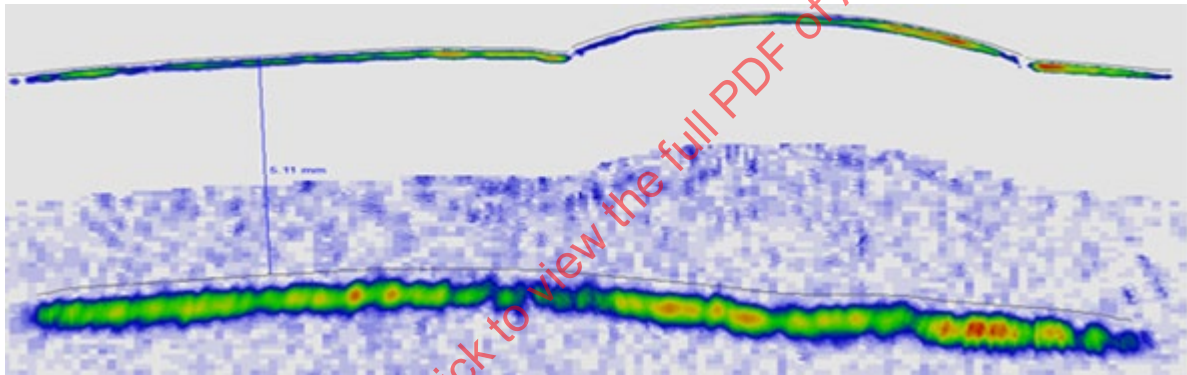


Image Courtesy of Ontario Power Generation, Inc.

**Figure 10-37: Plotting of the ID and OD interface in a 3D model**

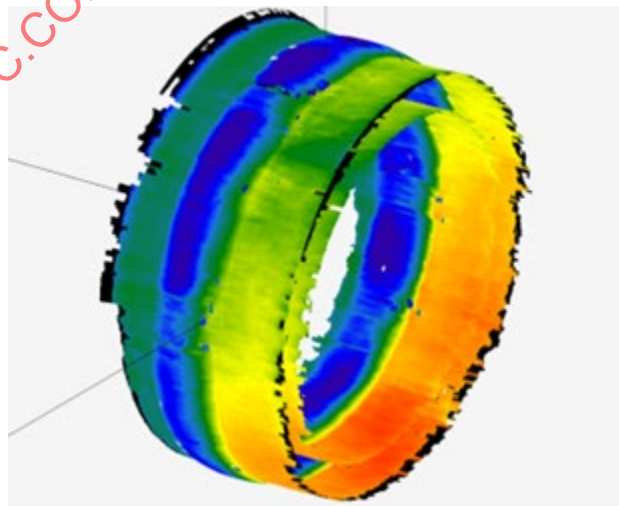


Image Courtesy of Ontario Power Generation, Inc.

### 10.2.18 Data Analysis Procedure

Data analysis begins immediately after the FMC data file has been uploaded to the analysis server. The TFM algorithm executes with the default set of analysis parameters.

The Analysis Operators will retrieve the following from the server:

FMC data file

Inspection Record

Calibration (verification) file

Calibration Record

The calibration file is checked for validity, the Analysis Operators will then review the FMC data file to make independent assessments of data quality and coverage metrics. Should the data quality not meet required standards, the analysis operators may call for a rescan of the affected component. The rationale for this function is to provide a QA check to the data obtained during the inspection campaign and enforce the process of reviewing the raw data as an input to analysis process. The Analysis Operators will also make notations of features and key metrics related to the scan. An Analysis Record is created to organize these notations. The information is used for plotting absolute position of the scan as well as potential adjustment to analysis parameters area of particular interest. Analysis parameters can be altered globally or isolated to a series of frames or even a region within a frame. Typically, this will be done to isolate and enhance a region of suspected minimum thickness. The Analysis Operators apply the revised parameters to applicable frames in the calibration block file to assess the effect of the parameters and confirm there is no adverse effect on measurement accuracy.

The next step in the analysis procedure is to retrieve the processed result. The Analysis Operators will page through the processed frames coordinated with the corresponding raw UT frame. The purpose of this step is to evaluate the frame result for congruency with the UT data and the trend in immediately adjacent frames. The Analysis Operator checks for potential missed minimum thickness regions as well as instances where the edge detector incorrectly identified a minimum reading. The Analysis Operator has various options to correct these conditions. The Operator can reprocess a series of affected frames, re-deploy the edge detector to a more narrowly defined region or trim the affected frame.

When the Analysis Operator has completed assessment of the TFM results, the analysis record form and results record form are completed. The modified TFM result is uploaded to the server along with electronic copies of the associated records. The results from two separate streams of analysis are compared for consistency of result. Discrepancies exceeding a prescribed threshold are sent to the Resolution Analyst for further assessment.

### 10.2.19 Results

The MIT process is capable of acquiring and generating the exterior and interior profiles of the fitting-to-fitting welds through a range of variable geometry in the fitting to fitting welds. Inspection through as formed weld caps to observe the interior volume has been achieved. In some instances, minor inclusions in the weld volume have been noted; see Figure 10-38. These inclusions have been verified on radiographs performed at the time of fabrication.

**Figure 10-38: Minor inclusion from fabrication welding**

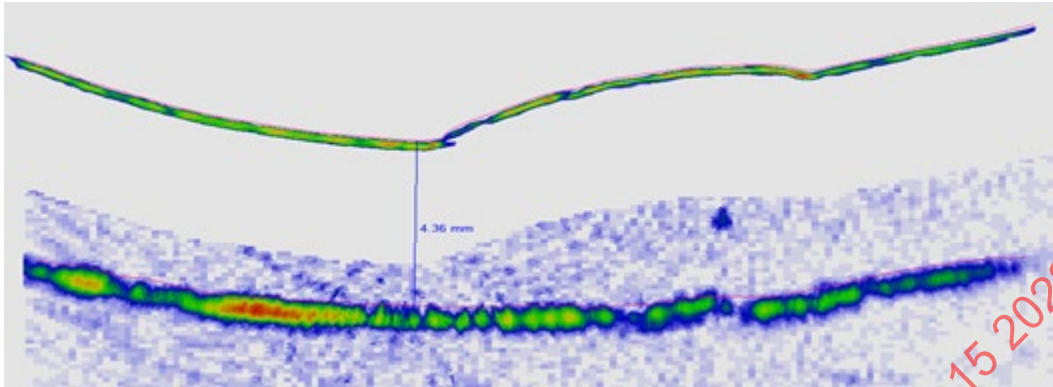


Image Courtesy of Ontario Power Generation, Inc.

Inspection results are linear in the lateral direction (along the inspection surface) and transverse direction (distance normal to the transducer face). The result is an accurate representation of the inspection geometry that is easily interpreted. Figure 10-39 is the result in the cheek region of a fitting to fitting weld. The FAC erosion pattern is observed under the weld cap with steps corresponding to the fusion lines of the weld preparation. A similar pattern is observed in a section of an ex-service feeder pipe, see Figure 10-40.

**Figure 10-39: Image(s) result in an accurate visualization of the component**

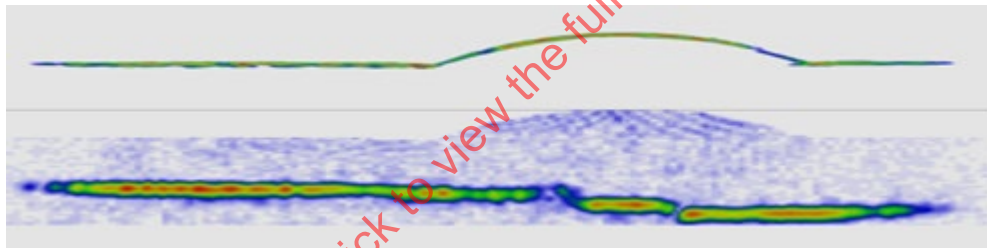


Image Courtesy of Ontario Power Generation, Inc.

**Figure 10-40: Section of an ex-service feeder demonstrating step erosion at the weld root. Flow is right to left in this image.**



Image Courtesy of Ontario Power Generation, Inc.

### 10.2.20 Discussion

The MIT technique provides a robust capability to resolve rapidly changing surfaces located beyond an arbitrary interface geometry. Figure 10-41 shows the results for a test sample where highly localized changes in thickness were introduced immediately adjacent a convex weld root.

**Figure 10-41: Example of the MIT result for a case where both the exterior and interior surfaces are independently and rapidly changing in profile. The hub is on the right, weld center and intrados of the fitting is on the left of the image.**

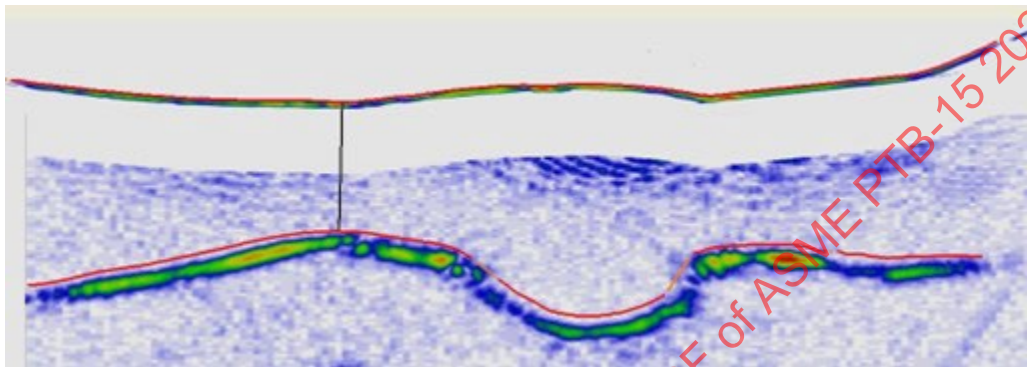


Image Courtesy of Ontario Power Generation, Inc.

The MIT concept was initially proposed in 2007 and developed over a 20-month period spanning 2008 to 2010. The system was first applied in the spring of 2010 and has been deployed more than 12 times in subsequent outages. The MIT system has been patented in several jurisdictions around the globe. Incremental improvements have been introduced to reduce inspection and analysis times. Current inspection times are on par with the time required using convention inspection tools. Inspection time savings are not a motivating factor to use this technology. The inspection manipulator can operate with minimal intervention by the Platform Operator compared to conventional methods. Reduced intervention in turn saves operator radiation exposure, increasing the number of locations the operator can inspect while decreasing the net dose for the inspection campaign. As with many immersion-based systems, reductions in data quality are invariably associated with air bubble formation on the inspection surface or transducer surface. The Acquisition Operators must be vigilant to these conditions and intervene to remove the accumulated air before scan quality is impaired. Scan data containing excessive air bubble artifacts invariably reduces the quality of the TFM result. Poor results in turn require time-consuming intervention by the Analysis Operators to correct and reprocess the affected frames to improve result quality. If air bubbles in a frame are too prominent, it is likely that no amount of correction can recover a useful result from the frame. In this case, the affected region is not inspected.

Figure 10-42 through Figure 10-45 are 3D representations of the feeder weld joint color coded for thickness. These plots can be exported for 3D printing reproducing the true inspection geometry. Furthermore, the same plots can be exported for FEA analysis. The profiles and 3D reconstructions represent a leap forward in inspection technology. The ability to map exterior and interior profiles independent of each other improves the determination of localized thinning rates for a particular location. A less conservative, more realistic value for thinning rate can be assigned increasing component longevity, thereby reducing the costs linked to premature component replacement. The 3D reconstructions can be exported in point cloud format to support Finite Element Analysis (FEA). FEA stress analysis provides a more accurate assessment to justify Fitness For Service in critical applications.



**Figure 10-42: 3D image of a fitting-to-fitting weld color coded for thickness. Note the areas in black are outside the range of color coding for thickness.**

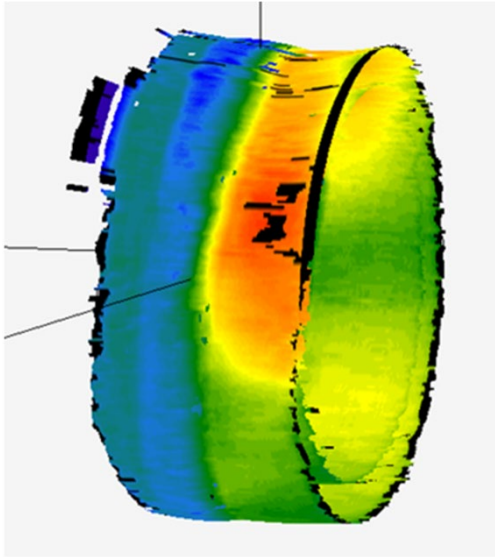


Image Courtesy of Ontario Power Generation, Inc.

**Figure 10-43: 3D image of a 2 1/2 inch fitting to fitting weld color coded for thickness.**

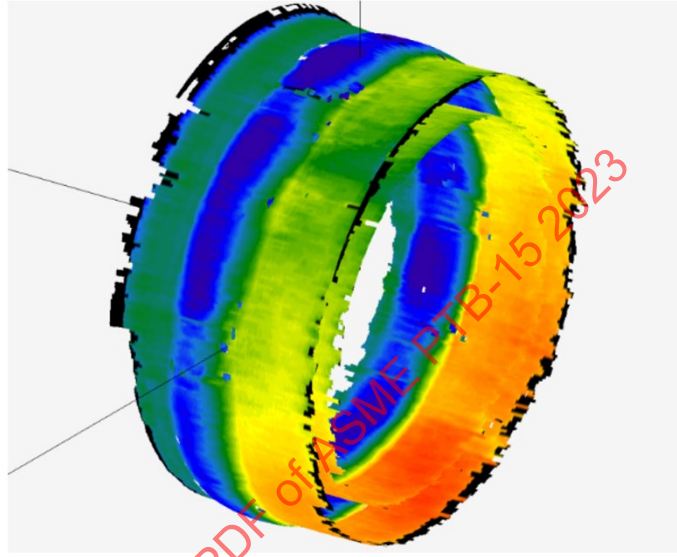


Image Courtesy of Ontario Power Generation, Inc.

**Figure 10-44: Color-coded 3D representation of a 2 inch feeder fitting to fitting joint.**

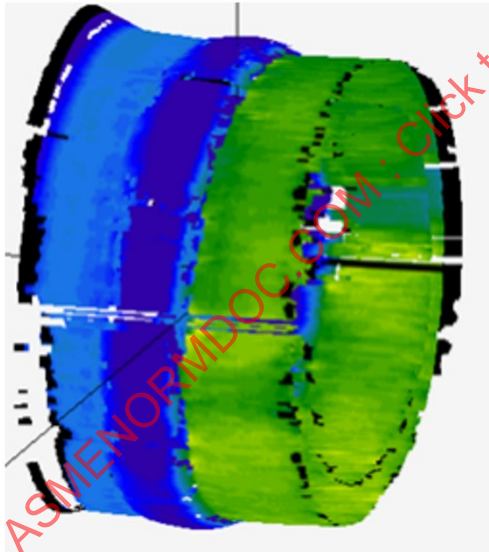


Image Courtesy of Ontario Power Generation, Inc.

**Figure 10-45: Rotation of the 3D model**

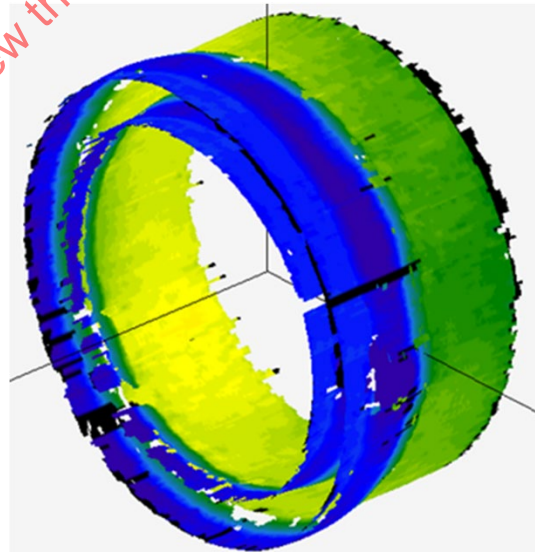


Image Courtesy of Ontario Power Generation, Inc.



Consider the result presented in Figure 10-46. The image on the left is a 3D reconstruction of an inspection location in the field that is colored in monotone grey and illuminated by a virtual light source. Visible are the weld pool ripple, the texture of the forged fitting on one side of the weld, and the smooth machined surface of the hub on the other side of the weld. This photo-realistic result compares favorably with a photograph of an ex-service sample taken in a laboratory setting. The missing line in the result represents a single failed frame, underscoring the data density of the result. The photo-realistic result is anecdotal evidence of the accuracy and resolution of the MIT process. However, the features in the result can be used in the following manner. Applying image analysis algorithms, a series of features unique to the inspected object can be extracted. These features can be used as a ‘fingerprint’ to be identified in future repeat inspections. The fingerprints can be compared to verify the correct object was inspected and more significantly as benchmarks to register the historical scan to future scan results. This would enable precise point for point comparison of inspection locations across two different scans. For some applications, this capability alone may be sufficient justification to deploy the MIT technology.

**Figure 10-46: Grey scale 3D model vs an actual photo of the component**

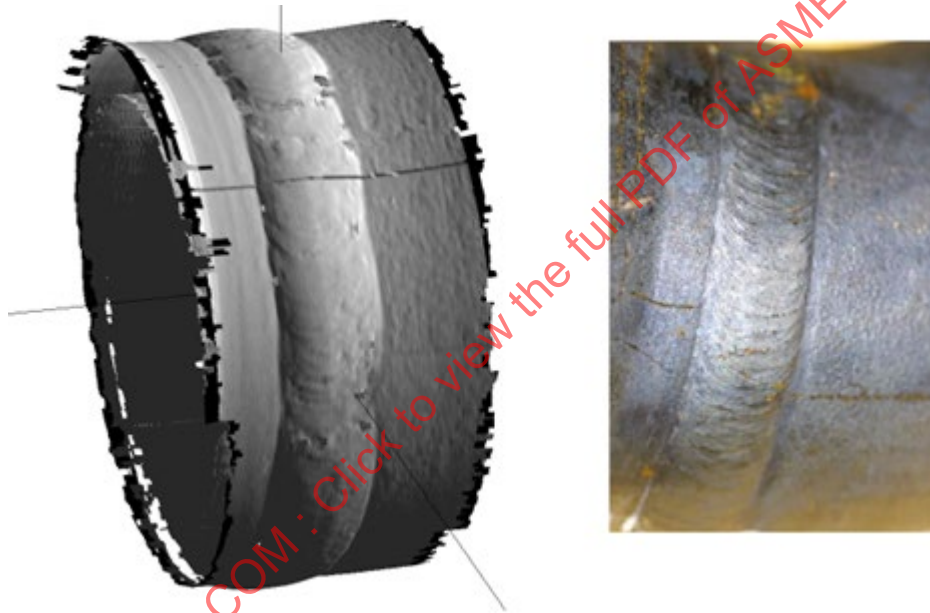


Image Courtesy of Ontario Power Generation, Inc.

Figure 10-47 depicts a series of sequential TFM images of the weld cap interface. The individual segments of ripple peaks and troughs can be observed to build in and recede in the series of frames. Ability to resolve the weld cap peaks and troughs is essential to define the sound path through the weld cap, a prerequisite to successful volumetric imaging within the weld material.

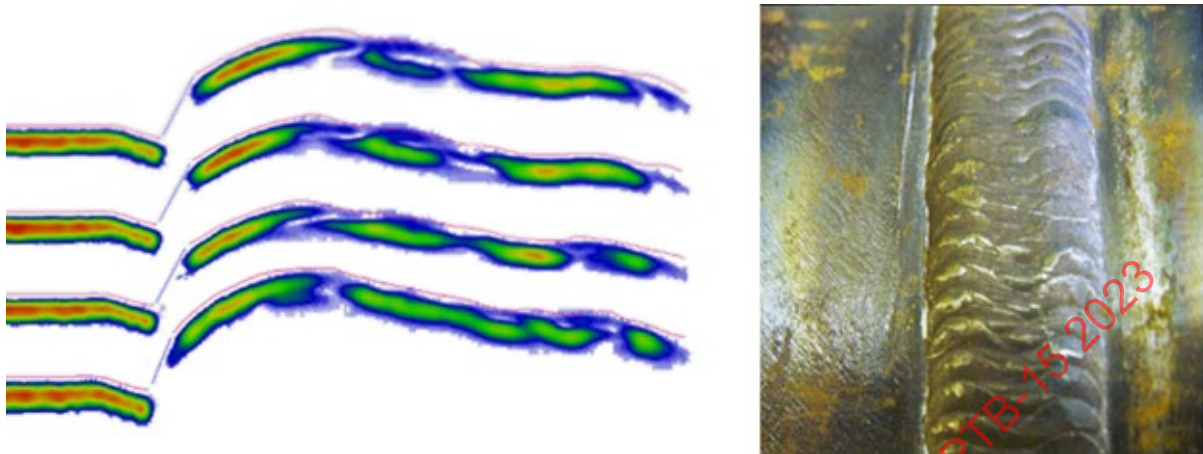
**Figure 10-47: OD imaged profiles vs the actual component**

Image Courtesy of Ontario Power Generation, Inc.

### 10.2.21 Further Developments

Various enhancements to the TFM beamforming strategy have been explored. One such enhancement is a 3rd iteration of TFM beamformer. The interior surface of the sample is considered and the path reflecting back into the inspection volume is solved. The modification is intended to image the corner trap reflector which is a characteristic of the defects open to the interior surface. The implementation solves for L wave, mode conversion and S wave signals. Initial results with EDM notches in reference blocks have been encouraging however, implementation on ex-service samples has not been as successful. Application of a 3rd iteration of TFM requires all error and uncertainty to be controlled to within a narrow margin across the surfaces through which the paths are calculated. The imaging performance is sensitive to the texture of the interior surface with smooth surfaces providing improved quality. Further development of this capability has not been pursued, as inspection for surface breaking defects is not required for the current application.

Another development that has been explored is the application of a material model in the TFM beamformer. Model based TFM imaging would be useful for the volumetric inspection of anisotropic material such as Austenitic weld material.

An application was developed for the inspection of 304 stainless steel weldments with 308L weld material. In this case, a macrograph of a weld fabricated with 308L fill material was used to create a model of the grain orientation within the weld material. The regions in the model corresponding to the grains were assigned group and phase velocities for the L wave mode. Transit times and orientations were solved by applying the group and phase velocity such that the minimum transit time between adjacent grain boundaries were determined. FMC data arrays were acquired using 3, 5, and 7.5 MHz linear arrays. The data sets were processed with the modified TFM code. Results obtained with the 3 MHz transducer demonstrated marked improvement in resolution of implanted defects, whereas the 5 MHz data sets yielded only modest improvements. The 7.5 MHz data sets did not yield discernible improvement when processed with the modified TFM analysis code.

### 10.2.22 Conclusions

A unique combination of FMC in immersion mode with iterative application of TFM has been developed and deployed for inspection use. This system, MIT, has provided unique capabilities that are inaccessible to contact modes of FMC/TFM.

The system is capable of inspection through as formed weld caps and can accommodate a wide range of rapidly changing geometries on both the interface surface and the interior. The results are graphics

that are easily interpreted by a layman. The MIT technology yields potential for input to FEA tasks in addition to imaging features that can be used as benchmarks for aligning repeat scans.

Extension to a 3rd iteration of the TFM beamformer have been introduced and holds potential to provide volumetric imaging bounded by complex geometries. Similarly, initial development work into application of TFM for anisotropic media has been conducted and the results have demonstrated potential for further development.

### 10.3 Crack Growth Monitoring with PAUT and TFM

#### 10.3.1 Introduction

Standard laboratory fatigue tests typically require monitoring of the crack height at various intervals to obtain an engineering relationship between applied loading and the rate at which the crack propagates. This allows calculation of the fatigue crack growth rate, which can be used in engineering assessments to predict the remaining service life of high-consequence, cyclically loaded structures such as cranes, bridges, aircraft wing spars, power generation turbines, etc. Crack growth rate can be material- and/or geometry-dependent, and thus can require some sophistication in monitoring crack size particularly at low crack growth rates or where environmental factors (i.e., corrosion) influence fatigue properties.

Conventional laboratory practice for monitoring crack size during fatigue testing involves the use of instrumentation such as clip gages, cameras, electric-potential drop (EPD) sensors, etc. While they have high sensitivity and resolution, these types of instruments usually measure an indirect property as a function of crack size rather than the crack itself. For example, a clip gage measures a change in compliance or stiffness of a test sample as the crack propagates. EPD sensors measure a change in the electric resistance during cracking and reduce the cross-sectional area of the specimen as a low-amperage electric current passes through the non-cracked portions. Cameras are useful for measuring crack height in thin materials but are far less accurate in quantifying crack height in thicker sections due to increased tendencies for crack tunneling. Consequently, while these techniques have been widely used in fatigue testing, they require careful setup, calibration and, in some cases, complicated data analysis to generate crack size information. EWI has evaluated the feasibility of using advanced NDE methods as an alternative approach for crack height measurement to simplify the process and gather better information about the nature of the crack during propagation (i.e., detect non-planar growth, tunneling, etc.).

#### 10.3.2 Approach

The test setup used a 50-kip servo-hydraulic test frame, a FlexTest GT Controller Version 3.5C 1815 to apply and control the cyclic loads, and an MTS 5 mm clip gage Model 632.02F-21 to monitor crack height using compliance methods on a standard, single-edge notched bend (SENB) fracture toughness specimen with a starter notch per ASTM E1820.

Figure 10-48 illustrates the typical SENB rectangular geometry with a machined notch and fatigue crack that emanates from the notch bottom. As part of the conventional specimen preparation for fracture toughness tests, a fatigue crack is grown to a prescribed height from the starter notch. Monitoring the crack height is done using a clip gage under standard practice.

In our study, the initiation and growth of a fatigue crack was monitored by three different ultrasonic testing (UT) methods along with the conventional clip-gage method. For most SENB specimens, the final height of the fatigue crack at the completion of the cyclic loading is 3.0 mm – 5.0 mm (0.12 in. - 0.20 in.). However, in this program, the crack was grown to more than 25 mm (1.0 in.) to comprehensively assess UT techniques for monitoring crack growth over an extended period of time and for much longer fatigue cracks.

The SENB test specimen was 300mm long, 40mm wide, and 45.9mm high. The notch, 11.2mm deep, was generated by electro-discharge machining (EDM) with a width of 1mm (Figure 10-49). The

recorded test parameters during the cyclic loading included number of load cycles, maximum applied load (to permit calculation of applied stress intensity factor) and crack height as predicted by compliance methods using the clip gage measurements. (See ASTM E1820 for more information about these parameters and how they are measured or calculated).

The cyclic loads were applied under three-point bending with the loading concentrated at the root of the notch. Figure 10-49 shows the three-point bend rig where the center roller at the top of the figure is positioned in-line with the machined notch during cyclic loading. A cyclic loading rate of about 5-10 hertz was applied at a predetermined load range to initiate fatigue cracking and growth to the target height, at which point the cyclic loading was stopped. The applied loads were based on the size of the test specimen, the material yield strength, and the depth of the machined notch to ensure that the resulting cyclic stresses at the notch tip were elastic and appropriate for fatigue crack initiation and growth (i.e. to prevent plastic deformation or ductile tearing during cyclic loading).

**Figure 10-48: Illustration of a conventional SENB test specimen geometry**

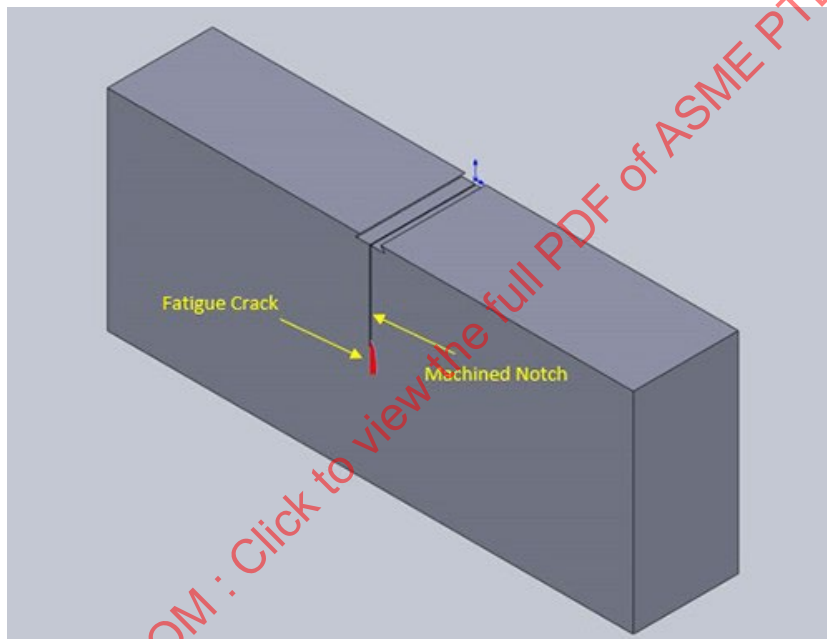


Image Courtesy of Oleg Volf

**Figure 10-49: Fatigue test setup on a servo-hydraulic test machine using an MTS clip gage**

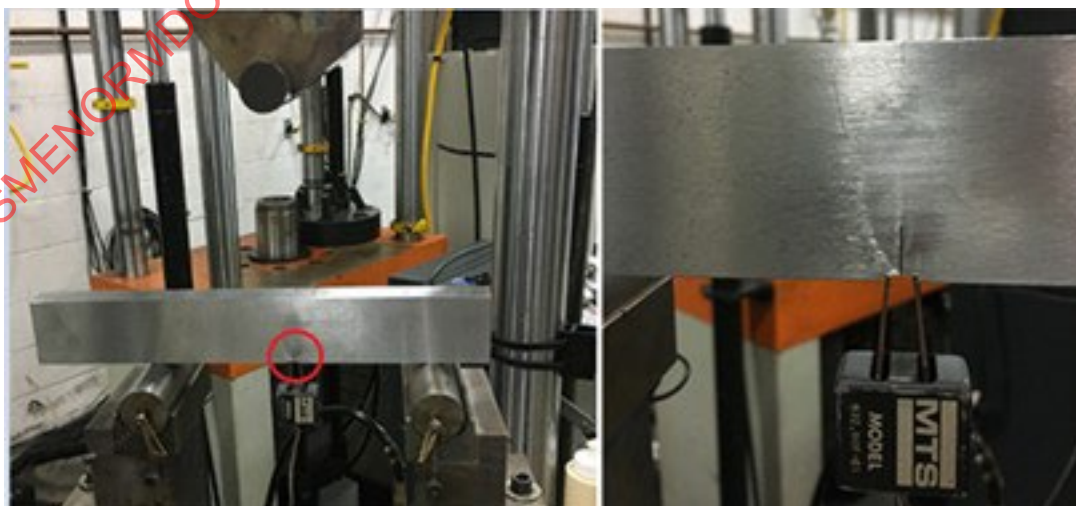


Image Courtesy of Oleg Volf



### 10.3.3 Description of the UT Setup

To achieve high resolution and sizing accuracy, an Olympus 7.5L60 PWZ1 7.5MHz linear array probe containing 60 elements at a pitch of 1 mm was placed on a Rexolite SPWZ1 N55S wedge to generate shear waves at natural refracted angles 55 degrees (Figure 10-50). The ultrasonic data was collected using an Olympus OmniScan X3 instrument. To prevent interference with the test fixture, the SENB sample was removed after each scan. After the UT measurements were made, the three-point bend fixture was re-positioned, and the cyclic loading re-initiated to continue crack propagation. Three different UT measurement techniques were evaluated: conventional phased-array ultrasonic testing (PAUT), full matrix capture/total focusing method in the T-T mode (FMC/TFM-T-T), and full matrix capture/total focusing method in the TT-T mode (FMC/TFM TT-T).

Figure 10-50: The phased array ultrasonic technique setup to monitor the notch

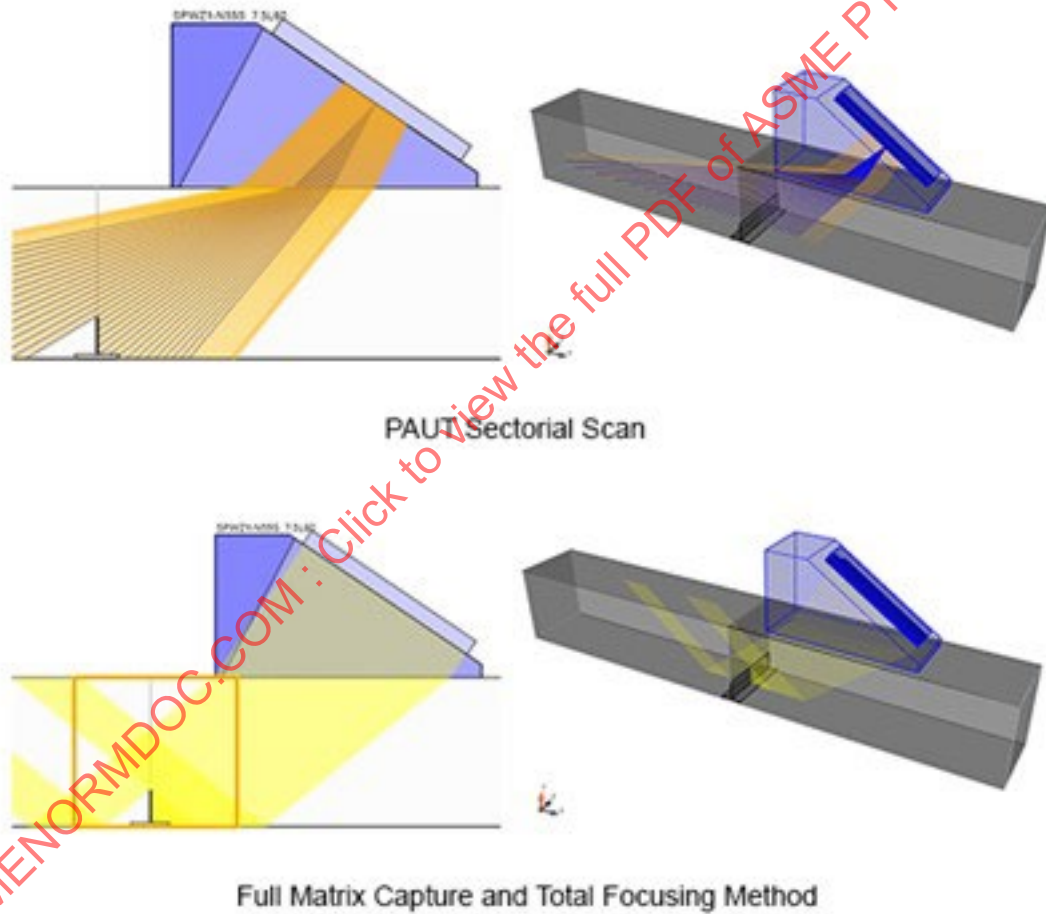


Image Courtesy of Oleg Volf



**10.3.4 Results**

UT readings were taken at 20-30 minute intervals throughout the fatigue test. The test images display the growth of a crack using the different UT approaches. To optimize the measurement, the sensitivity of the ultrasonic system was set high enough to detect weak diffraction signals from fatigue cracks in the pulse-echo mode.

**Table 10-10: Periodic Crack Measurement Values Using Various Measurement Techniques**

Number of Cycles	Crack Length from Clip Gage (mm)	Crack Length with TFM (mm)	Crack Length with PAUT (mm)
44914	11.88	12.38	12.61
66953	14.05	16.94	17.03
109833	20.25	22.17	21.77
129476	23.12	25.02	24.09
150378	26.22	26.83	27.08

Courtesy of Oleg Volf

**10.3.5 Analysis**

The data presented can be plotted on a graph of crack size from the original position of the notch tip against the number of cycles as shown in Figure 10-51 through Figure 10-63. These results provide valuable insight into the nature of the material and the variable rate of the crack growth as input to failure models.

**Figure 10-51: TFM images (left – T-T Mode, right – TT-T Mode), Number of Cycles = 0**

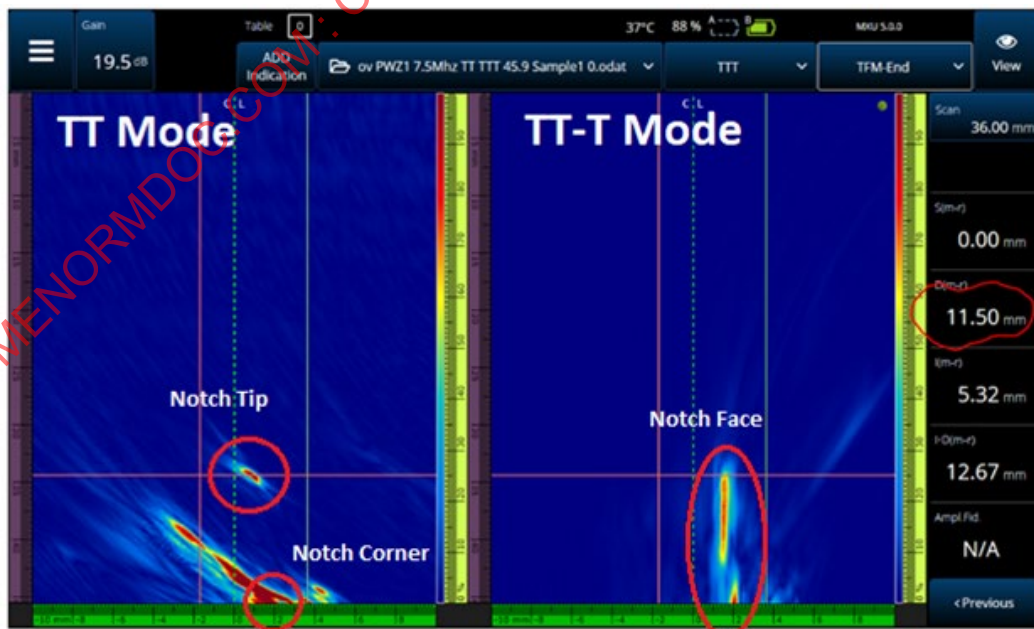


Image Courtesy of Oleg Volf

Figure 10-52: PAUT image (Sectorial Scan), Number of Cycles = 0

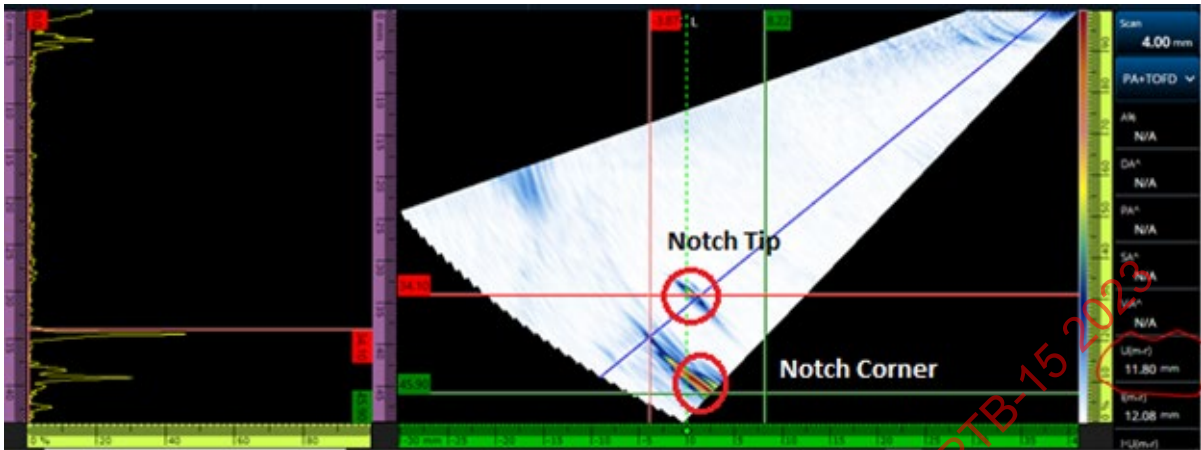


Image Courtesy of Oleg Volf

Figure 10-53: TFM images (left-T-T Mode, right-TT-T Mode), Number of Cycles = 44914

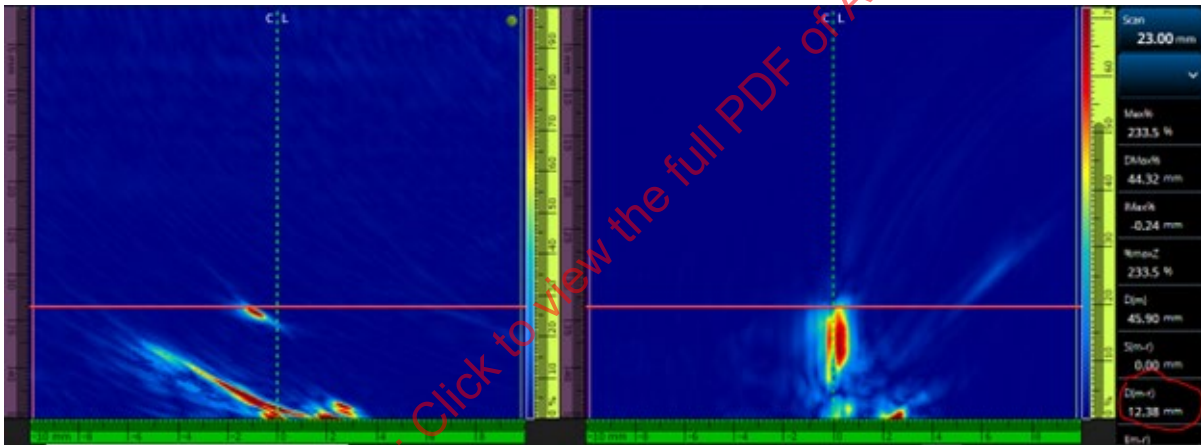


Image Courtesy of Oleg Volf

Figure 10-54: PAUT image (Sectorial Scan), Number of Cycles = 44914

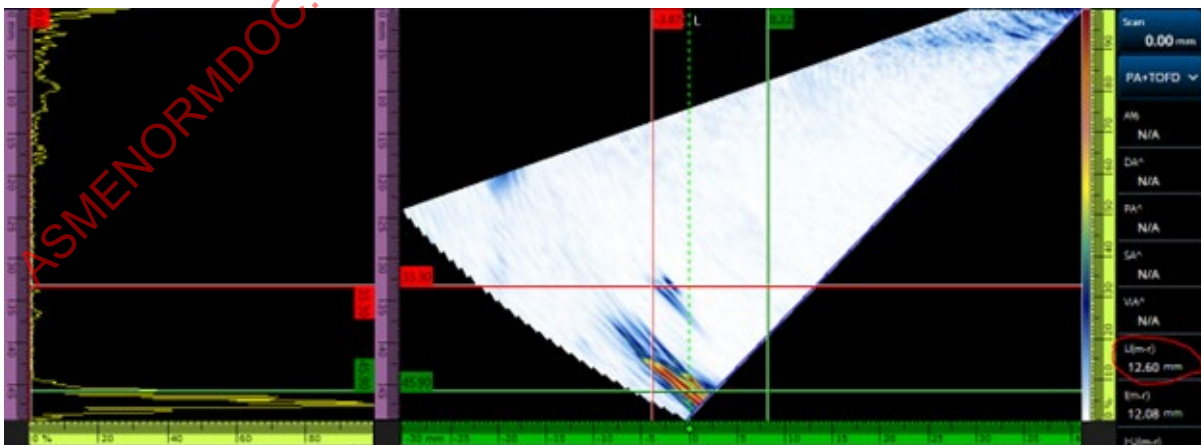


Image Courtesy of Oleg Volf

Figure 10-55: TFM images (left–T-T Mode, right–TT-T Mode), Number of Cycles = 66953

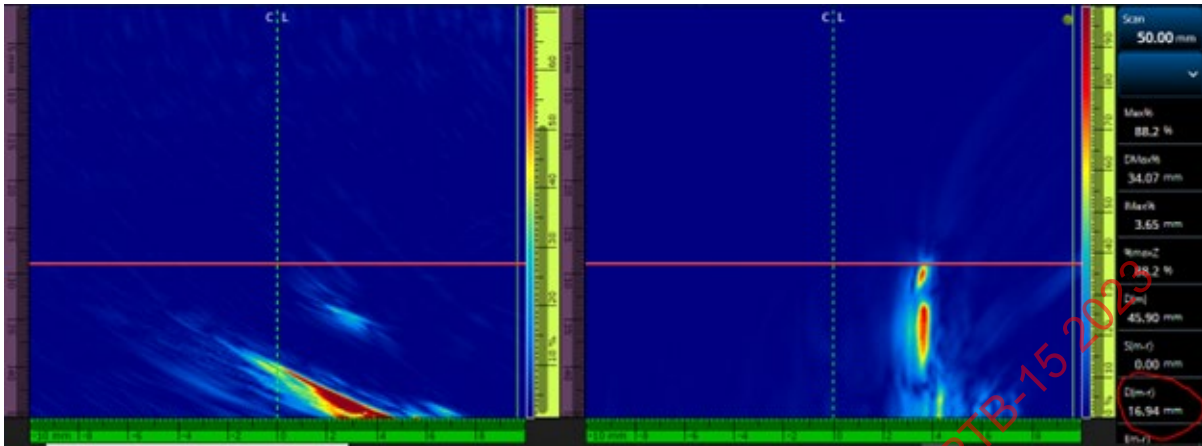


Image Courtesy of Oleg Volf

Figure 10-56: PAUT image (Sectorial Scan), Number of Cycles = 66953

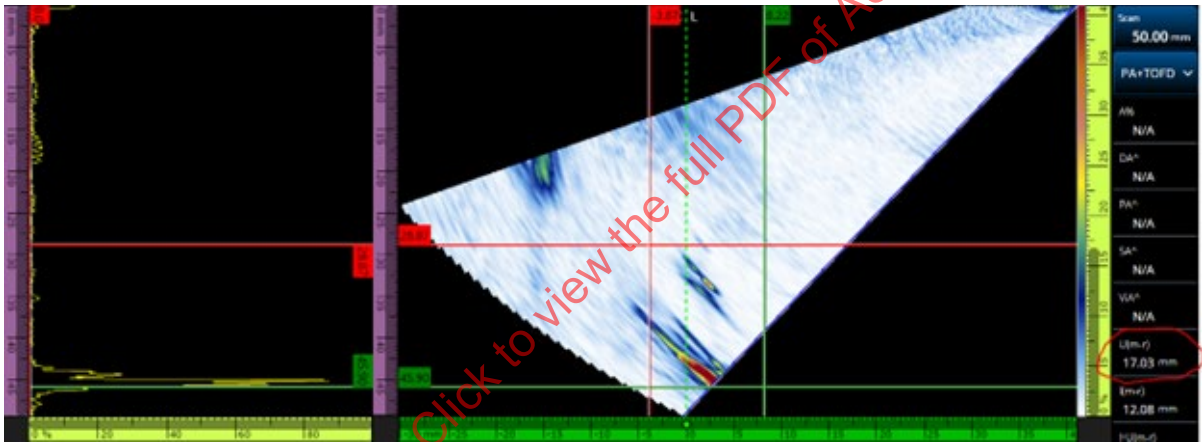


Image Courtesy of Oleg Volf

Figure 10-57: TFM images (left–T-T Mode, right–TT-T Mode), Number of Cycles = 109833

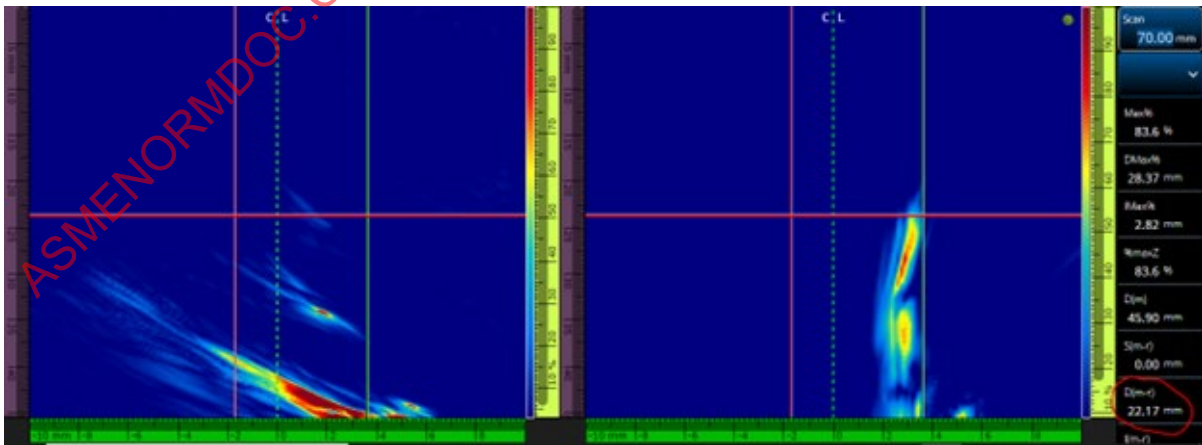


Image Courtesy of Oleg Volf



Figure 10-58: PAUT image (Sectorial Scan), Number of Cycles = 109833

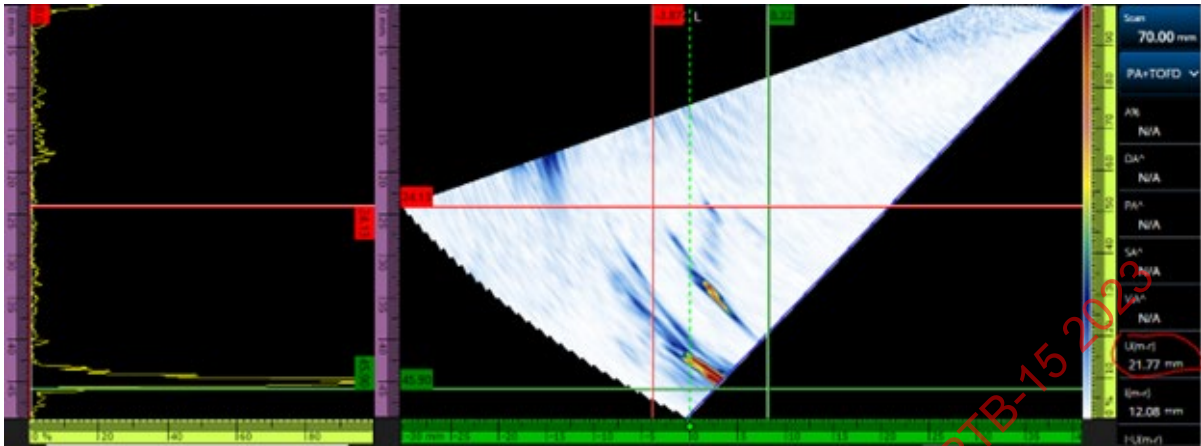


Image Courtesy of Oleg Volf

Figure 10-59: TFM images (left-T-T Mode, right-TT-T Mode), Number of Cycles = 129476

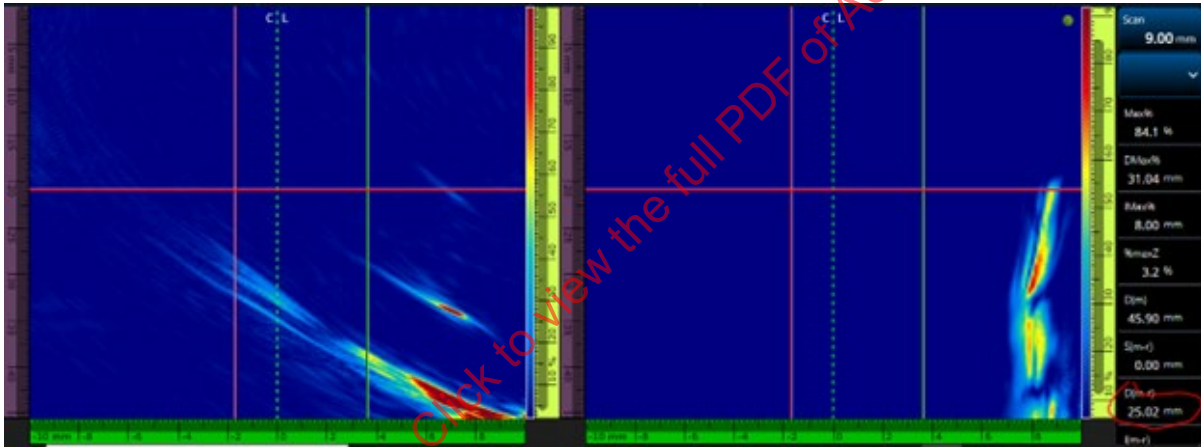


Image Courtesy of Oleg Volf

Figure 10-60: PAUT image (Sectorial Scan), Number of Cycles = 129476

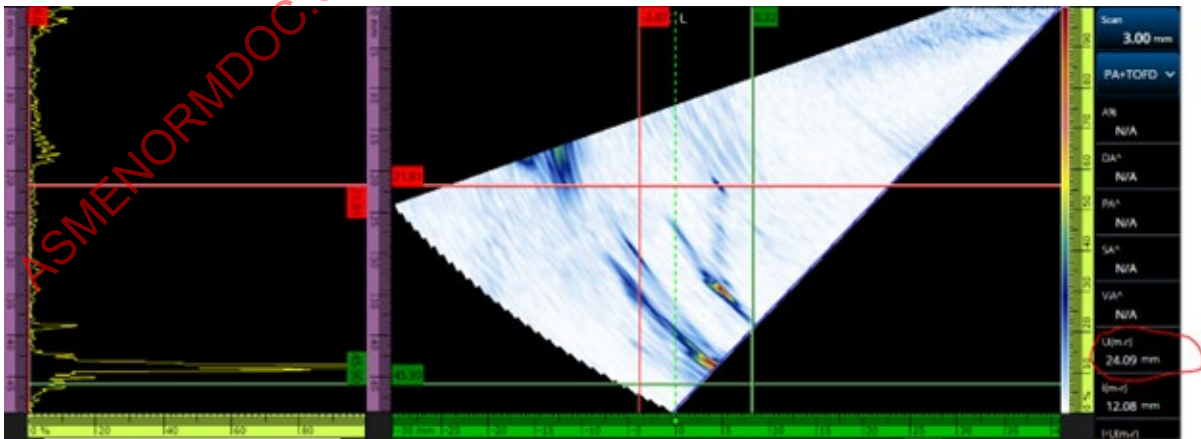


Image Courtesy of Oleg Volf

Figure 10-61: TFM images (left–T-T Mode, right–TT-T Mode), Number of Cycles = 150378

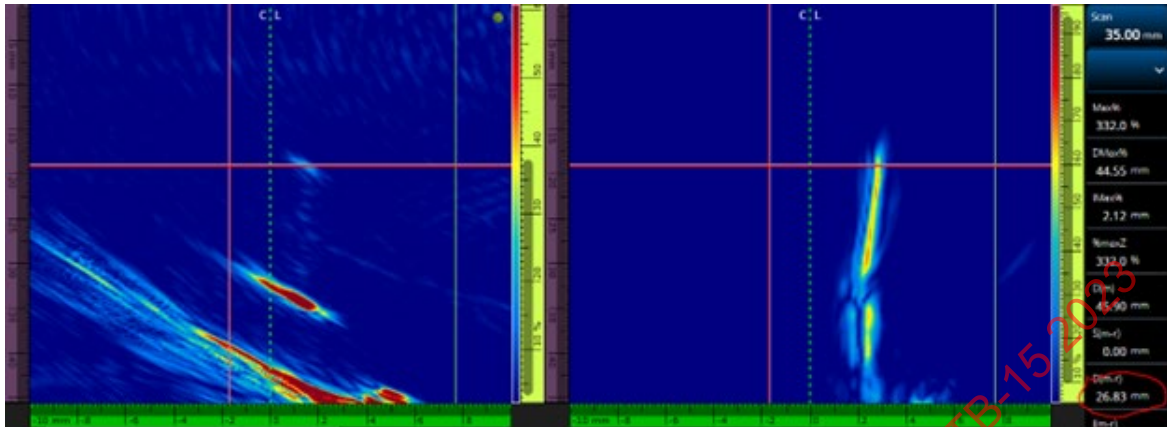


Image Courtesy of Oleg Volf

Figure 10-62: PAUT image (Sectorial Scan), Number of Cycles = 150378

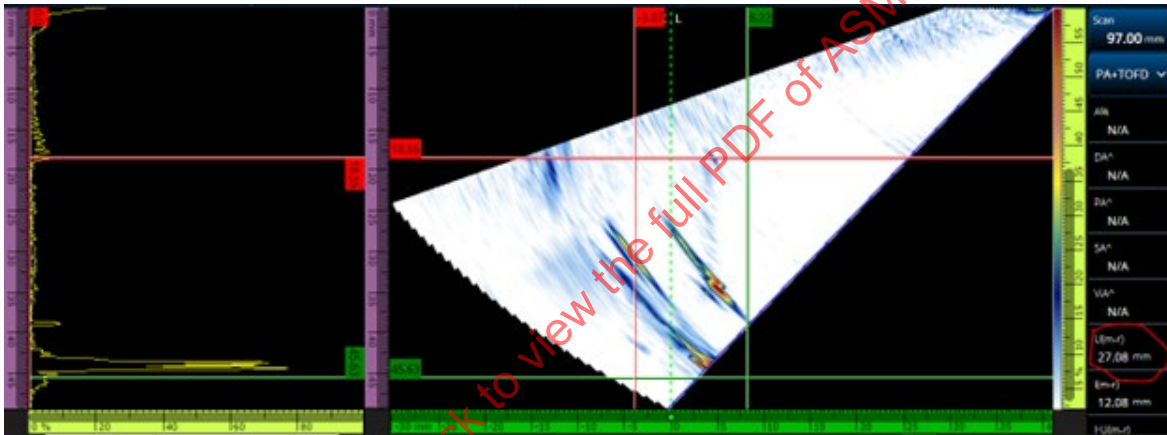
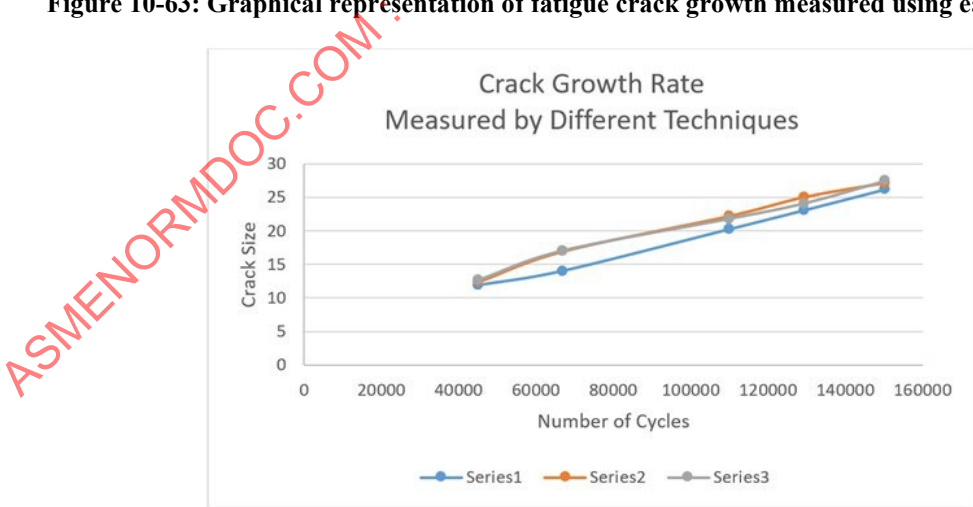


Image Courtesy of Oleg Volf

Figure 10-63: Graphical representation of fatigue crack growth measured using each technique



Series 1 - Crack Length from Clip Gage (mm)	Series 2 - Crack Length with FMC/TFM (mm)	Series 3 - Crack Length with PAUT (mm)
---	---	--

Image Courtesy of Oleg Volf



At the conclusion of testing, sample 17279-13 was opened to measure the crack physically. Table 10-11 lists nine post-test measurements, starting from the left side of the fatigue crack profile as viewed in Figure 10-64. The table also includes the average, minimum, and maximum measurements of the crack.

**Table 10-11: Post-test Measurements**

Sample 17279-4-13		
	Position (mm)	Crack Length (mm)
a(1)	0.23	25.66
a(2)	3.02	26.16
a(3)	5.81	26.50
a(4)	8.60	26.75
a(5)	11.40	26.89
a(6)	14.19	26.78
a(7)	16.98	26.49
a(8)	19.77	26.15
a(9)	22.56	25.53
<b>Average</b>	<b>Min</b>	<b>Max</b>
26.33	25.53	26.89

Courtesy of Oleg Volf

**Figure 10-64: Image of Sample 17279-4-13 used for detailed crack measurement**

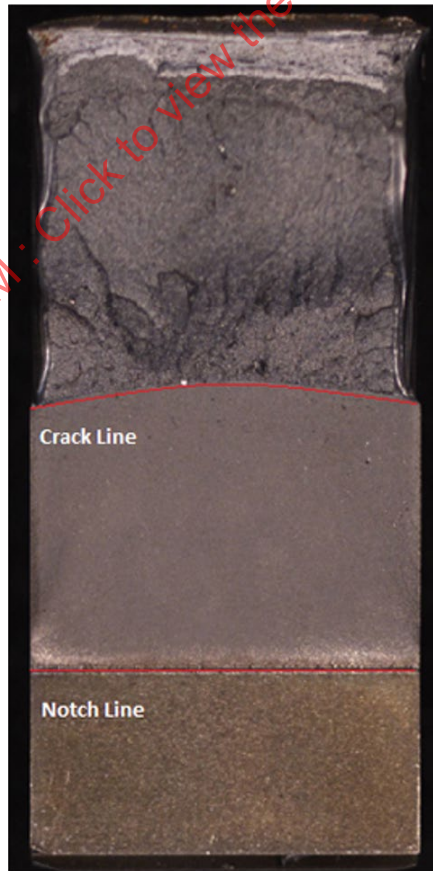


Image Courtesy of Oleg Volf

### 10.3.6 Conclusions and Next Steps

Results using conventional PAUT and TFM techniques demonstrated very similar sizing accuracy as shown in Table 10-12. The TFM-measured crack height nearly matched the visual confirming crack height measurements and was slightly more accurate than PAUT and the compliance-based clip-gage methods.

**Table 10-12: Comparison between the four different crack measurement techniques in this study**

Visually Measured Max Crack Length (mm)	Crack length from clip gage (mm)	Crack Length with TFM (mm)	Crack length with PAUT (mm)
26.89	26.22	26.83	27.08
% difference from visual measurement	-2.5	-0.2	+0.7

Courtesy of Oleg Volf

The UT measurement techniques show comparable results to the clip gage during the fatigue test and the gradient of this plot gives the growth rate of the crack at any given time during its propagation towards failure. Because UT is a nondestructive technique, this process shows promise for structural health and crack growth applications in the field. EWI plans to complete more testing to verify the accuracy of this technique for structural health monitoring.

Additionally, the FMC/TFM technique shows a significantly improved visual presentation of the crack including the orientation of crack propagation (crack angle). As shown in Figure 10-65, the TFM crack image is visualized as a cross-section of the sample, which provides more accessible data and eliminates the need for specially trained UT expertise to evaluate the images.

**Figure 10-65: SENB sample showing fatigue crack and corresponding FMC/TFM image of the crack**

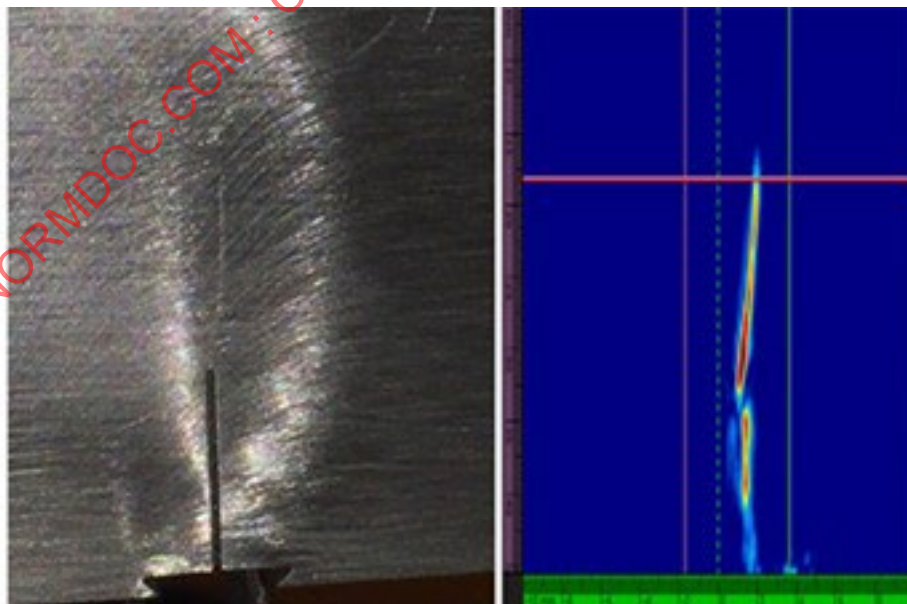


Image Courtesy of Oleg Volf

The laboratory feasibility work described here demonstrates the advantages of FMC/TFM over other conventional NDE and non-NDE methods commonly used to detect and monitor crack growth. Not only is crack sizing improved, but information regarding the nature and orientation of cracking can be visualized with FMC/TFM (i.e., crack orientation, degree of branching, etc.). Moreover, the improved resolution and accuracy obtained with FMC/TFM methods for inspection of fatigue-sensitive structures offers the potential for increased accuracy in fatigue crack detection and sizing, which would correspondingly improve the accuracy of engineering life assessments based on those crack measurements. To provide a basis for establishing field inspection protocols, additional work should consider more complex specimen crack geometries such as corner cracks, branched cracking, and buried cracks (i.e., cracks that do not extend to a free surface).

## 10.4 Weld Examination-Introduction

Weld examinations with FMC/TFM can provide comparable results to traditional phased array, while also possessing unique qualities that would be difficult or impossible to replicate with a traditional beam forming, single plane focused phased array examination. Notable examples include optimal focus, spatial resolution, ease of applying indirect modes, improved imaging and detection with divergent sound waves spreading in all directions, among others. These benefits can provide powerful tools for most weld examinations.

ASME BPVC Section V details the requirements for performing FMC for a fracture-mechanics-based acceptance criteria when the referencing code sections require ultrasonic testing [35]. The FMC requirements are applicable to any data reconstruction technique that uses FMC data, including TFM, provided the requirements can be met.

### 11.4.1 General Requirements

#### 10.4.1.1 Procedures

A procedure is defined in the ASME BPVC as “an orderly sequence of actions” detailing how the examination will be performed. In the case of FMC, the requirements to order into a sequence of actions can be found in ASME BPVC Section V. The requirements are broken into essential and non-essential variables which need to be addressed in the procedure, typically as a single value or a range of values.

**Table 10-13: Example of Essential and Non-essential variables**

Requirement	Essential Variable	Nonessential variable
Probe	X	-
Instrument	X	-
Exam Surface	X	-
Couplant	-	X

Courtesy of Mistras Group

Once complete, an FMC procedure needs to be qualified before use on production welds. Changes to any essential variable after a procedure has been qualified requires requalification. One possible exception to this for FMC is software revisions used by the instrument of choice. Software revisions are often updated adding new features and improving software performance. In this case it is advisable to review new software revisions. For example, revisions could be reviewed with existing data sets acquired during qualification and/or limited qualification sample(s) to assure the code requirements are met.

## 10.4.2 Equipment

### 10.4.2.1 Instruments

The instruments capable of performing FMC/TFM and other imaging processes are high performance specialized instruments with specific hardware and software needs. Real-time TFM requires fast processing capability and sufficient memory capacity to handle the large amount of data from the FMC acquisition. Alternatives to traditional FMC/TFM such as sparse array, Plane Wave Imaging (PWI) and others may be less demanding on the instrument memory and processing speed since they take advantage of less iterative acquisition routines and processes.

Instrument requirements are often reflected in the codes and standards addressing FMC/TFM, such as instrument bandwidth, A-scan sampling rate, and spatial resolution.

### 10.4.2.2 Probes

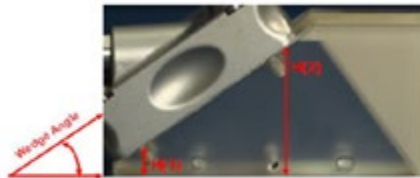
The probes used for FMC weld inspection are the same as those used for beam forming Phased Array. Probes are purpose built (contact or immersion) with a large selection of probe choices being widely available. The most popular probes used with FMC on weld applications are 1 or 2-D linear and dual linear or matrix probes.

Due to the nature of the FMC data collection and image reconstruction, such as TFM, it is essential the phased array probe be in good working order. This means checking the working condition of the individual elements in the array before use. ASME BPVC Section V includes a process any operator can easily implement for search unit element checks. This check is also included as an automated software tool in some instruments.

### 10.4.2.3 Wedges

The contact wedges used for FMC are the same as used for beam forming Phased Array and have the same considerations. Unique to the ASME FMC rules, flat wedges can be used in place of curved wedges for calibration, within certain guidelines. However, the correct curved wedge must be used during the examination. In all cases the focus of the operator should be on assuring very accurate wedge parameters including procedures to account for wedge wear, (i.e., changes to wedge delay and wedge cut angle). Some instruments may include a wedge tool to perform acoustic measurements. For instruments that don't, measurements can be made manually. Flexible (membrane) wedges can be used for specific weld inspections.

Figure 10-66: Wedge Measurements



$$\sin(\text{Wedge Angle}) = \frac{(H2-H1)}{(\text{Total Elements} - 1) \times (\text{Element Pitch})}$$

Image Courtesy of Evident Scientific, Inc.

## 10.4.3 Getting Started

Most ultrasonic examinations, regardless of the technique, begin with selecting the equipment based on application variables. Weld geometry, thickness, diameter, material, access and more all play into the choices made in selecting equipment and technical approach. One size does not fit all, and a considerable difference in approach and equipment is typical from weld to weld.

Figure 10-67: Considering variables

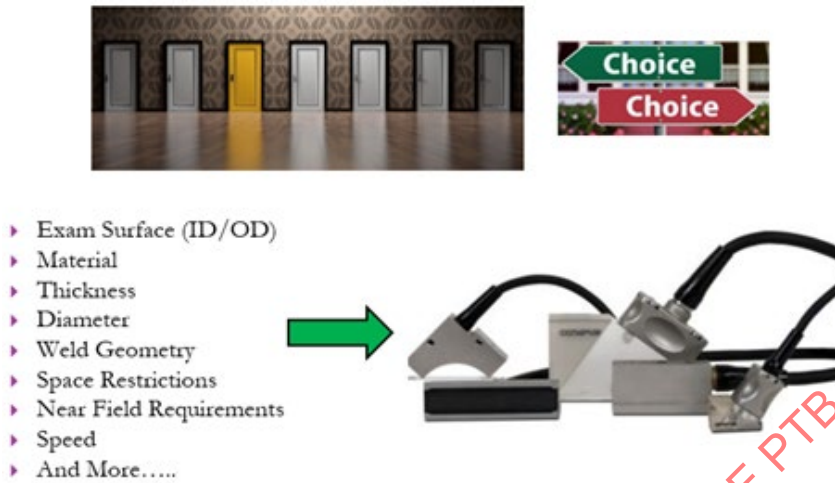


Image Courtesy of Mistras Group

#### 10.4.4 Scan Plan

The best way to consider all the application variables in aggregate is during the creation of a scan plan. While FMC is less mature than traditional phased array, robust tools are available to the operator when creating a scan plan, specifically acoustic modeling. While ray tracing is not applicable to FMC/TFM, in practice, designing a scan plan with acoustic modeling proceeds much the same way for the operator. Once the part information is entered, probes/wedges and image paths can be input and the resulting simulation informs probe positions and coverage approximations just like ray tracing, but also adds field intensity, much like a heat map through use of color coding. This means the variables can be modeled truer to the examination with respect to expected reflector responses. This makes acoustic modeling a powerful tool for designing FMC/TFM scan plans.

Figure 10-68: Example of acoustic simulation for FMC/TFM scan planning. Image clearly shows the probe needs to be moved forward to achieve coverage of the weld root/I.D. HAZ, and in this way acoustic simulation proceeds much like the use of Ray Tracing.

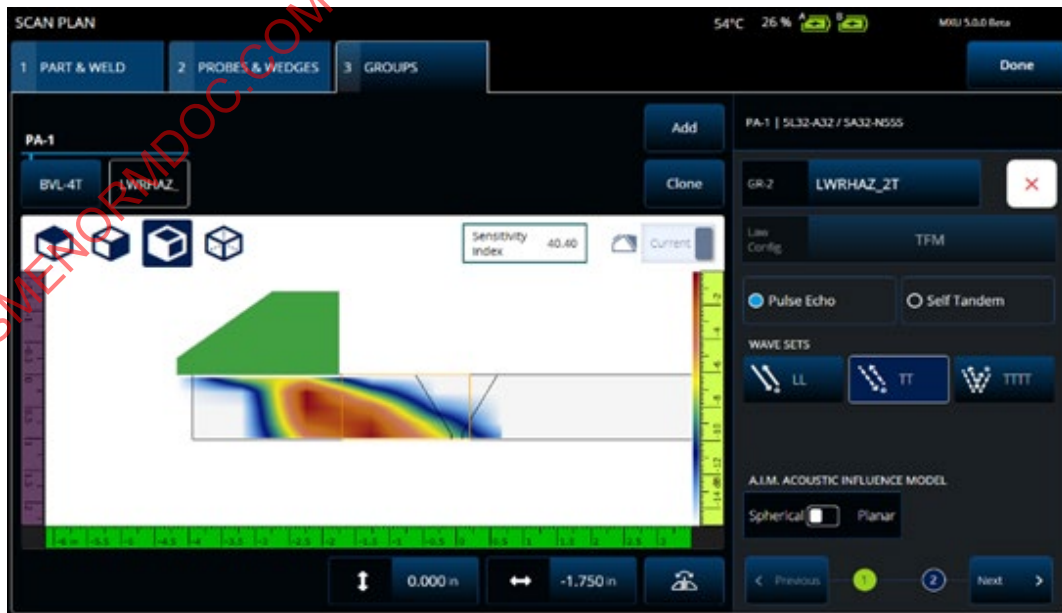


Image Courtesy of Mistras Group



#### 10.4.4.1 Search units

When modeling a search unit for weld examinations absolute performance is the most important measure, however when it comes to weld applications there are other considerations specific to FMC/TFM as well.

The maximum angular range of useful ultrasound, off axis to the probe, is a function of the single element beam spread. Additionally, focus can only be achieved within the nearfield of the probe, which is a function of the aperture, including effective aperture when off axis, probe frequency and velocity of the material. One might conclude from this that the best approach would simply be to use the largest probe with the smallest elements your instrument can handle. Not a bad starting point for FMC. However, the real world is always a balance of variables.

For example, FMC by nature is iteration and process intensive. For a 64 element x .5mm pitch probe the FMC process results in 64 pulse sequences and 4,096 elementary A-scans. There is an amount of time associated to perform that many steps. Compound this with multiple probes, several image paths, and the inherent ultrasonic time in the part and the acquisition speed can suffer quickly. However, a 32-element x 1mm pitch probe would reduce the FMC iterations substantially while providing the same aperture at a much-increased speed. Ultimately, the 64-element probe may well be the correct probe for the application, however, the operator should always consider all the variables during the scan planning process.

#### 10.4.4.2 Image Paths

As discussed in prior chapters, the image path selection informs the time of flight calculations used for TFM image reconstruction. This is important for weld examination, as in any application, because the image path(s) selected will weigh heavily on the results of the examination. FMC/TFM is still bound to the physics of ultrasound. What a particular image path can produce with respect to the expected flaws type, location, orientation, and of course probe position, relative to any flaw is paramount for the operator to understand. As shown in Figure 10-69, direct image paths alone would not be sufficient to cover most weld applications properly, a fact reflected in ASME BPVC Section V. Additionally, because the time of flight is a calculation, significant errors are seen when any of the time-of-flight variables are incorrect, such as velocity, wedge parameters, material thickness, and component curvature as can be seen on Figure 10-70 and Figure 10-71. Therefore, ensuring correct parameters is also critical.

**Figure 10-69: LOF and the response from differing image paths. From Left to right 2T Direct, 4T indirect, and Time Extended 2T**

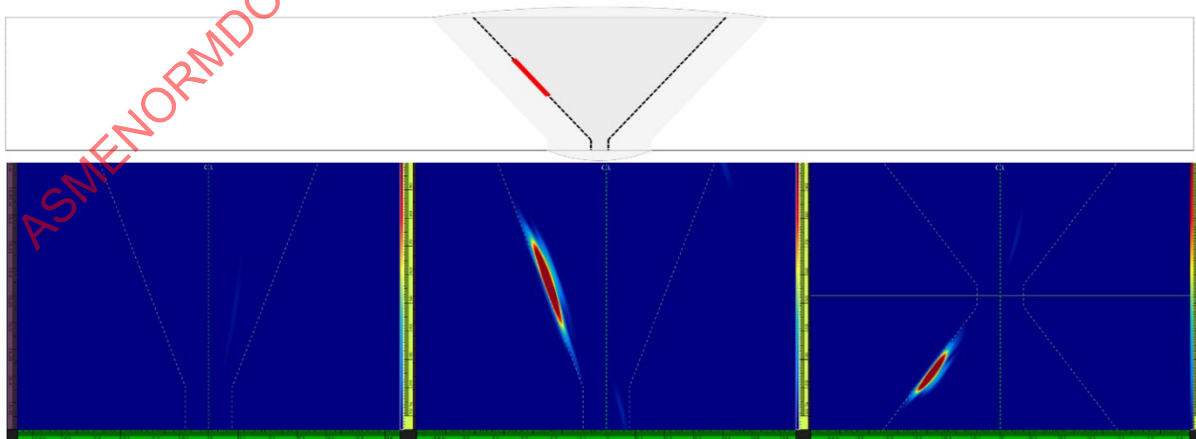
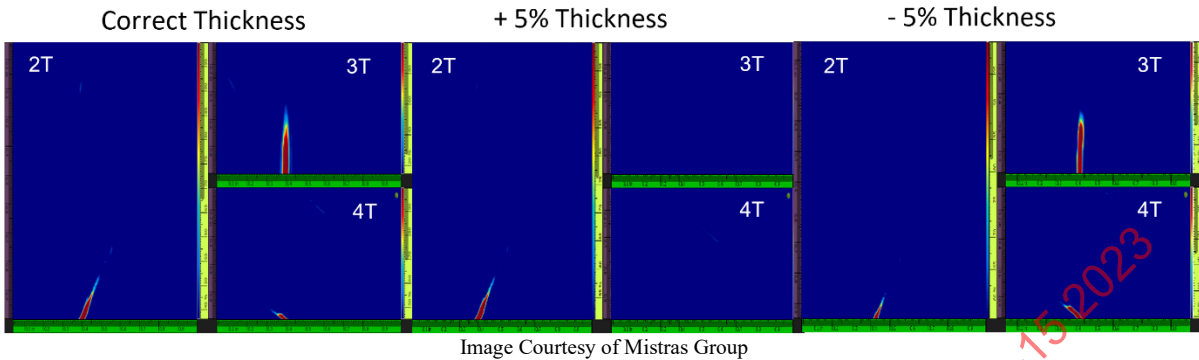
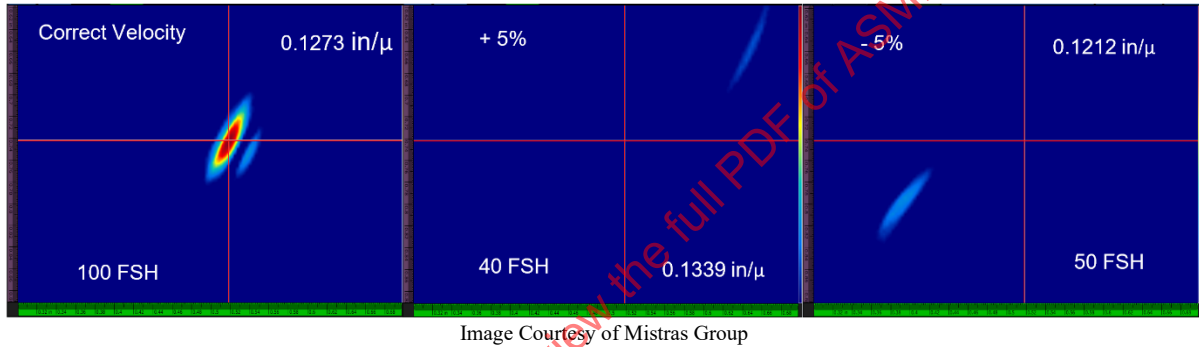


Image Courtesy of Mistras Group

**Figure 10-70: Example of the Influence an incorrect thickness parameter has on the signal response of an I.D notch**



**Figure 10-71: Example of the influence an incorrect velocity parameter has on signal response. 5Mhz, n=64, P=0.6mm, T-T direct,  $\lambda/7$ , SDH @ 0.8 in. deep**



### 10.4.5 Equipment Set-Up

There are several FMC/TFM capable instruments in the marketplace currently, and each has its own user interface and set-up procedure. However, there are a few topics in this area common to all worth discussion.

#### 10.4.5.1 Image Grid Density

For processed images such as TFM, the image grid density or resolution defines how many reconstruction points will be used to produce the image. This image frame parameter directly affects the amplitude precision represented in the processed image. To correctly represent the original amplitude, the image must be as accurate as possible to the original analog signal. This is known as amplitude fidelity. The ASME BPVC Section V requirement for amplitude fidelity is 2dB. All this might lead the operator to simply set the highest grid density possible, and for many applications this may be the correct approach. However, a balanced approach based on the application and expected flaws should be considered. As shown in Table 10-14 and Figure 10-72, increasing resolution has a cost in speed, and beyond a certain point there may be diminishing returns for the application.

**Table 10-14: General example of scan speed vs grid density for standard TFM. 5Mhz x 32-element probe. Changes to parameters such as PRF, algorithms and many others will affect results.**

Frame Size & Image path	Resolution (Pts/ $\lambda$ )	Scan Speed
0.500 in. $\downarrow$ by 1.500 in. $\leftrightarrow$ T-T Image path (*0.750 in <sup>2</sup> of coverage)	0.0051 in. (5.0)	2.36 in/sec.
	0.0031 in. (8.1)	1.83 in/sec.
0.500 in. $\downarrow$ by 1.500 in. $\leftrightarrow$ T-T & TT-TT Image path (*1.500 in <sup>2</sup> of coverage)	0.0051 in. (5.0)	2.00 in/sec.
	0.0031 in. (8.1)	0.98 in/sec.
1.000 in. $\downarrow$ by 2.000 in. $\leftrightarrow$ T-T Image path (*2.000 in <sup>2</sup> of coverage)	0.0051 in. (5.0)	1.81 in/sec.
	0.0031 in. (8.1)	0.80 in/sec.
1.000 in. $\downarrow$ by 2.000 in. $\leftrightarrow$ T-T & TT-TT Image path (*4.000 in <sup>2</sup> of coverage)	0.0051 in. (5.0)	0.97 in/sec.
	0.0031 in. (8.1)	0.41 in/sec.

Courtesy of Mistras Group

**Figure 10-72: A clear change is seen from  $\lambda/2$  to  $\lambda/5$ , but less from  $\lambda/5$  to  $\lambda/7$ . 1/64th SDH, 5Mhz, n=64, p=0.6 mm, L-L image path, Envelope on, 1.57 in. index x 2.26 in. depth TFM frame**

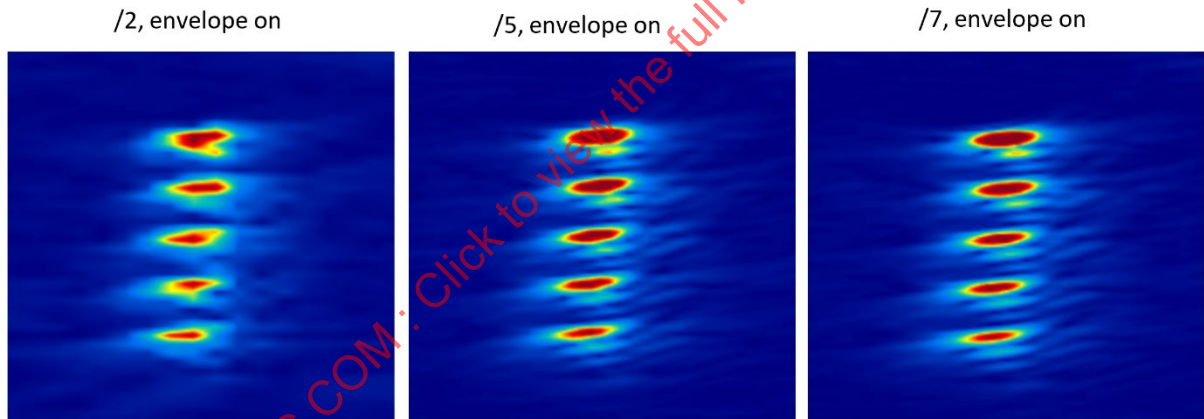


Image Courtesy of Mistras Group

#### 10.4.5.2 TFM Frame Size

Another consideration is the frame size that is used. While covering the area of interest with the image frame is required, beyond this, benefits diminish. As seen in Table 10-14, this has a direct relationship with scan speed. Larger than necessary frame sizes can also reduce the ability to see detail in the image, especially using smaller portable screens, and increase file size.

#### 10.4.5.3 Grouping

Examination coverage is most commonly achieved with two probes, one on each side of the weld. While this can be performed separately, performing the exam from both sides simultaneously decreases the inspection time, assures synced encoding between the two sides, and allows for easier understanding of flaw response from both sides without having to switch between or merge files.

There are other reasons for grouping unique to FMC/TFM. As discussed before, each image path is specific. Weld coverage will usually require multiple image paths. POD, imaging, and sizing will all be enhanced by using multiple image paths. Additionally, multiple image paths will be needed to satisfy the ASME BPVC Section V requirements of resolution verification and path verification. In short, no single image path can satisfy the requirements as shown in Figure 10-73.

**Figure 10-73: Image path verification on through wall slot in the ASME BPVC Section V calibration block. Satisfying the ASME requirements may require multiple image paths.**

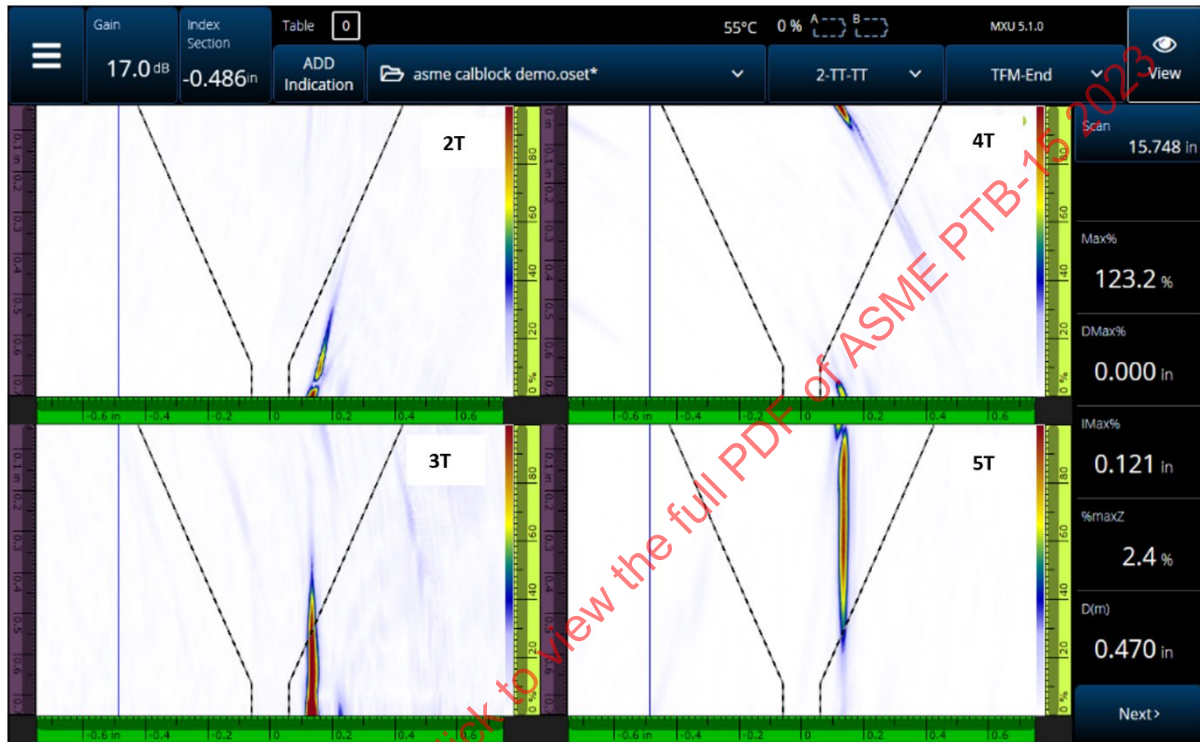
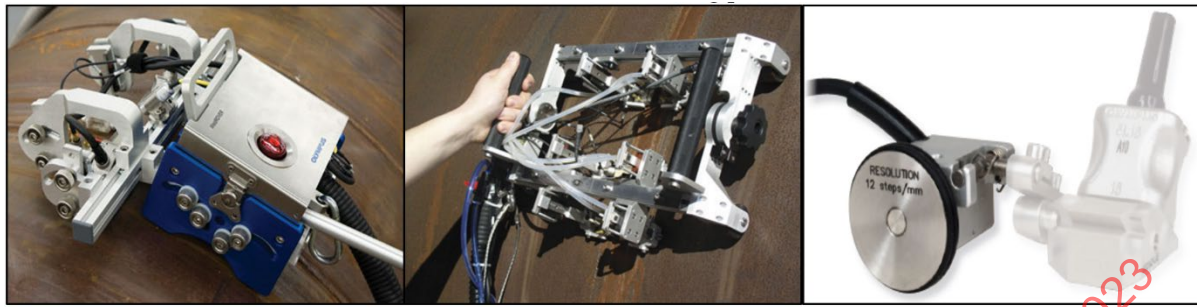


Image Courtesy of Mistras Group

#### 10.4.6 Scanning/Data Collection

Scanning with FMC/TFM (and associated techniques) is performed in an identical manner to that used with conventional Phased Array. The two primary methods are manual scanning and encoded scanning. ASME BPVC Section V requires the use of linear scanning techniques using Semi-Automated (SAUT) or Fully Automated (AUT) scanners for FMC weld examinations. The qualified image path configurations developed in the scan plan and used for calibration must be used for scanning. Linear scanning requires that the search unit be held at a fixed stand-off distance from the weld axis. Therefore, a means to maintain this distance is important, usually by a fixed guide or mechanical means. Figure 10-74 shows examples of encoded scanning and data collection techniques.

- Fully automated scanning (AUT)—A technique employing a 1 or more axis robotic scanner. The search unit(s) are held in a mechanical fixture onboard the scanner, the scanner is connected to a motion control device, engaging the motors that drive the scanner down the weld axis via computer control. An integrated encoder provides the means to record the ultrasonic data and scanning position.
- Semi-Automated scanning (SAUT)—A technique employing one or more axis scanners. The search unit(s) are held in a mechanical fixture onboard the scanner, and the scanner is manually manipulated down the length of the weld or inspection area. An integrated encoder records the ultrasonic data and scanning position.

**Figure 10-74: Examples of encoded scanning and data collection techniques**

Fully automated scanner

Semi-automated scanner

Probe with simple encoder

Image Courtesy of Evident Scientific, Inc.

Manual scanning techniques are typically used for proof-up of indications, verification of sizing, probe skewing techniques for signal characterization, looking for transverse indications, or non-new weld quality applications. With phased array, for example, often a simple A-scan and S-scan setup is used for this. An FMC/TFM correlation might be an A-scan and End View setup. Because ASME BPVC Section V requires SAUT or AUT for FMC, manual scanning is not allowed for data collection, but may be used as a follow up, provided the process was qualified in the procedure.

- Encoded Manual Scanning (EMUT)–The probe is handheld and manually moved along the scan axis. A wheel or string-type encoder is typical and is used to record the ultrasonic data and scanning position. A fixed guide may be included or used separately to maintain search unit position in relation to the scan axis. Typically used with 1 axis scanning but may be used with 2 axes by means of a mechanical or software indexer.
- Manual Scanning (MUT)–The probe is handheld and manually moved along the scan axis. No recording of data is performed.

#### 10.4.6.1 Encoding

When scanning a weld, it is important to maintain the encoding accuracy over the distance traveled. ASME BPVC Section V requires encoder calibration to be performed over a minimum of 20 in. (508 mm), with an accuracy of 1% of the actual distance traveled. That would equate to a +/- 0.2 in. (5 mm) tolerance. However, for very long scans greater accuracy may be required. Greater accuracy can be achieved by calibrating the encoder over longer distances.

Data quality must also be maintained. Scanning speed cannot exceed the instrument's acquisition rate or data drop out will occur. The ASME BPVC Section V requires that scan speed be such that data drop-out is less than 2 data lines/in. (25 mm) of the linear scan length, with no adjacent lines of data loss being present. An example of data drop-out is shown in Figure 10-75.

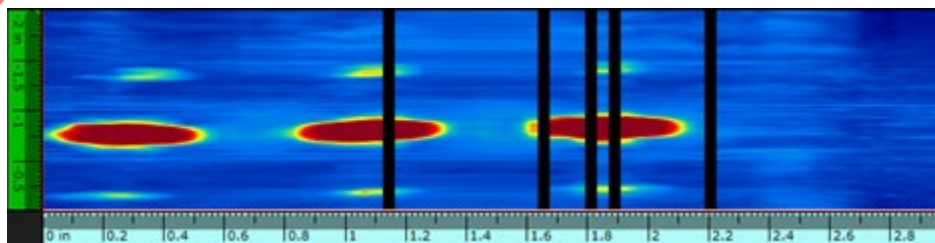
**Figure 10-75: Example of data drop-out**

Image Courtesy of Mistras Group